به نام خدا
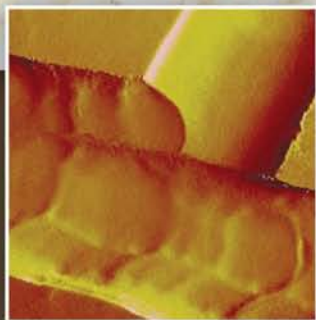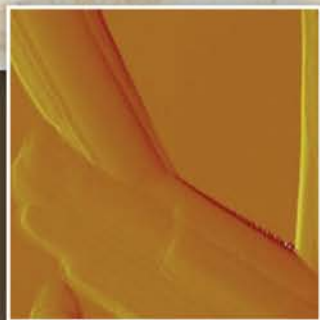
مرکز دانلود رایگان
مهندسی متالورژی و مواد

www.Iran-mavad.com

Electrochemistry of Porous Materials

Antonio Doménech-Carbó

CRC Press
Taylor & Francis Group

Electrochemistry of Porous Materials

Electrochemistry of Porous Materials

Antonio Doménech-Carbó

مرجع دانشجویان و مهندسین مواد

www.iran–mavad.com

مرجع دانشجویان و مهندسین مواد

Dedication

Als meus pares, in memoriam

Contents

Contents

Foreword

It is a remarkable feature of modern electrochemistry that research is directed on one side to a deeper understanding of the very fundamentals, of the elementary steps of charge transfer *at* interfaces and charge propagation *in* phases—that is, the most simple electrochemical systems—and on the other side, that more and more complex systems are experimentally investigated; for example, multi-phase systems in which sometimes several electrochemically active centers are present, in which charge propagation may proceed on complex pathways, where electrocatalysis may be involved and where electrochemically initiated chemical conversions may take place. These complex systems are not only of applied significance—for example, in batteries and fuel cells—but they also prompt new developments of the understanding of fundamental processes. Now the time is ripe for such complicated systems to be studied with all the modern techniques, of course including the most advanced spectroscopic and microscopic methods.

The author of this book has attempted to survey a specific but large area of modern electrochemical research, the electrochemistry of porous materials, and he was well prepared for this undertaking, as he has published extensively about such systems. Porous materials are very complex with respect to possible electrochemical reactions: The author covers materials with nanopores up to micropores, and he treats all these materials under the aspect of insertion electrochemistry, as electron and ion transfer processes are proceeding together. The range of different compounds and materials is impressive, and it is very rewarding for the reader to see a presentation of such great variety in one volume. This is a unique book in which for the first time a comprehensive treatment of the electrochemical features of porous materials is given. Because of the great technological importance of these materials, the book will be welcomed by the electrochemical community, and I am confident that the book will give an impetus to the theoreticians who may see in one glance what interesting and tempting systems the experimentalists have already studied and what tempting theoretical questions derive from these investigations.

Fritz Scholz
University of Greifswald, Germany

Preface

In the past decades, research on porous materials has increased considerably because of their wide-ranging applications (e.g., sensing, gas storage, catalysis, energy transformation and storage, among others). The term *porous materials* applies to a wide variety of substances, from clay minerals and silicates to metal oxides, metal-organic frameworks, or even thin films and membranes. Porous metals and carbons can also be included under such systems.

Electrochemistry plays an important role in both research and applications of porous materials via electroanalysis, electrosynthesis, sensing, fuel cells, capacitors, electro-optical devices, etc.

The purpose of this text is to provide an approach to the electrochemistry of porous materials that combines the presentation of a generalized theoretical modeling with a description of redox processes for different porous materials and a view of their electrochemical applications.

Because of the considerable variety of materials that can be classified as porous, the discussion will be limited to several groups: porous silicates and aluminosilicates, porous metal oxides and related compounds, porous polyoxometalates, metal-organic frameworks, porous carbons, carbon nanotubes, and several hybrid materials. All these materials can be viewed as relatively homogeneous from the electrochemical point of view. Metal and metal oxide nanoparticles, "organic metals," fullerenes, and dendrimers, which can also be regarded as nanostructured materials, also displaying distinctive electrochemical features, will not be treated here for reasons of brevity, although their appearance in hybrid materials as modifiers for microporous materials will be discussed.

This book is devoted to conjointly present the advances in electrochemistry of nanostructured materials. More specifically, the text presents the foundations and applications of the electrochemistry of microporous materials with incorporation of recent developments in applied fields (fuel cells, supercapacitors, etc.) and fundamental research (fractal scaling, photoelectrocatalysis, magnetoelectrochemistry, etc.). The book attempts to make electrochemistry accessible to researchers and graduate students working on chemistry of materials but also strives to approximate porous materials chemistry to electrochemists. To provide a reasonable volume of literature, citations are limited to fundamental articles. Whenever possible, textbooks and review articles have been cited or, alternatively, recent articles covering wide citations of previous literature have been used in order to facilitate access to a more extensive literature for readers who are interested in monographic topics.

The book includes part of research performed in collaboration with Elisa Llopis, María José Sabater, Mercedes Alvaro, Pilar Navarro, María Teresa Doménech, Antonio Cervilla, Javier Alarcón, Avelino Corma, and Hermenegildo García, as well

Author

Antonio Doménech holds a Ph.D. in chemistry (University of Valencia, 1989) and is currently professor in the Department of Analytical Chemistry, University of Valencia, Spain. His research is focused on supramolecular electrochemistry, electrochemistry of porous nanostructured materials, and electroanalytical methods applied to conservation and restoration of cultural heritage, as well as on educational problems in teaching of science. He has published more than 150 articles in scientific journals and several monographs, among them *Supramolecular Chemistry of Anions* and *Electrochemical Methods in Archeometry, Conservation and Restoration*. Dr. Doménech received the "Demetrio Ribes" award for original research (Valencian Regional Government) in 2006.

List of Acronyms

AFC: alkaline fuel cell
AFM: atomic force microscopy
ATR-FTIR: attenuated total reflectance–Fourier transform infrared spectroscopy
BET: Brunauer-Emmett-Teller surface area measurement
CA: chronoamperometry
CFC: chlorofluorocarbon compound
CNR: carbon nanoribbon
CNTs: carbon nanotubes
CPE: constant phase element
CV: cyclic voltammetry
DMFC: direct methanol fuel cell
EAFM: electrochemical atomic force microscopy
EIS: electrochemical impedance spectroscopy
EQCM: electrochemical quartz crystal microbalance
FC: fluorocarbon compound
FIA: flux injection analysis
FTIR: Fourier transform infrared spectroscopy
GCE: glassy carbon electrode
HCFC: hydrochlorofluorocarbon compound
HFC: hydrofluorocarbon compound
HPLC: high-performance liquid chromatography
HRTEM: high-resolution transmission electron microscopy
IES: ion-selective electrode
ITO: indium-doped tin oxide
LDH: layered double hydroxide
LSV: linear potential scan voltammetry
MeCN: acetonitrile
MCFC: molten carbonate fuel cell
MOFs: metal-organic frameworks
MWNTs: multiwall carbon nanotubes
OMCs: ordered mesoporous carbons
OMS: octahedral molecular sieves
PAFC: phosphoric acid fuel cell
PANI: polyaniline
PEFC: polymer electrolyte fuel cell
PFE: polymer film electrode
PIGE: paraffin-impregnated graphite electrode
POM: polyoxometalate
PPY: polypyrrole
PT: polythiophene
SCE: saturated calomel electrode

SECM: scanning electrochemical microscopy
SOFC: solid oxide fuel cell
SWCNTs: single-wall carbon nanotubes
SQWV: square-wave voltammetry
TEM: transmission electron microscopy
XRD: x-ray diffraction
YSZ: yttria-stabilized zirconia oxide

1 Porous Materials and Electrochemistry

1.1 POROUS MATERIALS, CONCEPT, AND CLASSIFICATIONS

Porous materials have attracted considerable attention since the 1960s because of their wide variety of scientific and technological applications. In its most generalized definition, the term *pore* means a limited space or cavity in a (at least apparently) continuous material. Porous materials comprise from inorganic compounds such as aluminosilicates to biological membranes and tissues. According to the International Union of Pure and Applied Chemistry, pores are classified into three categories: micropores (less than 2 nm), mesopores (between 2 and 50 nm), and macropores (larger than 50 nm).

Porous materials discussed at the International Conference on Materials for Advanced Technologies 2005 included clay minerals, silicates, aluminosilicates, organosilicas, metals, silicon, metal oxides, carbons and carbon nanotubes, polymers and coordination polymers, or metal-organic frameworks (MOFs), metal and metal oxide nanoparticles, thin films, membranes, and monoliths (Zhao, 2006).

Fundamental and applied research dealing with novel porous materials is addressed to improve template-synthesis strategies, chemical modification of porous materials via molecular chemistry, construction of nanostructures of metals and metal oxides with controlled interior nanospace, reticular design of MOFs with pore sizes ranging from the micropore to the mesopore scales, among others. Porous materials are useful for sensing, catalysis, shape- and size-selective absorption and adsorption of reagents, gas storage, electrode materials, etc. (Eftekhari, 2008).

Because of the considerable variety of materials that can be classified as porous, several classifications can be proposed. Thus, according to the distribution of pores within the material, we can distinguish between regular and irregular porous materials, whereas, according to the size distribution of pores, one can separate between uniformly sized and nonuniformly sized porous materials.

From a structural point of view, porous materials can be viewed as the result of building blocks following an order of construction that can extend from the centimeter to the nanometer levels. Porous materials can range from highly ordered crystalline materials such as aluminosilicates or MOFs, to amorphous sol-gel compounds, polymers, and fibers. This text will focus on materials that have porous structures, so that ion-insertion solids having no micro- or mesoporous structures, such as the metal polycyanometalates, whose electrochemistry was reviewed by Scholz et al. (2005), will not be treated here. To present a systematic approach

TABLE 1.1
Typical Values for Specific Surface Area
of Selected Porous Materials

Material	Specific Surface Area (m²/g)
Zeolite X	700
SBA-15	650
MCM-41	850
Activated carbon	2000
Nanocubes MOF-5	3500

from the electrochemical point of view, in this text, porous materials will be divided into:

- Porous silicates and aluminosilicates
- Porous metal oxides and related compounds (including pillared oxides, laminar hydroxides, and polyoxometalates)
- MOFs
- Porous carbons, nanotubes, and fullerenes
- Porous organic polymers and hybrid materials

Although it does not exhaust the entire range of porous materials, the list attempts to cover those that can be described in terms of extended porous structures and whose electrochemistry has been extensively studied. In addition, since 1990 there has been a growing interest in the preparation of nanostructures of metal and metal oxides with controlled interior nanospace, whereas a variety of nanoscopic porogens such as dendrimers, cross-linked and core-corona nanoparticles, hybrid copolymers, and cage supramolecules are currently under intensive research (Zhao, 2006). Several of such nanostructured systems will be treated along the text, although, for reasons of extension, the study *in extenso* of their electrochemistry should be treated elsewhere.

The most relevant characteristic of porous materials is the disposal of a high effective surface/volume relationship, usually expressed in terms of their specific surface area (area per mass unit), which can be determined from nitrogen adsorption/desorption data. Different methods are available for determining the specific surface area (Brunauer-Emmett-Teller, Langmuir, and Kaganer), micropore volume (*t*-plot, α_s, and Dubinin-Astakhov), and mesopore diameter (Barrett-Joyner-Halenda; Leroux et al., 2006). Table 1.1 summarizes the values of specific surface area for selected porous materials.

1.2 MIXED POROUS MATERIALS

Porous materials chemistry involves a variety of systems, which will generically be termed here as *mixed systems*, resulting from the combination of different structural moieties, resulting in significant modifications of the properties of the

pristine porous materials. In this group, we can include quite different materials, namely:

- Composites, formed by addition of a binder to porous materials and eventually other components forming mixtures for definite applications. This type of system is frequently used for preparing composite electrodes.
- Functionalized materials, prepared by attachment of functional groups to a porous matrix.
- Materials with encapsulated species, where molecular guests are entrapped in cavities of the porous host material.
- Doped materials, where a structural component of the material becomes partially substituted by a dopant species or when external species ingress in the original material as an interstitial ion. The term *doping* is thus applied to, for instance, yttria-doped zirconias used for potentiometric determination of O_2 but also to describe the incorporation of Li^+ in polymers and nanostructured carbons.
- Intercalation materials, in which different nanostructured components are attached to the porous matrix. This is the case of metal and metal oxide nanoparticles generated into zeolites and mesoporous silicates or organic polymers intercalated between laminar hydroxides.

From several applications, it is convenient to describe much of the above systems as resulting from the modification of the parent porous materials by a second component. In this sense, one can separate network modification, network building, and network functionalization processes. Network modification exists when the final structure of the parent material is modified as a result of its combination with the second component, thereby resulting in the formation of a new system of links. Network building occurs when the material is formed by assembling the units of both components. Finally, functionalization involves the attachment of selected molecular groups to the host porous material without modification of its structure.

1.3   ELECTROCHEMISTRY AND POROUS MATERIALS

All the aforementioned materials, in spite of their variety of physicochemical and structural properties, can be studied via electrochemical methods and can be treated as materials for electrochemical applications. In most cases, porous materials can be synthesized, modified, or functionalized via electrochemical methods. Intersection of electrochemistry with porous materials science can be connected to:

- Electroanalytical methods for gaining compositional and structural information on porous materials
- Electrosynthetic routes for preparing or modifying porous materials
- Design and performance of electrocatalysts for synthesis and sensing
- Characterization of photochemical and magnetochemical properties
- Design and performance of electrochemical, electro-optical, etc., sensors
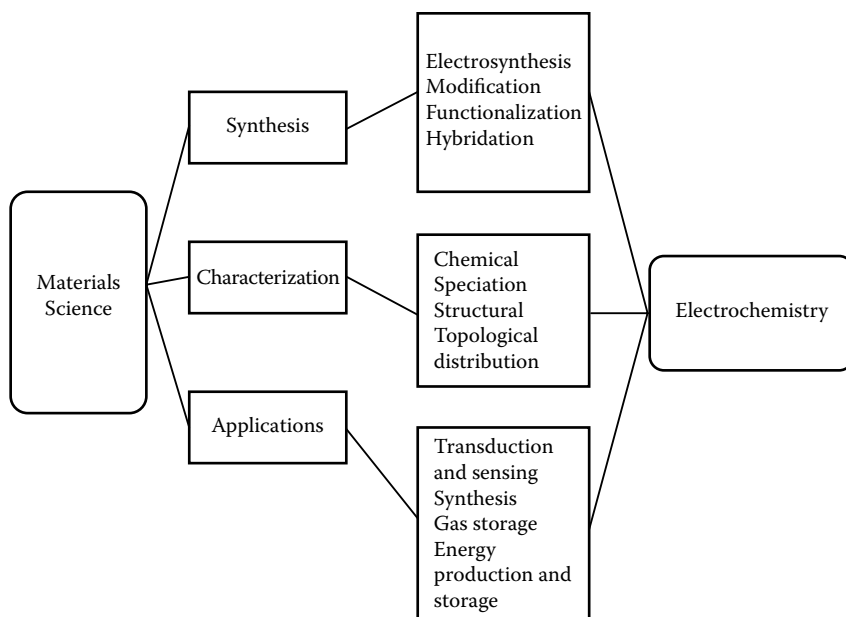
FIGURE 1.1 Schematic diagram depicting the relationships between electrochemistry and porous materials science.

- Design and performance of porous materials such as electrode materials, fuel cells, and the like
- Design and performance of capacitors, electro-optical devices, solar cells, and so forth

The relationship between electrochemical items and materials science can be grouped according to three main aspects as shown in Figure 1.1. It should be noted that electrosynthetic methods allow for preparing a variety of materials, from porous oxide layers in metal anodes, to MOFs (Mueller et al., 2006), layered double hydroxides (LDHs; Yarger et al., 2008), and porous carbons (Kavan et al., 2004). Furthermore, porous materials can be modified, functionalized, or hybridized (*vide infra*) via electrochemically assisted procedures, thus resulting in the preparation of novel materials.

Electrochemical methods can also be used for obtaining analytical information on porous materials. Voltammetric methods and related techniques have been largely used to acquire information on reaction mechanisms for species in solution phase, whereas impedance techniques have been extensively used in corrosion and metal surface studies. In the past decades, the scope of available methods has been increased by the development of the voltammetry of microparticles (Scholz et al., 1989a,b). This methodology, conceived as the recording of the voltammetric response of a solid material mechanically transferred to the surface of an inert electrode, provides information on the chemical composition, mineralogical composition, and speciation of solids (Scholz and Lange, 1992; Scholz and Meyer, 1994, 1998;

Grygar et al., 2000; Scholz et al., 2005). Recent developments in this frame comprise the determination of absolute quantitative composition of electroactive species (Doménech et al., 2004a, 2006a) and topological distribution of electroactive species attached to solid networks (Doménech et al., 2009).

Electrochemical applications of porous materials involve important issues, including transduction (electro-optical, magneto-optical devices) and sensing; gas production and storage; electrosynthesis at industrial scale; and pollutant degradation. In the analytic domain, porous materials can be used in electroanalytical techniques (potentiometry, amperometry) for determining a wide variety of analytes, from gas composition to pollutants or bioanalytes, with applications for tissue engineering, DNA sequencing, cell markers, and medical diagnosis (Zhao, 2006). Porous materials not only find application in batteries, capacitors and supercapacitors, and fuel cells but also in the preparation of high-performance dielectric materials for advanced integrated circuits in the microelectronics industry.

1.4   SYNTHESIS OF POROUS MATERIALS

Although traditional synthetic methods can be used for preparing a variety of porous materials, the development of template synthesis strategies has prompted an explosive-like growth of synthetic methods. Template synthesis roughly involves the use of a structure-directing reagent that facilitates the porous material to adopt the desired structure, followed by the template release. Three main types of templates, soft, hard, and complex, can be used (Zhao, 2006).

Soft templates, usually molecules and molecular associations such as amines, thermolabile organic polymers, and surfactants, can be removed by heat treatment. In addition, vesicles, ionic liquids, self-assembled colloidal crystals, and air bubbles have been used for soft templating synthesis.

Hard templates, whose release requires acid or basic attack such as zeolites and mesoporous silica, used as templates for porous carbon preparation (Kim et al., 2003; Yang et al., 2005), can be taken as examples.

Complex templates combine soft and hard template techniques. This methodology is used for synthesizing hierarchically bimodal and trimodal meso-macroporous materials with interconnected pore channels combining a surfactant template with a colloidal crystal template (Yuan and Su, 2004).

In parallel, sol-gel technologies have contributed to a significant growth of synthetic procedures for preparation of all types of materials (Wright and Sommerdijk, 2000).

In recent times, much attention has been paid to preparation of films of hybrid materials. Here, the composition (homogeneous, heterogeneous), structure (monolayer, multilayer), thickness, and texture (roughness) can notably influence the resulting optical and electrical properties of the system. Layer-by-layer (LbL) preparation involves the sequential deposition of oppositely charged building blocks modulated by their interaction with counterions.

A plethora of synthetic routes, however, is currently being developed. These include Ostwald ripening to build hollow anatase spheres and Au-TiO$_2$ nanocomposites (Li and Zeng, 2006), laser ablation (Tsuji et al., 2007), spray pyrolysis (Taniguchi and Bakenov, 2005), among others.

Interestingly, porous materials can act as templates for synthesizing other porous materials, as, for example, the application of MOFs (Liu et al., 2008) and organo-modified LDHs (Leroux et al., 2006) for porous carbon synthesis.

Techniques for thin-film deposition include vacuum thermal evaporation (Morales-Saavedra et al., 2007) and organized assembly.

In addition, electrosynthetic methods can be applied in preparing or modifying porous materials. Within an extensive list of procedures, one can mention the following:

- Preparation of porous oxide films by anodization of metal electrodes
- Electrosynthesis of metal-MOFs (Mueller et al., 2006)
- Electrosynthesis of porous carbons and nanotubes
- Electropolymerization forming porous polymers

Electrochemical modification of porous materials involves:

- Electrochemical doping via ion insertion in materials for lithium batteries
- Electropolymerization of polymers attached to porous substrates
- Nanoparticle electrogeneration and attachment to porous materials (Bessel and Rolison, 1997a)

1.5 MATERIAL-MODIFIED ELECTRODES

Roughly, electrochemical methods consist of recording the signal response of an electrode, which is immersed into an electrolyte solution, under the application of an electrical excitation signal. The potential of this electrode, the working electrode, is controlled with respect a reference electrode also immersed in the electrolyte. In solution electrochemistry, electroactive species are located in the liquid electrolyte, although eventually, formation of gas and/or solid phases can occur during electrochemical experiments. In solid state electrochemistry, the interest is focused on solid materials deposited on (or forming) the electrode, in contact with a liquid or, eventually, solid electrolyte.

A significant part of solid state electrochemistry is concentrated in the attachment of solid materials to the surface of a basal, inert electrode. This process will, in the following, be termed *electrode modification*.

The following methods have been proposed for electrode modification with porous materials.

- Direct deposition from suspensions. In this procedure, a drop of a suspension of the solid in a volatile liquid is placed on the surface of the basal electrode, allowing the solvent to evaporate (Li and Anson, 1985).
- Fixation/coverage into a polymer coating. Preparing a suspension of the solid in a solution of the polymer in a volatile solvent and allowing the solvent to evaporate (Ghosh et al., 1984). As a result, a coating of the solid particles embedded into the polymer coating is deposited onto a basal electrode. Alternatively, a microparticulate deposit obtained from evaporation of a suspension of the studied solid in a volatile solvent is covered by a polymer solution, followed by evaporation of the solvent (Calzaferri et al., 1995).

- Attachment to carbon paste electrodes and formation of material/carbon/polymer composites. Here, the powdered material is mixed with a paste formed with graphite powder and a binder. This is usually a nonconducting, electrochemically silent, and viscous liquid (nujol oil, paraffin oil), but electrolyte binders such as aqueous H_2SO_4 solutions have also been used (Adams, 1958; Kuwana and French, 1964; Schultz and Kuwana, 1965). Rigid electrodes can be prepared from mixtures of the material, graphite powder, a monomer, and a cross-linking agent, followed by radical-initiated copolymerization (Shaw and Kreasy, 1988).

- Formation of material/conductive powder mixtures (or pressed graphite-material pellets). This method involves powdering and mixing with graphite powder and pressing the powder mixture into electrode grids, as commonly done in the battery industry. The pressed mixture can be attached to a graphite electrode and immersed into a suitable electrolyte or, eventually, dry films of pressed pellets can be placed between planar electrodes (Johansson et al., 1977; Damertzis and Evmiridis, 1986).

- Coelectrodeposition with conducting polymers from a material-monomer slurry submitted to electropolymerization conditions. Thus, Rolison (1990) prepared uniform particle-polymer coatings from a drop of zeolite suspension in a pyrrole solution in $Et_4NClO_4/MeCN$ (see also Bessel and Rolison, 1997a).

- Mechanical transference. According to Scholz et al. (1989a,b), this method is based on the transference by abrasion of a few micrograms (or nanograms, if necessary) of solid particles of the sample to the surface of an inert electrode, typically paraffin-impregnated graphite electrodes (PIGEs).

- Adsorptive and covalent link to electrode surfaces. Particles of porous materials can be adsorptively or covalently bound to electrode surfaces via intermediate groups able to connect the basal conducting electrode and the porous particles. The use of silanes enables covalent binding, as originally described by Li et al. (1989) for the covalent attachment of bifunctional silane to a single dense layer of zeolite Y to an SnO_2 electrode. Adsorption can be facilitated by pendant groups, typically thiols with high affinity to gold surfaces. The use of thiol-alkoxysilanes has been applied to attach aluminosilicate materials to gold electrodes, here combining the thiol affinity for gold with the easy functionalization of aluminosilicates with alkoxysilanes (Yan and Bein, 1992).

- Layer and multilayer preparation methods. Under this designation, a variety of methods recently developed for preparing material-modified electrodes can be included: spin coating and formation of Langmuir-Blodgett films are accompanied by continuous film synthesis on electrodes (Kornik and Baker, 2002), self-assembled monolayer formation (Jiang et al., 2006), LbL deposition (Zhang et al., 2003), electrophoretic deposition (Zhang and Yang, 2007), and hydrothermal crystallization on conductive substrates (Kornik and Baker, 2002). The last method involves previous treatment of the basal electrode; for instance, zeolite-modified electrodes on glassy carbon electrode previously treated with a polycationic macromolecule to ensure

durable binding of the negatively charged zeolite seeds (Walcarius et al., 2004). Other methods involve silanization, charge modification, and seeding of the surface before hydrothermal crystallization of the porous material (Mintova et al., 1997). Among others, LbL assembly by ionic linkages mediated by multilayers of oppositely charged electrolytes has also been reported (Lee et al., 2001).

1.6   ELECTRODE-MODIFIED MATERIALS

Porous materials can be electrochemically synthesized and/or electrochemically modified by using electrolysis methodologies. Apart from synthesis of, for instance, MOFs (Mueller et al., 2006) or fullerenes (Kavan and Hlavaty, 1999), porous materials can be electrochemically modified in several ways.

One of the most intensively investigated possibilities results in the attachment of nanometric units to porous, electrochemically silent frameworks. This is the case of metal and metal oxide nanoparticles anchored to micro- and mesoporous aluminosilicates prepared by electrolyzing dispersions of, for instance, Pd(II)- and/or Cu(II)-exchanged zeolites in appropriate electrolytes. Application of reductive potentials leads to the formation of metal and/or metal oxide nanoparticles in the zeolite framework. With appropriate control of the synthetic conditions, metal nanoparticles can be predominantly confined to particular sites (e.g., supercages in zeolites) in the porous framework (Rolison, 1990; Rolison and Bessel, 2000). Zeolite-supported Pt or RuO_2 nanoparticles act as electron transfer mediators rather than as the controlling heterogeneous electron transfer surface and improve faradaic efficiency in electrolytic processes even in low-ionic-strength solutions (Bessel and Rolison, 1997a).

Metal nanoparticles housed in zeolites and aluminosilicates can be regarded as arrays of microelectrodes placed in a solid electrolyte having shape and size selectivity. Remarkably, the chemical and electrochemical reactivity of metal nanoparticles differ from those displayed by bulk metals and are modulated by the high ionic strength environment and shape and size restrictions imposed by the host framework. In the other extreme end of the existing possibilities, polymeric structures can be part of the porous materials from electropolymerization procedures as is the case of polyanilines incorporated to microporous materials. The electrochemistry of these types of materials, which will be termed, *sensu lato*, *hybrid materials*, will be discussed in Chapter 8.

Another interesting and widely studied case is the formation of porous metal oxides by anodization of metals. Here, the electrolytic procedure yields a thin layer of porous materials applicable in catalysis, in anticorrosion, batteries, and other applications. Such materials will be discussed in Chapter 6.

1.7   GENERAL ELECTROCHEMICAL CONSIDERATIONS

A variety of electrochemical techniques can be applied for obtaining information on the composition and structure of microporous materials. Roughly, we can divide such techniques into two main groups: first, "traditional" electrochemical methodologies,

mainly, cyclic voltammetry (CV), chronoamperometry, chronopotentiometry, and coulometry. Second, those involving impedance measurements particularly focused in electrochemical impedance spectroscopy (EIS). This brief enumeration, however, does not exhaust the scope of available techniques, because other extended methods, such as differential pulse- and square-wave voltammetries, electrochemical quartz crystal microbalance (EQCM), or electrochemical atomic force microscopy, can be used for characterizing microporous solids. Apart from this, electrochemical techniques can be combined with other experimental procedures so that coupling with ultraviolet-visible spectrometry, Fourier-transform infrared spectroscopy, x-ray diffraction, etc., is possible.

In a broad sense, electrochemical phenomena involve electron transfer processes through a two-dimensional boundary (interface) separating the electrode (metal-type conductor) and the electrolyte (ionically conducting). In the study of such phenomena, one can distinguish between electrodics, focused on the heterogeneous electrode/electrolyte charge transfer process, and ionics, devoted to the study of ionically conducting liquid or solid phases (Bockris and Reddy, 1977).

With regard to porous materials, it should be noted that more or less restricted ionic conductivity is a general property that can vary significantly depending on doping, type and concentration of defects, and temperature. Interestingly, several porous materials, such as hydrated aluminosilicates, can behave as liquid electrolyte-like conductors, whereas such materials behave as solid ionic conductors when dry.

The classical model for describing the electrode-liquid electrolyte junction considers a highly structured region close to the electrode surface, the double layer, with dipole-oriented solvent molecules and a double layer of charge-separated ions, which creates a capacitive effect. At a greater distance from the electrode surface, there is a less structured region, the diffuse layer, which finally reduces to the randomly organized bulk-electrolyte solution. The earlier formulation, according to Helmholtz, distinguished between the inner (Helmoltz) layer, which comprises all species that are specifically adsorbed on the electrode surface, and the outer (Helmholtz) layer, which comprises all ions closest to the electrode surface but are not specifically adsorbed (Bard et al., 2008). As far as the area and geometry of the electrode surface influence the double-layer capacitance, porous materials having large effective surface areas can yield significant capacitance effects, which will influence the electrochemical process.

When a difference of potential is established between the electrode and the electrolyte, there are several coupled processes occurring in the electrode/electrolyte region (the interphase): a process of charge transfer through the electrode/electrolyte interface (two-dimensional region of contact) and concomitant charge-transport processes in the electrolyte and the electrode, in particular involving ion restructuring in the double-layer zone. As a result, the current flowing when a potential positive or negative of the potential of zero charge of the system can be described in terms of the sum of a faradaic current, associated to the electron transfer process across the interface, and a capacitive (or double-layer charging) current, associated to ion restructuring in the vicinity of the electrode surface.

Let us first consider an ordinary electrochemical process consisting of the reduction (or oxidation) of a given electroactive species at an inert electrode. Because

the flow of faradaic current is a direct expression of the rate of the electron transfer reaction at the electrode/electrolyte interface, the rate of mass transport of the electroactive species from the bulk solution to the electrode surface influences decisively the magnitude of the faradaic current. Mass transport can occur via diffusion (whose driving force is concentration gradients), convection (driven by momentum gradients), and migration of charged species (driven by electric fields). Convection phenomena appear when the solution is stirred or undergoes unwanted room vibrations. Ionic migration is suppressed at relatively high concentration of supporting electrolyte. Under planar, semi-infinite diffusion conditions (*vide infra*), the faradaic current, *i*, for the reduction of a species whose concentration in the solution bulk is *c*, and its diffusion coefficient is *D*, at a plane electrode is then given by:

$$i = -nFAD\left(\frac{\partial c}{\partial x}\right)_{x=0} \tag{1.1}$$

where *A* represents the electrode area, *n* is the number of transferred electrons per mole of electroactive species, and *x* is the distance from the electrode surface. The current is proportional to the gradient of concentration of the electroactive species at the electrode/electrolyte interface.

The electron transfer process across the electrode/electrolyte interface is a heterogeneous reaction. The rate at which electron transfer takes place across that interface is described in terms of a heterogeneous electron transfer rate constant. The kinetics can be described via the Butler-Volmer equation:

$$i = -nFAk^{\circ}\left[c^{o}_{\text{red}}\exp\left[\frac{nF(1-\alpha)(E-E^{\circ\prime})}{RT}\right] - c^{o}_{\text{ox}}\exp\left[-\frac{\alpha nF(E-E^{\circ\prime})}{RT}\right]\right] \tag{1.2}$$

In this equation, c^{o}_{ox} and c^{o}_{red} represent the surface concentrations of the oxidized and reduced forms of the electroactive species, respectively; k° is the standard rate constant for the heterogeneous electron transfer process at the standard potential (cm/sec); and α is the symmetry factor, a parameter characterizing the symmetry of the energy barrier that has to be surpassed during charge transfer. In Equation (1.2), *E* represents the applied potential and $E^{\circ\prime}$ is the formal electrode potential, usually close to the standard electrode potential. The difference $E - E^{\circ\prime}$ represents the overvoltage, a measure of the extra energy imparted to the electrode beyond the equilibrium potential for the reaction. Note that the Butler-Volmer equation reduces to the Nernst equation when the current is equal to zero (i.e., under equilibrium conditions) and when the reaction is very fast (i.e., when k° tends to approach ∞). The latter is the condition of reversibility (Oldham and Myland, 1994; Rolison, 1995).

It should be noted that the overall electrochemical process can involve coupled chemical reactions in solution phase or involve gas evolution and/or deposition of solids and/or formation of adsorbates onto the electrode surface, so that electrochemical processes can, in general, be regarded as multistep reaction processes. As far as electrochemical responses are strongly conditioned, not only by the kinetics of

the interfacial electron transfer process, but also by the kinetics of coupled chemical processes, electrochemical methods are able to yield mechanistic information of interest in a wide variety of fields.

1.8 DIFFUSIVE ASPECTS

Oxidation or reduction of electroactive species at an electrode surface produces a depletion of its concentration in the diffusion layer, thus generating a concentration gradient between the interface and the bulk solution, which is the driving force for net diffusion of electroactive molecules from the bulk of the solution. In the following, it will be assumed that electrochemical experiments were conducted under conditions where no complications due to convection and migration effects appear. In short, this means that experiments are performed under quiescent, nonstirred solutions in the presence of an electrochemically silent (i.e., no redox activity) supporting electrolyte in sufficiently high concentration. The most single electrochemical experiment involves stepping the potential from an initial value, far from where electrode reaction occurs, to one where the electrochemical process proceeds at a diffusion-controlled rate. The corresponding current/time record is the chrono-amperometric curve.

For disk-type electrodes, usually with a radius of 0.1–1.0 cm^2, the thickness of the diffusion layer that is depleted of reactant is much smaller than the electrode size so that mass transport can be described in terms of planar diffusion of the electroactive species from the bulk solution to the electrode surface as schematized in Figure 1.2a, where semi-infinite diffusion conditions apply. The thickness of the diffusion layer can be estimated as $(Dt)^{1/2}$ for a time electrolysis t and usually ranges between 0.01 and 0.1 mm (Bard et al., 2008). For an electrochemically reversible n-electron transfer process in the absence of parallel chemical reactions, the variation of the faradaic current with time is then given by the Cottrell equation:

$$i = \frac{nFAcD^{1/2}}{\pi^{1/2}t^{1/2}} \tag{1.3}$$

(a)	(b)
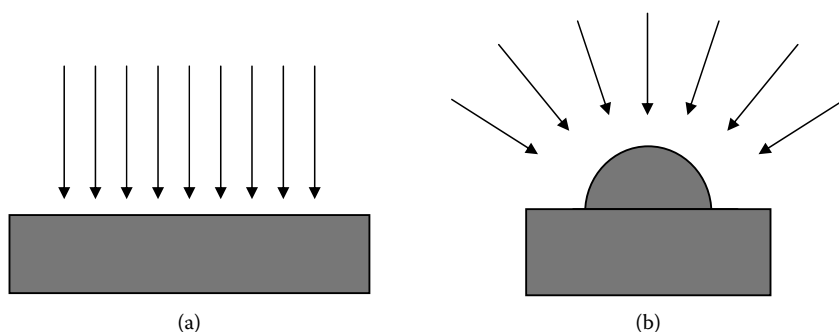
FIGURE 1.2 Schematic layout of (a) linear diffusion and (b) radial diffusion to electrodes.

It should be noted, however, that at short times in the experimentally recorded curves, deviations due to double-layer charging can appear, whereas at log times, convection can cause deviations from the expected response.

For microelectrodes, typically 5–10 µm in size, radial hemispherical diffusion conditions (Figure 1.2b) need to be considered. For the case of a spherical electrode of radius *r*, the chronoamperometric curve is described by:

$$i = \frac{nFADc}{r} + \frac{nFAcD^{1/2}}{\pi^{1/2}t^{1/2}} \tag{1.4}$$

At sufficiently short times, the second term of the above equation dominates over the first, so that the current/time response approaches that described by Equation (1.3). At long times, the second, Cottrell-type, term decays to the point where its contribution to the overall current is negligible and then the currents tend to be a constant, steady-state value in which the rate of electrolysis equals the rate at which molecules diffuse to the electrode surface (Forster, 1994).

At porous electrodes, diffusion will be conditioned by the electrode geometry and pore-size distribution, so that under several conditions, semi-infinite diffusion holds; however, under several other conditions, the porous electrode can be treated as an array of microelectrodes (Rolison, 1994).

1.9 VOLTAMMETRY AND RELATED TECHNIQUES

As previously noted, electrochemical methods are based on recording of the response of an electrode, in contact with an electrolyte, to an electrical excitation signal. Depending on the characteristics of the excitation potential signal applied to the working electrode and the measured signal response, one can distinguish different electrochemical techniques. Voltammetry consists of the recording of current (*i*) versus potential (*E*) that is applied between a working electrode and an auxiliary electrode, the potential of the working electrode being controlled with respect to a reference electrode. In conventional three-electrode arrangements, a potentiostat controls the potential so that the current flows almost exclusively between the working electrode and the auxiliary electrode while a very small, practically negligible current is passing through the reference electrode.

In linear potential scan (LSV) and cyclic (CV) voltammetries, a potential varying linearly with time is applied between an initial potential, E_{start}, usually at a value where no faradaic processes occur, and a final potential (LSV) or cycled between two extreme (or switching) potential values at a given potential scan rate *v* (usually expressed in mV/sec). In other techniques, such as normal and differential pulse voltammetries (NPV and DPV, respectively), or square-wave voltammetry (SQWV), the excitation signal incorporates potential pulses to a linear or staircase potential/time variation.

In a typical CV experiment, the potential scan is initiated at the open-circuit potential and directed in the positive or negative direction. For a reversible process, when the potential approaches the formal potential of the involved couple, the current increases rapidly while the concentration of the electroactive species in the vicinity of the electrode is depleted. As a result, a maximum of current is obtained,

thus defining a voltammetric (cathodic or anodic) peak. Note that the linear sweep voltammetric and the CV peak appear at a certain voltage fraction past the formal potential, from which the current slowly decreases. In the subsequent cathodic/anodic scan, a similar cathodic/anodic peak is recorded, defining a cathodic/anodic peak potential, E_{pc}/E_{pa}, and a cathodic/anodic peak current, i_{pc}/i_{pa}. Then, the current reaches a maximum and subsequently decays. About 150–200 mV after the voltammetric peak, the current becomes diffusion controlled. The general expression for the current in the case of a reversible n-electron transfer is

$$i = nFAcD^{1/2} \left(\frac{nF}{RT} \right)^{1/2} v^{1/2} \Psi(E - E^{\circ\prime}) \qquad (1.5)$$

where $\Psi(E - E^{\circ\prime})$ represents a tabulated function of the difference between the applied potential and the formal electrode potential of the redox couple (Nicholson and Shain, 1964). In the reverse scan, the oxidized (or reduced) species electrochemically generated, which remain in the vicinity of the electrode surface because the diffusion of products into the bulk of solution is slow, are reduced (or oxidized) to the parent reactant following a similar scheme. As a result, CVs for reversible electron transfer processes, involving two forms (oxidized and reduced) of an electroactive species in solution phase, consist of two peaks, cathodic and anodic, at potentials E_{pc} and E_{pa}, whose separation is related with the number of transferred electrons, n; but in the case of electrochemically irreversible or quasi-reversible electrode systems, they also depend on the kinetics of the electron transfer process and possibly also on the kinetics of coupled chemical reactions, adsorptions, etc. (Nicholson and Shain, 1964). Figure 1.3 shows a typical CV for ferrocene in MeCN solution, an essentially reversible one-electron couple.
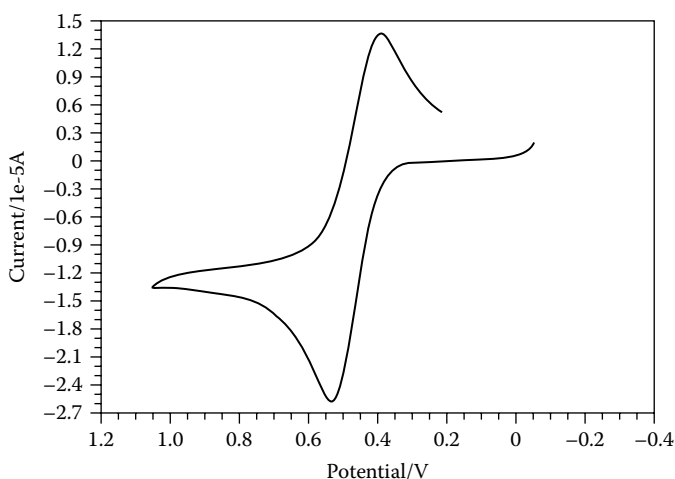
FIGURE 1.3 CV at Pt electrode for a 0.50-mM solution of ferrocene in 0.10 M Bu_4NPF_6/MeCN. Potential scan rate, 50 mV/sec.

For a reversible process involving species in solution, the absolute value of the peak potential separation, $|E_{pa} - E_{pc}|$, approaches $59/n$ (mV at 298 K), whereas the half-sum of such potentials can, in principle, be equal to the formal electrode potential of the couple. Under the above conditions, the peak current is given by the Randles-Sevcik equation (Bard et al., 2008):

$$i_p = 0.446nFAc\sqrt{\frac{nFvD}{RT}} \tag{1.6}$$

The peak current is then proportional to the concentration of the electroactive species and the square root of the potential scan rate. A case of particular interest is when the electroactive species is confined to the electrode surface where it reaches a surface concentration, Γ. Here, symmetric, bell-shaped current/potential curves, described by Bard and Faulkner (2001),

$$i = \frac{n^2F^2vA\Gamma_{ox}(b_{ox}/b_{red})\exp[nF(E-E^{\circ\prime})/RT]}{RT\{1+(b_{ox}/b_{red})\exp[nF(E-E^{\circ\prime})/RT]\}^2} \tag{1.7}$$

may be obtained again for reversible behavior. Here, b_i (i = ox, red) are equal to $\Gamma_i\exp(-\Delta G^{\circ}i/RT)$, ΔG_i° being the standard free energy for surface attachment. The peak current is then given by:

$$i_p = \frac{n^2F^2vA\Gamma}{4RT} \tag{1.8}$$

Now, the peak current becomes proportional to the potential scan rate. It should be noted that Equations (1.7) and (1.8) are formally analogous to those obtained for species in solution diffusing in a restricted space, under the so-called thin-layer conditions (by contraposition to unrestricted space diffusion, thick-layer conditions).

Laviron (1979) studied the voltammetric response of electroactive species confined to the electrode surface. Interestingly, interactions between species in the adsorbed layer may lead to peak splitting, a situation relevant with regard to the electrochemistry of solids.

The expressions for the cathodic and anodic peak potentials and rate constant in the case of small concentrations of surface-confined species are

$$E_{pc} = E^{\circ\prime} + \frac{RT}{\alpha nF}\ln[\alpha F/RT] \tag{1.9}$$

$$E_{pa} = E^{\circ\prime} + \frac{RT}{\alpha nF}\ln[(1-\alpha)F/RT] \tag{1.10}$$

$$\ln k_s = \alpha\ln(1-\alpha) + (1-\alpha)\ln\alpha - \ln(RT/nFv) - \alpha(1-\alpha)nF\Delta E_p/RT \tag{1.11}$$

Here, α represents the electron transfer coefficient, k_s is the apparent charge-transfer rate constant, and v is the potential scan rate. ΔE_p denotes the peak potential separation ($=E_{pa} - E_{pc}$).

Pulse voltammetric techniques are of interest because of its reluctance to charging effects. Their application is made difficult by the influence of pulse width in the shape of voltammetric curves. For SQWV under usual conditions, the net current flowing during the anodic and cathodic half-cycles can be approached by (Ramaley and Krause, 1969):

$$i_{\mathrm{dif}} = C \frac{n^2 F^2 A D^{1/2} c E_{\mathrm{SW}} f^{1/2}}{RT\pi^{1/2}} \frac{\exp(nF(E-E^{\circ\prime})/RT)}{\left[1+\exp(nF(E-E^{\circ\prime})/RT)\right]^2} \tag{1.12}$$

where f is the square-wave frequency, E_{SW} is square-wave amplitude (typically 25 mV), C is a numerical constant, and the other symbols have their customary meaning.

Obtaining information on the composition, structure, etc., of solid materials using voltammetric and related techniques can be performed by: (1) recording the response of the material attached to an inert electrode and immersed into a suitable electrolyte or (2) recording the modification of the response of an electroactive probe in the electrolyte solution in contact with the material-modified electrode. In addition, the electrochemical response of such systems under the application of optical or magnetic inputs can also be used.

In the first case, the voltammetric response can mainly be associated to reductive/oxidative dissolution processes and topotactic or epitactic solid-to-solid transformations, eventually confined to thin surface layers of the parent material (Scholz and Meyer, 1998; Grygar et al., 2000; Scholz et al., 2005). In the second case, among other possibilities, the solid can act as a preconcentrating system for enhancing the signal of the electroactive probe in solution, but also as a catalyst with regard to this process.

In the case of porous materials incorporating intercalated or entrapped electroactive species, the response of such species will be significantly conditioned by electrolyte ions, because, as will be discussed in Chapter 2, charge conservation imposes severe constraints for possible charge-transfer processes. This aspect is also relevant for doping of nanostructured carbons and conducting polymers, discussed in Chapters 7 and 8, respectively.

1.10   RESISTIVE AND CAPACITIVE EFFECTS

It is well known that experimental CVs for species in solution phase frequently diverge from theoretical ones for n-electron reversible couples. The divergence can be caused by a variety of factors: deviations from reversibility, occurrence of coupled chemical reactions and/or surface effects, and resistive and capacitive effects (Nicholson and Shain, 1964; Nicholson, 1965a). These last effects will be briefly treated here because of their potential significance when microheterogenous deposits or more or less homogeneous coatings of microporous materials cover the electrode surface.

In general, for a potential scan experiment initiated at a potential E_{start} and conducted with a potential scan rate v, the applied potential E satisfies the relationship (see, e.g., Bard and Faulkner, 2001):

$$E = E_{start} + vt = R(dq/dt) + q/C \qquad (1.13)$$

where q represents the charge passed at a time t, and R and C represent the resistance and the capacity of the system, respectively. This equation leads to the following expression for current i at time t:

$$i = vC + (E_{start}/R - vC)\exp(-t/RC) \qquad (1.14)$$

Then, the background current-potential curve will be given by:

$$i = vC + (E_{start}/R - vC)\exp[-(E - E_{start})/vRC] \qquad (1.15)$$

In short, the capacitive plus resistive effects mainly result in an enhancement of the background currents in both the positive- and negative-directed scans. Apart from this, resistive and capacitance effects also influence the peak profile so that the peak is flattened and decreased and shifted toward more negative (cathodic peak) or more positive (anodic peak) potentials.

Equation (1.15) predicts that the capacitive plus resistive current is proportional to v. Since, in the case of diffusion-controlled processes, the peak current will vary with $v^{1/2}$, one can expect that the capacitive plus resistive effects will decrease on decreasing potential scan rate. This can be seen in Figure 1.4, where CVs recorded
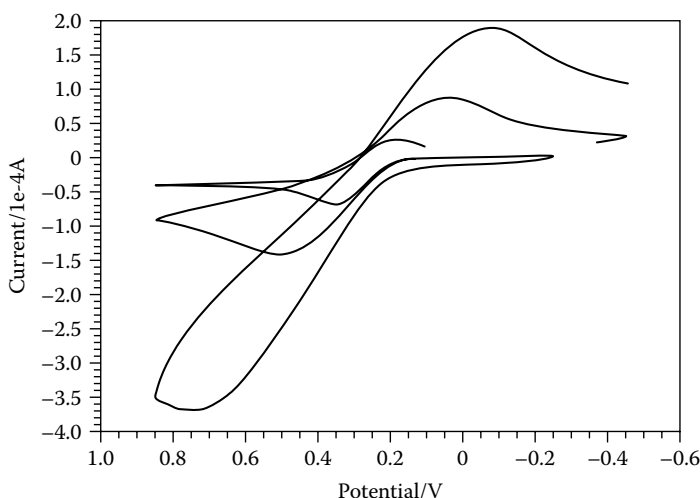
FIGURE 1.4 CVs for a 2.5-mM solution of $K_4Fe(CN)_6$ in water (0.15 M $NaClO_4$) at a zeolite Y-modified glassy carbon electrode. Potential scan rates of 10, 100, and 1000 mV/sec.
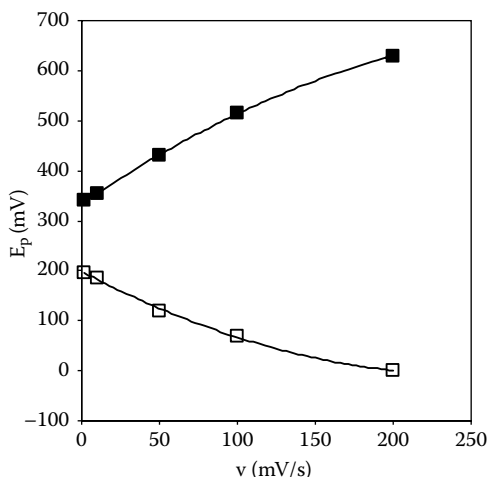
FIGURE 1.5 Variation in potential scan rate of peak potentials for the $Fe(CN)_6^{3-}/Fe(CN)_6^{4-}$ couple recorded from CVs in a 2.5-mM solution of $K_4Fe(CN)_6$ in 0.15 M $NaClO_4$ at a zeolite Y-modified glassy carbon electrode.

at different sweep rates for a zeolite Y-modified glassy carbon electrode immersed into an aqueous solution of $K_4Fe(CN)_6$ are shown. The cathodic-to-anodic peak potential separation, ΔE_p ($= |E_{pa} - E_{pc}|$), increases on increasing v but tends to the value in the absence of resistive effects when v tends to zero. The corresponding variation with the potential scan rate of peak potentials for the $Fe(CN)_6^{3-}/Fe(CN)_6^{4-}$ couple at a zeolite Y-modified glassy carbon electrode is depicted in Figure 1.5.

To separate kinetic and resistive effects, one can perform experiments at variable scan rate and at different concentrations of electroactive species. As a result, the peak potential separation increases on increasing v and the concentration of the depolarizer, allowing for estimation of the uncompensated resistance from the slope of the peak potential separation versus peak current plot for different analyte concentrations at a given potential scan rate (DuVall and McCreery, 1999, 2000) using the relationship:

$$\Delta E_p = (\Delta E_p)_{kin} + 2i_p R \qquad (1.16)$$

In this equation, ΔE_p represents the measured cathodic-to-anodic peak potential separation, and $(\Delta E_p)_{kin}$ denotes the value determined as the ordinate at the origin in the ΔE_p versus i_p plot for different concentrations of electroactive species. That $(\Delta E_p)_{kin}$ value can be directly related with kinetic parameters for the interfacial electron transfer reaction (Nicholson, 1965b). The slope of the above representation allows for calculation of the uncompensated ohmic resistance in the cell. Figure 1.6 shows ΔE_p versus i_p plots for the $Fe(CN)_6^{3-}/Fe(CN)_6^{4-}$ couple at zeolite Y- and hydrotalcite-modified glassy carbon electrodes immersed in $K_4Fe(CN)_6$ solutions in concentrations between 0.1 and 10.0 mM.
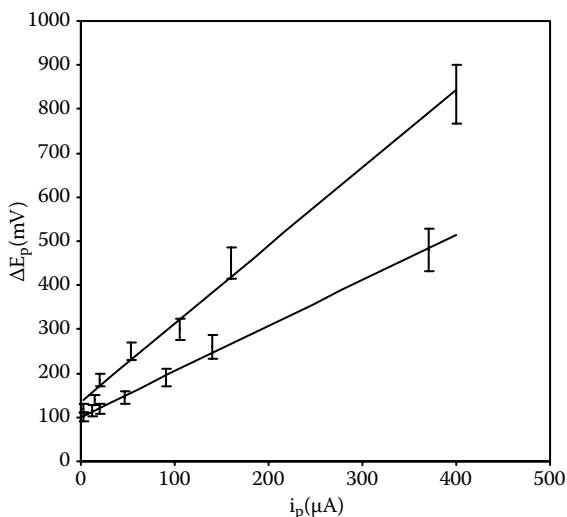
FIGURE 1.6   Plots of ΔE_p versus i_p for the $Fe(CN)_6^{3-}/Fe(CN)_6^{4-}$ couple recorded from CVs for $K_4Fe(CN)_6$ solutions (concentrations between 0.1 and 10.0 mM) in 0.15 M $NaClO_4$ at glassy carbon electrodes modified with zeolite Y (upper) and hydrotalcite (below). Potential scan rate, 50 mV/sec.

It should be noted, however, that cathodic-to-anodic peak potential separation can also be increased as a result of coupled chemical reactions. Frequently, resistive and capacitive effects are superimposed to more or less complicated reaction pathways. This can be seen in Figure 1.7, where a CV for a deposit of NiO in contact with 1.0 M KOH is depicted. Here, ill-defined cathodic and anodic signals appear over a large background current. The oxidation process can be described as (Srinivasan and Weinder, 2000; Xing et al., 2004):

$$NiO + OH^- (aq) \rightarrow NiOOH + e^- \tag{1.17}$$
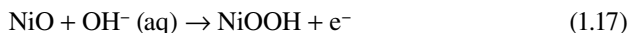
whereas the subsequent reduction step can be represented as:

$$NiOOH + H_2O + e^- \rightarrow Ni(OH)_2 \tag{1.18}$$

As far as two different couples with different electrode potentials are involved, the corresponding voltammetric profile differs from that expected for a single, uncomplicated electron transfer process involving a unique pair of species.

Interestingly, voltammetric methods provide information on purely capacitive responses characterized by CVs with characteristic rectangular, boxlike shape without any redox peaks. An example of this kind of response is shown in Figure 1.8, a PIGE modified with a microheterogeneous deposit of zeolite Y. The capacitive current satisfies the relationship $i_{cap} = ACv$. In this case, on increasing the potential scan rate the CV curves present a less rectangular response, thus suggesting that some limitations in the charging process occur.
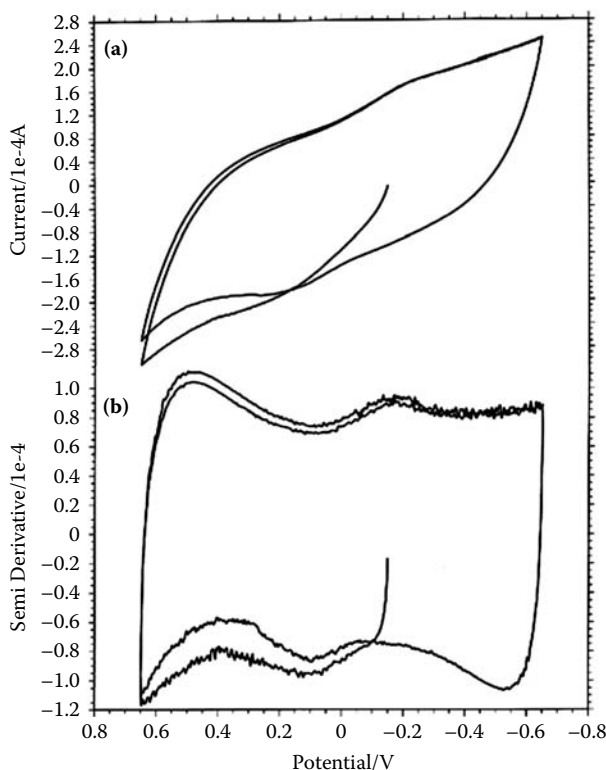
FIGURE 1.7 (a) CV and its (b) deconvolution for a NiO-modified graphite electrode immersed into 1.0 M NaOH. Potentials measured versus a Pt wire pseudoreference electrode. Potential scan rate, 50 mV/sec.

1.11   ELECTROCHEMICAL IMPEDANCE SPECTROSCOPY

Application of a time-dependent potential to an electrochemical cell in general gives rise to the appearance of a phase difference between the applied potential and the current response because diffusion, electron transfer, etc., processes yield an impedance effect similar to that typically observed in alternating current circuits. EIS is a technique based on the measurement, under steady-state conditions, of the complex impedance of the electrochemical cell as a function of frequency f (or angular frequency $\omega = 2\pi f$) of an imposed sinusoidal input of small amplitude. This situation can be represented in terms of a complex formulation where all involved quantities can, in general, be represented as having one real and one imaginary component. A vectorial formulation is usually used for representing impedances. The common circuit elements, resistors, capacitors, and inductances can be described as impedances of magnitude Z satisfying:

$$Z = Z_{real} + jZ_{imag} \quad (j = \sqrt{-1}) \tag{1.19}$$
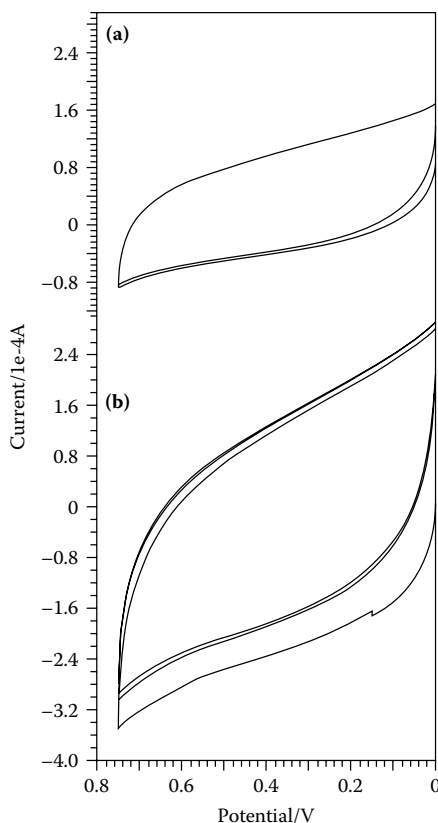
FIGURE 1.8 CV for a PIGE modified with a microheterogeneous deposit of zeolite Y. Potential scan rate, 50 mV/sec.

Considering a conventional electrical circuit submitted to an alternating potential input of angular frequency ω, the impedance for a resistor is $Z = R$, where R is the resistance of the resistor. For a capacitor of capacitance C, the impedance is $Z = -j/C\omega$, whereas for an inductance L, the impedance is $Z = jL\omega$. For an idealized alternating current circuit containing a resistor R, the phase angle φ is zero, whereas for a purely capacitive circuit and a purely inductive circuit, the phase angles would be $-90°$ and $90°$, respectively. Typical imaginary impedance versus real impedance plots are shown in Figure 1.9a and Figure 19b for R and C circuits, respectively.

Electrochemical cells can be represented via an equivalent circuit formed by an association of impedances that pass current with the same amplitude and phase angle of the real cell under a given potential input. Thus, for a series RC circuit, the impedance and the phase angle are given by:

$$Z = R - \frac{j}{C\omega} \tag{1.20}$$

$$\tan \varphi = -1 \,/\, RC\omega \tag{1.21}$$
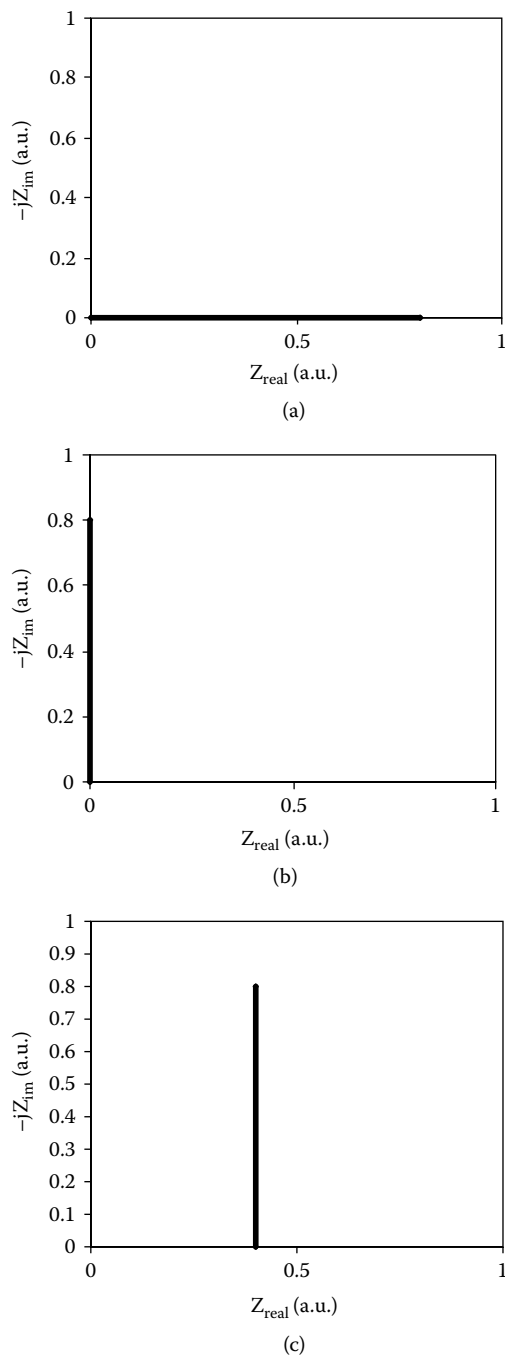
FIGURE 1.9 Nyquist representations for (a) R, (b) C, (c) series RC, and (d) parallel RC circuits.

(d)
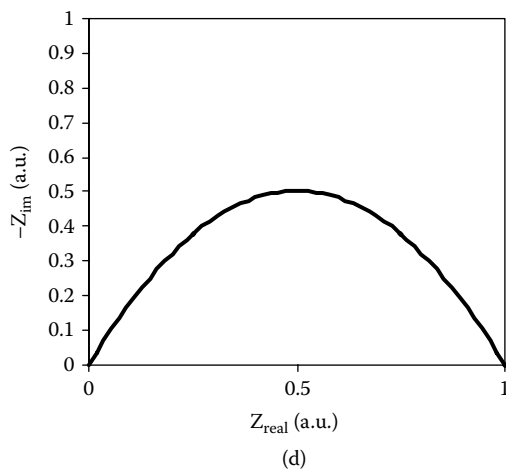
FIGURE 1.9   *(Continued)*

For this circuit, the representation of Z_{imag} versus Z_{real}, the so-called Nyquist plot, is shown in Figure 1.9c. For a parallel *RC* circuit, the total impedance and phase angle become:

$$Z = \frac{R}{1 + R^2 C^2 \omega^2} - \frac{jR^2 C\omega}{1 + R^2 C^2 \omega^2} \tag{1.22}$$

$$\tan \varphi = - RC\omega \tag{1.23}$$

The corresponding Nyquist representation, depicted in Figure 1.9d, corresponds to a circumference arc, whereas the phase angle varies with the angular frequency.

EIS is the experimental technique based on the measurement, under equilibrium or steady-state conditions, of the complex impedance of the cell at different frequencies of an imposed sinusoidal potential of small amplitude. As a result, a record of the variation of impedance with frequency (impedance spectrum) is obtained. Typically, EIS experiments are conducted from millihertz to kilohertz, so that available information covers a wide range of timescales (Retter and Lohse, 2005).

To properly describe the action of an alternating potential input on electrochemical cells, one can in principle consider at least two coupled interface processes influencing the impedance of the system: the electron transfer process across the electrolyte/electrode interface and the double-layer effect. The equivalent circuit typically used for representing this situation is the Randles circuit (Bard and Faulkner, 2001), constituted by a solution resistance, R_u, a charge transfer resistance, R_{ct} (often called polarization resistance with a meaning different to that used in other contexts), and a double-layer capacitance, C_{dl}. This circuit is schematized in Figure 1.10, where R_u represents the uncompensated resistance of the electrolyte and other possible ohmic resistances, whereas R_{ct} represents the ohmic drop that can be associated to the electron transfer process. The double-layer effect, which roughly consists of charge separation in the
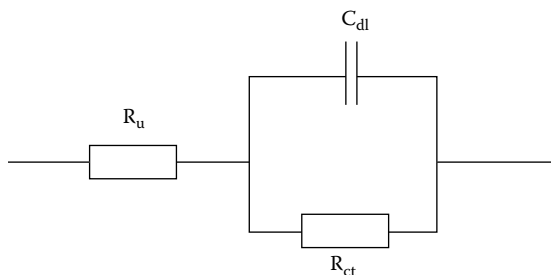
FIGURE 1.10   Schematic layout for the Randles circuit.

electrode/electrolyte interphase as a result of charge migration, can be assimilated to a capacitor of capacitance C_{dl}.

For this equivalent circuit, the Nyquist plot provides a circumference arc with a maximum of imaginary impedance located at $\omega_{max} = 1/R_{ct}C_{dl}$. The variation of the total impedance with the angular frequency (in double-logarithmic scale), termed the *Bode plot*, is shown in Figure 1.11a. Interestingly, at the high-frequency limiting ($\omega \to \infty$), the total impedance approaches R_u, whereas at the low-frequency limiting ($\omega \to 0$), Z approaches $R_u + R_{ct}$. For the Randles circuit, the phase angle varies with ω as depicted in Figure 1.11b, the maximum φ value being lower than 90°. At intermediate frequencies, there is a linear variation of the total impedance (absolute value) with the angular frequency ω (or frequency υ), so that the slope of the corresponding linear representation is $\partial(Z)/\partial(\log \upsilon) = -1$, whereas the ordinate at the origin equals to $1/C_{dl}$.

For properly describing electrochemical processes, additional impedance elements have been introduced. The Warburg impedance (Raistrick and Huggins, 1982; Honders and Broers, 1985) is representative of diffusive constraints, being defined, for the case of linear diffusion, as a frequency-dependent impedance given by:

$$Z(\omega) = Q_o (j\omega)^{-1/2} \tag{1.24}$$

where Q_o is a constant. The Warburg impedance, which represents a type of resistance to mass transfer, can be considered as a member of a family of the so-called constant-phase elements (CPEs), frequently introduced for describing the electrochemistry of solid phases. CPEs can be represented via (Jonscher, 1980; Almond and West, 1983; Boukamp and Wiegers, 1983; Bruce et al., 1983):

$$Z(\omega) = Q_o (j\omega)^{-n} \tag{1.25}$$

where n is a constant exponent. For $n = 0$, the CPE reduces to a resistance $R = Z_o$, whereas for $n = 1$, the CPE reduces to a capacitance.

One of the most remarkable aspects of this technique is that in a unique experiment, it provides information in phenomena occurring in considerably different time-scales because frequencies between millihertz (or even microhertz) and kilohertz (or even megahertz) are available. The critical frequency, ω_c, for an electrochemical process is defined as the frequency at maximum of the impedance arc associated
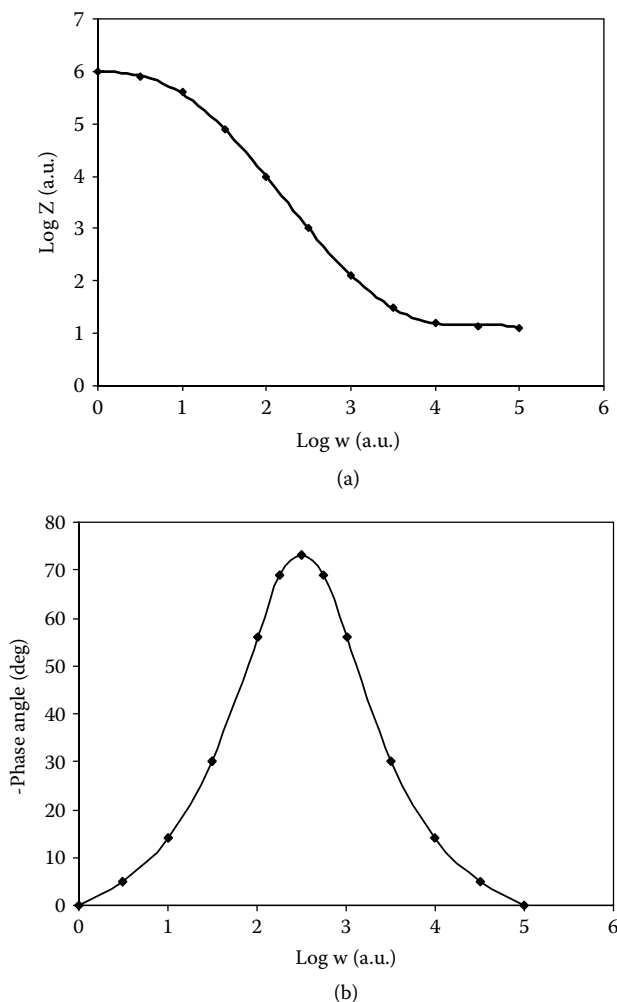
FIGURE 1.11 Bode plots representing (a) total impedance versus frequency and (b) phase angle versus frequency variations for a Randles circuit.

with the relaxation process. The relaxation time, τ, for this process, can be calculated from the value of the critical frequency as $\tau = 1/2\pi\omega_c$. This technique is of particular interest for studying electrode surfaces and has become an essential tool for examining electrode materials.

1.12 OTHER TECHNIQUES

Two additional electrochemical techniques, electrochemical quartz microbalance, EQCM and scanning atomic force electrochemical microscopy, can be mentioned. EQCM is based on the piezoelectric properties of quartz and permits the user to evaluate mass changes occurring on an electrode supported over a quartz lamina.

Mass changes are determined from the measurement of the change in the oscillation frequency of the quartz crystal (Chen, 2008), given by the Sauerbrey equation:

$$\Delta f = -\frac{2\pi f_o^{\,2}\Delta m}{(\mu\rho)^{1/2}} \tag{1.26}$$

where Δf represents the frequency change, Δm is the mass change per unit area, f_o is the fundamental frequency of the quartz resonator, μ is the shear modulus, and ρ is the density of quartz. Frequency changes can be monitored simultaneously to the charge passed during electrochemical cycles, Δq, so that for the deposition or dissolution of a compound of molar mass M, one can write:

$$\Delta m = \frac{M\Delta q}{nF} \tag{1.27}$$

Accordingly, M can be determined from the slope of the Δm versus Δq representation (Uchida et al., 1997, 1998). Adsorption/desorption of ions and solvent molecules, however, can complicate data interpretation (Salgado et al., 2006).

EQCM provides in situ measurement of mass changes accompanying electrochemical processes, namely, absorption, electrodeposition, electrocrystallization, electrodissolution, intercalation, electrochromism, etc. Studies dealing with, for instance, manganese oxides (Wu et al., 1997) and fullerenes (Bond et al., 2000, 2001) illustrate the capabilities of such technique in the context of the electrochemistry of porous materials.

Scanning electrochemical microscopy (SECM) is a technique based on the measurement of the current flowing through an ultramicroelectrode tip (diameter between 1 and 25 µm), submitted to potential inputs, whose position with respect the surface of the system to be studied remains constant or is changed. The tip electrode is associated to a three-electrode cell with a bipotentiostatic server. There are several modes of operation of SECM. In short, the tip can be regarded as a force sensor, thus providing topographic images of the studied surface, or as an electrochemical sensor, yielding an electrochemical image of the studied surface at nanometric scale. A detailed description of this technique and its applications can be seen in the text recently edited by Bard and Mirkin (2001), including concrete applications to the study of porous materials. An interesting comparison with other microscopy techniques, generically labeled as scanning probe-microscopy techniques, can be seen in the work of Bard et al. (2008).

2 Electrochemical Processes Involving Porous Materials

2.1 INTRODUCTION

In this chapter, existing theoretical approaches for describing the electrochemical behavior of microporous materials in faradaic processes will be treated. Such processes involve the transfer of electrons from/to a conducting electrode to/from electroactive species forming the framework of the porous material and/or attached as guests to this framework. The overall electrochemical process involves the propagation of the redox reaction across the solid via electron hopping between immobile redox centers. Charge conservation demands that this process be coupled with ion transport across the porous solid. Eventually, such charge transport processes can be restricted to the surface of the material particles.

With regard to the conducting characteristics of the microporous material, we can distinguish between "bulk" electron-conducting or semiconducting materials, those allowing for electron transport via conduction band of the material, and "bulk" nonelectron-conducting materials. In both cases, the material can either possess redox-active centers or not. If there are no electroactive centers in the material, this merely acts as a conducting layer, which can be seen as an electrode (bulk electron-conducting materials) or as an ionic "sponge," acting as a liquid electrolyte or, eventually, as an ionic conductor.

If the microporous material incorporates electroactive units, there is place for redox conductivity that is attained via electron hopping between immobile redox-active centers in the material coupled with ion transport across the pores. Depending on the distribution of electroactive centers, we can discern two extreme situations: first, when the material itself is electroactive, such as several transition metal oxides or metal-organic frameworks; second, when the electroactive centers are isolated within a nonconducting matrix, such as in zeolites incorporating electroactive cations. Remarkably, in the first case, the advance of the electrochemical reaction through the material can involve significant structural modifications and eventually phase changes. In the second case, there is a variety of possible electroactive units, the most frequent being simple ions or neutral molecules encapsulated into the pores, functional groups anchored to the microporous support, or metal nanoparticles or nanoclusters (polyoxometalates, silicates, etc.). Figure 2.1 shows a schematic representation of the case possibilities when redox center distribution and conductivity of the support are considered.

In this chapter, theoretical approaches for describing electrochemical processes in porous solids containing immobile redox-active centers will be discussed, whereas cases in which the entire porous material is electroactive will be further treated. In
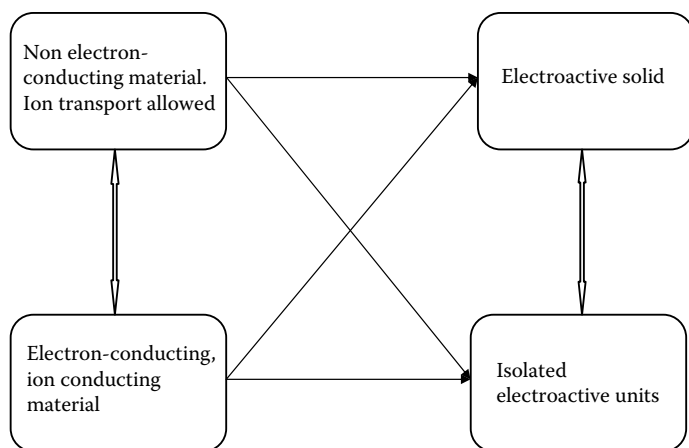
FIGURE 2.1 Schematics of possible combinations of conducting properties with redox-active centers distribution for porous materials.

the following, it will be assumed that conventional three-electrode arrangements are used. Here, the microporous material will be deposited onto the surface of an inert electrode, thus forming the working electrode. The reference and auxiliary electrodes complete the usual three-electrode arrangement. In general, the electrochemistry of microporous materials involves charge transfer in a (at least) three-phase system constituted by the material, a basal, electron-conducting electrode (usually a metal or graphite but also other materials such as boron-doped diamond or indium-doped tin oxide) and a liquid electrolyte. Depending on the spatial distribution of the corresponding interfaces, we can consider three separate situations, schematically depicted in Figure 2.2. In the first case (Figure 2.2a), a discontinuous set of microparticles of the porous material is deposited on the electrode surface, thus remaining in contact with the electrolyte. An almost equivalent situation is obtained when the particles of the microporous material are embedded into a conducting matrix such as a conducting polymer or a carbon paste, thus forming a composite. In the second case (Figure 2.2b),
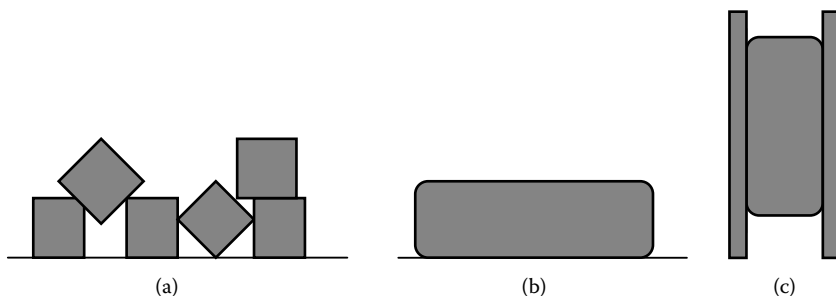
FIGURE 2.2 Schematic representation of possible configurations for studying the electrochemistry of microporous materials. (a) Discontinuous deposit of microparticles, (b) continuous layer, (c) material sandwiched between two electrodes.

a continuous layer of the microporous material is interposed between the basal electrode and the electrolyte. Finally, the electrolyte can be embedded within the microporous material, which is sandwiched between two metal electrodes (Figure 2.2c). The two first arrangements are those usually taken for characterizing the electrochemistry of solids, whereas the last situation relates directly to batteries and will be only tangentially treated here.

2.2 GENERAL APPROACH

Let us consider the case of a particle of microporous solid deposited on an inert electrode immersed into a suitable electrolyte. It will be assumed that the material is not a metallic conductor but incorporates immobile redox centers so that electron transport and ion transport are allowed through the solid via electron hopping between redox-active centers and ion diffusion across the micropores of the material. This situation can be treated based on the description from theoretical studies dealing with the electrochemistry of redox polymers (Andrieux and Savéant, 1980, 1982, 1984, 1988; Andrieux et al., 1982, 1984; Laviron, 1980) and the formulation of Lovric and Scholz (1997, 1999), Oldham (1998), and Schröder et al. (2000) for the voltammetry of redox-conductive microparticles. Although several aspects of the electrochemistry of porous materials can be approached via the concepts and methods developed for redox polymers, it should be noted that in such materials, a mixed-valent, self-exchange-based electron hopping mechanism occurs (Surridge et al., 1984) because the flexibility and ability of segmental motion of polymer chains make it possible to approach redox centers, thus facilitating electron hopping. Porous materials, however, cannot in general be treated as organic polymers capable of segmental motion, so that electron transfer between immobile redox centers attached to the porous matrix cannot be physically equated to polymeric motion-assisted processes occurring at redox polymer-modified electrodes (Rolison, 1995).

In the presence of a suitable monovalent electrolyte, MX, it will be assumed that each redox-active unit of the microporous material can be reduced (or oxidized) to an equally immobilized form. Charge conservation implies that the reduction process involves the ingress of electrolyte cations into the microporous system (denoted in the following by { }):

$$\{Ox\} + nM^+(sol) + ne^- \rightarrow \{Red\cdots nM^+\} \tag{2.1}$$
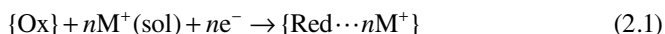
Equivalently, the oxidation of immobile redox centers in the material could involve the concomitant entrance of electrolyte anions into the microporous material:

$$\{Red\} + nX^-(sol) \rightarrow \{Ox\cdots nX^-\} + ne^- \tag{2.2}$$
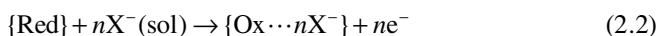
In cyclic voltammetric experiments, the inverse of the processes represented by Equations (2.1) and (2.2) should occur.

It is convenient to note that in most of the studied systems, such as in zeolites, the microporous solid frequently incorporates insertion ions (Li^+, Na^+, etc.). As a result,
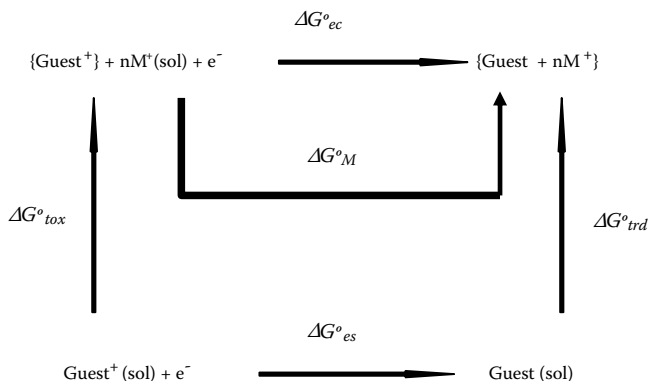
FIGURE 2.3 Thermochemical cycle for the electrochemical reduction of a monovalent cation guest attached to a porous solid.

the oxidation (reduction) process can occur via coupled issue of electrons and cations (anions) from the material to the electrolyte solution.

From a thermodynamic point of view, the variation of standard free enthalpy associated to the electron transfer process represented by Equation (2.1), ΔG_{ec}°, can be related with the variation of such thermodynamic quantity for the electron transfer process for species in solution phase, ΔG_{es}°, and for the transfer of the oxidized, ΔG_{tox}°, and reduced, ΔG_{tred}°, forms of the electroactive species and the electrolyte cations, ΔG_{M}°, from the solution phase to the porous solid. The corresponding Born-Haber-type cycle is shown in Figure 2.3 (Doménech et al., 2002a, 2003a). The relation between these quantities is

$$\Delta G^{\circ}_{ec} = \Delta G^{\circ}_{es} + \Delta G^{\circ}_{tred} - \Delta G^{\circ}_{tox} + n\Delta G^{\circ}_{M} \tag{2.3}$$

This equation reveals that not only the stability of the oxidized and reduced forms of the electroactive species but also the stability of the charge-balancing cations in the porous solid relative to their stability in solution phase are significant for determining the spontaneity of the redox process described via Equation (2.1).

Replacing, by simplicity, thermodynamic activities by concentrations, [ ], if equilibrium is reached, the reaction represented by Equation (2.1) should satisfy (Nernst equation):

$$[\{Ox\}] = [\{Red \cdots nM^+\}]\exp(nF(E - E_f)/RT) \tag{2.4}$$

In this equation, E represents the applied potential and E_f is a formal electrode potential that can be expressed as a function of the concentration of charge-balancing cations, M^+, in the electrolyte (Lovric et al., 1998):

$$E_f = E^{\circ} + (RT/nF)\ln K_{eq} + (RT/F)\ln[M^+] \tag{2.5}$$

Here, E° represents the standard potential of the {Ox}/{Red} couple and K_{eq} denotes the equilibrium constant for the ion transfer reaction:

$$\{Red\} + nM^+(sol) \rightarrow \{Red \cdots nM^+\} \tag{2.6}$$
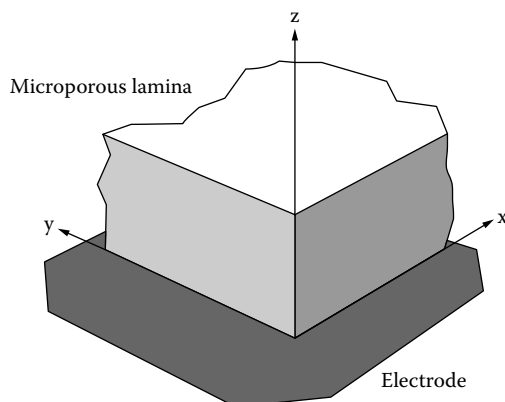
FIGURE 2.4 Coordinate system for the idealized representation of a lamina of a microporous material containing redox-active centers deposited on an electrode in contact with a suitable electrolyte.

In the following, it will be assumed that the concentration of electrolyte cations, M^+, in the solution is sufficiently high to ensure that ion transport phenomena occurring in the electrolyte can be neglected.

2.3 CONTINUOUS LAYER

Let us first consider the case of an infinite, uniform layer of microporous material attached to an infinite electrode. As depicted in Figure 2.4, the positive semiaxes x and y lie in the lamina/electrode interface, and the positive semiaxis z is placed along the lamina/electrolyte interface. It can be assumed that a redox reaction as described by Equation (2.1) occurs.

Then, the progress of the reaction across the microporous material involves a series of electron exchange plus ion exchange reactions between immobile redox centers, which can be represented via:

$$\{Red \cdots M^+\}_{site\ A} + \{Ox\}_{site\ B} \rightarrow \{Red \cdots M^+\}_{site\ B} + \{Ox\}_{site\ A} \tag{2.7}$$
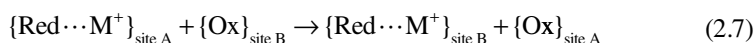
The charge exchange process represented by Equation (2.7) results in a net charge transfer along the z axis, which satisfies Fick's law:

$$\partial[Re\,d \cdots nM^+] / \partial t = D_z \partial^2 [Re\,d \cdots nM^+] / \partial z^2 \tag{2.8}$$

The electrochemical response of this system will depend on the timescale of the involved electrochemical experiment. Thus, if the charge transport rate is significantly faster than the experimental timescale, the oxidized/reduced site concentration ratio, $[\{Ox\}] / [\{Red \cdots nM^+\}]$, will be uniform throughout the microporous layer and in thermodynamic equilibrium with the applied potential. Thus, the concentration profiles (see Figure 2.5) for the oxidized and reduced forms of the electroactive
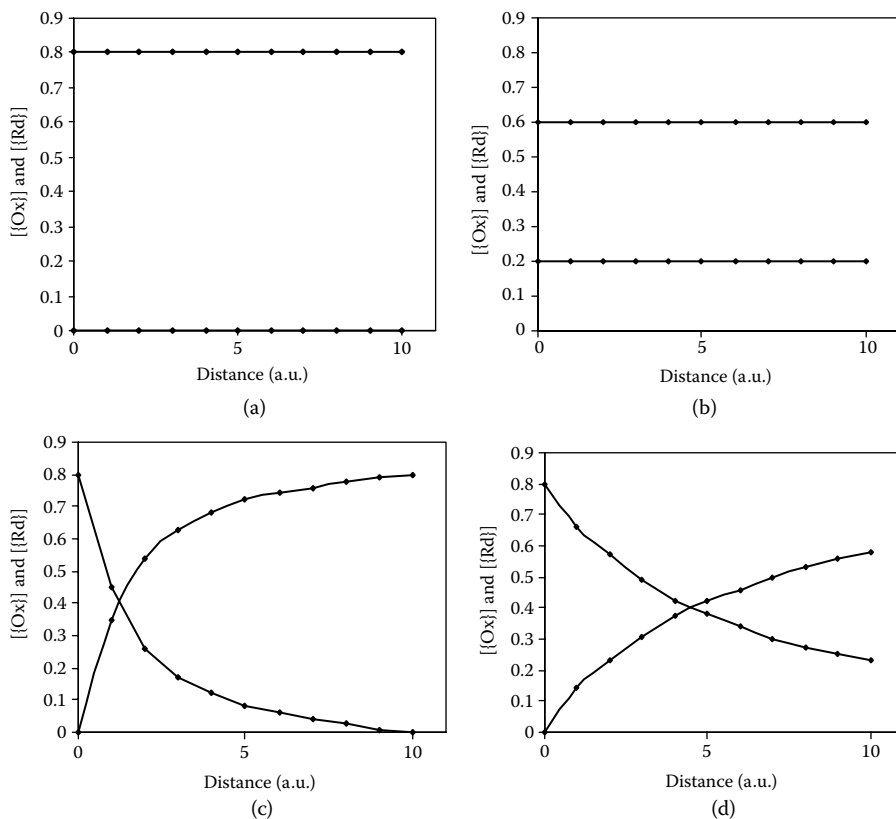
FIGURE 2.5 Concentration/distance profiles for the oxidized and reduced forms of an electro-active species uniformly distributed into a microporous layer deposited on a metallic electrode.

species will vary from the initial situation, depicted in Figure 2.5a for the case of a uniform concentration of the oxidized form, to that in Figure 2.5b.

If charge diffusion is significantly slower so that the distance of charge transport, L, $(=2(Dt)^{1/2})$ is clearly smaller than the thickness of the lamina, δ, the electrochemical response will be equivalent to that recorded when reactants freely diffuse from an infinite volume of solution to the electrode. This situation, often termed as *thick-layer behavior*, corresponds to semi-infinite boundary conditions, and concentration profiles such as that shown in Figure 2.5c are then predicted. Accordingly, Cottrell-type behavior is observed, for instance, in cyclic voltammetry (CV) and chronoamperometry (CA). In this last technique, a constant potential sufficiently cathodic for ensuring diffusion control in the reduction of {Ox} to {Red} is applied. The resulting current-time (i-t) curves should verify the Cottrell equation presented in the previous chapter (Equation (1.3)).

Here, c, represents the uniform concentration of the oxidized form of redox centers in the lamina of microporous material, A is the area of the upper and lower faces of the lamina, and the other symbols have their customary meaning.

Finally, at an intermediate charge transfer rate, the diffusion gradients will impinge on the outer boundary lamina and finite boundary conditions, resulting in a thin-layer response apply, with characteristic concentration profiles as shown in Figure 2.5d. The finite diffusion current-time relationship is as derived for redox polymers (Daum et al., 1980):

$$i = \frac{nFAcD^{1/2}}{\pi^{1/2}t^{1/2}} \left[\sum_{k=0}^{\infty} (-1)^k \left[\exp(-k^2\delta^2/Dt) - \exp(-(k+1)^2\delta^2/Dt) \right] \right] \quad (2.9)$$

Many situations can be described in terms of biphasic diffusion, where a given species diffuses through the electrolyte and the electrode phases. For this situation, which parallels that for codiffusion of electroactive species in solution phase (Blauch and Anson, 1991; Oldham, 1991), two limiting cases can be distinguished, following the description of Andrieux et al. (1984) for redox polymer films:

1. Full coupling of transport between the involved phases. This corresponds to a situation where there is a very fast cross-phase electron and/or mass transport exchange. Here, the "apparent" diffusion coefficient measured (e.g., via chronoamperometric experiments) should satisfy:

$$D_{app} = x_1 D_1 + x_2 D_2 \quad (2.10)$$

   In this equation, x_1, x_2 represent the molar fractions of the selected diffusing species in its partition between phases 1 and 2, and D_1, D_2 denote the respective diffusion coefficients.

2. Lack of coupling between phases. Here, one can expect that the flux of the diffusing species to be the sum of two independent contributions. Then, the apparent diffusion coefficient becomes:

$$D_{app}^{1/2} = x_1 D_1^{1/2} + x_2 D_2^{1/2} \quad (2.11)$$

This last equation is valid as long as the diffusion front of the diffusing species in solution phase remains within the electrode coating, a condition that applies for times shorter than 10–20 msec (Miller and Majda, 1986, 1988). Dynamics of electron hopping processes have been recently modeled by Denny and Sangaranarayan (1998) using kinetic Ising model formalism.

Another interesting situation arises when there is proton insertion within the solid film so that protonation of immobile redox centers accompanies electron transfer of the type $A + H^+ + e^- \rightarrow HA$, described by Wu et al. (1992) for redox polymers. Considering mass balance of protons over an infinitesimal film thickness in the boundary region of the film in contact with the electrolyte solution gives the diffusion equation:

$$D_H \left(\frac{\partial^2 c_H(x)}{\partial x^2} \right) = \frac{\partial c_H(x)}{\partial t} \pm \frac{\partial c_{HA}(x)}{\partial t} \quad (2.12)$$

where $c_H(x)$ and $c_{HA}(x)$ are the concentration of protons and protonated redox centers (HA) at a distance x from the electrolyte/film interface. The sign between the two terms in the above equation is + for reduction processes (ingress of protons and electrons into the film) or − for oxidation (issue of protons and electrons from the film). Mass balance for A yields $c_A(x) + c_{HA}(x) = c_A(0) + c_{HA}(0)$, where $c_A(0)$ and $c_{HA}(0)$ are the concentrations of A and HA at the interface, respectively. If protonation is faster than diffusion in the film, one can assume that chemical equilibrium is established at all points within the film and:

$$K = \frac{c_{HA}(x)}{c_H(x)c_A(x)} = \frac{c_{HA}(0)}{c_H(0)c_A(0)}$$
(2.13)

Combining the above relationships, one can arrive at the following expression for the effective diffusion coefficient of protons through the film, D_{eff}, available from chronoamperometric data:

$$D_{eff} = \frac{D_H}{1 \pm Kc_A(0)[1 + Kc_H(0)]}$$
(2.14)

This expression is of interest as far as it relates to the diffusional properties through the solid film with proton concentration at the solid/electrolyte interface.

2.4 MICROHETEROGENEOUS DEPOSITS

Let us consider the case of a set of crystals of a microporous material deposited on the surface of a metallic electrode.

Here (see Figure 2.6), the positive semiaxes x and y are located in the crystal/electrode interface, and the positive semiaxis z lies with the crystal/electrolyte interface. It can be assumed that a redox reaction as described by Equation (2.1) is initiated at the three-phase particle/electrode/electrolyte boundary, further expanding through the crystal. Fick's law can be expressed as:

$$\partial[\text{Red}\cdots n\text{M}^+]/\partial t = D_x \partial^2[\text{Red}\cdots n\text{M}^+]/\partial x^2 + D_y \partial^2[\text{Red}\cdots n\text{M}^+]/\partial y^2$$
$$+ D_z \partial^2[\text{Red}\cdots n\text{M}^+]/\partial z^2$$
(2.15)

In the above equation, D_x, D_y, D_z represent the charge diffusion coefficients along the x, y, and z directions. This formulation assumes that both electrons and ions are exchanged simultaneously and that no charge separation effects occur. The above diffusion coefficients will depend, in general, on the orientation of the particles of microporous material.

Theoretical modeling for redox processes in ion insertion solids predicts that, in the presence of a sufficiently high concentration of electrolyte, the voltammetric response of electroactive centers attached to porous materials will be similar, in the case of reversible electron transfer processes, to that displayed by species in solution (Lovric et al., 1998). Figure 2.7 shows the square-wave voltammetry (SQWV)
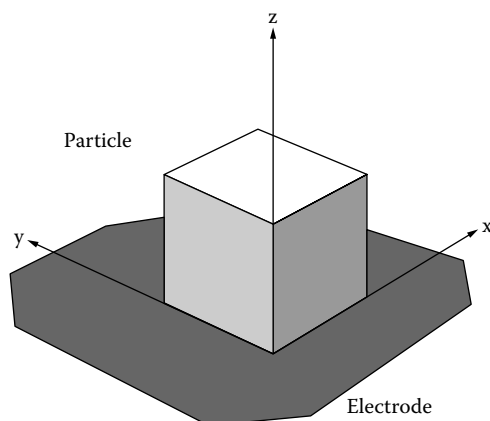
FIGURE 2.6 Coordinate system for the idealized representation of a particle of a microporous material containing redox-active centers deposited on an electrode in contact with a suitable electrolyte.

response of 2,4,6-triphenylpyrylium (PY$^+$) ion immobilized in zeolite Y (PY@Y), consisting of a well-defined peak at -0.26 V vs. AgCl/Ag. In contact with nonaqueous solvents with Li$^+$- or Et$_4$N$^+$-containing electrolytes, a reversible one-electron process occurs (Doménech et al., 1999a, 2002b), which can be represented as:

$$\{PY^+@Y\} + M^+(sol) + e^- \rightarrow \{PY@Y\cdots M^+\} \qquad (2.16)$$
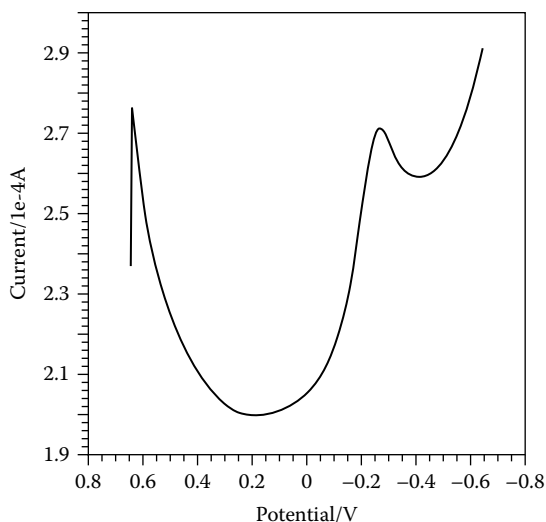
FIGURE 2.7 SQWV for microparticulate deposit of PY$^+$ ion attached to zeolite Y deposited on paraffin-impregnated graphite electrode in contact with 0.10 M Et$_4$NClO$_4$/MeCN. Potential step increment, 4 mV; square-wave amplitude, 25 mV; frequency, 5 Hz.

In the following, we will consider a deposit of N regular, cuboid-type crystals at rest on a plane basal electrode. Using the diagram shown in Figure 2.6, D_z can be identified as the diffusion coefficient for electrons (D_e), whereas D_x and D_y correspond to cation diffusion. Assuming isotropy ($D_x = D_y = D_M$), numerical simulation using finite difference method provides two different regimes. During the initial period, that is, at short experimentation times, quasi semi-infinite conditions apply to the diffusion of both electrons and cations into the crystal. The resulting chronoamperometric current can be expressed as (Schröder et al., 2000; Doménech, 2004):

$$i = nNFc\left\{ p\left[\left(\frac{\Delta z D_e^{1/2} + \Delta x D_M^{1/2}}{2\pi^{1/2}t^{1/2}}\right) + (D_e D_M)^{1/2}\right] - 4D_M(2D_e t)^{1/2}\right\} \quad (2.17)$$

In this equation, N represents the number of crystals, p is the length of the three-phase junction (i.e., the perimeter of the electrode/crystal interface), and Δx, Δz denote the size of the discrete boxes in which the crystal is divided for numerical simulation procedures.

The above equation contains a Cottrell-type term, characterized by $i \propto t^{-1/2}$, accompanied by a time-independent term and a third term for which $i \propto t^{1/2}$. The time-independent term can be associated to the restrictions imposed by the finite character of the crystals, whereas the third term can be described as an edge effect, resulting from overlapping of the cation diffusion near the corners of the crystal and thereby its influence on the entire diffusion process (Schröder et al., 2000).

Plots of the product $it^{1/2}$ vs. t yield characteristic curves with a maximum at a transition time t^* given by:

$$t^* = \frac{p^2}{128 D_M} \quad (2.18)$$

This transition time describes the point at which the transition from the three-dimensional diffusion conditions to the planar diffusion conditions occurs. This magnitude is of interest because it allows for easy determination of diffusion and crystal size parameters.

Experimental data for zeolite-associated species were found to be in agreement with that model, as can be seen in Figure 2.8 for PY$^+$ ion immobilized in zeolite Y immersed into 0.10 M Et$_4$NClO$_4$/MeCN (Doménech et al., 2002b) using CA data at an applied potential of -0.35 V vs. AgCl/Ag. This potential is sufficiently negative with respect to the voltammetric peak previously obtained (see Figure 2.7) to ensure diffusive control. Here, a well-defined maximum in the $it^{1/2}$ vs. t plot is obtained at $t = 15$ msec. Taking a mean perimeter for the crystal/electrode junction of 500 nm, estimated from transmission electron microscopy (TEM) examination of deposits, one obtains $D_M = 1.3 \times 10^{-9}$ cm^2/sec.

At relatively long experimentation times, semi-infinite diffusion does not hold, and the predicted behavior depends on the values of the diffusion coefficients for electrons and cations relative to the crystal dimensions. Roughly, when the diffusion of cations is fast compared to the diffusion of the electrons, the cations spread along the
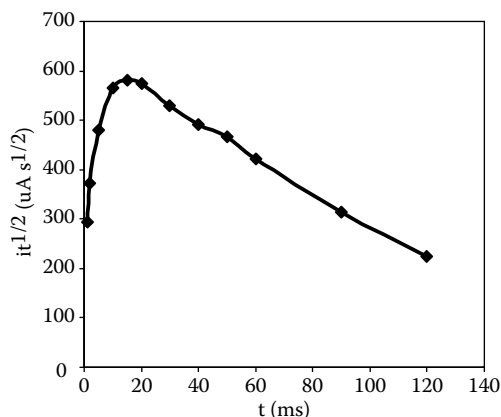
FIGURE 2.8 Plots of $it^{1/2}$ vs. t for microparticulate deposit of PY$^+$ ion attached to zeolite Y deposited on paraffin-impregnated graphite electrode in contact with 0.10 M Et$_4$NClO$_4$/MeCN. Chronoamperometric data at an applied potential −0.35 V vs. AgCl/Ag.

electrode/crystal interface into the bulk of the crystal so that the oxidized redox centers along this interface are exhausted. Now, electron diffusion becomes rate-determining and the orientation of the equiconcentration lines becomes increasingly parallel to the electrode surface so that the systems tend to reach a two-dimensional diffusion. Following Schröder et al. (2000), the chronoamperometric current becomes:

$$i = \frac{2nFNAD_e c}{H} \sum_{j=1}^{\infty} \exp\left(\frac{-(2j-1)^2 \pi^2 D_e t}{4H^2} \right) \tag{2.19}$$

where H denotes the crystal height and A an effective area. Here, the transition time for crystals of length L and width B is given by:

$$t^* = \frac{L^2 B^2}{4.45(L^2 + B^2)D_M} \tag{2.20}$$

When electron diffusion is clearly faster than cation diffusion, the reaction zone initially spreads along the z-axis and reaches the top surface of the crystal. Now, the cation diffusion in the x and y directions becomes rate-determining and the transition time is given by:

$$t^* = \frac{H^2}{1.1D_e} \tag{2.21}$$

The chronoamperometric long-time curves for crystals where $B \ll L$ can be approached by:

$$i = \frac{NnFLHcD_M}{B} \exp\left(\frac{-\pi^2 D_M t}{B^2} \right) \tag{2.22}$$

www.iran−mavad.com

مرجع دانشجویان و مهندسین مواد

Interestingly, this model predicts that there is redox conductivity even if one of the diffusion coefficients is equal to zero; that is, when one of the charge transport processes is hindered through the solid. If $D_e = 0$, the reaction propagates along the particle/electrode interface, whereas if $D_M = 0$, the reaction layer is confined to the lateral sides of the particle.

Comparable situations can be obtained when $D_M \gg D_e$ or $D_e \gg D_M$. This last condition appears to be the case for proton-assisted electron transfer processes involving organic molecules in contact with aqueous buffers. Here, charge transfer is ensured by proton hopping between immobile redox centers via chemical bond breaking and reforming rather than cation insertion into the organic lattice. As a result, one can assume that $D_e \gg D_M$, so that the electroactive region is confined to a narrow layer in the lateral sides of the crystals.

Interestingly, theoretical CVs for reversible electrochemical processes involving ion insertion solids, when the concentration of electrolyte is sufficiently high, are essentially identical to those predicted for reversible charge transfer processes between species in solution (Lovric et al., 1998). Then, the median potential, taken as the half-sum of the cathodic and anodic peak potentials, is equal to the formal potential in Equation (2.5). When the electrolyte concentration is low, the voltammetric peaks vanish and the median potential is given by (Lovric et al., 1998):

$$E_{\text{median}} = E^{\circ} + (RT/nF)\ln K_{\text{eq}} + (RT/2nF)\ln(D_{\text{solid}}/D_{\text{solution}}) + (RT/nF)\ln \rho \quad (2.23)$$

Here, ρ represents the density of the solid (mol/cm³) and D_{solid} and D_{solution} are the diffusion coefficients of the cation in the solid and the electrolyte, respectively.

2.5   DISTRIBUTION OF SPECIES

Equations (2.14) to (2.23) were obtained on the assumption that electroactive molecules are uniformly distributed in the entire volume of the solid. However, this is an unrealistic assumption in cases where bulky guest species are entrapped within the cavities of the porous material. Here, ship-in-a-bottle synthetic procedures most likely yield a nonuniform distribution of guest species in the network of the host porous material. Electrochemical data can then be used for obtaining information on the distribution of electroactive species.

Initial evidence of nonuniform electroactive species distribution can be obtained from crossing short-time and long-time CA data for zeolite-associated species. For instance, for PY^+@Y immersed into 0.10 M Et_4NClO_4/MeCN, the value of D_e can be estimated from the slope of the $it^{1/2}$ vs. t plot in the linear descending branch, which can be observed at times between 30 and 120 msec in Figure 2.8, using Equation (2.17). For deposits of 1.5 mg of PY^+@Y formally containing 3.7×10^{-4} mol/cm³ PY^+ ion, and assuming a volume particle of 1.2×10^{-16} cm³ and a material density of 2.3 g/cm³, the coefficient of diffusion for electrons is $D_e = 5.1 \times 10^{-10}$ cm²/sec. However, long-time CAs (times ranging from 1 to 300 sec), which provide a current-time dependence as predicted by Equation (2.19), lead to a lower D_e value of 2×10^{-11} cm²/sec. The discrepancy can be rationalized by considering that short-time experiments reflect the electrochemical response of the more external PY^+ ions, whereas

long-time experiments yield the response of a population of such ions more extensively distributed within the zeolite framework. Accordingly, the average concentration of PY^+ in the more external zeolite boundary should be larger than the average concentration when more depth layers are involved.

An estimate of the variation of the concentration of electroactive species with depth can be obtained from chronocoulometric data. In this technique, the charge passed (q) at time t upon application of a potential step is recorded. Roughly, the charge passed at time t can be associated to the number of electroactive species reached by the diffusion layer as it advances through the solid particle, so that the resulting q/t curves can be regarded as accumulated number of electroactive units/ depth profiles taking depth $= (Dt)^{1/2}$ (see Section 1.7). Accordingly, the concentration of electroactive species at depth x, $c(x)$, relative to the concentration at the external surface ($x = 0$), $c(0)$, can directly be estimated as the quotient between the slopes of the q/t curve at times $t = 0$ and t. An example of this treatment is shown in Figure 2.9 and Figure 2.10. Figure 2.9 presents the chronocoulometric curve recorded for PY^+@Y immersed into 0.10 M Et_4NClO_4/MeCN, consisting of a monotonically rising curve that tends to a horizontal line denoting the limiting q value corresponding to the completion of the process with reduction of all accessible PY^+ ions. The $c(x)/c(0)$ vs. x plot estimated from the above data, taking $D_e = 2 \times 10^{-11}$ cm²/sec, is depicted in Figure 2.10. As expected, a rapid decrease in the concentration of PY^+ ions on increasing depth is observed.

These concentration profiles, however, must be taken with caution. First of all, it should be noted that the obtained concentration profiles represent the distribution of effectively electroactive molecules within the solid but not necessarily the entire distribution of such molecules. As far as electron hopping and/or ion hopping can
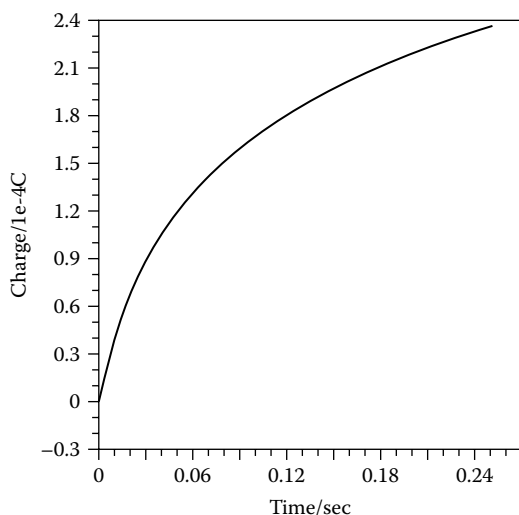
FIGURE 2.9 Chronocoulometric curve recorded under application of a potential of -0.35 V for PY^+@Y deposited on paraffin-impregnated graphite electrode in contact with 0.10 M Et_4NClO_4/MeCN.
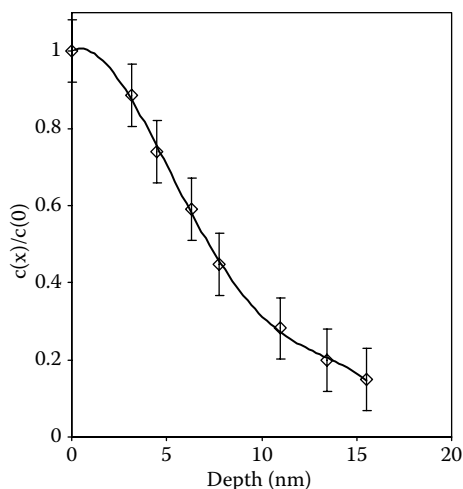
FIGURE 2.10 Concentration profiles estimated for the distribution of PY^+ ion in the boundary region of zeolite Y crystals estimated from chronocoulometric data in Figure 2.9.

be hindered in depth regions of the porous material, a significant portion of guest molecules do not exhibit electroactivity. Second, the advance of the diffusion layer is conditioned by the structural (bulk) and textural (surface) properties of the host material, and defects (cracks and crevices, dislocations, etc.) existing in the surface can significantly increase the external effective area exposed to the diffusion of charge-balancing electrolyte ions. At the same time, however, such defects produce more or less complicated topologies retarding charge diffusion and/or producing anisotropies in the same. As will be discussed in Chapter 4, in the case of systems such as zeolites, the electroactive layer, that is, the region of the crystals that is accessible to coupled electron and ion transport, is probably limited to an external boundary zone, so that depths in Figure 2.10 are probably overestimated. In spite of such limitations, the above treatment illustrates the capabilities of electrochemistry for providing relevant information for microporous materials.

2.6 REFINEMENTS

Dahms (1968) and Botár and Ruff (1985) studied exchange reactions such as those represented by Equation (2.6), stating that such processes can be described in terms of a second-order reaction kinetics, so that the apparent diffusion coefficient, D_{app}, measured in electrochemical experiments (e.g., CA) under diffusion-controlled conditions, can be expressed by:

$$D_{app} = D + \frac{k_e \delta^2 c}{s} \tag{2.24}$$

where $s = 2$, 4, and 6 for one-, two-, and three-dimensional diffusion, respectively. In the above equation, k_e is the second-order rate constant, and c and δ are

the concentration and the distance between the centers of the chemically equivalent species involved in the electron exchange, respectively.

The aforementioned picture of diffusion via electron hopping between localized centers and ion motion across the pore and channel system of the material does not specify whether the barriers for electron hopping or those for ion motion control the rate of charge transport. If the barrier is expressed in terms of a thermally activated diffusion, the following equation holds:

$$D^{1/2} = D_o^{\;1/2} \exp(-E_a/RT) \tag{2.25}$$

where E_a is the activation energy for the diffusion process. The preexponential factor can be obtained from the Eyring model (see, e.g., Bowers and Murray, 1966) as:

$$D_o = \frac{e\lambda^2 kT}{h} \exp(\Delta S^*/R) \tag{2.26}$$

where λ is diffusion jump distance and ΔS^* represents the activation entropy.

The above treatments are based on a series of simplifying assumptions. Real systems, however, can significantly deviate from the expected behavior. The main issues, similar to those appearing for redox polymers (Daum et al., 1980), are:

- Deviations from reversibility of the electrochemical process.
- Continuum deviation when the number of immobile redox centers is too large to ensure that the continuum approximation on which Fick's laws are based remains operative.
- Discontinuities and inhomogeneities in the microporous material and/or in the distribution of redox centers throughout the material.
- Uncompensated capacitive and resistive effects.
- Presence of ion transport control due to a strong disequilibrium between the concentration of cations in the electrolyte and the material, because ion diffusion constants vary over the gradients of ion activity coefficients, solvent content, and electrostatic ion size effects.
- Concentration polarization, associated to large changes in the ion concentration in the microporous material. As a result, ions in the solution contacting the microporous material may become concentration polarized.

Another set of refinements can arise when one considers diffusion in heterogeneous media containing obstructions of asymmetric shape (Ly and Cheng, 1997) and diffusion in periodic media (Koza, 2000; Jamnik et al., 2006).

2.7 FRACTAL SURFACES

Many systems exhibit fractal geometries, characterized by structures that look the same on all length scales (Mandelbrot, 1982). Fractal structures can be characterized by a scale law where the number of discrete units is proportional to the d_F power of the size of those units, where d_F represents the fractal dimension of the structure.

Diffusion in fractal media (Gefen et al., 1983; Giona and Roman, 1992) and diffusion toward and from/through interfaces (Le Mehaute and Crepy, 1983) are of interest in relation to electrochemical processes involving porous materials. Since the pioneering work of Nyikos and Pajkossy (1986), fractal geometry has provided a powerful tool in treating problems of mass transport toward and from/through interfaces between the electrode and the electrolyte (Nyikos et al., 1990; Borosy et al., 1991; Zuo et al., 1997).

It is well known that when mass transport is purely controlled by the reaction diffusion in the electrode or electrolyte, the electrochemical responses at the rough interface obey the generalized form of the Cottrell equation. For certain cases, however, classical fractal behavior under diffusion-controlled constraint is replaced by mixed kinetic/diffusive control (de Levie and Vogt, 1990; Kant and Rangarajan, 1995; Jung and Pyun, 2006a,b). Taking $\alpha = (d_F - 1)/2$, the chronoamperometric current becomes (Dassas and Duby, 1995; Stromme et al., 1995; Andrieux and Audebert, 2001):

$$i = \frac{nFAcD^{1/2}}{\pi^{1/2}t^{\alpha}} \tag{2.27}$$

This equation predicts a linear dependence of i on $t^{-\alpha}$, which can be tested from experimental CAs. An example is presented in Figure 2.11, where CA data at a polyacetylene-associated zeolite Y hybrid material (Doménech et al., 2006b) deposited over graphite in contact with aqueous $K_4Fe(CN)_6$ + 0.15 M $NaClO_4$ solutions are
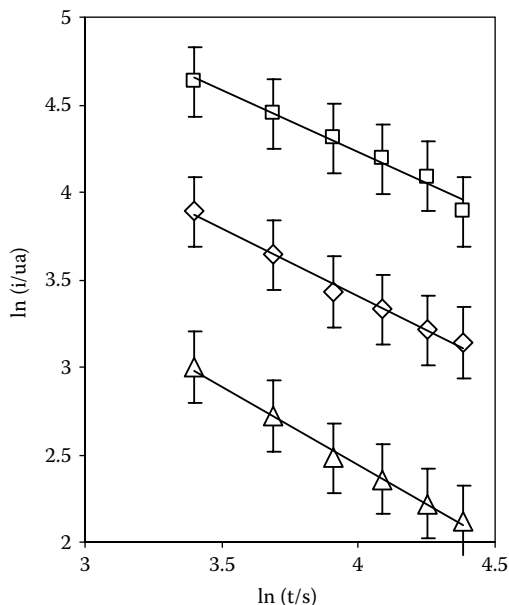
FIGURE 2.11 Plots of ln i vs. ln t for CAs at a polyacetylene-associated zeolite Y hybrid material deposited over graphite in contact with 3.5 (squares), 1.8 (rhombs), and 0.8 mM (triangles) $K_4Fe(CN)_6$ solutions in 0.15 M $NaClO_4$. Applied potentials +0.45 V vs. AgCl/Ag.

shown. An excellent linearity was obtained, with the slopes of such linear representations providing d_F values of 2.54 ± 0.15, which are clearly intermediate between those expected for planar electrodes and for ideally porous electrodes.

For a cyclic voltammetric experiment at a potential scan rate v, involving oxidized and reduced species with identical diffusion coefficient, D, the peak current, i_p, is given by (Stromme et al., 1995):

$$i_p = nFA \frac{\Gamma(1-\alpha)\Gamma(\alpha)(\gamma\lambda^2)^{\alpha-1/2}(nFv)^\alpha D^{1-\alpha} c \chi_{\max}(\alpha)}{\Gamma(1/2)(RT)^\alpha} \qquad (2.28)$$

Here, Γ is the gamma function, λ is the length corresponding to the inner cutoff for the fractal electrode, A is the macroscopic area, and γ is a geometric factor close to $1/\pi$. The dimensionless function $\chi(\alpha)$ can be determined numerically.

Equation (2.28) predicts that the peak current in CVs will be proportional to v^α, a relationship that can easily be tested. Interestingly, under such conditions, the diffusion layer length acts as a yardstick length for probing the fractal topography of the electrode surface (Pajkossy, 1991) and can be estimated as (Stromme et al., 1996a,b):

$$\delta = \frac{nFAcD}{i_p} \qquad (2.29)$$

In the above equations, d_F values should lie between 2 and 3, corresponding to a planar and a volumic electrode surface, respectively. Following Andrieux and Audebert (2001), both CA and CV experiments would be suitable in determining the fractal dimension d_F of a volumic modified electrode. In the first case (CA), plots of $\ln i$ vs. $\ln t$ from CA data should provide straight lines of slope $-\alpha$ [$= (d_F - 1)/2$]. In CV, successive experiments using different potential scan rates, v, have to be performed so that plots of $\log i_p$ vs. $\log v$ should yield straight lines of slope α.

Analogously, the generalized Warburg equation, representative of the response of constant phase elements in electrochemical impedance spectroscopy experiments, becomes (Nyikos and Pajkossy, 1990; Dassas and Duby, 1995):

$$Z(\omega) = \frac{1}{nFAD^{1/2}} \left(\frac{dE}{dc} \right) (j\omega)^{-\alpha} \qquad (2.30)$$

where E represents the applied potential and c is the concentration of the electroactive species. The thickness of the diffusion layer can now be determined from the frequencies in which the constant phase element (CPE) operates, f_{CPE}, as (Go and Pyun, 2004):

$$\delta = \sqrt{\frac{D}{f_{CPE}\gamma}} \qquad (2.31)$$

The corresponding interval of frequencies can be obtained from the $\tan^{-1}$ [$d(-Z_{imag})/dZ_{real}$] vs. f plots. Figure 2.12 shows the corresponding representation for
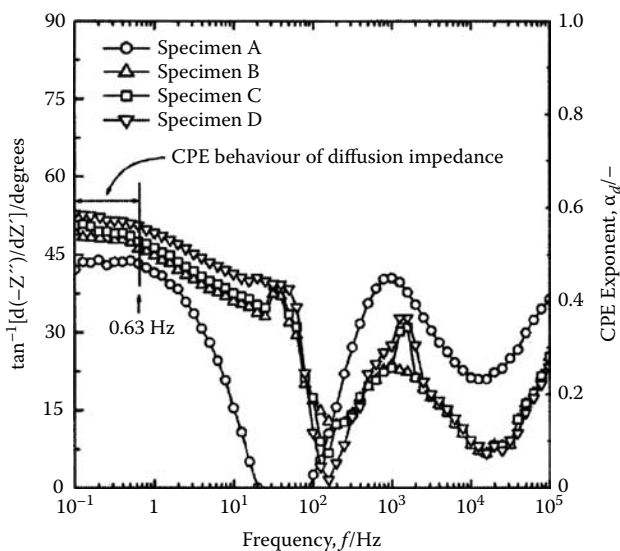
FIGURE 2.12 Plots of $\tan^{-1}[d(-Z_{imag})/dZ_{real}]$ vs. f for V_2O_5 film electrodes with various pore structures in 1 M LiClO$_4$/propylene carbonate solution at an electrode potential of 3.1 V vs. Li$^+$/Li. (From Jung and Pyun, 2006a. *Electrochim. Acta* 51, 2646–2655, with permission.)
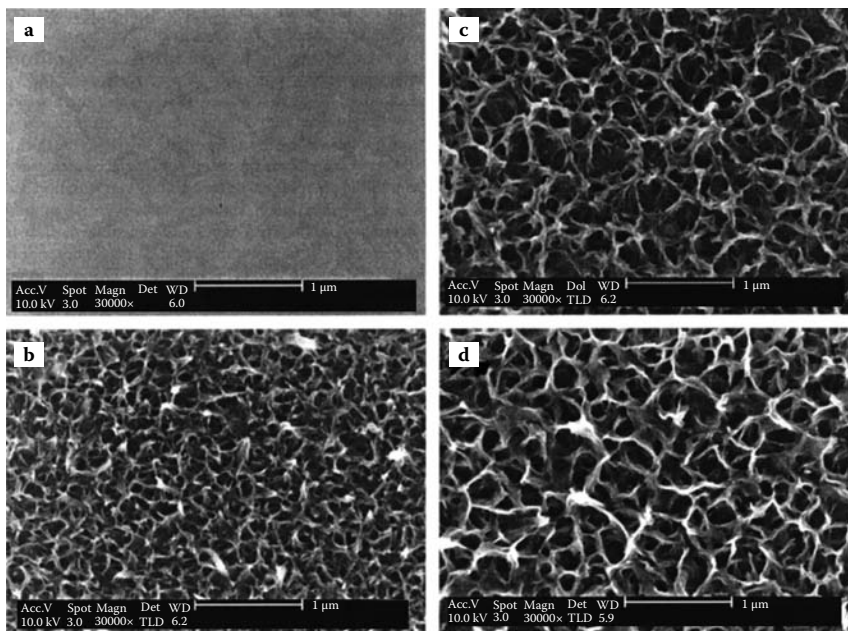
FIGURE 2.13 TEM images determined from different V_2O_5-porous film electrodes. (Adapted from Jung and Pyun, 2006a. *Electrochim. Acta* 51, 2646–2655, with permission.)

www.iran–mavad.com

مرجع دانشجویان و مهندسین مواد
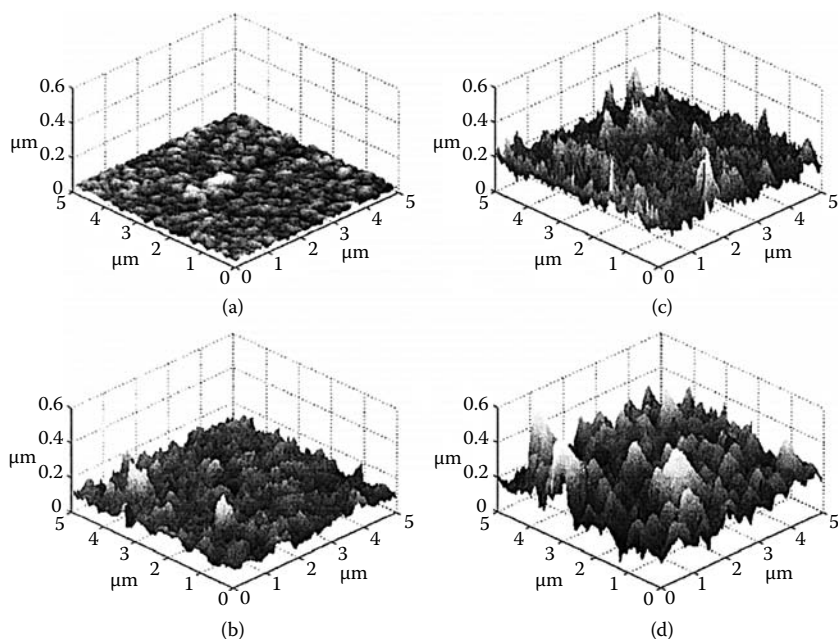
FIGURE 2.14 Three-dimensional AFM images determined from different V_2O_5-porous film electrodes. (From Jung and Pyun, 2006a. *Electrochim. Acta* 51, 2646–2655, with permission.)

V_2O_5 film electrodes with various pore structures in 1 M LiClO$_4$/propylene carbonate solution (Jung and Pyun, 2006a). In this context, the fractal dimension values of several oxide surfaces were first determined by Farin et al. (1985) and Ozeki (1985). Generation of fractal metallic surfaces from electrochemical reduction of oxides has been studied by Kessler et al. (1996). The effect of pore structure in porous V_2O_5 film electrodes has been investigated in terms of fractal geometry (Figure 2.13 and Figure 2.14) (Jung and Pyun, 2006a). Studies dealing with diffusion phenomena at fractal interfaces for diffusion-controlled and nondiffusion-controlled electron transfer processes have recently been reviewed by Go and Pyun (2007).

3 Electrocatalysis

3.1 INTRODUCTION

Electrocatalytic processes have received considerable attention in the last decades because of their application in synthesis and sensing. The term *catalysis* is used for describing the modification in the reaction rate of a given chemical reaction by effect of the addition of a catalyst species. Two essential conditions have to be accomplished by catalytic processes: the thermodynamics of the reaction becomes unaltered, and the catalyst stays unchanged. Additionally, a common demand for catalysis is that the catalytic process involves small concentrations of the catalyst. In the most general view, the rate of the reaction can be either increased (positive catalysis) or decreased (negative catalysis), although, obviously, positive catalysis is preferentially desired.

The term *electrocatalysis* will be used in the following for designing electrochemical processes involving the oxidation or reduction of a substrate species, *S*, whose reaction rate is varied in the presence of a given catalytic species, Cat. The effect of electrocatalysis is an increase of the standard rate constant of the electrode reaction resulting in a shift of the electrode reaction to a lower overpotential at a given current density and a current increase. The faradaic current resulting from the occurrence of a catalytic electrode mechanism is called *catalytic current*. For a positive electrocatalysis, the current obtained in the presence of the catalyst must exceed the sum of the currents obtained for the catalyst and the substrate, separately, under selected experimental conditions (Bard et al., 2008). Three possible situations can be discerned:

1. The catalyst and the substrate are in the same phase, usually dissolved in the bulk solution (homogeneous catalysis).
2. The catalyst or the substrate is immobilized (via fixation, functionalization, adsorption, etc.) at the electrode surface (heterogeneous catalysis).
3. The catalyst is electrochemically generated at the electrode/electrolyte interface.

Homogeneous electrocatalysis in solution phase can be described via a regeneration mechanism where the catalyst reacts with the product of the electrode reaction involving the substrate to regenerate the initial electroactive species. This can be represented by the reaction sequence:

$$S^{ox} + e^- \rightarrow S^{red} \tag{3.1}$$

$$S^{ox} + Cat^{red} \rightarrow S^{red} + Cat^{ox} \tag{3.2}$$
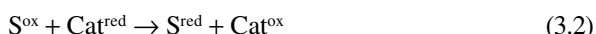
The reaction described by Equation (3.1) must have a formal potential that is larger (more positive) than the formal potential of the Cat redox system, but it must be so

مرجع دانشجویان و مهندسین مواد

irreversible that it is not significantly proceeding at potentials where Cat^{ox} is reduced according to:

$$Cat^{ox} + e^- \rightarrow Cat^{red} \tag{3.3}$$

The mentioned thermodynamic prerequisite that the formal potential of the substrate redox system must be more positive than the formal potential of the catalyst redox system means that, in principle, reduction of S^{ox} is easier compared to Cat^{ox}, but that kinetic constraints essentially hinder this process at potentials where the catalyst is oxidized. Then, the direct reduction of S^{ox} does not proceed electrochemically at potentials where Cat^{ox} is reduced (or maybe even at no accessible potential at all) but only via homogeneous redox reaction (Equation (3.2)) with Cat^{red}. In this context, the regeneration of the catalyst leads to much steeper concentration profiles of the catalyst in the diffusion reaction layer; that is, to a steeper concentration gradient that (see Chapter 1) means larger current.

The catalytic mechanism in solution phase described by Equations (3.1) and (3.2) is usually described in terms of a reversible electron transfer for the Cat system (Equation (3.3)) followed by a reaction operating under conditions of pseudo first-order kinetics (Nicholson and Shain, 1964). Thus, the shape of cyclic voltammograms (CVs) depends on the parameter $\lambda = kc_{cat}t$, where k is the rate constant for reaction (3.2) and c_{cat} is the concentration of catalyst. For low λ values, the catalytic reaction has no effect on the CV response and a profile equivalent to a single-electron transfer process is approached. For high λ values, s-shaped voltammetric curves are observed that can be described by (Bard and Faulkner, 2001):

$$i \approx \frac{nFAc\lambda^{1/2}}{1 + \exp[(nF/RT)(E - E^{o\prime})]} \tag{3.4}$$

Remarkably, the limiting current becomes independent of the potential scan rate ($i_{lim} = nFAcDKc_{cat}\lambda^{1/2}$), c being the concentration of substrate.

There are electrocatalytic systems where the catalyst is immobilized at the electrode surface. Typical examples involve the use of redox polymers or adsorbed species so that the substrate interchanges electrons with the catalyst, which is electrochemically regenerated (Murray et al., 1987). In this chapter, the electrocatalytic effects associated with porous materials will be discussed with regard to the two more frequent situations. The first one corresponds to cases in which the porous material acts as a catalyst for a given electrochemical process involving a substrate in solution phase, and the second corresponds to cases where the species in solution phase acts as a catalyst for an electrochemical process involving electroactive species in the porous material. Both situations can be applied to isolated electroactive centers that become attached to an electrochemically silent porous network, as in zeolites with encapsulated redox-active guests and cases where the entire porous material, which eventually can have semiconducting character and/or incorporate electroactive centers (Rolison, 1994), possesses electrocatalytic activity, as occurring in transition metal oxides (Lyons and Burke, 1987) and related materials.

3.2   ELECTROCATALYSIS BY SURFACE-CONFINED SPECIES

Rotating disk voltammetry is widely used for studying catalytic processes. For a reversible n-electron transfer process controlled by mass transport in solution, the limiting current, i_{lim} (μA), recorded in a linear potential scan voltammogram varies with the rotation rate, ω (sec^{-1}), following the Levich equation (Bard and Faulkner, 2001):

$$i_{lim} = 0.620 nFAcD^{2/3}\upsilon^{-1/6}\omega^{1/2} \tag{3.5}$$

where D denotes the diffusion coefficient (cm^2/sec) of the electroactive species, c is its bulk concentration (mol/cm^3), υ is the kinematic viscosity (cm^2/sec) of the solution, A is the electrode area (cm^2), and the other symbols have their customary meaning. This equation predicts that plots of i_{lim} vs. $\omega^{1/2}$ should be a straight line intersecting the origin. Deviations from the expected behavior can be attributed to deviations from ideality and kinetic complications.

Following Andrieux et al. (1982), for a mediated catalytic process, the limiting current should satisfy:

$$1/i_{lim} = 1/i_k + 1/nFAck\Gamma[1-(\delta/FAc_{cat}D_e)] \tag{3.6}$$

where the kinetic current, i_k, representing the current in the absence of mass transfer effect is introduced. In the above equation, Γ denotes the surface concentration of the catalyst in the film, k is the second-order rate constant for the catalytic reaction, δ is the film thickness, D_e is the diffusion coefficient for electrons in the film, and c_{cat} is the total volume concentration of the catalyst within the film. When the catalytic reaction becomes dominant, Equation (3.6) reduces to the Koutecky-Levich equation (Bard and Faulkner, 2001):

$$1/i_{lim} = 1/nFAck\Gamma + 1/0.620nFAcD^{2/3}\upsilon^{-1/6}\omega^{1/2} \tag{3.7}$$

and

$$i_k = nFAck\Gamma \tag{3.8}$$

3.3   ELECTROCATALYSIS AT MICROPARTICULATE DEPOSITS OF POROUS MATERIALS

Electrocatalytic sensing via microheterogeneous catalysts is based on the modification of electrode surfaces by attachment of solid materials having an electrocatalytic ability with respect to the oxidation/reduction of selected analytes in solution. As a result, the obtained electrochemical signal is enhanced, whereas eventually the signals of interfering species remain unchanged or are even depleted, thus enhancing the sensitivity and selectivity for determinations (Cox et al., 1991; Rolison et al., 1991). Electrode modification procedures include chemisorption of the modifier, formation of covalent bonds between the substrate electrode and the modifier, formation of homogeneous film coatings on electrodes, and formation of heterogeneous layers.

Microparticulate deposits of inorganic solids mechanically transferred to the surface of inert electrodes or dispersed in carbon paste or composite electrodes
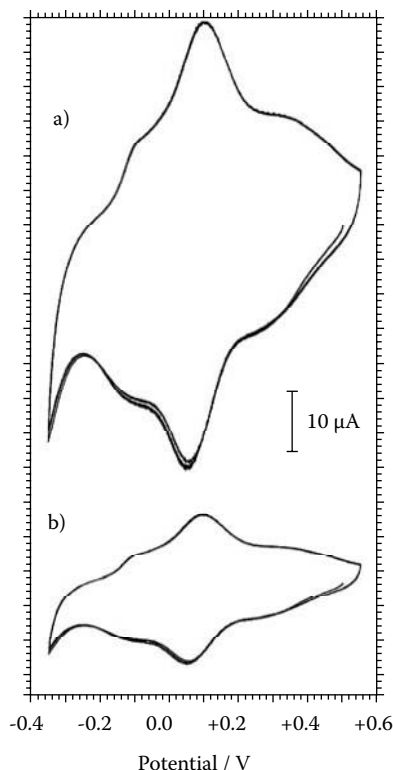
FIGURE 3.1 CVs for silicomolybdate-modified graphite electrodes immersed into 0.2 M H_2SO_4 containing: (a) 0.2 and (b) 0.0 mM concentrations of Cr(VI). Potential scan rate, 100 mV/sec.

or embedded into a conducting polymeric matrix, further fixed on the electrode surface, have been extensively used for electroanalytical sensing. Thus, coatings of transition metal oxides and related compounds have been used as effective catalysts for a variety of electrochemical processes (Trasatti, 1994). Such modi-fied electrodes are typically used as oxidizing agents in metal-based surface-modified glassy carbon electrodes for the amperometric sensing of substrates such as sugars and alditols, which are otherwise difficult to oxidize using conventional electrodes (see, e.g., Cataldi et al., 1995). Figure 3.1 shows an example of elec-trocatalytic behavior, corresponding to that exerted by silicomolybdate-modified electrodes with respect to Cr(VI) oxidation in aqueous acidic media. The voltam-metric response of the film electrode consists of three two-proton, two-electron couples, which can be represented by means of (Balamurugan and Chen, 2007):

$$H_4SiMo^{VI}_{12}O_{40} \xrightarrow{2H^+,2e^-} H_6SiMo^{VI}_{10}Mo^V_2O_{40} \xrightarrow{2H^+,2e^-}$$

$$H_8SiMo^{VI}_8Mo^V_4O_{40} \xrightarrow{2H^+,2e^-} H_{10}SiMo^{VI}_6Mo^V_6O_{40} \tag{3.9}$$
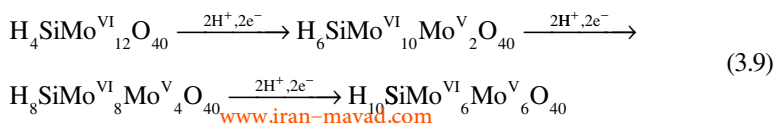
In the presence of Cr(VI) species, the currents for such processes are significantly enhanced and progressively increased on increasing the concentration of Cr(VI), as can be seen in Figure 3.1. The overall catalytic reaction can be represented as:

$$PPy/H_{10}SiMo^{VI}_{16}Mo^{V}_{6}O_{40} + Cr_2O_7^{2-} + 8H^+ \rightarrow PPy/H_4SiMo^{VI}_{12}O_{40} + 2Cr^{3+} \ 7H_2O$$

$$(3.10)$$
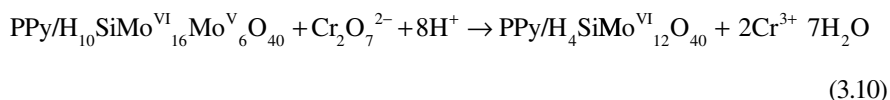
Dispersion of catalytic sites apparently enhances the electrocatalytic efficiency of such systems when compared to bulk metal electrodes (Casella et al., 1993). Accordingly, incorporation of catalytic centers into insulating materials can be considered a plausible methodology for obtaining sensitive and selective sensors. For this purpose, encapsulation of different redox-active species into micro- and mesoporous aluminosilicates has been described (Rolison, 1994; Rolison and Bessel, 2000). These systems combine site isolation, shape/size selectivity, and cation exchange capacity provided by the inorganic support with the intrinsic catalytic activity of redox centers. The protective effect exerted by the inorganic host can stabilize reactive organic intermediates (Scaiano and García, 1998; Doménech et al., 1999b; García and Roth, 2002) and enzymes (Inagaki et al., 1999) with highly specific catalytic properties (Doménech and Alarcón, 2002a; Doménech et al., 1999a, 2002b, 2003b, 2004b,c).

This scheme can be extended to nonconducting or semiconducting nanoporous solids incorporating redox-active centers via chemical doping prompted by sol-gel methodologies (Doménech and Alarcón, 2002b, 2003; Doménech et al. 2004b–d). Eventually, the materials can be electrochemically modified (Rolison and Bessel, 2000).

As occurring for thin films of redox polymers, there are three elements of porous electrode behavior crucial to its performance in electrocatalysis: the transport of a solution reactant to the catalytic sites within the porous system, the transport of electrolyte charge-balancing ions, and the electron transport across the solid, a process responsible for the regeneration of the initial oxidation state of the catalyst.

There are several possibilities depending on the conductivity of the porous support, its pore size distribution, the presence and mobility of electrolyte ions and/ or mobile redox mediators, and the type of attachment of catalytic centers to the support and its distribution. In the following, electrocatalysis at microheterogeneous deposits of insulating materials on inert electrodes will be described assuming that the microparticulate deposit, which is in contact with a given electrolyte solution, is distributed along a microheterogeneous layer covering the surface of a basal, metal-type conducting electrode. In the most direct electrocatalytic case, the solid incorporates electroactive centers, Cat, which can produce an electrocatalytic effect on the electrochemical oxidation/reduction of a given substrate, S, in solution. In classical electrocatalysis via redox films, there is a charge transfer process based on the diffusion of substrate molecules through the solution, interchange of electron with the immobile redox centers in the film, and subsequent electrochemical regeneration of the mediator, as schematically depicted in Figure 3.2. More complicated situations, however, can be handled; for instance, a redox mediator can be intercalated between the surface-confined catalyst and the substrate in solution (see Figure 3.3).
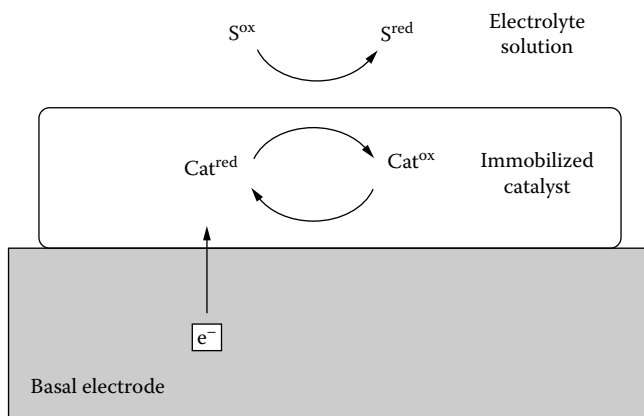
FIGURE 3.2   Schematic diagram of electrocatalysis performed with an immobilized catalyst.

Description of electrocatalytic processes in such modified electrodes can be derived from the intersection between the theory of Andrieux and Savéant (1980, 1988) for mediated electrocatalysis in redox polymers and those for metal oxide electrocatalysis (Lyons et al., 1992, 1994; Attard, 2001; Pleus and Schulte, 2001) and the recent models for the voltammetry of microparticles given by Lovric and Scholz (1997, 1999) and Oldham (1998) and combined by Schröder et al. (2000).

Following Schröder et al. (2000), electron transfer processes in these systems involve an initial reaction at the three-phase electrolyte/particle/electrode junction further extended via transport of electrons and charge-balancing ions in perpendicular directions. The propagation of the redox reaction in the particle implies electron hopping between immobile redox centers and the ingress/issue of charge-balancing
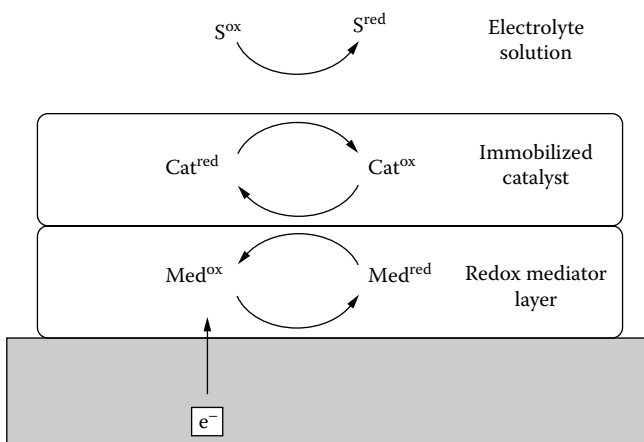
FIGURE 3.3   Schematic diagram of electrocatalysis via an immobilized catalyst aided by a redox mediator.

electrolyte ions into/from the lattice of the solid, as described in Chapter 2. Here, we consider that the catalyst can undergo a reduction process of the type:

$$\{Cat^{ox}\} + nM^+ + ne^- \rightarrow \{Cat^{red} \cdots nM^+\} \tag{3.11}$$
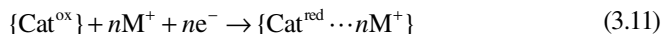
involving the entrance of electrolyte cations into the porous system. Following the same line of reasoning, oxidation processes involve the ingress of electrolyte anions into the solid:

$$\{Cat^{red}\} + nX^- \rightarrow \{Cat^{ox} \cdots nX^-\} + ne^- \tag{3.12}$$

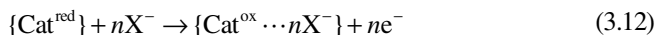Alternatively, reduction (oxidation) processes could involve the pass of mobile anions (cations) from the solid to the electrolyte, as previously discussed in Chapter 2. Unless stated, it will be in the following assumption that the above processes behave reversibly, the formal electrode potential of the Cat^{ox}/Cat^{red} couple being $E^{o\prime}_{cat}$.

In the case of microparticulate deposits, there is a possibility for different electrochemical pathways. First, we consider the catalyst immobilized and the substrate dissolved. The catalyst is electrochemically reduced via the process described by Equation (3.11) and, as previously noted, the direct reduction of S^{ox} (Equation (3.1) does not run electrochemically but only via heterogeneous redox reaction with Cat^{red}:

$$S^{ox} + \{Cat^{red} \cdots nM^+\} \rightarrow \{Cat^{ox}\} + S^{red} + nM^+ \tag{3.13}$$
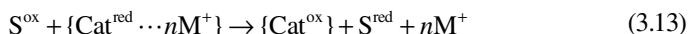
This situation is schematized in Figure 3.4. In several cases, the catalytic effect is exerted by electrochemically generated redox centers as described by Abbà et al. (1994) for the electroreduction of CO_2 at Ni(II) complexes of azacyclams.
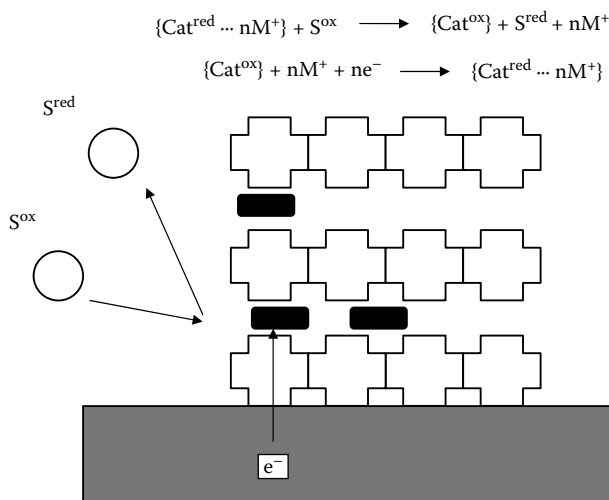
FIGURE 3.4 (See color insert following page 94.) Diagram for possible electrocatalytic processes involving immobilized catalyst species ($E_S^{o\prime} > E_{cat}^{o\prime}$).

$$\text{Cat}^{ox} + n\text{e}^- \longrightarrow \text{Cat}^{red}$$

$$\text{Cat}^{red} + \{\text{S}^{ox}\} + n\text{M}^+ \longrightarrow \text{Cat}^{ox} + \{\text{S}^{red} \cdots n\text{M}^+\}$$
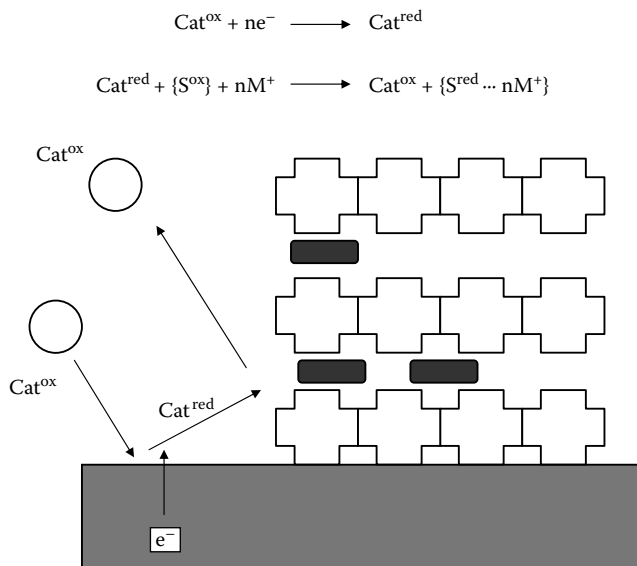
FIGURE 3.5 Diagram for possible electrocatalytic processes involving immobilized substrate species.

In the second case, the substrate is immobilized and the catalyst is dissolved. Now, the kinetically constrained electrochemical reduction of immobilized species $\{\text{S}^{ox}\}$ can be represented as:
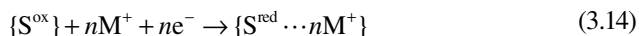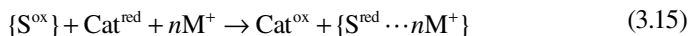
$$\{\text{S}^{ox}\} + n\text{M}^+ + n\text{e}^- \rightarrow \{\text{S}^{red} \cdots n\text{M}^+\} \tag{3.14}$$

Then, the catalyst species in solution, which can be electrochemically reduced as represented by Equation (3.3), can act as electrocatalyst for the oxidation or reduction of immobilized species, as schematized in Figure 3.5. The catalytic reaction can be represented as:

$$\{\text{S}^{ox}\} + \text{Cat}^{red} + n\text{M}^+ \rightarrow \text{Cat}^{ox} + \{\text{S}^{red} \cdots n\text{M}^+\} \tag{3.15}$$

Finally, electrocatalysis can proceed via adduct formation between immobilized sites and species in solution and subsequent solid-state reduction of that adduct species. For the case where the substrate is in solution and the catalyst is immobilized, this situation can be represented as (Figure 3.6):

$$\text{S}^{ox} + \{\text{Cat}^{red} \cdots n\text{M}^+\} \rightarrow \{\text{S}^{ox} \cdots \text{Cat}^{red} \cdots n\text{M}^+\} \tag{3.16}$$

$$\{\text{S}^{ox} \cdots \text{Cat}^{red} \cdots n\text{M}^+\} \rightarrow \{\text{S}^{red} \cdots \text{Cat}^{ox} \cdots n\text{M}^+\} \rightarrow \text{S}^{red} + \{\text{Cat}^{ox}\} + n\text{M}^+ \tag{3.17}$$

Depending on the possible interaction between substrate species and redox centers of the solid, one can consider: (1) outer sphere electron transfer processes in the electrolyte-particle interface and (2) inner-sphere mechanism, involving composition changes in the catalyst and the substrate.
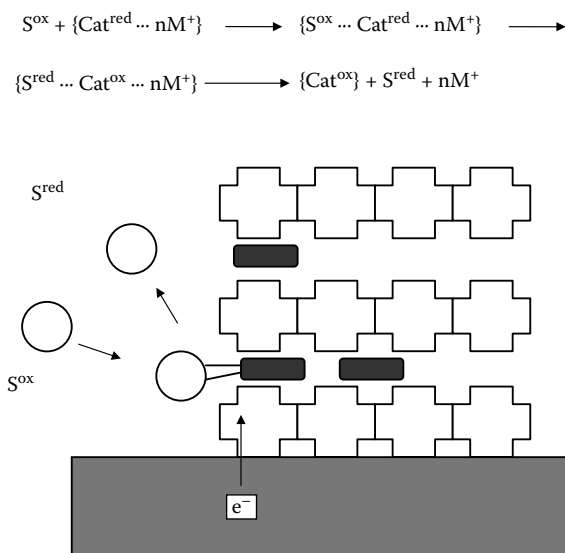
Depending on the site isolation of the catalyst centers two possible extreme cases appear: (1) close vicinity with unhindered electron hopping between adjacent redox centers; (2) extreme site isolation, so that there is no possible electron hopping between redox centers of the solid. In this case, substrate-mediated electron transfer is the unique possibility for propagating the redox reaction through the particle.

Depending on the size of electrolyte ions and substrate molecules with respect to the size of the pores and channels of the solid, one can consider the following: (1) Both substrate molecules and electrolyte counterions can move across the solid; then, the catalytic process can occur in the entire bulk of the (porous) solid. (2) Only electrolyte counterions can diffuse within the solid or only substrate molecules can move across the solid. (3) Neither substrate molecules nor electrolyte ions can diffuse in the solid; here, the catalytic process is confined to the surface of the solid particles.

The possibility of different electrocatalytic pathways can be illustrated by the oxidation of 1,4-dihydrobenzoquinone (H_2Q) in aqueous media at nicotinamide adenine nucleotide coenzyme (NADH) encapsulated within SBA-15 and MCM-14 mesoporous aluminosilicates—NADH@SBA and NADH@MCM, respectively (Doménech et al., 2006b). Here, a molecule with biocatalytic activity, NADH, and having a rich electrochemistry (Blaedel and Jenkins, 1975; Moiroux and Elving, 1978, 1979), was attached to two different mesoporous aluminosilicates that have in common an ordered structure based on hexagonal channels along with a complementary set of disordered micropores, which provides connectivity between the channels through the silica (Kruk et al., 2000; Ruthstein et al., 2003) but differing in their pore size and aluminum content (Si/Al molar ratio = 13 and ∞ for MCM-41 and for SBA-15, respectively). Figure 3.7 compares the CV response of a 2.5-mM solution of H_2Q in phosphate buffer (pH 7.0) at unmodified and NADH@MCM- and NADH@SBA-modified glassy carbon electrodes.

In contact with phosphate buffer, NADH@MCM- and NADH@SBA-modified electrodes display a weak, apparently irreversible oxidation peak at ca. +0.74 V. This process corresponds to the electrochemical oxidation of NADH to β-nicotinamide adenine dinucleaotide, NAD^+, which in turn, following literature (Moiroux and Elving, 1978), is electrochemically reduced to NADH at potentials ca. −1.0 V (small cathodic peak in Figure 3.7b).

At unmodified electrodes, the hydroquinone/quinone redox couple exhibits well-defined peaks at potentials of +0.22 V (anodic) and +0.04 V (cathodic), as depicted in Figure 3.7a. This response corresponds to a relatively complicated mechanism involving proton-assisted electron transfer processes (Laviron, 1984; Howell and Wightman, 1984) also mediated by solution electron transfer reactions (Evans, 1990). At NADH@MCM-modified electrodes, the voltammetric profile remained essentially unchanged, whereas H_2Q-centered peak currents were significantly enhanced (Figure 3.7b). At NADH@SBA, however, the response of H_2Q solutions consisted of two anodic peaks at +0.22 and +0.74 V (Figure 3.7c), both being significantly increased with respect to peaks recorded for NADH@SBA in the absence of H_2Q and in H_2Q solutions at unmodified electrodes.

$$S^{ox} + \{Cat^{red} \cdots nM^+\} \longrightarrow \{S^{ox} \cdots Cat^{red} \cdots nM^+\} \longrightarrow$$

$$\{S^{red} \cdots Cat^{ox} \cdots nM^+\} \longrightarrow \{Cat^{ox}\} + S^{red} + nM^+$$
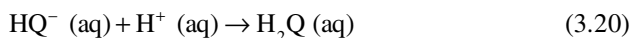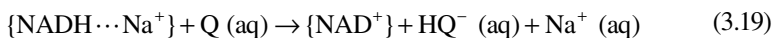

FIGURE 3.6 Diagram for possible electrocatalytic processes involving surface adduct formation between the substrate origin ally in solution and immobilized catalyst species.

This response can be rationalized by assuming that two different electrocatalytic pathways, where H_2Q acts as solution-phase catalyst on solid-state oxidation of NADH to NAD^+, are operative. First, for NADH@MCM, a reaction/regeneration mechanism as described by Equations (3.15) and (3.16) operates, the catalytic process being initiated by the electrochemical oxidation of hydroquinone to quinone, Q:

$$H_2Q \ (aq) \rightarrow Q + 2H^+ \ (aq) + 2e^- \tag{3.18}$$
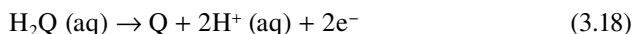
The resulting quinone diffuses across the mesoporous system and reacts with the NADH catalyst. As a result, the direct reduction of the immobilized NADH substrate does not proceed electrochemically but only via heterogeneous redox reaction with the oxidized form of the hydroquinone catalyst in solution (see Figure 3.5).

Because of the anionic nature of NADH (β-nicotinamide adenine dinucleotide reduced disodium salt), its attachment requires the parallel attachment of sodium ions, so that the materials can be represented as $\{NADH \cdots Na^+\}$. Then, the catalytic reaction can be represented as:

$$\{NADH \cdots Na^+\} + Q \ (aq) \rightarrow \{NAD^+\} + HQ^- \ (aq) + Na^+ \ (aq) \tag{3.19}$$

$$HQ^- \ (aq) + H^+ \ (aq) \rightarrow H_2Q \ (aq) \tag{3.20}$$

regenerating the hydroquinone catalyst, which reinitiates the catalytic cycle, thus resulting in significant current enhancement.

For NADH@SBA, a different mechanism can be proposed, assuming that H_2Q forms a surface-confined adduct with the substrate, following the reaction scheme

summarized by Equation (3.17). As a result, two successive substrate- and catalyst-centered electron transfer processes are observed:

$$\{NADH \cdots Na^+\} + H_2Q \ (aq) \rightarrow \{H_2Q - NADH \cdots Na^+\} \tag{3.21}$$

$$\{H_2Q - NADH \cdots Na^+\} \rightarrow \{Q - NADH \cdots Na^+\} + 2H^+ \ (aq) + 2e^- \tag{3.22}$$

$$\{Q - NADH \cdots Na^+\} \rightarrow \{Q - NAD^+\} + Na^+ \ (aq) + H^+ \ (aq) + 2e^- \tag{3.23}$$
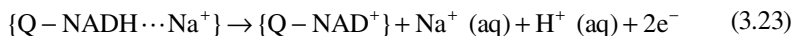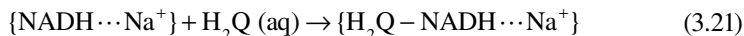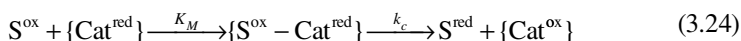
Charge conservation is ensured by the release of protons and/or sodium ions from the mesoporous system to the electrolyte solution. This mechanism is consistent with the observation of two peaks (see Figure 3.7c) at the potentials observed for the noncatalyzed oxidation of H_2Q and NADH in solution. Consistently, chronoamperometric data (*vide infra*) can be approached to those theoretically predicted for an electron transfer process preceded by a chemical reaction in solution phase, as demanded, roughly, by a process where adduct formation (Equation 3.16) acts as a rate-controlling step.

The remarkable differences between the electrocatalytic responses observed for NADH@MCM and NADH@SBA can be attributed to the existence of at least two competing pathways represented by Equations (3.19)–(3.20) (reaction/regeneration scheme) and Equations (3.21)–(3.23) (adduct formation), respectively, where H_2Q acts as catalyst in solution and NADH acts as immobilized substrate. Apparently, hydroquinone-NADH adduct formation is considerably slower at NADH@SBA than at NADH@MCM, a feature that would be associated to the different acidity/polarity of the lattices—because MCM-41 contains both Bronsted (Al(OH)Si groups) and Lewis (extraframework Al^{3+} centers) acid sites, whereas SBA-15 is a pure silica material—and pore size (3.2 nm for MCM-41 and 6.0 nm for SBA-15). Taking into account that adduct formation presumably requires a preorganization of NADH units to adopt the most favorable conformation for lying with H_2Q, larger cavities should favor conformational preorganizing and, consequently, adduct formation, in agreement with the aforementioned observations, but a significant influence of polarity/acidity effects (Corma et al., 2004) cannot be ruled out.

3.4 MODELING ELECTROCATALYSIS AT MICROHETEROGENEOUS DEPOSITS OF POROUS MATERIALS: THE STEADY-STATE APPROACH

Let us consider the formation of substrate-catalyst adducts that can be reduced/oxidized via electron hopping. This situation can be represented by (see Figure 3.7):

$$S^{ox} + \{Cat^{red}\} \xrightarrow{K_M} \{S^{ox} - Cat^{red}\} \xrightarrow{k_c} S^{red} + \{Cat^{ox}\} \tag{3.24}$$

$$\{Cat^{ox}\} + e^- \xrightarrow{k_e} \{Cat^{red}\} \tag{3.25}$$

In these and in subsequent equations, charge-compensating metal ions in the solid will be omitted for brevity. We are assuming that the catalyst is homogeneously
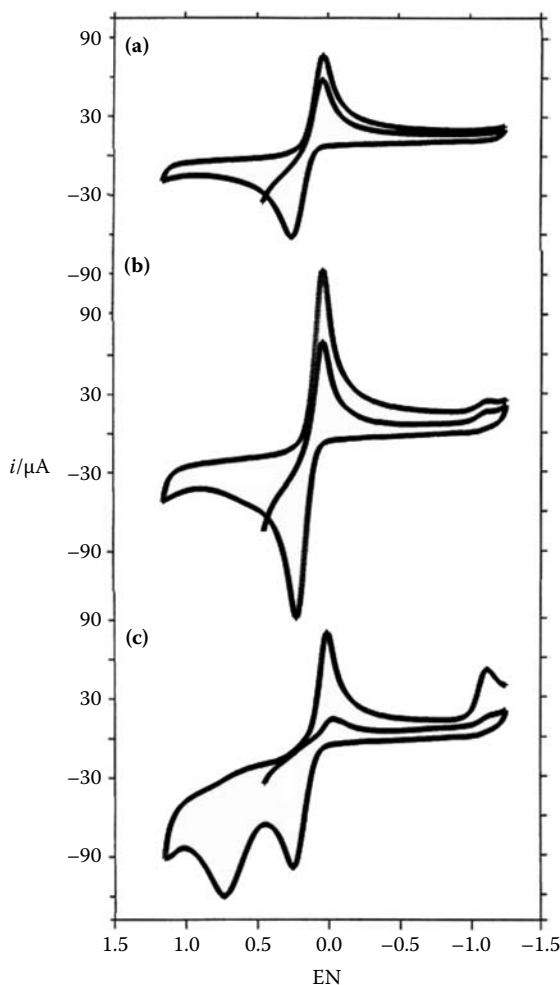
FIGURE 3.7 CVs at a 2.5 mM H$_2$Q solution in 0.50 M phosphate buffer, pH = 7, at (a) unmodified glassy carbon electrode; (b) NADH@MCM-modified electrode; and (c) NADH@ SBA-modified electrodes. Potential scan rate, 50 mV/sec. (From Doménech et al., 2006b. *Electrochim. Acta* 51, 4897–4908, with permission.)

distributed in a thin film of the surface of a basal electrode (see Figure 3.8). If the substrate can diffuse through the catalyst layer under steady-state conditions, the equation describing the transport and kinetics in the layer will be

$$D_S \frac{d^2[S]}{dx^2} - \frac{k_c c_{cat}[S]}{K_M + [S]} = 0 \tag{3.26}$$

where D_S represents the diffusion coefficient of the substrate through the layer, [S] is its concentration at distance x from the electrode, and c_{cat} is the total concentration
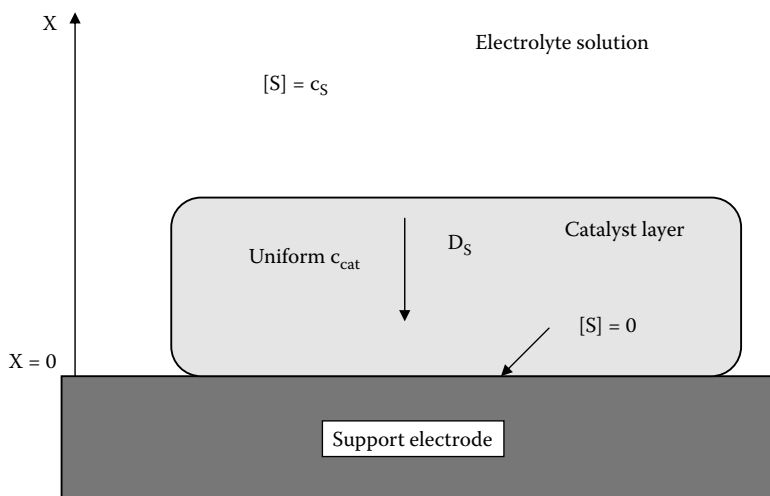
FIGURE 3.8 Schematic diagrams modeling electrocatalysis via microheterogenous systems under steady-state conditions.

of catalyst. Following Lyons et al. (1992), it will be assumed that Michaelis-Menten (or Langmuir-Hinshelwood) kinetics apply, k_c being the catalytic rate constant (sec^{-1}) and K_M the Michaelis constant (mol/cm^3). Neglecting concentration polarization in the solution, we consider several cases. First, if the concentration of the substrate can be taken as uniform throughout the catalyst layer, a situation approached by thin films, and assuming that there is no concentration polarization of the substrate in the film, the flux of substrate J_S (mol/cm^2 s) is given by:

$$J_S = \frac{k_c c_{cat} L c_S}{K_M + K c_S} \tag{3.27}$$

where L is the thickness of the catalyst layer, c_S is the concentration of substrate in the bulk of the solution, and K is the partition coefficient whose value can approach unity for porous materials. When the concentration of substrate in the film is not uniform, four extreme cases can be considered depending on film thickness and substrate concentration. For low substrate concentrations and thin films, the flux of substrate is described by:

$$J_S = k_c c_{cat} L K c_S / K_M \tag{3.28}$$

whereas for low substrate concentrations and thick films, the flux approaches:

$$J_S = K c_S (k_c c_{cat} DS / K_M)^{1/2} \tag{3.29}$$

Here, the reaction kinetics will be more rapid than the diffusive transport of the substrate and there is a large concentration gradient of substrate across the film.

For high substrate concentrations, the catalyst is saturated by the substrate. Then, the flux of independent substrate concentration as well as the rate-determining step is the decomposition of the intermediate substrate catalyst adduct, described by the rate constant k_c. Here, the flux of substrate satisfies:

$$\frac{1}{J_S} = \frac{k_M}{K_c L K c_{cat} c_S} + \frac{1}{k_c L c_{cat}}$$
(3.30)

This equation corresponds to the Lineweaver-Burk kinetic equation (Lyons et al., 1992, 1994) and can be transformed into an equation giving the dependence of kinetic currents, i_k, on the concentration of substrate in the solution bulk. Values of i_k at different concentrations of substrate can be determined from the limiting, steady-state currents, i_{lim}, obtained, for instance, as plateau currents in rotating disk voltammetry, using Equation (3.6). For the case of thin films with a surface concentration of catalytic centers Γ_{cat} (mol/cm^2) over an electrode of area A, one can write:

$$\frac{1}{i_k} = \frac{K_M}{nFAk_c\Gamma_{cat}c_S} + \frac{1}{nFAk_c\Gamma_{cat}}$$
(3.31)

Accordingly, plots of $1/i_k$ vs. $1/c_S$ should provide straight lines whose slope and ordinate at the origin enable calculating K_M and k_c, providing that Γ_{cat} is known.

The preceding expression can be rewritten to give the Eadie-Hofstee plot, which stems from the following equation:

$$\frac{i_L}{c_S} = \frac{nFAk_c\Gamma_{cat}}{K_M} + \frac{i_L}{K_M}$$
(3.32)

Application of such equations to the electrochemical oxidation of mannitol in 0.10 M NaOH aqueous solution (occurring at potentials greater than +0.90 V vs. AgCl/Ag) using rotating disk voltammetry at glassy carbon electrodes modified with α and μ cobalt cordierites Co$_2$Al$_4$Si$_5$O$_{18}$, (Doménech et al., 2004d) is shown in Figure 3.9 and Figure 3.10. In these experiments, the concentration of mannitol was varied between 2.0×10^{-5} and 2.0×10^{-3} M, and rotation rates ranged between 200 and 800 sec^{-1}.

3.5 MODELING ELECTROCATALYSIS AT MICROHETEROGENEOUS DEPOSITS OF POROUS MATERIALS: TRANSIENT RESPONSES

Electrochemical data recorded under no steady-state conditions can also be used for studying electrocatalytic processes involving porous materials. In cases where the catalytic system can be approached by homogeneous electrocatalysis in solution phase, variation of cyclic voltammetric profiles with potential scan rate (Nicholson and Shain, 1964) and/or, for instance, square-wave voltammetric responses with square-wave frequency (O'Dea et al., 1981; O'Dea and Osteryoung, 1993; Lovric, 2002) can be used. This situation can, in principle, be taken for highly porous materials where substrate transport, as well as charge-balancing ion transport, is allowed. On first examination, the catalytic process can be approached in the same manner
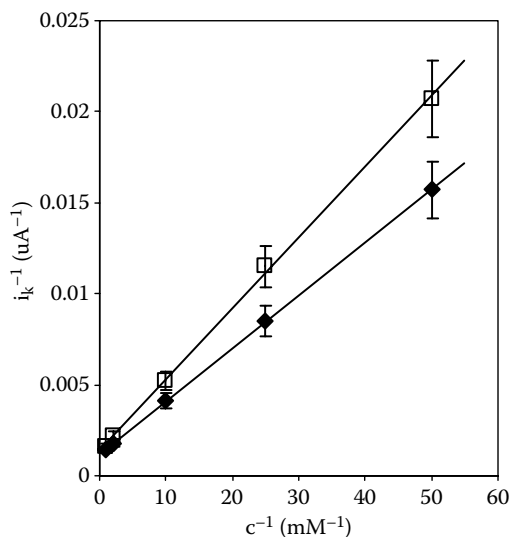
FIGURE 3.9 Linewaver-Burke plots of $1/i_k$ vs. $1/c$, from rotating disk voltammograms recorded for α (squares) and μ (rhombs) cobalt cordierite-modified glassy carbon electrodes (GCEs) in contact with a 1.25 mM mannitol plus 1.0 M NaOH aqueous solution. Potential scan rate, 50 mV/sec.
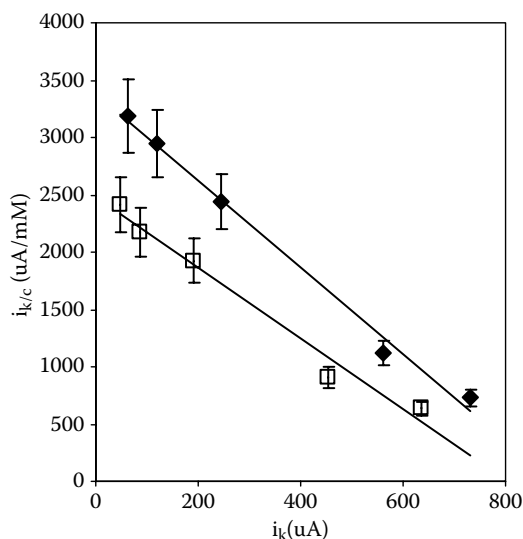
FIGURE 3.10 Eadie-Hofstee plots of i_k/c vs. i_k, from rotating disk voltammograms recorded for α (squares) and μ (rhombs) cobalt cordierite-modified GCEs in contact with a 1.25 mM mannitol plus 1.0 M NaOH aqueous solution. Potential scan rate, 50 mV/sec.

as in a solution phase described by Equations (3.1) and (3.2). The catalytic current is then expressed by:

$$i_{cat}/i_d = (kc_{cat}t)^{1/2}\{(kc_{cat}t)^{1/2}erf[(kc_{cat}t)^{1/2}]+(kc_{cat}t)^{-1/2}\exp(-kc_{cat}t)\} \qquad (3.33)$$

where i_d denotes the current for the unaltered, diffusion-controlled, single-electron transfer process described by Equation (3.1). When the term kc_{cat} exceeds 2, the error function (erf) reduces to 1 and the above equation can be approached to:

$$i_{cat}/i_d \approx (\pi kc_{cat}t)^{1/2} \qquad (3.34)$$

In several cases, when the electrocatalytic pathway involves adduct formation between immobilized units of the catalyst and the mobile substrate permeating the porous solid, the mechanism can be described in terms of a charge transfer process preceded by a relatively slow chemical reaction. Here, the chronoamperometric current can be approached by (Koutecky and Brdicka, 1947; Bard and Faulkner, 2001):

$$i = nFAcD^{1/2}(Kk_f)^{1/2}\exp[Kk_ft][erf(Kk_ft)^{1/2}] \qquad (3.35)$$

where k_f represents the rate constant of the direct preceding (adduct formation) reaction and K is the equilibrium constant for this process. Figure 3.11 compares experimental data for chronoamperometries (CAs) recorded at NADH@SBA-modified
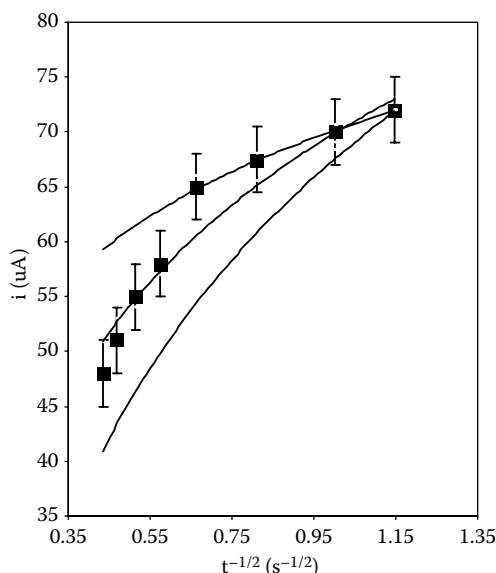
FIGURE 3.11 Plots of i vs. $t^{-1/2}$ for CAs recorded at NADH@SBA-modified glassy carbon electrodes immersed into 2.0 mM H_2Q solution in 0.50 M phosphate buffer (pH = 7.0). Experimental data points and theoretical curves from Equation (3.35) using different Kk_f values. Applied potential +0.95 V vs. AgCl/Ag. (Adapted from Doménech et al., 2006b. *Electrochim. Acta* 51, 4897–4908, with permission.)

glassy carbon electrodes in contact with H_2Q solution in aqueous phosphate with theoretical curves from Equation (3.35) using different values of the Kk_f parameter.

The case of charge transfer process preceded by a first-order bulk-surface reaction has been described by Guidelli (1971). Here, the parent electroinactive species is transformed into an electroactive species both through a homogeneous chemical reaction taking place within a thin solution layer adjacent to the electrode (with rate constant, k_f) and through a heterogeneous chemical reaction catalyzed by the electrode surface (with rate constant k_{ads}). The chronoamperometric current becomes:

$$\frac{i}{i_d - i} = t^{1/2} \frac{(3/5)[k_f K \Gamma + (k_{ads} D/K)^{1/2} t^{1/2}]}{(12 Dt/7\pi)^{1/2} + K\Gamma} \tag{3.36}$$

In this equation, i_d represents the diffusion limiting current given by $i_d = (12D/7\pi)^{1/2} nFAct^{1/2}$.

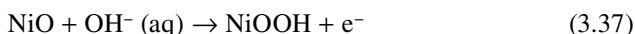## 3.6   ELECTROCATALYTIC MECHANISMS

Elucidation of the mechanism of the catalytic process is a relatively complicated task because of the variety of factors influencing the catalytic reaction. For instance, preconcentration of redox species in the porous films can result in an apparent surface excess, similar to adsorption. Here, semi-integral analysis of voltammetric curves can aid in separating diffusional and surface-confined components (Freund and Brajter-Toth, 1992).

One of the most intensively studied systems is probably the oxidation of sugars and polyalcohols in aqueous alkaline solutions at electrodes modified with transition metal oxides, typically NiO. Here, oxidation signals at ca. +0.6 V vs. AgCl/Ag were obtained in 0.20 M NaOH.

Electrochemical oxidation of sugars and alditols is a kinetically controlled process where the rate-determining step is the abstraction of hydrogen from the carbon atom in the α position with respect to the alcohol group, the overall electrochemical process being significantly influenced by molecular dimensions, preferred orientation, and steric hindrance as first described by Konaka et al. (1969).

Following Casella et al. (1993), one of the possible pathways can be represented by the following sequence of reactions:

$$NiO + OH^- \text{ (aq)} \rightarrow NiOOH + e^- \tag{3.37}$$

$$RCH_2OH \text{ (aq)} + NiO \rightarrow NiO(RCH_2OH) \text{ (ads)} \tag{3.38}$$

$$NiO(RCH_2OH) \text{ (ads)} + NiOOH \rightarrow NiO + NiO(R{\cdot}CHOH) \text{ (ads)} + H_2O \tag{3.39}$$

$$NiO(R{\cdot}CHOH) \text{ (ads)} + NiOOH \rightarrow NiO + NiO(RCOH) \text{ (ads)} + H_2O \tag{3.40}$$

where (ads) denotes adsorbed species. In this scheme, the rate-determining step would be reaction (3.39) (Xie and Huber, 1991). At more positive potentials, oxygen evolution is also catalyzed by active $\cdot OH$ radicals generated in the oxide surface:

$$NiOOH \rightarrow NiO + {\cdot}OH \tag{3.41}$$

$$2 \; {\cdot}OH \rightarrow H_2O + \tfrac{1}{2}O_2 \tag{3.42}$$

with NiOOH being electrochemically regenerated via the process described by Equation (3.37).

To study the kinetics of the catalytic process, Tafel representations from the current-potential data in the rising portion of the voltammetric curve can be used (Doherty and Vos, 1992). Under several conditions, plots of log i vs. E lead to straight lines whose slope (TSL) satisfies (Lyons et al., 1994):

$$(\text{TSL}) = \frac{\partial(\log i)}{\partial E} = \frac{\beta g F}{2.303 RT} \qquad (3.43)$$

Here, β represents the electrochemical symmetry factor (typically close to 0.5), and g is a numerical coefficient representative of the fraction of potential effectively experienced by the substrate. It is assumed that, if the initial electron transfer is rate-determining, then an inverse Tafel slope $(\text{TSL})^{-1}$ of 120 mV/decade would be predicted if the substrate was located at the outer Helmholtz plane (typically placed about 1 nm of the oxide surface) (Lyons et al., 1992, 1994). If the substrate is located in a reaction plane closer to the oxide surface than the outer Helmholtz plane when it undergoes a reaction, inverse Tafel slopes of ca. 240–300 mV/decade are predicted (Lyons et al., 1994).

An illustration of this type of analysis is provided by the catalysis associated to the electrochemical oxidation of cysteine at electrodes modified with vanadium-doped zircons, $V_x ZrSiO_4$, prepared from sol-gel methodologies (Doménech and Alarcón, 2003). Figure 3.12 shows x-ray diffraction patterns for $V_x ZrSiO_4$ specimens after annealing the corresponding gel precursor at 1600ºC for 24 h. Here, well-defined diffraction peaks of zircon, eventually accompanied by one cristobalite peak, appear.
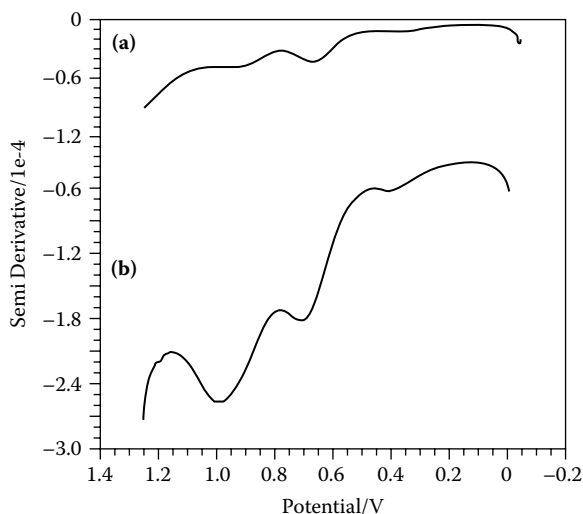
Figure 3.13 presents typical square-wave voltammograms for (a) an unmodified electrode and (b) a $V_{0.04} ZrSiO_4$-modified electrode immersed into an alkaline solution of cysteine plus 0.10 M NaOH. Here, three oxidation signals appear: at +0.20, +0.60, and +0.80 V vs. AgCl/Ag. Figure 3.14 shows E vs. log i inverse Tafel plots from data recorded in the rising portion of each voltammetric peak in CV experiments at relatively low scan rate. The slope of such representations was 220 ± 15, 100 ± 10, and 250 ± 15 mV/decade for oxidation processes at +0.20, +0.60, and +0.80 V, respectively. The existence of two different slopes, complemented by peak potential shift with scan rate and peak current variation with potential scan rate, led researchers to propose different electrochemical pathways. Peaks at +0.20 and +0.60 V can be attributed to thiolate-centered processes, whereas the peak at +0.80 V can be assigned to carboxylate oxidation, as judged via comparison with the electrochemistry of nonthiolated aminoacids. On the basis of the obtained inverse Tafel slope, the first thiolate-localized oxidation process involves a strong interaction between the substrate and the surface-confined vanadium centers, a situation that also applies to the oxidation wave at +0.80 V. In contrast, the oxidation at +0.60 V should involve cysteine molecules located in the outer Helmholtz plane. Since the oxidation potential is lower than that for the oxidation of vanadium centers (Doménech and Alarcón, 2003), the catalytic mechanism for strong cysteine
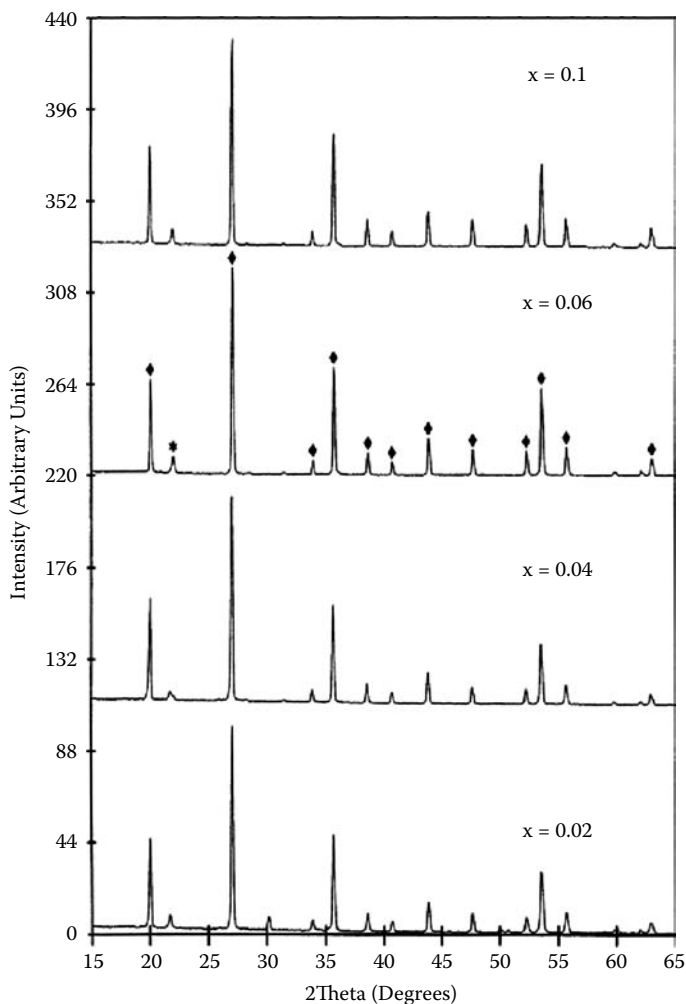
FIGURE 3.12 X-ray diffractograms for $V_x ZrSiO_4$ specimens with different vanadium loadings after annealing the corresponding gel precursor at 1600ºC during 24 h. ♦, zircon; *, cristobalite. (From Doménech and Alarcón, 2003. *Instrum. Sci. Technol.* 31, 121–140, with permission.)

fixation (peak at +0.20 V) can be attributed the formation of vanadium-cysteine adducts subsequently oxidized:
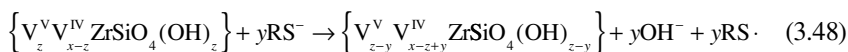
$$\left\{V_x^{IV} ZrSiO_4\right\} + yRS^- \rightarrow \left\{V_x^{IV} ZrSiO_4\right\} \cdots (RS^-)_y \tag{3.44}$$

$$\left\{V_x^{IV} ZrSiO_4\right\} \cdots (RS^-)_y \rightarrow \left\{V_x^{IV} ZrSiO_4\right\} \cdots (RS\cdot)_y + ye^- \tag{3.45}$$

$$\left\{V_x^{IV} ZrSiO_4\right\} \cdots (RS\cdot)_y \rightarrow \left\{V_x^{IV} ZrSiO_4\right\} + (y/z)(RS - SR) \tag{3.46}$$
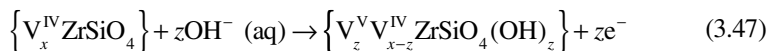
FIGURE 3.13 Square-wave voltammograms at (a) unmodified graphite and (b) $V_{0.04}ZrSiO_4$-modified graphite electrodes immersed into 2.50 mM cysteine plus 0.10 M NaOH. Potential step increment, 4 mV; square-wave amplitude, 25 mV; frequency, 5 Hz.
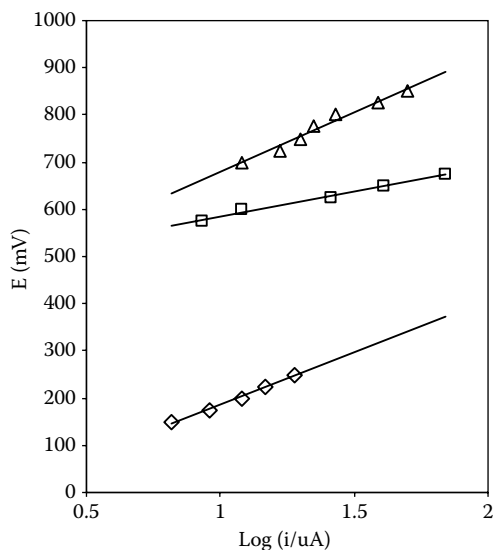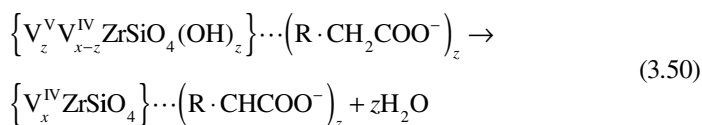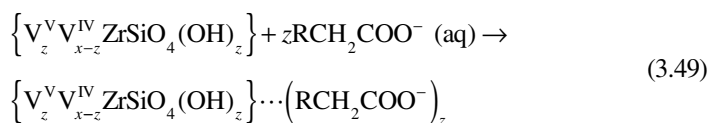

FIGURE 3.14 Tafel plots for oxidation waves recorded in CVs at a $V_{0.04}ZrSiO_4$-modified graphite electrode immersed into 2.50 mM cysteine plus 0.10 M NaOH. Potential scan rate, 20 mV/sec.

the oxidation product being presumably a dimeric dimercapto form, as described for several thiol compounds (Howie et al., 1977). The thiolate-centered, outer sphere oxidation process occurring at +0.60 V, a potential slightly more positive than that for V(IV) to V(V) oxidation in V_xZrSiO_4 materials, can be assigned to an oxidation/regeneration pathway of the type:

$$\left\{ V_x^{IV}ZrSiO_4 \right\} + zOH^- \ (aq) \rightarrow \left\{ V_z^V V_{x-z}^{IV}ZrSiO_4(OH)_z \right\} + ze^- \tag{3.47}$$

$$\left\{ V_z^V V_{x-z}^{IV}ZrSiO_4(OH)_z \right\} + yRS^- \rightarrow \left\{ V_{z-y}^V V_{x-z+y}^{IV}ZrSiO_4(OH)_{z-y} \right\} + yOH^- + yRS \cdot \tag{3.48}$$

The carboxylate-localized oxidation recorded at more positive potentials involves electron transfer between surface V(V) centers electrochemically generated and the substrate. Tentatively, the process should be initiated by the electron transfer process described by Equation (3.47) and followed by:

$$\left\{ V_z^V V_{x-z}^{IV}ZrSiO_4(OH)_z \right\} + zRCH_2COO^- \ (aq) \rightarrow$$
$$\left\{ V_z^V V_{x-z}^{IV}ZrSiO_4(OH)_z \right\} \cdots \left(RCH_2COO^- \right)_z \tag{3.49}$$

$$\left\{ V_z^V V_{x-z}^{IV}ZrSiO_4(OH)_z \right\} \cdots \left(R \cdot CH_2COO^- \right)_z \rightarrow$$
$$\left\{ V_x^{IV}ZrSiO_4 \right\} \cdots \left(R \cdot CHCOO^- \right)_z + zH_2O \tag{3.50}$$

The reaction progresses by involving a subsequent multistep pathway. Such schemes are, in principle, consistent with the observed variation in peak currents and potentials with frequency in square-wave voltammetries. In particular, it was observed that the height of peaks at +0.20 and +0.80 V, both involving strong substrate-catalyst interactions, increases at the expense of the peak at +0.60 V, which is associated to a weaker substrate-catalyst interaction, on decreasing square-wave frequency. This can be rationalized by considering that strong substrate-catalyst interactions are favored by long-time experiments, where penetration of the substrate in the external boundary region of the catalyst is larger than that in short-time ones.

For our purposes, the relevant point to emphasize is that electrocatalytic processes can involve different catalytically active sites and/or different catalytic mechanisms. These features are of considerable interest for sensing because they enhance the possibilities of obtaining highly selective responses for selected analytes by modulating the structural environment and concentration of catalytic sites in doped materials. This matter will be treated in more detail in Chapter 9.

# 4 Electrochemistry of Aluminosilicates

4.1 INTRODUCTION

Aluminosilicates can be regarded as a large group of nanostructured materials having in common a skeleton based on tetrahedral SiO_4 units in which a certain number of silicon atoms have been isomorphically substituted by aluminum ones. As a result, a defect of positive charge is produced in the lattice. Compensation of this excess of negative charge requires the attachment of cationic species to the aluminosilicate framework. SiO_4 and AlO_4 tetrahedral units act as building units for constructing a wide variety of structures, including porous (zeolites, sepiolite) to laminar aluminosilicates (montmorillonite, kaolinite). Since the preparation (Beck et al., 1992) of periodic mesoporous silica (MCM-41), a variety of silica-based mesoporous materials have been synthesized with variable degree of ordering, stability, and Al/Si ratios. An important group of materials is constituted by porous silica spheres (Hah et al., 2003).

The ionic nature of the cationic attachment allows for an easy ion exchange in such materials, but at the same time rigid porous structures exert a remarkable size- and eventually charge-selectivity for incorporating guest ions. It should be noted, however, that adsorption of guest species onto the external surface of the crystals of such materials can, in general, occur. In particular, laminar silicates can adsorb guest species in the interlaminar spaces, thus acting as flexible hosts with low size selectivity. The dynamic size of species that can enter through the zeolite pores is given by their kinetic diameter, taken as the intermolecular distance of the closest approach for two molecules colliding with zero initial kinetic energy (Breck, 1974).

4.2 ZEOLITES

Zeolites are microporous crystalline aluminosilicates characterized by its molecular sieving performance, cation exchange capacity, and catalytic ability (Rolison, 1994). The chemical composition of zeolites can be represented by the general formula $M_{x/n}{}^{n+}$ $(Al_xSi_yO_{2(x+y)})^{x-} \cdot zH_2O$, M being a cationic species, generally alkaline or alkaline-earth metal, proton, ammonium ion, etc. The Al/Si molar ratio can vary from 1 (sodalite) to ∞ (silicalites). The isomorphic substitution of silicon atoms by aluminum ones produces a negative charge in the lattice that has to be neutralized by such cationic species.

Remarkably, zeolites can be completely hydrated and dehydrated without damage to the crystalline network. The structure of zeolites is formally constructed from conjoining SiO_4 and AlO_4 tetrahedral building blocks so that a variety of ringed structures, generically labeled as secondary building units (SBUs), can be formed.
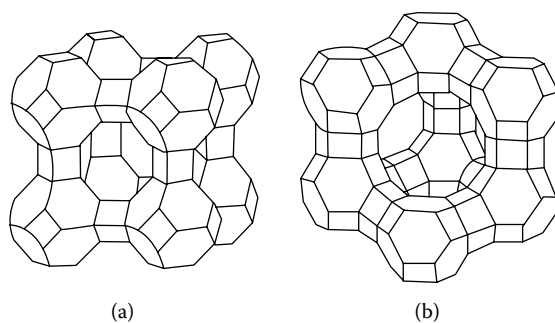
FIGURE 4.1 Three-dimensional representation of the framework structure of (a) zeolite A and (b) X and Y.

Figure 4.1 shows the structures of zeolites A and X, Y (faujasite). As previously noted, zeolites are capable of restricting the size and shape of the molecules that enter, reside within, or exit the lattice. Structures of such zeolites comprise pore opening, cage, and channel structures; for instance, the pore structure of zeolite Y consists of almost spherical 13-Å cavities interconnected tetrahedrally through smaller apertures of 7.4 Å. Table 4.1 and Table 4.2 show the characteristics of several types of zeolites used in electrochemical studies. Zeolites possess high porosity, with large surface areas, typically ranging from 400 to 650 m²/g and pore volumes of up to 0.1 cm³/g.

For every aluminum atom in the lattice, a fixed negative charge results. This negative charge is counterbalanced by mobile cations, typically alkaline or alkaline-earth cations. In contact with aqueous solutions, these mobile cations can easily be exchanged for other cations (metal cations, cationic complexes) of appropriate dimensions, thus determining the remarkable ion exchange properties of zeolites.

Zeolites are traditionally regarded as "acid" materials. There are two types of acidic centers in zeolites. First, protons held in the zeolite form bridging hydroxyl

TABLE 4.1
Characteristics of Several Zeolites

Type of Pore	Pore Size (Å)	Number of Tetrahedral Units	Channel Directions	Examples
Middle	4.8 × 3.5 [010]	8	2	Ferrierite
	5.4 × 4.2 [001]	10		
Middle	5.6 × 5.3 [010]	10	2	ZSM-5
	5.1 × 5.5 [100]	10		
Large	6.5 × 7.0 [001]	12	1	Mordenite
	5.7 × 5.6 [001]	10		
Large	7.6 × 6.4 [100]	12	3	β-zeolite
	5.6 × 5.6 [001]	12		
Large	7.4 × 7.4 [111]	12	3	Y zeolite
Extra large	8.2 × 8.1 [010]	14	1	UTD-1

TABLE 4.2
**Physical and Chemical Properties of Zeolites**

Zeolite Type	Unit Cell Composition[a]	Si/Al Molar Ratio	Unit Cell Volume (nm³)	Void Volume[b] (cm³/cm³)	Pore Openings (Å)	Supercage Diameter (Å)	Kinetic Diameter (nm)	t_c[c] (°C)
A	$Na_{12}[(AlO_2)_{12}(SiO_2)_{12}]·27H_2O$	0.7–1.2	1.870	0.47	4.1	11.4	0.39	660
X	$Na_{86}[(AlO_2)_{86}(SiO_2)_{106}]·264H_2O$	1–1.5	15.36–15.67	0.50	7.4	13	0.81	660
Y	$Na_{56}[(AlO_2)_{56}(SiO_2)_{136}]·250H_2O$	>1.5–3	14.90–15.35	0.48	7.4	13	0.81	700
L	$K_9[(AlO_2)_9(SiO_2)_{27}]·22H_2O$	2.6–3.5	2.205	0.32			0.81	845
Mord.	$Na_8[(AlO_2)_8(SiO_2)_{40}]·24H_2O$	4.17–5	2.794	0.28			0.39	

Source: Adapted from Breck (1974) and Rolison (1990).

[a] Typical composition for the fully hydrated zeolite.
[b] Void volume/total volume.
[c] Temperature at which structural changes are first noted by x-ray diffraction, for heating in air.
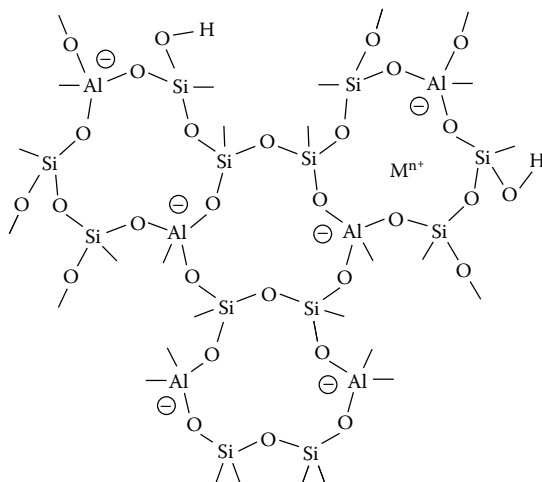
FIGURE 4.2 Two-dimensional representation of the Al-O-Si linkages creating the framework structure of aluminosilicates.

groups Si(OH)Al (Bronsted centers). A direct means of forming such centers is to interchange alkaline ions (e.g., Na^+) by NH_4^+ ions and further calcinations of the material. As a result, NH_3 is released, whereas Si(OH)Al groups are formed. In addition, charge-balancing cations and extra-lattice Al^{3+} ions act as Lewis acidic centers.

The density of Al atoms in the pores determines the polarity of internal spaces, thus determining the hydrophobicity/hydrophilicity of the material. In general, the hydrophobic character of the zeolites increases on decreasing the aluminum content. The coordinative environment of such aluminum centers notably influences their acidic properties, so that the incorporation of additional Al^{3+} centers alters the charge density of the original acid site. As schematized in Figure 4.2, increasing the number of aluminum atoms in the second coordination sphere of a given acid site decreases the acidity of the material.

Interestingly, zeolites can also present basic character, associated to oxygen atoms in the lattice having a large density of negative charge (Corma et al., 1990; Hattori, 1995). The alkalinity of zeolites has been related with the aluminum content and the nature of charge-balancing cations. By the first token, alkalinity is promoted by high aluminum contents; by the second, highly polarizable cations increase the alkalinity of the zeolite with respect to less polarizable ones.

4.3 ELECTROCHEMISTRY OF ZEOLITE-ASSOCIATED SPECIES

From the seminal work of Lunsford et al. in the early 1980s (DeWilde et al., 1980; Quayle and Lunsford, 1982), "ship-in-a-bottle" synthesis of metal complexes in the zeolite supercages, encapsulation of catalytically, optically, and/or electrochemically active species within micro- and mesoporous aluminosilicates, has received considerable attention (Alvaro et al., 2003). Site isolation of individual guest molecules, combined with shape and size restrictions imposed by the supercage steric limitations,

makes it possible for us to perform catalytic reactions combining the advantages of homogeneous and heterogeneous catalytic systems (Corbin et al., 1985; Tolman and Herron, 1988; Bresinska and Drago, 1990; Hanson, 1991). For instance, oxidation of water to O_2 by zeolite Y-encapsulated tris(2,2′-bipyridine)ruthenium(III), $Ru(bpy)_3^{3+}$, precludes multimetal-centered degradation reactions, resulting in ligand degradation and CO_2 evolution, typically observed in solution (Ledney and Dutta, 1995).

The electrochemistry of zeolite-associated species, however, has become controversial, the debate being focused on the extrazeolite/intrazeolite character of electrochemical processes occurring at zeolite-modified electrodes (Baker et al., 1995; Li et al., 1995a; Senaratne et al., 1996; Bedioui and Devynck, 1996; Rolison et al., 1996). Thus, Gemborys and Shaw (1986) first considered two possible electrochemical pathways: extrazeolitic and intrazeolitic. Shaw et al. (1989) and Li et al. (1989) considered a third mechanism—surface-mediated electron transfer—whereas Li et al. (1995b) further distinguished between ion transport and electron transport intrazeolitic mechanisms. Bessel and Rolison (1997a) concluded that the voltammetric response observed for zeolite-associated species essentially reflects the behavior of extrazeolite ion-exchanged molecules and/or those located in the more external "boundary" layer of the zeolite and proposed that different discernible responses can be attributed to electroactive species located in different sites in the zeolite matrix: the so-called topological redox isomers. Data on the electrochemistry of zeolite-associated transition metal complexes (Sabater et al., 1997; Doménech et al., 2000a, 2002a) and reactive organic intermediates (Doménech et al., 1999a,b, 2002a, 2003a, 2005b) provided results in agreement with such ideas.

Let us consider the electrochemical reduction of the oxidized form of an electroactive species. The extrazeolitic mechanism involves two steps: first, the zeolite-associated electroactive species is ion-exchanged with electrolyte cation, M^+:

$$\{Ox\} + M^+\,(sol) \rightarrow Ox\,(solv) + \{M^+\} \tag{4.1}$$
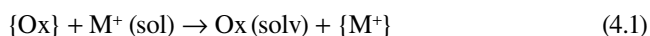
followed by reduction of the oxidized form in solution phase:

$$Ox\,(sol) + e^- \rightarrow Red\,(solv) \tag{4.2}$$

In these equations, (sol) denotes solvated species in electrolyte solution and { } species attached to the zeolite framework.

The intrazeolitic mechanism involves the reduction of intrazeolite species coupled with the ingress of charge-balancing electrolyte cations into the zeolite framework:

$$\{Ox\} + M^+\,(sol) + e^- \rightarrow \{Red \cdots M^+\} \tag{4.3}$$
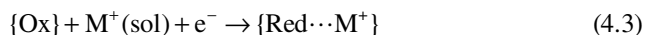
To elucidate reaction pathways, several experimental features have to be considered (Bessel and Rolison, 1997a; Doménech et al., 2002a, 2003a, 2004e):

1. Voltammetric and coulometric data indicate that under ordinary experimental conditions, only a small percentage (lower than 1–2%) of guest molecules is electroactive.
2. Voltammetric responses displayed by zeolite probes containing electroactive guests in contact with size-excluded electrolyte countercations such as

Hex_4N^+ and Bu_4N^+ are clearly lower than those of the same materials in contact with less size-excluded counteractions such as Et_4N^+ or Li^+.

3. In the presence of size-excluded electrolyte counteractions, the voltammetric signals are rapidly exhausted under repetitive cycling of the potential, whereas in the presence of less size-excluded counteractions, voltammetric signals decay slowly under repetitive voltammetry.

4. Voltammetry of zeolite-associated electroactive species in contact with size-excluded electrolyte counteractions produces single signals, whereas in the presence of less size-excluded counteractions, peak splitting frequently appears.

5. Electrocatalytic effects eventually exerted by zeolite-attached species on selected processes also become significantly dependent on the size of electrolyte cations.

Interestingly, anionic species can also be entrapped into zeolites and mesoporous aluminosilicates, although studied cases are currently limited to few inorganic (Breck, 1974; Barrer, 1978; Bresinska and Drago, 1990; Pastore et al., 1993) and organic (Kuchi et al., 1999; Chretien et al., 2002; Herance et al., 2005) anions. The reason for this paucity is that zeolite frameworks produce a significant energy barrier for the ingress of anions due to coulostatic repulsion exerted by the zeolite framework. Since no mobile negatively charged species exist in zeolites, anchorage of anionic species requires the coupled ingress of cations to maintain charge neutrality in the solid. Accordingly, the encapsulation of anionic species into zeolites occurs as the ionic pair ingress (Herance et al., 2005). This can be presented as:

$$\{\} + X^-(\text{solv}) + M^+(\text{sol}) \rightarrow \{X^- \cdots M^+\} \tag{4.4}$$
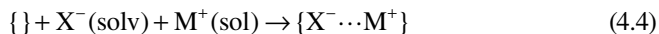
The electrochemistry of organic anions attached to zeolites can be described in terms of oxidation steps involving the issue of metal cations and reduction steps involving the ingress of electrolyte cations into the zeolite pore/channel system (Doménech et al., 2005a).

4.4   TOPOLOGICAL REDOX ISOMERS

Turro and García-Garibay (1991) introduced the idea that different topological isomers should be considered for explaining the photochemistry of zeolite systems. Bessel and Rolison (1997a) first applied this idea to electrochemistry of zeolites, coining the term *topological redox isomers* for designing redox-active guest species associated to different sites in the aluminosilicate framework. These authors distinguish four basic types of topological redox isomers:

1. Located outside the zeolite, with no bonding or sorptive association
2. Bound to the external surface of zeolite particles
3. Adsorbed into the voids of the zeolite but able to sample the global pore lattice topology
4. Size-included in the interior of supercages or channel intersections of the zeolite framework

Electrochemical methods provide information on the coexistence of different topological redox isomers. Discrimination between different redox isomers can

be obtained from differences in the electrolyte size influence and electrochemical mechanism that can be observed in zeolite-modified electrodes. The attachment of bulky cationic guests, unable to migrate within the zeolite framework, is of particular interest. It should be noted that zeolites are able to stabilize elusive cationic organic intermediates that tightly fit into the cavities of the aluminosilicate due to intense electrostatic fields experienced inside the pores, stabilizing cationic species, and by the blocking effect with respect the attack of nucleophilic reagents. In fact, several organic cations and radical cations became indefinitely persistent when they are encapsulated in appropriate zeolites (Scaiano and García, 1999).

A typical case is that of 2,4,6-triphenylthiopyrylium ion associated to zeolite Y ($TPY^+@Y$). The significant electrolyte dependency of the electrochemical response of zeolite-associated species can be seen in Figure 4.3, where square-wave voltammetries (SQWVs) for $TPY^+@Y$ immersed into different MeCN electrolytes can be compared. A one-electron reversible voltammetric response was obtained (Doménech et al., 1999a, 2002b) similar to that described via Equation (2.16).

In contact with size-excluded Hex_4N^+ and Bu_4N^+ cations, an apparently unique, broad reduction peak is obtained. In the presence of Et_4N^+, the voltammetric signal becomes significantly enhanced and reduced to a tall peak. Chronoamperograms
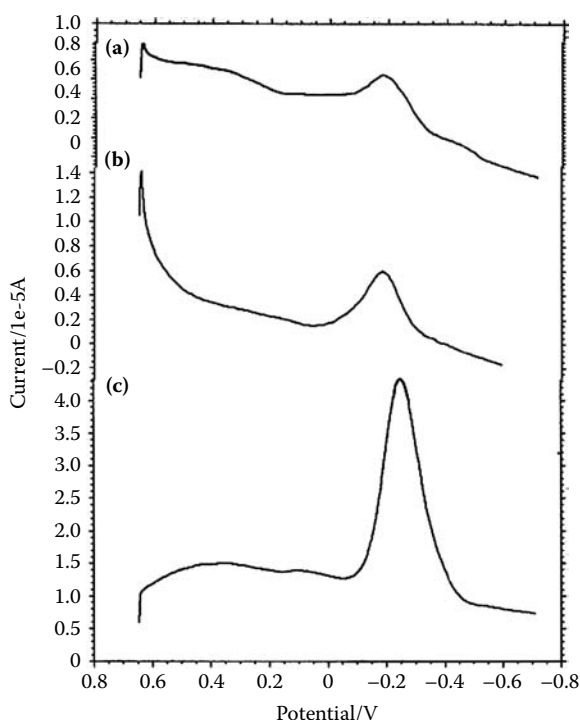
FIGURE 4.3 Deconvoluted SQWVs for $TPY^+@Y$-modified paraffin-impregnated graphite electrodes in contact with 0.10 M solutions of (a) Hex_4NPF_6, (b) Bu_4NPF_6, (c) Et_4NPF_6 in MeCN. Potential step increment, 4 mV; square-wave amplitude, 25 mV; frequency, 10 Hz.
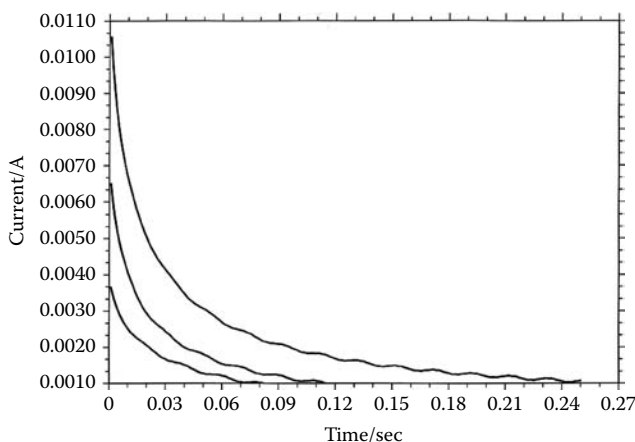
FIGURE 4.4 CAs for TPY$^+$@Y-modified paraffin-impregnated graphite electrodes in contact with 0.10 M solutions of (from upper to below): Et$_4$NPF$_6$, Bu$_4$NPF$_6$, and Hex$_4$NPF$_6$, in MeCN. Applied potential, -0.35 V vs. AgCl/Ag.

for TPY$^+$@Y-modified paraffin-impregnated graphite electrodes in contact with the above electrolytes also reveal significant differences, as shown in Figure 4.4.

These features can be rationalized on assuming that the observed electrochemical response corresponds to the superposition of that due to at least two different topological redox isomers: guest TPY$^+$ ions externally adsorbed onto the zeolite surface ("surface isomers"), thus displaying a genuine extrazeolite mechanism, and guest TPY$^+$ located in sites in the more external, electrochemically accessible regions of the zeolite grains ("boundary isomers"). In addition, it has been observed that the voltammetric response of external surface isomers approaches diffusive control under semi-infinite conditions, or thick-layer behavior, whereas the response of boundary isomers approaches thin-layer conditions (Doménech et al., 2002a).

As described in Chapter 2, diffusion coefficients for electrons and electrolyte cations can be calculated from chronoamperometry (CA) using the model developed by Schröder et al. (2000) (Doménech, 2004). Values for D_e and D_M are listed in Table 4.3 using data for graphite electrodes modified with Mn(salen)N$_3^-$ and 2,4,6-triphenylthiopyrylium-containing zeolite Y, immersed into Et$_4$NClO$_4$/MeCN, LiClO$_4$/MeCN, and Bu$_4$NPF$_6$/MeCN electrolytes. CA data for the first two electrolytes fit well with the theoretical model, whereas data obtained in the presence of Bu$_4$N$^+$ deviate from theory, in agreement with the expected purely extrazeolitic nature of electrochemical processes in contact with that electrolyte cation. Accordingly, estimated D values contained in Table 4.3 for Bu$_4$N$^+$ represent merely the result of a forced fit of experimental data with theory.

It should be noted that the high site isolation of electroactive guest molecules into zeolite hosts suggests that electron hopping between zeolite-encapsulated species, demanded by the propagation of the redox reaction (see Chapter 2) through the material particles, should be highly hindered. Voltammetric data suggest that although restricted to external zeolite regions, there is a place for a certain degree of redox reaction propagation across the boundary zone. Consistently, spectroscopic

TABLE 4.3

Diffusion Coefficients for Electrons and Electrolyte Cations Calculated from CA Data for Graphite Electrodes Modified with Mn(Salen)N$_3$-Containing Zeolite Y and Immersed into Et$_4$NClO$_4$/MeCN, LiClO$_4$/MeCN, and Bu$_4$NPF$_6$/MeCN Electrolytes (All in Concentration 0.10 M)

Electrolyte Cation	Mn(Salen)N$_3$@Y D_M (cm²/sec)	Mn(Salen)N$_3$@Y D_e (cm²/sec)	TPY$^+$@Y D_M (cm²/sec)	TPY$^+$@Y D_e (cm²/sec)
Bu$_4$N$^+$	(1×10^{-12})	(2.3×10^{-12})	(1×10^{-12})	(1×10^{-12})
Et$_4$N$^+$	1.1×10^{-9}	3.5×10^{-11}	5.0×10^{-9}	2.0×10^{-11}
Li$^+$	7.8×10^{-10}	2.0×10^{-11}	4.6×10^{-9}	2.2×10^{-11}

Source: Data taken from Doménech et al. (2002a, 2003b)

Figures in parenthesis are uncertain values.

studies reveal that significant electronic interactions between adjacent entrapped molecules occur when assisted by small, mobile charge-balancing ions. Thus, studies on intrazeolitic photochemical charge transfer for methylviologen and Ru(bpy)$_3^{2+}$ indicate that an efficient electron transfer coupled with recombination occurs at high guest loadings (Dutta and Turbeville, 1992; Ledney and Dutta, 1995; Yoon and Park, 1996; Sykora et al., 1999; Vitale et al., 1999).

4.5 SPECIES DISTRIBUTION

As mentioned in Chapter 2, it appears reasonable to assume that molecules entrapped into the voids of microporous aluminosilicates will be not uniformly distributed in the bulk of the material. The determination of distribution of guest molecules in the voids of the aluminosilicate host is an obvious target for elucidating the chemical and photochemical reactivity of the resulting materials (Bruhwiler and Calzaferri, 2004). Thus, Layné et al. (1996), while studying the distribution of tris(2,2′-bipyridine)ruthenium(II) complex (Ru(bpy)$_3^{2+}$) in the supercages of zeolite Y, concluded that at low complex loadings, a mean distribution of one complex per two supercages occurs, whereas for relatively high ruthenium loadings, there is an increasing amount of biproducts, formally Ru(bpy)$_n$(NH$_3$)$_{6-2n}^{2+}$. For larger ruthenium loadings, the complex tends to accumulate toward the surface of the zeolite microcrystals instead of a random distribution in the aluminosilicate bulk.

In support of the foregoing considerations, variation of peak currents for cyclic voltammetries (CVs) and SQWVs of selected zeolite-associated systems exhibits a significant variation with the potential scan rate and the square-wave frequency, respectively. Figure 4.5 shows SQWVs for TPY$^+$@Y deposited on a graphite electrode upon immersion into 0.10 M Et$_4$NClO$_4$/MeCN at two different frequencies. Variation in peak current with square-wave frequency is depicted in Figure 4.6. At $f < 50$ Hz, the peak current increases on increasing frequency; at larger frequencies, however, the peak current decreases on increasing frequency, contrary to that observed for diffusion-controlled processes in solution phase. This behavior can be rationalized on assuming that
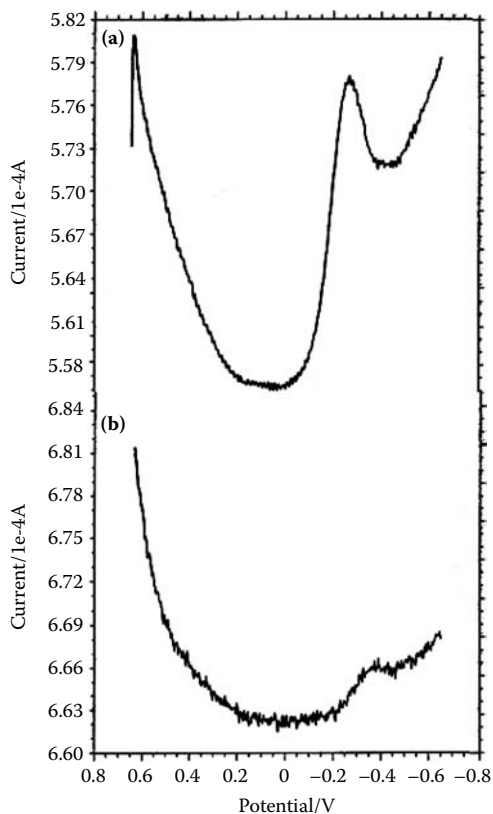
FIGURE 4.5 SQWVs for microparticulate deposit of 2,4,6-triphenylpyrylium ion attached to zeolite Y deposited on paraffin-impregnated graphite electrode in contact with 0.10 M Et_4NClO_4/MeCN. Potential step increment, 4 mV; square-wave amplitude, 25 mV; frequency: (a) 50 Hz, (b) 500 Hz.

the electrochemically accessible TPY^+ ions are concentrated in the external boundary of zeolite crystals, their concentration decreasing rapidly with depth.

As previously noted (see Section 2.5), the depth reached in a given experiment can, in principle, be approached by the advance of the diffusion layer if the diffusion coefficient for the rate-determining charge transport is known. Then, at short times, only the electrochemical response of the guest molecules externally adsorbed or located in the more external layers of the crystals will be electroactive. At longer times, the observed response will reflect the contribution of molecules located deeper in the host crystals.

Then, the quotient between the concentrations of accessed molecules at a given depth and the total electrochemically accessible molecules in the solid can roughly be estimated from CVs or SQWVs. In this second case, taking a characteristic time, t_D, for the advance of the diffusion layer as a function of the square-wave frequency (SQWV), $t_D = 1/f$. Accordingly, the depth, x, can roughly be estimated as $(Dt_D)^{1/2}$. Since the peak current can be taken as representative of the average concentration of electroactive species in the accessed zones of zeolite grains, the quotient between the
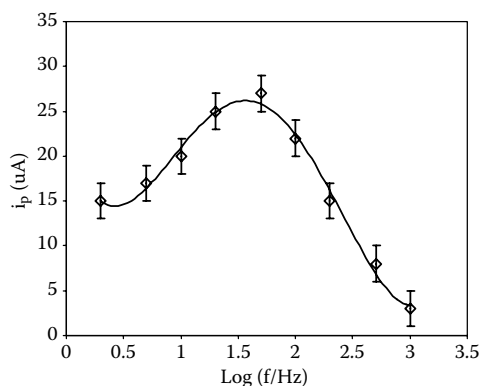
FIGURE 4.6 Variation of the peak current with the square-wave frequency for deposits on graphite of microparticles of zeolite Y having attached 2,4,6-triphenylthiopyrylium ion (TPY$^+$) upon immersion into 0.10 M Et$_4$NClO$_4$/MeCN.

concentration at a given depth and the concentration in the surface can be approached by the quotient between the peak current at a given frequency and the peak current at low frequencies (or extrapolated at frequency zero).

Figure 4.7 compares the concentration profiles calculated for TPY$^+$@Y in contact with different MeCN electrolytes using chronocoulometric data, as described in Section 2.5. It was assumed that electron diffusion acts as a rate-determining step and D_e values listed in Table 4.3 were taken for estimating depths.

It should be emphasized, however, that the above calculations involve a simplified view of zeolite structure and species distribution because an ideal, semi-infinite
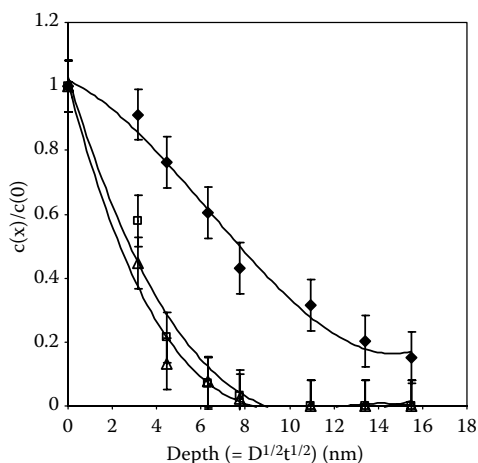

FIGURE 4.7 Variation of the $c(x)/c(0)$ ratio with depth for TPY@Y in contact with different MeCN electrolytes from chronocoulometric data at sample-modified paraffin-impregnated graphite electrodes immersed into 0.10 M Hex$_4$NPF$_6$/MeCN (triangles), 0.10 M Bu$_4$NPF$_6$/MeCN (squares), and 0.10 M Et$_4$NPF$_6$/MeCN (rhombs).
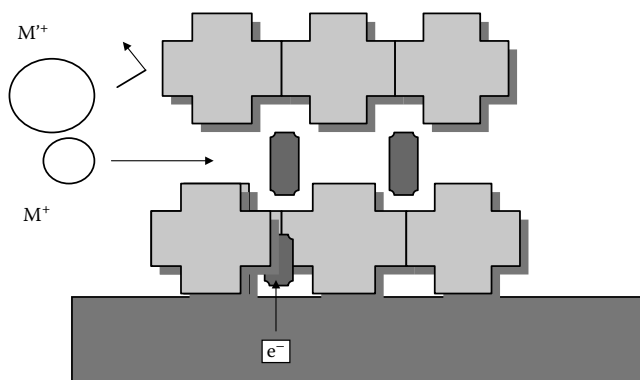
FIGURE 4.8 (See color insert following page 94.) Schematics for the electrochemical reduction of a species immobilized into the voids of a porous aluminosilicate involving the ingress of size-allowed electrolyte cations (M^+). Size-excluded electrolyte cations cannot contribute to intrazeolite redox conductivity.

diffusion through homogeneous zeolite particles is assumed. A pictorial scheme for the reduction of guest electroactive species attached to porous aluminosilicates is depicted in Figure 4.8. A more accurate description should take into account a more precise description of the zeolite topology where truncated cages, fractures, etc., provide opportunity for the access of bulky electrolyte counterions to regions beyond the ideal external surface of crystals (see Figure 4.9).
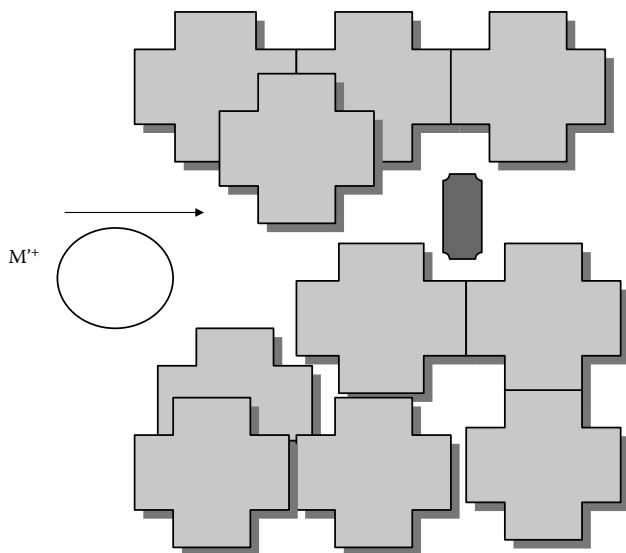
FIGURE 4.9 Schematics for the electrochemical reduction of a species immobilized into the voids of a porous aluminosilicate involving considering surface defects.
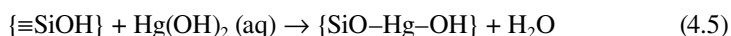
4.6   MESOPOROUS MATERIALS

The electrochemical response of mesoporous aluminosilicates has attracted attention because of their potential applications in catalysis, separations, adsorption, coatings, and microelectronics. Such materials (MCM-41 periodic mesoporous silica as representative example) provide considerably less exigent size restrictions than zeolites with regard to ion diffusion, the electrochemical response being dependent on: (1) the electrochemical properties of the guest, (2) its concentration, (3) the size of the separation between cavities able to attach electroactive guest species, (4) the type of association of the electroactive species with the aluminosilicate framework, and (5) the more or less ordered nature of the mesoporous host. As in the case of zeolites, however, charge conservation requires the ingress/issue of charge-balancing electrolyte ions coupled to electron transfer steps. As described in Chapters 1 and 2, the advance of the redox reaction across the porous materials involves electron hopping between immobile redox centers coupled with the transport of mobile ions through the pore/channel system of the aluminosilicate framework. Obviously, there is opportunity for charge transport associated to the motion of redox-mediators, a situation that was discussed in Chapter 3. Eventually, charge transport could involve proton hopping between silanol groups and acid sites.

Given the adsorbent properties of mesoporous aluminosilicates, these materials can be used for preconcentrating more or less selectively species in solution, following a scheme also used in zeolites (Kruk et al., 2000). Accumulation is driven by the ease of transport of the analyte to binding sites, so that efficiency is high when using materials displaying high specific surface area and regular channels of tailor-made monodispersed dimensions. Compared to amorphous silica gel, the regular tridimensional structure of systems such as MCM-41 makes it easier for guest species to bind with host-binding sites (Walcarius and Bessière, 1999).

As described in Chapter 1, a variety of functionalization and electrode modification procedures are available. These include formation of self-assembled monolayers (Jiang et al., 2006), layer-by-layer deposition (Zhang et al., 2003), electrophoretic deposition (Zhang and Yang, 2007), and hydrothermal crystallization on conductive substrates (Kornik and Baker, 2002), among others. Figure 4.10 schematizes the assembly of mercapto-trimethoxysilanes and zeolite nanocrystals on gold electrode (Jiang et al., 2006).

Preconcentration of transition metal cations, of obvious interest for environmental sensing and remediation, involves reaction with silanol groups via condensation processes. For instance, for mercury in aqueous solution, the prevailing species at pH values between 4 and 7 are the complexes $Hg(OH)_2$ and $Hg(OH)^+$. Their attachment to mesoporous silicates can be presented as (Schindler and Stumm, 1987):

$$\{\equiv SiOH\} + Hg(OH)_2 \text{ (aq)} \rightarrow \{SiO–Hg–OH\} + H_2O \qquad (4.5)$$

$$\{\equiv SiOH\} + Hg(OH)^+ \text{ (aq)} \rightarrow \{SiO–Hg^+\} + H_2O \qquad (4.6)$$

In general, immobilization of selected species into mesoporous aluminosilicates provides opportunity for studying their electrochemistry under site isolation
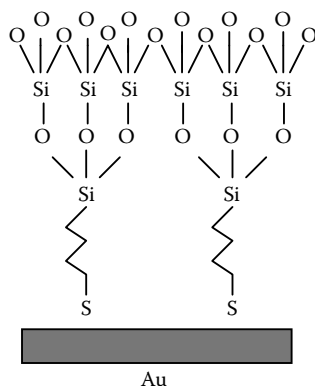
FIGURE 4.10 Schematics of the assembly of mercapto-trimethoxysilanes and zeolite nano-crystals on gold electrodes.

conditions; that is, bypassing parallel chemical reactions in solution and/or undesired electrode surface effects. This is the case of studies dealing with protein electrochemistry. The facilitation of electron transfer between proteins and the electrode is of interest for fabricating biosensors, bioreactors, and biomedical devices without using mediators (Hamachi et al., 1997; Armstrong and Wilson, 2000). The inaccessibility of the electroactive units in the large three-dimensional structure of proteins and the pre- and post-electron transfer passivation due to protein adsorption makes it difficult to establish direct electron transfer between proteins and conventional electrodes. Thus, the immobilization of the protein on micro- or mesoporous surfaces is a plausible strategy that has aroused interest among researchers (Heering et al., 2004). Micro- and mesoporous aluminosilicates can provide an electron-transfer-facilitating environment, block undesired adsorption effects, and protect proteins from biodegradation. The use of electrode modification methods such as self-assembled monolayer formation layer-by-layer deposition favors the acquisition of well-defined electrochemical responses, as described by Dai et al. (2004) for cytochrome *c* immobilized on NaY zeolite and Sun et al. (2008) for hemoglobin assembled with Al-MSU-S particles.

It should be noted that chemical modification of the mesoporous host—for instance, by thiol groups—can provide not only functional attachment to electrode surfaces but also specific binding sites for preconcentration of selected analytes. The modified electrode configuration (monolayer, multilayer, etc.) can significantly influence the final electrochemical response.

4.7 ELECTROCHEMISTRY OF RELATED MATERIALS

In the above-studied systems, the aluminosilicate framework merely acts as a porous, electrochemically inert support embedding the redox-active guests. In contrast to this, the presence of electroactive atoms in the composition of the aluminosilicates renders the solid electroactive. This applies to the case of titanium

silicalite, whose framework contains isolated, tetrahedrally coordinated Ti^{4+} ions. De Castro-Martins et al. (1994) studied the voltammetric behavior of titanium silicalites in contact with aqueous electrolytes obtaining a single-peak couple at a midpoint potential of +0.59 V vs. SCE, corresponding to the Ti(IV)/Ti(III) inter-conversion. A further study on different alkaline-free calcined Ti/beta zeolites, synthesized by hydrothermal crystallization, differing in their aluminum content and crystallinity, provided a more complicated electrochemical response attributable to the distribution of Ti centers between different sites (Doménech et al., 2000b). The reduction of titanium centers can be presented as:

$$\{\equiv Ti^{IV}-O\} + H^+ (aq) + e^- \rightarrow \{\equiv Ti^{III}-OH\} \tag{4.7}$$
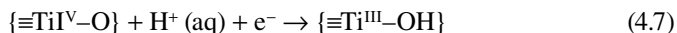
It should be noted that thermal treatments applied to aluminosilicates can vary significantly with their properties. For instance, silica calcination at temperatures ca. 900°C produces condensation of neighboring silanol groups to form silanoxy bridges (Hozumi et al., 2000; Naono et al., 2000). This process can be schematized as:

$$\{\equiv Si-OH\} + \{HO-Si\equiv\} \rightarrow \{\equiv Si-O-Si\equiv\} \tag{4.8}$$
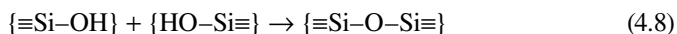
From the electrochemical point of view, an important class of materials is that constituted by aluminosilicates incorporating cobalt, iron, etc., centers. In the case of Fe-based zeolites with Mobil Five structure (FeZSM-5) materials, different forms of iron can coexist. These include isolated ions either in framework positions (isomorphously substituting silicon centers), isolated ions in cationic positions in zeolite channels, binuclear and oligonuclear iron complexes in extra-framework positions, iron oxide nanoparticles (size <2 nm), and large iron oxide particles (Fe_2O_3) in a wide distribution (up to 25 nm in size) located in the surface of the zeolite crystal (Pérez-Ramírez et al., 2002). The electrochemistry of such materials will be reviewed in Chapter 8.

4.8   SPECIATION: THE MAYA BLUE PROBLEM

The study of Maya Blue (MB), an ancient nanostructured organic-inorganic hybrid material, illustrates the capabilities of electrochemical methods to obtain information on microporous systems and, in particular, for facing speciation problems. MB is a pigment widely used in wall paintings, pottery, and sculptures (see Figure 4.11) by the ancient Mayas and other Mesoamerican people for centuries (Reyes-Valerio, 1993). This material claimed attention by its peculiar palette, ranging from a bright turquoise to a dark greenish blue, and its enormous stability with regard to the attack of acids, alkalis, organic reagents, and also biodegradation. The nature of MB, however, has challenged chemists for decades and, in fact, despite intensive research, several controversial aspects remain unsolved.

Shepard (1962) first introduced the idea of MB being an unusual material consisting of a dye attached to certain Yucatán clays. Van Olphen (1967) prepared synthetic specimens with chromatic and chemical properties analogous to those of MB by crushing

FIGURE 4.11 (See color insert following page 94.) Image of Maya wall paintings in the Substructure I of Calakmul (Campeche, México), Early Classical Maya period. Photograph courtesy of María Luisa Vázquez de Agredos Pascual. (From Doménech et al., 2007b. *Anal. Chem.* 79, 2812–2821, with permission.)

palygorskite, a local clay, and indigo. Arnold et al. identified palygorskite in Yucatán clays and localized sites for its extraction (Arnold, 1967, 1971; Arnold and Bohor, 1975).

Currently, it is known that MB is a material resulting from the attachment of indigo, a blue dye extracted from leaves of *añil* or *xiuquitlitl* (*Indigofera suffruticosa* and other species) to the clay matrix of palygorskite, a fibrous phyllosilicate of ideal composition $Si_8(Mg_2Al_2)O_{20}(OH)_2(OH_2)_4 \cdot 4H_2O$ whose structure can be described as a continuous set of layers formed by two-dimensional tetrahedral and octahedral sheets. The tetrahedral and octahedral mesh gives rise to a series of rectangular tunnels of dimensions 6.4×3.7 Å. Palygorskite crystals are therefore crossed by zeolite-like channels and permeated by weakly bound, nonstructural (zeolitic) water. Magnesium and aluminum cations complete their coordination with tightly bound water molecules (structural water).

The nature of the indigo-palygorskite association and the reasons for the hue and durability of MB have become controversial. Thus, José-Yacamán et al. (1996) reported the presence of nanoparticles of iron metal encapsulated in an amorphous silicate substrate accompanied by iron oxide nanoparticles on the surface of that substrate. On the basis of those observations, it was suggested that Mie-type light dispersion in nanoparticles should produce the characteristic hue of MB.

Subsequent studies reported by Sánchez del Río et al. (2004, 2005) did not find either iron in metallic form or goethite in archeological MB. In the most recent literature, it is commonly accepted that MB coloration is mainly due to batochromic shift of the indigo absorption bands as a result of the association of the dye to the inorganic support (Reinen et al., 2004).
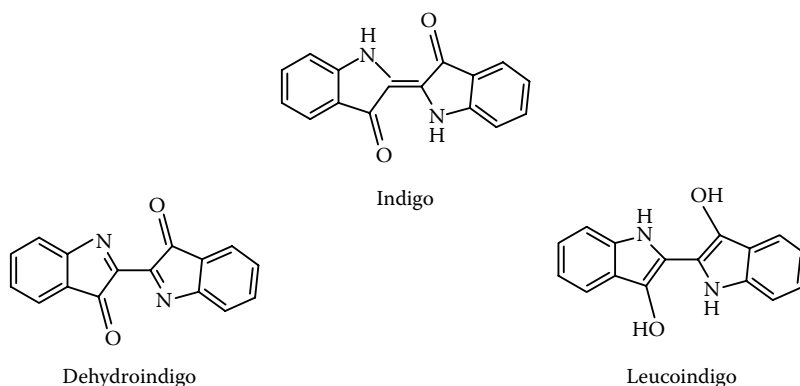
FIGURE 4.12 Structural diagrams for indigo, dehydroindigo, and leucoindigo.

The application of solid-state electrochemical methods, supported by visible and infrared spectroscopies and nuclear magnetic resonance (NMR) data, led Doménech et al. (2006c) to insert a new piece into the MB puzzle: dehydroindigo (see Figure 4.12). Comparison of square-wave voltammograms of indigo and MB samples allowed researchers to detect unambiguously the presence of the dye associated to the palygorskite matrix. The common presence of indigo and dehydroindigo attached to the palygorskite matrix could be responsible for the peculiar hue of MB, as clearly suggested by spectral data (Doménech et al., 2006c). In addition, electrochemical data, confirmed by spectral measurements, made it possible to detect the presence of MB in wall paintings of Substructure IIC in the archeological site of Calakmul, dated in the Early Classical period (440–450 BC), thus providing evidence on the use of this pigment 700–750 years before the date currently accepted. Thermochemical data (see Table 4.4) for the association of indigo, dehydroindigo, and

TABLE 4.4

Thermochemical Parameters for the Association of Indigo, Dehydroindigo, and Leucoindigo to Palygorskite Calculated from the Variation with Temperature (Temperature Range 0–60°C) of Peak Potentials Recorded in SQWVs of Maya Blue Samples Attached to Paraffin-Impregnated Graphite Electrodes in Contact with 0.50 M Acetate Buffer and 0.10 M NaOH

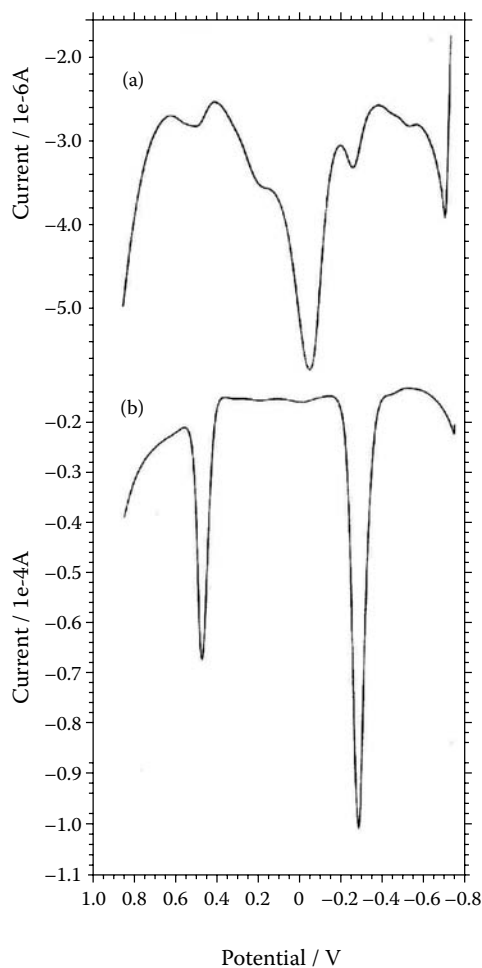| Process Dye (solid) + palygorskite (solid) → Maya Blue (solid)	ΔH^o (kJ/mol)	ΔS^o (kJ/mol K)
Indigo-palygorskite	+101	0.32
Dehydroindigo-palygorskite	+65	+0.46
Leucoindigo-palygorskite	+118	+0.25

Source: Described in Doménech et al. (2006a)

FIGURE 4.13 SQWVs of (a) indigo microparticles and (b) MB sample from Calakmul, Substructure II-C, immersed into 0.50 M acetate buffer, pH 4.85. Potential scan initiated at −750 mV in the positive direction. Potential step increment 4 mV; square-wave amplitude 25 mV; frequency 5 Hz. The sample, dated in the Late Preclassical period, may be the most ancient sample of MB currently detected. (Adapted from Doménech et al., 2007b. *Anal. Chem.* 79, 2812–2821, with permission.)

leucoindigo, the reduced form of indigo, to the palygorskite framework were also calculated from temperature-dependent electrochemical parameters (Doménech et al., 2006c, 2007a,b). Figure 4.13 shows SQWVs of paraffin-impregnated graphite electrodes modified with indigo microparticles (Figure 4.13a) and the MB sample (Figure 4.13b) from Substructure II-C in the archeological site of Calakmul. The sample, dated in the Late Preclassical period, may be the most ancient sample of MB currently detected. Aqueous acetate buffer was used as electrolyte. In the voltammograms, the peaks at +0.45 and −0.30 V corresponding to the oxidation of indigo

to dehydroindigo and the reduction of indigo to leucoindigo, respectively, can be observed. The first process can be presented as:

$$\{H_2IN\} \rightarrow \{IN\} + 2H^+ \text{ (aq)} + 2e^- \tag{4.9}$$
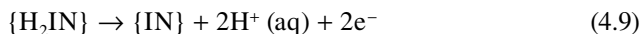
where { } denotes palygorskite-associated species.

In turn, the reduction of palygorskite-attached indigo to palygorskite-attached leucoindigo can be formulated as:

$$\{H_2IN\} + 2H^+ \text{ (aq)} + 2e^- \rightarrow \{H_4IN\} \tag{4.10}$$
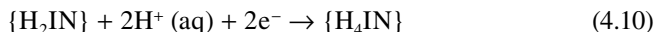
Notice that in both processes, charge conservation is ensured by the ingress/issue of protons to/from the palygorskite framework.

The aforementioned data are consistent with the idea that the ancient Mayas were probably able to change the hue of the pigment by crushing indigo and palygorskite and submitting the system to different thermal treatments (heating at 100–190°C; Doménech et al., 2006c, 2007a,b,c). Increasing the temperature should result in an increase in the dehydroindigo/indigo ratio, thus increasing the greenish hue of the pigment, as can be deduced from the consideration of visible spectra for indigo, dehydroindigo, and MB samples from Ek Balam (Yucatán, Mexico, Late Classical period), depicted in Figure 4.14. Further studies allowed researchers to propose that different procedures (evolving along the Maya times) for the preparation of MB were probably used by the ancient Mayas, eventually involving the use of additives such
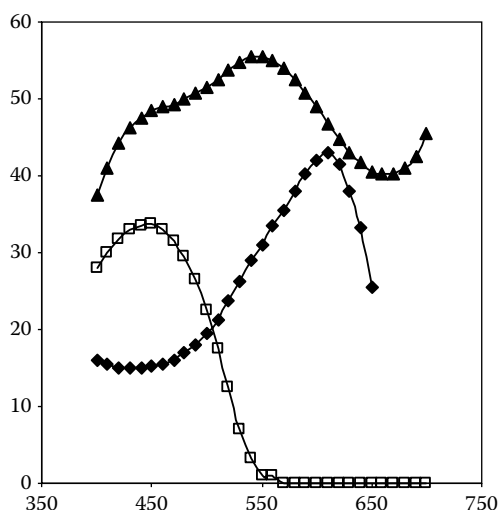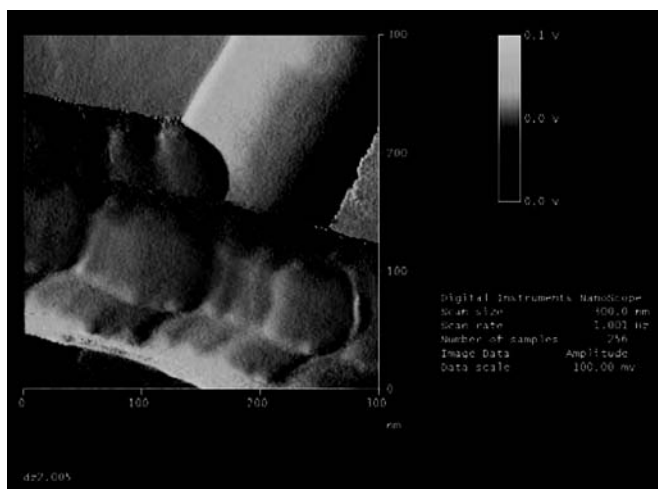

FIGURE 4.14 Visible spectra for indigo (rhombs), dehydroindigo (squares), and MB sample from Ek Balam (triangles). Spectra are vertically translated for clarity. Spectra of indigo and dehydroindigo were translated from Klessinger and Lüttke (1963).
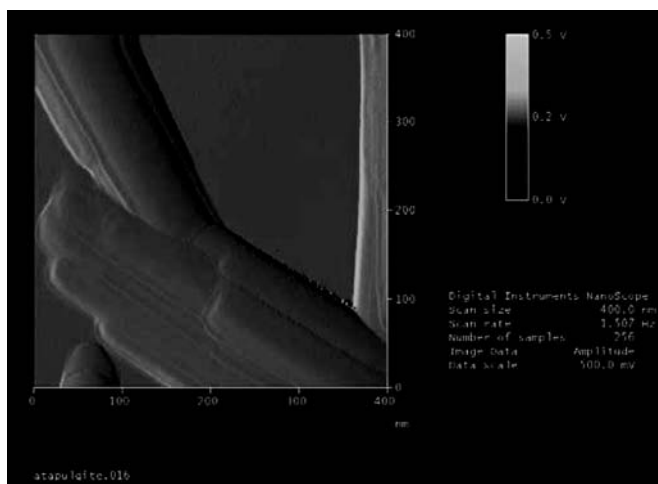
(a)

(b)

FIGURE 4.15   (See color insert following page 94.) AFM images for (a) pristine palygorskite crystals from Sacalum and (b) MB sample from Dzibilnocac (Yucatán, Maya Late Classical period). (From Doménech et al., 2006c. *J. Phys. Chem. B* 110, 6027–6039, with permission.)

as ochre (Doménech et al., 2007b), and the appearance of minority indigoid products such as indirubin (Doménech et al., 2007c, 2009). More recently, Arnold et al. (2008) have reported that burning incense was one means used by ancient Mayas to make MB in the context of ritual ceremonies, a proposal consistent with the foregoing set of considerations.

Microscopic examination of palygorskite and MB samples provides support for the ideas described above. Figure 4.15 shows atomic force microscopy (AFM) images of pristine palygorskite and a genuine MB sample from the archeological

(a)

(b)
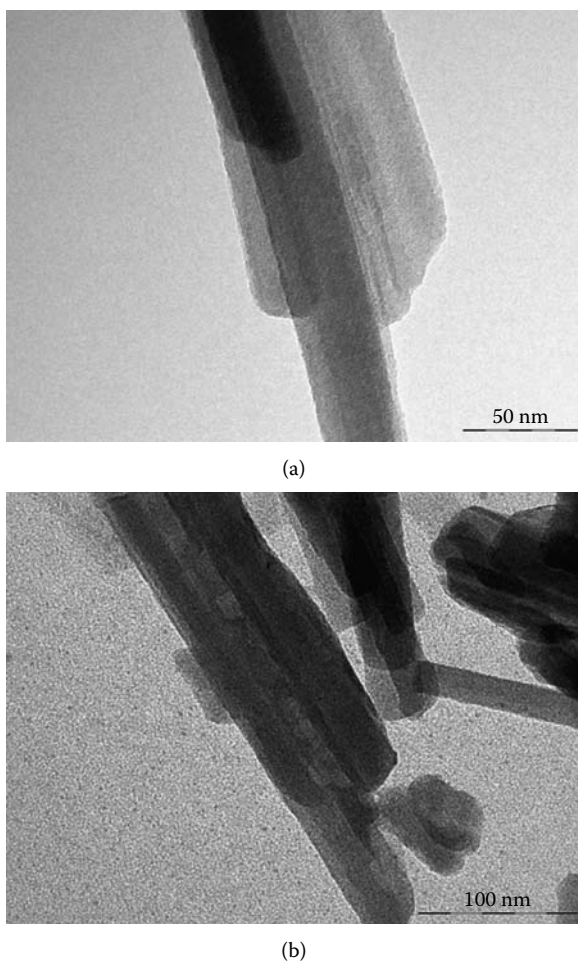
FIGURE 4.16 Micrographs obtained by TEM for (a) pristine palygorskite from Sacalum and (b) MB sample from Mayapán, Postclassical period.

site of Dzibilnocac, Late Classical period. Palygorskite crystals show an elongated shape of 0.5–1 μm having fine fiber structures of 30–60 nm, whereas MB samples contain irregularly shaped palygorskite crystals divided into almost square domains of rough texture. These features can be attributed to the effect of thermal treatments resulting in the loss of zeolitic water. In agreement with that idea, transmission electron microscopy (TEM) offers different images of MB samples, including from irregular-shaped palygorskite crystals to crystals crossed by a dense array of pores whose sizes range from 2 to even 20 nm (see Figure 4.16). Since such pores can unambiguously be attributed to the segregation and evacuation of physisorbed and zeolitic water, the observed differences in their shape, size, and distribution on the surface of palygorskite crystals can be taken as indicative of the use of different preparation procedures for MB.

Interestingly, such textural differences can be correlated with the observed variation of electrochemical parameters, so that a classification of MB voltammograms into different "electrochemical types" can be made. Then, application of multivariate chemometric techniques allows for establishing definite relationships between samples from different archeological sites. It was concluded that a ramified scheme applies with regard to the evolution of MB preparation procedures, thus enabling for obtaining a fine chronology of Maya history (Doménech et al., 2007b).

The nature of the indigo-palygorskite association, however, remains unsolved. Van Olphen (1967) suggested that indigo molecules are too large to enter the channels of palygorskite, so that they become, to an extent, sealed at their ends by dye molecules. Kleber et al. (1967) suggested that in view of the dimensions of indigo molecules and palygorskite channels, partial or even deep penetration of indigo molecules into the palygorskite channels cannot be excluded. Recent formulations include formation of hydrogen bonds between the carbonyl and amino groups of indigo with edge silanol units of the clay, thus closing palygorskite channels (Hubbard et al., 2003), hydrogen bonds between indigo carbonyl and structural water (Fois et al., 2003), and formation of hydrogen bonds between C=O and N–H groups of indigo molecules and structural water molecules (Giustetto et al., 2005). It should be noted that there is a serious discrepancy between computational methods applied to the refinement of the indigo-palygorskite structure, which indicates that structural water lies only with carbonyl groups of indigo, and molecular modeling coupled to spectroscopic data, which suggests that both C=O and N–H indigo groups are involved in hydrogen bond formation with structural water. Apart from hydrogen bonding, however, van der Waals interactions and a direct interaction between indigo and clay octahedral cations, not mediated by structural water, could also play an important role in anchoring indigo molecules (Fois et al., 2003), as suggested by thermochemical data (Doménech et al., 2007a).

The most recent electrochemical data (Doménech et al., 2009) suggest that there are different topological redox isomers of indigo attached to the palygorskite matrix. This can be seen in Figure 4.17, where the SQWV in contact with aqueous acetate buffer for different Maya blue-type specimens prepared by crushing indigo (1% w/w) and palygorskite and submitted to different thermal treatments, are shown. In the unheated sample (Figure 4.17a), two main peaks at +0.45 and −0.28 V vs. AgCl/Ag appear, attributable to the aforementioned oxidation of indigo to dehydroindigo and the reduction of indigo to leucoindigo. Upon heating in a furnace above 130–180°C, the voltammetric response of the MB-type specimens changed significantly, with the peak at +0.45 V appearing like several overlapping signals (Figure 4.17b). This is in agreement with current ideas on MB preparation—the heating process favoring the attachment of indigo to the palygorskite framework. Specimens treated at 180°C can exhibit up to three different topological redox isomers as judged by peak splitting observed in voltammograms. ^{13}C NMR data in Figure 4.18 suggest the presence of different indigo/dehydroindigo isomers.

Similar features were obtained for sepiolite-based specimens, but no comparable variation of the electrochemical response was obtained for indigo associated to laminar clays such as kaolinite and montmorillonite or for alizarin-palygorskite
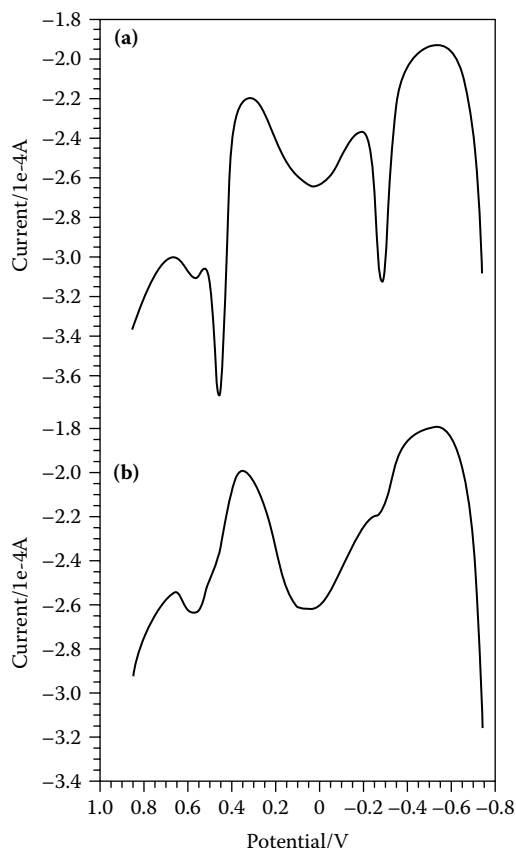
FIGURE 4.17 SQWVs for paraffin-impregnated graphite electrodes modified with indigo (1% w/w) plus palygorskite specimens, (a) unheated and (b) treated at 180°C for 24 h in a furnace, in contact with 0.50 M acetate buffer at pH 4.75. Potential step increment, 4 mV; square-wave amplitude, 25 mV; frequency, 5 Hz.

specimens. All these features clearly suggest that peak splitting can be attributed to a specific indigo-palygorskite and indigo-sepiolite interaction that differs for a merely external adsorption, as occurring for alizarin-sepiolite, alizarin-palygorskite, indigo-montmorillonite, and indigo kaolinite specimens.

Consistently, upon repetitive scanning of the potential for palygorskite-based samples, the peak recorded at more positive potentials in freshly prepared electrodes vanishes, whereas the other signals remain essentially unchanged, with only a slow peak current decay in successive scans. This is just one of the conditions characterizing the electrochemistry of species strongly attached to microporous aluminosilicates (Bessel and Rolison, 1997a), thus suggesting that such signals can be attributed to a strongly palygorskite- or sepiolite-associated species.

Further support for the above scheme was obtained in experiments for MB-type samples in contact with MeCN solutions containing Hex_4N^+, Bu_4N^+, and Et_4N^+
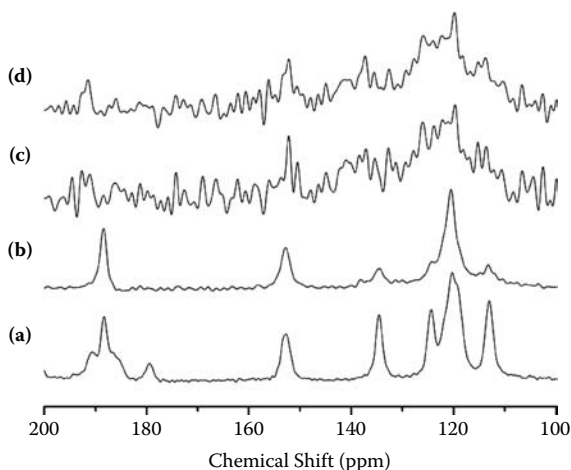
FIGURE 4.18 ^{1}H-^{13}C CP/MAS NMR for (a) indigo and MB-type samples prepared by crushing palygorskite with indigo; (b) 6% w/w of dye; (c) 1% w/w of dye, heated at 130°C; (d) as before, but heated at 180°C.

electrolyte ions. As shown in Figure 4.19, samples in contact with (a) Hex$_4$NPF$_6$/MeCN and (b) Bu$_4$NPF$_6$/MeCN electrolytes displayed a unique, weak peak at a potential almost identical to that recorded for indigo dissolved in organic solvents. This signal can be assigned to the reduction of external indigo to its corresponding radical anion, as described by Bond et al. (1997). This process can be presented as:

$$H_2IN \text{ (ads)} + e^- \rightarrow H_2IN^{\cdot-} \text{ (ads)} \tag{4.11}$$
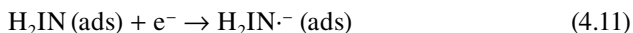
where (ads) denotes adsorbed species.

In contrast, in the presence of Et$_4$N$^+$ electrolyte, the voltammogram consists of two well-separated peaks at −0.54 and −0.76 V (see Figure 4.19c). This electrochemistry can be described assuming that palygorskite-associated molecules remain electrochemically silent as far as the electrolyte contains bulky Hex$_4$N$^+$ and Bu$_4$N$^+$ cations, both unable to enter into the palygorskite channel system. If the electrolyte contains Et$_4$N$^+$ cations, which can enter into the clay framework, palygorskite-associated species can be reduced, thus yielding the peak at −0.54 V. This peak can unambiguously be assigned to the reduction of palygorskite-associated species:

$$\{H_2IN\} + Et_4N^+ + e^- \rightarrow \{H_2IN^{\cdot-} \cdots Et_4N^+\} \tag{4.12}$$
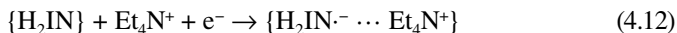
Concentration profiles for the variation of the concentration of the different topological redox isomers with depth were estimated from chronoamperometric and chronocoulometric data. Application of methods described in Section 2.5 led researchers to establish that the electrochemical process represented by Equation (4.9) is controlled by electron diffusion with $D_e = 1 \times 10^{-11}$ cm^2/sec (Doménech et al., 2009). Resulting curves are shown in Figure 4.20 for a three-isomer system.

Application of available methods (Scholz and Hermes, 1999; Doménech et al., 2000a, 2002c) for voltammetric measurements provides information concerning
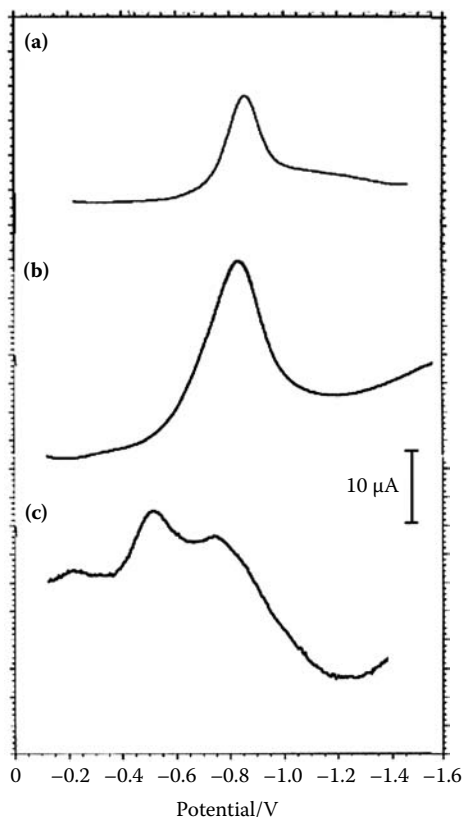
FIGURE 4.19 SQWVs for paraffin-impregnated graphite electrodes modified with indigo (1% w/w) plus palygorskite specimen heated at 180°C for 24 h in a furnace, in contact with 0.10 M solutions of (a) Hex_4NPF_6, (b) Bu_4NPF_6, and Et_4NClO_4 in MeCN. Potential step increment, 4 mV; square-wave amplitude, 25 mV; frequency, 10 Hz.

the oxidation state of the electroactive centers in porous materials (Doménech et al., 2007c). The method of Scholz and Hermes is based on the fact that the entire CVs for solutions of the reduced and the oxidized forms of the depolarizer, although identical in shape, are shifted along the current axis depending on the redox state. As a result, a direct estimate of the molar fraction of the oxidized form of the couple, α_{ox}, can be obtained from the currents at the extreme potentials of the voltammogram (switching potentials). The second method derives from the comparison of peak currents in the first and second potential scans in CVs initiated just at the midpoint potential between cathodic and anodic peaks. For minimizing disturbing effects due to ohmic drops in the cell and capacitive effects, a calibration was performed using CVs for microparticulate deposits of indigo using peaks I and II as representative of systems containing $\alpha_{ox} = 0$ and $\alpha_{ox} = 1$, respectively (Doménech et al., 2009). Using CVs at different potential scan rates, an estimate of the variation of the molar fraction of indigo, α_{DI}, with the depth in palygorskite
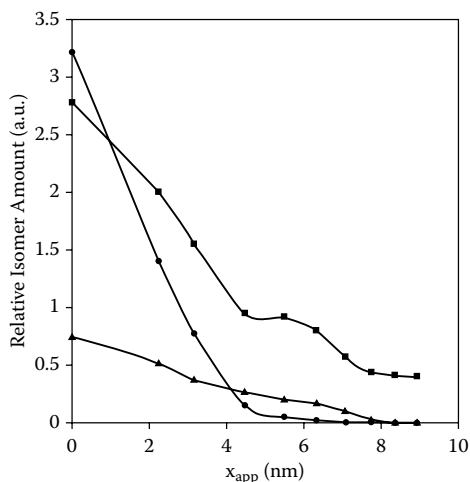
FIGURE 4.20 Variation with the apparent depth, x_{app} ($=(D_e t)^{1/2}$), of estimated amount of different topological isomers responsible for signals (see Figure 4.17b) at +0.45 V (squares), +0.55 V (triangles), and +0.62 V (rhombs) in synthetic MB-type samples prepared from indigo and palygorskite and heated at 180°C for 24 h. From chronocoulometric data.
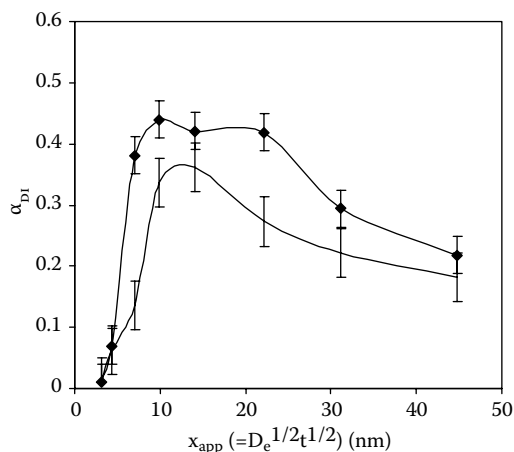
FIGURE 4.21 Variation with the apparent depth, x_{app} ($=(D_e t)^{1/2}$), estimated molar fraction of dehydroindigo, for synthetic MB-type samples prepared from indigo and palygorskite (rhombs) and sepiolite (bars), heated at 180°C for 24 h; from coulometric and cyclic voltammetric data, respectively.

or sepiolite crystals can be made. The resulting α_{DI} vs. x_{app} plots for MB@P$_{180}$ and MB@SP$_{180}$ are shown in Figure 4.21.

All these results are illustrative of the inherent capability of electrochemical methods to provide information relevant to the knowledge of structure and reactivity of electroactive species incorporated into porous materials.

# 5 Electrochemistry of Metal-Organic Frameworks

5.1 INTRODUCTION

Metal-organic frameworks (MOFs) are crystalline systems that can be described as infinite networks resulting from the bonding of metal ions, which act as coordination centers, with polyfunctional organic molecules. First prepared by Tomic (1965) and Yaghi et al. (1996), MOFs can be regarded as coordination polymer "sponges" by virtue of their large surface area, high porosity, and permeability to guest molecules (Kitagawa et al., 2004; Rowsell and Taghi, 2005). Remarkably, and in contrast with other microporous materials, there is a lack of any volume inaccessible to guest molecules or ions. Organic linkers contain carboxylate, cyanide, or pyridine coordinating groups. A schematic representation of the $Cu(bpy)(H_2O)_2(BF_4)_2(bpy)$ MOF (Jiang et al., 2008) is shown in Figure 5.1.

The singular porosity of MOFs allows for a significant redox conductivity that, in contrast with zeolites and other microporous aluminosilicates, can involve all units of the material. This is the case of Cu^{2+}- and Zn^{2+}-based MOFs with terephtalic acid; in these materials, both metal centers and organic units are potentially electroactive in contact with suitable electrolytes.

The relevant properties of MOFs have prompted their use for catalysis, gas storage, and separation (Janiak, 2003; Chun et al., 2005; Kaye and Long, 2005; Rowsell and Yaghi, 2006), as well as for fuel cells (Mueller et al., 2006), Li-based batteries (Li et al., 2006; Férey et al., 2007), and electrocatalysis (Wang et al., 2008). Conversely, MOFs can be synthesized electrochemically, as described by Mueller et al. (2006). MOFs are indirectly related with other electrochemical applications acting as a template for the synthesis of porous carbon to be applied as double-layer electrochemical capacitor (Liu et al., 2008).

The electrochemistry of MOFs should, in principle, be based on redox processes for both metal ions and polyfunctional organic molecules coupled with the ingress/issue of electrolyte ions in/from the MOF lattice. In view of the large ionic permeability of MOFs, one can expect that an internal diffusion occurs. This means that the redox reactivity can be significantly (and rapidly) extended along the crystal. Accordingly, redox conductivity should be heavily influenced by the structure of the material and possible structural conditioning (anisotropy, reticular defects). Conversely, cooperative, large-scale structural effects (crystalline domains, secondary phases) might be produced as a result of the application of electrochemical inputs.

In addition, the involvement of certain transition metal ions makes it possible for us to study electrochemical processes resulting in the formation of metal particles or deposits from MOFs. This is of interest with regard to recent developments in oscillatory

Metal ion or cluster

Organic linkers
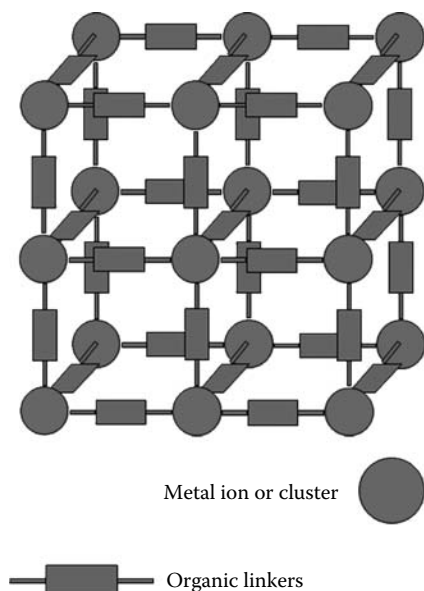
FIGURE 5.1   Schematic representation of the *ab* plane of the Cu(bpy)(H$_2$O)$_2$(BF$_4$)$_2$(bpy) MOF crystal. (Adapted from Jiang et al., 2008. *J. Catal.* 257: 390–395, with permission.)

electrodeposition (Strasser et al., 1999). Thus, formation of ordered metallic nanostructures by modulating oscillatory electrodeposition through changes in electrochemical parameters (Switzer et al., 1998; Saliba et al., 2002; Zhang et al., 2004) or using organic additives (Yu et al., 1999; Trejo et al., 2001) has been recently reported.

In this chapter, the electrochemistry of MOFs will be studied with particular attention to their peculiarities with respect to other microporous materials. Two general types of electrochemical processes will be considered: those involving an ion insertion–driven electrochemical process that, in principle, does not demand sharp structural changes and those involving formation of metal particles, thus requiring the formation of a new phase. The electrochemistry of solid materials with miscibility gaps has been theoretically treated by Lovric et al. (2000).

Several related materials, such as metal coordination oligomers and polymers (Ye et al., 2005), interpenetrating two-dimensional cationic coordination frameworks (Wang et al., 2008), "organic metals," among others, are currently under intensive research, and their electrochemistry will probably be attracting attention in the next few years.

5.2   ION INSERTION–DRIVEN ELECTROCHEMISTRY OF MOFS

The first remarkable feature is the significant dependence of the electrochemical response on the size of electrolyte ions (Doménech et al., 2006d, 2007d). This is illustrated in Figure 5.2 for the reduction of a deposit of Cu-MOF immersed into different MeCN electrolytes. In contact with Bu$_4$NPF$_6$/MeCN, weak reduction peaks were obtained in the +0.60 to −1.85 V vs. AgCl/Ag potential region. In the
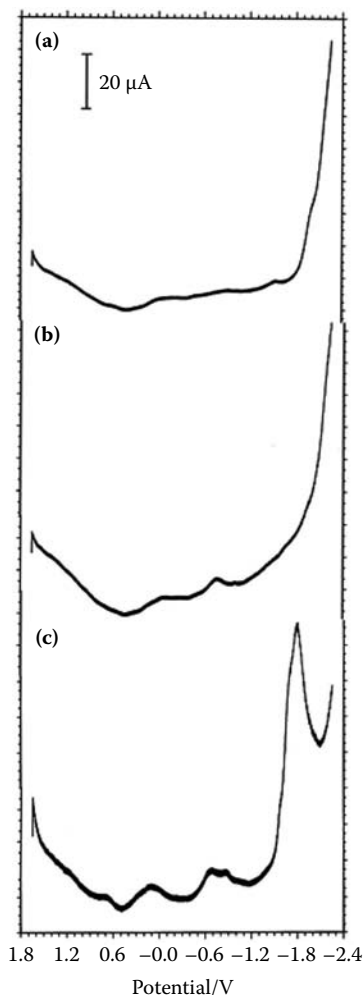
FIGURE 5.2 Square-wave voltammograms of Cu-MOF immersed into (a) 0.10 M Bu$_4$NPF$_6$/MeCN, (b) 0.10 M Et$_4$NClO$_4$/MeCN, and (c) 0.10 M LiClO$_4$/MeCN. Potential scan initiated at +1.65 V vs. AgCl/Ag in the negative direction. Potential step increment, 4 mV; square-wave amplitude, 25 mV; frequency, 5 Hz. (From Doménech et al., 2006d. *Electrochem. Commun.* 8: 1830–1834, with permission.)

presence of Et$_4$NClO$_4$/MeCN, reduction peaks at +0.20 and −0.65 V were recorded. Upon immersion into LiClO$_4$/MeCN electrolytes, the above peaks are enhanced and exhibit peak splitting, whereas a prominent cathodic peak appears at −1.75 V. These features can be rationalized on assuming that the reduction of Cu^{2+} centers existing in the MOF involves the coupled ingress of electrolyte cations into the solid microporous lattice. This ingress of such cations should be significantly size hindered, so that bulky Bu$_4$N$^+$ ions cannot enter into the MOF. In contact with Bu$_4$N$^+$/MeCN electrolytes, only ill-defined cathodic waves, which can be attributed to the reduction

of external Cu^{2+} centers, appear. In contrast, for Et_4N^+/MeCN and Li^+/MeCN electrolytes, the ingress of Li^+ ions and, partially, Et_4N^+ ions should be allowed, thus permitting the record of well-defined voltammetric peaks corresponding to the propagation of the redox reaction to the Cu-MOF bulk. Consistently, the net amount of charge transferred was found to be dependent on the electrolyte concentration, as expected for ion insertion solids (Scholz and Hermes, 1999).

Reduction of Cu^{2+} centers to Cu^+ ones can, in principle, occur via four different electrochemical pathways:

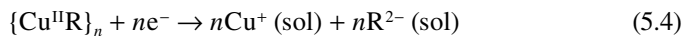1. Topotactic solid-state transformation coupled with the ingress of electrolyte cations, M^+, into the solid:

$$\{Cu^{II}R\}_n + nM^+ \, (sol) + ne^- \rightarrow \{Cu^IR\cdots M^+\}_n \tag{5.1}$$

2. Proton-assisted topotactic solid-state transformation involving the protonation of organic groups in the solid lattice:

$$\{Cu^{II}R\}_n + nH^+ \, (sol) + ne^- \rightarrow \{Cu^I(RH)\}_n \tag{5.2}$$
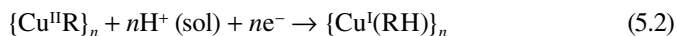
3. Reductive reorganization involving the loss of organic polyfunctional units:

$$\{Cu^{II}R\}_n + ne^- \rightarrow \{Cu^IR_{1/2}\}_n + (n/2)R^{2-} \, (sol) \tag{5.3}$$

4. Reductive dissolution process:

$$\{Cu^{II}R\}_n + ne^- \rightarrow nCu^+ \, (sol) + nR^{2-} \, (sol) \tag{5.4}$$
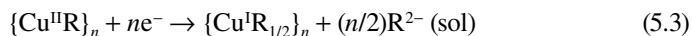
In all these expressions, {} denotes, as customary along the text, solid phases, whereas (sol) represents solvated species existing in solution phase. Processes (3) and (4) can eventually be proton assisted.

Evidence for the ingress of electrolyte cations into the Cu-MOF lattice clearly suggests that the reaction schemes (1) and (2) would be operative.

The ingress of electrolyte cations into the MOF framework was confirmed by scanning electron microscopy/energy-dispersive x-ray (EDX) analysis of electrochemically treated deposits of Cu-MOF. Results obtained after application of a reductive potential step to Cu-MOF crystals in contact with acetate buffers are shown in Figure 5.3. Here, EDX spectra for (a) pristine Cu-MOF and (b) Cu-MOF after application of a constant potential of -1.0 V for 10 min are shown. EDX spectra of original Cu-MOF crystals exhibits prominent Cu peaks at 1.0, 8.0, and 8.4 keV accompanied by a Si signal at 1.9 keV. After the electrolysis step, an additional Na peak at 1.1 keV appears.

Interestingly, electrochemical processes associated with redox changes in the organic polyfunctional units are also dependent on the composition of the supporting electrolyte. Voltammograms in Figure 5.4, initiated at -2.05 V in the positive direction, correspond to Cu-MOF immersed into: (a) 0.10 M Bu_4NPF_6/MeCN, (b) 0.10 M Et_4NClO_4/MeCN, and (c) 0.10 M $LiClO_4$/MeCN. In these voltammograms, the
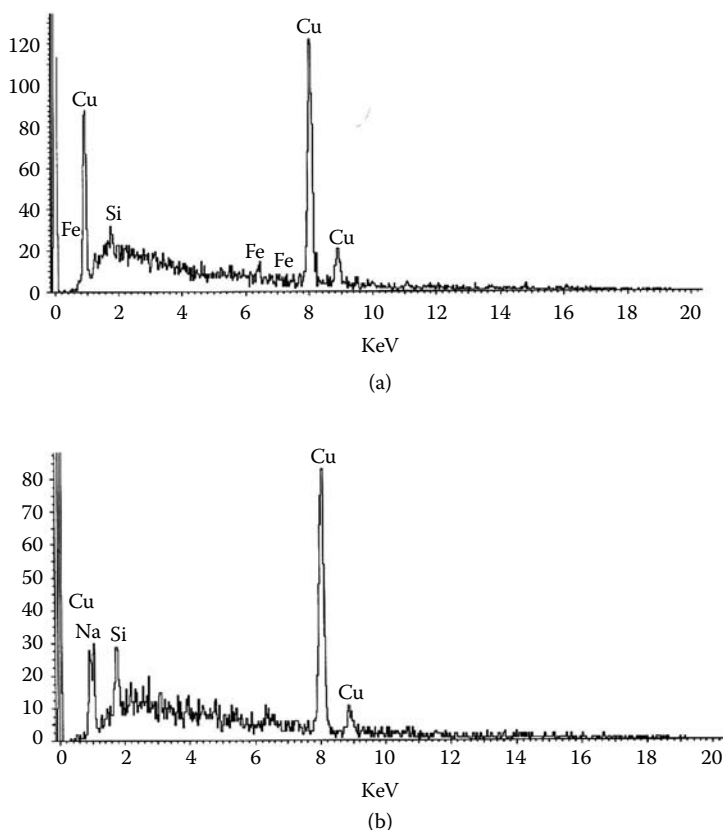
FIGURE 5.3   EDX spectra recorded for a Cu-MOF deposit (a) before and (b) after application of a constant potential of -1.0 V during 10 min in contact with 0.50 M acetate buffer (pH 4.85). (From Doménech et al., 2006d. *Electrochem. Commun.* 8, 1830–1834, with permission.)

prominent anodic peak at $+0.05$ V corresponds to the stripping oxidation of Cu metal generated by electrochemical reduction of Cu^{2+} centers at the negative potentials applied at the beginning of the voltammetric scan. This peak results in the release of Cu^+ ions to the solution, further oxidized to Cu^{2+} at $+1.6$ V:

$$Cu^+ \text{ (sol)} \rightarrow Cu^{2+} \text{ (sol)} + e^- \qquad (5.6)$$
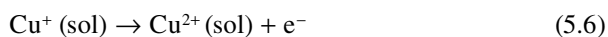
Remarkably, a prominent Cu stripping was obtained in contact with Bu_4NPF_6/ MeCN and M Et_4NPF_6/MeCN electrolytes but not in contact with $LiClO_4$/MeCN. This difference can be attributed to a different metal deposition mode associated with the different permeability of the material to cation transport (*vide infra*).

Oxidation pathways involve anion insertion coupled to electron transfer process. In experiments performed on Cu-MOF modified electrodes such as those shown in Figure 5.4, additional anodic peaks located in the $+0.60$ to $+1.80$ V potential region are attributable to the oxidation of polyfunctional organic groups. Such oxidation
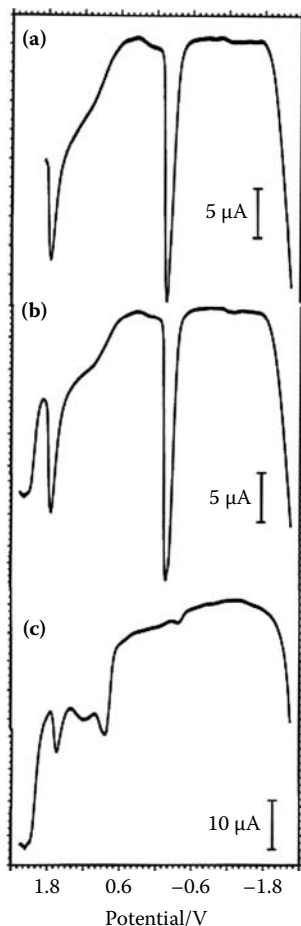
FIGURE 5.4 Square-wave voltammograms of Cu-MOF immersed into: (a) 0.10 M Bu$_4$NPF$_6$/
MeCN, (b) 0.10 M Et$_4$NClO$_4$/MeCN, and (c) 0.10 M LiClO$_4$/MeCN. Potential scan initiated
at −2.05 V vs. AgCl/Ag in the positive direction. Potential step increment, 4 mV; square-wave
amplitude, 25 mV; frequency, 5 Hz.

processes should involve the ingress of electrolyte counteranions coupled with the
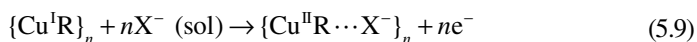issue of electrons into/from the MOF lattice:

$$\{Cu^{II}R\}_n + nX^- \ (\text{sol}) \rightarrow \{Cu^{II}R^{ox} \cdots X^-\}_n + ne^- \tag{5.7}$$
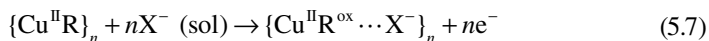
Now, in the presence of bulky PF$_6^-$ anions, only Cu-associated oxidation peaks
appear (Figure 5.4a,b), whereas in the presence of ClO$_4^-$ ions, additional anodic peaks
are recorded (Figure 5.4c). Differences in these last processes in LiClO$_4$/MeCN and
Et$_4$NClO$_4$/MeCN electrolytes are attributable to the coexistence of a competing

mechanism, involving the issue of cations previously entered into the MOF material as a result of reductive processes. This can be represented as:

$$\{Cu^I R \cdots M^+\}_n \rightarrow \{Cu^I R^{ox}\}_n + nM^+ \text{ (sol)} + ne^- \tag{5.8}$$

Simultaneously, the oxidation of Cu(I) to Cu(II) can occur via such competing pathways:

$$\{Cu^I R\}_n + nX^- \text{ (sol)} \rightarrow \{Cu^{II} R \cdots X^-\}_n + ne^- \tag{5.9}$$

$$\{Cu^I R \cdots M^+\}_n \rightarrow \{Cu^{II} R\}_n + nM^+ \text{ (sol)} + ne^- \tag{5.10}$$

5.3 METAL DEPOSITION ELECTROCHEMISTRY OF MOFS

Figure 5.5 shows a typical cyclic voltammetry (CV) for Cu-MOF in contact with aqueous acetate buffer. Here, two overlapping cathodic peaks at -0.21 and -0.46 V, preceding an ill-defined wave near -1.0 V, appear. In the reverse scan, a typical stripping peak at $+0.37$ V is recorded. This peak, associated with the oxidation of copper metal electrochemically formed, disappears when the potential is switched at potentials ca. -0.25 V but is clearly recorded for switching potentials more negative than -0.35 V. As a result, it is concluded that Cu^{2+} centers are reduced to Cu^+ ones at potentials less negative than -0.30 V. At more negative potentials, metallic copper is formed.
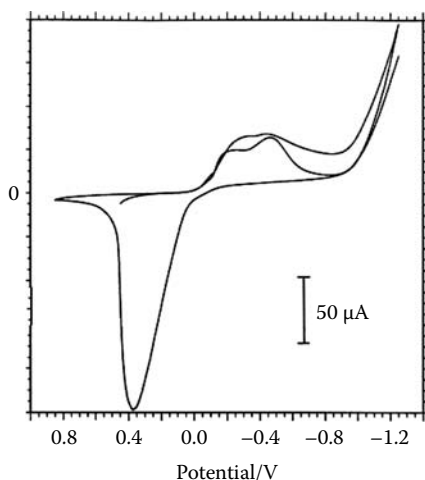
FIGURE 5.5 CV of a polymer film electrode modified with Cu-MOF immersed into 0.25 M HAc + 0.25 M NaAc, pH 4.85. Potential scan rate, 50 mV/sec. (From Doménech et al., 2007d. *J. Phys. Chem. C* 111, 13701–13711, with permission.)
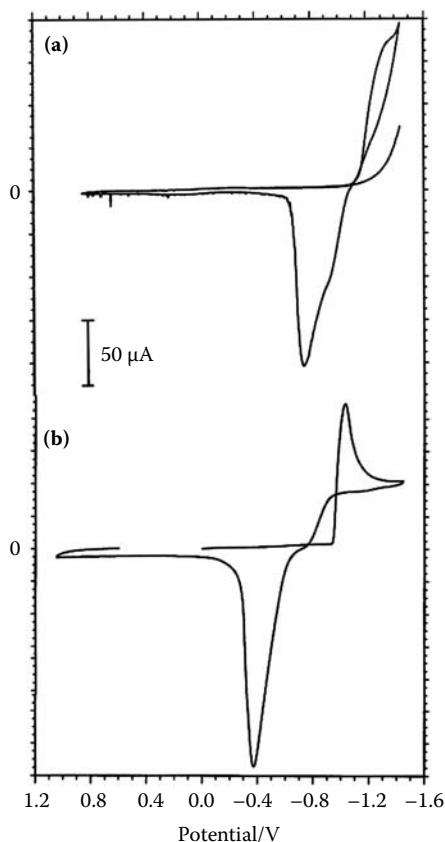
FIGURE 5.6 CVs of: (a) PFE modified with Zn-MOF immersed into 0.25 M HAc + 0.25 M NaAc, pH 4.85; (b) an unmodified GCE in contact with a 1.0 mM solution of $Zn(NO_3)_2$ in the above electrolyte. Potential scan rate, 50 mV/sec. (From Doménech et al., 2007d. *J. Phys. Chem. C* 111, 13701–13711, with permission.)

Figure 5.6 shows CVs of (a) polymer film electrode (PFE) modified with Zn-MOF immersed into acetate buffer and (b) an unmodified GCE in contact with a 1.0 mM solution of $Zn(NO_3)_2$ in the above electrolyte. In both cases, although with different profiles, a reduction wave at highly negative potentials is recorded, followed, in the subsequent anodic scan, by a prominent stripping peak.

The Cu^{2+} to Cu^+ reduction, however, appears as a relatively complicated process, as denoted by peak splitting observed in square-wave voltammetric experiments, as shown in Figure 5.7. Here, peak splitting features are significantly sensitive to variations in the square-wave frequency (i.e., in the timescale) of the voltammetric experiment, thus denoting that different electrochemical pathways are probably involved.

This is consistent with data from atomic force microscopy (AFM) examination of Cu-MOF deposits submitted to a cathodic input. As shown in Figure 5.8a, pristine Cu-MOF particles appeared as elongated crystals 100–200 nm in size with a corrugated surface texture. Upon application of a constant potential step at −250 mV
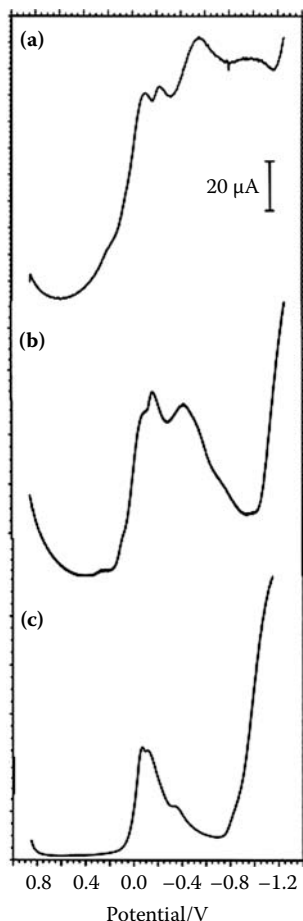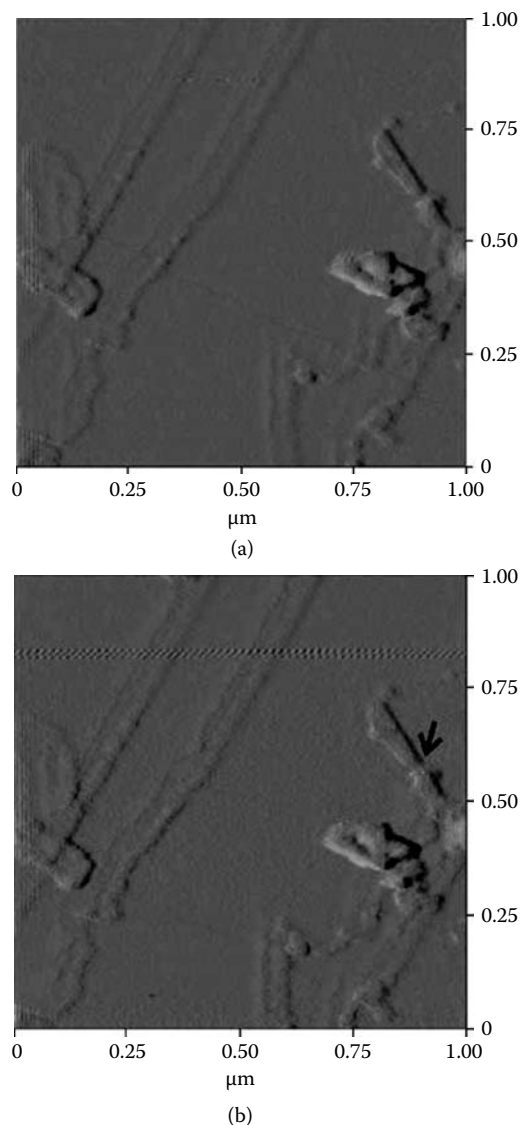
FIGURE 5.7 SQWVs of Cu-MOF-modified electrodes in contact with 0.25 M HAc + 0.25 M NaAc, pH 4.85. Potential step increment, 4 mV; square-wave amplitude, 25 mV; frequency: (a) 500, (b) 100, (c) 15 Hz. (From Doménech et al., 2007d. *J. Phys. Chem. C* 111, 13701–13711, with permission.)

during 5 min, a contraction of the crystals was observed, accompanied of a small variation in their profile, as shown in Figure 5.8b (Doménech et al., 2007d).

Peak splitting observed for the reduction signals at potentials less negative than −0.50 V (see Figure 5.7) can be attributed to: (1) reduction of different topological redox isomers of Cu^{2+} located, for instance, in the external faces of Cu-MOF crystals, in near surface cracks and crevices, or in the bulk of the crystal; (2) reduction via different mechanisms (probably pathways (a) and (b)); (3) appearance of anisotropic effects for electron hopping between Cu^{2+} centers and cation diffusion across the MOF lattice (and/or, eventually, proton hopping between organic polyfunctional units).

Reduction of Zn-MOF and Cu-MOF can lead to the formation of metallic Zn and Cu, respectively, as indicated by CV in Figure 5.6 for Cu-MOF. In the case of

FIGURE 5.8 (See color insert following page 94.) AFM images recorded on a Cu-MOF-modified electrode in contact with 0.50 M acetate buffer (pH 4.85): (a) pristine sample; (b) after application of a potential step at −250 mV for 5 min. (Adapted from Doménech et al., 2007d. *J. Phys. Chem. C* 111, 13701–13711, with permission.)

Zn-MOF in contact with aqueous electrolytes, potentials of ca. −1.0 V are required (see Figure 5.6). As in the case of Cu-MOF, reduction of Zn-MOF involves the ingress of electrolyte cations so that voltammetric profiles are strongly electrolyte dependent, as shown in Figure 5.9.
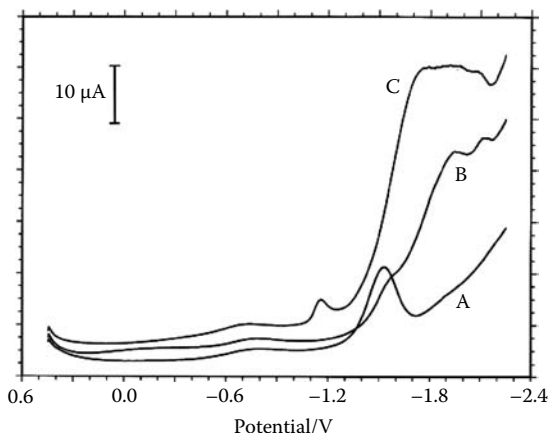
FIGURE 5.9 SQWVs of Zn-MOF immersed into: (A) 0.10 M Bu$_4$NPF$_6$/MeCN, (B) 0.10 M Et$_4$NClO$_4$/MeCN, (C) 0.10 M LiClO$_4$/MeCN. Potential step increment, 4 mV; square-wave amplitude, 25 mV; frequency, 5 Hz. (From Doménech et al., 2007d. *J. Phys. Chem. C* 111, 13701–13711, with permission.)

Formation of metal deposits in such cases, however, is strongly influenced by the electrochemical conditions (potential and time of electrodeposition in constant potential steps, potential scan rate in scanning methods). As can be seen in AFM images shown in Figure 5.10 for Cu-MOF, application of a potential stage at −0.50 V, a series of discrete, lightly marked, transversal structures appear crossing pristine Cu-MOF crystals. By applying a potential step at more negative potentials (−0.85 V), a different series of marked transversal structures 10–15 nm in size and regularly spaced at 45–50 nm appear. If more negative potentials are reached, formation of external deposits of metal particles, similar to those obtained in conventional electrodeposition experiments from Cu^{2+} ions in solution, is observed. Such transversal sheets can unambiguously be attributed to Cu metal deposits because (1) such sheets increased in thickness on prolonging the time duration of the potential step and/or applying more negative potentials, and (2) on returning the potential at values close to −0.35 V, the above features entirely disappear.

AFM images recorded during the application of different potential steps to microheterogeneous deposits of Zn-MOF presented significant differences with those obtained for Cu-MOF. As shown in Figure 5.11a, Zn-MOF consisted of irregular 20- to 30-nm-sized particles. Upon application of potentials of −0.94 V, the crystals show a set of small circular-like surface features, ca. 10 nm in size, growing in the MOF crystal body, as can be seen in Figure 5.11b. Application of potentials of −1.25 V or more negative ones produced similar features with the parallel appearance of external Zn deposits.

These features suggest that the formation of metal deposits occurs via structure-driven processes; that is, that preferential reduction directions are involved. The overall reduction process can be described for Zn-MOF in terms of three extreme models:

(a)

(b)
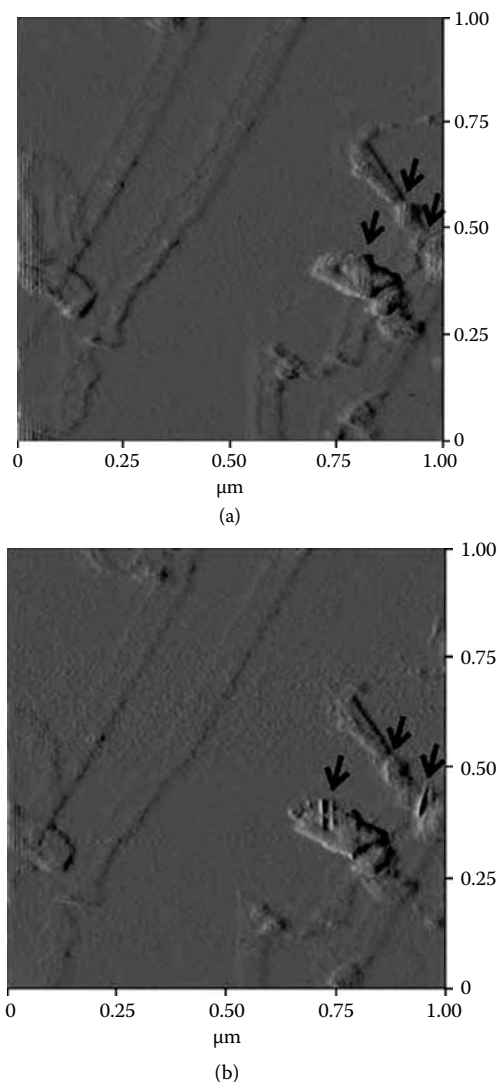
FIGURE 5.10 (See color insert following page 94.) AFM images recorded on a Cu-MOF-modified electrode in contact with 0.50 M acetate buffer (pH 4.85): (a) after application of a potential step at −0.50 *V* for 5 min; (b) id. at −0.85 *V*. (Adapted from Doménech et al., 2007d. *J. Phys. Chem. C* 111, 13701–13711, with permission.)
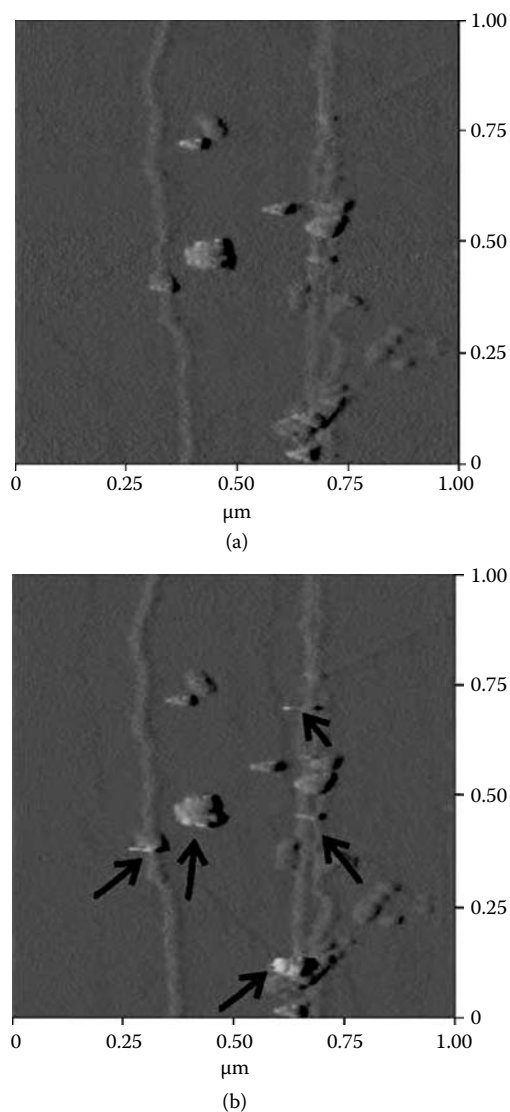
1. Extensive bulk reduction with epitactic formation of an external metal deposit
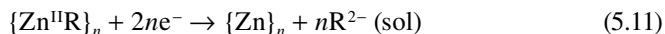
$$\{Zn^{II}R\}_n + 2ne^- \rightarrow \{Zn\}_n + nR^{2-} \text{ (sol)} \tag{5.11}$$

2. Cation-assisted reduction with formation of metal clusters incorporated within the MOF framework ($0 < x < 1$)

$$\{Zn^{II}R\}_n + 2nxM^+ \text{ (sol)} + 2nxe^- \rightarrow \{Zn^{II}_{1-x}(Zn)_x(M^+)_{2x}R\}_n \tag{5.12}$$

(a)

(b)

FIGURE 5.11 (See color insert following page 94.) AFM images of Zn-MOF-modified electrode immersed into acetate buffer: (a) pristine sample; (b) after application of a potential step at −935 mV for 5 min.

3. Proton-assisted reduction with formation of metal clusters incorporated within the MOF framework (0 < x < 1)

$$\{Zn^{II}R\}_n + 2nxH^+ \text{ (sol)} + 2nxe^- \rightarrow \{Zn^{II}_{1-x}(Zn)xR_{1-x}(RH_2)_x\}_n \qquad (5.13)$$
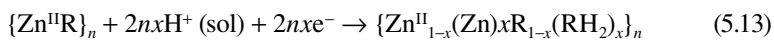
At moderate reduction potentials, the electrochemical pathways (2) and (3) apply, thus resulting in the formation of intercalated structures. Differences in Cu-MOF
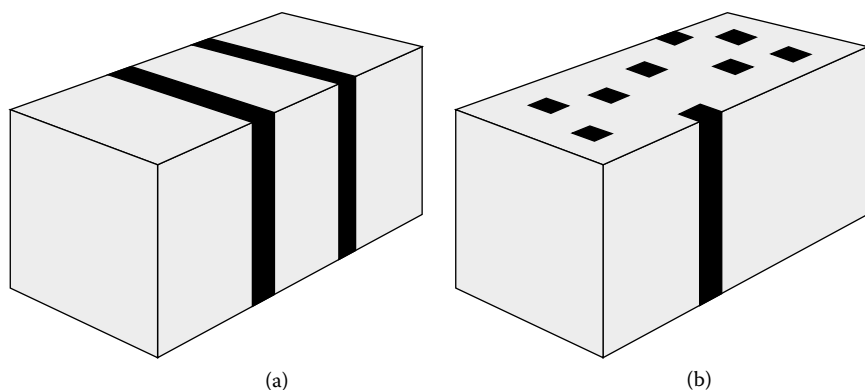
FIGURE 5.12 Pictorial representation of metal deposition modes for (a) Cu-MOF, (b) Zn-MOF.

and Zn-MOF metal intercalated deposits schematized in Figure 5.12 can be correlated with the different symmetry of such materials (see Figure 5.1).

Transmission electron microscopy (TEM) monitoring of morphological changes occurring in Cu-MOF crystals during the application of highly cathodic potentials yields significant results. As shown in Figure 5.13a, pristine crystals of Cu-MOF show a cubic structure 1–1.5 μm in size. After the application of a constant potential of −1.0 V for 5 min, Cu-MOF crystals presented a surface divided into rectangular domains separated by holes (Figure 5.13b). These images can be rationalized by assuming that a fast reductive dissolution with issue of Cu^{2+} ions from the Cu-MOF lattice with concomitant formation of external deposits of Cu metal occurs. As before, privileged crystallographic directions are involved, so that a regular distribution of holes results. Figure 5.14 shows a pictorial representation of reduction processes along selected crystallographic directions.

Description of the overall electrochemical processes requires consideration of at least two steps: (1) reduction of solid materials coupled with ion insertion and (2) formation of metal deposits via nucleation and nuclei growth/diffusion processes. In this regard, the model of Lovric, Scholz, and Oldham and coworkers (see Schröder et al., 2000) for the propagation of electrochemical reactions through ion-permeable solids can be combined with different models for metal electrodeposition: two-dimensional (Schultze and Lohrengel, 1983), three-dimensional (Sharifker and Hills, 1983), layer-by-layer (Obretenov et al., 1994), among others (Nakanishi et al., 2005). The model of Sharifker and Hills (1983) considers two extreme cases involving three-dimensional instantaneous nucleation and progressive nucleation. In the first case, predicted chronoamperometry (CA) curves are given by:

$$i = \frac{nAFcD^{1/2}}{\pi^{1/2}t^{1/2}} [1 - \exp(-N^* \pi kDt)] \qquad (5.14)$$

1 μm   Electron image 1

(a)

1 μm   Electron image 1

(b)
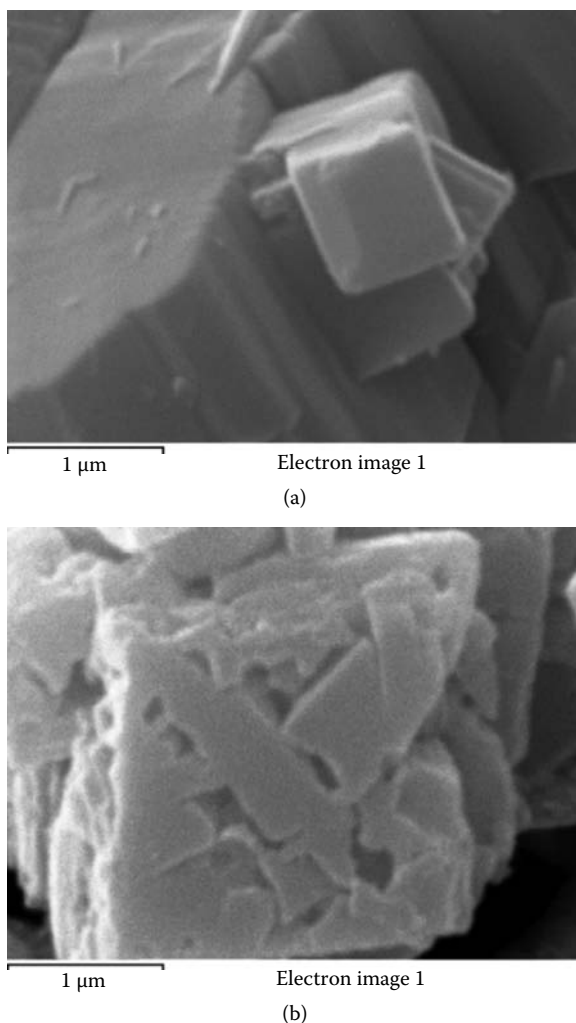
FIGURE 5.13 TEM images recorded for Cu-MOF crystals (a) before and (b) after application of a constant potential of −1.0 V during 5 min in contact with 0.50 M acetate buffer (pH 4.85).

whereas for progressive nucleation, it is predicted:

$$i = \frac{nAFcD^{1/2}}{\pi^{1/2}t^{1/2}} [1 - \exp(-AN^{*}\pi kDt^{2}/2)] \tag{5.15}$$

In these equations, A represents the electrode area and D is the diffusion coefficient of the electroactive ions in the bulk of the solution. For layer-by-layer

(a)

(b)
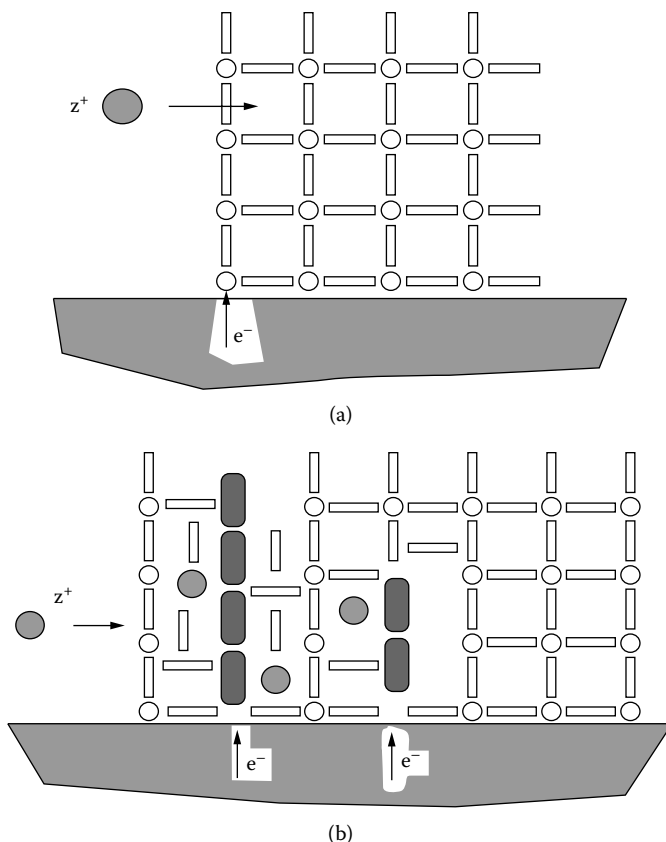
FIGURE 5.14 Schematic diagram of ion insertion/metal deposition in Cu-MOF. (From Doménech et al., 2006d. *Electrochem. Commun.* 8, 1830–1834, with permission.)

deposition with instantaneous nucleation, CA curves can be described by (Milchev and Heerman, 2003):

$$\ln \ln \left[1 - \frac{\pi^{1/2}}{nFcAD^{1/2}} it^{1/2} \right] - 1 = \ln (N^* \pi kD) + \ln t \qquad (5.16)$$

whereas for progressive nucleation, the following current-time variation is predicted:

$$\ln \ln \left[1 - \frac{\pi^{1/2}}{nFcAD^{1/2}} it^{1/2} \right] - 1 = \ln (N^* \pi kDA/2) + 2\ln t \qquad (5.17)$$

In these equations, N^* represents the density of nuclei (cm^{-2}) and k a material constant.

Chronoamperometric data for Cu-MOF in contact with aqueous acetate buffer revealed the existence of different current/time responses depending on the applied potential (Doménech et al., 2007d). At increasingly negative applied potentials, such responses can be associated to diffusion-controlled ion insertion process, a three-dimensional nucleation/growth deposition, and a layer-by-layer deposition process, respectively, in agreement with AFM and TEM observations. From such data, the diffusion coefficient for electrons was calculated as $D_e = 2.0 \times 10^{-11}$ cm^2/sec, whereas the diffusion coefficients for Li$^+$, Na$^+$, and K$^+$ ions were $D_M(Li^+) = 1.4 \times 10^{-7}$, $D_M(Na^+) = 4.4 \times 10^{-8}$, and $D_M(K^+) = 4.1 \times 10^{-8}$ cm^2/sec, respectively.

5.4 SENSING AND ELECTROCATALYSIS

The high specific surface area and the presence of redox-active centers make MOFs interesting materials for electrochemical sensing and electrocatalysis. By the first token, size selectivity can be combined with the coordinating ability of redox-active centers. An example of the possibility of selective electrochemical sensing using MOFs is shown in Figure 5.15, which displays the square-wave voltammetries
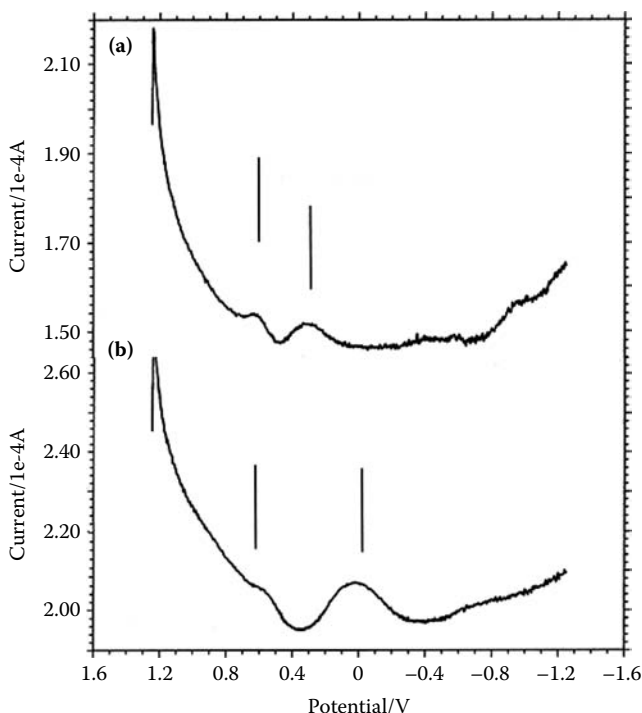

FIGURE 5.15 SQWVs for Cu-MOF attached to paraffin-impregnated graphite electrode in contact with a 0.10 M LiClO$_4$/DMF solution in the (a) absence and (b) presence of 2.0 mM Bu$_4$NF. Potential step increment, 4 mV; square-wave amplitude, 25 mV; frequency, 5 Hz.
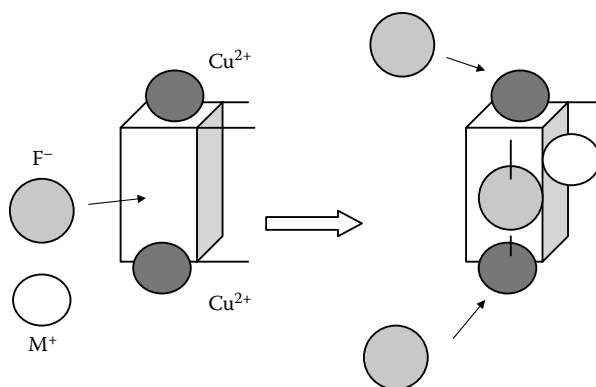
FIGURE 5.16   Scheme for possible coordination schemes of fluoride ions to Cu-MOF.

(SQWVs) for Cu-MOF attached to paraffin-impregnated graphite electrode in contact with a 0.10 M LiClO₄/DMF solution in the (a) absence and (b) presence of Bu₄NF. In the absence of fluoride ions, two cathodic signals at +0.62 and +0.36 V appear, being attributable to the reduction of external and boundary Cu(II) centers to Cu(I) ones. In the presence of fluoride, the first peak is weakened, whereas the second is replaced by a signal at +0.03 V. This electrochemistry can be described in terms of the formation of copper-fluoride adducts favored by the permeability of the MOF framework to ion transport. Tentatively, this attachment could involve fluoride ion coordination with axial positions of copper centers and/or fluoride encapsulation and coordination to metal ions coupled, by reasons of electroneutrality, to the ingress of charge-balancing cations (schematized in Figure 5.16):

$$\{Cu^{II}R\}_n + nz F^- \text{ (sol)} + nz M^+ \text{ (sol)} \rightarrow \{(F^-)_z \cdots Cu^{II}R \cdots (M^+)_z\}_n \qquad (5.18)$$
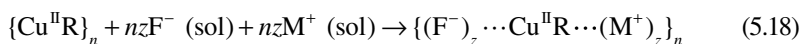
As a result, the reduction potential of Cu(II) centers becomes significantly shifted.

     The electrocatalytic performance of MOFs is illustrated in Figure 5.17, where CVs for a O₂-saturated 0.10 M Bu₄NPF₆/MeCN /MeCN solution at (a) unmodified and (b) Cu-MOF-modified glassy carbon electrode are depicted. At the unmodified electrode, O₂ is reduced in an essentially reversible one-electron step to superoxide radical anion, $O_2^{\cdot-}$,

$$O_2 \text{ (sol)} + e^- \rightarrow O_2^{\cdot-} \text{ (sol)} \qquad (5.19)$$
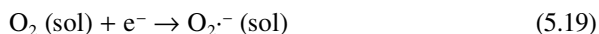
the peak potentials being −0.90 V (cathodic) and −0.72 V (anodic) vs. AgCl/Ag in the plotted voltammogram. The presence of proton impurities and/or water traces modifies the voltammetric response, as described by Sawyer et al. (Barrette et al., 1984; Cofré and Sawyer, 1986). Here, perhydroxyl radical (HO₂·) is formed but rapidly disproportionates into H₂O₂ and O₂. Thus, in the presence of millimolar concentrations
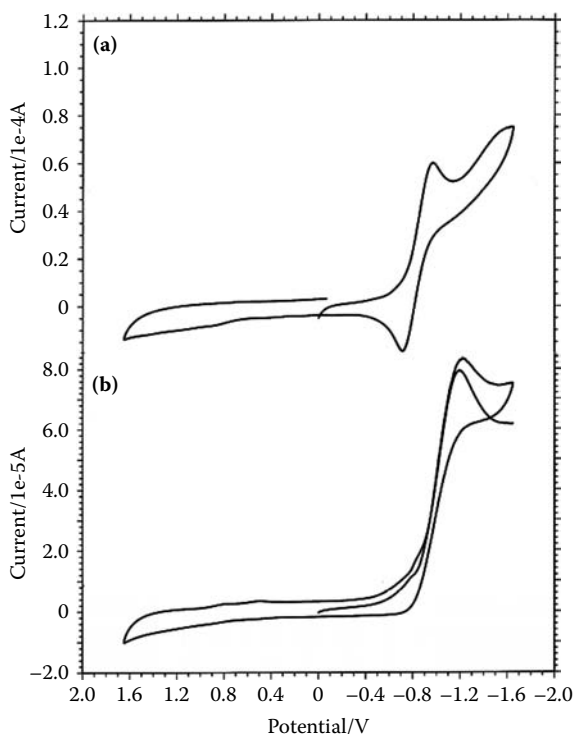
FIGURE 5.17 CVs for a O_2-saturated 0.10 M Bu_4NPF_6/MeCN solution at (a) unmodified and (b) Cu-MOF-modified glassy carbon electrode. Potential scan rate, 50 mV/sec.

of water, reduction of O_2 dissolved in nonaqueous solvents appears like an irreversible process, the overall reaction being:

$$O_2(sol) + 2H^+ (sol) + 2e^- \rightarrow 2H_2O_2 \qquad (5.20)$$
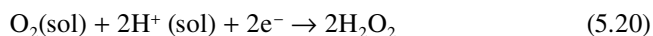
At Cu-MOF-modified electrodes, a reduction wave with a slightly larger intensity is recorded at -1.22 V. The cathodic peak, which is preceded by a weak shoulder at -0.90 V, looks like an irreversible voltammetric wave, because no anodic counterpart is detected.

Remarkably, the electrocatalytic process is modulated by electrolyte counterions. This can be seen in Figure 5.18, which displays CVs at Cu-MOF-modified paraffin-impregnated graphite electrodes immersed into 1.0 mM H_2O plus O_2-saturated (a) 0.10 M Et_4NClO_4/MeCN and (b) 0.10 M $LiClO_4$/MeCN solutions. In the presence of size-hindered Et_4N^+ ions, only the oxygen-localized reversible reduction process at a midpoint potential of ca. -0.80 V is observed. In the presence of Li^+ ions, however, two reduction waves at ca. -0.60 and -1.20 V are recorded, followed, in the subsequent anodic scan, by anodic peaks at -0.85, -0.45, $+0.40$, $+0.90$, and $+1.40$ V.
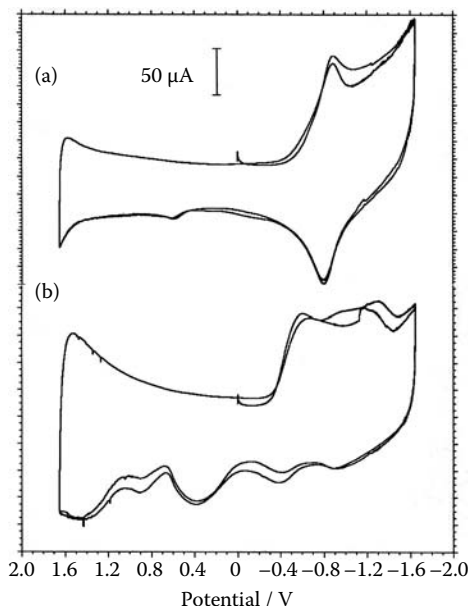
FIGURE 5.18 Deconvoluted CVs at Cu-MOF-modified paraffin-impregnated graphite electrodes immersed into 1.0 mM H_2O plus O_2-saturated (a) 0.10 M Et_4NClO_4/MeCN and (b) 0.10 M $LiClO_4$/MeCN solutions. Potential range: +1.65 to −1.65 V vs. AgCl/Ag. Potential scan rate, 50 mV/sec.

These features can be rationalized by assuming that, for size-hindered electrolytes such as Bu_4NPF_6 and Et_4NClO_4, the catalytic effect only involves external copper centers and operates via an outer scheme pathway where water does not play a significant role, so that the reduction process described by Equation (5.19) is operative. In the presence of size-allowed cations, the electrochemical pathway changes significantly, the reduction apparently occurring in two steps.

More information on the role of metal centers can be obtained by comparing CVs at Cu-MOF-modified electrodes in deoxygentated and O_2-saturated 0.10 M $LiClO_4$/MeCN solutions, shown in Figure 5.19. In the absence of oxygen, copper-localized reduction occurs in two steps: Cu(II) to Cu(I) reduction at ca. +0.40 V (see also Figure 5.2) and subsequent Cu(I) reduction to Cu metal at −0.62 V. This process is followed, in the subsequent anodic scan, by the stripping oxidation of Cu to Cu^+ ions in solution. As previously described, additional oxidation waves are recorded (see Figure 5.4), probably associated with the oxidation of different Cu(I)-MOF species. In the presence of oxygen (see Figure 5.19b), the voltammetric response was essentially identical, but all peaks become significantly enhanced, whereas an additional anodic peak, attributable to the oxidation of peroxo-species generated during previous reductive steps, is recorded at +0.18 V. At the expense of a detailed study of this system, the catalytic effect can be associated to the Cu(I) to Cu(0) interconversion,
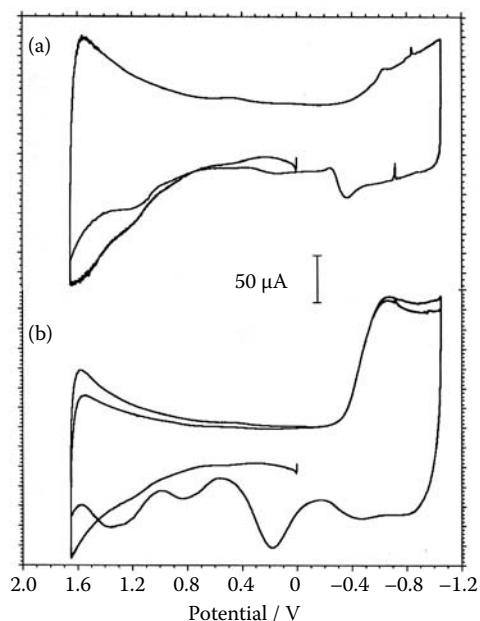
FIGURE 5.19 Deconvoluted CVs at Cu-MOF-modified paraffin-impregnated graphite electrodes immersed into (a) deoxygentated and (b) O_2-saturated 0.10 M $LiClO_4$/MeCN solutions. Potential range: +1.65 to −1.05 V vs. AgCl/Ag. Potential scan rate, 50 mV/sec.

so that eventually the formation of metal clusters of metallic layers can influence the catalytic performance of the MOF. Remarkably, however, the voltammetric profile is maintained upon repetitive cycling the potential scan. This suggests that eventually, zerovalent copper can be formed under these conditions, with no formation of metal deposits, as described in recent literature for heteropolymetallic transition metal complexes (Packheiser et al., 2008).

6 Electrochemistry of Porous Oxides and Related Materials

6.1 OVERVIEW

Most oxide materials adopt microporous structures formed by oxometal units tailored to form cage and tunnel cavities. The electrochemistry of metal oxides in contact with aqueous electrolytes is dominated, as briefly introduced in Section 3.6, by surface redox reactions involving tightly bound hydrated oxometal groups. Porous oxides, however, can undergo, apart from the above, electron transfer processes coupled with ion insertion issue from/to the electrolyte, with the possibility of adopting interstitial positions or binding to metal centers via formation of hydroxo and aquo groups.

In contact with aqueous alkaline media, metal oxide electrochemistry is dominated by hydroxylation processes. However, in contact with acidic media, proton and cation insertion processes occur, eventually leading to complicated responses where reductive or oxidative dissolution processes frequently take place (Scholz and Meyer, 1998; Grygar et al., 2002; Scholz et al., 2005). As far as such processes involve disintegration of the porous structure of the material, electrochemically assisted dissolution processes will be taken only tangentially here.

Related materials comprise, among others, layered double hydroxides (LDHs) and compounds based on polyoxometalate (POM) groups. LDHs form lamellar structures entrapping charge-balancing anions. Polyoxovanadates, molybdates, and tungstates are representative of POM compounds where complicated geometries are obtained from MO_6 octahedral units containing charge-balancing ions occupying cavities. Finally, a fourth group of materials of electrochemical interest is that obtained by doping the above and related materials. Typically, electroactive ions substitute parent metal centers in the lattice of the original material.

Finally, the electrochemistry of porous metal oxides prepared as films from anodic treatment of metal electrodes will also be discussed. Porous metal oxide films on electrodes have applications in a variety of fields, from corrosion protection to batteries and catalysis.

6.2 ELECTROCHEMISTRY OF METAL OXIDES AND METAL OXOHYDROXIDES

A number of metal oxides can be described as porous materials. For instance, porous manganese oxides define octahedral molecular sieves (OMS) that have been introduced in recent years as possible materials for batteries, separations, and chemical
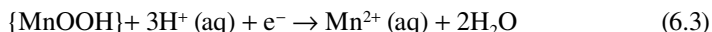
مرجع دانشجویان و مهندسین مواد
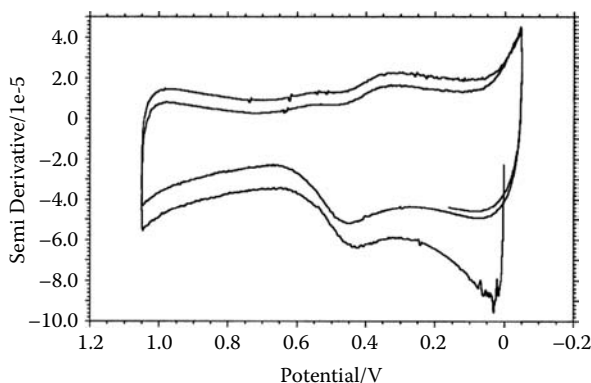
FIGURE 6.1   CVs at pyrolitic graphite electrode for a 5 mM solution of $Mn(NO_3)_2$ in 0.10 M H_2SO_4. Potential scan initiated at 0.0 V in the positive direction. Potential scan rate, 10 mV/sec.

sensing (Cai et al., 2001). Interestingly, metal oxides and related materials can eventually be electrochemically obtained. This is the case of MnO_2, which is deposited on solid electrodes upon oxidation of Mn^{2+} salts in aqueous media, as shown in Figure 6.1. The two basic MnO_2 forms, pyrolusite and ramsdellite, are constituted of MnO_6 octahedral units with edge or corner sharing resulting in 1×1 (pyrolusite) or 1×2 (ramsdellite) tunnels. The oxidation process can be represented as:

$$Mn^{2+} (aq) + 2H_2O \rightarrow \{MnO_2\} + 4H^+ (aq) + 2e^- \qquad (6.1)$$
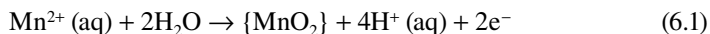
The reduction of MnO_2, however, is a complex process involving proton insertion into the crystal lattice with formation of a scarcely conductive thin surface layer of MnOOH, further reduced to Mn^{2+} in solution, the film limiting the reduction rate of MnO_2 (Bodoardo et al., 1994; Amarilla et al., 1994). These processes can be presented as:

$$\{MnO_2\} + H^+ (aq) + e^- \rightarrow \{MnOOH\} \qquad (6.2)$$

$$\{MnOOH\} + 3H^+ (aq) + e^- \rightarrow Mn^{2+} (aq) + 2H_2O \qquad (6.3)$$

Among the first studied synthetic porous oxides were the so-called manganese OMS with the structures of todorokite (OMS-1) and hollandite (OMS-2; De Guzman et al., 1994). The potassium form of the mineral hollandite (cryptomelane), KMn_8O_{16}, includes one-dimensional tunnels among rigid MnO_2 framework composed of edge-shared and corner-shared MnO_6 octahedra with tunnel size 4.6×4.6 Å, whereas the composition of OMS-1 is $Mg_{0.98-1.35}Mn^{II}_{1.89-1.94}Mn^{IV}_{4.38-4.54}O_{12} \cdot (4.47-4.55)H_2O$ and its structure defines cavities of 6.9 Å. The electrochemistry of such materials is complicated by the fact that both Mn(IV) and Mn(II) centers coexist. For instance, the average manganese oxidation state of cryptomelane is 3.8 (Malinger et al., 2006). The mixed valency of manganese makes this material a good semiconductor and oxidation catalyst.
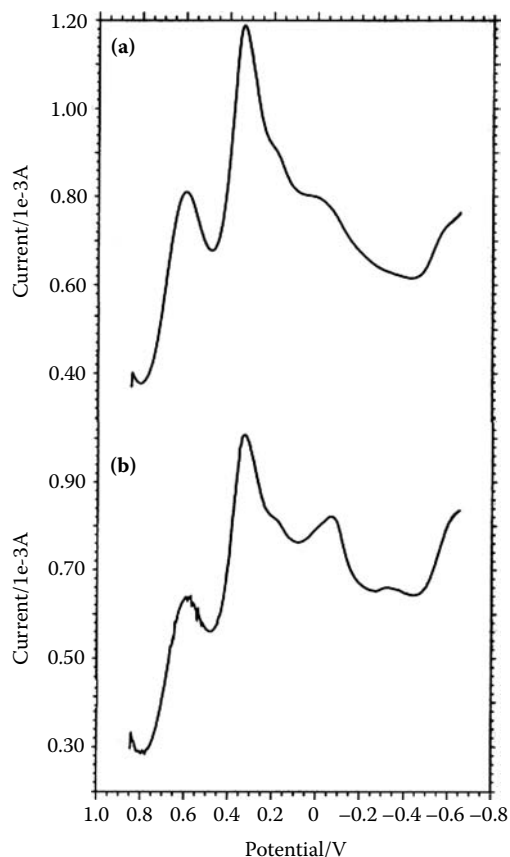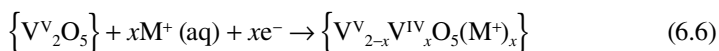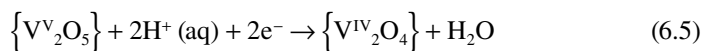
FIGURE 6.2 SQWVs for V_2O_5 attached to paraffin-impregnated graphite electrode immersed into: (a) 0.50 M phosphate buffer; (b) 0.50 M phosphate buffer plus 0.05 M $LiNO_3$. Potential step increment, 4 mV; square-wave amplitude, 25 mV; frequency, 5 Hz.
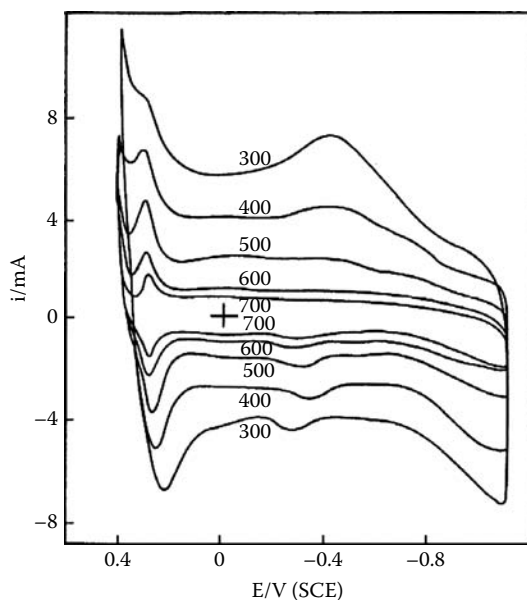
The electrochemistry of V_2O_5 in contact with aqueous media is also representative of this complex behavior, as can be seen in Figure 6.2a. Here, two main peaks at +0.65 and +0.34 V appear, accompanied by weak, overlapping signals at +0.15 and −0.08 V. In the presence of Li^+ ions (Figure 6.2b), the peak at −0.08 V becomes significantly enhanced. This electrochemistry can be described (Barrado et al., 1997) in terms of the superposition of reductive dissolution processes:

$$\left\{V^V_2O_5\right\} + 6H^+ \text{(aq)} + 2e^- \rightarrow 2V^{IV}O^{2+} \text{(aq)} + 3H_2O \qquad (6.4)$$

and proton-assisted and metal-cation-assisted solid-state transformation processes:

$$\left\{V^V_2O_5\right\} + 2H^+ \text{(aq)} + 2e^- \rightarrow \left\{V^{IV}_2O_4\right\} + H_2O \qquad (6.5)$$

$$\left\{V^V_2O_5\right\} + xM^+ \text{(aq)} + xe^- \rightarrow \left\{V^V_{2-x}V^{IV}_xO_5(M^+)_x\right\} \qquad (6.6)$$

FIGURE 6.3 CVs for a RuO₂-poly(vinylchloride) film electrode in contact with 3 M NaOH. (From Dharuman and Chandrasekara Pillai, 2006. *J. Solid State Electrochem.* 10, 967–979, with permission.)

With regard to the electrochemistry of transition metal oxides in contact with alkaline aqueous electrolytes, it is, in general, assumed that surface aqua- and oxo-metal species have a low degree of bridging oxygen coordination to the bulk oxide lattice (Lyons et al., 1994). A widely studied case is that of RuO_2, whose cyclic voltammetry (CV) response in contact with alkaline solutions consists of a main pair of peaks at potentials ca. +0.30 V vs. saturated calomel electrode (SCE) accompanied by a second, weak pair of peaks at potentials around −0.20 V, as shown in Figure 6.3, corresponding to RuO_2-poly(vinylchloride) (PVC) film electrode in contact with 3 M NaOH. Such peaks are attributable to the Ru(VII)Ru(VI) and Ru(VI)/Ru(IV) couples (Dharuman and Chandrasekara Pillai, 2006). A third couple, assigned to the Ru(IV)/Ru(III) couple, at potentials ca. −0.60 V can also be detected. Electrochemical reversibility is approached by this system, as judged by symmetrical peak shapes, nearly equal anodic and cathodic peak heights, linear increase of anodic peak current with potential scan rate, scan rate anodic peak potential, and electrode-rotation independent profiles (Brown and Anson, 1967; Smith et al., 1979). The two first processes were formulated by Lyons et al. (1994) as:

$$\left\{ (-O-)_2 Ru^{IV}(OH)_2(H_2O)_2 \right\} + 2OH^- (aq) \rightarrow \left\{ (-O-)_2 Ru^{VI}(OH)_4 \right\} + 2H_2O + 2e^- \quad (6.7)$$

$$\left\{ (-O-)_2 Ru^{VI}(OH)_4 \right\} + OH^- (aq) \rightarrow \left\{ (-O-)_2 Ru^{VII}O(OH)_3 \right\} + H_2O + e^- \quad (6.8)$$
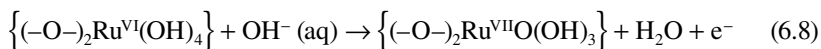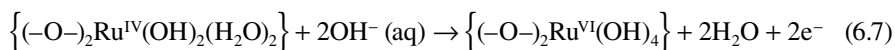
The variation of peak potentials with the pH can lead to an estimate of the number of OH⁻ ions per electron, n_{OH}, involved in each electron transfer step. As in

the case of processes in the solution phase, reversible systems should yield linear E_p vs. pH plots of slope $[\partial E_p / \partial \mathrm{pH}] = 59 n_{OH}/n$. Based on such plots, Dharuman and Chandrasekara Pillai (2006) have recently proposed for RuO_2-PVC film electrodes in contact with NaOH solutions:

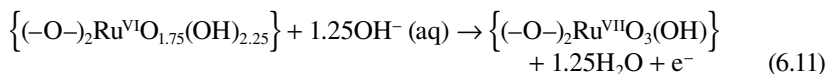$$\left\{ (-O-)_2 Ru^{III} O(H_2O)_3 \right\} + 1.25 OH^- \text{ (aq)} \rightarrow \left\{ (-O-)_2 Ru^{IV} O(OH)_{1.25}(H_2O)_{1.75} \right\}$$
$$+ 1.25 H_2O + e^- \qquad (6.9)$$

$$\left\{ (-O-)_2 Ru^{IV} O(OH)_{1.25}(H_2O)_{1.75} \right\} + 2.5 OH^- \text{ (aq)} \rightarrow \left\{ (-O-)_2 Ru^{VI} O_{1.75}(OH)_{2.25} \right\}$$
$$+ 2.5 H_2O + 2e^- \qquad (6.10)$$

$$\left\{ (-O-)_2 Ru^{VI} O_{1.75}(OH)_{2.25} \right\} + 1.25 OH^- \text{ (aq)} \rightarrow \left\{ (-O-)_2 Ru^{VII} O_3(OH) \right\}$$
$$+ 1.25 H_2O + e^- \qquad (6.11)$$
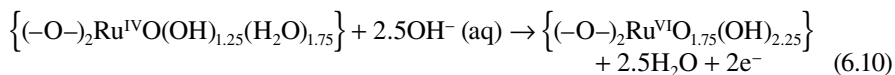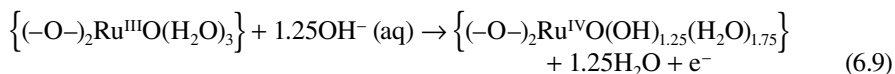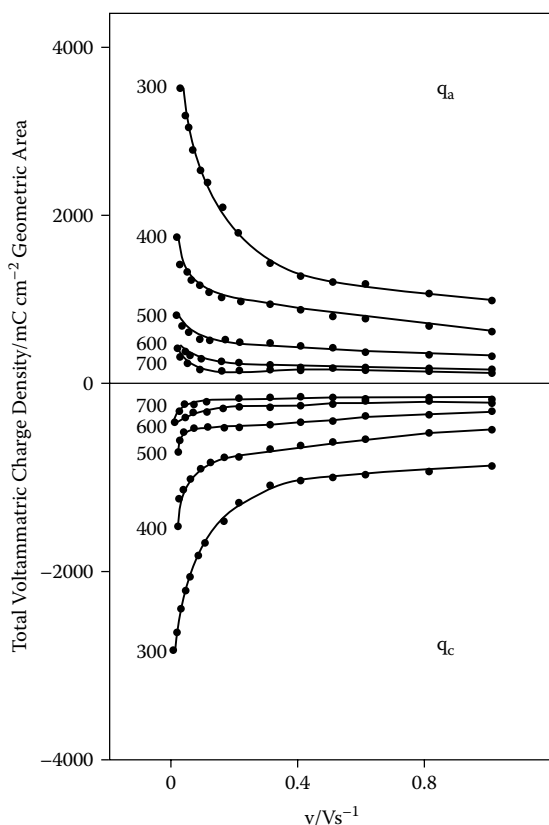
Figure 6.4 shows the charge/potential scan rate plots for different RuO_2-PVC film electrodes in contact with 3 M NaOH.

FIGURE 6.4 Variation with potential scan rate of charge passed in CVs for different RuO_2-PVC film electrodes (temperature of preparation of RuO_2 probes is indicated) in contact with 3 M NaOH. (From Dharuman and Chandrasekara Pillai, 2006. *J. Solid State Electrochem.* 10, 967–979, with permission.)

It should be noted that, in general, two regions can be distinguished in metal oxides: the external oxide/electrolyte interface and the internal oxide/electrolyte interface located inside the fissures and cracks. Obviously, this region becomes less accessible for OH^- ions than the first, so that the charge passed decreases on increasing potential scan rate, as depicted in Figure 6.4. Typically, preparation of this type of material uses thermal treatments at different temperatures, so that charges passed through voltammetric experiments increase on decreasing the temperature of preparation of the material. This can be rationalized by considering that under decreasing oxide preparation temperature, high surface area material having countless fissures, cracks, crevices, etc., results (Trasatti and Lodi, 1981). Nuclear reaction analysis coupled with radiometric methods indicated that a thickness of about 50 nm below the surface is involved in the proton exchange process (Lodi et al., 1991). The sweep rate variation of electrical charge passed, q, measured from the area under voltammetric peaks, can be approached, at low potential scan rates to (Ardizzone et al., 1990):

$$1/q = 1/q^* + gv^{1/2} \tag{6.12}$$

where $q*$ is the maximum surface charge arising due to infinitely slow OH^- ion exchange and g is a constant of proportionality. Thus, $q*$ denotes the charge related to the whole active surface. Complementarily, plots of q vs. $v^{-1/2}$ and extrapolation to $v \to \infty$ gives an ordinate at the origin of $q_{outer}*$, representing the net amount of charge associated to the outer surface of the oxide being forwardly accessible to OH^- ion exchange.

$$q = q^*_{outer} + sv^{-1/2} \tag{6.13}$$

where s is a second constant of proportionality. Then, the charge associated to the internal oxide/solution interface, $q_{in}*$, can easily be calculated as $q_{in}* = q* - q_{outer}*$.

Real systems deviate frequently from ideal behavior due to large uncompensated electrolyte resistance, slow kinetics of electron transfer, and site-to-site interactions (Ilangovan and Chandrasekara Pillai, 1997). Such deviations from Nernstian behavior can be expressed by an interaction term, r, which can be estimated from the variation of peak potential with potential scan rate:

$$i_p = \frac{n^2 F^2 A \Gamma v}{RT(4 - 2r\Gamma)} \tag{6.14}$$

In this equation, A denotes the geometrical area of the electrode and Γ is the surface concentration of electroactive adsorption sites. This last parameter can be calculated from determination of the charge pass associated to solid-state redox reaction, q_s, because $q_s = nFA\Gamma$, or from capacitance determination using the relationship (Brown and Anson, 1977; Smith et al., 1979):

$$C = \frac{n^2 F^2 \Gamma}{RT(4 - 2r\Gamma)} \tag{6.15}$$

In this scheme, each oxide particle has an outer, hydrated catalytically active layer consisting of dangling oxometal surface groups.

Remarkably, reaction of surface metal centers can significantly influence the observed electrochemistry. For instance, nanoparticle mesoporous films of ceria, CeO_2, presumably forms a new $CePO_4$ phase during electrochemical reduction of aqueous phosphate buffer solution (Cummings et al., 2008).

6.3 ELECTROCHEMISTRY OF LAYERED HYDROXIDES AND RELATED MATERIALS

LDHs of Al, Ni, Zn, and other metals are composed of rigid layers where anions and water molecules can move. Typical LDHs can be represented by the formula $[M_{1-x}M'_x(OH)_2][A^{n-}]_{x/n} \cdot mH_2O$, where M is a divalent metal cation, M′ could be a trivalent metal cation or a mix of trivalent and divalent metal cations, and A^{n-} represents an interlayer anion or mix of anions. Both divalent and trivalent cations are located at the center of octahedral composed of OH^- ions, $M(OH)_6$ and $M'(OH)_6$ units share edges forming two-dimensional layers, whereas the interlayer space incorporates anions (and water molecules) to maintain electroneutrality. These materials exhibit a stable lamellar structure while $0.2 \leq x \leq 0.5$, and the interlayer A^{n-} anions can be freely exchanged by foreign anions (Khan and O'Hare, 2002).

Due to their ability to accommodate anionic guests in the interlayer region, such materials have been tested for different applications, from catalysis to sensing and as electrode materials for Ni batteries, as described in Chapter 10. Figure 6.5 shows the CV response of Co-Al LDH immersed into 0.10 M NaOH at two different potential
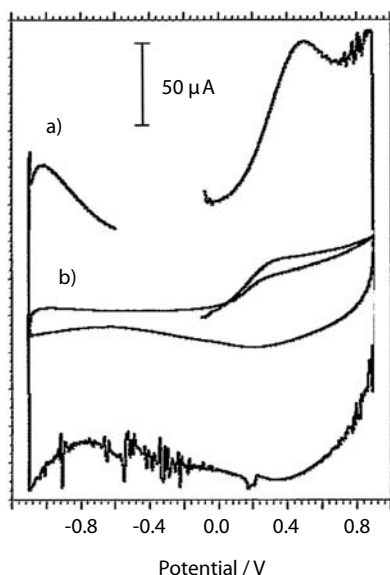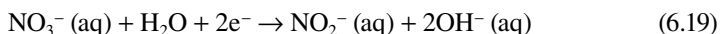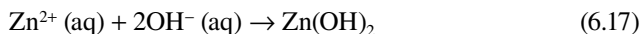

FIGURE 6.5 CVs at different scan rates recorded at Co-Al LDH attached to graphite electrode in contact with 0.10 M NaOH. Potential scan rate: (a) 520; (b) 5 mV/s.

scan rates. Most of this research is focused on hybrid materials and composites, as described by Su et al. (2008). At a potential scan rate of 5 mV/sec, the voltammograms exhibit a cathodic wave at +0.22 V vs. SCE and an anodic wave at +0.41 V whose separation markedly increases on increasing potential sweep rate. The cathodic peak current becomes proportional to the square root of the potential scan rate, thus denoting that the electrochemical process is diffusion controlled. This response, following Scavetta et al. (2005), can be described in terms of a fast entrance of OH$^-$ ions into the interlayer region, so that the electrochemical process can be represented as:

$$\{LDH \cdots Co^{II}\} + OH^- \text{ (aq)} \rightarrow \{LDH \cdots Co^{III} \cdots OH^-\} + e^- \qquad (6.16)$$

Zn-Al LDHs can be prepared by electrodeposition from aqueous solutions of the nitrates of such metals (Yarger et al., 2008). Cathodic depositions, conducted at room temperature without stirring over noble metal-coated electrodes, were achieved by reducing nitrate ions to generate hydroxide ions on the working electrode, the optimal potential being −1.65 V vs. AgCl/Ag in 4 M KCl. The overall reactions involved are

$$Zn^{2+} \text{ (aq)} + 2OH^- \text{ (aq)} \rightarrow Zn(OH)_2 \qquad (6.17)$$

$$Zn(OH)_2 \rightarrow ZnO + H_2O \qquad (6.18)$$

$$NO_3^- \text{ (aq)} + H_2O + 2e^- \rightarrow NO_2^- \text{ (aq)} + 2OH^- \text{ (aq)} \qquad (6.19)$$

Composition, in terms of oxidation state of metal cations, and the nature of intralayer anions can determine significant modifications in the electrochemical response. In the case of $[Ni_4Al(OH)_{10}]OH$, upon oxidation, the average oxidation state of Ni increases from 2 to ca. 3.7, as calculated from charge passed, thus denoting that Ni^{3+} and Ni^{4+} centers are formed. It has been proposed that due to the high polarization ability of such ions, some protons drop off from the hydroxyl and react with interlayer OH$^-$ anions to give water molecules (Lei et al., 2008). When the oxidized form is reduced, protons are removed from the interlayer water molecules. As a result, OH$^-$ ions are easily interchanged with the electrolyte. However, if the interlayer anions are NO$_3^-$, the OH$^-$ transport is significantly hindered by electrostatic repulsion, thus resulting in a different electrochemical performance between $[Ni_4Al(OH)_{10}]OH$ and $[Ni_4Al(OH)_{10}]NO_3$. Water relay and proton and anion migration play an important role in the electrochemistry of such materials, but the degree of crystallinity, crystal morphology, defects, and additives can also significantly influence their electrochemical properties (Ren et al., 2006). In this regard, it should be noted that network-doping metal cations can enhance the electronic conductivity of the material, whereas introduction of interlayer anions can modulate its ionic conductivity.
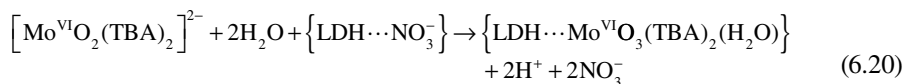
The electrochemistry of LDH-attached species has received relatively little attention compared with that of zeolite-associated species. The electrochemistry of LDH-supported bis(2-mercapto-2,2-diphenyl-ethanoate) dioxomolybdate(VI) complex, $[Mo^{VI}O_2(TBA)_2]^{2-}$ (TBA = $O_2CC(S)Ph_2$) is representative, however, of the capabilities of electrochemical methods for obtaining information on this type of system. The mineralogical composition of the used Zn-Al hydrotalcite was $Zn_{2.20}Al_{0.79}(OH)_6(NO_3)_{0.79} \cdot H_2O$. X-ray absorption spectroscopy and other techniques (Cervilla et al., 1994a), suggested that the complex, which, in solid phase exhibits
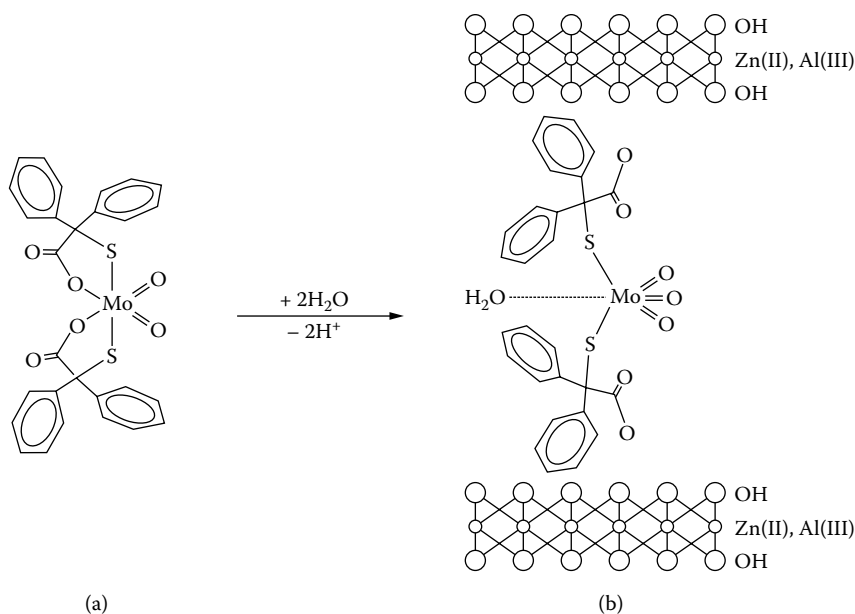
FIGURE 6.6 Scheme for the possible attachment of the bis(2-mercapto-2,2-diphenyl-ethanoate) dioxomolybdate(VI) complex, $[Mo^{VI}O_2(TBA)_2]^{2-}$, to Zn-Al hydrotalcite framework. (From Doménech et al., 1998. *J. Electroanal. Chem.* 458, 31–41, with permission.)

a *cis*-dioxo Mo(VI) arrangement, is accommodated as a pillar in the interlamellar space of the host layered hydroxide, as shown in Figure 6.6. It was presumed that the hydrotalcite-associated complex exhibits a *fac*-trioxo Mo(VI) arrangement due to the disassociation of coordinated carboxylate groups. This disassociation would sufficiently induce the positive charge on the oxomolybdenum core to allow an oxygen atom transfer from a contiguous molecule of water with no change in the oxidation state of the metal:

$$\left[Mo^{VI}O_2(TBA)_2\right]^{2-} + 2H_2O + \left\{LDH \cdots NO_3^-\right\} \rightarrow \left\{LDH \cdots Mo^{VI}O_3(TBA)_2(H_2O)\right\} + 2H^+ + 2NO_3^- \tag{6.20}$$
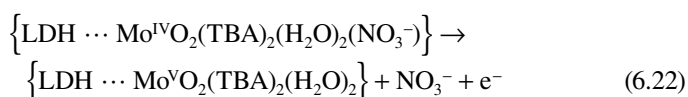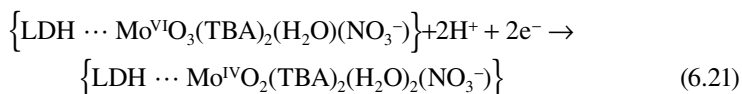
Application of voltammetry of microparticle techniques revealed the appearance of significant differences between the response of the complex in solution (Cervilla et al., 1994b) and that of hydrotalcite-associated species (Doménech et al., 1998). Repetitive cycling of the potential scan for {LDH $\cdots$ $Mo^{VI}O_3(TBA)_2(H_2O)$}-modified, paraffin-impregnated graphite electrodes in Figure 6.7 reveals a stable response, suggesting, in agreement with the requirement expressed by Bessel and Rolison (1997a) for zeolite-associated species, that electrochemical processes involve electroactive species firmly attached to the boundary of the LDH grains. Here, a main reduction peak appears at ca. −0.95 V vs. AgCl/Ag, preceded by two overlapping reduction signals between −0.05 and −0.25 V coupled with two superimposed anodic peaks at −0.10 and +0.03 V.

مرجع دانشجویان و مهندسین مواد
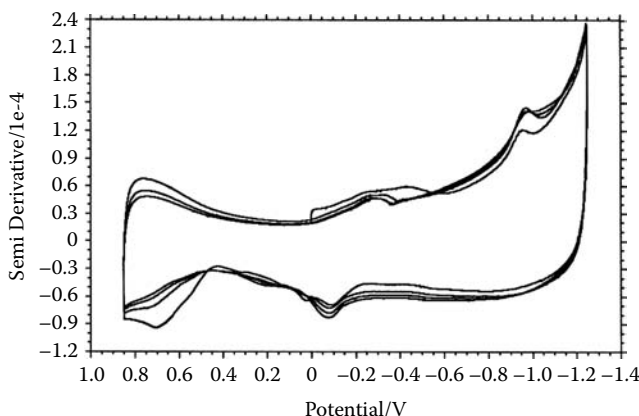
FIGURE 6.7 Repetitive CV at {LDH ··· Mo^{VI}O$_3$(TBA)$_2$(H$_2$O)}-modified paraffin-impregnated graphite electrodes immersed into 0.50 M phosphate buffer, pH 7.0. Potential scan rate, 20 mV/sec.

These last signals are enhanced at the expense of the main reduction process at −0.94 V in successive potential scans, thus denoting that a net interconversion of the original Mo(VI)-LDH-associated species to molybdenum species in other oxidation states occurs. This voltammetry can be represented in terms of the reduction of the *fac*-trioxo Mo(VI) complex to a Mo(IV) analogue accompanied by the loss of an oxo group, followed by oxidation to an Mo(V) analogue (Doménech et al., 1998). The sequence of electrochemical processes can be represented as:

$$\left\{ \text{LDH} \cdots \text{Mo}^{VI}\text{O}_3(\text{TBA})_2(\text{H}_2\text{O})(\text{NO}_3^-) \right\} + 2\text{H}^+ + 2e^- \rightarrow$$
$$\left\{ \text{LDH} \cdots \text{Mo}^{IV}\text{O}_2(\text{TBA})_2(\text{H}_2\text{O})_2(\text{NO}_3^-) \right\} \tag{6.21}$$

$$\left\{ \text{LDH} \cdots \text{Mo}^{IV}\text{O}_2(\text{TBA})_2(\text{H}_2\text{O})_2(\text{NO}_3^-) \right\} \rightarrow$$
$$\left\{ \text{LDH} \cdots \text{Mo}^{V}\text{O}_2(\text{TBA})_2(\text{H}_2\text{O})_2 \right\} + \text{NO}_3^- + e^- \tag{6.22}$$

This system illustrates the possibility of electrochemically promoting structural changes in anionic species attached to LDH systems.

6.4 ELECTROCHEMISTRY OF POMS

It is well known that several transition metals form POM ions in solution, eventually incorporating other elements. Thus, acidification of aqueous solutions of ammonium or sodium molybdates yields different so-called iopolyanions. As an example, condensation reactions for molybdate in aqueous solution can be represented as a sequence of equilibria initiated by the formation of heptamolybdate ion:
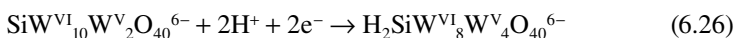
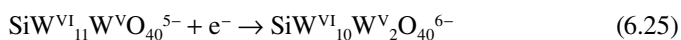$$7\text{MoO}_4^{2-} + 8\text{H}^+ \rightarrow \text{Mo}_7\text{O}_{24}^{6-} + 4\text{H}_2\text{O} \tag{6.23}$$
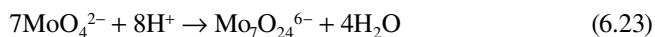
During condensation processes, oxo-anionic hetero groups of p-block atoms (PO$_4^{3-}$, SiO$_4^{4-}$, etc.) can be incorporated into the structures, so that the so-called
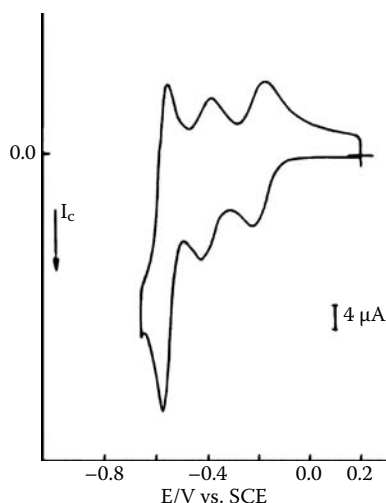
FIGURE 6.8 CV at glassy carbon electrode of 1 mM $SiW_{12}O_{40}^{4-}$ in 1 M $HClO_4$ aqueous solution. Potential scan rate, 100 mV/sec. (From Keita and Nadjo, 1987. *J. Electroanal. Chem.* 217, 287–304, with permission.)

heteropolyanions ($PMo_{12}O_{40}^{3-}$, $SiW_{12}O_{40}^{3-}$, etc.) are formed. The architectures of most POMs are based on specific structural types, such as the Lindquist ($M_6O_{19}^{2-}$), Keggin ($XM_{12}O_{40}^{3-}$), or Dawson (e.g., $X_2M_{18}O_{62}^{6-}$) metalates. When the condensation involves the acids (H_3PO_4, H_3BO_3) rather than their salts, hydrated forms can be obtained where the rigid, primary heteropolymetalate structure is surrounded by a secondary hydrate layer with a pseudo-liquid structure and heteropolyacids are formed (Keita and Nadjo, 2006).

The electrochemistry of POMs in solution and attached to electrode surfaces has received considerable attention, as reviewed by Sadakane and Steckhan (1998). Typical multiple peak profiles were obtained, as depicted in Figure 6.8, corresponding to a CV of 1 mM $SiW_{12}O_{40}^{4-}$ in 1 M $HClO_4$ aqueous solution (Keita and Nadjo, 1987). Here, three couples were obtained, corresponding to two essentially reversible one-electron and a two-electron transfer processes:

$$SiW^{VI}_{12}O_{40}^{4-} + e^- \rightarrow SiW^{VI}_{11}W^V O_{40}^{5-} \tag{6.24}$$

$$SiW^{VI}_{11}W^V O_{40}^{5-} + e^- \rightarrow SiW^{VI}_{10}W^V_2 O_{40}^{6-} \tag{6.25}$$

$$SiW^{VI}_{10}W^V_2 O_{40}^{6-} + 2H^+ + 2e^- \rightarrow H_2 SiW^{VI}_8 W^V_4 O_{40}^{6-} \tag{6.26}$$

The electrochemistry of POMs is characterized by reversible multistep redox processes resulting in the formation of mixed valence species and electron self-exchange between mixed-valence metal sites (e.g., $Mo^{VI,V}$) via electron hopping. Extensive reduction of POMs leads to the formation of heteropolybrown species in which such distinct ionic sites (e.g., W^{VI} and W^{IV}) can coexist.

The electrochemistry of Fe-, Ru-, and lanthanide-substituted heteropolyanions has also been studied. Now, metal-substituent- and POM-centered electrochemical

signals can be recorded. In particular, the iron-substituted heteropolyanions have large negative charge densities favoring ion pairing with counteractions and protons. Then, the formal potentials for both the iron-localized and POM-localized electron transfer processes depend on the pH and counteraction concentration because of the competition between protonation and ion pairing (Sadakane and Steckhan, 1998). The electrochemistry of novel Fe_2 and Fe_4 clusters encapsulated in vacant polyoxo-tungstates via hydrothermal synthesis has been described in terms of Fe-localized and POM-localized signals (Pichon et al., 2008).

POMs have found application in homogeneous electrocatalysis but also after attachment to electrode surfaces via adsorption (dip coating; Martel and Kuhn, 2000), entrapment into polymers (Mahmoud et al., 1999), electrodeposition (Keita and Nadjo, 1988), or droplet evaporation (Carapuça et al., 2006). Multilayer assemblies can be obtained because of the strong interaction of POMs with cations (Ingersoll et al., 1994). For instance, polypyrrole coating doped by molybdo-phosphate anions can be used for corrosion prevention in carbon steels (Ohtsuka et al., 2006). Structural protons in POM single crystals can provide electroneutrality during redox processes, thus allowing electroanalytical investigation in the absence of external electrolyte phase (Bard et al., 2008).

Solid isopoly- and heteropolymetalate compounds have been synthesized. Within this group of materials, one can include the so-called metal oxide bronzes (typically tungsten bronzes). Starting from WO_3, electrochemical reduction processes yield intercalation materials with electrochromic properties (Grandqvist, 1999).

6.5   ELECTROCHEMISTRY OF DOPED MATERIALS

The development of new synthetic routes has prompted the preparation of a variety of metal-oxide-type materials doped with different metal species. A significant part of research efforts in this field have been focused on doped materials for gas sensing and ion sensing and will be explained in Chapter 9. In this chapter, the voltammetric behavior of doped metal-oxide-based materials will be discussed. Two characteristic aspects can be noted: (1) the response of doping species is, in general, superimposed to that eventually displayed by the supporting material; (2) in general, the response of doping species will be confined to surface sites in the crystal lattice.

The interpretation of electrochemical data can be complicated, however, by the coexistence of solid solutions and multiphase systems. For instance, in vanadium-doped zirconias ($V_xZr_{1-x}O_2$) at low vanadium loadings, V^{4+} ions substitute isomor-phously Zr^{4+} ions in the lattice but, at relatively high vanadium loadings, some V^{5+} ions enter into the lattice, thereby promoting cation vacancies. At sufficiently larger vanadium loadings, finely dispersed vanadium oxide accompanies both monoclinic and tetragonal zirconias (Doménech and Alarcón, 2002b).

In this case, voltammetry of microparticle methods allows us to discern between monoclinic (m) and tetragonal (t) vanadium-doped zirconias, as can be seen in Figure 6.9, corresponding to square-wave voltammetries (SQWVs) of m-$V_{0.015}Zr_{0.985}O_2$ and t-$V_{0.015}Zr_{0.985}O_2$ materials attached to graphite electrodes in contact with 0.10 M H_2SO_4, after subtracting the blank voltammograms recorded for the corresponding parent materials, namely, m-ZrO_2 and t-ZrO_2. In contact with 0.10 M H_2SO_4,
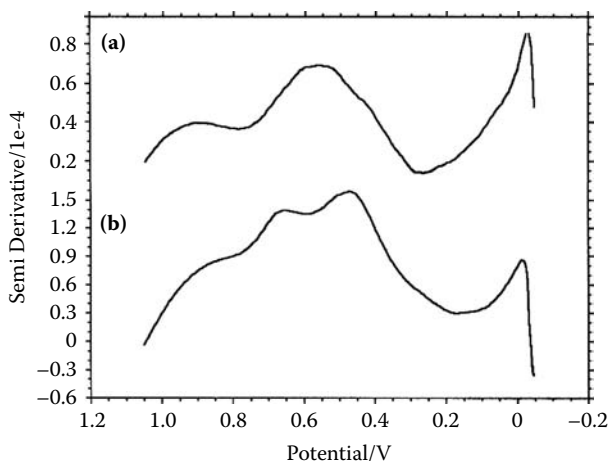
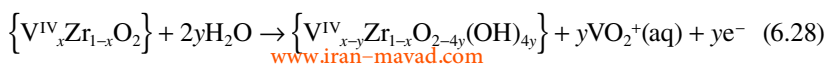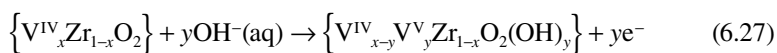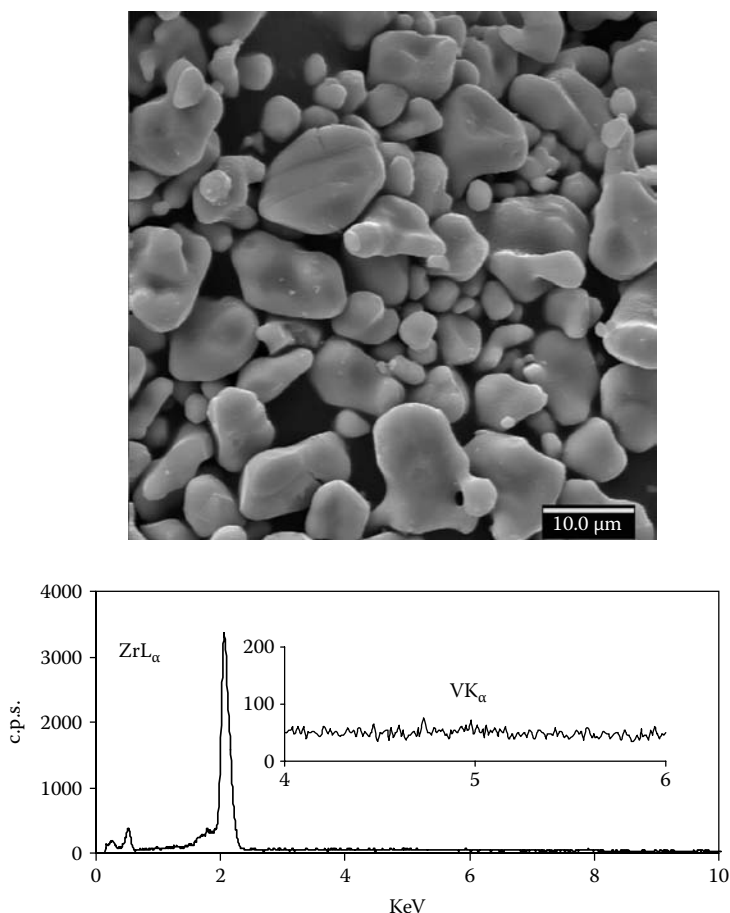**FIGURE 6.9** SQWVs, after subtracting the blank voltammogram recorded for m-ZrO_2 and t-ZrO_2, respectively, for: (a) m-$V_{0.015}Zr_{0.985}O_2$ and (b) t-$V_{0.015}Zr_{0.985}O_2$ attached to paraffin-impregnated graphite electrodes in contact with 0.10 M H_2SO_4. Potential scan initiated at −0.05 V in the positive direction. Potential step increment 4 mV; square-wave amplitude 25 mV; frequency 2 Hz.

m-$V_xZr_{1-x}O_2$ display anodic peaks at +0.20 and +0.75 V, accompanied, in the case of t-V_xZrO_2, by an additional peak at +0.58 V. Figure 6.10 shows field emission scanning electron micrograph and energy-dispersive x-ray spectroscopy of monoclinic $V_{0.075}Zr_{0.925}O_2$ solid solution prepared after heating gels at 1300°C for 3 h (Doménech and Alarcón, 2007).

To rationalize this voltammetric response, it should be kept in mind that in monoclinic zirconias, Zr^{4+} ions (and V^{4+} ions in vanadium-doped zirconias) are seven-coordinated with three oxygen atoms at 2.07 Å and four oxygen atoms at 2.21 Å, whereas in tetragonal zirconias, Zr^{4+} ions are eight-coordinated to four oxygen atoms at 2.065 Å and four oxygen atoms at 2.455 Å. As far as electroactive V^{4+} centers in vanadium-doped zirconias should be located in the external surface of crystals, where truncated coordination exists, the coordination of surface metal centers should be completed with OH^- or H_2O units. Accordingly, voltammetric signals can be attributed to the oxidation of vanadium species located in different sites in the external surface of doped zirconia grains and/or involving different electrochemical pathways. On comparing with the electrochemistry of vanadium in solution and solid-state electrochemistry of V_2O_5 and $NaVO_3$ (Barrado et al., 1997; Friedrich et al., 1998), voltammetric peaks at ca. +0.2 V can be attributed to the V(IV)/V(III) couple, whereas remaining peaks can be attributed to the V(V)/V(IV) pairs. In alkaline media, electrochemical oxidation of vanadium centers can be represented by means of the following processes:

$$\left\{V^{IV}_xZr_{1-x}O_2\right\} + yOH^-(aq) \rightarrow \left\{V^{IV}_{x-y}V^V_yZr_{1-x}O_2(OH)_y\right\} + ye^- \qquad (6.27)$$

$$\left\{V^{IV}_xZr_{1-x}O_2\right\} + 2yH_2O \rightarrow \left\{V^{IV}_{x-y}Zr_{1-x}O_{2-4y}(OH)_{4y}\right\} + yVO_2^+(aq) + ye^- \quad (6.28)$$

FIGURE 6.10 (See color insert following page 94.) Field emission scanning electron micrograph and energy-dispersive x-ray spectroscopy of monoclinic $V_{0.075}Zr_{0.925}O_2$ solid solution prepared after heating gels at 1300°C for 3 h. (From Doménech and Alarcón, 2007. *Anal. Chem.* 79, 6742–6751, with permission.)

accompanied by solution-phase redox processes such as:

$$VO_2^+(aq) + 2H^+(aq) + e^- \rightarrow VO^{2+}(aq) + H_2O \quad (6.29)$$
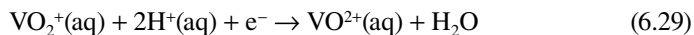
The appearance of common peaks for tetragonal and monoclinic vanadium-doped zirconias suggests that identical electrochemical pathways are operative for vanadium centers in these materials. Additional peaks recorded in t-V_xZrO$_2$ materials can be attributed, however, to vanadium centers with a coordinative arrangement characteristic of tetragonal zirconias.

Interestingly, electrochemical data can provide information on the oxidation state of doping centers, as described for high oxidation states of chromium in chromium-doped cassiterite (SnO$_2$) and tin-sphene (or malayaite, CaSnSiO$_5$; Doménech et al., 2006e).
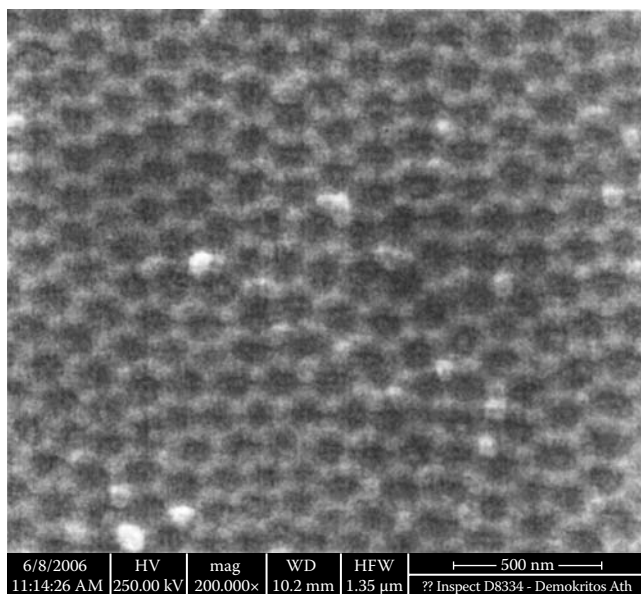
6.6 POROUS ANODIC METAL OXIDE FILMS

Porous films of more or less hydrated metal oxides are electrochemically formed by surface oxidation of metallic electrodes immersed in suitable electrolytes. As previously noted, porous anodic metal oxide films can be regarded as technological materials with applications, among others, in anticorrosion (Diggle et al., 1969), rechargeable batteries (Mozalev et al., 2001), templates for metal nanowires (Zhang et al., 1999), synthesis of porous carbons (Li et al., 1999) and nanostructured catalysts (Patermarakis and Pavlidou, 1994; Patermarakis and Nikolopoulos, 1999). Lastly, there is interest in porous anodic membranes, which can be obtained after dissolving the remaining metal and oxide barrier film separating metal from the pore bottom. This type of membrane is of interest because of its possible use in aggressive environments where the most common polymeric membranes do not resist (Asoh et al., 2001).

Porous anodic alumina films have found application in nanotechnology due to their nanometer-scale porous structure and sizes of particles forming the pore-wall material. Such films are formed by galvanostatic anodization of Al electrodes immersed into solutions of, for instance, H_2SO_4 plus $Al_2(SO_4)_3 \times 18H_2O$ under vigorous stirring. The phenomena inside the pores during Al anodizing are complex and substantially affect the mechanism of film growth. The pore generally broadens toward the film surface as a result of the pore-wall chemical dissolution reaction by the electrolyte inside the pores during the film growth (Patermarakis, 2006), but pores can also open toward the surface owing to the similar open-circuit oxide dissolution, which is a first-order reaction with respect to proton activity and is hindered by incorporated electrolyte anions (Patermarakis and Moussoutzanis, 2002; Patermarakis et al., 2007).

Figure 6.11 shows a schematic representation of migration processes accompanying the formation of porous oxide films by anodization of metals, illustrated here for
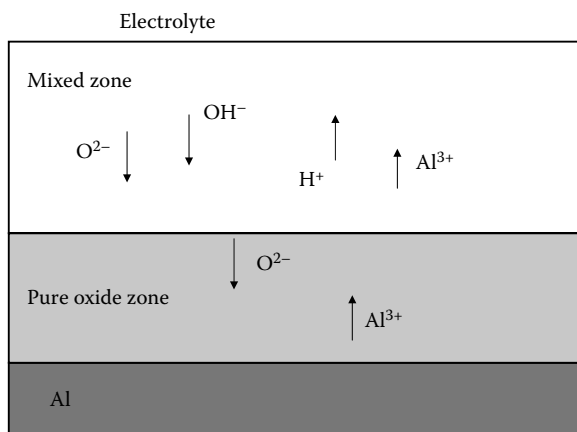
FIGURE 6.11 Schematic diagram shown migration processes accompanying the formation of porous oxide films by anodization of metals.

6/8/2006	HV	mag	WD	HFW	├── 500 nm ──┤
11:14:26 AM	250.00 kV	200.000×	10.2 mm	1.35 µm	?? Inspect D8334 - Demokritos Ath

FIGURE 6.12   SEM image of the imprints of anodic films of Al surface prepared in oxalic acid baths. (From Patermrakis et al., 2007. *J. Solid State Electrochem.* 11, 1191–1204, with permission.)

the case of aluminum. Two layers can be distinguished: that adjacent to the metal, where O^{2-} and Al^{3+} are the only migrating species, and the outer layer (mixed or barrier layer), where H^+ and OH^- also migrate and electrolyte ions are embodied (Patermarakis et al., 2007). Al is consumed according to Faraday's law and oxide forms in the metal/oxide interface, and O^{2-} and Al^{3+} migrate through vacancies in the pure oxide and barrier layers in this last reaction, accompanied by migration of H^+ and OH^- ions (*vide infra*).

Figure 6.12 shows a scanning electron microscopy (SEM) image of the imprints of anodic films of Al surface prepared in oxalic acid baths (Patermarakis et al., 2007), where a hexagonal structure can be clearly seen. A schematic representation of a section parallel to the pore axis of an elongated, columnar cell of a porous anodic alumina film is depicted in Figure 6.13. Here, the double layer on the pore base surface and the attached layer on the film surface are shown. In these regions, nuclei and microcrystallites of metal salts, typically $Al_2(SO_4)_3$ for Al anodizing, are formed. In this case, the growth of nuclei and microcrystallites as colloidal micelles, negatively charged by the anions being in excess in the first layer or those attached to the wall surface, takes place. Micelles uptake Al^{3+} ions and gradually the oxide is dissolved.

It should be noted, however, that different mechanisms of anodic oxide film formation are operative in acidic and alkaline media. This is clearly suggested by the variation with the film formation potential of the resistance and the inverse of capacitance for anodic oxide films on pure aluminum rod specimens reported by Moon and Pyun (1998) and depicted in Figures 6.14 and 6.15. It should be noted that the
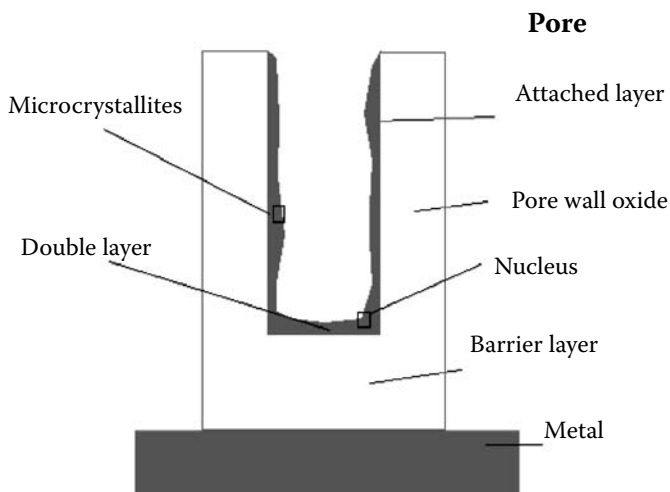
Pore

FIGURE 6.13 Schematic representation of a section parallel to the pore axis of an elongated, columnar cell of a porous anodic alumina film.
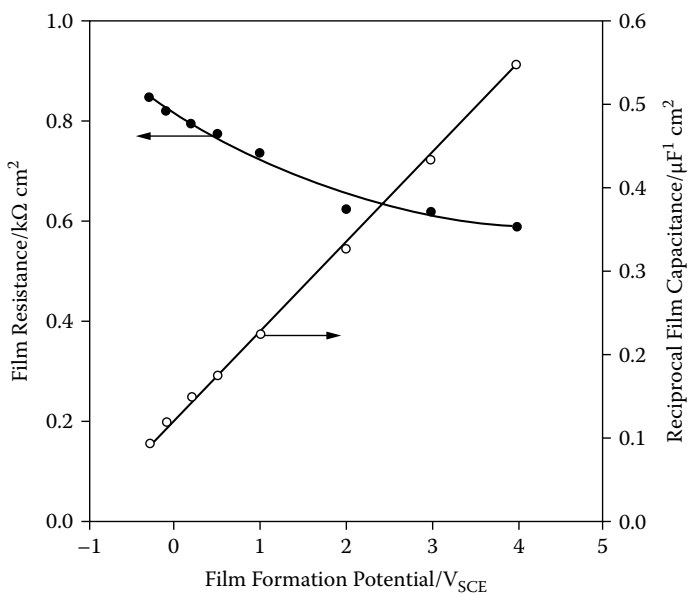
FIGURE 6.14 Variation of the reciprocal capacitance and resistance of anodic oxide film on pure aluminum rod specimen with film formation potential in contact with 0.5 M H_2SO_4 solution. (From Moon and Pyun, 1998. *J. Solid State Electrochem.* 2, 156–161, with permission.)
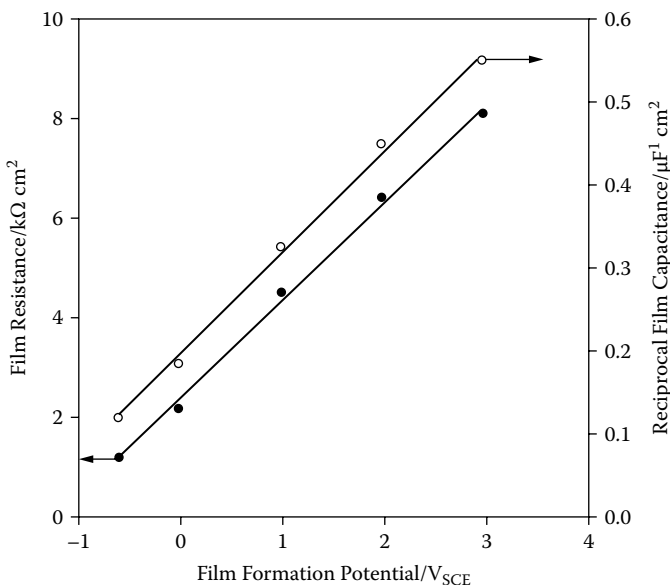
FIGURE 6.15 Variation of the reciprocal capacitance and resistance of anodic oxide film on pure aluminum rod specimen with film formation potential in contact with 1 mM NaOH solution. (From Moon and Pyun, 1998. *J. Solid State Electrochem.* 2, 156–161, with permission.)

capacitance, C_{ox}, and resistance, R_{ox}, of the oxide film depend on its thickness, δ_{ox}, according to:

$$C_{ox} = \frac{\varepsilon_o \varepsilon_{ox}' A_{ox}}{\delta_{ox}} \tag{6.30}$$

$$R_{ox} = \frac{\rho_{ox} \delta_{ox}}{A_{ox}} \tag{6.31}$$

In these equations, A_{ox} represents the exposed area of the specimen, ρ_{ox} is the film resistivity, ε_o is the vacuum permittivity, and ε_{ox}' is the relative permittivity of the metal oxide. Consistently, with such equations, the reciprocal capacitance of anodic aluminum oxide films increases on increasing the formation potential in both alkaline (Figure 6.15) and acidic media (Figure 6.14). This behavior reflects the increase in the film thickness on increasing the formation potential.

In agreement with the foregoing set of considerations, the film resistance increases linearly with film formation potential in alkaline solution (Figure 6.15). However, in acidic media, the resistance of the oxide film decreases on increasing the film formation potential, as can be seen in Figure 6.14. This can be attributed to an increase in the vacancy concentration within the oxide film, which could be explained by a field-assisted dissolution of anodic oxide film at the oxide/solution interface generating aluminum vacancies:

$$Al_{Al} \rightarrow Al^{3+} (aq) + V''_{Al} \tag{6.32}$$

In the above equation, Al_{Al} represents the "normal" aluminum ion in the regular site of the oxide film and V_{Al}'' represents the negatively charged aluminum vacancy in the oxide film. Here, the Kröger-Vink notation for representing point defects in solids is used (for a more detailed view, see Chapter 9). In alkaline media, generation of aluminum vacancies can be explained by the occurrence of a process involving water molecules adsorbed on the oxide film:

$$H_2O \text{ (ads)} \rightarrow O_O + 2/3 \ V_{Al}'' + 2H^+ \text{ (aq)} \tag{6.33}$$
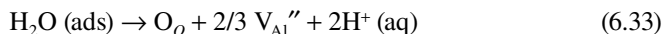
Here, O_O represents normal oxygen ion in the regular site of the oxide film. Since water is an uncharged species, its adsorption on the oxide film is scarcely influenced by the applied electric field, thus resulting in small change in the concentration of aluminum vacancies with the applied potential.

The current (i) measured during the growth of the porous film can be taken as the sum of the ionic current, i_{ion}, due to the oxidation of the metal at the metal/oxide interface, and the electronic current, i_{el}, due to faradaic processes occurring at the oxide/electrolyte interface. The former can be described as the sum of the formation current density, i_{form}, associated to oxide formation, and the dissolution current, i_{dis}, related to the dissolution of metal ions into the electrolyte at the pore bottom. Then,

$$i = i_{ion} + i_{el} = i_{form} + i_{dis} + i_{el} \tag{6.34}$$

The average currents can be evaluated from weight measurements by applying Faraday's law (Bocchetta et al., 2007) using the following relationships:

$$(i_{ion})_{av} = \frac{z(\Delta m)_M F}{S_m M_M \Delta t} \tag{6.35}$$

$$(i_{form})_{av} = \frac{z(\Delta m)_{MO} F}{S_m M_{MO} \Delta t} \tag{6.36}$$

$$(i_{dis})_{av} = (i_{ion})_{av} - (i_{form})_{av} \tag{6.37}$$

where S_m is the apparent surface area of the sample; $(\Delta m)_M$ and $(\Delta m)_{MO}$ are the masses of consumed metal and metal oxide formed, respectively, at a time Δt; and z is ionic charge. Porosity, P, defined as the pore volume (S_p)/total volume (S_m) ratio, can be calculated as (Sunseri et al., 2006):
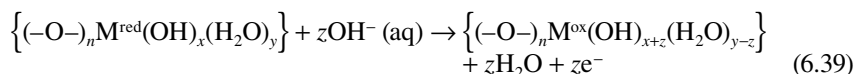
$$P = \frac{S_p}{S_m} = \frac{i_{dis}}{i_{ion}} \tag{6.38}$$

Regular films of low porosity are desired for mechanical applications, whereas high pore-surface density, high pore-base diameter (probably), thickness, and real surface are desired for catalysis. The growth of low-porosity films is favored by low temperatures, low electrolyte concentrations, and high current densities. Sulfate additives such as $Al_2(SO_4)_3$, $MgSO_4$, Na_2SO_4, however, favor the appearance of pitting, which is due to the nonuniform growth of film, yielding to undesired porosity,

roughness, cracks, etc. (Patermarakis and Moussoutzanis, 2001). Current developments attempt to obtain regularly grown, low-enough porosity, and high surface density and base diameter of the pores.
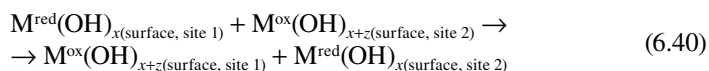
6.7   ELECTROCATALYSIS AT METAL OXIDES AND RELATED MATERIALS

The foregoing considerations have been mainly addressed to describe electrocatalytic processes where catalytic centers remain attached to an inert porous substrate. Such models can be applied to ion insertion microporous and mesoporous solids, typically zeolites, where ion transport through the pore/channel system of the particles can easily occur. Here, our attention will be focused in electrocatalytic processes involving porous materials that are electrocatalytically active. This is the case for most porous metal oxides, whose use as electrocatalyst has attracted considerable attention (Trasatti, 1994). On first examination, general ideas concerning electron and ion transfer through the material/electrode/electrolyte interfaces and charge transport across the solid previously detailed can be used. Electrochemical processes for electroactive oxides in contact with alkaline aqueous electrolytes involve the formation of surface-confined metal hydroxo- and oxo-complexes (Trasatti, 1994). This is supported by the fact that surface oxy groups hydrate or hydroxylate are in contact with aqueous media (Edgell et al., 1983; Lyons et al., 1987) and that rapid redox reactions can occur owing to the simultaneous gain or loss of electrons and hydroxide ions. The oxidation of a metal center in an oxide-type material can be represented as:

$$\left\{ (-O-)_n M^{red}(OH)_x (H_2O)_y \right\} + zOH^- (aq) \rightarrow \left\{ (-O-)_n M^{ox}(OH)_{x+z}(H_2O)_{y-z} \right\} + zH_2O + ze^- \tag{6.39}$$

where {} denotes surface-confined species. In this equation, it is assumed that the coordination number of the metal center remains unchanged upon oxidation.

In the case of metal oxides, the eventual electron transport between contiguous metal centers should involve the coupled transport of hydroxo and eventually oxo groups, namely:

$$M^{red}(OH)_{x(\text{surface, site 1})} + M^{ox}(OH)_{x+z(\text{surface, site 2})} \rightarrow \\ \rightarrow M^{ox}(OH)_{x+z(\text{surface, site 1})} + M^{red}(OH)_{x(\text{surface, site 2})} \tag{6.40}$$

This situation can be reconciled with the general ideas for describing electrochemistry of nonconducting solids with possible ion insertion (Lovric and Scholz, 1997, 1999; Oldham, 1998; Schröder et al., 2000) of unambiguous application to zeolites and related materials (Doménech, 2004a). This modeling states that there is redox conductivity even for: (1) highly restricted electron diffusion and (2) highly restricted ion diffusion. The second limiting case applies for insulating metal oxides, the reaction being confined to the particle/electrolyte interface.

With regard to electrocatalytic processes, it is pertinent to note that in the case of insulating oxides, there is, in general, no possibility of substrate permeation

within the material. Accordingly, electrocatalysis should involve the formation of surface-confined adducts between the substrate and the metal centers in the surface of the particles of catalyst. A widely studied case is the oxidation of glucose in alkaline solution at RuO_2-modified electrodes (Lyons et al., 1994). Here, oxometal surface groups act as mediators in a cyclic heterogeneous catalytic process (Lyons, 1994). The catalytic process can be represented as:

$$\{Ru^{VI}\} + glucose \rightarrow \{Ru^{IV} \cdots glucanolactone\} \rightarrow \{Ru^{IV}\} + glucanolactone \quad (6.41)$$

$$\{2Ru^{VII}\} + glucose \rightarrow \{2Ru^{VI} \cdots glucanolactone\} \rightarrow \{2Ru^{VI}\} + glucanolactone \quad (6.42)$$

It is assumed that glucose experiences a keto-enol transformation to form an anionic enol species:

$$R\text{-}CHOH \cdot CHO \leftrightarrow RCOH = CHOH \leftrightarrow RCOH = CHO^- + H^+ \quad (6.43)$$
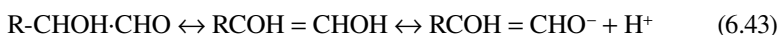
Then, the electrostatic interaction between cationic species and the anionic glucose form can be taken as an important factor for promoting glucose oxidation.

This applies when catalytic centers are incorporated as dopants to the lattice of the base porous material. In fact, site isolation of electroactive centers immobilized in microporous materials and doping units in inorganic supports appears to promote efficient electrocatalysis for a variety of analytically significant processes. Some remarks can be made:

1. Such systems can provide notable selective effects. These can be due to size- and charge-exclusion effects in microporous solids but also to symmetry effects associated to the coordinative arrangement of doping centers in metal oxides and related materials. Formation of surface-confined complexes between the substrate and the immobile redox-active center in the solid may involve exigent structural constraints, thus resulting in large selectivity.
2. The electrocatalytic activity of the studied systems can be modulated by changing the composition and abundance of the catalytic centers but also the structural characteristics of the solid (Doménech and Alarcón, 2002a).
3. Chiral electrocatalysis can be achieved via formation of chiral surfaces (Attard, 2001; Pleus and Schulte, 2001; Hazzazi et al., 2004) but also by inserting chiral centers into the inorganic matrix. This should apply to the case of monoclinic and cerium- and vanadium-doped zirconias (Doménech and Alarcón, 2007), which will be presented in Chapter 9.

6.8   SITE-CHARACTERISTIC ELECTROCHEMISTRY

An interesting but relatively unexplored aspect is the existence of site-characteristic electrochemical responses in porous materials containing electroactive centers. As far as the electrochemical processes involve an interfacial electron transfer between the electroactive species and the electrode surface, it is reasonable to expect that the kinetics of that electron transfer should be conditioned by the
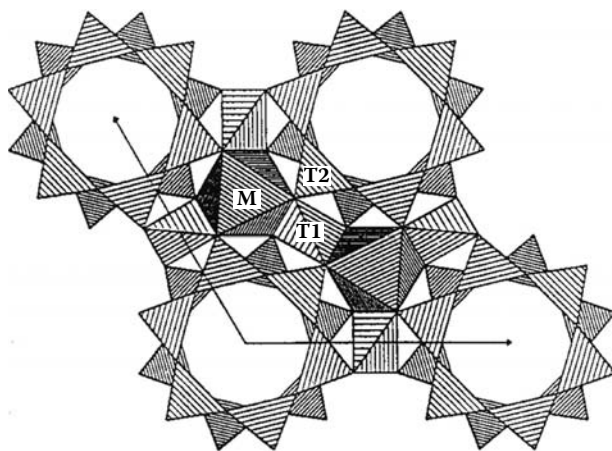
FIGURE 6.16 Schematic representation of the pore structure of cordierites.

structural arrangement of the electroactive center, thus resulting in discernible electrochemical responses. In addition, the electrochemical response could also be influenced by the crystallinity, porosity, and distribution of electroactive centers in the porous material. In the following, these types of effects will be termed *mesostructural effects*.

An example of this possibility is provided by magnesium-cobalt cordierites. Magnesium and cobalt cordierites, $Co_xMg_{2-x}Al_4Si_5O_{18}$ ($0 < x < 2$), can exist in different α and β forms characterized by six-membered rings of tetrahedrally coordinated cations (labeled as T_2 units) linked through tetrahedral (T_1) and octahedral polyhedra (Figure 6.16). Alternate layers of the hexagonal rings are connected through octahedral and tetrahedral units. In magnesium cordierites, silicon occupies T_2 tetrahedra, whereas aluminum occupies mostly T_1 tetrahedra and magnesium occupies octahedral sites. In α-cordierite form, aluminum-containing tetrahedral units do not occupy definite positions, whereas in β-cordierite, the aluminum-rich tetrahedral are located in fixed sites. An additional metastable form, μ-cordierite can also be formed. This material can be described as a solid solution with a μ-quartz structure.

During preparation from gel precursors via a semi-wet method (Villegas and Alarcón, 2002), different crystalline forms of cobalt-magnesium cordierites can be prepared. A cordierite glass can be first obtained from gel precursors, subsequently yielding a crystalline phase with μ-cordierite structure. This last structure is further converted, upon thermal treatment, into α- and β-cordierite. Spectral data suggested that Co^{2+} ions, which occupied tetrahedral sites in the glasses, move into octahedral sites during crystallization. Similar considerations apply for nickel cordierites. Cyclic voltammograms for cobalt-glass and nickel-glass cordierites in contact with aqueous HCl are shown in Figure 6.17. As can be seen in this figure, different metal-centered electrochemical processes are recorded for such materials.
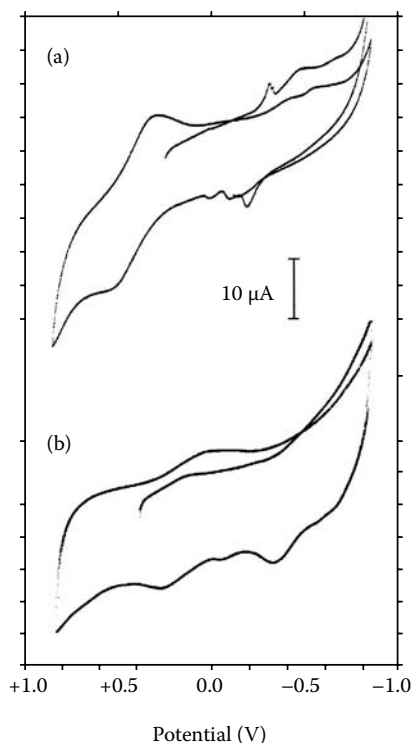
FIGURE 6.17 Cyclic voltammograms for: (a) cobalt-, and (b) nickel-glass cordierites attached to paraffin-impregnated graphite electrodes immersed into 1 M HCl. Potential scan rate 20 mV/sec. Materials courtesy of Prof. Javier Alarcón, University of Valencia.

Comparing voltammetric data (Doménech et al., 2004d) for cobalt cordierites and CoO (with octahedral Co^{2+} coordination) and cobalt spinel ($CoAl_2O_4$, with tetrahedral Co^{2+} coordination) revealed a significant site dependency of the electrochemical response of cobalt centers. This can be seen in Figure 6.17, which shows linear scan voltammograms for: (a) cobalt spinel, (b) cordierite glass, (c) μ-cordierite, (d) α-cordierite, (e) β-cordierite, and (f) CoO immersed into 1.0 M NaCl. Cathodic peaks were obtained for all materials in the 0.0- to −0.70-V potential range. Such electrochemical processes lead to the formation of a deposit of Co metal, as denoted by well-defined stripping peaks recorded at −0.15 V in anodic scan voltammograms corresponding to the oxidation of cobalt metal to Co^{2+} ions in solution. Again, significant differences between the electrochemical responses of the studied materials appear. Remarkably, the most definite stripping peaks are recorded for cordierite glass and α-cordierite, the most "disordered" materials, whereas the responses of more "ordered" materials (μ- and β-cordierite, CoO) consisted of weaker stripping processes at −0.15 V preceding additional oxidation signals, particularly at +0.40 V (Doménech et al., 2004d).
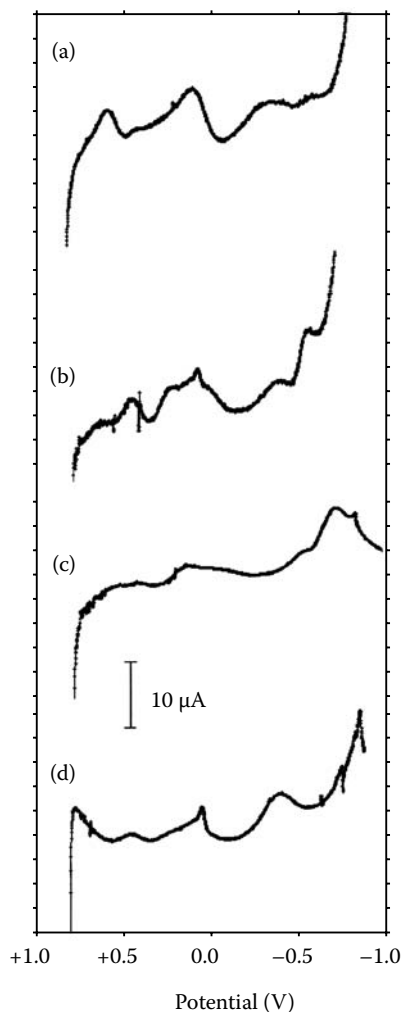
FIGURE 6.18 Linear scan voltammograms for: (a) cobalt spinel, (b) α-cordierite, (c) β-cordierite, and (d) CoO, attached to paraffin-impregnated graphite electrodes immersed into 1.0 M HCl. Potential scan rate 20 mV/sec.

The observed response (Figure 6.18) can be attributed to the superposition of voltammetric responses for octahedrally coordinated Co^{2+} ions (broad peak at −0.65 V) and tetrahedrally coordinated Co^{2+} centers (peaks at −0.38 and −0.58 V). For a cobalt cordierite, the cathodic process in acidic media can be described as a reductive dissolution/metal deposition:

$$Co_2Al_4Si_5O_{18} + 6H^+ + 4e^- \rightarrow Co + 5SiO_3^{2-} + 4Al^{3+} + 3H_2O \qquad (6.44)$$
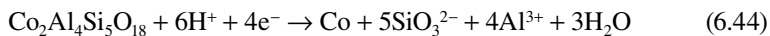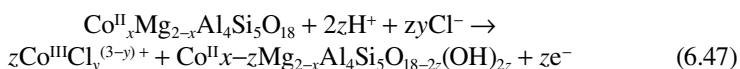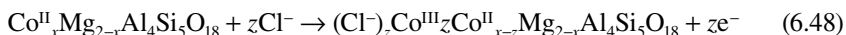
For magnesium-cobalt cordierites, however, the electrochemical process can be represented as a partial dissolution of cobalt centers with concomitant coordinative rearranging:

$$Co_xMg_{2-x}Al_4Si_5O_{18} + 2xH^+ + 2xe^- \rightarrow Co + Mg_{2-x}Al_4Si_5O_{18-2x}(OH)_{2x} \quad (6.45)$$
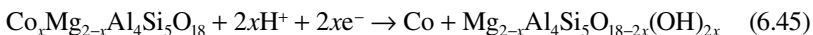
Obviously, the kinetics of the overall process will be influenced by both the partial reductive dissolution and the kinetics of the nucleation/growth of the deposit of Co metal. This process may involve intermediate cobalt species in solution or proceed via solid-to-solid conversion to a metal phase, as described by Hasse and Scholz (2001) for the reduction of lead oxide. The properties of the metallic deposit are remarkably different for each of the studied materials, as denoted by the observed differences in their anodic behavior. The oxidation signal at +0.40 V can be described in terms of total or partial oxidative dissolution processes:

$$Co^{II}_2Al_4Si_5O_{18} + 6H^+ + 2yCl^- \rightarrow 2Co^{III}Cl_y^{(3-y)+} + 5SiO_3^{2-} + 4Al^{3+}$$
$$+ 3H_2O + 2e^- \quad (6.46)$$

$$Co^{II}_xMg_{2-x}Al_4Si_5O_{18} + 2zH^+ + zyCl^- \rightarrow$$
$$zCo^{III}Cl_y^{(3-y)+} + Co^{II}x{-}zMg_{2-x}Al_4Si_5O_{18-2z}(OH)_{2z} + ze^- \quad (6.47)$$

Or a solid-state oxidation process involving chloride coordination of surface cobalt centers:

$$Co^{II}_xMg_{2-x}Al_4Si_5O_{18} + zCl^- \rightarrow (Cl^-)_zCo^{III}zCo^{II}_{x-z}Mg_{2-x}Al_4Si_5O_{18} + ze^- \quad (6.48)$$

An interesting implication of this site-characteristic electrochemistry is the possibility of promoting different catalytic effects. In the case of cobalt cordierites, significant differences were obtained in their catalytic ability with respect to the oxidation of polyalcohols in aqueous alkaline media (Doménech et al., 2004d). This can be seen in Figure 6.19, which shows the linear scan voltammograms for paraffin-impregnated graphite electrodes modified with: (a) cordierite glass, (b) μ-cordierite, (c) α-cordierite, and (d) β-cordierite immersed into 2.0 mannitol plus 0.10 M NaOH. Remarkably, the catalytic currents are considerably larger for crystalline cordierites than for cordierite glass. For this material, anodic waves at +1.04 and +1.35 V are recorded, whereas for μ-, α-, and β-cordierites overlapping anodic signals at +1.04 and +1.20 V appear. In the case of cordierite glass, the two signals could be attributed to the coexistence of: (1) two different mechanisms involving location of the substrate at the outer Helmholtz plane and closer to the oxide surface than the outer Helmholtz plane and/or (2) the action of two different catalytic sites (tetrahedral and octahedrally coordinated Co^{2+} ions). For crystalline cordierites, differences in their "mesostructures" (crystallinity and ordering in tetrahedral/octahedral units) can also be invoked for explaining the differences in catalytic response. Existing data support the idea that octahedral Co^{2+} environments in ordered crystalline structures yields more efficient and "clean"
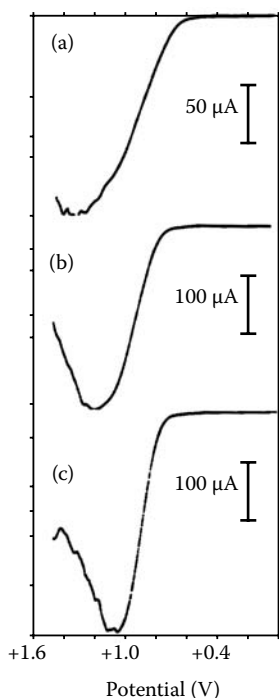
FIGURE 6.19   Deconvoluted linear scan voltammograms for paraffin-impregnated graphite electrodes modified with different cobalt cordierites: (a) cordierite glass, (b) μ-cordierite, and (c) α-cordierite, immersed into 2.0 mM sorbitol plus 0.10 M NaOH. Potential scan rate 20 mV/sec.

electrocatalytic responses, but further research is needed for properly elucidating structural conditioning of electrocatalytic processes. In this sense, it should be noted that visualization of electroactive sites is available to scanning electrochemical microscopy. This technique has been recently used for monitoring the highly localized electroactivity at titanium surfaces on which a native or anodically grown semiconducting oxide film has been deposited (Basame and White, 1998).

7 Electrochemistry of Porous Carbons and Nanotubes

7.1 CARBONS AS ELECTROCHEMICAL MATERIALS

Elemental carbon is usually handled in three forms: graphite, diamond, and amorphous carbon. Graphite and amorphous carbon have been extensively used in electrochemistry because of their high electrical conductivity, chemical stability, versatility, and low cost. For electrochemical applications, such materials can be manufactured in bars, powders, and fibers or can even form conducting composites when appropriate binders are used. A number of carbon-based materials, such as pyrolytic carbon, carbon blacks, activated carbons, graphite fibers, whiskers, glassy carbon, etc., have been used in electrochemistry for decades (Yoshimura and Chang, 1998).

Numerous new carbon materials have recently been introduced in the field of electrochemistry. These materials include boron-doped diamond electrodes, fullerenes, porous carbons, carbon fiber electrodes, carbon nanotubes (CNTs), etc. (for a general overview, see Echegoyen et al., 2006 and Yoshimura and Gallage, 2008). Several properties of carbons make these materials of particular interest in most electrochemical applications—carbon materials are relatively inert in contact with most electrolytes, while retaining a high degree of surface activity, and allow different functionalization/derivatization procedures. Novel carbon materials have attracted attention for their use as adsorbents, gas storage and catalyst supports, and electrode materials in batteries, fuel cells, etc. Highly porous carbons can be used as electrodes in supercapacitors and batteries. Graphitic carbons reversibly intercalate lithium, used as the main anode material in lithium batteries (Liu et al., 2008).

7.2 POROUS CARBONS

The term *porous carbons* is used to designate the materials prepared by carbonization of organic felts or fibers (cellulose, polyacrylonitrile) under inert atmosphere or under reducing conditions. Complex pyrocarbon structures are formed depending on temperature. Ordered mesoporous carbons (OMCs) possess a uniform, periodic distribution of mesopores with high surface area (Ryoo et al., 2001). Such materials can be prepared by nanocasting ordered mesoporous silicas such as MCM-48 or SBA-15 and mesocellular silica foams (Ryoo et al., 1999). During the OMC replication process, the internal porous structure of the silica template is inversely replicated while the external morphology of the primary
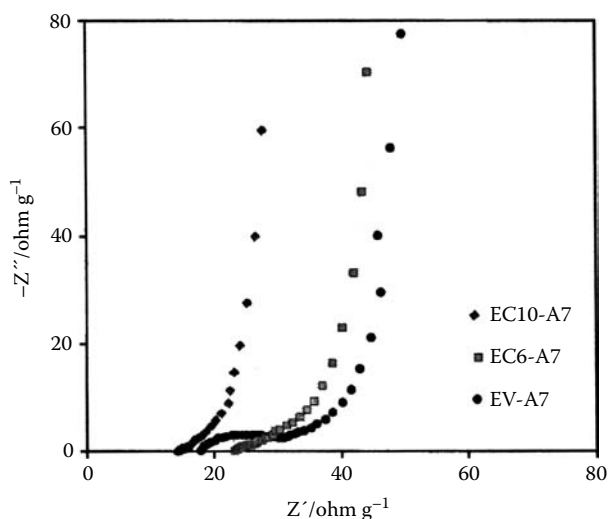
مرجع دانشجویان و مهندسین مواد
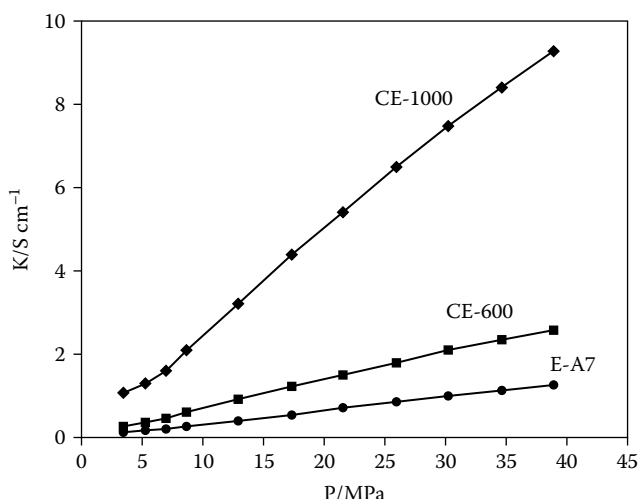
FIGURE 7.1 Conductivity of activated carbon electrodes prepared from naphthalene-derived mesophase chemically activated by KOH and thermally treated at 600 and 1000ºC, mixed with polyvinylidene fluoride, and subsequently thermally activated at the above temperatures. (Adapted from Ruiz et al., 2008. *J. Electroanal. Chem.* 618, 17–23, with permission.)

particles is preserved, the control of particle sizes being of interest (Joo et al., 2008). Chemical and thermal treatments are used for the activation of carbons. Chemical activation, usually done via KOH, introduces oxygen functionalities in the carbon surface.

A frequent strategy for preparing carbon electrodes is pressing the carbonaceous material with a polymeric binder for compact carbon particles. Figure 7.1 shows the variation in conductivity (using the four-point method; Bard et al., 2008) with pressure for activated carbon electrodes chemically prepared from naphthalene-derived mesophase. The material was activated by KOH, thermally treated at 600 and 1000ºC, mixed with polyvinylidene fluoride, and then thermally activated at the above temperatures (Ruiz et al., 2008). Thermal treatment of electrodes leads to a recovery of the surface area blocked by the polymer. Increase in pressure leads to a compact electrode with concomitant increase in conductivity because of the improved contact between carbonaceous particles. This effect is more pronounced after thermal treatment at relatively high temperatures due to conductivity increase associated with reordering of the structure of carbonaceous particles and the greater conductivity of the residue that leaves the polymer compared to the pristine polymer.

Electrochemical impedance spectroscopy (EIS) analysis of such electrodes is shown in Figure 7.2. At high frequencies, the imaginary part of the impedance tends to zero, whereas at low frequencies it increases sharply, thus approaching the variation of impedance with the frequency expected for a pure capacitor (see Chapter 1). In the intermediate frequencies, a semicircle can be observed, the amplitude of the loop varying with the nature of the activated material. This semicircle can be

FIGURE 7.2 Nyquist plots for activated carbon electrodes prepared from naphthalene-derived mesophase chemically activated by KOH and thermally treated at 600 and 1000°C, mixed with polyvinylidene fluoride, and subsequently thermally activated at the above temperatures. Electrolyte, 1 M H_2SO_4; voltage window, 1 V. (Adapted from Ruiz et al., 2008. *J. Electroanal. Chem.* 618, 17–23, with permission.)

associated to the resistance that arises from the porous structure of the electrode, the contact at the electrode/current collector, and/or the occurrence of faradaic phenomena. For thermally treated electrodes, the loop disappears as a result of the decrease in conductivity of the material and the removal of surface functionalities and, consequently, of faradaic effects.

Figure 7.3 shows the variation in specific capacitance, determined from galvanostatic charge/discharge measurements, with the current density for such electrodes in contact with 1 M H_2SO_4. One can observe that the capacitance of thermally treated electrodes is lower than those of untreated ones. Although there are several factors influencing capacitance, it appears that the unexpected appearance of constrictions at the entrance of the porous network has a negative effect on capacitance that cannot be compensated for by the increase in surface area of the electrodes (Ruiz et al., 2008).

7.3   CARBON NANOTUBES AND NANORIBBONS

CNTs (Oberlin and Endo, 1976; Wiles and Abrahamson, 1978; Iijima, 1991; Kavan et al., 2001; Yang et al., 2005) and carbon nanoribbons (CNRs) (Novoselov et al., 2004) are graphene-type nanostructured materials having in common a fiber-type structure (Figure 7.4). In CNTs, sp²-hybridized carbon atoms are arranged in graphite-type sheets building up seamless hollow tubes capped by fullerene-type (*vide infra*) hemispheres.

Single-walled carbon nanotubes (SWNTs) are composed of single hollow tubes having a diameter between 0.4 and 2 nm. Multiwalled carbon nanotubes (MWNTs)
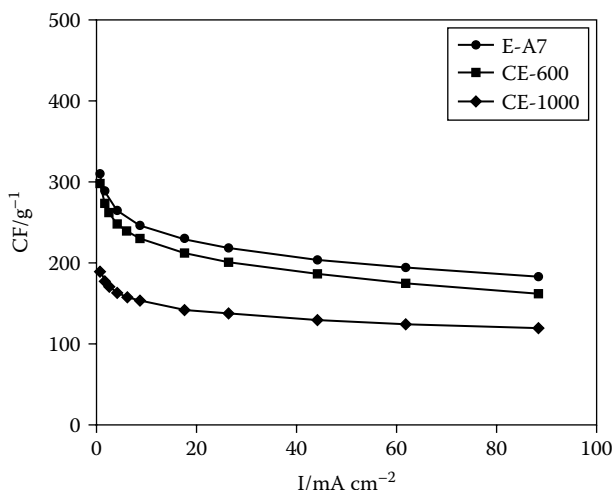
FIGURE 7.3 Variation in the specific capacitance with the current density for activated carbon electrodes in Figures 7.1 and 7.2. (Adapted from Ruiz et al., 2008. *J. Electroanal. Chem.* 618, 17–23, with permission.)

are formed by concentric tubes with a diameter between 2 and 100 nm. SWNTs can act as semiconductors or as metallic conductors, whereas MWNTs behave as metallic conductors. In the case of carbon powders, different activation strategies typically involving chemical activation protocols with acids or alkalis can be used. Figure 7.5 shows transmission electron microscopy (TEM) images of untreated carbon nanotubes (ACNT) and activated with KOH and thermally treated at 800ºC using different KOH/ACNT weight ratios of 3 (ACNT-3) and 5 (ACNT-5) (Xu et al., 2008). Unactivated nanotubes are multiwalled with diameters ranging
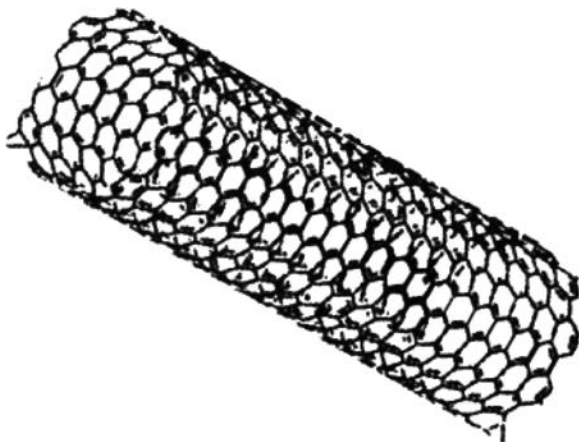
FIGURE 7.4   Typical structure of SWCNTs.
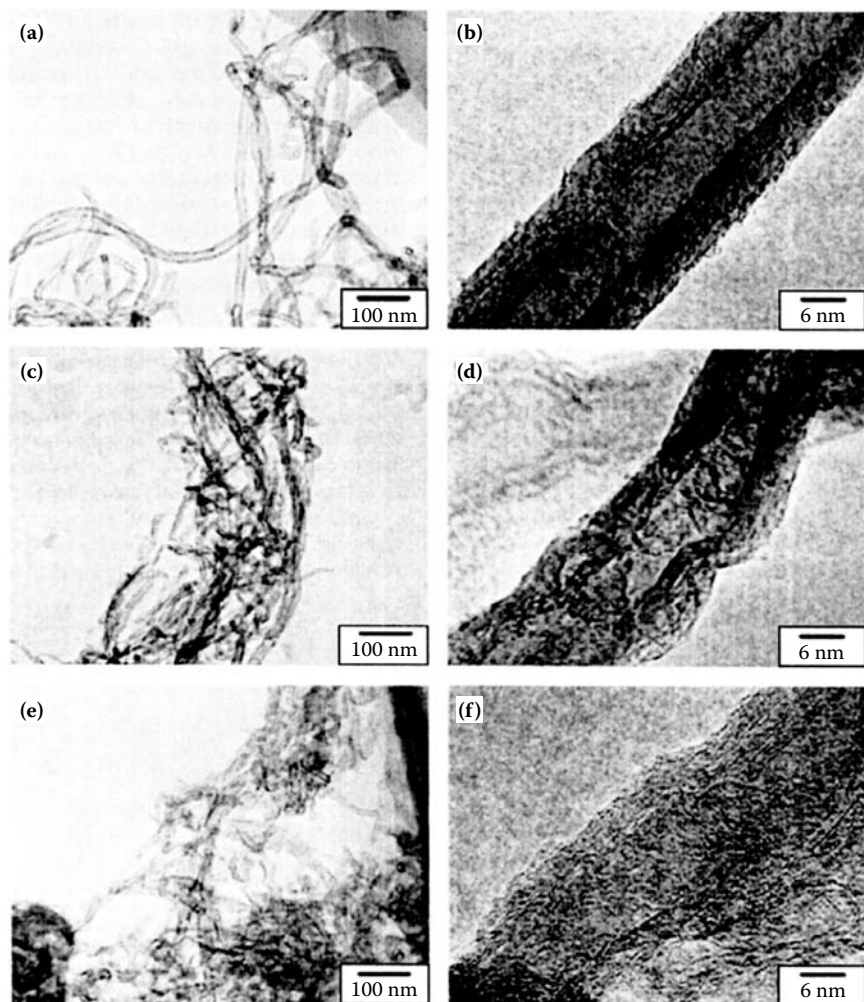
FIGURE 7.5 TEM images of untreated CNTs (a, b; ACNT) and activated with KOH and thermally treated at 800°C using different KOH/ACNT weight ratios of 3 (c, d; ACNT-3) and 5 (e, f; ACNT-5). (From Xu et al., 2008. *Electrochim. Acta* 53, 7730–7735, with permission.)

between 10 and 20 nm with both outer and inner walls being smooth. After activation, both the morphology and structure of nanotubes change—the tubes becoming short and distorted, and some of the nanotubes becoming fractured or even powdered. These effects can be attributed to the strong chemical reaction between KOH and CNTs at high temperature, the structural alteration being more severe as the KOH/ACNT ratio increases. Interestingly, some of the active sites of the surface of nanotubes are etched with KOH and become pores, thus increasing the surface area of the material. Concomitantly, the destruction of the graphitic structure of the nanotubes produces a decrease in conductivity.
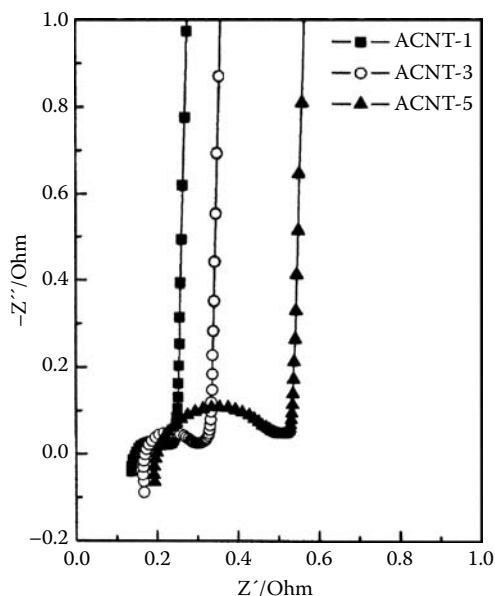
FIGURE 7.6 Nyquist plots of ACNT-based electrodes in Figure 7.5 immersed into 7 M KOH. (From Xu et al., 2008. *Electrochim. Acta.* 53, 7730–7735, with permission.)

Figure 7.6 shows Nyquist representations of the impedance spectrum for such nanotubes in contact with 7 M aqueous KOH. A semicircle appears at high frequency and abruptly changes to an almost vertical line at low frequency, this last denoting the capacitive behavior typical of CNTs.

CNRs can be described as quasi-one-dimensional systems consisting of basically elongated stripes of single layered graphene with a finite width. Graphene nanoribbons can either be metallic or semiconducting, depending on the crystallographic direction of the ribbon axis; the main difference between CNRs and CNTs is the existence of sharp edges in CNRs, so that edge effects are currently under intensive research (Barone et al., 2006). Both n- and p-doping of CNTs can be obtained in electrochemical turnovers; for instance, in $Bu_4NBF_4/MeCN$ electrolytes:

$$\{CNT\} + zBu_4N^+ \text{ (sol)} + ze^- \rightarrow \left\{ CNT \cdots \left(Bu_4N^+ \right)_z \right\} \tag{7.1}$$

$$\{CNT\} + zBF_4^- \text{ (sol)} \rightarrow \left\{ CNT \cdots \left(BF_4^- \right)_z \right\} + ze^- \tag{7.2}$$
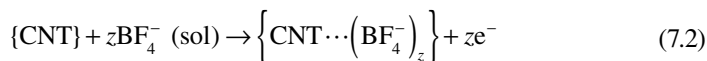
The electrochemical response of CNTs is dominated by double-layer charging with only a small contribution of faradaic pseudocapacitance due to surface oxides (Frackowiak and Beguin, 2000; Kavan et al., 2001), so that faradaic processes are essentially absent. In contact with aqueous electrolytes, however, weak peaks may eventually appear. These peaks are presumably due to faradaic pseudocapacitance associated with oxygen-containing surface functionalities on CNTs and/or

carbonaceous impurities. Such processes were found to be pH dependent and can be represented by the generic expression (Barisci et al., 2000a):

$$=C=O + H^+ + e^- \rightarrow \equiv COH \tag{7.3}$$

The appearance of weak voltammetric peaks in contact with nonaqueous electrolytes can be attributed to water traces (Claye et al., 2000) or to Li^+ insertion (Barisci et al., 2000b). Lithium insertion into SWNTs exhibits fast kinetics and absence of staging, and Li^+ ions are presumably accommodated in nanochannels occurring inside the nanotube bundles and ropes (Claye et al., 2000).

Correlation between spectral and electrochemical features for CNTs has been studied by Kavan et al. (2004). Spectral features for SWNTs in the near infrared–visible region can be explained in terms of resonance enhancement and optical band-gap excitation in a one-dimensional conductor with Van Hove singularities in the electronic density of states (Kavan et al., 2000). Chemical redox processes can modify the population of such states so that the electronic structure of SWNTs can be tuned by chemical doping with molecules having different redox potentials or by controlling the interfacial potential of SWNTs in contact with an electrolyte solution, as studied in detail by Kavan et al. (2001).

Doping of CNTs with some types of heteroatoms may lead to the formation of electron excess (n-type, e.g., doping with N) of electron-deficient (p-type, e.g. doping with B) semiconducting nanotubes (Saito, 1997). Depending on the position and distribution of such heteroatoms, various types of nanostructured junctions with different electronic properties would be possibly prepared. This involves double coaxial CNTs of doped and undoped multiwalls or double coaxial CNTs composed by N- and B-doped multiwalls. Doping CNTs with N or B presumably modifies the electronic structure and, presumably, the conducting properties of the materials. In these materials, an increase in conductivity with respect to that of undoped CNTs, attributed to the increase in hopping frequency between the conduction and valence bands, has been obtained by Yang et al. (2005). As pointed out by these authors, it is interesting to note that this type of systems may exhibit p-n junction characteristics of interest for obtaining nanoelectronic devices.

With regard to their application in lithium batteries, CNTs exhibit large hysteresis and irreversible capacity, two properties that made their practical application difficult. The mesoporous character of CNTs is responsible for the ease in evacuation of Li^+, thus determining hysteresis, as well as for the ease in access of solvated ions to the active surface, thereby determining irreversible capacity (Frackowiak and Béguin, 2002).
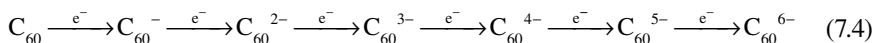
7.4 FULLERENES

The term *fullerenes* is used to design a family of carbon allotropes whose structure is based on fused five- and six-membered rings forming spherical or elongated closed-cage structures (Kroto et al., 1985) (see Figure 7.7). The most popular structure is that of C_{60}, composed by spherical polyhedra containing 12 pentagons and 20 hexagons where carbon atoms are located at the vertices of the resulting truncated icosahedron.
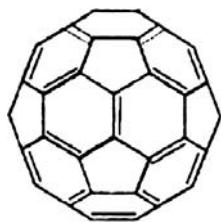
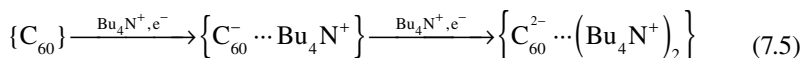**FIGURE 7.7** Structural representation of C_{60} fullerene.

Carbon atoms in fullerenes possess an sp^2-type electronic configuration, but, in contrast with graphitic carbons, addition reactions at the double bond junction between six-membered rings are allowed. This is due to the pyramidalization of sp^2 carbons as a result of the curvature of the structure (Bard et al., 2008). Accordingly, a variety of functionalized fullerenes can be prepared (Hirsch, 1993). In addition, fullerenes can encapsulate anions and neutral molecules, thus forming the so-called endohedral fullerenes (Guha and Nakamoto, 2005) and form different types of polymeric chains.

Fullerenes have high electron affinity so that electrochemical reduction processes are easily observed. The solution-phase electrochemical response of C_{60} and C_{70} fullerenes in MeCN/toluene mixtures at low temperature consisted of six reversible one-electron reductions at potentials between −0.97 to −3.26 V vs. Fc/Fc$^+$ (Xie et al., 1992). This can be represented as successive one-electron transfer processes:

$$C_{60} \xrightarrow{e^-} C_{60}{}^- \xrightarrow{e^-} C_{60}{}^{2-} \xrightarrow{e^-} C_{60}{}^{3-} \xrightarrow{e^-} C_{60}{}^{4-} \xrightarrow{e^-} C_{60}{}^{5-} \xrightarrow{e^-} C_{60}{}^{6-} \quad (7.4)$$

However, higher fullerenes and endohedral fullerenes provide a more complicated electrochemistry (Anderson et al., 2000).

The electrochemistry of solid fullerenes in contact with aqueous (Szucs et al., 1996) and nonaqueous (Bond et al., 2000) electrolytes has also been studied. Following Bond et al. (2000), microcrystalline C_{60} adhered to gold, glassy carbon, and platinum electrodes in contact with Bu_4NClO_4/MeCN can be reduced by 3–5 electrons to species in solution, whereas one- and two-electron reduction steps only lead to a minor level of dissolution of $C_{60}{}^-$ and $C_{60}{}^{2-}$. The electrochemical pattern is complicated by adsorption processes of electrochemically generated ions, the adsorption strength decreasing on increasing the charge of the fullerene anionic species. Solid-state electron transfers are, in principle, limited to the processes:

$$\{C_{60}\} \xrightarrow{Bu_4N^+,e^-} \left\{ C_{60}{}^- \cdots Bu_4N^+ \right\} \xrightarrow{Bu_4N^+,e^-} \left\{ C_{60}{}^{2-} \cdots \left(Bu_4N^+ \right)_2 \right\} \quad (7.5)$$

Electrochemical quartz crystal microbalance (EQCM) experiments confirmed that $C_{60}{}^{3-}$ species can be oxidatively precipitated on gold, the corresponding process being represented as:

$$C_{60}{}^{3-} \text{ (sol)} + 2Bu_4N^+ \text{ (sol)} \rightarrow \left\{ C_{60}{}^{2-} \cdots \left(Bu_4N^+ \right)_2 \right\} + e^- \quad (7.6)$$
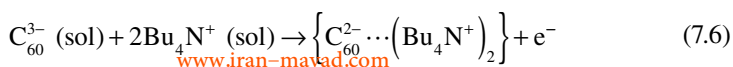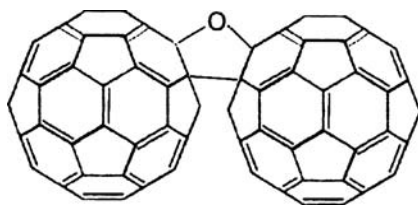
FIGURE 7.8   Structural representation of C_{60} fullerene epoxide.

Fullerenes are versatile components able to form different macro- and supramo-
lecular structures by virtue of their ability to entrap small molecules but also by their
capacity to be embedded into large macrocyclic molecules (cyclodextrins, caliza-
renes, porphyrins, crown ethers) and derivatized with dendrimer structures (Winkler
et al., 2006). Fullerenes can form homopolymers (Yamawaki et al., 1993) but can
also be incorporated into polymeric chains forming a "pearl necklace" structure
(Loy and Assink, 1992) or acting as pendant substituents in the side chains of poly-
mers (Hirsch et al., 1991), forming the so-called *charm bracelet* polymers. Fullerene
epoxide–based polymers containing an epoxy ring connecting two adjacent fuller-
ene cages can be used as precursors for a large group of epoxy resins, which can be
synthesized from fullerene epoxides such as $C_{60}O$ (see Figure 7.8). Fullerene-epoxide
polymerization can be electrochemically promoted in O_2-containing aprotic sol-
vents. Electropolymerization is initiated by the well-known one-electron reversible
reduction of O_2 to $O_2\cdot^-$, followed by nucleophilic addition of the radical superoxide
to the fullerene:

$$O_2 \xrightarrow{\;e^-\;} O_2\cdot^- \xrightarrow{\;C_{60}\;} C_{60}-O-O^- \xrightarrow{\;C_{60}\;} C_{60}O^- + C_{60}O \qquad (7.7)$$
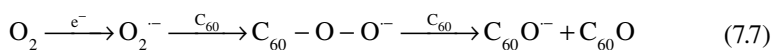
$C_{60}O\cdot^-$ and $C_{60}O$ are capable of inducing further polymerization of the fullerene.

Polymers of fullerenes with transition metal complexes exhibit electrochemical
activity due to the reduction of fullerene moieties. This process is accompanied
by the transport of cations from the supporting electrolyte into the film. Figure 7.9
shows repetitive CV for C_{60} plus Pd(acetate)$_2$ in MeCN plus toluene, using Bu$_4$NClO$_4$
as a supporting electrolyte (Grodzka et al., 2008). Here, the current is enhanced in
successive scans due to polymer deposition. Parallel monitoring of microgravimet-
ric changes by EQCM, shown in Figure 7.10, shows a decrease in frequency due to
the polymer deposition process. A small decrease in frequency in the positive scan
direction is related to film oxidation followed by egress of supporting electrolyte
cations from the polymer film to the solution. For experiments performed in sup-
porting electrolyte alone that such systems can be considered good electrochemical
capacitors, the pseudocapacitance performance of the polymer depended on the
amount of polymeric material deposited on the electrode surface.

Poly $C_{60}M$ films can be electrochemically reduced due to the electroactivity of
fullerene moieties. A typical process is (Winkler et al., 2006):

$$(\text{Pd-}C_{60}\text{-Pd})_n + n\text{TAA}^+ + ne^- \rightarrow (\text{Pd-}C_{60}^-\text{-Pd} \cdots \text{TAA}^+)_n \qquad (7.8)$$
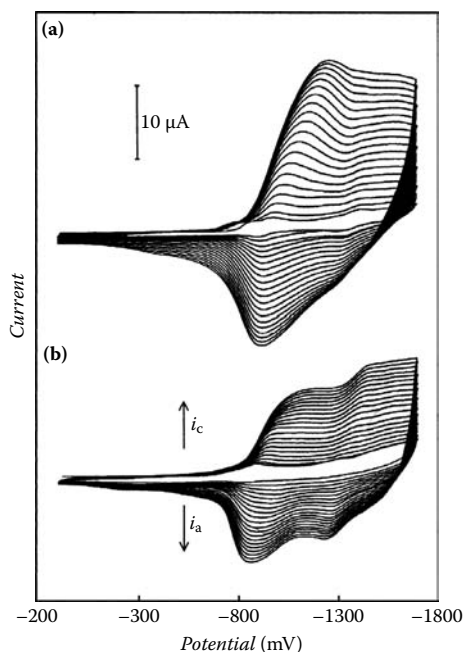
FIGURE 7.9 Repetitive CV for (a) 0.25 mM C_{60} + 0.85 mM Pd(acetate)$_2$ and (b) 0.25 mM C_{70} + 0.85 mM Pd(acetate)$_2$, in 0.10 M Bu$_4$NClO$_4$/MeCN + toluene (1:4 v/v). Potential scan rate, 100 mV/sec. (Adapted from Grodzka et al., 2008. *J. Solid State Electrochem.* 12, 1267–1278, with permission.)
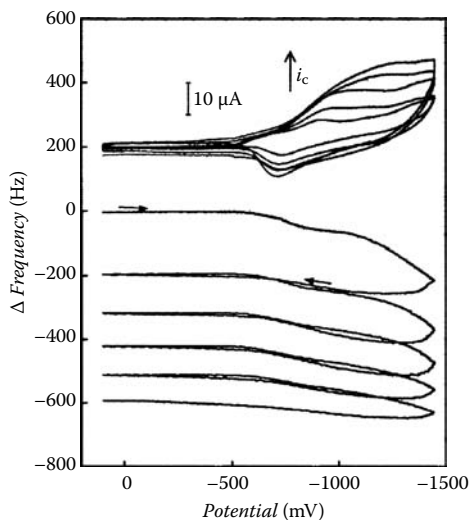
FIGURE 7.10 Multicyclic voltammetric curves and frequency changes in microgravimetric experiments at Au/quartz electrode in 0.25 mM C_{60} + 0.85 mM Pd(acetate)$_2$ in 0.10 M Bu$_4$NClO$_4$/MeCN + toluene (1:4 v/v). Potential scan rate, 25 mV/sec. (Adapted from Grodzka et al., 2008. *J. Solid State Electrochem.* 12, 1267–1278, with permission.)
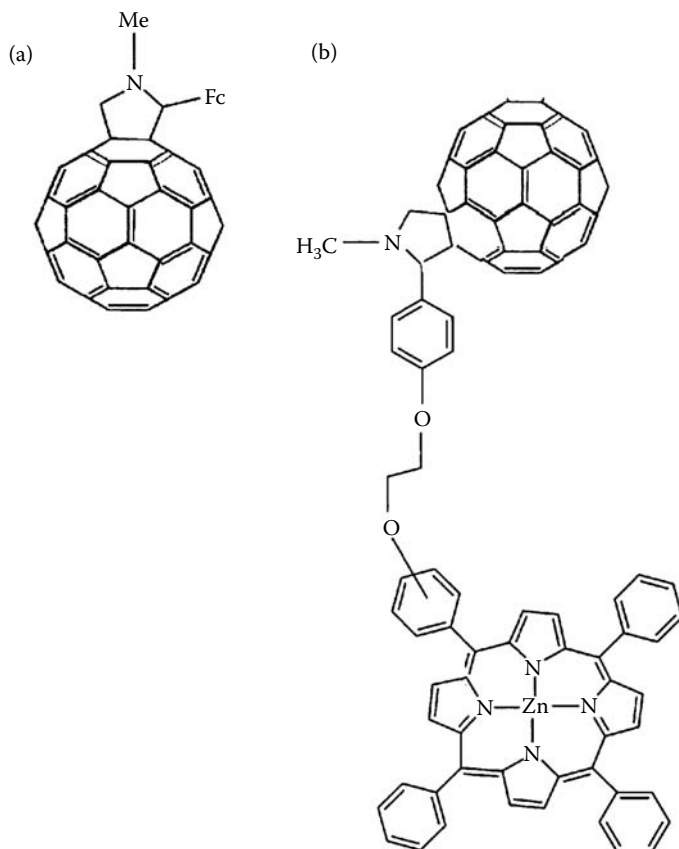
FIGURE 7.11 Structure of 2′-ferrocenylpyrrrolidino[3′,4′;1,2]C_{60} (a) and zinc meso-tetraphenylporphyrin (b) fullerenes.

where TAA$^+$ denotes a tetraalkylammonium ion from the electrolyte. Remarkably, the electrochemical reduction of the polymeric film results in an increase in conductivity (Balch et al., 1998). Electropolymerizations in the presence of high concentration of metal give rise to the formation of metal nanoparticles.

A variety of hybrid materials involving fullerene building blocks has been described. "Double cables" are polymers of transition metal cations and fullerene derivatives for instance, 2′-ferrocenylpyrrrolidino[3′,4′;1,2]C_{60} and zinc meso-tetraphenylporphyrin fullerenes, whose structures are depicted in Figure 7.11. Fullerene peapods (Smith et al., 1998) can be described as supramolecular complexes formed by filling SWNTs by fullerenes, but their electrochemistry and spectroelectrochemistry are currently under research. Recent studies on fullerene peapods with single-wall CNTs (e.g., C_{60}@SWCNT) with $LiClO_4$ in MeCN and ionic liquid electrolytes do not display voltammetric peaks, thus denoting that the electrochemical reduction of intratubular fullerene is hampered (Kavan et al., 2004).

7.5 DIRECT ELECTROCHEMICAL SYNTHESIS OF FULLERENES AND NANOTUBES

According to Kavan (1997), electrochemical carbons are synthetic solids consisting mainly of atoms of elemental carbon, which can be prepared electrochemically from suitable precursors. Electrochemical carbonization is characterized by three specific features (Kavan et al., 2004): (1) ability to obtain relatively unstable carbon chains; (2) easy templating of carbon nanostructured materials by the precursors; and (3) defined kinetics of certain reactions, allowing for the control of film thickness.

Electrochemical carbonization leads to carbines and polyynes, materials that can also be prepared by the action of laser or synchrotron radiations on graphitic carbons or from methods such as cluster beam deposition or hot filament–assisted sputtering. As a result, polymeric structures constituted by sp-hybridized carbon chains of the type $-(C\equiv C)_n-$ and $=(C=C)_n=$ can be obtained. Electrosynthesis of carbon materials started from poly(tetrafluoroethylene), originally discovered by Janska and Dousek (1973), using reduction with a liquid amalgam of alkali metal. Here, the reaction yields a polyyne stabilized by interdispersed nanocrystalline alkali metal fluoride, which in turn protects the carbynoid skeleton against cross-linking and/or chemical attack from the reactive environment. This can be represented as:

$$-(CF_2-CF_2)_n- + 4nM^+(Hg) + 4ne^- \rightarrow (-C\equiv C-)_n + 4nMF \tag{7.9}$$
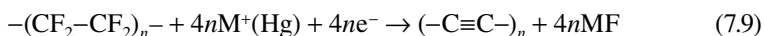
The resulting carbon possesses a small superstoichiometric overreduction, equivalent to an n-doping, the extra negative charge being compensated for by the corresponding cations of alkali metals. Actual reaction products, however, are mesoscopic sp^2-hybridized carbons with short oligoyne sequences ($n < 8$), whereas polyyne is spontaneously cross-linked to graphene (see Figure 7.12).

Direct synthesis of fullerenes and nanotubes can be performed by electrochemical dehalogenation of perhalogenated hydrocarbons. For instance, C_{60} can be prepared from octafluoroanthracene:

$$6C_{10}F_8 + 48e^- \rightarrow C_{60} + 48F^- \tag{7.10}$$
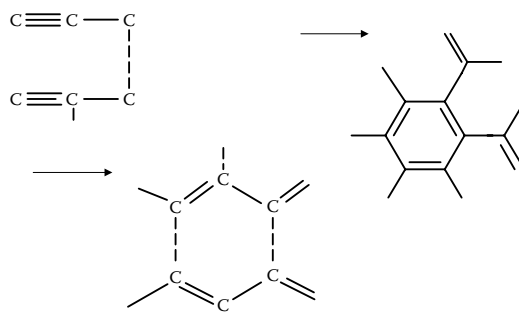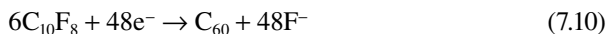
**FIGURE 7.12** Schematics for cross-link reactions producing graphene from polyynes.

Although currently yields obtained in electrochemical synthesis of fullerenes and nanotubes are not yet competitive compared to those prepared via the usual processes (carbon arc, laser ablation, etc.), such procedures are of considerable interest (Kavan et al., 2004).

7.6   CAPACITANCE RESPONSE

Porous carbons and nanotubes have attracted considerable attention in relation to such practical issues as hydrogen storage, lithium batteries, and supercapacitors. In general, the electrochemical behavior of porous carbons and CNTs solely consists of double-layer charging processes with small or zero contribution of faradaic pseudo-capacitance of surface oxide functionalities. This is in sharp contrast with the rich electrochemistry of fullerenes.

Cyclic voltammetries (CVs) of CNTs A/CoSi700 modified by electrodeposited polypyrrole present the characteristic boxlike shape of an ideal capacitor even at moderate scan rates of 2 mV/sec, as shown in Figure 7.13 (Frackowiak and Béguin, 2002). Values of specific capacitance of nanotubes are significantly enhanced after modifications such as electrodeposition of a thin layer of conducting polymers, because of the contribution of pseudofaradaic properties of the polymer.

Electrochemical capacitors based on carbon materials can be divided into double-layer capacitors, where only a pure electrostatic interaction between ions and charged electrode surfaces occur, and supercapacitors, based on the occurrence of faradaic pseudocapacitance reactions (see Chapter 10). It is generally assumed that the charge is mainly stored, in porous carbons, in the double layer at the electrode/electrolyte
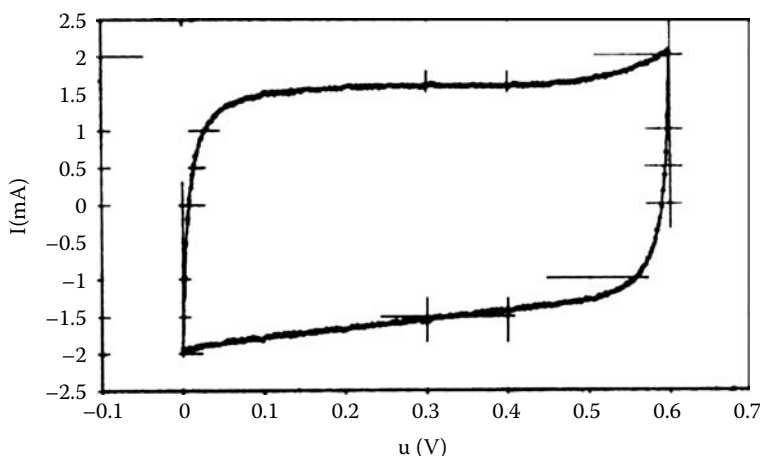
FIGURE 7.13   CV of CNTs A/CoSi700 modified by electrodeposited polypyrrole in contact with 1 M H_2SO_4. Potential scan rate, 2 mV/sec. (From Frackowiak and Béguin, 2002. *Carbon* 40, 1775–1787, with permission from Elsevier.)

interface. Remarkably, several studies indicate that there is no clear relationship between capacitance and specific surface area (Kim et al., 2004; Leroux et al., 2006). In principle, the specific capacitance increases as the specific surface area of the carbon increases, but as far as this quantity depends on the distance between polarized carbon surface and solvated ions, the presence of mesopores becomes a determinant for ion transport.

For an ideal "carbonaceous" double-layer capacitor (see Chapter 10), the change in the number of electrons transferred per one carbon atom, Δn, is (Kavan et al., 2004)

$$\Delta n = \frac{C_{\mathrm{sp}} M_C V}{F} \tag{7.11}$$

where M_C represents the atomic mass of carbon, V the potential difference, and C_{sp} the specific capacitance of the system.

7.7   CARBON FUNCTIONALIZATION

The use of redox mediators as electrode modifiers increases the catalytic ability of carbon electrodes toward selected electrochemical processes. Among other strategies, adsorption, deposition, covalent attachment, in-site functionalization of self-assembled monolayers, and electropolymerization have been reported (see Zhang and Lian, 2008). Functionalization of carbon materials by promoting the formation of covalent bonds can be performed mainly by: (1) direct electrochemical oxidation by applying a sufficiently positive oxidizing potential, high enough to produce oxygenated functional groups on carbon surface; and (2) electrochemically assisted reaction with a functionalizing substrate. Nonelectrochemical methods for covalent modification of graphitic carbon substrates were recently reviewed by Barrière and Downard (2008).

Among others, derivatization of carbons through reduction of dizonium salts has found application in electrochemical sensing (Wildgoose et al., 2005). Figure 7.14 shows scanning electron microscopy (SEM) images of native and chloronitrophenyl-functionalized carbon powder (Pandurangappa and Ramakrishnappa, 2008) prepared via chemical reduction of 4-chloro-2-2dinitrobenzene-dizaonium chloride salt with hypophosphorous acid. Although chloronitrophenyl group–functionalized carbon particles exhibit a similar surface morphology to its unfunctionalized counterparts, the voltammetric response of functionalized carbon powder consists of well-defined features. This can be seen in Figure 7.15, where CVs for 4-chloro-2-nitrophenyl-derivatized carbon powder immobilized on basal plane pyrolitic graphite electrode in contact with HCl plus KCl aqueous solution is shown. In the first potential scan, an irreversible peak at −0.52 V vs. AgCl/Ag appears. This peak is followed, in the subsequent scans, by an oxidation/reduction couple at ca. + 0.30, while the initial reduction signal disappears. This response can be interpreted in terms of the initial reduction of 4-chloro-2-nitrophenyl moiety to the corresponding chlorophenyl hydroxyl amine through a four-proton, four-electron irreversible process. This last form undergoes a reversible two-electron, two-proton oxidation yielding the chloronitroso-phenyl species, as schematized in Figure 7.16. Here, the quotient between
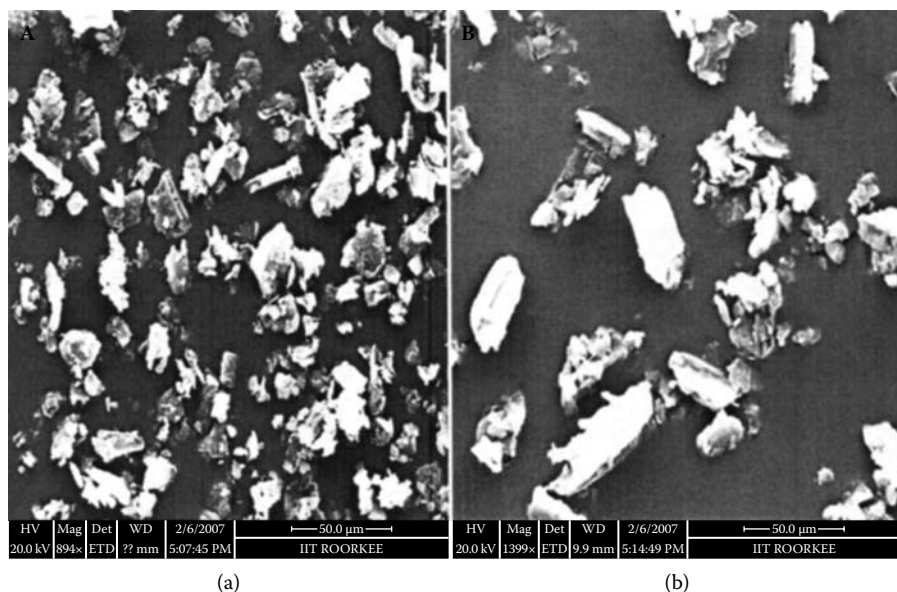
FIGURE 7.14   SEM images for (a) native and (b) chloronitrophenyl-functionalized carbon powder. (From Pandurangappa and Ramakrishnappa, 2008. *J. Solid State Electrochem.* 12, 1411–1419, with permission from Springer.)
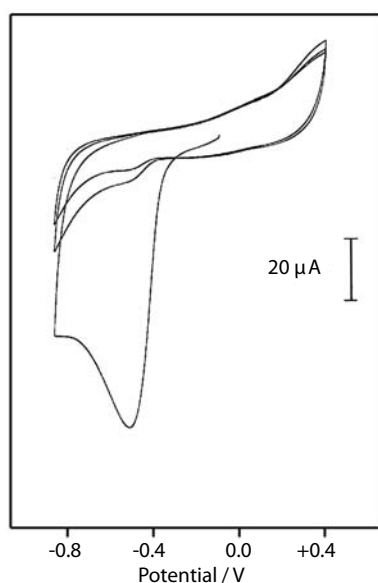
FIGURE 7.15   CVs for 4-chloro-2-nitrophenyl-derivatized carbon powder immobilized on basal plane pyrolitic graphite electrode in contact with 0.10 M HCl aqueous solution. The potential scan rate, 50 mV/sec.
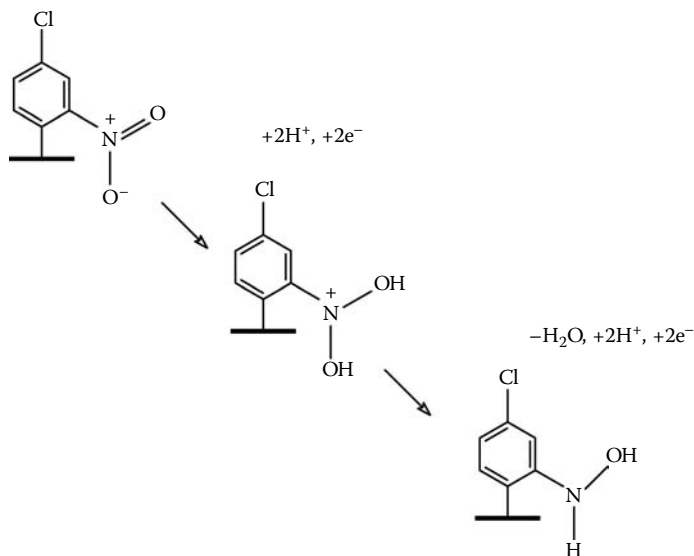
FIGURE 7.16 Reaction scheme proposed by Pandurangappa and Ramakrishnappa (2008) for the voltammetry of 4-chloro-2-nitrophenyl-derivatized carbon powder immobilized on basal plane pyrolitic graphite electrode in contact with aqueous electrolytes.

the number of protons, n_p, and the number of electrons, n, involved in the electrochemical process can be estimated from the slope of the linear peak potential vs. pH dependence using the well-known relationship (Leventis et al., 2004):

$$E_p = E^{o\,\prime} - \frac{2.303 R T n_p}{nF} \qquad (7.12)$$

7.8 ELECTROCATALYTIC ABILITY

Electrocatalytic processes at carbon materials have been widely studied. First of all, it should be noted that porous carbons and nanotube systems are able to enhance voltammetric signals recorded at conventional metal or carbon electrodes because of the increase in specific surface area. This can be seen in Figure 7.17, which shows the CVs recorded at unmodified and SWNT-modified glassy carbon electrodes in contact with a dopamine solution in aqueous phosphate buffer. The voltammetric profile is essentially identical, but a general increase of the currents is observed at the nanotube-modified electrode, accompanied by large capacitive current, as denoted by the background box-shaped response.

The high electron transfer ability of porous, activated carbon materials can improve their electrochemical performance with respect to that at conventional pyrolitic and glassy carbon electrodes. It should be noted, however, that—as occurring for these latter electrodes—electrode conditioning and electrochemical
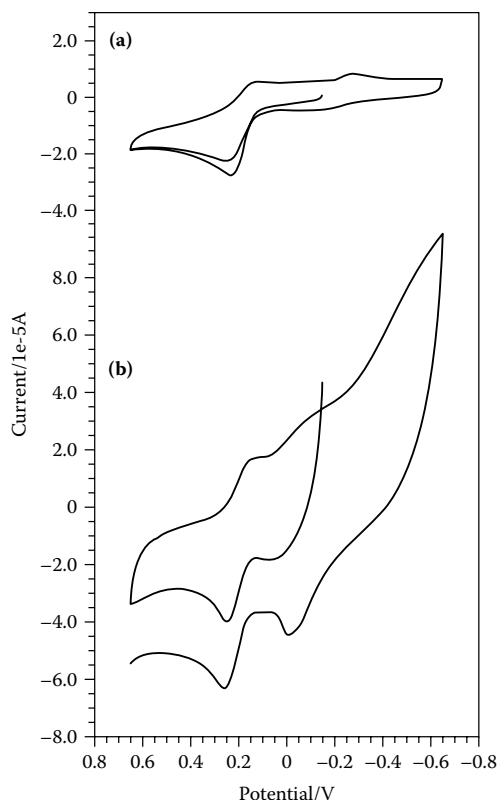
FIGURE 7.17 CVs for a 2.5 mM solution of dopamine in 0.50 M phosphate buffer, pH 7.0, at (a) unmodified glassy carbon electrode, (b) SWNT-modified glassy carbon electrode. Potential scan rate, 50 mV/sec.

activation treatments can significantly modify the electrochemical properties of carbon electrodes.

The electrocatalytic ability of CNTs was first investigated by Wang and Mushameh (2003). A variety of electrode configurations, from powder microelectrodes (Zhao et al., 2003) to aligned deposits of CNTs (Gao et al., 2003), have been proposed. Aligned deposits of CNTs on electrode surfaces provide additional advantages for a maximized access of the nanotubes electrode surface and efficient device construction. Formation of composites and functionalization with other redox-active species has attracted attention. For instance, modification of aligned CNTs with thionine, a purple-type dye used in several bioassays, provides electrocatalytic behavior to the oxidation of nitrite (Zhao et al., 2007). Figure 7.18 compares SEM and TEM images for well-aligned pristine and thionine-functionalized CNT arrays on Au. For the nonfunctionalized system, CNTs are vertically and orderly aligned together and have a slick outer wall, as can be seen in the TEM image. Thionine-modified CNTs become blurred in the SEM image and individual
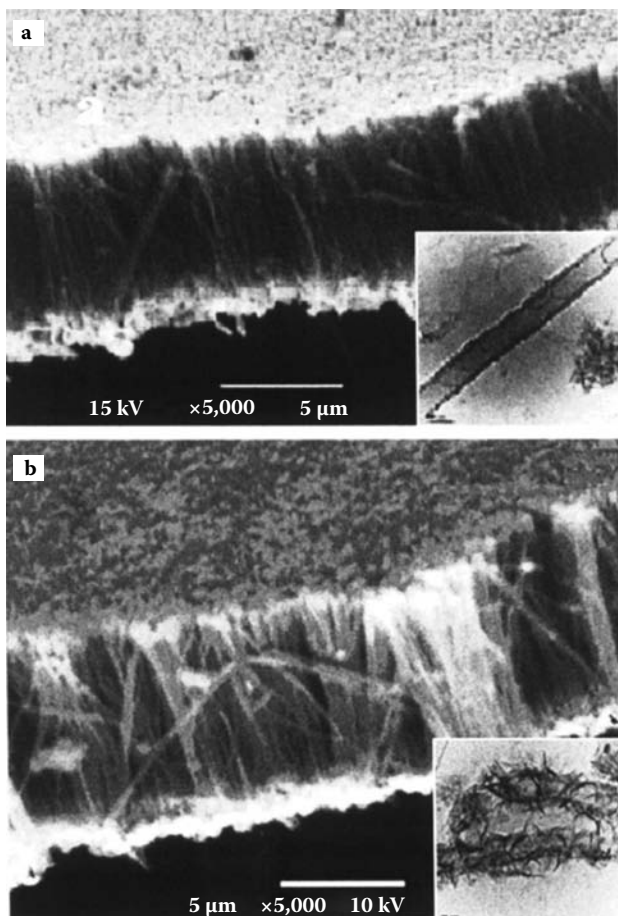
FIGURE 7.18 SEM images of (a) aligned CNTs electrode and (b) thionine-modified aligned CNTs electrode. Insets in (a) and (b) illustrate the corresponding TEM images. (From Zhao et al., 2007. *Electrochem. Commun.* 9, 65–70, with permission.)

CNTs look like bigger feathers. The TEM image shows that there is much fleecy stuff on the surface of CNTs.

Figure 7.19 shows CVs recorded at an aqueous nitrite solution at pH 3.5 in phosphate-buffered saline (PBS) at glassy carbon electrode, aligned CNT electrode, and thionine-modified aligned CNT electrode. At glassy carbon electrode, a weak signal at +0.90 V vs. AgCl/Ag was obtained. At the bare aligned CNTs electrode, both the peak and background currents increase significantly, the peak potential being negatively shifted (+0.80 V). These effects can be attributed to the higher specific surface area provided by CNTs and novel electron transfer ability. At thionine-modified aligned CNTs electrode, a prominent oxidation peak appears. The catalytic mechanism proposed by Zhao et al. (2007) is schematically depicted in Figure 7.20.
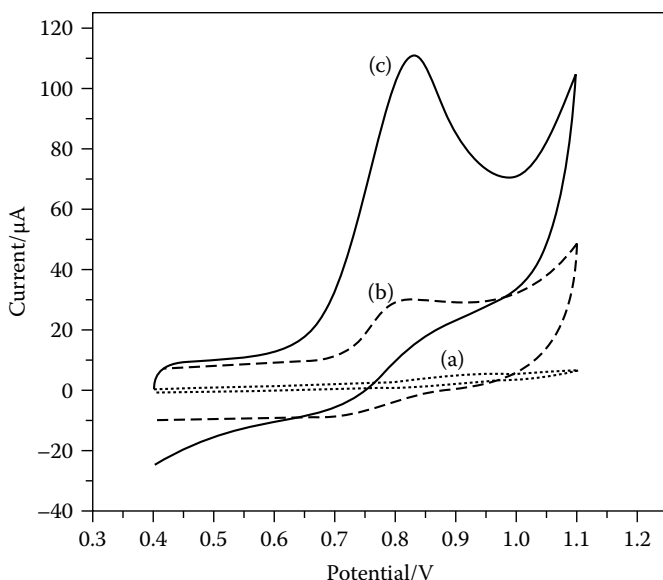
FIGURE 7.19 CVs of 0.10 mM NO_2^- in PBS buffer solution, pH 3.5, on (a) glassy carbon electrode, (b) aligned CNTs electrode, and (c) thionine-modified aligned CNTs electrode. Potential scan rate, 100 mV/sec. (From Zhao et al., 2007. *Electrochem. Commun.* 9, 65–70, with permission.)

Another plausible strategy consists of the functionalization of CNTs via covalent attachment of selected groups. This is the case of thiol and thiol-plus macrocyclic *m*-crown-*n* ether (*m* = 12, *n* = 4, and *m* = 15, *n* = 5)–functionalized single-wall CNTs (*m*C$_n$SHα-SWNT) prepared by Alvaro et al. (2007). The functionalization process and the structure of pendant units are depicted in Figure 7.21. Attachment of such
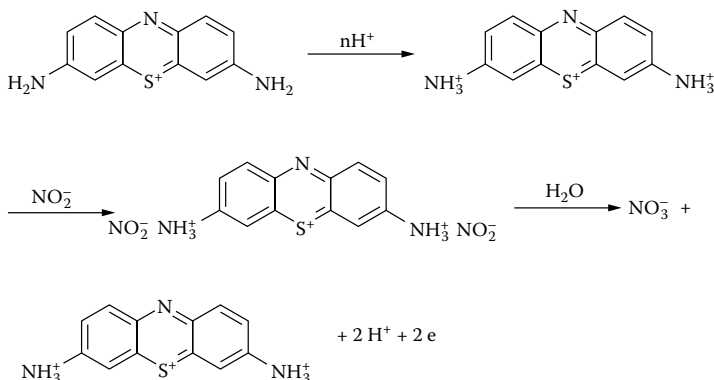
FIGURE 7.20 Electrocatalytic mechanism operating for nitrite oxidation at thionine-modified aligned CNTs electrode according to Zhao et al. (2007. *Electrochem. Commun.* 9, 65–70, with permission.)
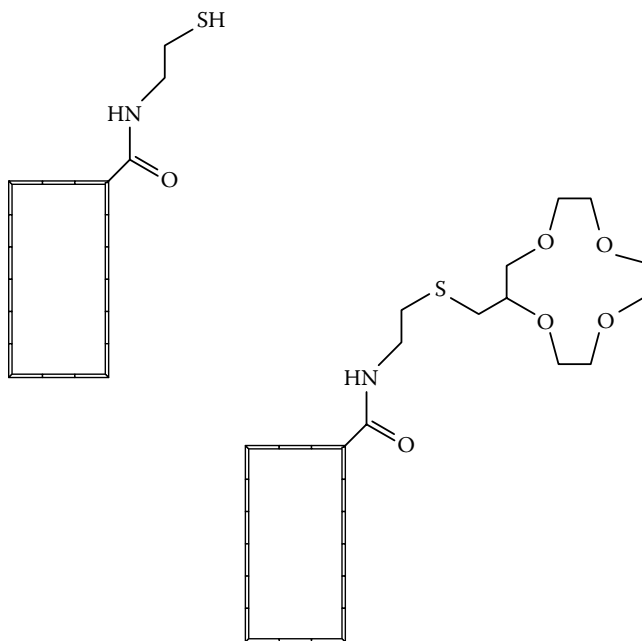
FIGURE 7.21 Scheme for thiol- and macrocyclic polyether crown doubly functionalized CNTs.

CNTs to gold electrodes provides an efficient and selective electrocatalytic response with respect to the oxidation of 3,4-methylenedioxymethyl metamamphetamine (MDMA, "ecstasy") and 3,4-methylenedioxymethyl amphetamine (MDA), two well-known designer drugs, in aqueous phosphate buffer. This procedure combines the conducting and catalytic ability of nanotubes with their efficient attachment to gold substrates through the thiol group. A high selectivity is obtained with respect to the common interferents in the electrochemical determination of MDA and MDMA: dopamine, ascorbic, and uric acids.

The selective electrocatalytic response can be seen in Figure 7.22, corresponding to the CV responses at unmodified and 15C₅SHα-SWNT thiol–modified and macrocyclic polyether crown, doubly functionalized CNT–modified gold electrodes in an MDMA solution in aqueous phosphate buffer. The anodic peak ca. +1.20 V becomes considerably enhanced at CNT-modified electrodes, where the crown ether groups act as preconcentration units by selectively complexing the analytes and provide charge and lipophilic/hydrophilic selectivity with regard to their interferents.

The possibility of MDA or MDMA determination in the presence of the aforementioned interfering compounds is illustrated in Figure 7.23, which shows the CV responses recorded at solutions of *p*-methoxyamphetamine (PMA), a model compound for MDA and MDMA containing an excess of (a) uric acid, (b) dopamine,
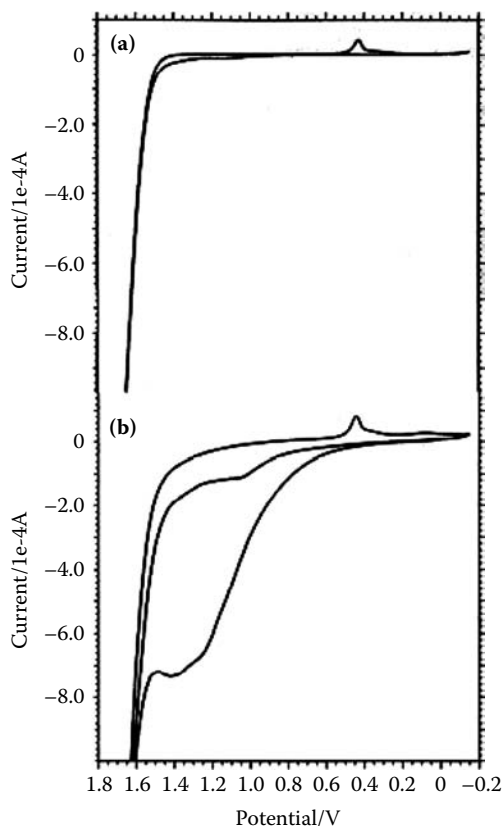
FIGURE 7.22 CVs for a 0.72 mM MDMA solution in 0.50 M aqueous phosphate buffer (pH 7.4) at: (a) unmodified gold; (b) 15C5SHα-SWNT thiol- and macrocyclic polyether crown doubly functionalized CNTs electrode. Potential scan rate, 50 mV/sec. (Disposal of materials courtesy of Hermenegildo García, Polytechnical University of Valencia.)

and (c) ascorbic acid. In all cases, the oxidation peak of MDMA becomes well defined, whereas weak voltammetric peaks recorded for the interferents, all exhibiting oxidation waves in the +0.20 to +0.40 V range at nonmodified electrodes, remain weaker.

First of all, the catalytic ability of $mC_nSH\alpha$-SWNT-modified electrodes for MDMA and MDA oxidation can be associated to the preconcentrating effect due to the coordination of ammonium groups to the polyether macrocyclic crown (Figure 7.24). The weak electrochemical response of such interferents at $mC_nSH\alpha$-SWNT-modified electrodes with respect to those obtained at unmodified ones can be attributed, in the case of ascorbic and uric acids, to the absence of ammonium groups capable of being coordinated with the macrocyclic ring of SWNTs. In addition, the anionic nature of these species under our experimental conditions can contribute to hindering their electrochemical response by electrostatic repulsion. Given the pK_a values (4.2 for ascorbic acid and 5.4 for uric acid), at pH 7.4, the anionic forms ascorbate and urate
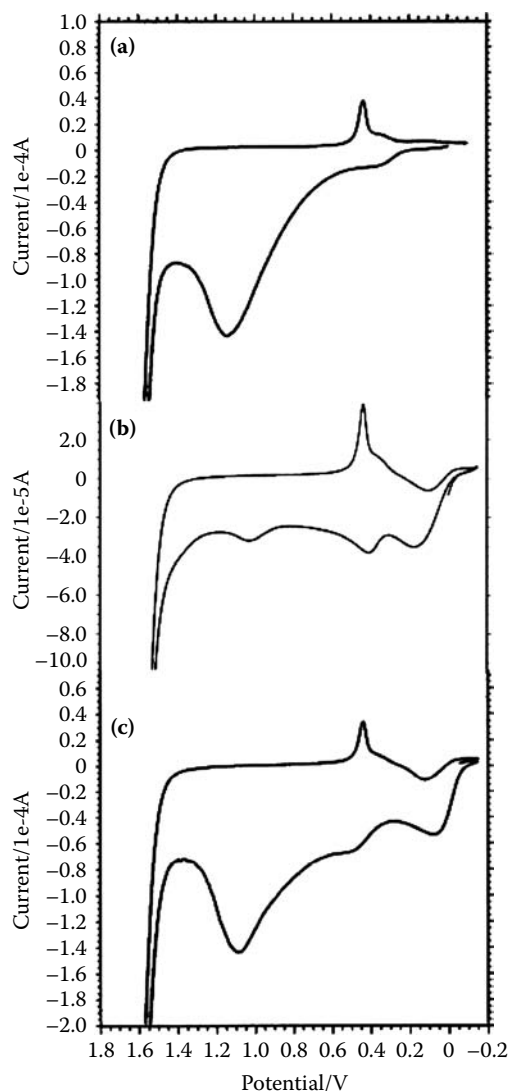
FIGURE 7.23 Deconvolution of CVs at 15C5SHa-SWNT-modified gold electrodes immersed into 0.50 M phosphate buffer solutions (pH 7.4) containing: (a) 0.12 mM PMA + 1.25 mM uric acid; (b) 20 μM PMA + 0.25 mM dopamine; (c) 0.18 mM PMA + 0.88 mM ascorbic acid. Potential scan rate, 50 mV/sec. (Disposal of materials courtesy of Hermenegildo García, Polytechnical University of Valencia.)

largely prevail in solution. As a result, electrochemical oxidation of ascorbate and urate are disfavored at SWNT-modified electrodes.

In the case of dopamine, however, there is an ammonium group capable of binding with the pendant macrocyclic units of SWNTs, but apparently there is no
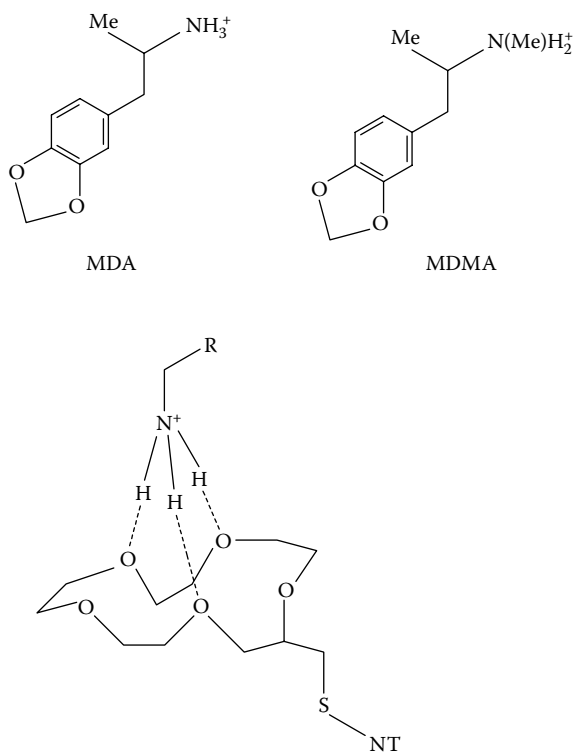
FIGURE 7.24 Scheme for the coordination of MDA and MDMA to 15C5SHα-SWNT thiol- and macrocyclic polyether crown doubly functionalized CNTs.

significant dopamine-receptor interaction. On comparing the macrocycle-substrate interaction, for PMA, MDA, MDMA, and dopamine, one can take into account that the strength of that interaction and, consequently, the extent of analyte-crown ether recognition, depend significantly on electronic and solvation factors, so that equilibrium formation constants can be factorized from several parameters (Reviriego et al., 2002). Accordingly, the lipophilic character of PMA, MDA, and MDMA should justify the existence of a strong interaction with the macrocyclic receptor units inserted in the SWNTs.

8 Electrochemistry of Porous Polymers and Hybrid Materials

8.1 ORGANIC-INORGANIC HYBRID MATERIALS AND NANOCOMPOSITES

The label of hybrid materials can be assigned to a variety of systems having in common a combination of organic and inorganic components blended on the molecular scale. Following Kickelbick (2007), one can distinguish between organic-inorganic hybrids *sensu stricto*, when inorganic units are formed *in situ* by molecular precursors, and nanocomposites, when discrete structural units are used in the respective size regime. Nanocomposites are usually formed by embedding nanoparticles, nanowires, nanorods, carbon nanotubes, etc., in an organic polymer.

Preparation strategies involve either the combination of building blocks, which retain, to a great extent, their molecular integrity throughout the process of material formation, or the transformation of building precursors into a novel material. Most of the development of hybrid materials derives from the use of sol-gel technologies. Hybrid materials can involve relatively weak interactions such as van der Waals forces or hydrogen bonding (class I hybrid materials) or covalent bonding between the building blocks (class II).

Since 1990, a wide variety of composites and hybrid materials has been prepared and electrochemically characterized. In this chapter, only a fraction of these materials will be presented. In the case of materials that can be described as a result of the attachment of an organic moiety to an inorganic network, one can distinguish between network modification, network building, and network functionalization. In the first case, the organic units are anchored to the inorganic support, which results in modifying only its surface properties. In a functionalized system, a reactive organic group is bonded to the inorganic support, whereas if a mixed network is formed by combining both the organic and inorganic moieties, both moieties are termed as *network builders*. In this context, the term nanocomposite is used when the size of one of the structural units falls in the 1- to 100-nm range. Nanoparticles, nanorods, metal-oxo clusters, fullerenes, carbon nanotubes, spherosilicates, and oligomeric silsesquioxanes are included in this group. Applications of hybrid materials and composites comprise catalysis, batteries, optoelectronic devices, corrosion inhibition and so forth. In most cases, multifunctional materials can be prepared from different molecular precursors.

In this chapter, attention will be focused on hybrid materials involving polymeric species. However, it should be noted that a wide variety of composites are currently under research—for instance, NiO plus yttrium-stabilized zirconia (Lee et al., 2001)

or nanocomposite materials formed by dispersion of metal oxide catalysts such as RuO_2 into different support materials (silica, zeolites, titania, carbon, carbon nanotubes, organic functionalized mesoporous silicas) (Rassaei et al., 2008). In addition, new types of hybrid nanomaterials enter into the scene: functionalized and structured metal nanoparticles and binary and ternary hybrid nanocrystals, for instance, $Au-Fe_3O_4$ (Shi et al., 2006).

8.2   POROUS POLYMERS

In recent years, special attention has been paid to porous polymers that could be used as electrolytes, such as poly(acrylonitrile) or poly(methyl methacrylate), in high power applications (Devaraj et al., 1990; Yan et al., 1996). In the search for higher ionic conductivities at room temperature, several strategies have been achieved either by varying the conductivity of the polymers or lowering their glass transition temperature. Such strategies include copolymerization (Wieckzorek and Stevens, 1997), comb branch polymers (Booth et al., 1989), cross-linked networks (MacCallum et al., 1981; Watanabe et al., 1987), and combinations (Kim et al., 1996). In the last case, the working system consists of films prepared from polymer solutions plus a lithium or sodium salt (typically, $NaClO_4$) and a plasticizer, as described by Reddy et al. (2007). Figure 8.1 shows the impedance plot for a zeolite Y–associated
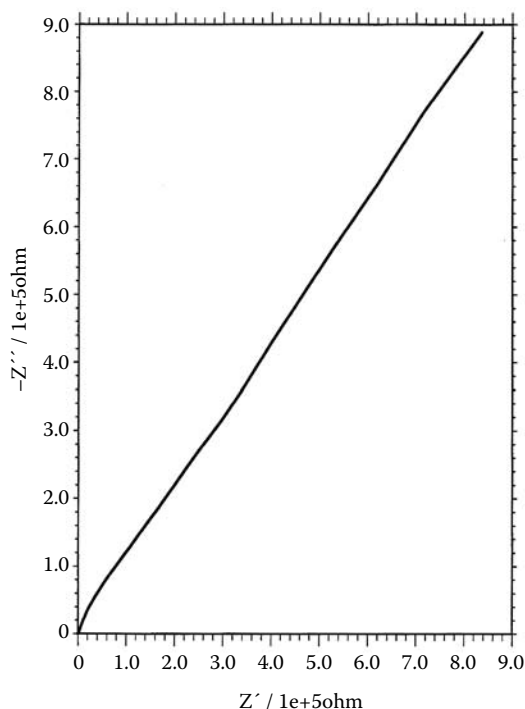
FIGURE 8.1   Nyquist impedance plot for a zeolite Y-associated poly(p-phenylenevinylene) film in contact with 0.10 M H_2SO_4.

poly(p-phenylenevinylene) (Álvaro et al., 2007) in contact with 0.10 M H_2SO_4. The conductivity of the system results from the summation of electronic and ionic conductivities; this last can be calculated from the area, thickness, and bulk resistance of the film using EIS data.

Electrochemical impedance spectroscopy (EIS) spectra suggest that the migration of ions may occur through the free volume of the matrix polymer, which can be represented by an ohmic resistance. The immobile polymer chains become polarized in the alternating field, and can be represented by a capacitor. When the concentration of plasticizer increases up to a certain value, the resistive component of polymer electrolyte prevails. Factors influencing conductivity are the degree of crystallinity, dielectric permittivity of the polymer, and coupling ions with the polymer chain. The conductivity of solid polymer electrolytes can be enhanced by using polymer hosts with high dielectric permittivity for favoring electrolyte dissociation and low glass transition temperature and/or two-phase polymer blends (Choe et al., 1995).

8.3 HYBRID MATERIALS BASED ON MODIFICATION OF CONDUCTING ORGANIC POLYMERS

From the seminal work of Shirakawa et al. (1977), redox-active π-conjugated conducting polymers have received considerable attention not only because of their conducting properties but also for their frequently reversible redox chemistry, ionic transport properties, tunable doping states, and electro-optical properties (Miller, 1993a,b). These include, among others, polypyrrole, polyaniline (PANI), polythiophene, and different copolymers. Figure 8.2 shows the typical response (see Pournaghi-Azar and Habibi, 2007) of PANI films during formation by electropolymerization from
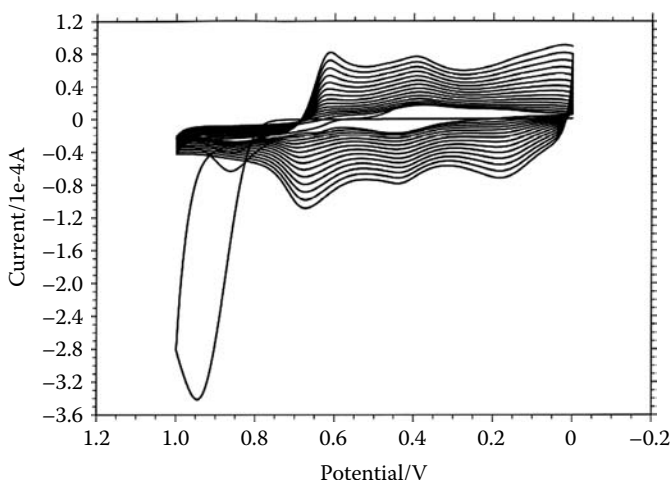
FIGURE 8.2 Repetitive CV response at glassy carbon electrode for a 10-mM aqueous solution of aniline in 0.10 M H_2SO_4. Potential scan rate, 50 mV/sec.

an aqueous solution of aniline in 0.10 M H_2SO_4 aqueous solution. In the first anodic scan, a prominent oxidation peak ca. $+0.95$ V appears. This process promotes radical cation formation and subsequent polymerization. Upon repetitive cycling the potential scan, overlapping couples at $+0.18$, $+0.40$, and $+0.65$ V vs. AgCl/Ag, appears. The height of the voltammetric peaks is enhanced in repetitive scans, a feature characterizing electropolymerization processes.

Polymers possess a characteristic size and dimensionality in between those of molecular and extended species. Two distinct classes of polymer-based, hybrid organic-inorganic materials can be distinguished: those in which the polymers constitute the matrix where inorganic species are inserted or integrated and those where the organic polymer in inserted into a more extended inorganic matrix, although, obviously, there are borderline materials challenging this classification such as V_2O_5-polyaniline (Cuentas-Gallegos et al., 2004).

In the context of porous hybrid materials, one can note that preparation of composites of inorganic materials with conducting organic polymers is currently under intensive research in order to combine catalytic properties of inorganic materials with conductivity and redox properties of such polymers.

The insertion of molecular inorganic species into a conducting organic polymer network can be obtained via copolymerization and functionalization but also by using doping strategies, so that charged inorganic species can be attached as charge-balancing ions in the polymer network. Different conducting polymers modified with anionic inorganic species, namely, oxometalates, complexes with organic ligands, macrocyclic compounds, etc., have been described. As an example, polymers embedded in porous aluminosilicates show EIS responses as depicted in Figure 8.3. In log Z vs. log f plots, a horizontal-like plateau is obtained at high frequencies, thus providing an ohmic resistance, R_u, which can be identified as the electrolyte resistance, $R_{electrol}$, in series with the polymer resistance, R_{poly}. At low frequencies, the charge transfer resistance, R_{ct}, also contributes significantly, so that the $R_u + R_{ct}$ sum can be read at the low-frequency intercept.

The EIS response depends on the film thickness and morphology, applied potential, and, obviously, the nature of the components of the hybrid system. The hydrophobic nature of the polymer, the level of doping within the film, and the size of ions in contact with the polymer surface are factors to be considered for studying the response of such materials. In short, the kinetics of the overall charge transfer process should take into account (1) electron hopping between adjacent redox sites (Andrieux et al., 1986) usually described in terms of a Warburg diffusion impedance element (Nieto and Tucceri, 1996) and (2) double-layer charging at the metal-film interface, represented in terms of a double-layer capacitance element.

When the polymer film is oxidized, its electronic conductivity can exceed the ionic conductivity due to mobile counterions. Then, the film behaves as a porous metal with pores of limited diameter and depth. This can be represented by an equivalent circuit via modified Randles circuits such as those shown in Figure 8.4. One Warburg element, representative of linear finite restricted diffusion of dopants across the film, is also included. The model circuit includes a charge transfer resistance, associated with the electrode/film interface, and a constant phase element representing the charge accumulation that forms the interfacial double
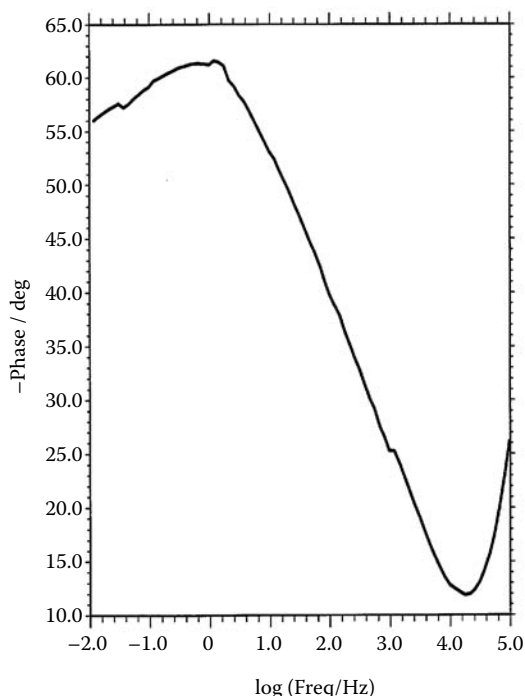
FIGURE 8.3 Bode plots Ru(bpy)-PA attached to MCM-41 immersed into 0.10 M of H_2SO_4. (Material courtesy of Prof. Hermenegildo García, Polytechnical University of Valencia.)

layer (Galal et al., 2007). In the low-frequency region, the impedance of the Warburg element, Z_D, can be expressed as a function of a diffusion pseudoresistance, R_D, a diffusion pseudocapacitance, C_D, and a diffusion time constant, τ_D, related by:

$$Z_D = \frac{(\tau_D/C_D)\coth(jC_D\tau_D)^{1/2}}{(j\omega C_D)^{1/2}} \tag{8.1}$$
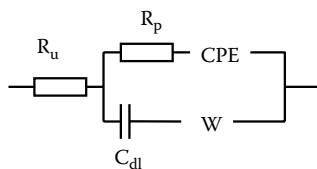
FIGURE 8.4 Equivalent circuit for describing EIS of conducting polymers.

The impedance of a one-dimensional cylindrical pore structure with invariant interfacial impedance Z_o along the wall of the pores can be described in terms of the electrolyte resistance; the impedance for a single pore, Z_p; the impedance of the pore wall, Z_{wall}; the pore radius, r_p; and the pore length, l_p, using the relationships:

$$Z_p = (R_{electrol} Z_{wall})^{1/2} \coth (R_{electrol} / Z_{wall})^{1/2} \tag{8.2}$$

$$Z_{wall} = \frac{Z_o}{2\pi r_p l_p} \tag{8.3}$$

$$R_{electrol} = \frac{l_p}{\sigma \pi r_p} \tag{8.4}$$

Here, σ represents the Warburg coefficient, which can be estimated from the slope of the $\log Z_{real}$ vs. $\log f$ representation in the region of intermediate frequencies, where:

$$Z_{real} = R_u + R_{ct} + \sigma/\omega^{1/2} \tag{8.5}$$

PANI is one of the most remarkable materials of this type of compounds because of its stability, conductivity, catalytic ability, and electrochemical properties. Its characteristics can be modified by incorporation of inorganic particles although it can also be regarded as a conducting network to be combined with inorganic components (Fusalba and Bélanger, 2000). It is known that PANI polymers can exist in five differently colored forms or "states," usually labeled as leucoemeraldine (light yellow), protoemeraldine (green), emeraldine (deep green), nigraniline (blue), and pernigraniline (violet) (Prakash, 2002), whose interconversion is schematized in Figure 8.5 and Figure 8.6. In the more reduced form, leucoemeraldine, all nitrogen units remain as amine groups, whereas the protoemeraldine and emeraldine forms incorporate until one half of nitrogen units remain as protonated imine groups. The nigraniline form possesses amine groups, protonated imine units, and deprotonated imine groups. Finally, the pernigraniline state of the PANI chain corresponds to a fully oxidized form where all imine groups become deprotonated. Film thickness, δ, can be estimated from:

$$\delta = \frac{qM}{zFA\rho} \tag{8.6}$$

where q represents the charge necessary to switch from one form to another, M is the molecular mass of the monomer, A is the electrode area, ρ is the density, and z is the number of charge of the monomer in polymer chains (Duic and Grigic, 2001).
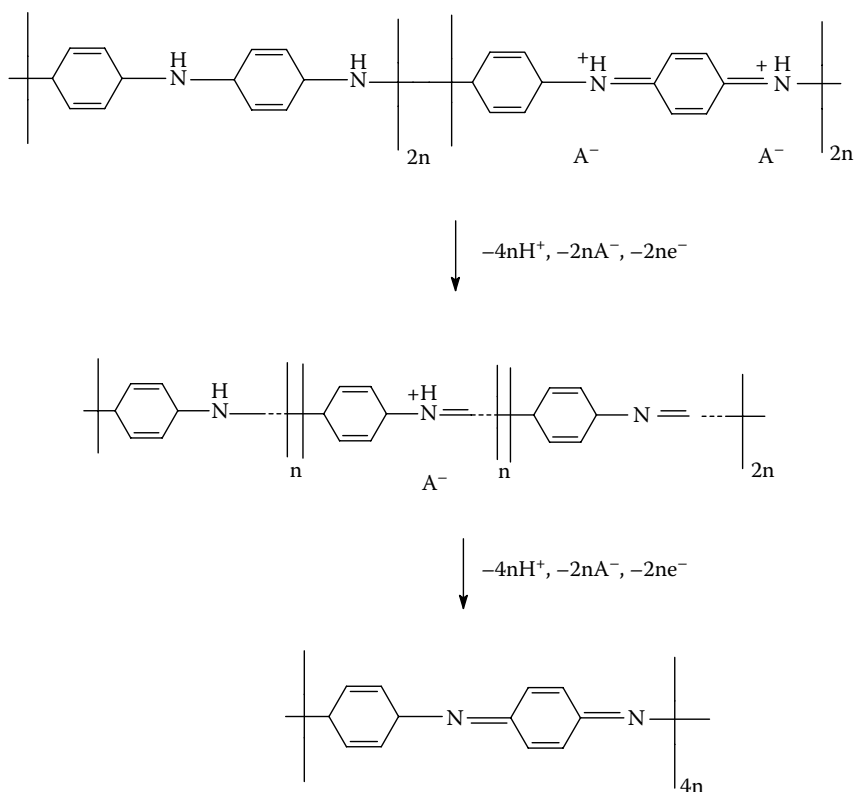
FIGURE 8.5 Schematics for the electrochemical oxidation of the emeraldine form of PANI. (From Doménech et al., 2008. *J. Electroanal. Chem.* 624, 275–286, with permission.)

Composite films of conducting polymers with other materials have been prepared; for instance, polyaniline and molybdenum oxide formed by electrocodeposition in aqueous media (Liu et al., 2007). Polyoxometalate-polymer hybrid materials have been widely studied. The strong oxidizing potential and acid character of acidic forms of oxometalates (e.g., "phosphomolybdic acid") are convenient properties for polymerizing monomers, such as aniline, pyrrol, or thiophene, to yield the corresponding p-doped polymers where bulky polyoxometalate species become trapped within the polymeric matrix via oxidative doping. The amount of electroactive guest anions incorporated within the polymer matrix is, in principle, limited by the doping level attainable for the polymer, the spatial distribution within the polymeric matrix depending on the conditions of preparation of the hybrid material. It should be noted that deinsertion of doping species can occur when the polymer is reduced, thus resulting in the loss of the desired activity. This is one of the reasons for studying polyoxometalate/conducting polymer hybrid materials, because the low diffusion rate of these species relative to that of common doping
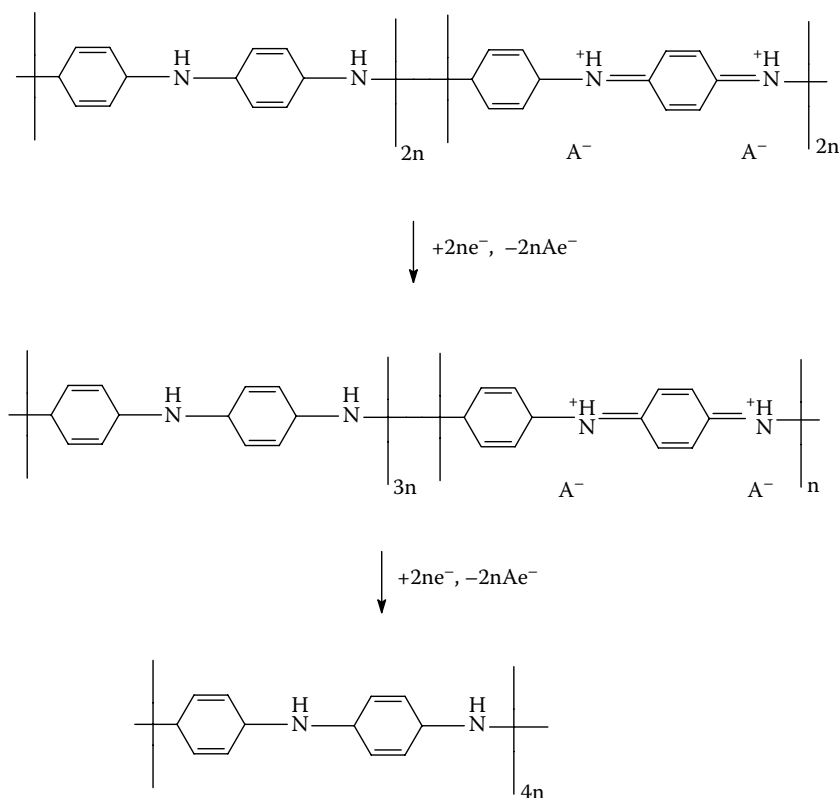
FIGURE 8.6 Schematics for the electrochemical reduction of the emeraldine form of PANI. (From Doménech et al., 2008. *J. Electroanal. Chem.* 624, 275–286, with permission.)

anions (ClO_4^-, Cl^-) makes them appropriate candidates for remaining anchored to the polymer network during oxidative steps. In fact, polyoxometalate-doped polymers can run as cation-inserting redox materials, a property of interest, for instance, in lithium batteries.

8.4 HYBRID MATERIALS BASED ON MODIFICATION WITH CONDUCTING POLYMERS

Different hybrid materials formed by insertion of organic polymers into inorganic substrates have been prepared. Layered materials are well known as host matrices for the incorporation of a large variety of polymeric organic species. Generally, the inorganic part is finely dispersed or exfoliated within the polymer, but, alternatively, the polymer can form laminae intercalated in laminar solids. This is the case for layered double hydroxides (LDHs, see Chapter 6), whose structure is closely related to that of the brucite, $Mg(OH)_2$, in which the partial substitution of some of the divalent

cations in octahedral positions with trivalent metallic ions results in the generation of positive charge supported by the hydroxyl layer. The substitution of the interlamellar anions by negatively charged species allows for the preparation of hybrid materials. This goal can be achieved via different procedures, of which delamination/restacking is one of the most versatile (Liu et al., 2006). This method consists of the delamination of the LDH system by mechanic shaking in organic solvents and subsequent addition of the anionic substituent molecule to the delaminated material, thus promoting the flocculation of the intercalated material. Using this methodology, an LDH-supported polyaniline material can be prepared by the intercalation of an emeraldine-conductive PANI solution into a $ZnAlNO_3^-$-LDH inorganic host (Doménech et al., 2008).

Attachment of PANI to this inorganic support determines a significant variation in the electrochemistry of the polymer, as can be seen by comparing cyclic voltammetries (CVs) in Figure 8.2 and Figure 8.7. Modulation of the electrochemical properties of the polymer in its different oxidation states as a result of the interaction with the inorganic support can be seen in Figure 8.8, which displays the CVs for a glassy carbon electrode modified with $ZnAlNO_3^-$-LDH-PANI immersed into 0.50 M phosphate buffer. On scanning the potential from the open circuit potential in the positive direction (Figure 8.7a), a weak oxidation wave appears at +0.20 V vs. AgCl/Ag preceding a prominent anodic peak at +0.60 V, followed by a shoulder near +0.85 V. In the subsequent cathodic scan, no cathodic counterparts of the above signals were detected and only a cathodic peak at −0.60 V is recorded. When initiating the potential in the negative direction (Figure 8.7b), a cathodic shoulder at ca. −0.60 V is accompanied, in the subsequent anodic scan, by the oxidation peak at +0.60 V. This voltammetry clearly differs from that obtained for PANI films in contact with aqueous electrolytes, illustrated in Figure 8.2.

A significant electrolyte-dependent response was obtained for $ZnAlNO_3^-$-LDH-PANI in contact with different MeCN electrolytes, thus denoting that PANI-intercalated species are responsible for the electrochemistry of $ZnAlNO_3^-$-LDH-PANI material. As shown in Figure 8.7, upon immersion of $ZnAlNO_3^-$-LDH-PANI-modified electrodes in Bu_4NPF_6/MeCN electrolytes, weak cathodic signals were recorded in initial cathodic scan voltammograms, whereas two prominent overlapping oxidation peaks at +1.20 and +1.46 V appeared in the subsequent anodic scan and in initial anodic scan voltammograms. In contrast, initial cathodic scan CVs in $LiClO_4$/MeCN electrolytes exhibit a well-defined cathodic signal at −1.86 V, whereas the response in the positive region of potentials becomes similar to that described when in contact with Bu_4NPF_6/MeCN.

A plausible—but tentative—representation of oxidation processes recorded for $ZnAlNO_3^-$-LDH-PANI-modified electrodes in contact with aqueous phosphate buffers involves the issue of NO_3^- ions as depicted in Figure 8.9. Subsequent reduction of the generated nigraniline and pernigraniline forms should be conditioned by the need for adding anions and protons or cations from the electrolyte. As a result, no cathodic counterparts of the oxidation peaks at +0.60 and +0.85 V are recorded.
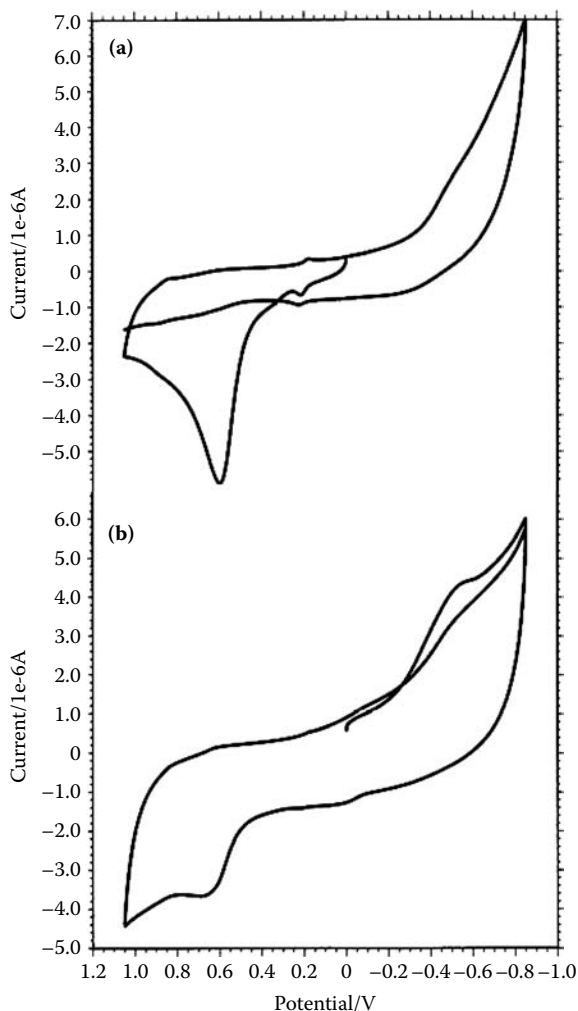
FIGURE 8.7 CVs of glassy carbon electrodes modified with $ZnAlNO_3^-$-LDH-PANI immersed into 0.50 M phosphate buffer (pH 7.0). (a) Initial anodic scan; (b) initial cathodic scan. Potential scan rate, 50 mV/sec. (From Doménech et al., 2008. *J. Electroanal. Chem.* 624, 275–286, with permission.)

Reduction of $ZnAlNO_3^-$-LDH-PANI involves the ingress of electrolyte charge-balancing cations, essentially hindered for bulky Bu_4N^+ species. A schematic representation of reduction processes from the emeraldine form is presented in Figure 8.10. Cathodic processes also behave irreversibly, attributable to the difficulty in removing anions from the LDH framework and the concomitant ingress of electrolyte cations into the LDH-PANI system. Oxidation of PANI species generated by electrochemical reduction of the parent emeraldine-type LDH-PANI should occur at potentials
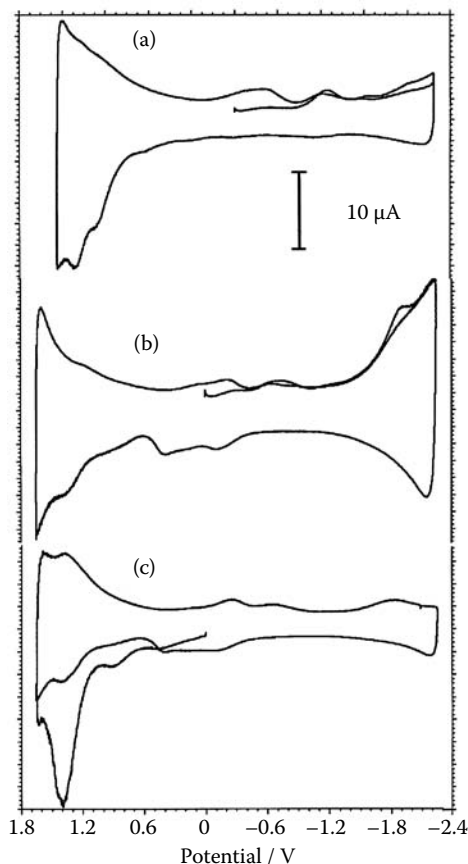
FIGURE 8.8 Semiderivative convolution of CVs for $ZnAlNO_3^-$-LDH-PANI-modified glassy carbon electrode. (a) Initial cathodic scan, 0.10 M Bu_4NPF_6/MeCN; (b) initial cathodic scan, 0.10 M $LiClO_4$/MeCN; (c) initial anodic scan, 0.10 M $LiClO_4$/MeCN. Potential scan, rate 100 mV/sec. (From Doménech et al., 2008. *J. Electroanal. Chem.* 624, 275–286, with permission.)

of −0.05 and +0.20 V, being highly constrained by ion transport across the LDH-PANI system. A tentative representation of electrochemical oxidation of emeraldine is shown in Figure 8.10.

Atomic force microscopy (AFM) examination of LDH-PANI deposits over a graphite plate during application of different potentials shows changes in the volume and morphology of LDH-PANI particles depending on the applied potentials. This can be seen in Figure 8.11, which shows the AFM images recorded for an LDH-PANI immersed into phosphate buffer: (a) at open circuit potential, (b) after scanning the potential to +1.20 V at 10 mV/sec, and (c) upon scanning the potential again from +1.20 to −1.00 V. Initially, irregular aggregates of hydrotalcite nanoparticles 100–150 nm in size were observed. After scanning the potential to +1.20 V,
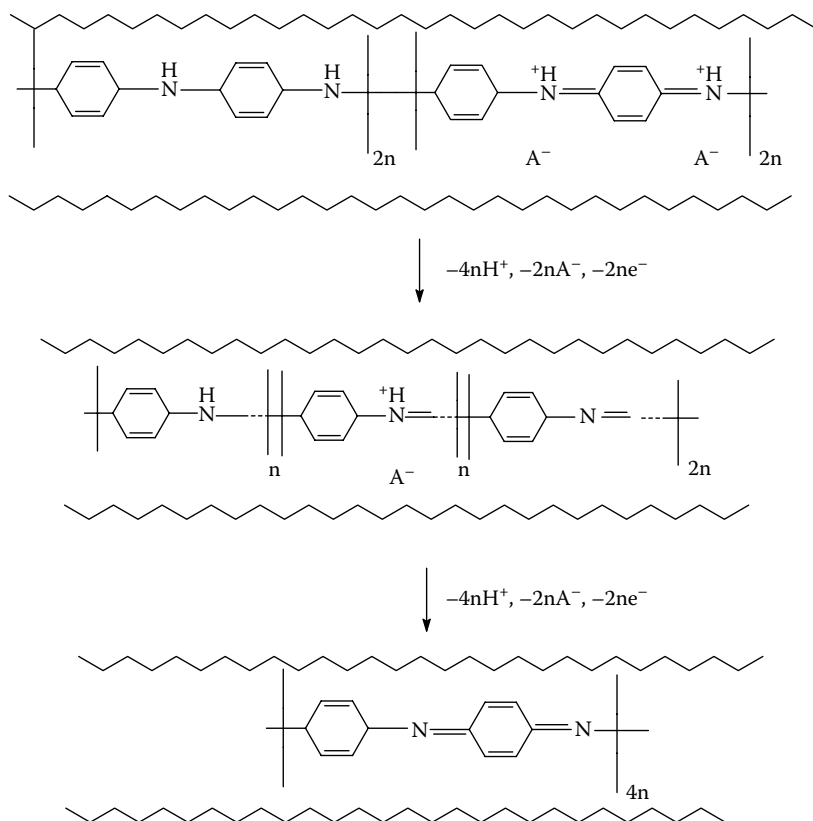
FIGURE 8.9 Schematics for the electrochemical oxidation of the ZnAlNO$_3^-$-LDH-PANI system starting from the emeraldine form of PANI. (From Doménech et al., 2008. *J. Electroanal. Chem.* 624, 275–286, with permission.)

a very small decrease in the volume of several particles was observed in large crystals, whereas when the potential is brought back to 0.0 V and further to −1.00 V, a significant expansion in the volume of such particles is observed, and even particle interconnections appear. These features can be rationalized, on the basis of the previous reaction scheme, by assuming that: (1) oxidation of the parent emeraldine form results in proton loss and extensive double bond formation in nitrogenated chains of the polymer, thus slightly lowering the volume of the polymer incorporated to the hydrotalcite particles; (2) reduction of emeraldine implies single-bonded chains with concomitant ingress of cations (see reaction schemes in Figure 8.9 and Figure 8.10) and electrons in the LDH-PANI system. As a result, the volume of polymeric chains becomes significantly enlarged, even forming links between PANI units from different hydrotalcite crystals, as suggested by AFM image in Figure 8.11c.

Changes in conductivity of LDH-PANI associated to the above electrochemical processes were monitored by EIS upon application of potentials of 0 (open circuit),
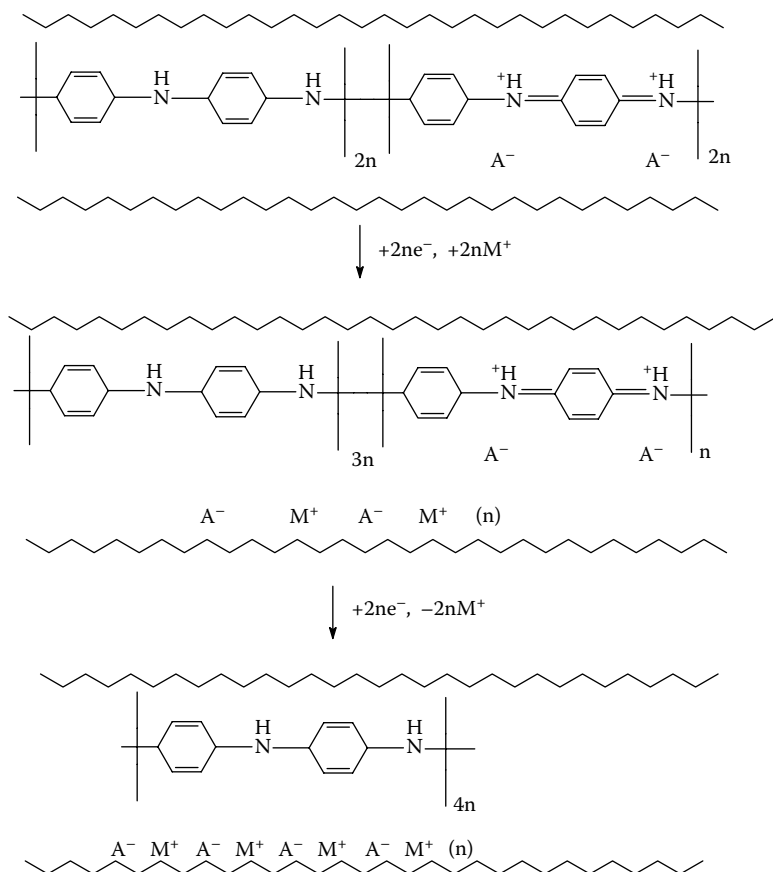
FIGURE 8.10 Schematics for the electrochemical reduction of the ZnAlNO$_3^-$-LDH-PANI system starting from the emeraldine form of PANI. (From Doménech et al., 2008. *J. Electroanal. Chem.* 624, 275–286, with permission.)

+0.90, and −0.80 V. The corresponding representations are shown in Figure 8.12. In all cases, the total impedance decreases on increasing frequency. Remarkably, at all frequencies, the impedance upon application of a potential of +0.60 V is ten times larger than that obtained at open circuit. This result is consistent with the idea that emeraldine is oxidized to nigraniline at that potential. It has been proposed that the extensive π conjugation in the polymer chain of the emeraldine form of PANI, and hence, the high conductivity of the polymer came from the preferential protonation of the imine nitrogen, although the amine nitrogens are stronger bases (Prakash, 2002). The extent of the protonation of the polymer decreases as the oxidation state increases, so that the pernigraniline form should be little or not protonated in these forms. Formation of nigraniline then results in a significant decrease in the conductivity.

Upon application of a potential of −0.90 V, however, the total impedance at low frequencies is close to that obtained at +0.80 V, further decreasing to values close

(a)

(b)

(c)
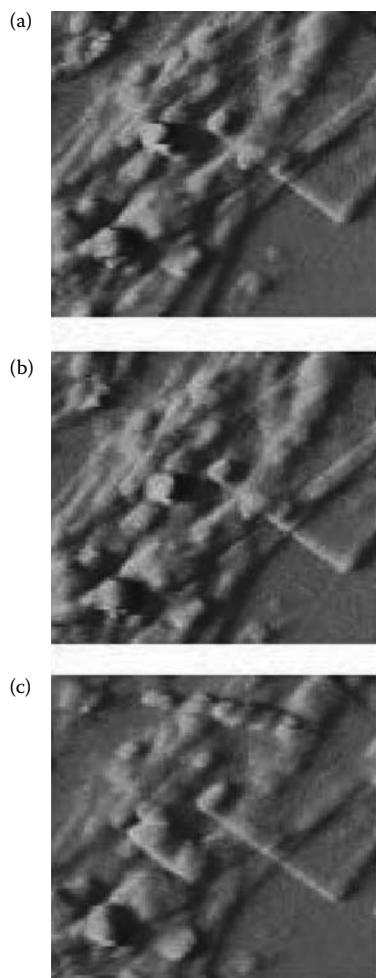
FIGURE 8.11 (See color insert following page 94.) AFM images (750–750 nm in size) recorded for a ZnAlNO$_3^-$-LDH-PANI deposit on graphite plate immersed into 0.50 M phosphate buffer at (a) open-circuit conditions, (b) upon scanning the potential to +1.20 V at 10 mV/sec, and (c) upon scanning again the potential from +1.20 to −1.00 V at 10 mV/sec. (From Doménech et al., 2008. *J. Electroanal. Chem.* 624, 275–286, with permission.)

to those recorded at open circuit at frequencies greater than 10 kHz. This variation can be seen in Figure 8.13, where the Nyquist representation at frequencies above 10 Hz is depicted. This peculiar variation of impedance should be consistent with the electrochemistry of LDH-PANI described above. At low frequencies, electrochemical reduction of LDH-PANI occurs, thus forming protoemeraldine and leucoemeraldine and decreasing conductivity with respect to that of the parent emeraldine. At relatively high frequencies, ion transport becomes considerably slower and reduction processes are hindered. Accordingly, the impedance response is equal to that obtained for emeraldine at open circuit.
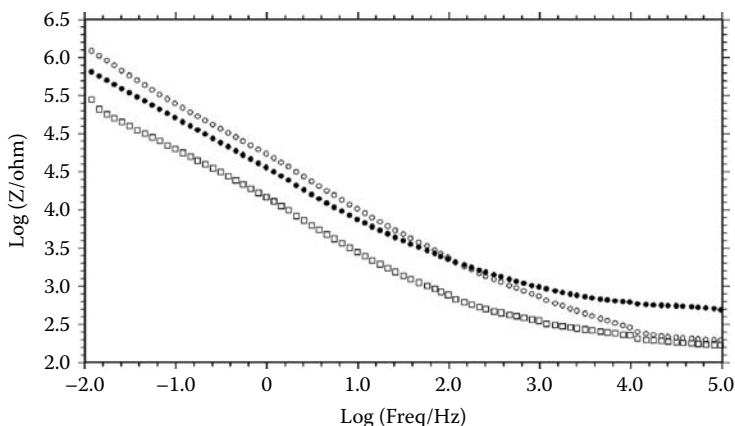
FIGURE 8.12 Representation of the variation of the total impedance with the frequency for EIS obtained for glassy carbon electrodes modified with LDH-PANI immersed into 0.50 M phosphate buffer (pH 7.0) at applied potentials of 0 V (squares), +0.90 V (solid circles), and −0.80 V (circles).

8.5 ELECTROCHEMICAL MONITORING OF POLYMERIZATION IN HYBRID SYSTEMS

Redox conductivity of conducting polymers involves anion insertion associated to oxidation processes (p-type doping) and cation insertion coupled with reduction ones (n-type doping). Efficient polymer-based electronic devices require lowering of the redox potential of the involved electron transfer processes, and electrochemical reversibility is necessary to allow repetitive charge/discharge processes. In the
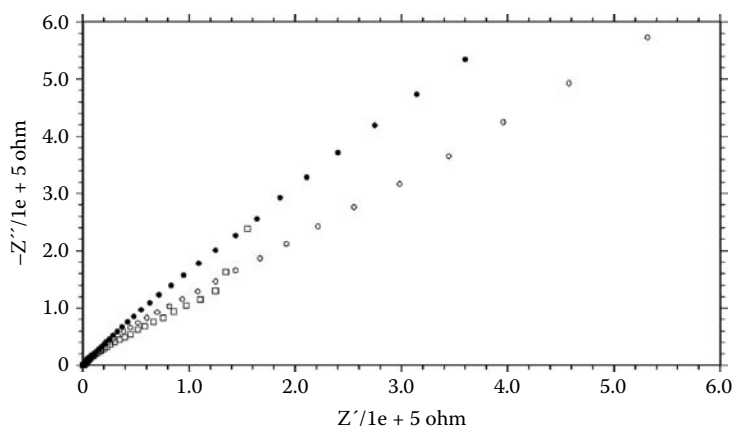
FIGURE 8.13 Nyquist representations for EIS obtained for glassy carbon electrodes modified with LDH-PANI immersed into 0.50 M phosphate buffer (pH 7.0) at applied potentials of 0.0 V (circles), +0.60 V (solid circles), and −0.80 V (squares).

attempt to accomplish the above conditions, different functional groups have been attached to polyacetylene chains (Alvaro et al., 2005); however, achievement of electrochemical reversibility is made considerably difficult by chemical reactions accompanying electron transfer processes.

In this context, an alternative means of stabilizing reactive charged species resulting from p- and n-doping of polyacetylenes consists of their anchorage to a nonconducting inorganic matrix. This strategy has been widely used for stabilizing organic reactive species into inorganic hosts, particularly zeolites (see Chapter 4). This type of material combines the redox activity of the organic guest with the ability of zeolites for stabilizing positively charged species, thus stabilizing reactive cations, blocking cross-link reactions, and protecting such reactive species from the attack of external reagents, particularly oxygen.

Figure 8.14 compares the CV response of zeolite Y-associated poly (thienylacetylene) (PTA@Y) in contact with Bu_4NPF_6/MeCN, Et_4NClO_4/MeCN, and $LiClO_4$/MeCN electrolytes. In all electrolytes, a well-defined oxidation peak appears at +1.44 V, followed by an ill-defined wave near +2.4 V. In contact with Bu_4NPF_6/MeCN and Et_4NClO_4/MeCN electrolytes, no coupled cathodic peaks were recorded in the subsequent cathodic scan even at potential scan rates of 1000 mV/ sec, denoting that the main oxidation process corresponds to an irreversible electron transfer or an electron transfer followed by a fast chemical reaction. At more negative potentials, a weak reduction wave near −1.0 V was recorded. In contrast, in contact with $LiClO_4$/MeCN, a well-defined cathodic peak appears at +0.82 V, followed by overlapping cathodic signals at −1.05 and −1.51 V.

Remarkably, peak currents for PTA@Y immersed into $LiClO_4$/MeCN were considerably larger than those recorded for PTA@Y-modified electrodes in contact with Bu_4NPF_6/MeCN and Et_4NClO_4/MeCN electrolytes. As can be seen in Figure 8.14, in the second and successive scans, peak currents decreased rapidly for PTA@Y immersed into Bu_4NPF_6/MeCN and Et_4NClO_4/MeCN electrolytes, whereas a slow decay of peak currents was observed for such modified electrodes in contact with $LiClO_4$/MeCN.

Separation of the cathodic and anodic components of the net current (measured at the end of forward and backward pulses) in square-wave voltammetries (SQWVs) provided only anodic components for PTA@Y electrodes immersed into Bu_4NPF_6/ MeCN, as depicted in Figure 8.15. In contrast, SQWVs display well-developed anodic and cathodic components for PTA@Y electrodes in contact with $LiClO_4$/ MeCN. This feature, indicative of reversible electron transfer processes, was found to be more pronounced on decreasing square-wave frequency.
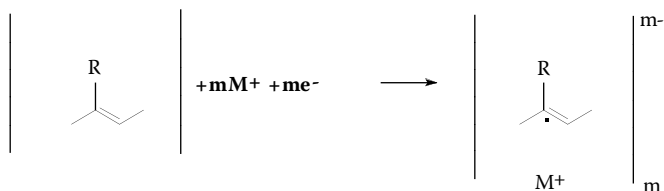
Reduction of zeolite-associated poly(thienylacetylene) oligomers can be represented as a one-electron per monomer electron transfer process schematized in Figure 8.16, where an anion radical is formed. Reduction of zeolite-associated poly(thienylacetylene) can be described in terms of the formation of radical anion species coupled with the ingress of electrolyte cations M^+ (=Bu_4N^+, Et_4N^+, Li^+) into the zeolite framework (equivalent to the n-type doping in redox polymers in solution). Now, radical anion species are formed, being eventually stabilized into the zeolite pore/channel system, as described for zeolite-associated Meisenheimer anions (Doménech et al., 2005b). Since the reduction process requires the ingress of
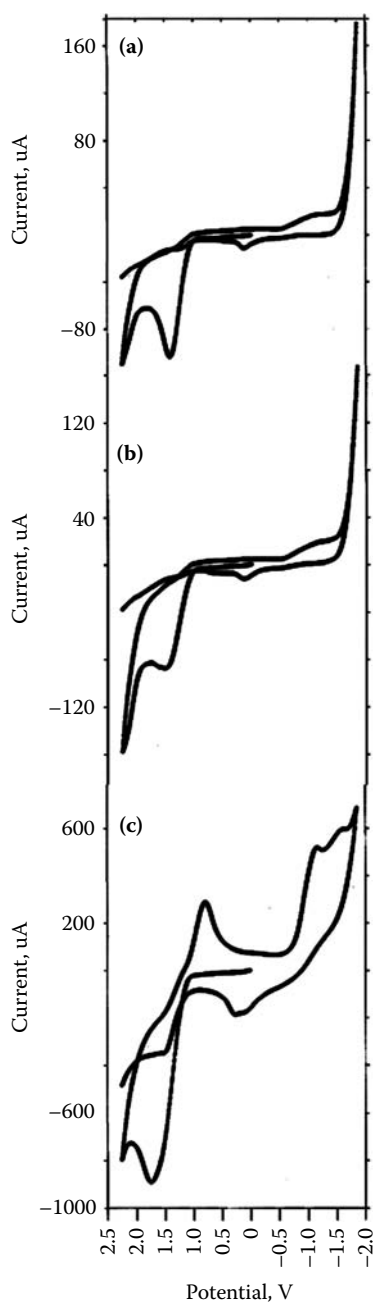
FIGURE 8.14 CVs of PTA@Y-modified electrodes immersed into: (a) 0.10 M Bu$_4$NPF$_6$/MeCN, (b) 0.10 M Et$_4$NClO$_4$/MeCN, and (c) 0.10 M LiClO$_4$/MeCN. Potential scan initiated at 0 V in the positive direction at 50 mV/sec.
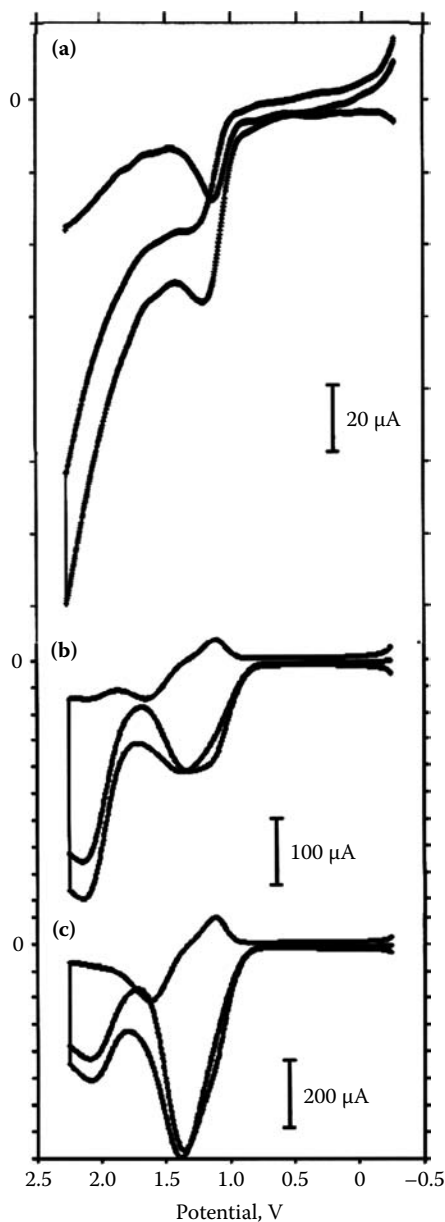
FIGURE 8.15 Separate plots of the cathodic and anodic components and the net current in SQWVs of PTA@Y-modified electrodes immersed into (a) 0.10 M Bu_4NPF_6/MeCN and (b,c) 0.10 M $LiClO_4$/MeCN at frequencies of (a,b) 5 and (c) 15 Hz. Potential step increment, 4 mV; square-wave amplitude, 25 mV.

FIGURE 8.16 Schematics for the electrochemical reduction of zeolite-associated polyacetylene oligomers.

electrolyte cations (M^+) into the zeolite system, reduction of zeolite-associated species will be allowed for Li^+ ions, whereas bulky, size-excluded Bu_4N^+ and, to a lesser extent, Et_4N^+ ions block reduction processes.

Oxidation of zeolite-associated poly(thienylacetylene) can be described via anion insertion (i.e., the typical p-type doping process in redox polymers) or via desorption of charge-balancing Na^+-exchanged cations from the zeolite system to the solution phase. These two possible electrochemical pathways are depicted in Figure 8.17, where $X^- = PF_6^-$, ClO_4^-. Following the general concepts for the electrochemistry of electroactive species attached to porous solids previously described, the voltammetric response of PTA@Y in contact with Bu_4NPF_6/MeCN and Et_4NClO_4/MeCN electrolytes should be attributed to the population of poly(thienylacetylene) chains located on the particle surface, thus producing a unique, weak oxidation peak. In contrast, the response of PTA@Y immersed into $LiClO_4$/MeCN results from the superposition
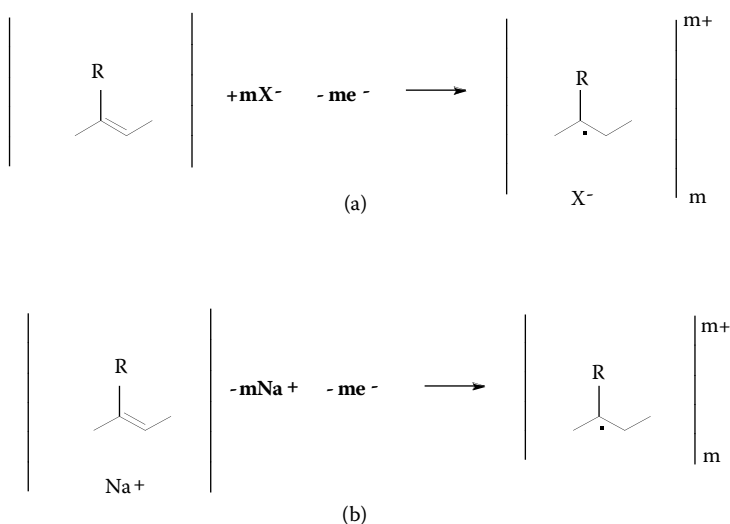
FIGURE 8.17 Schematics for possible pathways in the electrochemical oxidation of zeolite-associated polyacetylene oligomers.

of that due to external (displaying an irreversible behavior) and that due to zeolite-associated poly(thienylacetylene) (this one displaying an essentially reversible behavior). Consistently, the response in the second and subsequent scans in repetitive voltammetry is rapidly exhausted for PTA@Y immersed into Bu_4NPF_6/MeCN and Et_4NClO_4/MeCN, whereas it is significantly more reversible for $LiClO_4$/MeCN.

In this scheme, zeolite-associated species display a reversible electrochemistry because of the compartmentalization effect due to the encapsulation of poly(thienylacetylene) oligomers into the zeolite framework. It should be noted that the electrochemical oxidation of thiophenes having free 2 or 5 positions can result in dimerization and oligomerization arising from post–electron transfer reactions. These processes can frequently result in apparently irreversible voltammetric profiles (Garcia et al., 1992). In the case of thiophene-substituted polymers, such oxidation processes may result in the formation of cross-links via α,α' or α,β' coupling between thiophene units (Roncali, 1992). Then, the reversibility of electron transfer processes of PTA@Y in contact with $LiClO_4$/MeCN electrolytes can be attributed to the exigent spatial constraints due to the rigidity of the zeolite framework, thus stabilizing thiophene substituents by impeding side reactions of polarons to occur.

The redox potentials, electrochemical HOMO and LUMO energies (E_{HOMO} and E_{LUMO}, respectively) and energy gap, E_{gap}, can be calculated—as described in the literature—from the onset potentials, defined as the potential values obtained from the intersection of the two tangents drawn at the rising current and the baseline charging current of the CV curves. Data obtained from CV for PTA@Y-modified electrodes immersed into different MeCN electrolytes are summarized in Table 8.1. The potentials were calculated as E_{HOMO} (E_{LUMO}) = $-[-(E_{onset} - 0.45) - 4.75]$ eV (Nguyen et al., 2000). In this equation, E_{onset} represents the onset potential vs. Ag^+/Ag, 4.75 eV represents the energy level of ferrocene below the vacuum, and 0.45 is the value of the ferricinium/ferrocene couple vs. Ag^+/Ag.

The net amount of charge passed through the oxidation step, determined as the area under voltammetric peak A_1, was 1250 μC for zeolite deposits of 0.20 mg, corresponding to a charge of 0.18 mol of electrons/mol monomer (Doménech et al., 2006f). This result indicates that a significant amount (ca. 20%) of the zeolite-associated


TABLE 8.1

Redox Potentials (vs. AgCl (3M NaCl)/Ag), Electrochemical HOMO and LUMO Energies and Energy Gap Obtained from Cyclic Voltammetry at 298 K (v = 100 mV/s) for PTA@Y-Modified Electrodes Immersed into Different MeCN Electrolytes. E^{HOMO} (E^{LUMO}) = -[-(E_{onset} − 0.45) − 4.75] eV, [a] All in Concentration 0.10 M

Electrolyte[a]	E_p (V)	E_p (V)	E^{onset} (V)	E^{onset} (V)	E^{HOMO} (eV)	E^{LUMO} (eV)	E^{gap} (eV)
Bu_4NPF_6/MeCN	+1.28	−0.89	+1.08	−0.68	−5.38	−3.62	1.76
Et_4NClO_4/MeCN	+1.41	−0.88	+1.07	−0.68	−5.37	−3.62	1.77
$LiClO_4$/MeCN	+1.43	−1.00	+1.08	−0.68	−5.38	−3.62	1.76

polymer is electroactive, in sharp contrast with the values for zeolite-associated dis-crete species for which less than 1% of the encapsulated molecules were electroactive (Chapter 4). The high degree of guest charging is a manifestation of the conducting nature of conjugated monomer.

Chronoamperometric curves obtained by applying a constant potential above +1.50 V yield rapidly decaying current-time curves, similar to those obtained for species freely diffusing in solution phase. Interestingly, however, significant cur-rent fluctuations were obtained along the chronoamperometry (CA) curve, as can be seen in Figure 8.18. On first examination, these current fluctuations can be
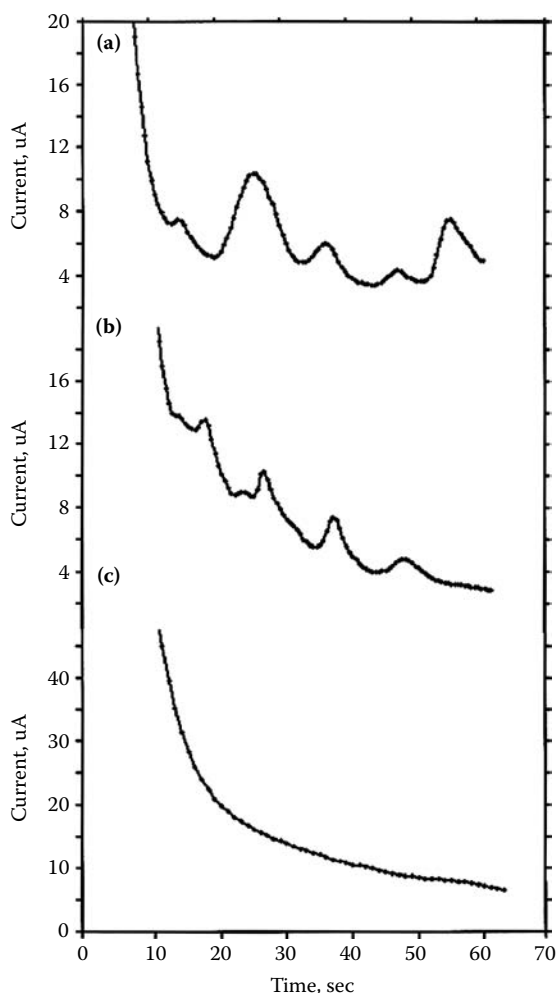
FIGURE 8.18 Long-time chronoamperometric curves recorded for (a) bulky deposit and (b) fine deposit of PTA@Y over a glassy carbon electrode. Curve (c) corresponds to the response at zeolite Y–modified electrodes with no attached polymer.

associated to the attachment of polymer chains to zeolite framework. As described by Egbe et al. (2003), the electronic and optical properties of conjugated polymers are controlled by the primary molecular structure, providing π conjugation, and by the supramolecular organization given by intermolecular interactions, governed by π stacking and doping (cation/anion insertion) effects (Yamamoto et al., 2003). Accordingly, it is conceivable that ordering of polymer chains along zeolite crystals may promote a certain degree of cooperative electron transfer resulting in quasi-periodic current fluctuations. Consistently, such current fluctuations disappear in CAs recorded while stirring the electrolyte solution, as depicted in Figure 8.18b. Tentatively, CA current fluctuations can be attributed to a "discrete" charge transfer process associated to the transfer of successive electrons to polymer chains governed, to any extent, by supramolecular ordering induced by the zeolite framework.

The net amount of charge transferred during the crust in chronoamperometric curves was typically found to be $q = 15$ µC. This quantity can be tentatively used for estimating the mean size of tiophene oligomers assuming that the charge corresponds to the n-electron oxidation of a layer of N oligomers perpendicularly distributed to the electrode surface. Taking the oligomers as elongated chains whose monomer length is $b = 0.8$ nm, as estimated from molecular modeling, and assuming that the maximum area covered is just the electrode area, A, one can write: $q_{crusts} = zFAbc$. Inserting the values for the nominal monomer concentration $c = 2 \times 10^{-3}$ mol/cm^3 and geometrical electrode area $A = 0.071$ cm^2, one obtains $z = 13.6$. This value, which corresponds strictly to the mean oligomer number resulting from the coverage of the electrode surface, is consistent with values for polyalkynes attached to zeolites reported by Alvaro et al. (2005).

8.6 DISPERSION OF METAL AND METAL OXIDE NANOPARTICLES INTO POROUS SOLIDS

Metal and metal oxide nanoparticles are currently under intensive research because of their applications in sensing, optics, electronics, and information storage. Nanoparticle stabilization from solutions requires the use of a protecting agent (capping) to prevent aggregation phenomena resulting in peculiar nanoparticle properties. Adsorbed polymer coatings, adsorbed ion layers, monolayers of organic ligands, and dendrimers, among others, have been used for this purpose.

Since the desired property of metal nanoparticles is loss by particle aggregation, confinement of metal nanoparticles on mesoporous materials has received attention. Here, the porous material can act as a template for forming nanoparticles, which then have controlled size and high dispersion. Interestingly, in such pore structure, metal particles can interact with each other only in the same pore; between neighboring pores, no interaction occurs (Bore et al., 2005). Electrochemical deposition of gold nanoparticles occurs on amine-functionalized mesoporous silica films (Yu et al., 2007). Preparation methods involve impregnation of porous materials by gold salts followed by chemical or electrochemical reduction, introduction of gold salts in the template-synthesis of such porous materials followed by chemical reduction, and eventually thermal
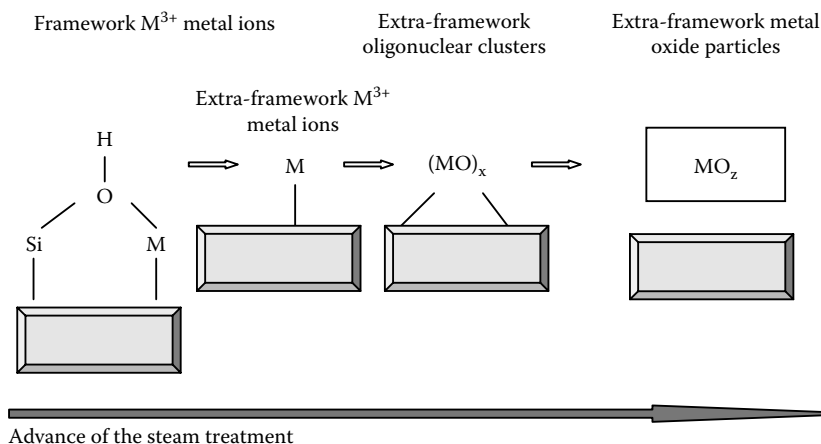
FIGURE 8.19 Scheme for the extraction and clustering of metal species in MZSM-5 (M = Fe, Co, Ni) materials upon steam activation.

treatment (Asefa and Lennox, 2005) or encapsulation of premade nanoparticles during the synthesis of such mesoporous materials (Aprile et al., 2005).

One of the possible means of obtaining nanoparticles consists of application of hydrothermal treatments to aluminosilicate materials incorporating metal ions in their lattice. This is the case of Fe, Co (etc.)-doped zeolites. Thus, FeZSM-5 materials are prepared from H-ZSM5 using solid and liquid ion exchange methods (Joyner and Stockenhuber, 1999), chemical vapor deposition of volatile iron compounds ($FeCl_3$) (Chen and Sachtler, 1998), or hydrothermal synthesis of isomorphously substituted FeZSM-5 (Panov et al., 1998) followed by calcinations and steam treatment. Steam activation produces extraction and clustering of iron species, as depicted in Figure 8.19 (Pérez-Ramírez et al., 2003). These treatments induce the migration of iron toward extra-framework positions by cleavage of Si–O–Fe bonds and dealumination of the zeolite framework.

Figure 8.20 shows a transmission electron microscopy (TEM) image of iron oxide nanoparticles generated in FeZSM-5 zeolite after calcinations and steam treatment. Dark spots in this image correspond to homogeneously dispersed iron oxide nanoaggregates of 1–2 nm (Doménech et al., 2002d,e). Changes in iron species can be monitored by ^{57}Fe Mössbauer spectroscopy, as illustrated in Figure 8.21. This figure shows spectra taken at 300 K in the air for FeZSM-5 (a) as-synthesized, (b) calcined, and (c) steamed (Pérez-Ramírez et al., 2002). The spectrum of the as-synthesized sample shows a broad singlet that can be assigned to tetrahedrally coordinated Fe^{3+} ions homogeneously distributed in the zeolite framework. The calcined sample exhibits a significant narrowing of the Mössbauer signal accompanied by the onset of a paramagnetic doublet. This can be attributed to the shortened electron spin relaxation times, thus denoting a shortening in the Fe-Fe distances, presumably as a result of the appearance of extra-framework iron in cationic positions, small oligonuclear
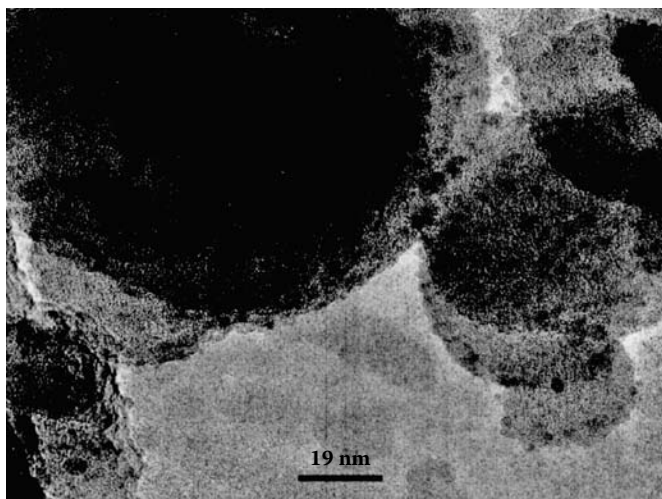
FIGURE 8.20   TEM image for iron oxide nanoparticles generated in FeZSM-5 zeolite. (From Doménech et al. 2002e. *J. Electroanal. Chem.* 519, 72–84, with permission.)
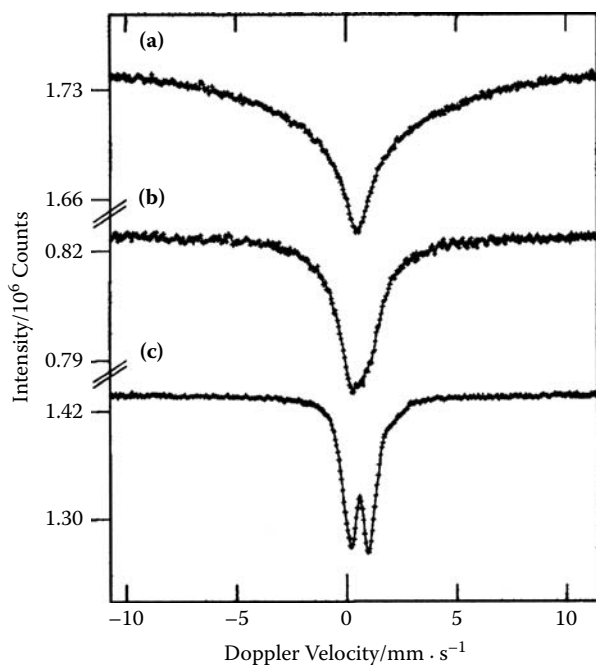

FIGURE 8.21 ^{57}Fe Mössbauer spectra at 300 K in air for FeZSM-5 samples: (a) as-synthesized, (b) calcined, (c) steamed. (From Pérez-Ramírez et al., 2002. *J. Catal.* 207, 113–126.)

oxometallic species, and, to a lesser extent, clusters in metal nanoparticles. Finally, for the steamed sample, a well-resolved paramagnetic doublet is recorded. This spectrum corresponds to further increases in electron spin relaxation rate, attributable to continued clustering of Fe^{3+} ions and small oxometal complexes into larger particles. A small shoulder on the high-energy line of this doublet can be fitted to a second doublet, probably due to a small amount of Fe^{2+} generated during the steam treatment.

For our purposes, the relevant point to emphasize is that voltammetry of microparticles permits us to discriminate between electron transfer processes for the different iron species. This can be seen in Figure 8.22, which shows the square-wave
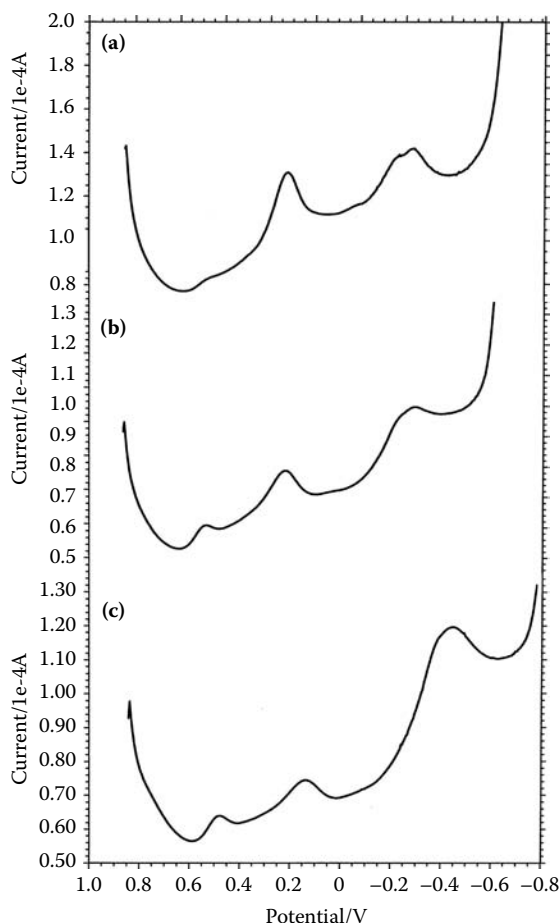
FIGURE 8.22 Square-wave voltammograms for (a) as-synthesized, (b) calcined, and (c) steamed FeZSM-5 samples attached to polymer film electrodes immersed into 0.10 M HCl. Potential scan initiated at +0.85 V vs. AgCl/Ag in the negative direction. Potential step increment, 4 mV; square-wave amplitude, 25 mV; frequency, 5 Hz. (From Doménech et al., 2002e. *J. Electroanal. Chem.* 519, 72–84, with permission.)

voltammograms for FeZSM-5 samples [(a) as-synthesized, (b) calcined, and (c) steamed] immersed into 0.10 M HCl. For the as-synthesized sample, reduction peaks at +0.15 and −0.35 V vs. AgCl/Ag appear. For the calcined sample, the first signal is weakened with respect to the second while an additional peak appears at +0.45 V. For the calcined plus steamed sample, the peak at −0.45 V largely prevails over the other signals, now including a weak shoulder at ca. +0.65 V. Upon comparison of this electrochemistry with that of iron oxides (Doménech et al., 2001), a reasonable description of such electrochemical processes involves solid-state reduction of framework iron centers (peak at +0.15 V) accompanied by reduction of isolated, extraframework iron ions in the more external zeolite sites (peak at +0.45 V), solid-state reduction of oligonuclear iron oxo species (shoulder at +0.65 V) and reductive dissolution of extrazeolite iron oxide nanoparticles (peak at −0.45 V). These processes can be represented, respectively, by the equations (Doménech et al., 2002c,d):

$$\{O_3Fe^{III}(OH)\} + H^+ \,(aq) + e^- \rightarrow \{O_3Fe^{II}(H_2O)\} \tag{8.7}$$

$$\{O_3Fe^{III}(OH)(Fe^{3+})_z\} + zH^+ \,(aq) + ze^- \rightarrow \{O_3Fe^{III}(OH)_{1-z}(H_2O)_z(Fe^{2+})_z\} \tag{8.7}$$

$$\{Fe^{III}_xO_y\} + xH^+ \,(aq) + xe^- \rightarrow \{Fe^{II}_xO_{y-x}(OH)_x\} \tag{8.8}$$

$$\{Fe^{III}O_x\} + 2xH^+ \,(aq) + (2x-2)e^- \rightarrow Fe^{2+} \,(aq) + xH_2O \tag{8.9}$$
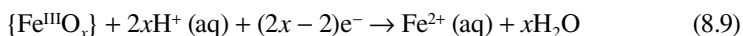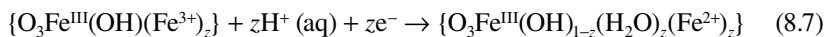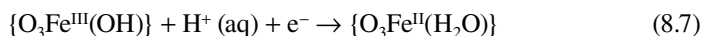
Peak splitting (see Figure 8.22) can be attributed to the superposition of processes due to iron species in different zeolite sites (topological redox isomers, see Chapter 4) and also to the occurrence of chloride-assisted reduction processes.

A similar electrochemistry can be observed for CoZSM-5 materials in contact with 0.10 M HCl, as depicted in Figure 8.23. The as-synthesized material incorporates Co^{3+} centers into the framework of ZSM-5 zeolite, displaying a sharp reduction peak at +0.40 V vs. AgCl/Ag. Upon calcination and steam activation, extra-framework cobalt ions and cobalt oxide nanoparticles are formed, yielding signals at +0.20 and −0.50 V. Similar features were obtained in phosphate buffer, as shown in Figure 8.24. Here, cobalt oxide species show a prominent reduction peak due to the reductive dissolution of cobalt oxide forms.

Interestingly, cobalt oxide forms act as efficient catalysts with respect to the electrochemical reduction of oxygen in water. It is known that electrochemical reduction of O_2 in aqueous solution involves two main processes, which can be represented as:

$$O_2 + 2H_2O + 2e^- \rightarrow H_2O_2 + 2OH^- \tag{8.10}$$

$$O_2 + 2H_2O + 4e^- \rightarrow 4OH^- \tag{8.11}$$

The thermodynamic electrode potentials of these two reactions at pH 7.0 are +0.06 and +0.60 V vs. SCE, respectively. However, reduction of dissolved oxygen in water at conventional electrodes involves kinetic complications so that, at graphite electrodes, very weak reduction signals appear.
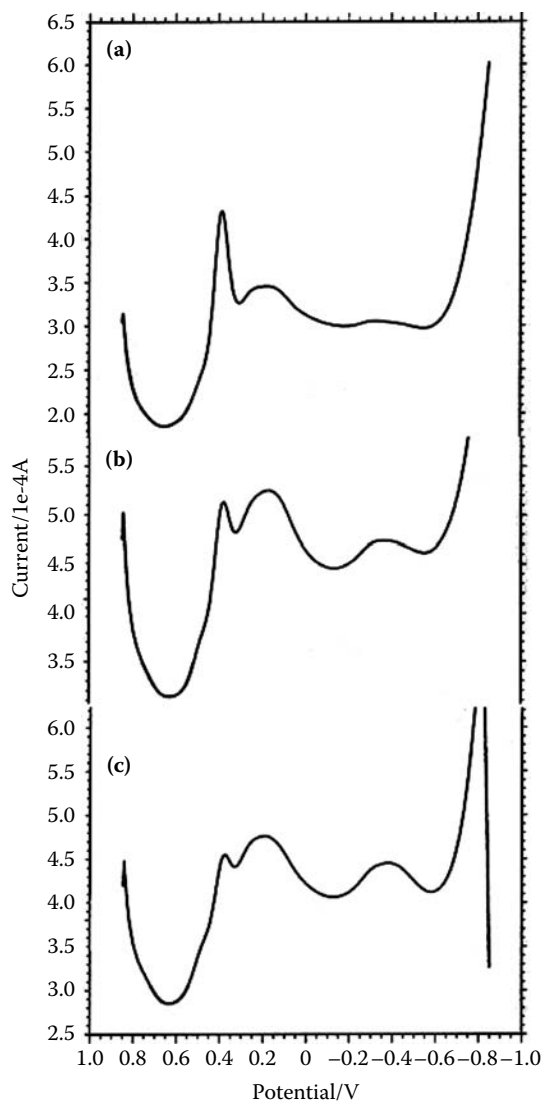
FIGURE 8.23 SQWVs for (a) as-synthesized, (b) calcined, and (c) steamed CoZSM-5 samples attached to paraffin-impregnated graphite electrodes immersed into 0.10 M HCl. Potential step increment, 4 mV; square-wave amplitude, 25 mV; frequency, 5 Hz.
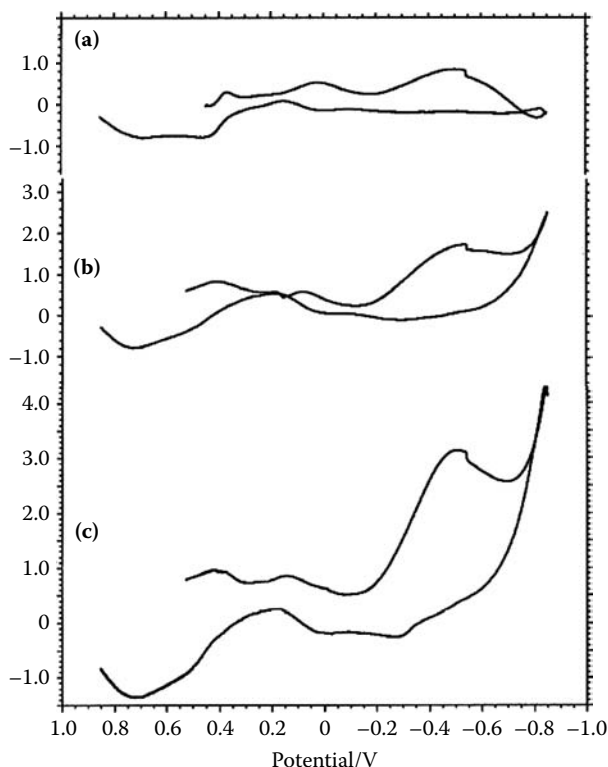
FIGURE 8.24 Deconvoluted CVs for CoZSM-5-modified, paraffin-impregnated graphite electrodes immersed into aqueous phosphate buffer at pH 7.0: (a) as-synthesized, (b) calcined, and (c) calcined samples. Potential scan rate 50, mV/sec.

The different catalytic activity of CoZSM-5 materials can be seen by comparing CVs in O_2-saturated aqueous phosphate buffer at paraffin-impregnated graphite electrodes modified with (a) as-synthesized and (b) steamed CoZSM-5 materials shown in Figure 8.25. For the as-synthesized material, weak cathodic peaks at −0.40 and −0.60 V appear, attributable to the reduction signals for dissolved oxygen and small amounts of cobalt oxide forms existing in the CoZSM-5 sample. At electrodes modified with steamed CoZSM-5, a prominent reduction peak at −0.70 V is recorded. This peak is considerably larger than those obtained for all CoZSM-5 zeolites in deoxygenated solutions (see Figure 8.24), denoting that a significant electrocatalytic effect exists.
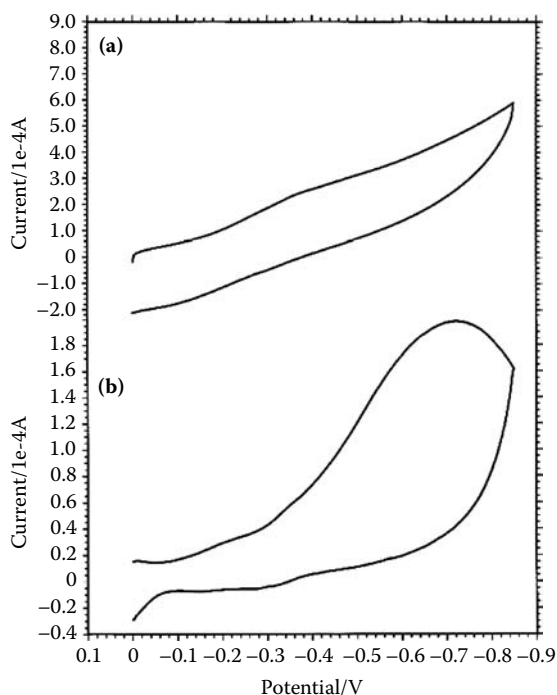
FIGURE 8.25 CVs recorded at CoZSM-5-modified, paraffin-impregnated graphite electrodes immersed into O_2-saturated, aqueous phosphate buffer at pH 7.0: (a) as-synthesized and (b) steamed samples. Potential scan rate, 50 mV/sec.

9 Electrochemical Sensing via Porous Materials

9.1 ELECTROCHEMICAL SENSING

In general, sensors can be defined as devices that perceive changes in physical properties of the environment and turn them into a measurable signal (Gründler, 2007; Bard et al., 2008). Electrochemical sensing, in general, is devoted to identifying and/or quantifying selected analyte(s) and involves:

- Monitoring any electrochemical process experienced by electroactive analytes.
- Monitoring an auxiliary electrochemical process whose parameters are modified by the presence of the analyte. This approach can correspond to two basic possibilities:
- The analyte participates in the electrochemical process via catalysis, complexation, etc.
- The analyte competes with electroactive species blocking of modifying their electrochemical response (competitive methods).

There are three types of electrochemical sensors: potentiometric, amperometric, and potentiodynamic sensors.

Potentiometric sensors are based on the measurement of the voltage of a cell under equilibrium-like conditions, the measured voltage being a known function of the concentration of the analyte. Potentiometric measurements involve, in general, Nernstian responses under zero-current conditions; that is, the measurement of the electromotive force of the electrochemical cell.

Amperometric sensing is based on the record of the current response of an electrode in contact with the system to be analyzed under the application of a given potential input. Amperometric sensors operate under conditions where mass transport is limiting.

Potentiodynamic sensors are based on the measurement of the current response of the working electrode under no mass transport limiting conditions. Potentiodynamic methods typically involve accumulation (or preconcentration) steps, such as in stripping voltammetry for analyzing trace metals in solution.

It should be noted that electrochemical methods for determining a given analyte can, in general, be affected by interfering species (whose analytical signal is superimposed or can distort the analyte signal) and matrix effects (species disturbing the signal from the analyte by complexation, adsorption, etc.). The search for highly sensitive and highly selective sensors reluctant to undergo interference and matrix effects is the focus of most of the work in electroanalytical chemistry.

Social demands (e.g., miniaturization for monitoring processes *in vivo*) involve improved sensing methods accomplishing so-called analytical properties (accuracy and precision, repeatability and reproducibility, sensibility, selectivity, traceability) but also short response time (suitability), economy (power consumption), safety (for operators and for environment), etc.

9.2   GAS SENSORS WITH POROUS MATERIALS

Solid-state electrochemical gas sensors exploit the conductivity of metal oxides and related compounds. In the case of conventional potentiometric gas sensors, the gas to be detected is converted to the mobile component in a solid electrolyte that separates a reference compartment and a test compartment, as schematized in Figure 9.1. The difference in potential then established between the two sides of the solid electrolyte is dependent on the difference in thermodynamic activity across the solid electrolyte of the species that will equilibrate with the charge-transporting ions in the solid electrolyte. Here, sensing involves, to any extent, charge transport across the solid, so that the sensing process is extremely sensitive to temperature and the presence of doping species in the solid. Solid electrolyte sensors are applied for sensing three types of gaseous systems (Bard et al., 2008):

1. Gas mixtures in chemical equilibrium
2. Gas mixtures containing the analyte beside inert gases
3. Gas mixtures of nonequilibrated gases

In all three cases, the measurement cell consists, schematically, of two porous electrodes (usually Pt) pressing a layer of the sensing material (Zhuiykov, 2007).

Potentiometric sensors for oxygen measurement are typically formed by a layer of stabilized zirconia pressed between two porous Pt electrodes, as schematized in Figure 9.1 (Bard et al., 2008; Pasierb and Rekas, 2009). Such electrodes are in contact with the gas sample and a reference gas, respectively. A typical example is constituted by O_2 sensors based on yttrium- or scandium-doped zirconias. The
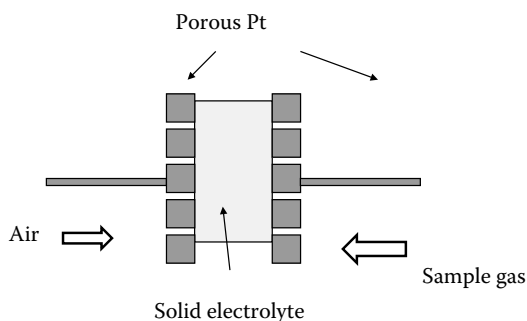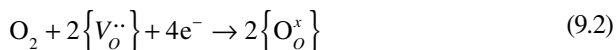

FIGURE 9.1   Schematic diagram for potentiometric gas sensors.

electrode reaction, occurring at the three-phase metal/electrolyte/gas boundary can be presented as (Pasierb and Rekas, 2009):

$$O_2 \text{ (g)} + 4e^- \text{ (metal)} \rightarrow 2O^{2-} \text{ (electrolyte)} \tag{9.1}$$

or, using the Kröger-Vink notation,

$$O_2 + 2\left\{V_O^{\cdot\cdot}\right\} + 4e^- \rightarrow 2\left\{O_O^x\right\} \tag{9.2}$$

where $\{V_O^{\cdot\cdot}\}$ denotes oxygen vacancies in the yttria-stabilized zirconia (YSZ) lattice. The cell can be considered an oxygen concentration cell, where the overall reaction can be described in terms of the transfer of oxygen from one side to the other.

The electromotive force of the cell is given by the Nernst equation:

$$E_{eq} = \frac{RT}{4F} \ln \frac{p'_{ox}}{p''_{ox}} \tag{9.3}$$

where p'_{ox} and p''_{ox} are the partial pressures of O_2 in the gas sample and the reference gas (usually air with defined humidity), respectively.

Conductivity in solid oxide-type compounds can be associated to defect formation and oxygen absorption/desorption processes. The following defect-forming reactions are possible:

$$\text{Null} \rightarrow e' + h^{\cdot} \tag{9.4}$$

$$\text{Null} \rightarrow 2e' + V_O^{\cdot\cdot} + (1/2)O_2 \tag{9.5}$$
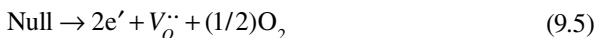
where e' and $h^{\cdot}$ represent electrons and holes (defect electrons) in the Kröger-Vink notation. This notation, schematized in Table 9.1, will be used here.

In its most single version, the oxygen absorption process can be represented as a reaction between the oxygen vacancies and gaseous oxygen in which holes are generated (Logothetis, 1980):

$$V_O^{\cdot\cdot} + (1/2)O_2 \rightarrow O_O^x + 2h^{\cdot} \tag{9.6}$$
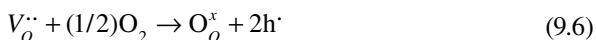
Conversely, the transition of oxygen from the oxide phase to the gas phase involves the generation of excess electrons, e':

$$O_O^x \rightarrow (1/2)O_2 + V_O^{\cdot\cdot} + 2e' \tag{9.7}$$

As a result, under equilibrium conditions, the concentration of excess electrons and, hence, their contribution to electrical conductivity is proportional to $p(O_2)^{-1/4}$ or $p(O_2)^{-1/6}$. Similarly, the concentration of defect electrons becomes proportional to $p(O_2)^{1/4}$ or $p(O_2)^{1/6}$ (Bard et al., 2008).

Moderate doping with rare earth cations such as Y^{3+} or Sc^{3+} stabilizes cubic zirconia at relatively low temperatures and increases conductivity, the maximum of this quantity being reached when the concentration of acceptor-type dopants is close to the minimum necessary for stabilizing the cubic phase (Kharton et al., 2004). For YSZ,

TABLE 9.1
Kröger-Vink Notation for Representing Point Defects in Solids

Point Defect	Symbol
Vacancies	V (or □ when vanadium is present)
Position occupied in the ideal lattice	Denoted as lower index (M: metal site, X: anion site)
Interstitial position	Lower index i
Formal charge defect with respect to the ideal structure	Superscript $n+$ or $n-$
Effective positive charge defect with respect to the ideal structure	Superscript dot ($\cdot$)
Effective negative charge defect with respect to the ideal structure	Superscript prime (')
Zero effective charge defect with respect to the ideal structure	Superscript cross (×)
Free electrons	e'
Free holes	$H^{\cdot}$
Polarons	P
Interstitial M^{3+} cation	$M_i^{\cdot\cdot\cdot}$
M^{2+} cation vacancy	V_M''
X^{2-} anion vacancy	$V_X^{\cdot\cdot}$
X^- anion occupying M^+ cation site	X''_M
Z^- anion occupying X^{2-} anion site	Z_X'
A^{2+} cation at the M^{2+} site	$A_M^{\times}$
A^{4+} cation at the M^{2+} site	$A_M^{\cdot\cdot}$
Cluster formed by one X^{2-} vacancy and one A^{2+} cation occupying M^{3+} site	$(V_X^{\cdot\cdot} A_M')$ or $(V_X A_M)$

Source: Data summarizes the notation introduced by Kröger and Vink (1956)

$Y_x Zr_{1-x} O_{2-x/2}$ ceramics, the maximum conductivity is obtained for $x \approx 0.10$. Higher concentrations of dopant cations decrease conductivity by the effect of their progressive association with oxygen vacancies. The working temperature range extends from 400 to 1600°C for partial pressures of oxygen between 10^{-20} and 10 bar.

It should be noted that the conductivity in ionic solids involves ion transport mechanism between coordinating sites (site-to-site hopping) and local structural relaxation. In general, the conductivity measured by ac measurements, σ_{ac}, can be expressed as a function of the conductivity from dc measurements, σ_{dc}, and the frequency (Bruce et al., 1983a,b; Skinner and Munnings, 2002; Girdauskaite et al., 2006; Khrokunov et al., 2006; Berenov et al., 2007):

$$\sigma_{ac} = \sigma_{dc} + A\omega^{\alpha} \tag{9.8}$$

where α is the power law exponent and A is a constant. According to the jump relaxation model (Funke et al., 1998), α represents the quotient between the back-hop rate

and the site relaxation time. For conductivity in ionic solids, the variation of conductivity with temperature satisfies an Arrhenius-type variation given by:

$$\sigma = (\sigma_o / T) \exp(-E_a / K_B T) \tag{9.9}$$

E_a being the activation energy.

The total conductivity of an oxide-type material with mixed ionic-electronic conduction, σ, can be expressed as:

$$\sigma = \sigma_{ion} + G(T) p(O_2)^{\pm 1/m} \tag{9.10}$$

where σ_{ion} denotes the ionic conductivity of the material and the subsequent term represents the electronic conductivity of the material, expressed as the product of a temperature-dependent constant, $G(T)$, and the partial pressure of O_2, $p(O_2)$. The sign in front of $1/m$ is positive when the electronic conductivity is primarily due to electron holes (p-type conductivity) and negative when it is primarily due to excess electrons (n-type conductivity; Larose and Akbar, 2006).

High coordination numbers of oxygen, such as in fluorite- and perovskite-type structures, are desirable in enabling moderate metal ion–oxide ion bonding forces, thus resulting in more interchangeable oxygen sites. Mixed ionic-electronic conductors of the perovskite-type structure provide high oxide ion and electron transport (Teraoka et al., 1985). Doping with isovalent cations of different ionic radii generates mechanical tension in the crystal lattice, whereas heterovalent cations additionally generate acceptor- or donor-type electrical charge defects. Oxide ions are transported through lattice defects, mostly by a vacancy mechanism and rarely by oxygen interstitial sites. The vacancies in the oxygen sublattice are generated by partial reduction of transition metal cations or by heterovalent cationic substitution. Above a certain concentration, oxygen vacancies, which are randomly distributed, play an essential role. Increasing concentrations of ionic and electronic defects in the crystal cause an increase in the transport rate of oxide ions with a parallel decrease in the thermochemical stability of the oxide material. At high defect concentration, formation of clusters and new crystalline phases can occur, a process that in general is accompanied by a decrease in the mobility of oxide ions.

For a substituted perovskite-type material with oxygen vacancy-type defect structure, the overall formula can be written as $A_{1-a}A'_aB_{1-b}B'_bO_{3-x}$, where A, A' denotes rare earth or earth-alkaline cations, B, B' transition metal cations of the fourth row of the periodic system.

The equilibrium at a temperature T with a gas phase containing oxygen with a partial pressure $p(O_2)$ can be presented as:

$$A_{1-a}A'_aB_{1-b}B'_bO_{3-x-\delta} + \delta O_2 \rightarrow A_{1-a}A'_aB_{1-b}B'_bO_{3-x} \tag{9.11}$$
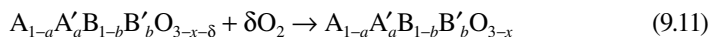
In this equation, $A_{1-a}A'_aB_{1-b}B'_bO_{3-x-\delta}$, represents the oxygen-poorer state and $A_{1-a}A'_aB_{1-b}B'_bO_{3-x}$ the oxygen-richer state. For the overall equilibrium reaction (9.1), one can write:
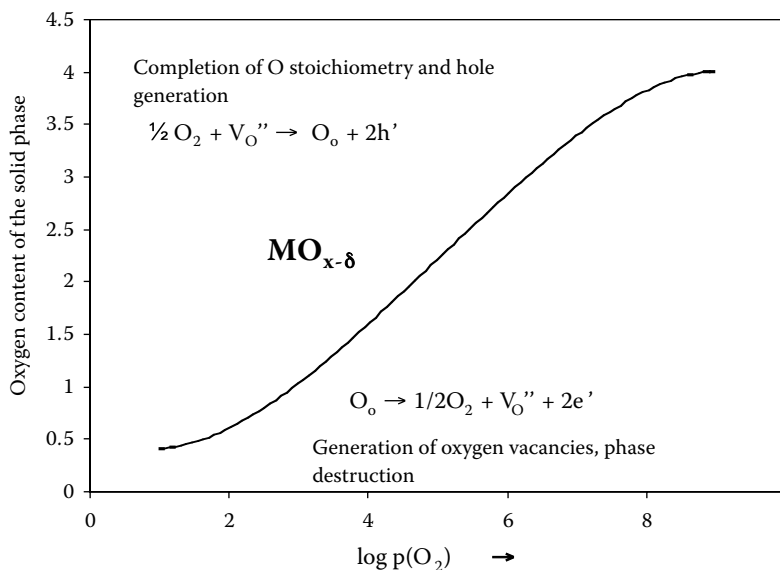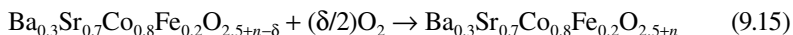
$$K_p = (p(O_2))^{-\delta/2} \tag{9.12}$$

FIGURE 9.2   Typical δ vs. $p(O_2)$ for a $MO_{x-\delta}$ material.

Related to the reaction of 1 mol of atomic oxygen, the usual thermochemical equations yield:

$$\Delta G^{\circ} = (\delta/2)RT \ln(p(O_2)) \tag{9.13}$$

$$\ln(p(O_2)) = -\frac{\Delta H^{\circ}}{RT} + \frac{\Delta S^{\circ}}{R} \tag{9.14}$$

Thermobalance measurements allow for determining δ values at different temperatures, whereas the concentration of defects is reflected in the unit cells of the crystals, determined from x-ray diffraction data. Typical δ vs. $p(O_2)$ plots are depicted in Figure 9.2. The process for the iron material can be represented as (Girdauskaite et al., 2007):

$$Ba_{0.3}Sr_{0.7}Co_{0.8}Fe_{0.2}O_{2.5+n-\delta} + (\delta/2)O_2 \rightarrow Ba_{0.3}Sr_{0.7}Co_{0.8}Fe_{0.2}O_{2.5+n} \tag{9.15}$$

The oxygen exchange capacity is directly related with the oxygen/metal stoichiometry. The amount of reversibly exchangeable oxygen in a $A_{1-a}A'_aB_{1-b}B'_bO_{3-x}$ perovskite-type oxide, x, is a function of temperature and gradient of the thermodynamic oxygen activity between the surface and the center of the crystal. Complete occupation of the oxygen sublattice, that is, $x = 3$, is reached at higher partial pressure of O_2 in the gas phase. At decreasing $p(O_2)$, such materials approach a level of $p(O_2)$-independent stoichiometry, where $x = a/2$. This situation corresponds to the average oxidation state of 3+ of the B cations (Ullmann
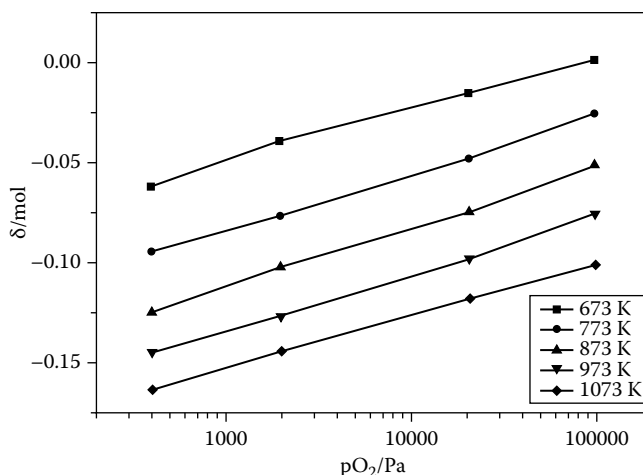
FIGURE 9.3 Diagram for the variation of the oxygen/metal stoichiometry with the partial pressure of oxygen for different perovskite-type oxides. (From figure 1 of Girdauskaite et al., 2007. *J. Solid State Electrochem.* 11, 469–477, with permission.)

and Trofinenko, 2001). At lower partial pressures of O_2, the concentration of oxygen vacancies increases until phase destruction occurs. The corresponding variation of the oxygen/metal stoichiometry with $p(O_2)$ is depicted in Figure 9.3 (Girdauskaite et al., 2007).

A second group of solid-state gas sensors is constituted by those involving equilibration with the mobile component of solid electrolyte. A typical example is CO_2 sensor with K_2CO_3 solid electrolyte. Here, K^+ ions are the only mobile ions in the solid electrolyte, so that the overall electrochemical process can be represented as (Pasierb and Rekas, 2009):

$$2K^+ \text{ (electrolyte)} + CO_2 \text{ (g)} + \tfrac{1}{2}O_2 \text{ (g)} + 2e^- \text{ (metal)} \rightarrow K_2CO_3 \text{ (electrolyte)} \quad (9.16)$$
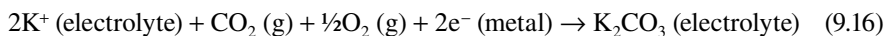
A third group of potentiometric gas sensors involves the use of an additional auxiliary phase. This class was subdivided by Yamazoe and Miura (1996) depending on whether the mobile ions of solid electrolyte are the same, different but of the same sign, or different and of a different sign than those of the auxiliary phase. An example of this type of electrode is the CO_2 sensor incorporating Na_2CO_3 and N-alumina. Details are given in a recent review by Pasierb and Rekas (2009).

9.3 SOLID-STATE pH AND ION-SELECTIVE ELECTRODES

Casting metals consisting of Sb or Bi covered by a thin hydroxide layer and membranes of transition metal oxide bronzes show a relatively high selectivity for hydrogen ions, as recently reviewed by Vonau and Guth (2006). Metal/metal oxide electrodes display non-Nernstian responses, but applications in food control and medicine have

been proposed. Electrochemical reactions for tungsten and molybdenum bronze electrodes can be represented as:

$$\{Na_xWO_3\} + yH^+ (aq) + ye^- \rightarrow \{Na_xH_yWO_3\} \tag{9.17}$$

$$\{A_xMo_zO_w\} + yH^+ (aq) + ye^- \rightarrow \{A_xH_yMo_zO_w\} \tag{9.18}$$

$$\{A_xMo_zO_w\} + yH^+ (aq) \rightarrow \{A_{x-y}H_yMo_zO_w\} + yA^+ \tag{9.19}$$
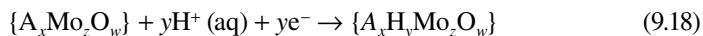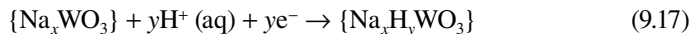
More recently, lithium tungsten bronzes have been studied as materials for reference electrodes (Gabel et al., 2004).

Ionophore-based ion-selective electrodes (IES) have been extensively studied over the past decades for selectively determining the concentration of selected ions in solution. Their practical use, however, has been limited to a relatively narrow range of fields because of the limited concentration interval that can be determined with such devices. Lowering detection limits can be obtained, among other strategies, through solid-contact IES, prepared by direct contact of a ionophore-doped polymeric membrane with a metallic conductor. To avoid problems associated with poorly defined metal/membrane interfaces and unstable phase-boundary potentials, intermediate layers with conducting polymers or localized redox-active units separating the sensing membrane and the metallic conductor can be used (Back, 1987). More recently, ordered macroporous carbon contacts have been tested (Lai et al., 2007). The used carbons consist of a skeleton of glassy carbon surrounding a periodic array of uniform spherical pores that are interconnected in three dimensions. Pore sizes are of a few hundred nanometers, whereas skeletal walls are tens of nanometers thick. As a result of the mutually interconnected pore-wall structure of such materials, filling pores with an electrolyte solution results in a nanostructured material with both ionic and electronic conductivities (Lai et al., 2009).

Solid-state reference electrodes for potentiometric sensors are currently under research. The main problem to be faced in developing this type of electrode lies in connecting the ionic conducting (usually aqueous) solution with an electronic conductor. Since the reference electrode has to maintain a defined potential, the electrochemical reaction with components of the electrolyte has to be avoided. Oxides, mixed oxides, and polyoxometalate salts of transition elements can be proposed for preparing solid-state reference electrodes. Tested compounds include tungsten and molybdenum oxides (Guth et al., 2009).

9.4 AMPEROMETRIC SENSING

Amperometric sensing of gases is based on solid ion-conducting materials, as described for potentiometric gas sensors. Solid-state amperometric gas sensors measure the limiting current (i_L) flowing across the electrochemical cell upon application of a fixed voltage so that the rate of electrode reaction is controlled by the gas transport across the cell. The diffusion barrier consists of small-hole porous ceramics. The limiting current satisfies the relationship:

$$i_L = \frac{4FAD_{ox}T}{RTL} p_{OX} \tag{9.20}$$
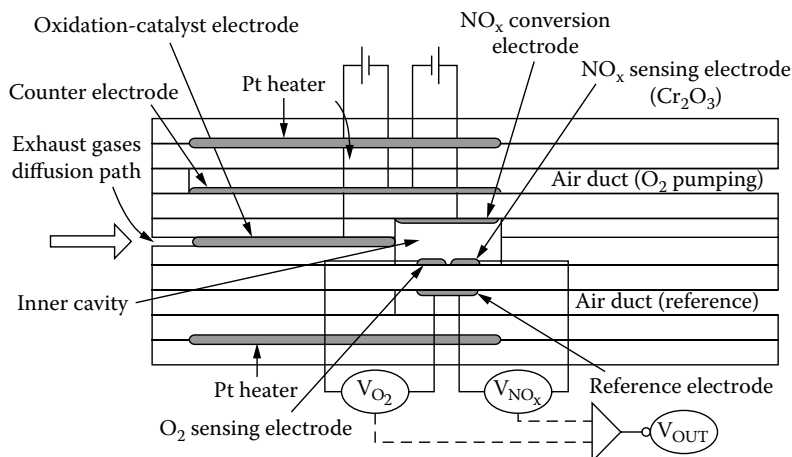
FIGURE 9.4 Cross section of the laminated-type NOx sensor using a YSZ-based oxidation-catalyst electrode. (From Ono et al., 2004. *Solid State Ionics.* 175, 503–506, with permission.)

Here, *A* represents the area of holes, *L* their length, and D_{OX} the coefficient of diffusion of O_2 (Tsipis and Kharton, 2008).

Figure 9.4 shows a cross-sectional view of a laminated-type sensor for atmospheric nitrogen oxides based on YSZ, acting as an oxidation-catalyst electrode (Ono et al., 2004). The cell was fabricated by firing YSZ sheet on which the oxidation-catalyst platinum anode and the platinum counterelectrode were screen-printed. The porosity of the electrode is adjusted by adding resin powder into each electrode paste.

Amperometric sensing of selected species in liquids is widely extended with an enormous variety of materials and applications, which include electrochemical detection coupled with high-performance liquid chromatography and flux injection analysis. In these cases, high sensitivity and high reproducibility are required. These properties are conditioned by electrode fouling associated to formation of solid deposits and adsorbates on the electrode surface. As a result, the electrode experiences "memory effects" with concomitant loss of analytical performance.

Correction of such memory effects can often be made by applying electrochemical pre- and posttreatments. These treatments, consisting of the application of successive potential steps, are able to regenerate the electrode surface before/after measuring.

Most of the amperometric sensors are based on the electrocatalysis of the electrochemical reduction/oxidation of the analyte. A typical amperometric test is shown in Figure 9.5, corresponding to H_2O_2 sensing in buffered aqueous solution (pH 6.9) at hemoglobin (Hb) adsorbed in mesoporous molecular sieves (MSU), prepared as layer-by-layer films alternating with poly(diallyldimethylammonium) (PDDA). MSU was prepared from the precursor of zeolite Y using ionic liquids as templates. Layer-by-layer films, labeled {MSU/Hb}$_n$/PDDA, *n* being the number of deposited layers, were deposited over glassy carbon electrode by alternative adsorption of positively
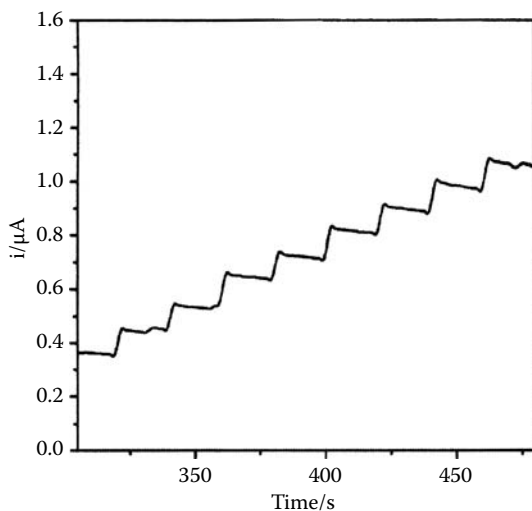
FIGURE 9.5 Amperograms at a glassy carbon electrode modified with hemoglobin adsorbed in mesoporous molecular sieves {MSU/Hb}$_5$/PDDA upon successive additions of 10 μM H$_2$O$_2$ to 0.2 M potassium phosphate buffer solution at pH 6.9. Applied potential −0.30 V vs. SCE. (Adapted from Sun et al., 2008. *Talanta* 74, 1692–1698.)

and negatively charged species from their solutions (Sun et al., 2008). The staircase current-time variation depicted in Figure 9.5 corresponds to successive injections of H$_2$O$_2$ into the electrochemical cell. The height of the different steps remains essentially constant, thus denoting that no significant memory effects appear under the reported experimental conditions.

Impedance spectra for electrodes with increasing number of layers are shown in Figure 9.6 using a K$_4$Fe(CN)$_6$ solution as a redox probe. The spectra recorded at the formal potential of the Fe(CN)$_6^{3-}$/Fe(CN)$_6^{4-}$ couple (−0.295 V) exhibit a semicircle, corresponding to the electron transfer–limited process, whose diameter increases on increasing the number of layers. The increase in diameter indicates that the charge transfer rate for the redox probe is gradually reduced as a result of the deposition of successive insulating layers on the electrode surface.

The electrocatalytic effect exerted by {MSU/Hb}$_5$/PDDA-modified electrodes on the electrochemical reduction of H$_2$O$_2$ can be seen in Figure 9.7, where cyclic voltammetries (CVs) at the bare glassy carbon electrode and at the modified electrode in contact with blank and H$_2$O$_2$-containing solutions can be compared. The essentially reversible hemoglobin couple

$$HbFe^{III} + H^+ + e^- \rightarrow HbFe^{II} \tag{9.21}$$

observed at {MSU/Hb}$_5$/PDDA-modified electrode in the blank solution is replaced by an apparently irreversible, significantly more intense cathodic wave in the presence of H$_2$O$_2$.
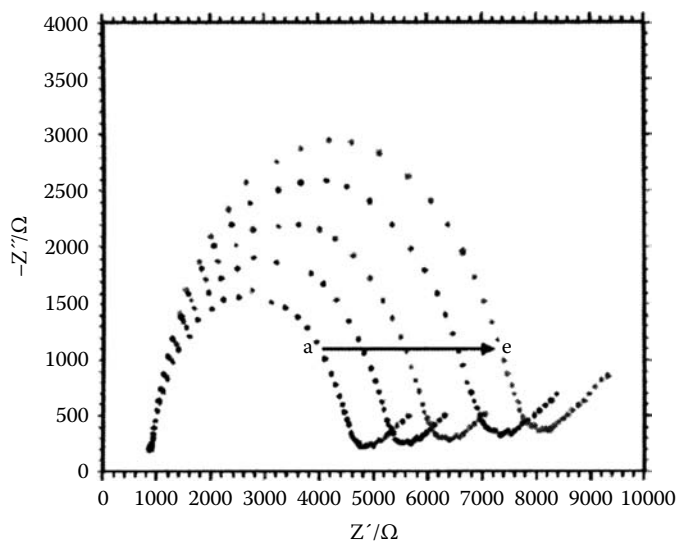
FIGURE 9.6 EIS of different {MSU/Hb}n/PDDA electrodes (n varying from 1 to 5) in 5.0 mM $K_4Fe(CN)_6$ plus 0.10 M KCl under application of a potential of −0.295 V vs. SCE. (Adapted from Sun et al., 2008. *Talanta* 74, 1692–1698.)
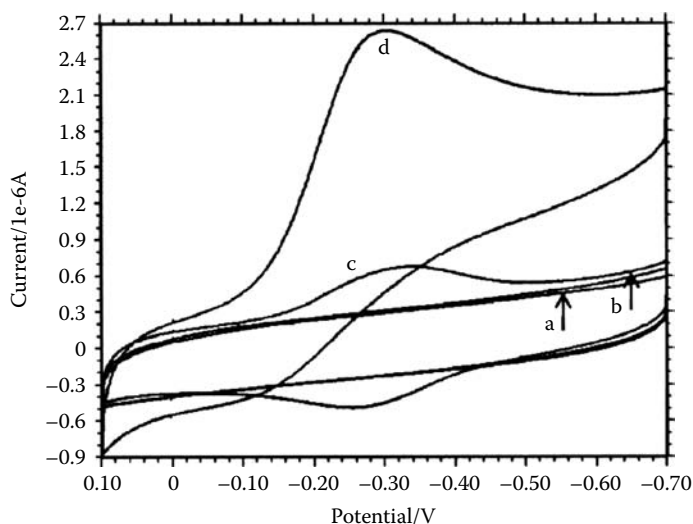
FIGURE 9.7 CVs at (a, b) bare glassy carbon electrode; (c, d) {MSU/Hb}$_5$/PDDA for (a, c) a blank 0.2 M aqueous phosphate buffer (pH 6.9) and (b, d) 100 μM H_2O_2 solution in the above electrolyte. Potential scan rate, 100 mV/sec. (From Sun et al., 2008. *Talanta* 74, 1692–1698.)

9.5 VOLTAMMETRIC SENSING AND SELECTIVITY

As previously noted, potentiodynamic, voltammetric sensing involves the measurement of the current response of the working electrode under no mass transport–limiting conditions. Typical analytical strategies involve the concentration of the analyte in the electrode surface via the application of a reductive (or oxidative) potential step, followed by the application of an oxidative (or reductive) potential scan. In stripping voltammetry devoted to the determination of trace metals in solution, metal ions are reduced to a metal deposit (or an amalgam at Hg electrodes) and their concentration is monitored by measuring the peak current in the oxidative dissolution process recorded upon application of a scan in the positive direction of potentials (Wang, 1985).

Porous materials, used as electrode modifiers, can act as preconcentrating agents in order to increase the effective concentration of the analyte in the vicinity of the electrode. Large pore size, uniform pore structure, and high loading capacity are general requirements for porous materials used for sensing purposes. Thus, the use of zeolites (Wang and Walcarius, 1996) and nontronite clays (Zen and Chen, 1997) for determining dopamine (*vide infra*) have been reported.

A variety of porous materials can be used for analytical applications. For instance, layer-by-layer films assembled by alternate adsorption of mesoporous silica and poly(diallyldimethylammonium chloride) onto glassy carbon electrode can be used for highly sensitive determination of ultratrace nitroaromatic compounds in aqueous solution (Shi et al., 2007).

Voltammetric methods are of particular interest with regard to the selective determination of analytes in the presence of interferents. As a widely studied case, one can mention the determination of dopamine and other neurotransmitter catecholamines in the presence of interfering compounds, namely, ascorbic acid and/or uric acid. It is known that dopamine exerts a significant physiological role as extracellular chemical messenger whose loss in neurons can be associated to serious diseases such as Parkinsonism. Consequently, its determination *in vitro* and *in vivo* is an obvious target in neurochemical studies.

Electrochemical determination of dopamine is made possible by virtue of its well-defined oxidation signal at ca. +0.2 V vs. saturated calomel electrode (SCE) in aqueous media at physiological pH values. Unfortunately, ascorbic acid accompanies dopamine in biological samples; thus, in the extracellular fluid of the central nervous system, ascorbic acid is present in concentrations between 100 and 500 μM, whereas the concentration of dopamine is less than 100 nM (O'Neill, 1994). The electrochemical oxidation of dopamine is an apparently irreversible process, due to the occurrence of post–electron transfer reactions. The initial two-proton, two-electron product, dopaminequinone, can undergo a deprotonation accompanied by fast 1,4 (Michael) addition to yield a bicyclic derivative, leucoaminochrome, further oxidized to its quinonic form, aminechrome, either electrochemically or chemically by reaction of dopaminequinone (Amatore and Savéant, 1978; Ciolkowski et al., 1994), as schematized in Figure 9.8. As a result, the apparent number of electrons consumed during the electrochemical oxidation of dopamine varies from two to four, depending on the timescale of observation. In addition, electrochemical runs can be accompanied by polymerization processes producing melanine, a process that results in electrode fouling.
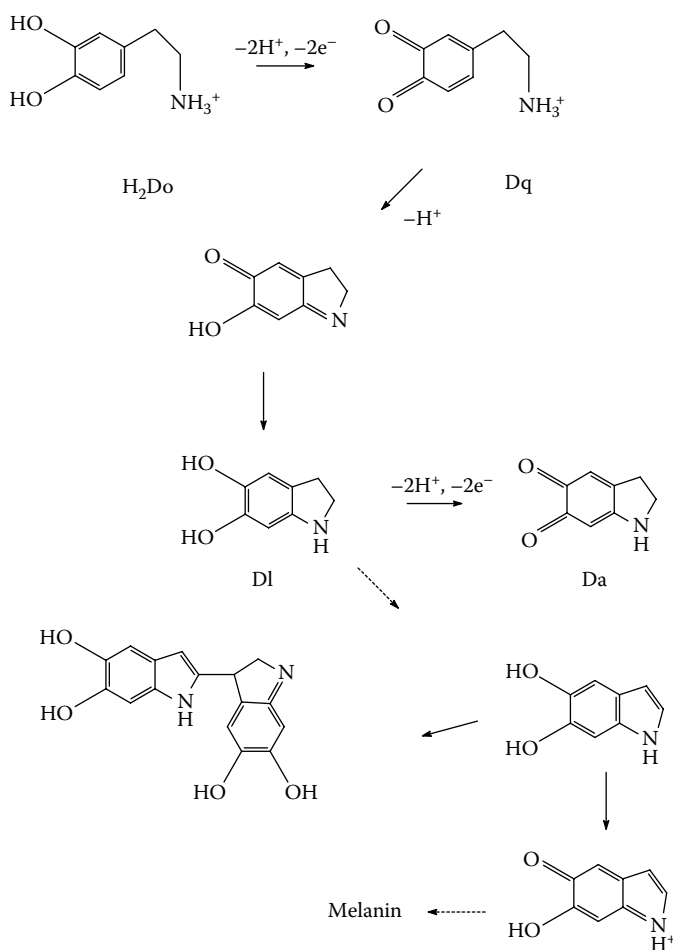
FIGURE 9.8 Scheme for the electrochemical oxidation of dopamine at physiological pH values.

A plausible strategy for electrochemically determining dopamine in the presence of excess amounts of ascorbic acid is the use of zeolites incorporating catalytic centers. This is the case of polymer film over glassy carbon electrodes modified with 2,4,6-triphenylpyrylium ion encapsulated into zeolite Y (Doménech et al., 1999a, 2000b) This strategy combines the size- and charge-exclusion properties of the zeolite matrix with the electrocatalytic ability of the redox center, in turn increased by effect of site isolation provided by encapsulation into the aluminosilicate host. By the first token, it should be noted that at physiological pH values, ascorbate ion ($pK_a = 4.2$) and protonated dopamine ($pK_a = 10.6$) exist in solution, so that the zeolite host acts as a selective membrane repelling ascorbate anion. By the second token, 2,4,6-triphenylpyrylium ion encapsulated into zeolite Y (TPY+@Y) can
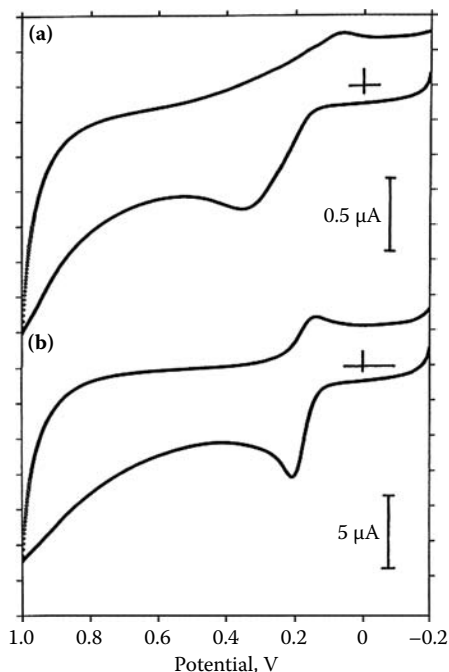
**FIGURE 9.9** CVs at (a) unmodified and (b) TPY$^+$@Y-modified glassy carbon electrodes in a 0.12 mM solution of dopamine in potassium phosphate buffer, pH 7.4. Potential scan rate 10 mV/sec. (From Doménech et al., 2002b. *Anal. Chem.* 74, 562–569, with permission.)

be involved in an electrocatalytic cycle for dopamine oxidation. These effects are illustrated in Figure 9.9 and Figure 9.10, where the voltammetric responses of dopamine (Figure 9.9) and ascorbate (Figure 9.10) at bare and TPY$^+$@Y-modified glassy carbon electrodes are compared. Remarkably, the oxidation peak of dopamine at +0.20 V is significantly enhanced at TPY$^+$@Y-modified electrodes with respect to that signal at unmodified electrodes. In contrast, the oxidation signal at +0.38 V recorded for ascorbate at unmodified electrodes decays when TPY$^+$@Y-modified electrodes are used. In addition, as can be seen in Figure 9.9, the cathodic counterpart of the anodic peak for dopamine oxidation is clearly enhanced at TPY$^+$@Y-modified electrodes. This feature suggests that post–electron transfer reactions are significantly inhibited. Figure 9.11 shows a scheme for the possible catalytic cycle associated to dopamine oxidation at TPY$^+$@Y-modified electrodes.

Under optimized conditions, using differential pulse or square-wave voltammetries, linear peak current vs. dopamine concentration plots can be obtained in the 1–200 μM dopamine concentration range in the presence of 0.1 mM ascorbate, with detection limits ($S/N = 3$) of ca. 0.3 μM.

A second possibility for the selective determination of analytes is provided by materials incorporating redox-active centers as dopants (Doménech and Alarcón, 2002a, 2003; Doménech et al., 2004b,c). Figure 9.12 presents a typical case of electrocatalysis involving doped materials, concerning the electrochemical oxidation of
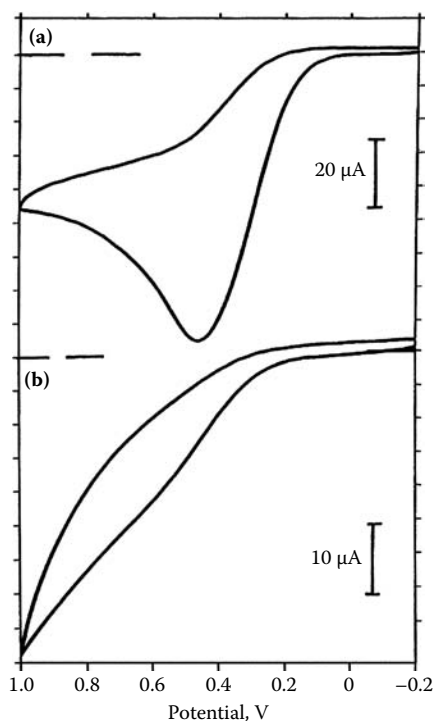
FIGURE 9.10 CVs at (a) unmodified and (b) TPY$^+$@Y-modified glassy carbon electrodes in a 5.5 mM solution of ascorbic acid in potassium phosphate buffer, pH 7.4. Potential scan rate, 100 mV/sec. (From Doménech et al., 2002b. *Anal. Chem.* 74, 562–569, with permission.)
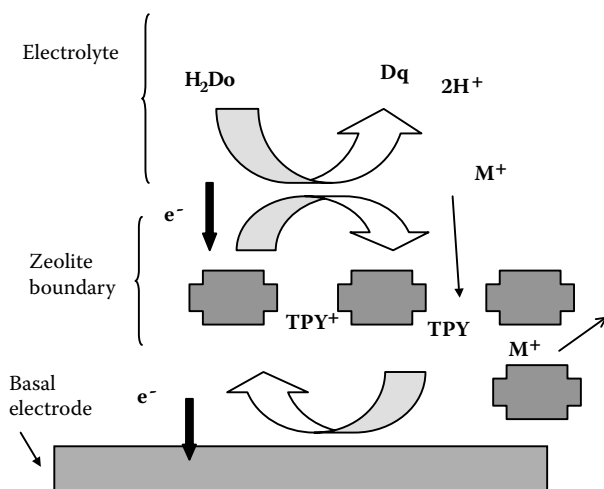
FIGURE 9.11 Catalytic scheme for the electrochemical oxidation of dopamine at TPY$^+$@Y-modified glassy carbon electrodes at physiological pH values.

www.iran–mavad.com

مرجع دانشجویان و مهندسین مواد
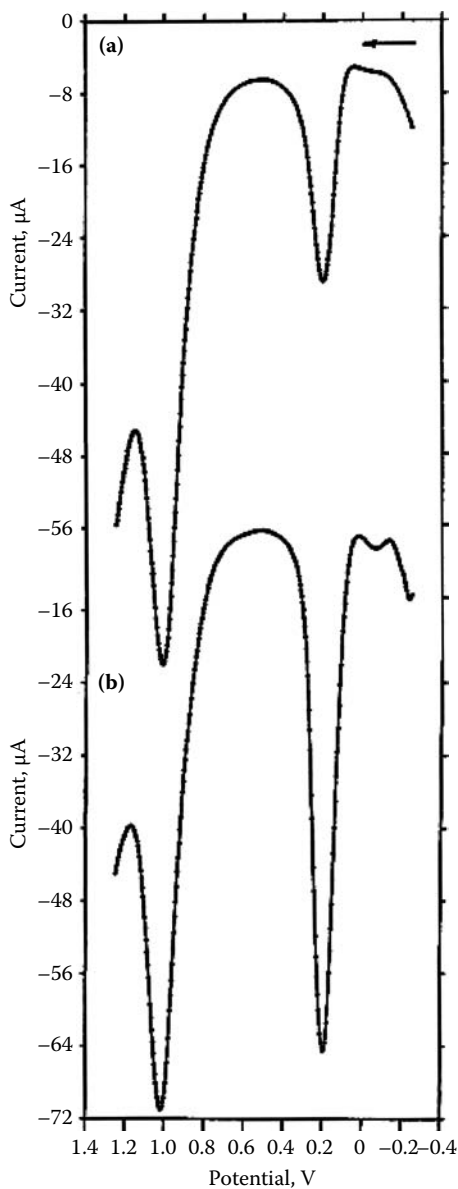
FIGURE 9.12 SQWVs at monoclinic $Ce_{0.10}Zr_{0.90}O_2$-modified polymer film electrodes deposited over glassy carbon for: (a) 0.14 mM MDA plus 0.30 mM dopamine and (b) 0.14 mM MDA plus 1.28 mM ascorbate, in 0.50 M potassium phosphate buffer, pH 7.0. Potential step increment 4 mV; square-wave amplitude 25 mV; frequency 15 Hz. (From Doménech et al., 2004b. *Electrochem. Comm.* 6, 719–723, with permission.)

methylenedioxyamphetamine [1-(3,4-methylenedioxyphenyl)-2-aminopropane (MDA)] and its *N*-methyl analogue, MDMA, two well-known psychedelic agents. Following Squella et al. (1993), such compounds are electrochemically oxidized in aqueous electrolytes through a one-electron transfer followed by a relatively slow chemical reaction (EC mechanism) near +1.0 V at physiological pH values. Electrochemical determination of MDA is made difficult by the fact that its oxidation process occurs at potentials where it is overlapped with the solvent discharge and by the eventual interference, in biological samples, of other oxidizable analytes such as neurotransmitter catecholamines (dopamine, norepinephrine), serotonin, and ascorbic acid. Using cerium-doped tetragonal and monoclinic zirconias ($Ce_xZr_{1-x}O_2$, $0 < x < 0.1$), the anodic peak for MDA oxidation is considerably enhanced. A lower electrocatalytic effect was caused by the electrochemical oxidation of dopamine and norepinephrine, so that there is an opportunity for determining MDA in the presence of relatively large amounts of dopamine (Doménech et al., 2004b).

This can be seen in Figure 9.12, where square-wave voltammetries (SQWVs) at monoclinic $Ce_{0.10}Zr_{0.90}O_2$-modified electrode immersed into MDA plus dopamine and MDA plus ascorbate solutions in aqueous phosphate buffer are depicted. Here, the MDA-localized oxidation peak at +1.0 V vs. AgCl/Ag is clearly separated from peaks corresponding to the oxidation of dopamine and ascorbate at ca. +0.20 V. Remarkably, the sensitivity for MDA is greater than those for its possible interferents, dopamine and ascorbate.

9.6   ENANTIOSELECTIVE ELECTROCHEMICAL SENSING

The possibility of chiral electrocatalytic sensing is one of the interesting analytical applications of the studied materials. In the past decade, a variety of chiral materials with electrochemical activity has been reported (Scholz et al., 2002), including trischelated complexes adsorbed by montmorillonite (Yamagishi and Aramata, 1984), chiral CuO films deposited onto single-crystal Au (Khotari et al., 2004), and epitaxial electrodeposition of ZnO on Au(III) (Limmer et al., 2006).

The possibility of electrochemical chiral sensing can be seen in Figure 9.13, corresponding to experimental SQWV data for monoclinic and tetragonal (m-V_xZrO$_2$ and t-V_xZrO$_2$, respectively) vanadium-doped zirconias attached to paraffin-impregnated graphite electrodes and immersed into 0.10 M NaOH. A main oxidation peak near +1.0 V vs. AgCl/Ag appears for both m-$V_{0.075}Zr_{0.925}O_2$- and t-$V_{0.075}Zr_{0.925}O_2$-modified electrodes (Doménech and Alarcón, 2007). In contact with alkaline solutions of glucose, the voltammetric signals become significantly enhanced and remarkably enantioselective, as can be seen in Figure 9.14. Here, SQWVs for t-$V_{0.050}Zr_{0.95}O_2$ (Figure 9.14a and b) and m-$V_{0.50}Zr_{0.95}O_2$ (Figure 9.14c and d), immersed into 0.10 M NaOH plus 2.0 mM L-glucose (Figure 9.14a and c) and D-glucose (Figure 9.14b and d), are depicted. Clearly, t-V_xZrO$_2$ materials display an essentially identical response for both D- and L-glucose, consisting of overlapping anodic peaks at +0.92 and +1.15 V vs. AgCl/Ag. In contrast, m-V_xZrO$_2$-modified electrodes discriminate between D- and L-glucose. Measured currents at +0.92 V for monoclinic vanadium-doped zirconias in contact with L-glucose solutions are 10–20 times larger than those recorded for D-glucose solutions under identical conditions.
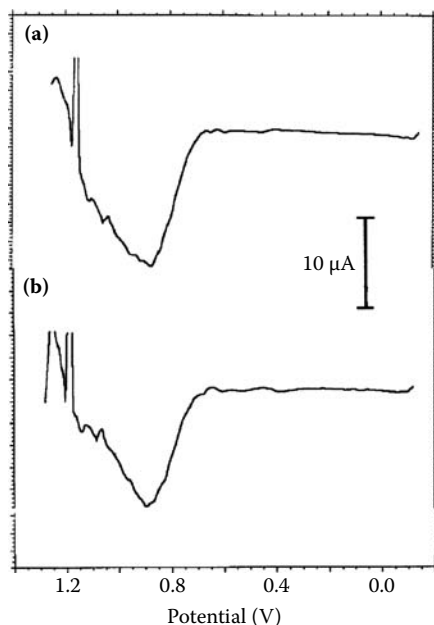
FIGURE 9.13 Deconvolution of SQWVs for paraffin-impregnated graphite electrodes modified with (a) t-$V_{0.10}Zr_{0.90}O_2$ and (b) m-$V_{0.10}Zr_{0.90}O_2$ immersed into 0.10 M NaOH. Potential scan initiated at -0.15 V vs. AgCl/Ag in the positive direction. Potential step increment, 4 mV; square-wave amplitude, 25 mV; frequency, 2 Hz. (Adapted from Doménech and Alarcón, 2007, *Anal. Chem.* 79, 6742–6751, with permission.)

This enantioselective catalytic effect can be rationalized by considering the different coordinative arrangement of metal centers in tetragonal and monoclinic vanadium-doped zirconias. As previously noted (Chapter 6), in tetragonal zirconias, each M^{4+} ion (M = Zr, V) is eight-coordinated, whereas in monoclinic zirconias, M^{4+} ions are seven-coordinated. In this case, there is a no centrosymmetric coordinative arrangement around each metal center, so that a necessary condition for enantioselectivity activity—the existence of chiral centers—is achieved. Consistently, monoclinic V_xZrO_2 materials become electrochemically enantioselective with regard to oxidation of glucose, whereas tetragonal V_xZrO_2 ones remain nonenantioselective.

As previously noted, electrochemical oxidation of alcohols and carboxylic acids at transition metal oxide–based materials occurs via intermediate radical species, the rate-determining step in alcohol oxidation being radical formation in the carbon in the alpha position with respect to the alcohol group. Following Kokoh et al. (1992), at Pt electrodes in acidic solution, the oxidation mechanism involves an initial one-electron, one-proton electrochemical oxidation step involving the dehydrogenation of the anomeric atom followed by adsorption of glucose onto the metal surface. In alkaline media, Burke and Ryan (1992) postulated that
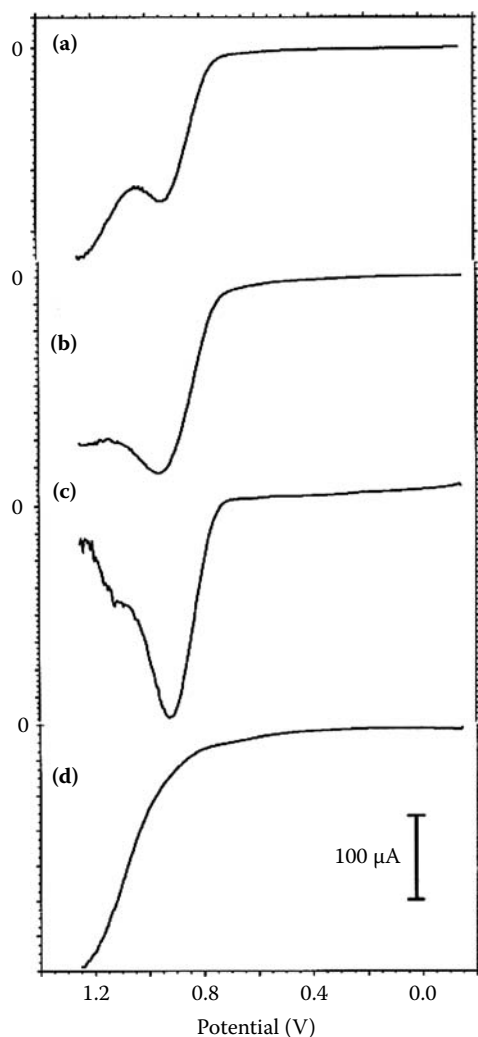
FIGURE 9.14 Deconvolution of SQWVs for paraffin-impregnated graphite electrodes modified with (a,b) t-$V_{0.050}Zr_{0.95}O_2$ and (c,d) m-$V_{0.50}Zr_{0.95}O_2$, immersed into 0.10 M NaOH plus (a,c) 2.0 mM L-glucose and (b,d) D-glucose. Conditions are as in Figure 9.15. (From Doménech and Alarcón, 2007. *Anal. Chem.* 79, 6742–6751, with permission.)

glucose undergoes a keto-enol transformation to form anionic enol species. It should be noted that an open-cyclic equilibrium is established in glucose solutions. Electrochemical oxidation of cyclic forms leads to gluconolactone (or gluconate) as illustrated in Figure 9.15. Open forms, however, can lead to six-electron products (glycolate and glucarate) and even 12- and 18-electron products (formate and oxalate, respectively), as schematized in Figure 9.16 (Tominaga et al., 2006).
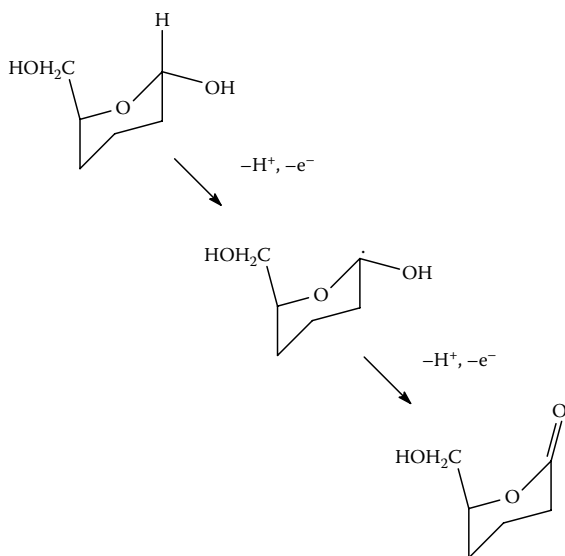
FIGURE 9.15 Schematics for the electrochemical oxidation of cyclic glucose forms. (From Doménech and Alarcón, 2007. *Anal. Chem.* 79, 6742–6751, with permission.)
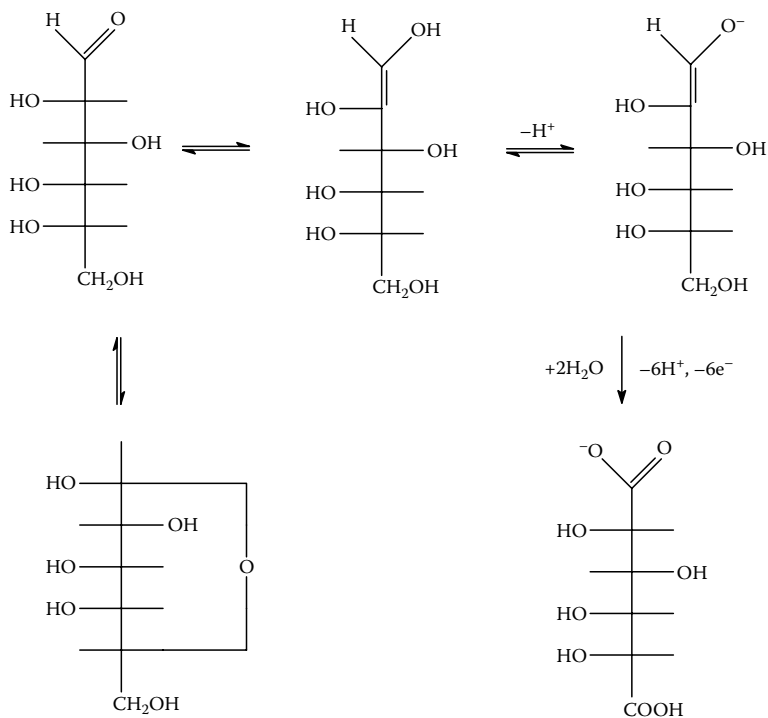
FIGURE 9.16 Schematics for the electrochemical oxidation of open glucose forms. (From Doménech and Alarcón, 2007. *Anal. Chem.* 79, 6742–6751, with permission.)

Controlled potential electrolysis data suggest that under our experimental conditions, the two-electron product of glucose oxidation is almost exclusively formed at +0.92 V, whereas for the process at +1.15 V, coulometric experiments indicated the consumption of more than two electrons per mole of glucose.

Tafel analysis of voltammetric curves (see Chapter 3) allows us to attribute the electrocatalytic process at +0.92 V to the formation of relatively strong vanadium-glucose adducts, whereas the electrocatalytic process at +1.15 V involves the oxidation of glucose molecules located at the outer Helmholtz plane. The catalytic pathway can be described on assuming that the electrochemical process is initiated by the formation of vanadium-glucose surface-confined complexes:

$$\{V^{IV}_xZrO_2(H_2O)_z\} + xC_6H_{12}O_6 \rightarrow \{V^{IV}_xZrO_2(H_2O)_w \cdot xC_6H_{12}O_6\} + (z-w)H_2O \quad (9.22)$$
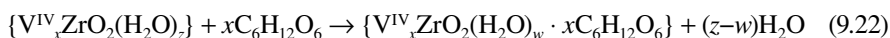
For simplicity, it is assumed that all vanadium centers participate in the reaction. This step should be followed by vanadium-centered and glucose-centered electrochemical oxidation of the V^{4+}-anionic glucose complex:

$$\{V^{IV}_xZrO_2(H_2O)_w \cdot xC_6H_{12}O_6\} + xOH^- \rightarrow$$
$$\{V^{V}_xZrO_2(OH)_x(H_2O)_{w-x} \cdot xC_6H_{12}O_6\} + xH_2O + xe^- \quad (9.23)$$

$$\{V^{V}_xZrO_2(OH)_x(H_2O)_{w-x} \cdot xC_6H_{12}O_6\} \rightarrow$$
$$\{V^{V}_xZrO_2(OH)_x(H_2O)_{w-x} \cdot xC_6H_{11}O_6\} + xH^+ + xe^- \quad (9.24)$$
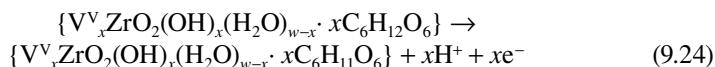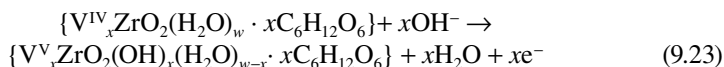
The resulting radical probably experiences an electron exchange with the oxidized vanadium centers, resulting in the formation of gluconolactone and regenerating the parent V^{4+} centers:

$$\{V^{V}_xZrO_2(OH)_x(H_2O)_{w-x} \cdot xC_6H_{11}O_6\} \rightarrow$$
$$V^{IV}_xZrO_2(H_2O)_w + xC_6H_{10}O_6 \quad (9.25)$$
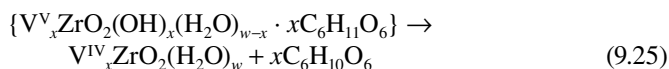
In agreement with the foregoing set of considerations, chloride ions significantly decrease the electrocatalytic effect of all tested materials with respect to glucose oxidation. This effect can be attributed to the competence of chloride with glucose and water for coordinating vanadium centers. Interestingly, this effect can be minimized using diphasic materials, composed by either monoclinic or tetragonal vanadium-doped zirconias included in an amorphous silica matrix (see transmission electron microscopy image of tetragonal $V_{0.075}Zr_{0.925}O_2$ coated with a layer of amorphous silica in Figure 9.17). Here, the layer of amorphous silica covering zirconia grains acts as an ion-selective barrier partially blocking the access of chloride ions to vanadium centers (Doménech and Alarcón, 2007).

9.7   ELECTROCHEMICAL MODELING OF ELECTRONIC SYSTEMS

Modeling of electronic circuitry via photochemical and electrochemical systems has received attention in the past two decades. On first examination, a variety of electrochemical systems can be regarded as frequency filters, rectifiers, or amplifiers because their operating properties are parallel to those typical of vacuum and
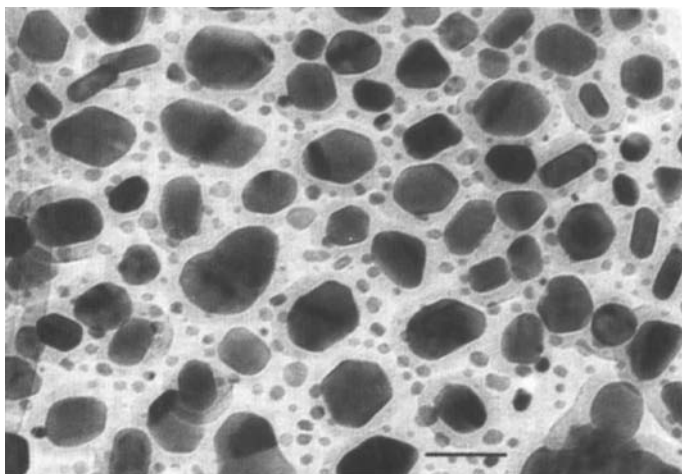
FIGURE 9.17 Transmission electron microscopy of tetragonal $V_{0.075}Zr_{0.925}O_2$ coated with a layer of amorphous silica prepared from gels heated at 1200°C for 3 h. (From Doménech and Alarcón, 2007. *Anal. Chem.* 79, 6742–6751, with permission.)

semiconducting electronic devices. This is potentially interesting for transduction, sensing, and information storage.

A first example of electrochemical modeling is provided by the oxidation of N,N,N',N''-tetramethylbenzidine in nonaqueous media at zeolite Y-encapsulated poly(thienylacetylene) (PTA@Y), a hybrid material described in Chapter 8 (Doménech et al., 2006f). As can be seen in Figure 9.18, at the PTA@Y-modified glassy carbon electrode, two consecutive oxidation peaks appear for benzidine oxidation in 0.10 M Bu_4NPF_6/MeCN. Upon addition of $LiClO_4$, the voltammetric response becomes essentially identical, but the peak currents are significantly enhanced. This effect can be interpreted as the result of the easier entrance of ClO_4^- ions than PF_6^- ones in the zeolite network demanded by charge neutrality in electrochemical cycles. Interestingly, the electrode modifier enhances the signal with no concomitant increase in background currents as observed in, for instance, nanotube-modified electrodes (see Figure 7.20). This effect can be attributed to the conjunction of the preconcentrating effect due to the zeolite host and electrocatalytic effect associated to the conducting oligomer/polymer system.

Examination of Figure 9.18 suggests that one can consider the PTA@Y-modified electrode as an electrolyte-driven amplifier system as far as (a) the amplitude of the input signal is enhanced and (b) the profile of the output signal is identical to that of the input signal (see Figure 9.19).

The use of molecular switches in solution phase has recently received attention (de Silva et al., 1997). Photochemical logic gates shown AND, OR, XOR, NOR, and INH functionality have been reported, whereas electrochemical storage of information via electroswitchable systems (Katz et al., 2004), electrochemical transduction of photonically or electrochemically encoded information, and electrochemical/photochemical information processing (Willner et al., 2001; Pérez-Inestrosa
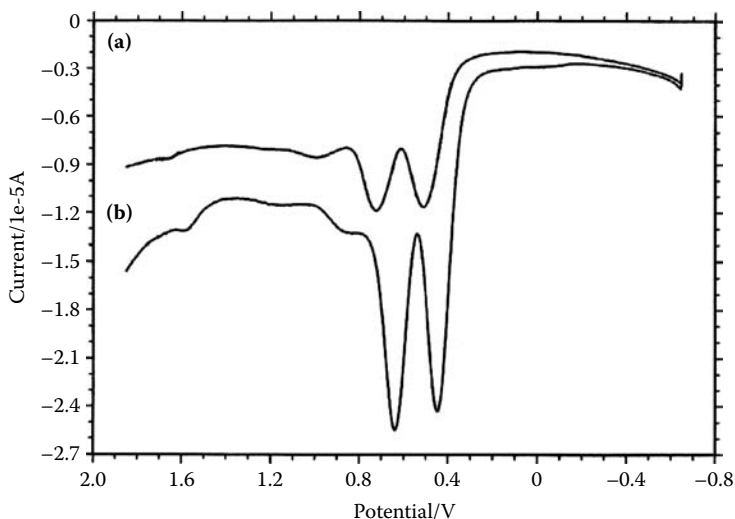
FIGURE 9.18 SQWVs for PTA@Y-modified glassy carbon electrodes immersed into (a) 0.50 mM N,N,N′,N″-tetramethylbenzidine plus 0.10 M Bu₄NPF₆/MeCN solution and (b) the same plus 0.05 M LiClO₄. Potential scan initiated at −0.75 V vs. AgCl/Ag in the positive direction. Potential step increment 4 mV; square-wave amplitude 25 mV; frequency 15 Hz. (From Doménech et al., 2006e. *Electrochem. Commun.* 8, 1335–1339, with permission.)

et al., 2007) are possible. A three-state chemical/electrochemical system can be approached from polyaniline attached to layered double hydroxides (LDH-PANI) described in Chapter 8. For this purpose, the voltammetric response of aqueous $Fe(CN)_6^{4-}$ solutions at LDH-PANI-modified electrodes is modulated upon application of different potential inputs, the system being able to be operated as an ionic/electronic switch (Doménech et al., 2008).

Figure 9.20 compares CVs for a 2.0 mM solution of $K_4Fe(CN)_6$ in phosphate buffer at unmodified GCE (Figure 9.20a) and LDH-PANI-modified electrode (Figure
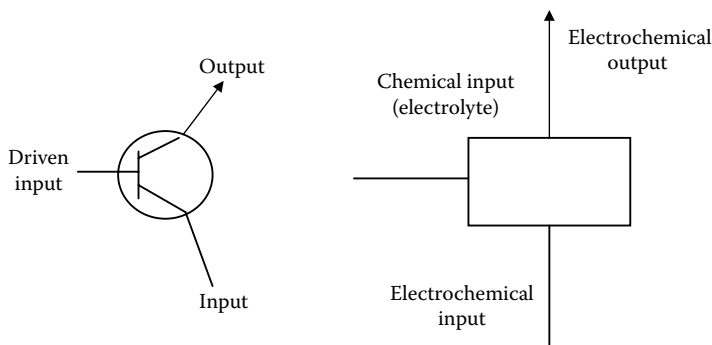
FIGURE 9.19 Schematic representation of (left) a transistor-type amplifier system and (right) an electrolyte-driven PTA@Y/benzidine electrochemical amplifier.
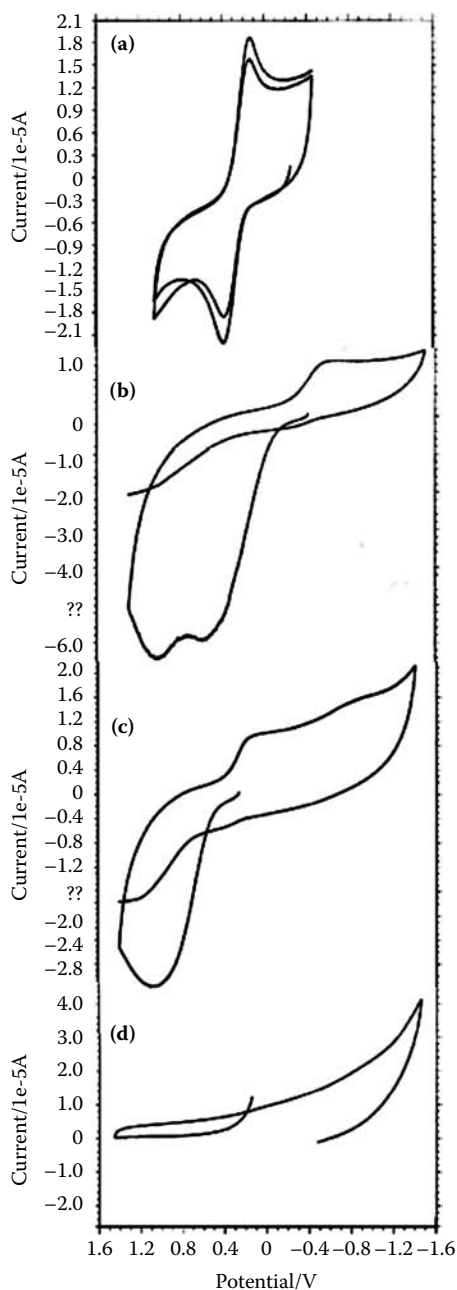
FIGURE 9.20 CVs for a 2.0 mM $K_4Fe(CN)_6$ solution in 0.50 M phosphate buffer at pH 7.0 at (a) unmodified GCE and (b–d) LDH-PANI-modified GCE after application of a constant potential step of (b) 0.0 V, (c) −1.25 V, (d) +0.85 V for 2 min. Potential in the CVs initiated at 0.0 V in the positive direction. Potential scan rate 100 mV/sec. (From Doménech et al., 2008. *J. Electroanal. Chem.* 624, 275–286, with permission from Elsevier.)

9.20b–d) after conditioning the modified electrode by applying different constant potential steps between 1 and 5 min. At unmodified electrodes, a well-defined quasi-reversible couple appears at peak potentials of +0.28 V (anodic) and +0.14 V (cathodic). At LDH-PANI, when no conditioning potential is applied, anodic peaks at +0.28 and +0.60 V, attributable to LDH-PANI-mediated oxidation of $Fe(CN)_6^{4-}$, and the LDH-PANI oxidation, respectively, appear, as denoted by the increased cathodic-to-anodic peak potential separation, and the significant decrease of the cathodic peak for the $Fe(CN)_6^{4-}/Fe(CN)_6^{3-}$ couple. If a conditioning potential of −1.25 V is applied, CVs exhibit only the second oxidation peak at +0.60 V. Finally, when a conditioning potential of +0.90 V is applied to pristine LDH-PANI electrodes, the subsequent CV initiated at 0.0 V in the anodic direction shows no oxidation or reduction peaks.

This behavior suggests that LDH-PANI can be described in terms of a three-state system where the three states can be accessed by applying the adequate potential inputs from the parent emeraldine form. Under potentials ranging between +0.90 and −0.80 V in contact with aqueous phosphate buffer, the three states are stable (as denoted upon repetitive cycling the potential scan), although, as can be observed on comparing Figure 9.20a and b, there is no entirely reversible switching between all states.

Application of such potential inputs can lead to modeling two combinational logic functions, the electrochemical system acting, as with a switch, able to transduce one chemical and one electrochemical input (I1, I2) into two electrochemical outputs (O1, O2), corresponding to the oxidation peaks for LDH-PANI and $Fe(CN)_6^{4-}$.

Combinational logic circuits equivalent to the LDH-PANI switch are depicted in Figure 9.21. A positive logic convention (absence = 0, presence = 1) is used for $Fe(CN)_6^{4-}$ input (I1), as customary. Two alternative encodings can be used for the electrochemical input (I2) by combining preconditioning potentials of (a) 0.0 V (off = 0) and +1.0 V (on = 1) and (b) 0.0 V (off = 0) and −1.25 V (on = 1). The corresponding

(a)

(b)
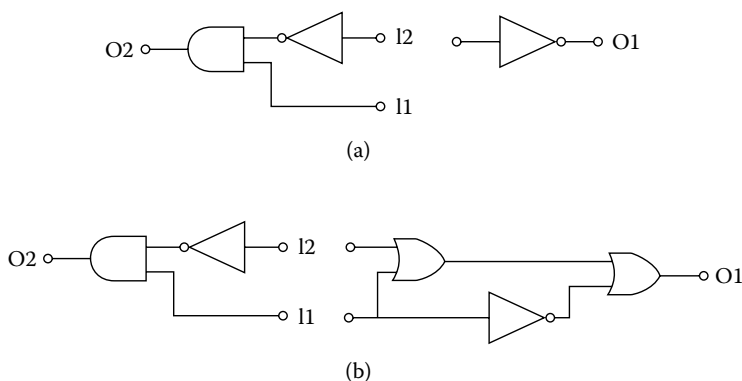
FIGURE 9.21 Schematics for the LDH-PANI-based logic circuits acting in modes (a) and (b). (From Doménech et al., 2008. *J. Electroanal. Chem.* 624, 275–286, with permission from Elsevier.)

TABLE 9.2
Truth Table for the ZnAl-PANI Switch
Operating in Mode I

I1	I2	O1	O2
0	0	1	0
0	1	0	0
1	0	1	1
1	1	0	0

TABLE 9.3
Truth Table for the ZnAl-PANI Switch
Operating in Mode II

I1	I2	O1	O2
0	0	1	0
0	1	1	0
1	0	1	1
1	1	1	0

truth tables are shown as Table 9.2 and Table 9.3. Analysis of the logic behavior of the LDH-PANI switch in mode (a) reveals that the input I1 has no influence on the output O1, which is equivalent to a NOT connected to the input I2. I1 and I2 issues can be combined through NOT and AND gates (INHIBIT gate) producing the output O2. This situation is repeated in mode (b), whereas input O1 can be represented as a combination of one NOT and two OR gates.

10 Supercapacitors, Batteries, Fuel Cells, and Related Applications

10.1 ELECTRICAL ENERGY STORAGE AND CONVERSION

Production, storage of electrical energy, and its conversion into other energy forms are obvious demands from current society. Batteries are power sources where chemical energy is converted into electrical energy via spontaneous electrochemical reactions. Batteries contain one or several cells where a reduction process and an oxidation process occur in two electrodic compartments lined by a solid or liquid electrolyte. Primary batteries are not designed to be recharged, whereas secondary batteries allow repeated cycles of charge/discharge.

Capacitors are devices for storing electric energy consisting, ideally, of two conducting elements separated by a dielectric. Under application of a difference of potential between the conducting elements, the capacitor acquires a charge that can be further released through a consumer circuit. Accordingly, capacitors, apart from their use as frequency filters, rectifiers, etc., in electronic circuitry, can be used for energy storage, especially for shorter periods (Bard et al., 2008).

Remarkably, charge/discharge processes in batteries proceed via interconversions of electrode materials involving phase changes and a certain level of irreversibility resulting in limited cycle of life. Increasing stability and cycleability in energy storage devices using nonpollutant and inexpensive materials are the focus of considerable research efforts. In this context, the use of porous materials with high surface area plays an essential role.

10.2 CAPACITORS AND SUPERCAPACITORS

Traditional capacitors use nonpolarized dielectrics such as ceramic materials or polymers (polystyrene, polypropylene), working typically in the picofarad to microfarad capacitance range. Polarized (or electrochemical) capacitors involve anodic oxides of Al, Ta, or Nb (electrolytic capacitors), the capacitance being extended to the microfarad to millifarad range. In recent times, new families of electrochemical capacitors, generically called supercapacitors, have been devised. These involve two possible mechanisms for charge storage: double layer and charge transfer reactions, the latter resulting in the so-called pseudocapacitances (Conway, 1991). Double-layer capacitance arises from the separation of charge at the interface between a solid electrode and an electrolyte (Sarangapani et al., 1990), whereas pseudocapacitance arises from fast, reversible faradaic reactions occurring at or near a solid electrode

مرجع دانشجویان و مهندسین مواد
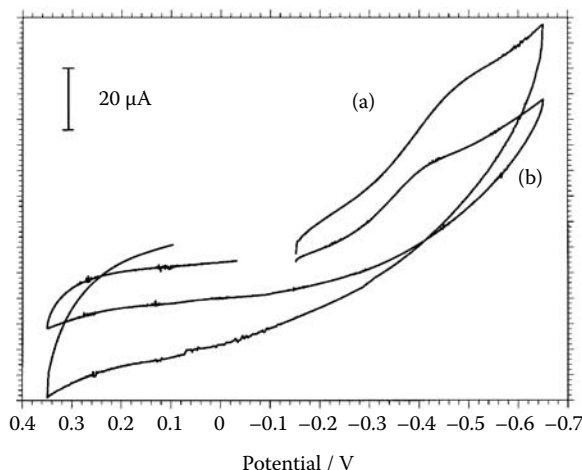
FIGURE 10.1 CVs for NiO attached to a graphite plate in contact with 0.10 M NaOH. Potential scan rate of (a) 50, (b) 5 mV/sec.

surface over an appropriate range of potential (Zheng and Jow, 1995). Such redox reactions can go beyond the surface area and penetrate into the bulk of these materials (Hu and Tsou, 2002). Noble metal oxides such as RuO_2 and IrO_2 provide the most specific capacitance values (about 750 F/g), but they are toxic and expensive. Thus, porous transition metal oxides such as CoO_x, NiO_x, and MnO_2 are currently under intensive research as materials for supercapacitors.

Electrochemical analysis of their performance is usually conducted via preparing electrodes by pressing a mixture of the powdered material with a binder (e.g., acetylene black plus polytetrafluorene-ethylene) onto metal foam current collectors (typically 1×1 cm^2). Cyclic voltammetric analysis of electrodes prepared from such materials allows researchers to discern between a purely capacitive behavior and a pseudocapacitance response. The purely capacitive response results in box-shaped voltammograms such as depicted in Figure 7.13. A typical pseudocapacitance behavior can be seen in Figure 10.1, which shows the cyclic voltammetric response of a deposit of microparticulate NiO on a graphite plate in contact with 0.10 M NaOH. Here, faradaic processes can be clearly seen as more or less defined peaks in the voltammogram.

The specific capacitance, C_{sp} (F/g), can be evaluated from CVs as the quotient between the "box" current, I, and the product of the potential scan rate and the mass of the composite layer, m:

$$C_{sp} = \frac{I}{mv} \tag{10.1}$$

Analogously, the specific capacitance can be calculated from charge/discharge curves at a given current rate by using the relationship:

$$C_{sp} = \frac{I\Delta t}{m\Delta V_d} \tag{10.2}$$
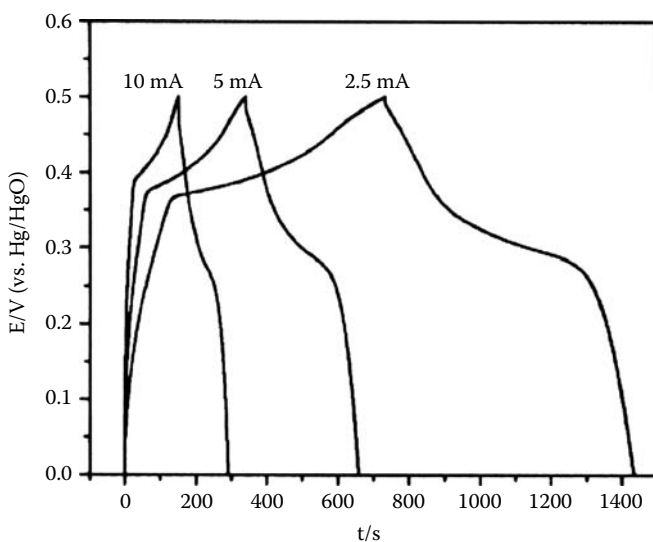
FIGURE 10.2 Charge/discharge curves at different current rates for mesoporous NiO (obtained using supramolecular template) in contact with 0.10 M KOH. (From Xu et al., 2007. *J. Solid State Electrochem.* 11, 372–377, with permission.)

where I represents the discharge current density, m is the mass of the composite, Δt is the total time of discharge, and ΔV_d is the potential drop during discharge. Typical curves are illustrated in Figure 10.2 for NiO in contact with 0.10 M KOH obtained using a supramolecular template (Xu et al., 2007). The specific capacitance can also be calculated from the imaginary part of impedance at the low-frequency limit at an electrochemical impedance spectroscopy (EIS) experiment at open circuit potential by using the relationship:

$$C_{sp} = \frac{1}{mj\omega Z_{imag}} \tag{10.3}$$

Figure 10.3 shows the Nyquist plot obtained for a coating of Ru(bpy)-PA-functionalized polyacetylene on graphite in contact with 0.10 M H$_2$SO$_4$. The EIS response is sensitive to the application of different potentials. At high frequencies, a small semicircle arc appears, data fitting to the equivalent circuit consisting of a parallel combination of double-layer capacitance, charge transfer resistance, and a Warburg diffusion impedance (Z_W) are taken. The high-frequency intercept of the real axis leads to a low value of the internal resistance (electrolyte resistance plus active material resistance plus contact resistance at the active material-collector interface), whereas at intermediate frequencies, the appearance of a 45° inclined line in the Nyquist diagram suggests that the Warburg impedance dominates. At low frequencies, the linear region leans more toward the imaginary axis, thus approaching purely capacitive behavior.
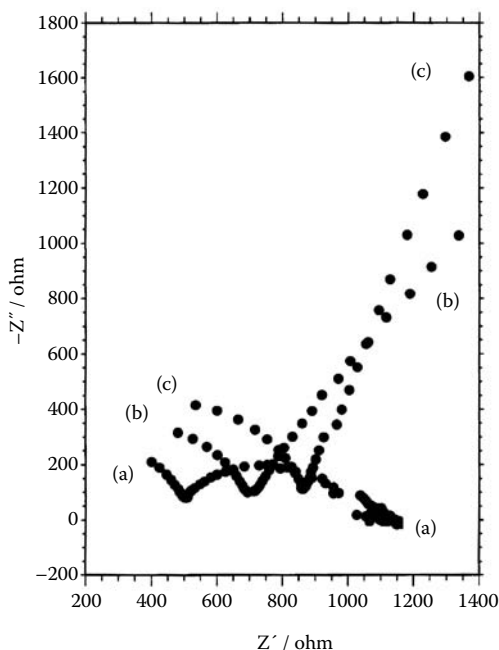
FIGURE 10.3 Nyquist plot in the $10^5 – 10^{-1}$ Hz frequency range for Ru(bpy)-PA-functionalized polyacetylene on graphite in contact with 0.10 M H_2SO_4. Applied potentials of: (a) +1.0; (b) 0.0; and (c) -1.0 V vs. AgCl/Ag. Material courtesy of Prof. Hermenegildo García, Polytechnical University of Valencia.

The fraction of metal electroactive sites involved in the faradaic reaction, z_{ac}, can be calculated from the specific capacitance of the composite using the relationship (Srinivasan and Weidner, 2000):

$$z_{ac} = \frac{C_{sp}M\Delta V}{F} \tag{10.4}$$

where ΔV represents the potential window and M is the average molecular mass of the material.

The specific energy, W_{sp} (W h/kg), can be estimated as (Schneuwly et al., 1999):

$$W_{sp} = \frac{CU^2}{2m_{ac}} \tag{10.5}$$

In this equation, C represents the capacitance of the system, U is the working voltage, and m_{ac} is the total amount of active materials. Typical values of W_{sp} are ca. 50 W h/kg. The specific power density is given by (Yuan et al., 2008):

$$P_{sp} = \frac{IU}{4m_{ac}} \tag{10.6}$$
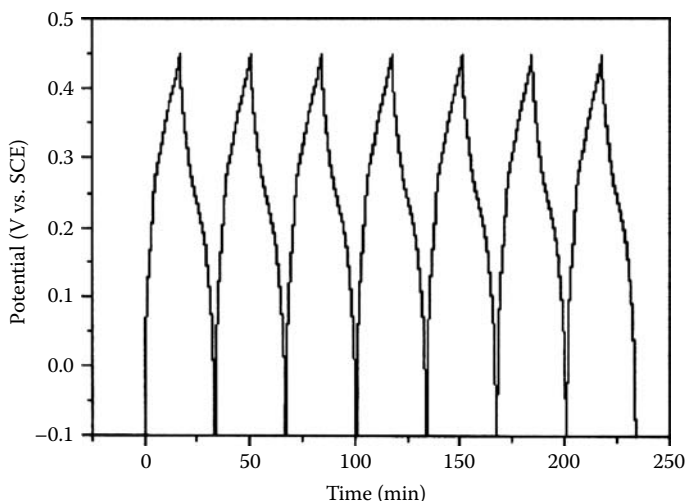
FIGURE 10.4   First seven charge/discharge cycles of a $Co(OH)_2$-$Ni(OH)_2$/ultrastable Y zeolite composite electrode immersed into 1 M KOH within the potential window between −0.1 and +0.45 V vs. SCE (From Liang et al., 2007. *J. Solid State Electrochem.* 11, 571–576, with permission from Springer.).

In this equation, I and U represent the constant charge-discharge current and the potential range corrected by ohmic drop, respectively. When constant current is used for charging and discharging processes, coulombic efficiency, η, can be calculated as:

$$\eta\ (\%) =\ 100\frac{t_D}{t_C} \tag{10.7}$$

Here, t_D and t_C represent the discharge and charge characteristic times, respectively. Figure 10.2 shows the charge/discharge curves at different current rates for mesoporous NiO obtained using supramolecular template (Xu et al., 2007). A crucial aspect for practical applications is the stability of the response, so that multiple cycling tests (typically 500–100 cycles) are routinely performed. Figure 10.4 shows the first seven charge/discharge cycles of a $Co(OH)_2$-$Ni(OH)_2$/ultrastable Y zeolite composite electrode immersed into 1 M KOH within the potential window between −0.1 and +0.45 V vs. SCE (Liang et al., 2007). It can be seen that the specific capacitance loss after several cycles is negligible.

A high rate discharge capability is one of the most important properties of supercapacitors in the application of electrode battery (Ye et al., 2004).

The surface faradaic reactions for NiO are, in general, described in terms of (Srinivasan and Weinder, 2000; Xing et al., 2004):

$$NiO + OH^- \rightarrow NiOOH + e^- \tag{10.8}$$
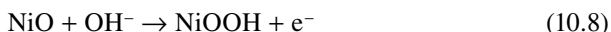
The reversible pseudocapacitance redox reaction might be represented as:

$$NiOOH + H_2O + e^- \rightarrow Ni(OH)_2 + OH^- \tag{10.9}$$
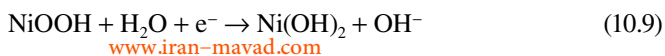
Recent developments include the use of hybrid electrochemical capacitors, in which intercalations compounds ($Li_4Ti_5O_{12}$) were used as the negative material and activated carbon was used as the positive material (Amatucci et al., 2001). Cheng et al. (2006) have recently reported a β-FeOOH-based hybrid capacitor where the iron hydroxide, acting as negative electrode, is assembled with activated carbon positive electrode in ethylene carbonate/dimethyl carbonate with 1.0 M $LiPF_6$ electrolyte.

With respect to capacitors, supercapacitors offer such advantages as virtually unlimited life cycle, typically ca. 10^6 cycles coupled with high cycle efficiency (95% or more), low impedance, high rates of charge and discharge with concomitant low charging time (seconds), no danger of overcharge, and relatively low cost/power ratios.

As for disadvantages (with respect to batteries), one can mention that supercapacitors possess relatively low energy density (ranging from one-fifth to one-tenth of a conventional electrochemical battery), low cell voltages, and high self-discharge rates. In addition, it should be noted that linear discharge voltage of capacitors prevents use of the full energy spectrum, whereas their use in electrical vehicle applications requires electronic control and switching equipment.

10.3 NICKEL BATTERIES

Nickel batteries use β-$Ni(OH)_2$ as electrode material. This material converts to β-NiOOH during the charging process and this rearranges to γ-NiOOH when it is overcharged. This last process is accompanied by a significant expansion, because of the difference in density between β-NiOOH and γ-NiOOH, which may result in poor electric contact between the current collector and β-$Ni(OH)_2$/β-NiOOH, with concomitant decrease in the discharge capacity of the battery. Among others, layered double hydroxides of Ni and other metals, often termed *stabilized* α-$Ni(OH)_2$ or doped $Ni(OH)_2$, have been tested as electrode materials (Bernard et al., 1996). The effect of the interlayer anions on the electrochemical performance of layered double hydroxide electrode materials has been recently studied by Lei et al. (2008) (see Chapter 6).

Ferrate(VI)-based materials were studied in 1999 (Licht et al., 1999) and reviewed by Yu and Licht (2008). The cathodic charge storage of ferrate(VI) can be represented as the reduction processes:

$$FeO_4^{2-} + 3H_2O + 3e^- \rightarrow FeOOH + 5OH^- \tag{10.10}$$

$$FeO_4^{2-} + 5/2\,H_2O + 3e^- \rightarrow \tfrac{1}{2}\,Fe_2O_3 + 5OH^- \tag{10.11}$$

CVs for the oxidation of ferrate ions in alkaline solution are shown in Figure 10.5 (Licht et al., 2001), where an apparently irreversible diffusion-controlled oxidation process is recorded. A primary ferrate(VI) battery contains a Fe(VI) cathode and can use a zinc anode and an alkaline electrolyte such as a conventional alkaline battery. For Ag_2FeO_4, the general discharge reaction would be:

$$Ag_2FeO_4 + 5/2Zn \rightarrow 2Ag + 1/2Fe_2O_3 + 5/2\,ZnO \tag{10.12}$$
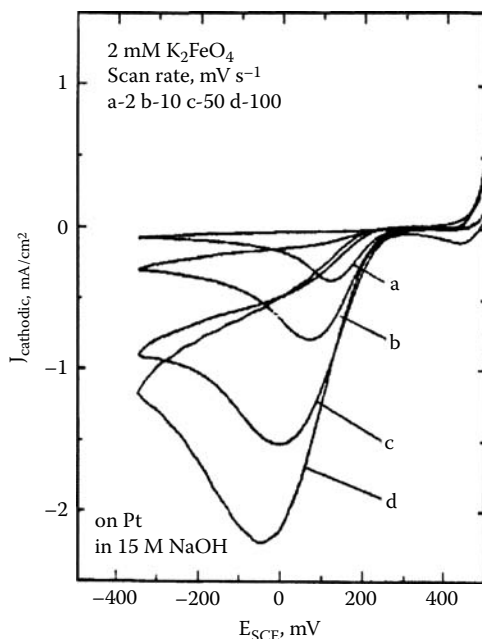
FIGURE 10.5 CVs at Pt electrode for 2 mM K_2FeO_4 solution in 15 M NaOH. (From Licht et al., 2001. *J. Power Sources* 101, 167–176, with permission from Elsevier.)

10.4 LITHIUM BATTERIES

Following Bard et al. (2008), the term *lithium batteries* refers to a family of different devices having in common a lithium metal anode whose discharge reaction is Li $\rightarrow Li^+ + e^-$. Lithium batteries have found application in portable electronic devices because of their high working voltage (up to 4 V), high energy density, excellent cyclability, flat discharge characteristics, and long shelf life (up to 10 years) (Nazri and Pistoia, 2004).

Lithium was initially used as a cathode material and was later replaced (due to its reactivity) by Li-carbon intercalation materials. Cathode materials include lithiated transition metal oxides such as $LiCoO_2$, $LiNiO_2$, $LiMn_2O_4$, and related compounds (Ammunsdsen and Paulsen, 2001). Apart from these materials, different porous materials have been studied for lithium batteries. Thus, V_2O_5 and vanadates (LiV_3O_8, V_6O_{13}) have been described by Abraham et al. (1981), Desilvestro and Haas (1990), and Delmas et al. (1994); recent advances include sol-gel chromium-modified V_6O_{13} (Leger et al., 2007). Structurally related materials are MoO_2, MoS_2, and $MnMoO_4$ (Auborn and Barberi, 1987; Martos et al., 2000; Xie et al., 2003; Guo et al., 2007). Such materials possess high cycling capability. A second group of widely studied materials comprises MnO_2 and related compounds (Bach et al., 2000; Soudan et al., 2000), iron phosphate-based materials (Pahdi et al., 1997; Yang et al., 2002; Santos-Peña et al., 2006), and iron sulfides (FeS, FeS_2) (Strauss et al., 2002).

Lithium batteries can operate over a wide temperature range (−40 to 70ºC), the most common solvents being polar organic liquids such as acentonitrile, propylene carbonate, methyl formate, etc. Thionyl chloride ($SOCl_2$) and sulfuryl chloride (SO_2Cl_2) are inorganic liquids that can be used as both the solvent and the active cathode material in lithium batteries. $LiClO_4$, $LiBF_4$, and $LiAsF_6$ are the most common salts for supporting electrolyte dosage. Recent developments include the use of solid electrolytes, namely, polyethers, thin films of conducting ceramic materials, among others.

The electrochemical performance of cathodes depends significantly on their behavior with regard to lithium diffusion, in turn, depending on particle size, surface morphology, homogeneity, and porosity. Porous composite cathodes can be regarded as two contiguous interwoven networks. The cathode-active material network consists of electronically conducting particles, whereas the second network is a polymer electrolyte that fills the pores between the active cathode material particles. Lithium ions participating in the cathode reaction and originating from the lithium electrode migrate through the composite into the polymer electrolyte-filled pores of the composite cathode to react with the cathode-active material. The mechanism of charge-discharge may be affected by ion transport in the electrolyte network and redox insertion kinetics of the cathode-active material. General requirements are as follows: (1) electrical contact has to be ensured between the particles of the cathode-active material; (2) the electrolyte must completely fill the pores to prevent the separation of cathode-active particles and provide ion conductivity between them; (3) the mobility of ions in the polymer-electrolyte phase should be comparable with that in the cathode-active material phase.

The cycle life can be defined as the number of charge/discharge cycles that a battery can go through, under given conditions, before it reaches predefined minimum performance limits (Bard et al., 2008). The cycle of life depends on rates of charge and discharge, charge and discharge cutoff limits, depth of discharge, self-discharge rate, and temperature of operation.

Figure 10.6 shows the CV of a $LiMn_2O_4$ electrode on a cell with Li foil for both the reference and auxiliary electrodes in ethylene carbonate plus dimethyl carbonate solution of $LiAsF_6$ (1 M) (Sinha and Munichandraiah, 2008). The pair of peaks at larger potential corresponds to the deintercalation/intercalation of Li in the range $0 \leq x \leq 0.5$ for $Li_xMn_2O_4$, whereas the pair of peaks at lower potentials is attributable to this process for $0.5 \leq x \leq 1$, both accompanied by reversible Mn(IV)/Mn(III) redox reactions. Following Xia and Yoshio (1996), the later electrochemical process corresponds to the removal/addition of Li^+ ions from/into half of the tetrahedral sites in which the lithium intercalation occurs. The former couple is then attributed to this process at the other tetrahedral sites where lithium intercalations do not occur.

EIS for a $LiMn_2O_4$ electrode at 20ºC is shown in Figure 10.7, whereas the equivalent circuit used for fitting experimental impedance data is depicted in Figure 10.8 (Sinha and Munichandraiah, 2008). The Nyquist plot can be described in terms of two superimposed semicircles. Because the semicircles are depressed with their centers below the real axis, constant phase elements are introduced in this circuit. Here, R_1 and Q_1 represent the resistance of the surface film on $LiMn_2O_4$ and the constant phase element (CPE) representing the film
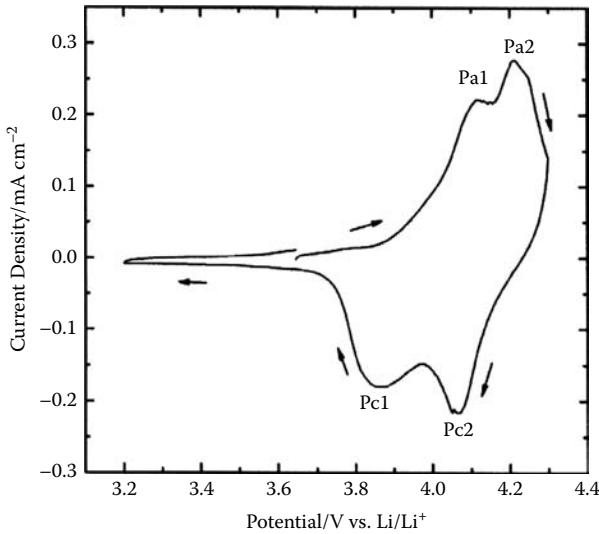
FIGURE 10.6 CV of a LiMn$_2$O$_4$ electrode (surface density, 5 mg/cm^2) in 1 M LiAsF$_6$/ (ethylene carbonate + dimethyl carbonate). Potential scan rate, 0.05 mV/sec. (From Sinha and Munichandraiah, 2008. *J. Solid State Electrochem.* 12, 1619–1627, with permission from Springer.)

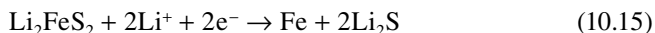capacitance, both corresponding to the high-frequency region of the impedance spectrum. R_2 and Q_2 denote, respectively, the resistance and CPE corresponding to the electrochemical intercalation/deintercalation process and double-layer capacitance. R_2 is equivalent to the charge-transfer resistance (R_{ct}) of the Mn^{4+}/Mn^{3+} redox process. This magnitude exhibits an Arrhenius-type variation
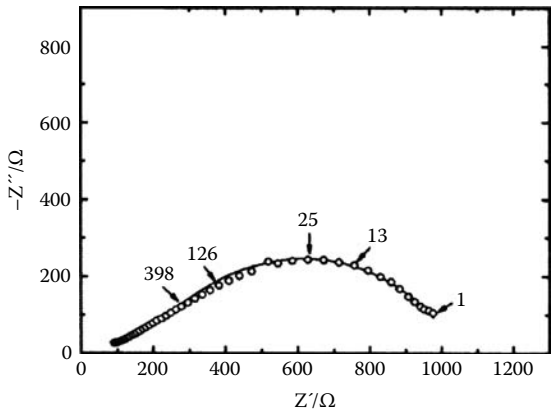
FIGURE 10.7 EIS of a LiMn$_2$O$_4$ electrode in 1 M LiAsF$_6$/(ethylene carbonate + dimethyl carbonate) at 20°C. (From Sinha and Munichandraiah, 2008. *J. Solid State Electrochem.* 12, 1619–1627, with permission from Springer.)
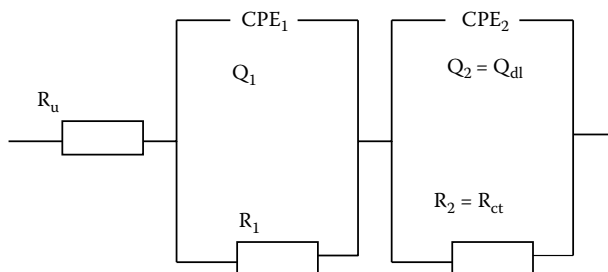
FIGURE 10.8 Representation of the equivalent circuit used by Sinha and Munichandraiah (2008) to describe the EIS of $LiMn_2O_4$ electrode in 1 M LiAsF6/(ethylene carbonate + dimethyl carbonate) depicted in Figure 10.7.

with temperature so that the activation energy, E_a, of the electrochemical process can be obtained from the slope of $\ln(R_{ct}/T)$ vs. $1/T$ linear relationship (Suresh et al., 2002):

$$\frac{\Delta(\ln(R_{ct}/T))}{\Delta(1/T)} = \frac{E_a}{R} \tag{10.13}$$

In the case of pyrite batteries, Strauss et al. (2002) proposed a multistep mechanism for the charge–discharge of pyrite in polymer electrolytes in the temperature range 90–135ºC. In the first cycle, the reduction of pyrite occurs in two steps:

$$FeS_2 + 2Li^+ + 2e^- \rightarrow Li_2FeS_2 \tag{10.14}$$

$$Li_2FeS_2 + 2Li^+ + 2e^- \rightarrow Fe + 2Li_2S \tag{10.15}$$

The second cycle charge/discharge curve for the Li/composite polymer electrolyte/ FeS_2 cell is shown in Figure 10.9. Region b in the voltage/capacity curve in the figure
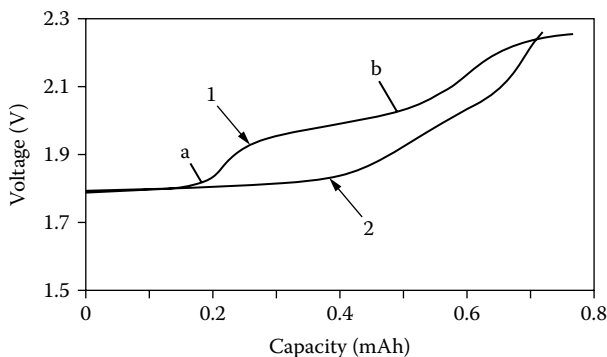
FIGURE 10.9 Plot of voltage vs. capacity corresponding to the second charge-discharge cycle of Li/composite polymer electrolyte/FeS_2 cell. (From Strauss et al., 2002. *J. Solid State Electrochem.* 6, 468–474, with permission from Springer.)
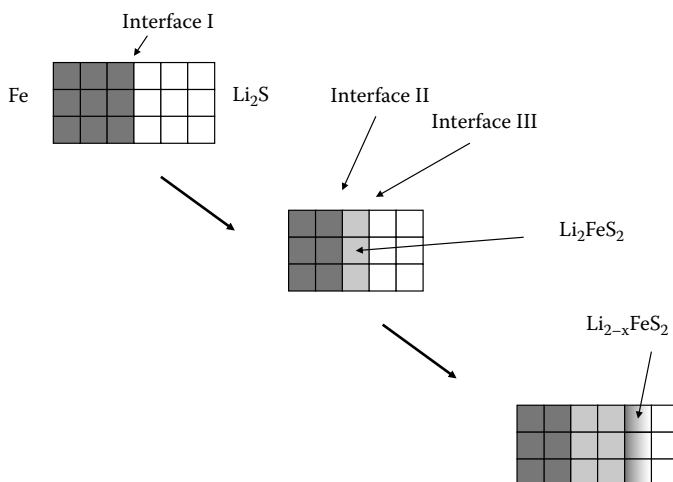
FIGURE 10.10 Schematics for charge solid-phase transitions in a pyrite-based composite cathode as described by Strauss et al. (2002).

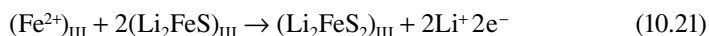corresponds to the reversible electrochemical reaction:

$$Fe + 2Li_2S \rightarrow Li_2FeS_2 + 2Li^+ \tag{10.16}$$
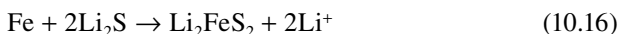
whereas region a is associated to the reversible insertion/deinsertion of lithium in the Li_2FeS_2 host, complicated by phase change. The phase evolution of the system is schematized in Figure 10.10. In the first step, iron metal is oxidized to Fe^{2+} at the Fe/Li_2S interface (I) and a Li_2FeS_2 layer is formed in that interface:

$$(Fe)_I \rightarrow (Fe^{2+})_I + 2e^- \tag{10.17}$$

$$(Fe^{2+})_I + 2(Li_2S)_I \rightarrow (Li_2FeS_2)_I + 2Li^+ \tag{10.18}$$
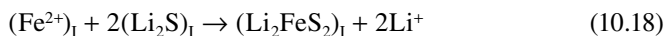
Here, Li^+ ions are released, whereas two interfaces, Fe/Li_2FeS_2(II) and Li_2FeS_2/Li_2S(III), are generated. Fe^{2+} cations formed at interface II migrate and diffuse through lattice defects in the Li_2FeS_2 phase until they reach interface III, where they react with Li_2S:

$$(Fe)_{II} \rightarrow (Fe^{2+})_{II} + 2e^- \tag{10.19}$$

$$(Fe^{2+})_{II} \rightarrow (Fe^{2+})_{III} \tag{10.20}$$

$$(Fe^{2+})_{III} + 2(Li_2FeS)_{III} \rightarrow (Li_2FeS_2)_{III} + 2Li^+ 2e^- \tag{10.21}$$

This step continues until all iron particles electrically connected to the current collector react with Li_2S particles. This produces a thickening of the intermediate layer of Li_2FeS_2. When a given threshold thickness is reached, a potential jump appears,
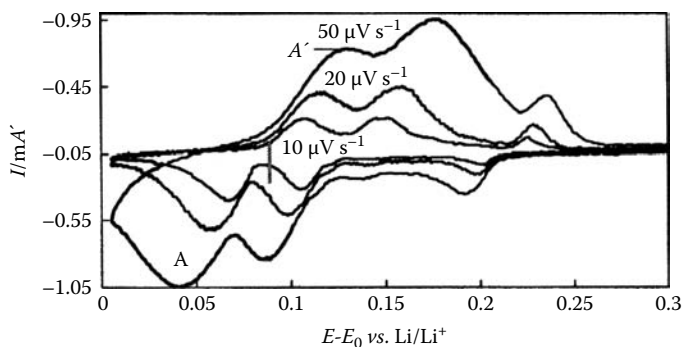
FIGURE 10.11 CVs at different sweep rates for composite graphite electrode immersed into 1 M $LiPF_6$ in 1:3 ethylene carbonate plus dimethylcarbonate mixture. The region between 0.080 and 0.085 V corresponds to the almost complete $LiC_{12} \rightarrow LiC_6$ interphase transition. (From Levi and Aurbach, 2007. *J. Solid State Electrochem.* 11, 1031–1042, with permission from Springer.)

due to the transport limitations of Fe^{2+} in Li_2FeS_2. Final steps lead to the formation of a layer of $Li_{2-x}FeS_2$, in which Fe^{2+} is oxidized to Fe^{3+} coupled to deinsertion of lithium ions, and a change in iron occupancy at an advanced stage of the reaction (Blandeau et al., 1987).

The charging and discharging processes of lithium batteries involve the transfer of Li^+ from one ion insertion electrode to another. This process can be regarded as a topotactic intercalation reaction of Li^+ ions into interstitial sites in the crystalline host matrices, eventually accompanied by first-order phase transitions. Electrochemical detection of such phase transitions is conditioned by slow solid-state diffusion of ions into the solid matrix and uncompensated ohmic drops. Phase transition can be associated to the two-peak response in CVs such as those shown in Figure 10.11, corresponding to a composite graphite electrode immersed into $LiPF_6$/(ethylene carbonate plus dimethylcarbonate) electrolyte. Figure 10.12 depicts the electrochemical conversion of $LiC_{12} \rightarrow LiC_6$. The most singular picture of the phase transition/insertion process is provided by chronoamperometric curves such as shown in Figure 10.13, corresponding to the intermittent titration of graphite electrode across the major
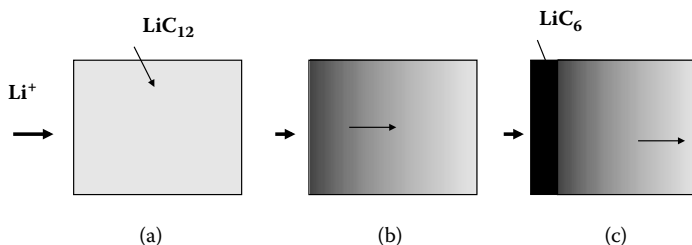
FIGURE 10.12 Schematic representation for the advance of a moving boundary during the electrochemical conversion of LiC_{12} into LiC_6 following the description of Levi and Aurbach (2007). It is assumed that lithium ions from the electrolyte (left) intercalate into the LiC_{12} phase.
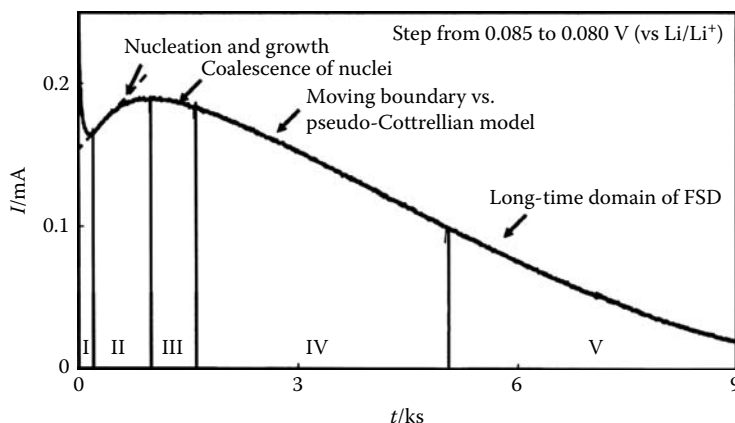
FIGURE 10.13 Current/time curve for the intermittent titration of graphite electrode across the major intercalation peak for $LiC_{12} \rightarrow LiC_6$ transition, potential step from 0.085 to 0.080 V. Electrolyte: 1 M $LiPF_6$ in 1:3 ethylene carbonate plus dimethylcarbonate mixture. (From Levi and Aurbach, 2007. *J. Solid State Electrochem.* 11, 1031–1042, with permission from Springer.)

intercalation peak for $LiC_{12} \rightarrow LiC_6$ transition, potentiostatic titration between 0.085 and 0.080 V (Levi and Aurbach, 2007). Here, the low mass film of powdery composite electrodes in a coin-type cell configuration, in contact with a small amount of $LiPF_6$ in ethylene carbonate plus dimethylcarbonate electrolyte, was used to improve data resolution.

Five regions, labeled I–V, can be distinguished in the chronoamperometry (CA) curve in Figure 10.13: At short times (region I), double-layer charging is accompanied by saturation of the initial phase, LiC_{12}, with Li^+ ions. Here, nuclei with a subcritical size are formed, further undergoing coalescence to form larger size, supercritical nuclei, a well-known phenomenon in metal deposition electrochemistry (Simmons et al., 1997). In region II, the current increases almost linearly with time, a process that can be associated to the growth of supercritical nuclei, overlapping with each other and finally forming a continuous layer. The coalescence of nuclei of the new phase (region III) determines the end of the growth of the total surface area. The current decreases through region IV, where the boundary between the two coexisting phases advances toward the electrode bulk (see scheme depicted in Figure 10.12). Finally, the current decreases monotonically when the electrode reaches equilibrium with lithium ions in the solution at the applied potential (region V). The current decrease in region IV can be interpreted by two alternative models: a quasi-Cottrellian approach and a progressive boundary motion model. In the quasi-Cottrellian approach, it is assumed that the quotient between the charge passed at time t' after the maximum current, $Q_{t'}$, and the total charge passed at infinite time, Q_∞, are proportional to the square root of time:

$$\frac{Q_{t'}}{Q_\infty} = 4\left(\frac{Dt'}{\pi a}\right)^{1/2} \tag{10.22}$$

assuming that diffusion of lithium ions (with diffusion coefficient D) occurs from two opposite edges of a particle of size a. In the moving boundary model, the Q_t/Q_∞ ratio becomes:

$$\frac{Q_{t'}}{Q_\infty} = 2\gamma(D_{phase}t)^{1/2} \tag{10.23}$$

where D_{phase} is the diffusion coefficient for the propagating phase and γ is a numerical coefficient whose value approaches 0.52 (Levi and Aurbach, 2007). Diffusion influences notably EIS responses for this kind of system (Dell'Era and Pasquali, 2009). When conditions of semi-infinite diffusion hold, the Nyquist plot comprises a semicircle followed by a linear branch. When the thickness of the stagnant layer is finite (transmissive finite diffusion), two semicircles are obtained, while if transmission takes place at a limited distance (reflective finite diffusion), two consecutive linear regions follow to the high-frequency semicircle (Kuang et al., 2009) (see Figure 10.14).

10.5   FUEL CELLS

Fuel cells can be defined as energy-producing devices where chemical energy from a fuel and an oxidant is directly converted into electricity and heat, without involving combustion cycles, generally involving a steady-state electrode-electrolyte system. In contrast with batteries, closed systems that chemically store electrical energy, fuel cells can be described as open systems that can operate continuously by maintaining the appropriate flow of reactants. Here, the electrodes act as catalysts for the overall fuel oxidation reaction, also in contrast with batteries, where the electrodes react during charge/discharge cycles. Fuel cells provide advantages with respect to other energy conversion systems by virtue of their high efficiency, environmental safety, and possibility of recovering exhaust heat.

If the fuel cell system is in thermal and mechanical equilibrium and operates at constant pressure and temperature, through a chemical reaction whose changes of free energy, enthalpy end entropy are, respectively, ΔG, ΔH, and ΔS, the intrinsic maximum efficiency, η_t, is given by:

$$\eta_t = \frac{\Delta G}{\Delta H} = 1 - \frac{T\Delta S}{\Delta H} \tag{10.24}$$

The theoretical efficiency in such systems is close to unity, but in practice, the practical efficiency is significantly lower. This is attributable to the different mechanical and thermal losses in the system but also to the direct chemical reactions between the reactants and secondary electrochemical reactions in the cell. The voltage efficiency of the cell, η_v, is defined as the quotient between the cell voltage, V, at a given cell current, I, and the cell voltage at open circuit, V_r (the maximum value of the cell voltage, equivalent, if the cell is in equilibrium, to the reversible cell potential, E_f):

$$\eta_v = \frac{V}{V_r} \tag{10.25}$$
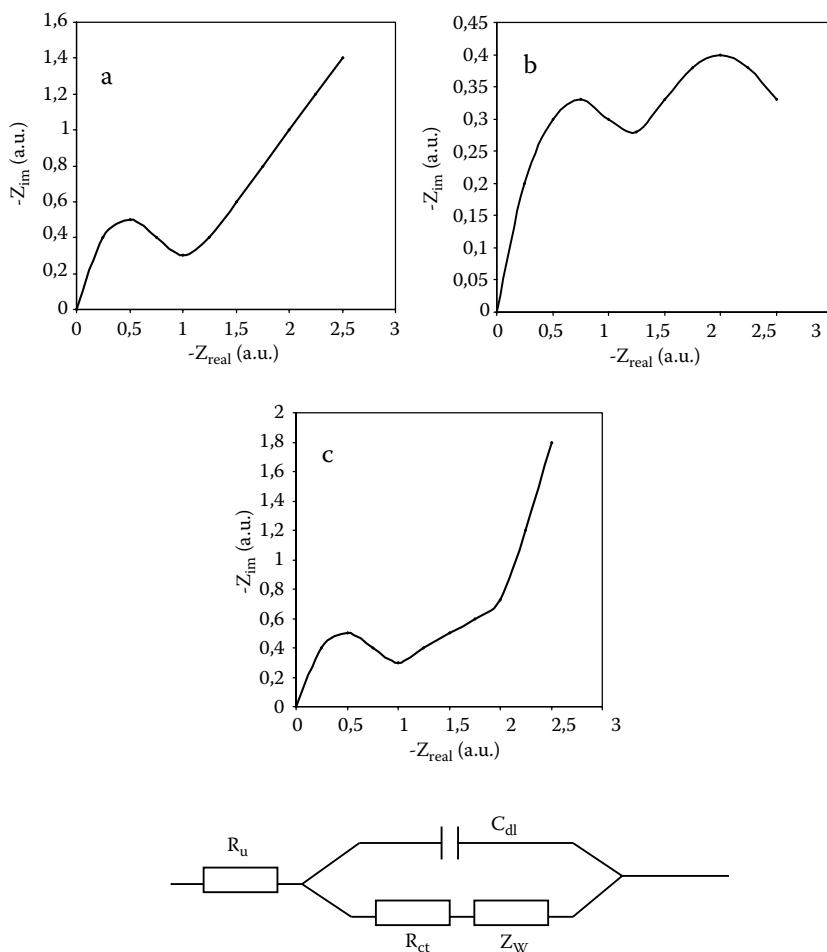
FIGURE 10.14   Nyquist responses for (a) semi-infinite diffusion; (b) transmissive finite diffusion, and (c) reflective finite diffusion, using the equivalent circuit represented below.

It should be noted that, in general, the electrochemical equilibrium is not fully attained in fuel cells. Then, stationary open circuit potentials reached in fuel cells are not equilibrium potentials. When the electrodes are connected through an external circuit, a current flows and the cell voltage departs from the stationary open circuit value, a situation generically labeled as polarization of the cell. All phenomena leading from the departure of the equilibrium potential of the cell are also termed polarization phenomena.

The faradaic efficiency, η_f, is defined as the quotient between the cell current and the theoretical cell current, I_m, calculated by assuming that the reactants are completely consumed and that reactions do not take place:

$$\eta_f = \frac{I}{I_m} \tag{10.26}$$

The overall efficiency of the cell, η_c, is taken as the product between the three efficiencies described above:

$$\eta = \eta_t \eta_v \eta_f \qquad (10.27)$$

The so-called polarization of a fuel cell can be attributed to different phenomena, each one being, in general, quantified by an overpotential. Three main types of over-potentials can be considered:

1. Activation overpotential, due to the existence of slow charge transfer steps in the electrochemical reaction.
2. Concentration overpotential, due to slow diffusion processes in the electro-lyte. This arises, in particular, in porous gas diffusion electrodes.
3. Resistance overpotential, associated to the difference of potential arising between the ends of resistive components of the cell. This can be minimized by using highly conductive electrolytes, electrodes of high area, and small interelectrode gap.

Typical polarization curves are represented in Figure 10.15, corresponding to nanoscale membrane assemblies based on porous anodic alumina functioning in a H_2/O_2 fuel cell (Bocchetta et al., 2007). In the region of low current, activation con-trol predominates, whereas in the central, essentially linear region of the diagram, ohmic control exists. Finally, in the region of almost constant current, mass transfer
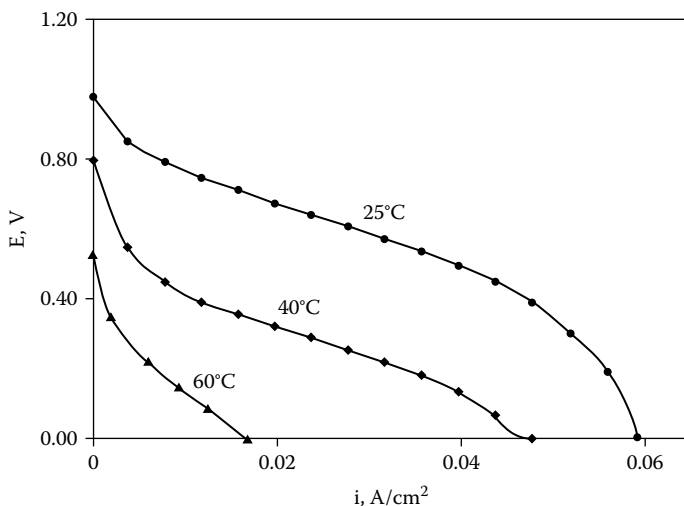
FIGURE 10.15 Polarization curves (E cell voltage) at different cell temperatures recorded under linear potential scan conditions (sweep rate, 5 mV/sec) for a 5-cm^2 H_2/O_2 fuel cell working with membrane assemblies based on porous anodic alumina. (From Bocchetta et al., 2007. *J. Solid State Electrochem.* 11, 1253–1261, with permission from Springer.)
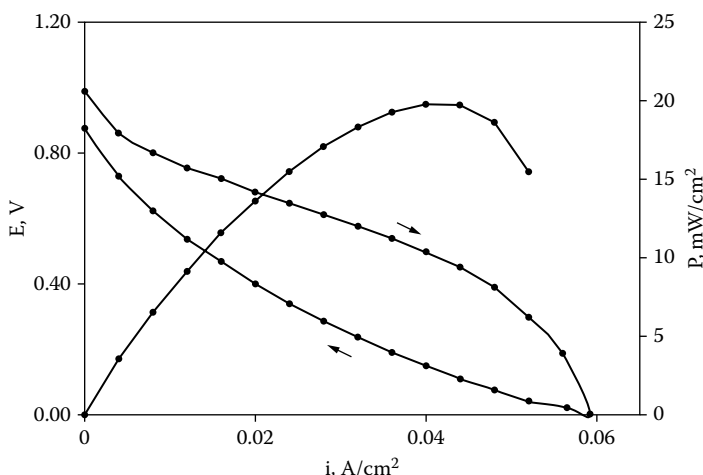
FIGURE 10.16 Polarization curve (*E* cell voltage) at 25°C and power density (*P*) recorded under linear potential scan conditions (sweep rate 5 mV/sec) for a 5 cm^2 H$_2$/O$_2$ fuel cell working with membrane assemblies based on porous anodic alumina. (From Bocchetta et al., 2007. *J. Solid State Electrochem.* 11, 1253–1261, with permission from Springer.)

control exists. Figure 10.16 shows the variation in power density (*P*, W/cm^2), with current density recorded under linear potential scan conditions for the above fuel cell working at 25°C. The maximum performance is obtained in the central current density region.

Taking into account the different existing activation and resistive limitations, the cell voltage can be expressed as:

$$V = V_r - |\eta_a| - |\eta_c| - IR_{tot} \tag{10.28}$$

Here, R_{tot} represents the total resistance of all ohmic components in the cell, whereas η_a and η_c represent the overpotentials of the anodic and cathodic reactions, respectively.

Fuel cells are usually classified according to their electrolyte and working temperature. The main types are alkaline fuel cells (AFCs), polymer electrolyte fuel cells (PEFCs), direct methanol fuel cells (DMFCs), phosphoric acid fuel cells (PAFCs), molten carbonate fuel cells (MCFCs), and solid oxide fuel cells (SOFCs), whose essential characteristics are listed in Table 10.1. Different fuels have been used, mainly hydrocarbons, natural gas and biogas, hydrogen, and alcohols. Oxygen from air is the main oxidant agent, although other oxidants, such as CO$_2$/oxygen/air mixtures and chlorine and chlorine dioxide, have been tested.

In proton exchange membrane fuel cells, perhaps the most divulgate type of fuel cells, a proton-conducting polymer membrane acts as the electrolyte separating the anode and cathode sides. Porous anaodic alumina (Bocchetta et al., 2007) and mesoporous anastase ceramic membranes have been recently introduced in this field (Mioc et al., 1997; Colomer and Anderson, 2001; Colomer, 2006).
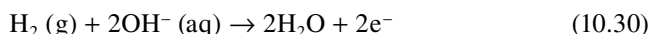
TABLE 10.1
Main Types of Fuel Cells

Type of Fuel	Electrodes	Electrolyte	Primary Fuel	Operation Temperature (ºC)
Alkaline (AFC)	Metal or carbon	NaOH/KOH	Hydrogen	60–90
Polymer electrolyte (PEFC)	Pt on carbon	Polymeric membrane	Reformate hydrogen	80–110
Direct methanol (DMFC)	Pt on carbon	Polymeric membrane	Methanol	80–110
Phosphoric acid (PAFC)	Pt on carbon	H_3PO_4	Reformate hydrogen	160–200
Molten carbonate (MCFC)	Ni + Cr	Li_2CO_3-K_2CO_3	H_2/CO reformate	600–800
Solid oxide (SOFC)	Ni/Y_2O_3-ZrO_2	ZrO_2 doped with Y_2O_3	H_2/CO/CH_4 reformate	800–1000

Source: Data taken from Alcaide et al., 2004.

SOFCs are based on the use of doped metal oxides. Remarkably, there is production of chemicals in the fuel cell in the course of its operation, so that it can also be considered an electrosynthetic reactor. Formally, the anodic reaction produces the electrons that flow through the external circuit toward the cathode, where they are transferred to the cathodic reactant. The cathode reaction can be written as:

$$O_2 (g) + 2H_2O + 4e^- \rightarrow 4\ OH^- (aq) \tag{10.29}$$

whereas the anode reaction can be represented as:

$$H_2 (g) + 2OH^- (aq) \rightarrow 2H_2O + 2e^- \tag{10.30}$$

Thermal and mechanical stability and oxygen ionic conductivity are general requirements for materials that can be used as electrode materials in SOFCs. Increase in stability and reduction of costs require lowering of the operation temperature. However, this prerequisite is accompanied by an increase of electrode polarization, which may be critical for the overall performance (Tsipis and Kharton, 2008). This is because the apparent activation energies for the interfacial processes are, in general, higher than those for oxygen ionic transport in solid electrolytes (Yamamoto, 2000). The reduction of the working temperature results in a lower oxygen vacancy concentration with concomitant increase of the role of ionic conductivity of electrode material.

As cathode materials, one can cite perovskite-type manganites, $(Ln,A)(Mn)O_{3\pm\delta}$ (Ln = La-Yb or Y; A = Ca, Sr, Ba, Pb), ferrites, $(Ln,A)FeO_{3\pm\delta}$, cobaltites, (Ln,A)

$CoO_{3\pm\delta}$, nickelates, and cuprates (Yu and Fung, 2003; Gasik, 2008). Perovskite-type manganites show high electrical conductivity, substantial electrocatalytic activity toward oxygen reduction at temperatures above 1000–1100 K and moderate thermal expansion coefficients, predominant electronic conductivity, and low oxygen ion diffusivity, with transport properties and electrochemical activity being dependent on oxygen nonstoichiometry. Here, electrocatalytic activity under high cathodic polarization is usually correlated with the generation of oxygen vacancies in the electrode surface. Doping with acceptor species, in general, leads to an increase in the p-type conductivity and electrochemical activity of $Ln_{1-x}A_xMnO_{3\pm\delta}$ manganites. Ferrites, in general, exhibit higher electronic or mixed conductivity than manganites but provide high thermal expansion coefficients due to oxygen losses at elevated temperatures and may lead to thermochemical incompatibility with common solid electrolytes. Oxygen diffusivity is enhanced by extensive acceptor doping, but this is usually accompanied by increasing thermal and chemical expansion due to weakening of metal-oxygen bonds and rising the atomic vibration unharmonicity (Tsipis and Kharton, 2008).

Perovskite-related cobaltites show better cathodic and transport properties compared to manganites and ferrites but also higher chemical and thermal expansion. It is accepted that the performance of ferrite and cobaltite electrodes is essentially governed by the exchange processes at the electrode and electrolyte surfaces and by ion transfer across the cathode/electrolyte interface, with the bulk ionic transport in the electrode being important but less critical than the above processes. Nickelates and cuprates are also considered interesting materials, although their thermomechanical stability and compatibility with solid oxide electrolyte ceramics are, in general, lower with respect to the aforementioned materials.

Manganite-, cobaltite-, and ferrite-based perovskites, however, cannot be thermodynamically stable under anodic conditions. The most common materials for anodes consisted of ceramic-metal composites (cermets) containing yttria-stabilized zirconia (YSZ) and Ni or other metals. In such systems, the metallic phase acts as electronic conductor and catalyst. Here, composite layers should provide percolation paths for electrons, oxygen ions, and gas, so that the electrochemical performance of the anode material is strongly dependent on its microstructure. The YSZ fraction in the composite, its porosity, and the sizes of the Ni and YSZ particles play a crucial role in determining the properties of the electrode. For cermets having components with similar grain sizes, the percolation threshold is expected to correspond to a ca. 30% v/v of metallic phase (Sunde, 1996). Microstructural differences are important in this context. It should be noted that, at elevated temperatures, Ni-YSZ cermets with high metal content experience fast degradation due to coarsening of metal particles. Problems due to microtructural reconstruction, strains, and failure, accompanied by rising overpotentials during redox cycling, are also associated to high metal contents in these composites.

Doped cerias have also been extensively used as anodes in SOFC cells. The main advantage of such materials is the high catalytic ability of ceria with regard to combustion reactions involving oxygen, particularly those using hydrocarbons and biogas as fuels. Reduced $CeO_{2-\delta}$ materials possess a significant amount of mixed oxygen ionic and n-type electronic conductivity, properties that can be enhanced

by acceptor-type doping (Kharton et al., 2001). An additional metal has to be added because the electronic conduction in cerias is lower than necessary to avoid critical ohmic losses and/or current constriction effects on the overall anodic polarization. Other materials, namely, spinels, fluorites, pyrochlores, and molybdates, among others, have been proposed for SOFC anodes.

Composite cathode materials, surface modification of solid electrolytes and electrodes, insertion of nano-sized particles of catalysts, and application of oxide-activating agents onto the electrode surface, recently reviewed by Tsipis and Kharton (2008), are strategies for improving the overall electrochemical performance of fuel cells. There is a growing interest in preparing porous anodes with gas permeability, chemical stability, mechanical resistance, high electrical conductivity, and high thermal shock resistance.

Theoretical modeling of porous cermets can be ascribed to two general approaches simulating random packing of particles (Monte Carlo simulations) and via macroscopic averaged models in terms of corrugated layers covered by a thin electrolyte film or vice versa (Sunde, 1997).

DMFCs are based on the electrochemical oxidation of methanol at an anode. The main problem is the disposal of a suitable catalyst for the complete oxidation of methanol to CO_2:

$$CH_3OH + H_2O \rightarrow CO_2 + 6H^+ + 6e^- \tag{10.31}$$
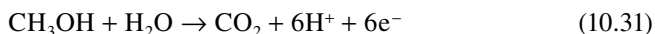
Intensive research is currently being carried out to obtain efficient catalysts for this reaction. Most of the research is devoted to different metal (Pt, in particular)-based materials, but several approaches include porous materials such as Ni-impregnated zeolites, obtained from soaking of zeolites in, for instance, $NiSO_4$ solutions (Abdel Rahim et al., 2006). The performance of gold-zeolite–modified electrodes toward electrocatalytic oxidation of ethanol, an alternative to methanol fuel, has been recently reported by Ouf et al. (2008).

10.6 ELECTROCOGENERATION

There is a continuously growing interest in the development of cogenerative fuel cells, fuel cells involving generation of useful chemicals. The cogeneration processes require favorable thermodynamic and kinetic conditions. Such systems involve a conventional fuel cell, an external circuit for using electrical energy, and a system for recovering the useful chemicals produced (Alcaide et al., 2004). Ideally, this methodology can be extended to portable devices.

The use of porous materials attracts a significant part of research efforts because of their ability to provide electrodes with high specific area and their capacity for storing reaction products (gaseous products, in particular).

One remarkable aspect is that, frequently, a variety of products result from electrochemical reactions in the fuel cell, so that selectivity for a given product is another factor to be considered in cell design. For instance, SOFC cells using bismuth
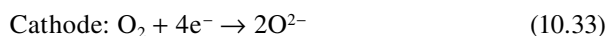
TABLE 10.2

Some Examples of Cogenerative Processes in Fuel Cells Involving the Use of Porous Materials

Electrode	Anode Reaction	Cathode Reaction	Type of Fuel Cell/Source
Porous Pt	$C_4H_8 + H_2O \rightarrow$	$O_2 + 4H^+ + 4e^- \rightarrow 2H_2O$	AFC[a]
		$CH_3COC_2H_5 + 2H^+ + 2e^-$	
Porous Pt	$H_2 \rightarrow 2H^+ + 2e^-$	$C_6H_6 + 6H^+ + 6e^- \rightarrow C_6H_{12}$	AFC[b]
Active carbon	$H_2 \rightarrow 2H^+ + 2e^-$	$O_2 + 2H^+ + 2e^- \rightarrow H_2O_2$	AFC[c]
$(Bi_2O_3)_{0.85}(La_2O_3)_{0.15}$	$2C_3H_6 + 3O^{2-}$	$O_2 + 4e^- \rightarrow 2O^{2-}$	SOFC[d]
	$\rightarrow C_6H_6 + 3H_2O + 6e^-$		
$ZrO_2(Y_2O_3)$	$PhCH_2CH_3 + O^{2-} \rightarrow$	$O_2 + 4e^- \rightarrow 2O^{2-}$	SOFC[e]
	$PhCH = CH_2 + H_2O + 2e^-$		

Source: Data taken from: [a]Langer and Colucci-Rios (1985), [b]Langer and Yurchak (1969), [c]Yamanaka et al. (2002), [d]Di Cosmo et al. (1986), [e]Michaels and Vayenas (1984). See also Alcaide et al. (2004).

oxide–based catalysts can produce the oxidative dehydrogenation of propylene to 1,5-hexadiene and benzene via the following reactions (Jiang et al., 1994):

$$\text{Anode: } C_3H_6 + O^{2-} \rightarrow C_3 \text{ dimers} + 2e^- \qquad (10.32)$$

$$\text{Cathode: } O_2 + 4e^- \rightarrow 2O^{2-} \qquad (10.33)$$

The cell operates at 600ºC under atmospheric pressure and provides a selectivity of 77% for the production of 1,5-hexadiene and benzene at 3.2% conversion.

A variety of cogeneration processes has been recently described in the literature. A brief list is shown in Table 10.2, where representative examples involving porous materials and different types of fuel cells are included. In most cases, electrocogeneration allows for a simultaneous removal of organic pollutants and flue gas emissions. Examples of this possibility will be treated in Chapter 12.

11 Magnetoelectrochemistry and Photoelectrochemistry of Porous Materials

11.1 MAGNETOELECTROCHEMISTRY

The term *magnetoelectrochemistry* refers to the study of electrochemical phenomena under the application of magnetic fields. The influence of magnetic fields on electrochemical reactions is well known and involves from metal electrodeposition to electropolymerization (Fahidy, 1999). Conversely, magnetic fields can be induced by electrochemical reactions (Juzeliūnas, 2007). The effect of magnetic fields on electrochemical processes in solution phase is threefold: (1) may cause energy-level splitting in radicals (Zeeman effect); (2) may bring about diamagnetic orientation of aromatic molecules; (3) may cause convection in the electrolytic solution (magneto-hydrodynamic effect.

From the seminal work of Fahidy (1983), the magnetohydrodynamic effect has been studied by several authors (Waskaas, 1993, 1996, 1997; O'Brien and Santhanam, 1997; Ragsdale et al., 1996, 1998). This effect is explained in terms of a gradient of paramagnetic ions in the vicinity of an electrode surface; i.e., in terms of magneto-convection. More recently, Waskaas and Kharkats (1999) have suggested that the magnetic field will cause a transport of all ions because of the difference in the magnetic susceptibility in the solution at the electrode surface. Lorentz force (F_B) due to moving charges in an electrolyte solution can be expressed as:

$$\vec{F}_B = (nz_+ e\vec{v}_+ + nz_- e\vec{v}_-) \times \vec{B} \tag{11.1}$$

where B denotes the externally applied magnetic field, z_+, z_-, are the formal charge of ions, and v_+, v_-, their respective velocities. Notice that although the velocities and positive and negative mobile charges point in opposite directions, the corresponding charges have opposite signs. Accordingly, cations and anions experience magnetic forces in the same direction. The average low-field magnetic moment per magnetic dipole of a given species, j, with spin ½ (including common organic radicals) is given by

$$\overrightarrow{<m>}_j = \left(\frac{g\mu_B}{2}\right)^2 \frac{\vec{B}}{kT} \tag{11.2}$$

مرجع دانشجویان و مهندسین مواد

In this equation, g is the Lande factor and μ_B is the Bohr magneton. The total paramagnetic force acting on the unit volume element, F_{pm}, is given by:

$$\vec{F}_{pm} = N_A \left(\frac{gm_B}{4} \right)^2 \left(2c_j \frac{\vec{B} \cdot \nabla \vec{B}}{kT} + \frac{|\vec{B}|^2}{kT} \nabla c_j \right) \tag{11.3}$$

Here, c_j designates the concentration of radical species and N_A is Avogadro's number. The first term in the above equation describes the field gradient paramagnetic force exerted in areas where the magnetic field gradient is ≠0, typically occurring in the vicinity of ferromagnetic particles (Leventis et al., 2007). The second term in Equation (11.3) describes the effect due to the presence of gradients in the concentration of radical species. This occurs, for instance, in the diffusion layer during electrochemical experiments and can be obscured by other phenomena like convection (Leventis et al., 2007).

In the context of the electrochemistry of porous materials, it can be expected that application of magnetic fields can promote alterations in charge transport through materials, electrolyte, and interfaces, and eventually, variations in the orientation of guest molecules potentially able to be reflected in the electrochemical response of the materials. The effect of static magnetic fields effects on the electrochemistry of bipyrylium bication [1,4-bis(3,5-diphenyl-4-pyrylium)phenylene] (=BTP^{2+}) associated to zeolite Y and MCM-41 mesoporous aluminosilicate (BTP@Y and BTP@ MCM, respectively) has been described by Doménech et al. (2005c). Molecular modeling indicates that the BTP^{2+} bication cannot be accommodated in a single cavity of zeolite Y and should occupy two neighboring supercages. Upon attachment to polymer film electrodes immersed into Et$_4$N$^+$/MeCN and Bu$_4$N$^+$/MeCN electrolytes, BTP@MCM and BTP@Y probes provide clearly separated voltammetries. As shown in Figure 11.1, BTP@MCM displays an almost identical response in both electrolytes consisting of two main cathodic signals at 0.5 and −0.12 V versus AgCl/Ag and an additional more or less marked peak at −0.28 V. This voltammetry can be described in terms of a solution-like response consisting of two one-electron reduction processes mediated by a comproportionation reaction. The additional signal at more negative potentials can be ascribed to the reduction of BTP^{2+} species more strongly attached to the MCM matrix.

The response of BTP@Y in Bu$_4$N$^+$/MeCN is restricted to a unique reduction process near to −0.40 V, but it differs significantly in the presence of Et$_4$N$^+$. Here, two reduction processes at −0.22 and −0.36 V appear (Figure 11.2). As described in Chapter 4, this response can be associated to the presence of different boundary-associated topological redox isomers for which no significant comproportionation reaction occurs, namely,

$$\{BTP^{2+}\} + Et_4N^+ (sol) + e^- \rightarrow \{BTP^{\bullet+} \cdots Et_4N^+\} \tag{11.4}$$

$$\{BTP^{\bullet+} \cdots Et_4N^+\} + Et_4N^+ (sol) + e^- \rightarrow \{BTP \cdots (Et_4N^+)_2\} \tag{11.5}$$
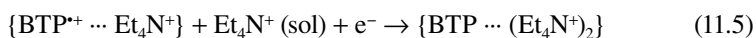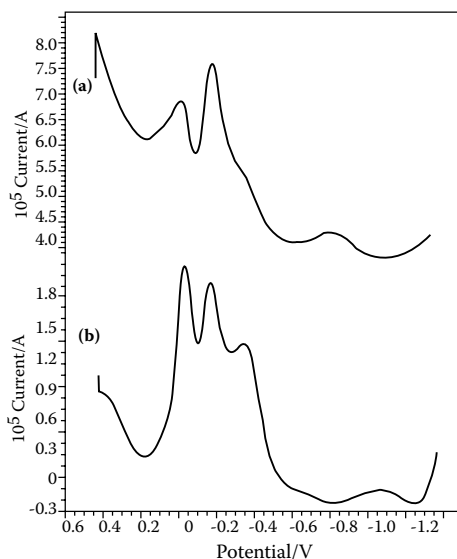
FIGURE 11.1   Square-wave voltammetries (SQWVs) for BTP@MCM immersed into (a) 0.10 M Bu_4NPF_6/MeCN and (b) 0.05 M Et_4NClO_4 + 0.10 M Bu_4NPF_6/MeCN. Potential scan initiated at 0.45 V in the negative direction. Potential step increment, 4 mV; square-wave amplitude, 25 mV; frequency, 15 Hz. (Adapted from Doménech et al., 2005. *J. Electroanal. Chem.* 577, 249–262, with permission from Elsevier.)
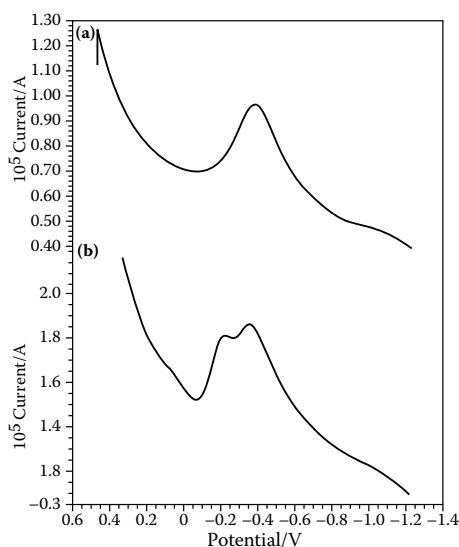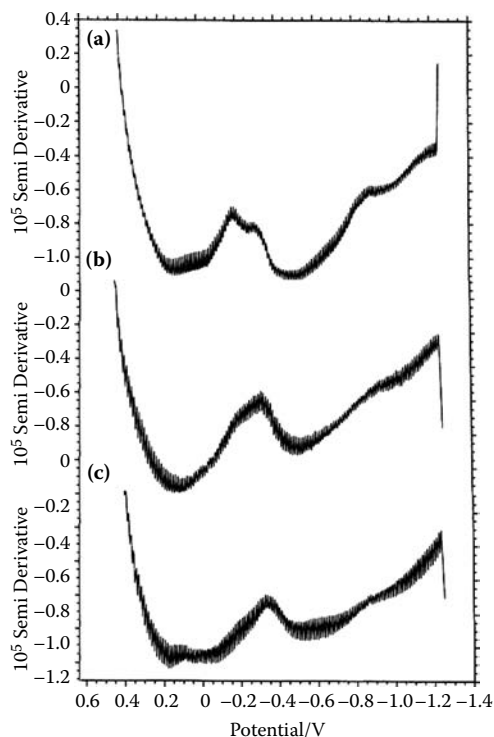

FIGURE 11.2   SQWVs for BTP@Y immersed into (a) 0.10 M Bu_4NPF_6/MeCN and (b) 0.05 M Et_4NClO_4 + 0.10 M Bu_4NPF_6/MeCN. Potential scan initiated at 0.45 V in the negative direction. Potential step increment, 4 mV; square-wave amplitude, 25 mV; frequency, 15 Hz. (Adapted from Doménech et al. 2005. *J. Electroanal. Chem.* 577, 249–262, with permission from Elsevier.)
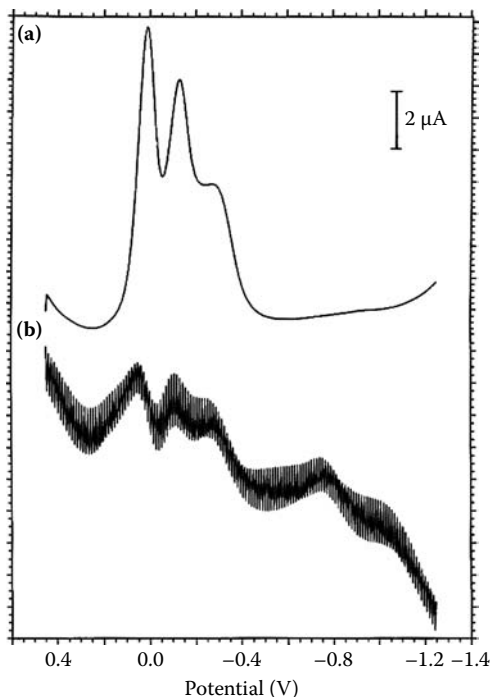
FIGURE 11.3   SQWVs for BTP@MCM immersed into 0.05 M Et_4NClO_4 + 0.10 M Bu_4NPF_6/ MeCN (a) in the absence and (b) under the application of a horizontal magnetic field of 0.2 T. Potential scan initiated at 0.45 V in the negative direction. Potential step increment, 4 mV; square-wave amplitude, 25 mV; frequency 15 Hz. (Adapted from Doménech et al., 2005. *J. Electroanal. Chem.* 577, 249–262, with permission from Elsevier.)

     Application of moderate magnetic fields (0.02–0.2 T) produces significant modifications in the voltammetric behavior of BTP@MCM and BTP@Y. As shown in Figure 11.3, corresponding to the application of a horizontal magnetic field (0.2 T) to a vertical BTP@MCM-modified electrode immersed into Et_4NClO_4 plus Bu_4NPF_6/ MeCN electrolyte, the main effect appears to be a lowering of peaks while the overall voltammetric profile becomes slightly unchanged. Similar features were obtained for BTP@Y in contact with Bu_4N^+/MeCN electrolytes. In the case of BTP@Y-modified electrodes immersed into Et_4NClO_4 plus Bu_4NPF_6/MeCN electrolytes, however, the relative height of voltammetric peaks becomes changed, apparently depending on the angle between the applied magnetic field and the electrode axis, as depicted in Figure 11.4.

     These features can be rationalized by considering the magnetoconvective effect–associated ion motion, paramagnetic effect associated with concentration gradients, and, eventually, orientation effects induced by the applied magnetic field. First of all, for BTP@MCM, the main effect due to magnetic fields is peak current variations with no significant change in relative peak currents. These features suggest that in this

FIGURE 11.4   SQWVs for BTP@Y immersed into 0.05 M Et_4NClO_4 + 0.10 M Bu_4NPF_6/ MeCN under the application of a magnetic field of 0.2 T forming angles of (a) −60°, (b) 0°, and (c) 60° with the vertical electrode axis. Potential scan initiated at 0.45 V in the negative direction. Potential step increment, 4 mV; square-wave amplitude, 25 mV; frequency, 15 Hz. (Adapted from Doménech et al., 2005. *J. Electroanal. Chem.* 577, 249–262, with permission from Elsevier.)

system, where there are no restricted ionic mobility and a solution-like response was obtained, magnetoconvection is the main factor determining changes in the voltammetric response. In the case of BTP@Y in the presence of Et_4N^+ electrolytes, however, the magnetoconvection on charge-balancing cations can be superimposed, to any extent, to orientation effects. In fact, magnetic effects appear to influence the reaction rate in conformationally constrained macrocyclic systems in the solution phase (Doménech et al., 2004f). Future developments should consider magnetically assisted electrochemical formation of porous layers and the effect of nonstationary magnetic fields because relaxation effects associated with encapsulation would be possibly detected.

11.2   PHOTOELECTROCHEMISTRY

The term *photoelectrochemistry* is in general applied to all phenomena where photon absorption is accompanied by electrochemical processes. The usual requirements for photoelectrochemical activity are (1) the semiconductor character of the electrode

material, (2) the existence of an electrolyte concentration high enough to significantly exceeding the density of charge carriers in the semiconductor, and (3) that the semiconductor should be reverse biased with respect to the solution (Bard et al., 2008).

A significant part of such systems are addressed to produce hydrogen for water, pioneered by Honda and Fujishima (1972), who discovered that water can be decomposed into H_2 and O_2 by using a photocell comprising a TiO_2 electrode under light irradiation. Due to their wide band gaps, the majority of the photocatalysts are only active under UV light irradiation, thus limiting their application for hydrogen production from water and sunlight.

For all types of cells, the position of the valence and conduction bands of the semiconductor relative to the redox energy levels of the redox couple is an important parameter with regard to estimate the efficiency of the cell in energetic terms.

As previously noted, photoelectrochemical cells involve semiconductor/electrolyte junctions. To describe this system, it should be kept in mind that for an intrinsic semiconductor at room temperature, the Fermi level (the energy value, E_F, where the probability of a level being occupied by an electron is equal to the probability of being occupied by a vacant) is at the midpoint in the band gap region between valence and conduction bands. For a doped material, the location of the Fermi level depends on the doping level and dopant concentration. Roughly, for doped n-type materials, E_F lies just below of the conduction band edge, whereas for doped p-type materials the Fermi level is located slightly above the valence band edge. E_F can be determined from measurements of work functions or electroaffinities and is usually expressed with respect to the vacuum scale of energies, i.e., taking as zero the energy for a free electron in vacuum.

When equilibrium is established between a semiconductor and an electrolyte solution, the Fermi level in both phases is equalized via charge transfer between phases. In the case of an n-type semiconductor, this implies the pass of electrons from the semiconductor to the solution phase, so that the semiconductor becomes positively charged and the electrolyte negatively charged. The excess charge in the semiconductor resides (contrary to a metal, where excess of charge resides at the surface) in a space charge region. This region can be considered as analogous to the diffuse double layer (see chapter 1) formed near the electrolyte/semiconductor junction. Then the surface region of the semiconductor (50–2000 Å) becomes depleted of majority carriers and a depletion layer is formed. This situation is represented in energy diagrams by the bending of the bands for p- and n-type semiconductors (Figure 11.5). The potential at which no charge excess exists in the semiconductor is the potential of zero charge or flat band potential, E_{FB}. It should be noted, however, that this ideal, reversible behavior of the semiconductor/electrolyte junction is rarely found, with deviations from reversibility arising by inherently slow charge transfer across the semiconductor/electrolyte interface, surface oxide formation, corrosion, etc. (Bard and Faulkner, 2001).

In ideal semiconductor/electrolyte junctions, the presence of an energetic barrier in the semiconductor phase, originated from the equilibrium of the Fermi level in the solid and liquid phases, can be approached by the semiconductor depletion layer capacitance or space charge capacitance, C_{SC}. Measurement of capacitance versus
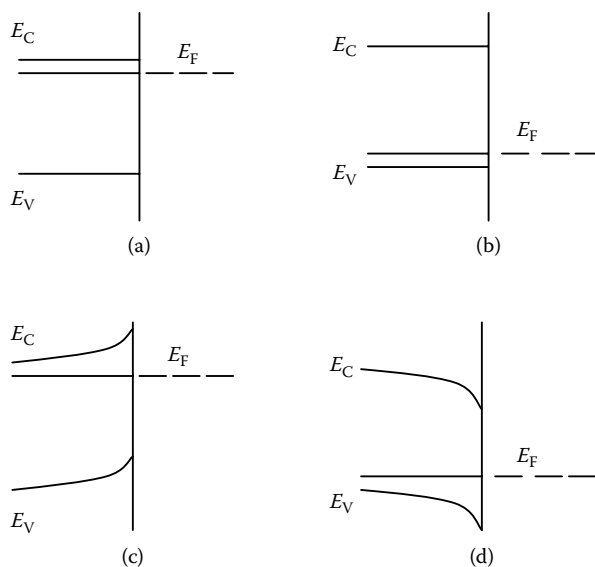
FIGURE 11.5   Energy diagrams for the semiconductor/electrolyte junction under dark conditions (a, b) before contact and (c, d) after contact and electrostatic equilibration for (a, c) n-type and (b, d) p-type semiconductors.

applied potential at a given frequency gave information regarding types of conductivity of solid electrodes and the carrier concentrations, which can be derived from capacitance measurements for electrodes in contact with aqueous electrolytes. Here, the Mott-Schottky relationship applies:

$$\frac{1}{C_{SC}^{2}} = \frac{2(E - E_{FB} - k_{B}T/e)}{\varepsilon\varepsilon_{o}N_{D}e} \tag{11.6}$$

where E represents the electrode potential, E_{FB} is the flat band potential (both relative to a given reference electrode), e is the carrier charge, N_{D} is the ionized donor or acceptor concentration, k_{B} is the Boltzmann's constant, and ε and ε_{o} are the permittivities in the medium and in vacuum, respectively. At 298 K and taking C_{SC} in farads per square centimeter, N_{D} in cubic centimeters, and all potentials in volts, Equation (11.6) becomes (Bard and Faulkner, 2001)

$$\frac{1}{C_{SC}^{2}} = \frac{\text{constant}}{\varepsilon N_{D}}(E - E_{FB} - 0.0257) \tag{11.7}$$

Mott-Schottky plots of $1/C_{SC}^{2}$ versus E using capacitance data at different applied potentials for semiconductor electrodes in contact with aqueous media
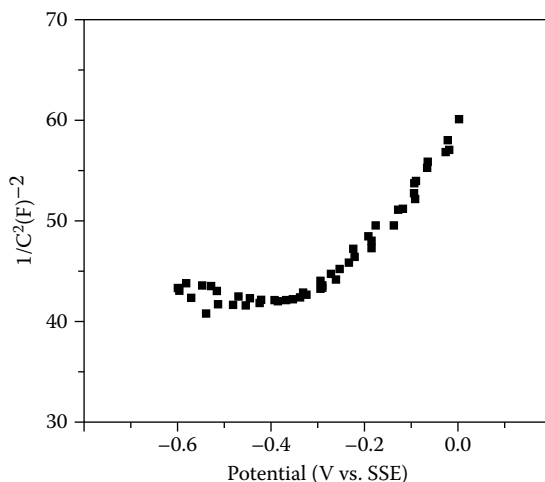
FIGURE 11.6 Mott-Schottky plots from capacitance measurements at commercial TiO_2 in contact with 0.1 M H_2SO_4. Frequency, 10 Hz; potential scan, 10 mV/sec. (From Rincón et al., 2007. *J. Solid State Electrochem.* 11, 1287–1294, with permission from Springer.)

allows to estimate the flat band potential (from the intersection with the potential axis), while the slope is proportional to the inverse of N_D. Figure 11.6 shows typical Mott-Schottky plots for commercial TiO_2 oxide in contact with 0.1 M H_2SO_4 (Rincón et al., 2007).

For the case of metal oxides and related compounds, using potentials versus SCE, the position of the valence band edge with respect to the vacuum level, E_{VB}, can be expressed as

$$E_{VB} = V_{FB} + 4.4 + \Delta E_F + V_H \qquad (11.8)$$

In this equation, the term 4.4 corresponds to the position of the SCE with respect to the vacuum level and ΔE_F represents the difference between the Fermi level and the valence band edge ($\Delta E_F = E_F - E_{VB}$), a parameter that can be estimated from thermoelectric power measurements. V_H is the Helmholtz potential between the electrode, and the solution originated from the preferential adsorption of either OH^- or H^+ ions from the solution on the metal oxide surface. V_H depends on the pH according to

$$V_H = 0.059(pH_{zc} - pH) \qquad (11.9)$$

where pH_{zc} is the pH of zero charge, a parameter that can be estimated with an accuracy of 1–2 pH units from electronegativity considerations (Koffyberg and Benko, 1982). Figure 11.7 shows the energy band scheme calculated by Koffyberg and Benko (1982) for CuO.
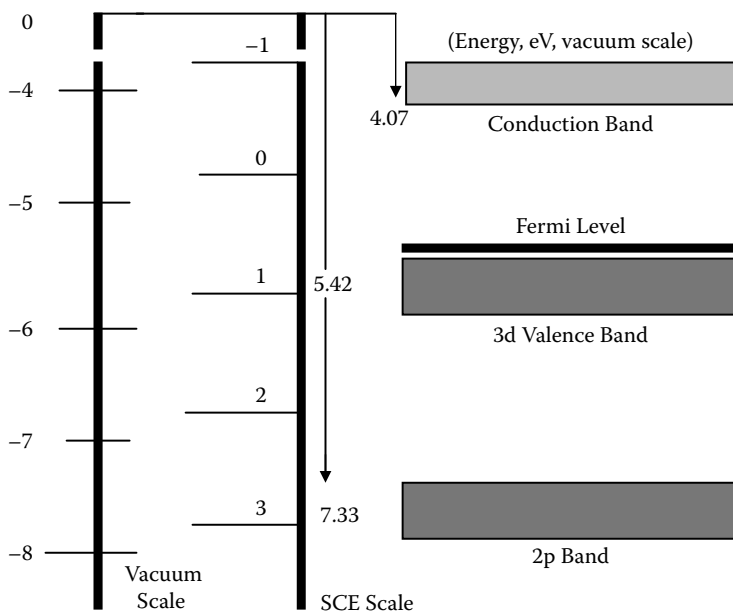
FIGURE 11.7   Energy band scheme for CuO calculated by Koffyberg and Benko (1982).

11.3   PHOTON ENERGY AND REDOX PROCESSES

When the semiconductor surface being in contact with a redox couple Ox/Red is irradiated with a light of sufficiently low wavelength (i.e., when the photon energy, $h\nu$, is larger than the band gap energy), photons are absorbed and electron-hole pairs are created. Although some electron-hole pairs are recombined, the space charge field favors their separation and promotes the oxidation process for the redox pair in solution when the electrode potential is larger than the flat band potential. As a result, the oxidation process in solution takes place at electrode potentials less positive than those required for developing this process at inert metal-conducting electrodes. Similarly, p-type semiconductors produce photoassisted electrochemical reduction processes, as schematized in Figure 11.8.

It should be noted that these effects are generally not observed at potentials for redox couples located at potentials negative (n-type semiconductors) or positive (p-type semicoductors) of the flat band potential. In these cases, the majority carriers (electrons for n-type semicoductors, holes for p-type ones) tend to accumulate near the semiconductor/electrolyte interface and the semiconductor behavior approaches that of a metal electrode.

Correlation between electrochemical and spectroscopic data usually focuses on the determination of band gap energy and the estimation of the position of upper edge of the valence band (HOMO energy) and the lower edge of the conduction band (LUMO energy). Formal electrode potentials are correlated to the vacuum level as previously indicated. In most cases, the corresponding energies, E_{HOMO}, E_{LUMO},
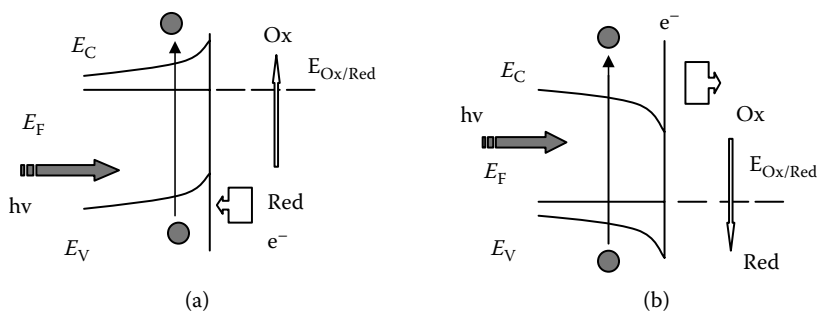
FIGURE 11.8 Schematic representation of (a) n- and (b) p-type semiconductor in contact with an electrolyte solution containing an Ox/Red redox couple under irradiation of photons with energy larger than the band gap energy.

and corresponding electrochemicalband gap can be approached by the voltammetric onset potentials from extreme oxidation and reduction voltammetric peaks, as described by Chen et al. (2000) for polymer systems. There are, however, discrepancies between band gap energies calculated from electrochemical and spectral data (Alhalasah and Rolze, 2007).

11.4 PHOTOELECTROCHEMICAL CELLS

Photoelectrochemical cells are formed by a semiconductor electrode and a suitable counterelectrode immersed into the electrolyte. Three types of photoelectrochemical cells can be distinguished. In photovoltaic cells, the reaction at the counterelectrode is simply the reverse of the photo assisted reaction occurring at the semiconductor electrode so that the cell converts radiant energy into electricity with no change in the composition of the solution or electrodes.

In photoelectrosynthetic cells, the Ox′/Red′ reaction at the counterelectrode is different than that occurring at the semiconductor electrode, Ox/Red. As a result, the overall reaction occurring in the cell is driven by light in a direction opposite that of the thermodynamically spontaneous one. Then light energy is converted into chemical energy stored in the resulting products of the electrochemical reaction. For an n-type semiconductor, this requires that the potential of the Ox/Red couple lies above the valence band edge while the potential of the Ox′/Red′ couple becomes lower than the flat band potential.

Finally, in photocatalytic cells, the reaction, which is kinetically hindered, is conducted in its thermodynamically spontaneous direction by applying an external potential bias to the cell, with the light providing the necessary activation energy for the process. Here, the location of the potentials of the Ox/Red and Ox′/Red′ couples is inverse to the case of photoelectrosynthetic cells.

Because the light used for photoelectrochemical processes must have photon energy greater than the band gap of the semiconductor, UV irradiation is needed

in most cases. A strategy for using visible light is the sensitization of the semi-conductor with a layer of a photomediator (typically, dyes), which is capable of absorbing visible light. The photonically excited mediator injects an electron in the semiconductor band, thus becoming oxidized. If a suitable redox couple exists in the adjacent electrolyte solution, the original mediator form is regenerated via electron exchange with species in solution. This can be described as the sequence of react ions:

$$\{Med\} + h\nu \rightarrow \{Med^+\} + e^- \tag{11.10}$$

$$\{Med^+\} + Red \rightarrow \{Med\} + Ox \tag{11.11}$$
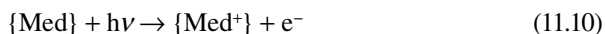
Here, { } denote the layer of mediator deposited over the semiconductor surface.

Figure 11.9 compares the energy levels for CdS and $LaMnO_3$ in water at pH = 14 (Kida et al., 2003). Under illumination, photogenerated electrons in the conduction band of CdS can react with water to produce hydrogen. This is not the case for $LaMnO_3$ because the conduction band edge of this material is more positive than the H_2/H_2O redox potential.

Apart from oxides such as TiO_2, ZnO, and ZrO_2, sulfides (typically CdS), nio-bates, tantalates, titanates, and other compounds have been tested as photocatalytic materials for splitting water. Composites (Kida et al., 2003; Rincón et al., 2007) and porous materials (Velaski et al., 2006) have been introduced as electrode materials in photovoltaic cells in the last years.
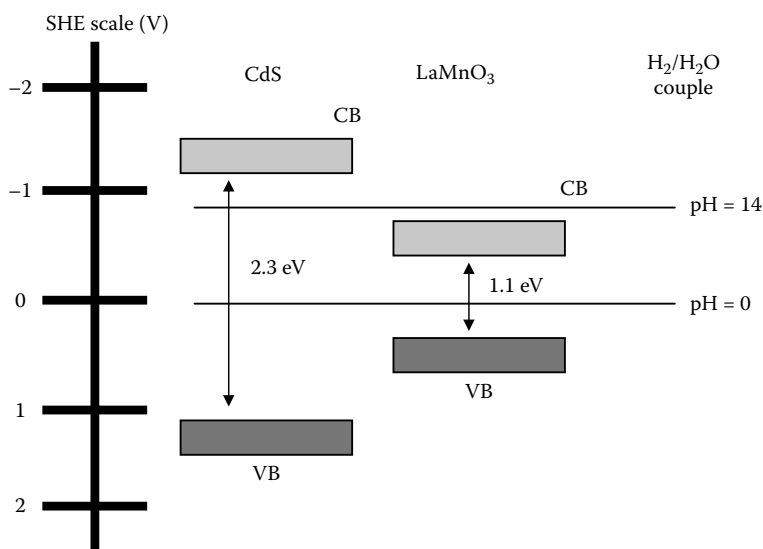
FIGURE 11.9   Energy levels for CdS and $LaMnO_3$ following Kida et al. (2003). CB, conduction band; VB, valence band.

11.5   ELECTROCHEMICALLY INDUCED LUMINESCENCE AND ELECTROCHROMIC MATERIALS

Another interesting phenomenon is producing luminescence from electrochemical reactions. This can be achieved by doping crystalline metal oxides and related materials or anodic metal oxide layers (Meulenkamo et al., 1993) or depositing organic molecules onto nanostructured porous materials such silicon (Martín et al., 2006).

Electrochromic materials are of interest for displays, smart windows, sunroofs, etc., and are characterized by the reversible change in their color upon application of light or electrical inputs. The electrochromic effect is generally associated with the ingress/issue of electrons and metal cations.

Typical electrochromic materials are oxides that can be colored anodically (IrO_2, Rh_2O_3, NiO_x) or cathodically (MoO_3, WO_3, TiO_2). A typical example is that of tungsten (VI) oxide. This compound is transparent when forming thin films. Upon electrochemical reduction, W^V sites are generated to give an electrochromic material:

$$\{W^{VI}O_3\} + xM^+ + xe^- \rightarrow \{M_xW^V_xW^{VI}_{1-x}O_3\} \tag{11.12}$$
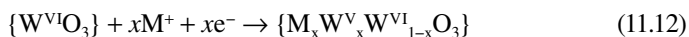
At low x values, the films acquire a blue coloration caused by intervalence charge transfer between adjacent W^V and W^{VI} sites. At higher x values, irreversible insertion occurs, yielding a metallic "bronze" (Bard et al., 2008).

Since the electrochromic properties are strongly related with the ability of the base material for incorporating doping ions, the synthesis of porous materials is receiving a growing interest. Tested materials include anastase films and amorphous TiO_2 (Ohtsuka et al., 1987). Figure 11.10 shows a diagram for an electrochromic device assembled by separating indium-doped tin oxide (ITO)/glass and TiO_2/ITO/glass junctions by means of a spacer and filling the volume between the two electrodes with the electrolyte (Lin et al., 2008). The optical transmittance spectra of different
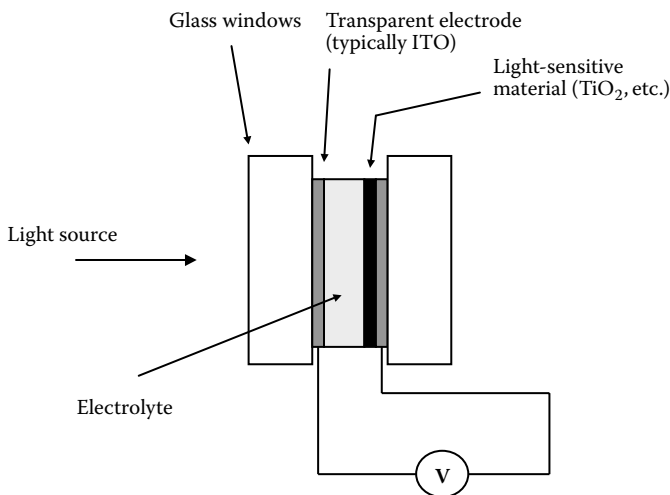
FIGURE 11.10   Schematics for a typical electrochromic device.
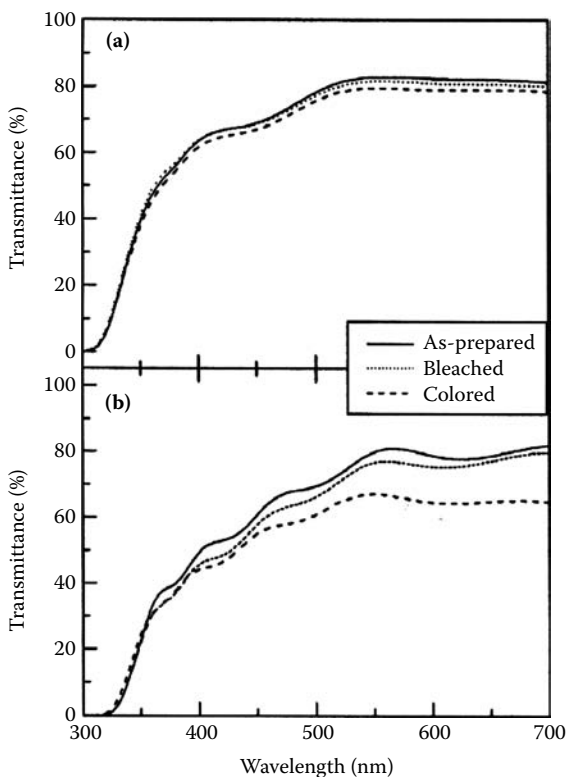
FIGURE 11.11   Transmittance spectra of (a) 100- and (b) 350-nm-thick pristine TiO_2 thin films heated at 300°C for 10 min. (From Lin et al., 2008. *J. Solid State Electrochem.* 12, 1481–1486, with permission from Springer.)

films in the 350- to 700-nm wavelength range are shown in Figure 11.11. One can observe that the transmittance at 550 nm varies significantly from the bleached to the colored (blue) state; this last state was reached upon Li^+ insertion. Cyclic voltammograms of such films in contact with 1 M $LiClO_4$/propylene carbonate show a reduction peak at −3.8 V versus AgCl/Ag and an oxidation peak at ca. −0.10 V associated to the Li^+ insertion/deinsertion processes (Figure 11.12). The electrochromic efficiency at a given wavelength, $\eta(\lambda)$, can be calculated from spectrochronocoulometric experiments as (Gaupp et al., 2002)

$$\eta(\lambda) = \frac{\log T(\lambda)_{\text{bleach}} - \log T(\lambda)_{\text{color}}}{\sigma} \tag{11.13}$$

In the above equation, $T(\lambda)_{\text{bleach}}$ and $T(\lambda)_{\text{color}}$ represent, respectively, the transmittance of the bleached and colored forms at the selected wavelength and σ the charge density (C/cm^2) necessary to produce the observed chromatic change.
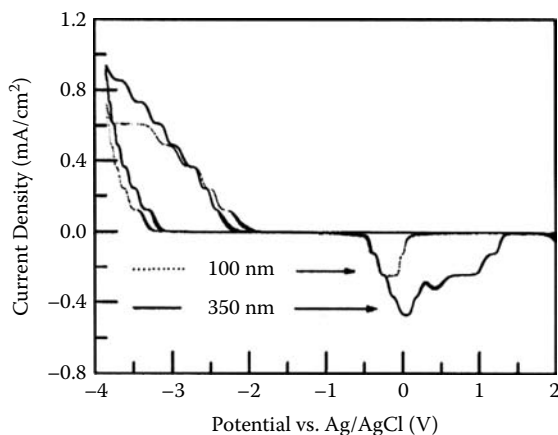
FIGURE 11.12 CVs of 100- and 350-nm-thick TiO_2 thin films. Electrolyte, 1 M $LiClO_4$ in propylene carbonate. (From Lin et al., 2008. *J. Solid State Electrochem.* 12, 1481–1486, with permission from Springer.)

Electrochromic electrodes are frequently based on a conducting polymer film supported on a conducting substrate. Changes in color upon application of different potentials can be seen in Figure 11.13, which correspond to the spectra recorded for a poly(3-methylthiophene)-mesoporous TiO_2 nanocomposite deposited on ITO upon application of different negative-going potentials in contact with a pure ionic liquid, 1-butyl-3-methylimidazolium hexafluorophosphate (Ma et al., 2008). Changes of
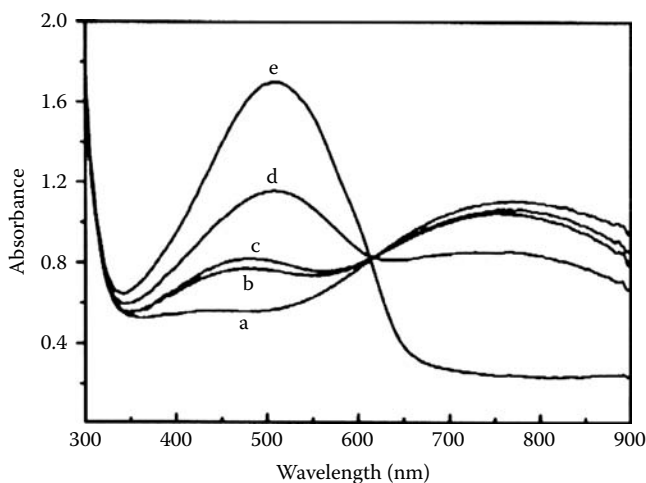
FIGURE 11.13 Spectra recorded for a poly(3-methylthiophene)-mesoporous TiO_2 nanocomposite deposited on ITO in contact with 1-butyl-3-methylimidazolium hexafluorophosphate upon application of negative-going potentials of (a) 1, (b) 0.5, (c) 0, (d) −0.5, and (e) −1 V. (From Ma et al., 2008. *J. Solid State Electrochem.* 12, 1503–1509, with permission from Springer.)

(a)

(b)
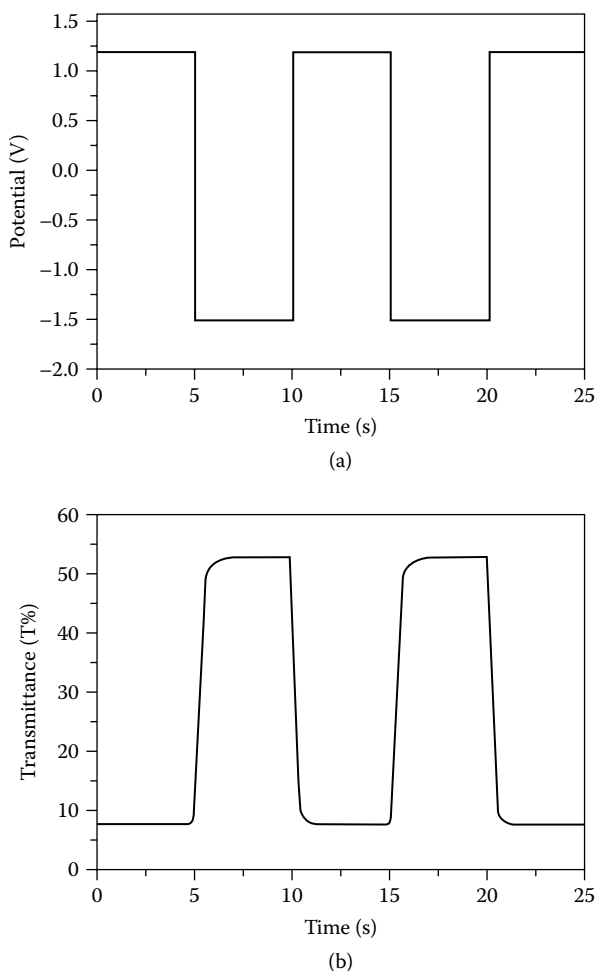
FIGURE 11.14   (a) Applied potential and (b) changes of transmittance at 500 nm on poly(3-methylthiophene)-mesoporous TiO$_2$ nanocomposite deposited on ITO in contact with 1-butyl-3-methylimidazolium hexafluorophosphate electrodes when switched between 1.2 and −1.5 V in 5 s. (From Ma et al., 2008. *J. Solid State Electrochem.* 12, 1503–1509, with permission from Springer.)

transmittance at 500 nm on such electrodes when switched between 1.2 and −1.5 V in 5-s intervals are depicted in Figure 11.14.

11.5   PHOTOCHEMICAL MODULATION OF ELECTROCATALYTIC PROCESSES

Modulation of the electrocatalytic response by electrochemically or photochemically induced changes in the electroactive centers anchored to porous solids is another possibility in photoelectrochemistry. This can be illustrated by the voltammetric
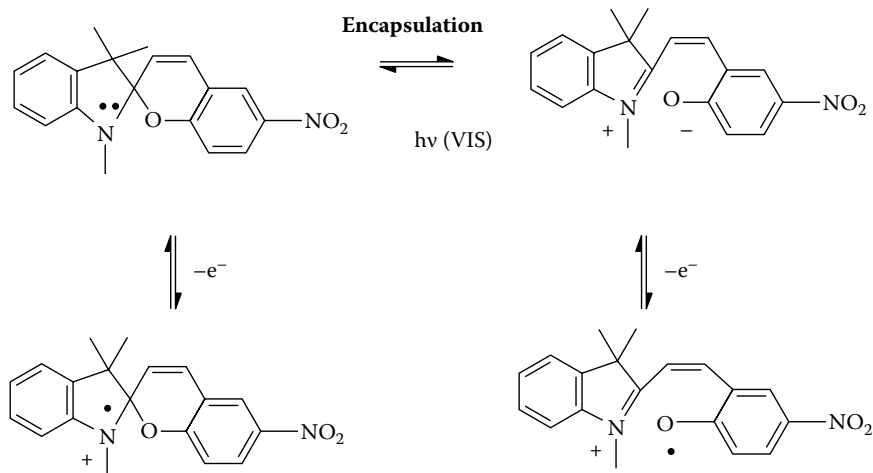
FIGURE 11.15 Main photoelectrochemical processes involved in the voltammetric response of SP@Y systems. (From Doménech et al., 2004. *J. Phys. Chem. B*. 108, 20064–20075, with permission.)

behavior of spiropyrans attached to zeolite Y, SP@Y. Spiropyrans are composed of an indoline and a chromene moiety that are linked by a spirocarbon atom. In solution, irradiation with near-UV light ($\lambda < 350$ nm) induces heterolytic cleavage of the spiro-carbon-oxygen bond of the original closed spiropyran to produce a ring-opened species whose structures are depicted in Figure 11.15. In the absence of UV irradiation, this undergoes ring closure to reform the parent spiropyran. However, upon attachment to aluminosilicates, spiropyrans show a reverse photochemical behavior in which, under illumination with visible light ($\lambda > 450$ nm), the predominant open form undergoes ring closure to the closed spiropyran one (Guglielmetti, 1990). In addition, a third form consisting of protonated open spiropyran is also detected in the solids. Thus, there is a distribution of three different species (closed, unprotonated open, and protonated open forms) whose populations vary depending on the polarity and acidity of the solid, the open protonated form being the predominant species in the solids (Casades et al., 2000).

Due to the frozen orthogonal configuration of the indolic and phenolate moieties, the closed spiropyran form is a rigid molecule. In contrast, the open forms are significantly more flexible due to the allowed rotation through the single C–C bond connecting the indole and chromene units. In the interior of cages of zeolite Y, in which the spiropyran molecule must occupy a little more space than that available in a single cavity, the conformational freedom should be, at least partially, hindered, so that the *cis* configuration with respect to the central C–C bond of the open chain is probably retained (Figure 11.15).

Electrochemical data for SP@Y probes were consistent with these above considerations (Doménech et al., 2004e). For our purposes, the relevant point to emphasize is that a light-sensitive effect on the voltammetric response for benzidine oxidation
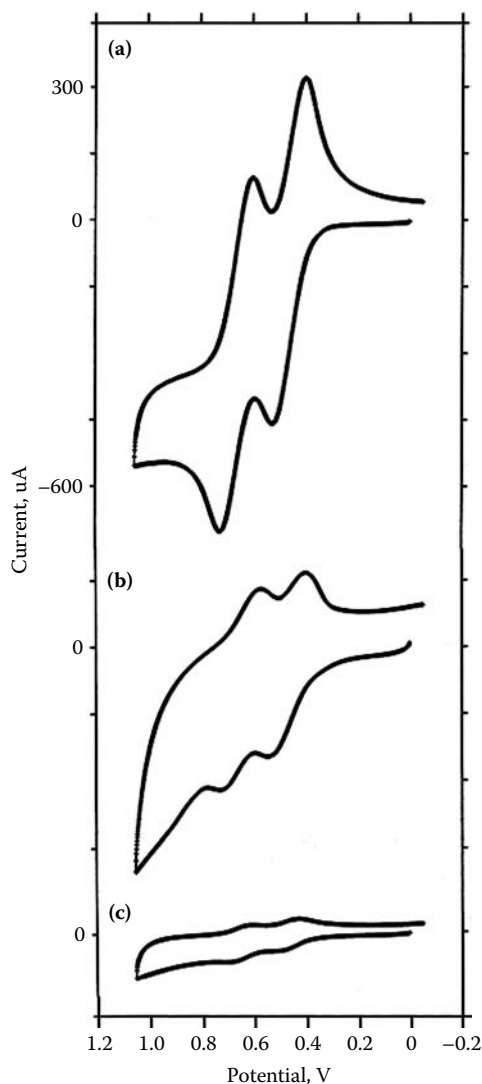
FIGURE 11.16 CVs at paraffin-impregnated graphite electrodes modified by (a) bleached SP@Y, (b) partly bleached SP@Y, and (c) pristine SP@Y, immersed into 3.0 mM *N,N,N′,N′*-tetramehylbenzidine solution in 0.10 M Et₄NClO₄/MeCN. Potential scan rate 100 mV/sec. (From Doménech et al. 2004. *J. Phys. Chem. B*. 108, 20064–20075, with permission.)

in nonaqueous media at SP@Y-modified electrodes occurs. This can be seen in Figure 11.16, where CVs at paraffin-impregnated graphite electrodes modified with bleached, partially bleached, and pristine SP@Y specimens in contact with a MeCN solution of *N,N,N′,N′*-tetramehylbenzidine are shown. The two-peak response of benzidine recorded for pristine SP@Y specimens is essentially identical to that
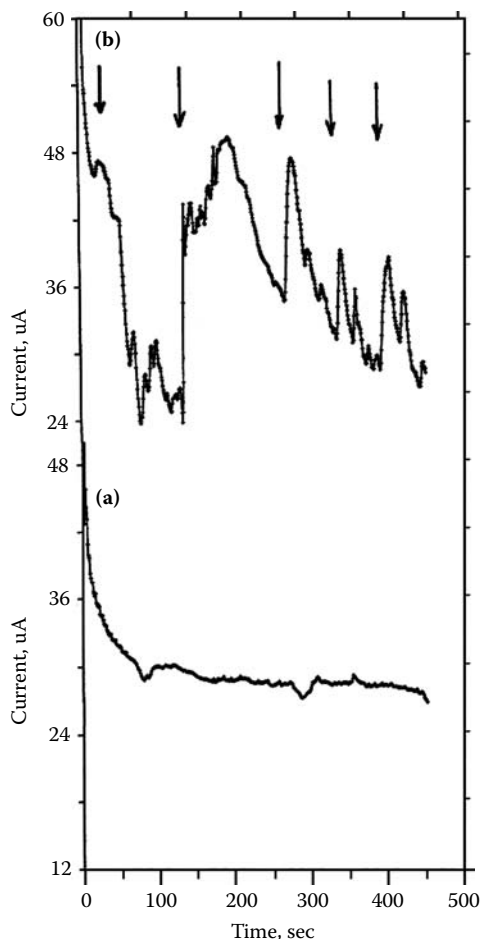
FIGURE 11.17 Current-time curves obtained upon application of a constant potential of 1.0 V to a SP@Y-modified paraffin-impregnated graphite electrode immersed into a 1.0-mM solution of *N,N,N′,N′*-tetramehylbenzidine in 0.10 M Et$_4$NClO$_4$/MeCN. The electrode was (a) maintained under dark conditions or (b) submitted to illumination with visible light during periods of 1 min (marked by arrows). (From Doménech et al., 2004. *J. Phys. Chem. B*. 108, 20064–20075, with permission.)

recorded at unmodified graphite electrodes, but peak currents are clearly enhanced upon bleaching the SP@Y specimen. These features are attributable to an electro-catalytic effect that is associated with the closed spiropyran form attached to the zeolite boundary. This effect can be modulated by irradiation of the electrodes as can be seen in Figure 11.17. Here CA data were obtained upon application of a constant potential of 1.0 V to a SP@Y-modified electrode immersed into a quiescent benzidine solution. Upon maintaining the electrode under dark conditions, a smooth, monotonically decreasing curve is obtained. If intermittent irradiation steps with
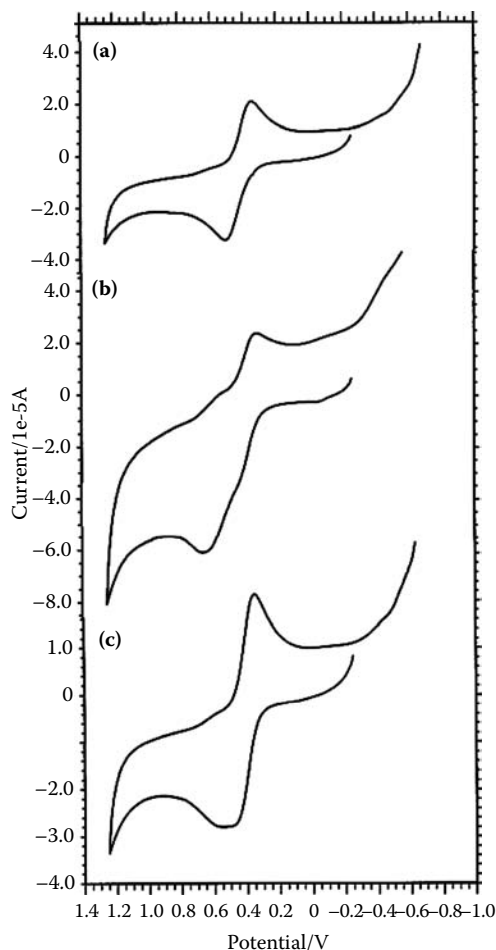
FIGURE 11.18 CVs recorded in a 0.50-mM $K_4Fe(CN)_6$ aqueous solution in 0.50 M H_2SO_4 at (a) bare paraffin-impregnated graphite electrode and $Ca_{0.95}Y_{0.05}Sn_{0.95}Cr_{0.05}SiO_5$-modified electrode under (b) dark conditions and (c) irradiation with visible light. Potential scan rate 50 mV/sec. (From Doménech et al., 2006. *Eur. J. Inorg. Chem.* 638–648, with permission from Wiley.)

visible light during periods of 1 min are applied, prominent currents are recorded in agreement with the reversible nature of the open-closed spiropyran interconversion and the different electrocatalysis associated to such forms.

Comparable results can be obtained for electrochemically active doped materials (Figure 11.18) for chromium-doped sphene samples prepared from sol-gel techniques (Doménech et al., 2006e). Here, Cr(V), Cr(IV), and Cr(III) centers, providing different redox properties, exist. Figure 11.18 compares CVs recorded in a $K_4Fe(CN)_6$ aqueous solution at a paraffin-impregnated graphite electrode modified with $Ca_{0.95}Y_{0.05}Sn_{0.95}Cr_{0.05}SiO_5$ under dark conditions and under irradiation with

visible light. The response of the modified electrodes consists of two overlapping couples attributable to the nonmediated (midpoint potential of ca. 0.44 V versus AgCl/Ag) and modifier-mediated oxidation (midpoint potential of ca. 0.62 V) of hexacyanoferrate(II) ions. Under irradiation, the mediated process, attributed to Cr(IV) centers in the surface of the sphene crystals, is significantly decreased with respect to nonmediated $Fe(CN)_6^{4-}$ oxidation, as expected from a decrease in the population of Cr(IV) centers, induced by light irradiation.

12 Microporous Materials in Electrosynthesis and Environmental Remediation

12.1 ELECTROSYNTHESIS

Electrosynthetic procedures are those devoted to prepare chemical products using electrochemistry, ordinarily using controlled current or controlled potential electrolysis in a cell or electrochemical reactor. An electrochemical reactor can be defined as a device where a chemical product is obtained from one or more reagents using electrical energy. Electrolysis cells or electrochemical reactors mainly differ from chemical reactors by the use of electrical energy as a driving force for promoting chemical changes and by the existence of an interface where the electrochemical reaction takes place.

Different classifications of electrochemical reactors can be made depending on their configuration (divided, undivided cathodic, and anodic compartments) electrode geometry (bi- and tri-dimensional), the fluid flow through the reactor (mixing, plug-flow, fluidized baths), among others. There are several demands for electrochemical reactors (Pletcher and Walsh, 1990; Molina et al., 2004):

- Security, safety, low cost, ease in operation, and, eventually, automatic control
- Controlled, uniform potential distribution, and current density between the electrodes
- Low cell voltage as possible for minimizing energetic cost
- Electrode surface/reactor volume ratio must be as high as possible
- Low pressure drop and easy gas evacuation
- Control of mass transport and heat transport in the reactor

The methodology used in chemical engineering to describe the performance of chemical reactors can be adapted to the study of electrochemical cells. Electrosynthesis of a variety of industrially relevant products has been studied; for instance, the synthesis of ammonia from natural gas at atmospheric pressure (Marnellos et al., 2001; Wang et al., 2007).

12.2   ELECTROLYTIC PROCEDURES INVOLVING POROUS ELECTRODES

Porous metallic structures have been used for electrocatalysis (Chen and Lasia, 1991; Kallenberg et al., 2007). Porous electrodes are made with conductive materials that can degrade under high temperatures at high anodic potential conditions. This last problem is of less importance for fuel cell anodes, which operate at relatively low potentials, but it can be of importance for electrochemical reactors. Porous column electrodes prepared by packing a conductive material (carbon fiber, metal shot) forming a bar are frequently used. Continuous-flow column electrolytic procedures can provide high efficiencies for electrosynthesis or removal of pollutants in industrial situations. Theoretical analysis for the electrodeposition of metals on porous solids has been provided by Masliy et al. (2008).

Industrially relevant products can be prepared by means of electrosynthetic procedures using microporous materials. Two general approaches can be used:

1. Electrosynthesis at conventional electrodes immersed into dispersions of the porous material in the electrolyte
2. Electrosynthesis at porous electrodes

In most cases, a catalyst is deposited over the basal electrode, but it is also possible to interpose an electron mediator between the catalyst and the electrode (Zhong et al., 2007).

12.3   ELECTROCATALYTIC PROCESSES

As discussed in Chapter 10, most of synthetically or energetically relevant electrochemical processes involve high kinetic constraints, represented by cathodic and/or anodic overpotentials. Electrocatalysis allows lowering such overpotentials and obtaining effective electrosynthetic procedures.

The encapsulation of catalytically active species into porous solids is one of the possible strategies of particular interest. Thus, Bessel and Rolison (1997b,c) compared the electrocatalytic effect of zeolite Y-encapsulated Co(salen) (salen = N,N'-bis(salicylidene)ethylenediamine) on the reaction between benzyl chloride and carbon dioxide in tetrahydrofuran/hexamethylphosphoramide, with that exerted by the same complex in solution. Using a large surface area reticulated vitreous carbon electrode immersed into suspensions of Co(salen)@NaY in solutions of the reagents, the effective electrocatalytic turnover is ca. 3000 times that of homogeneous Co(salen) under comparable conditions. Remarkably, coulometric experiments indicated that only 0.1% of encapsulated Co(salen) is electroactive.

It should be noted that electrocatalytic effects in zeolites can be influenced by

- Lewis base effects associated to framework oxygens (Teunisson et al., 1993)
- "Docking" of the substrate into the supercages (Derouane et al., 1988; Chen et al., 1994)
- "Boxing effect" due to electronic confinement for the guest molecule entrapped into the zeolite framework (Zicovich-Wilson et al., 1997)

Microheterogeneous electrocatalysis can be performed with zeolite-based catalysts using suspensions of such materials in organic solvents with low ionic strength by applying a DC voltage to suspensions of zeolite particles, as described by Rolison and Stemple (1993) for the Pd^{II}-Cu^{II}-NaY catalyzed oxidation of propene, but a wide variety of systems has been studied.

In the case of electron transfer mediators immobilized on electrode surfaces, one can define a specific activity, S_A, as the quotient between catalytic peak current, i_{pcat}, and catalyst deposition charge, Q_{cat} ($S_A = i_{pcat}/Q_{cat}$) (Wang et al., 2004). In most systems, one can define apparent activation energy, E_a, satisfying an Arrhenius-type equation:

$$i_p = k \exp(-E_a / RT) \tag{12.1}$$

Then, the specific activity should vary with temperature as

$$S_A = -E_a / RT + \text{constant} \tag{12.2}$$

12.4   OXYGEN EVOLUTION REACTION

Oxygen evolution reaction (OER) can be considered as one of the most relevant processes in electrochemistry involved in, for instance, chlor-alkali and ozone productions. One of the challenges is seawater electrolysis in order to store pure hydrogen and oxygen gases and prevent Cl_2 formation. The overall OER,

$$2H_2O \rightarrow O_2 + 4H^+ + 4e^- \tag{12.3}$$

can be described in terms of the sequence of elementary steps:

$$H_2O \rightarrow OH\cdot \text{ (ads)} + H^+ + e^- \tag{12.4}$$

$$OH\cdot(\text{ads}) \rightarrow O\cdot \text{ (ads)} + H^+ + e^- \tag{12.5}$$

$$2O\cdot \text{ (ads)} \rightarrow O_2 \tag{12.6}$$
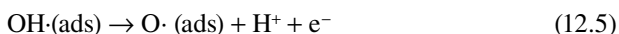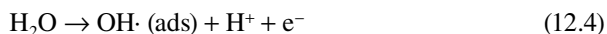
where the process described by Equation (12.4) acts as a rate-determining step (Silva et al., 2003). The mechanism for OER at metal oxide electrodes is a subject of discussion, although it is generally accepted that adsorbed or chemisorbed $OH\cdot$ and $O\cdot$ radicals are involved, but probably adsorbed or chemisorbed O^- and O_2^{2-} species participate in the process (Bockris and Otagawa, 1984; Oliveira et al., 1994). Different electrode configurations (packed bed, gas diffusion, trickle bed, rotating porous cylinders, etc.) have been described. Figure 12.1 shows hydrodynamic voltammograms at reticulated vitreous carbon in O_2-saturated 0.5 M H_2SO_4 at different rotation rates (Awad et al., 2008). Here, the electrode was pretreated by applying an anodic potential of 2 V in 0.1 M H_2SO_4 during 1 min for enhancing the values of the limiting currents, H_2O_2 being the product of the reduction wave recorded at −0.70 V versus AgCl/Ag. Simulation of oxygen evolution at porous anodes from flowing electrolytes has recently been performed by Saleh (2007).
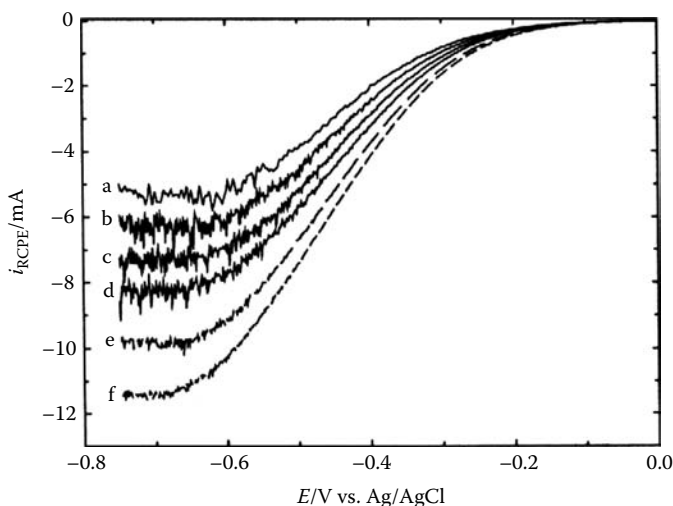
FIGURE 12.1 Hydrodynamic voltammograms at reticulated vitreous carbon in O_2-saturated 0.5 M H_2SO_4 at different rotation rates (a) 400, (b) 600, (c) 800, (d) 1000, (e) 1500, and (f) 2000 rpm. Potential scan rate 20 mV/s. (From Awad et al., 2008. *J. Solid State Electrochem.* 12, 251–258, with permission from Springer.)

12.5 HYDROGEN EVOLUTION REACTION

Obtaining hydrogen gas from water electrolysis has received considerable attention due to the possible use of H_2 as fuel. Mainly, noble metal electrodes displaying low overpotentials for hydrogen evolution have been investigated. The mechanism of the electrochemical hydrogen evolution reaction (HER) has been described as a two-step process with high electrocatalytic character (Bard et al., 2008). In the first step, adsorbed hydrogen is formed from H^+ or water (Volmer reaction):

$$H^+ (aq) + e^- \rightarrow H\cdot (ads) \tag{12.7}$$

$$H_2O + e^- \rightarrow H\cdot (ads) + OH^- (aq) \tag{12.8}$$
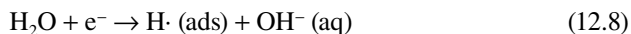
In the second step, adsorbed hydrogen is removed from the electrode either through a chemical process (Tafel reaction):

$$2H\cdot (ads) \rightarrow H_2 (g) \tag{12.9}$$

or by means an electrochemical process:

$$H\cdot (ads) + H^+ (aq) + e^- \rightarrow H_2 (g) \tag{12.10}$$
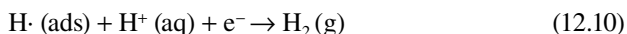
Thermally prepared thin films of RuO_2 and IrO_2 on titanium have been tested as cathodes for use in water electrolysis cells (Kondintsev and Trasatti, 1994; Burke and Naser, 2005). The mechanism of the HER at oxide electrodes, however, should differ significantly from that studied at metal electrodes (Burke et al., 2007).

12.6   ELECTROCATALYTIC OXIDATION OF ALCOHOLS

With the development of fuel cells, electrocatalytic oxidation of small organic molecules, such as methanol or formic acid, has attracted great interest recently (Rice et al., 2003). Ethanol oxidation to acetaldehyde can be performed by means of the reactions:

$$\text{Anode: } CH_3CH_2OH \rightarrow CH_3CHO + 2H^+ + 2e^- \tag{12.11}$$

$$\text{Cathode: } O_2 + 4H^+ + 4e^- \rightarrow 2H_2O \tag{12.12}$$
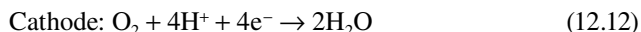
Since 1990, cogeneration strategies have grown considerably. These imply the production of useful chemical together with energy. The chemical cogenerative processes can be classified according to the different types of fuel cells (Alcaide et al., 2004). Hydrogenations, dehydrogenations, oxygenations, halogenations, among others have been reported.

12.7   ELECTROCHEMICAL DEGRADATION OF CONTAMINANTS

Preservation and improvement of the environment is a contemporary necessity that involves all the humanity. Terms like *sustainable development* or *green chemistry* have become something more than a literary topic and are currently converted into widely claimed social demands. Destruction of environmental pollutants is one of the aspects dealing with environmental management, a term where concepts such as environmental preservation, environmental remediation, etc., are included. Here, the attention will be focused in the electrodegradation of pollutants.

Electrochemical methods for degradation of environmental contaminants are more advantageous with respect to other treatments (incineration, chemical attack) because of, among other factors, the use of low operating temperatures and the possibility of an accurate control of variables influencing the overall process.

Electrochemical methods play a prominent role in the degradation/destruction of environmental pollutants, a strategy addressed to the conversion of pollutants into environmentally innocuous substances. The most divulgated method for the electrochemical degradation of organic contaminants in waters is anodic oxidation, often also called *electrochemical incineration*. This methodology is based on the oxidation of pollutants by adsorbed hydroxyl radical (OH·) formed at the surface of the anode as a result of water oxidation.

The hydroxyl radical is a powerful oxidizing agent that can react with organic compounds to give dehydrogenated or hydroxylated derivatives until they achieve complete mineralization and yield water and carbon dioxide. Typically, the contaminated water is treated in the anodic compartment of a divided cell with high-oxygen overvoltage anodes such as Pt or undoped or doped PbO_2, SnO_2, or IrO_2.

Lastly, indirect methods have been introduced. These involve continuous supply of H_2O_2 to the contaminated solution. Hydrogen peroxide can be electrochemically obtained in acidic media from

$$O_2 + 2H^+ + 2e^- \rightarrow H_2O_2 \tag{12.13}$$

The Fenton procedure involves the addition of Fe^{2+} ions to the solution, thus resulting in the generation of hydroxyl radicals:

$$H_2O_2 + Fe^{2+} \rightarrow Fe^{3+} + OH\cdot + OH^- \tag{12.14}$$
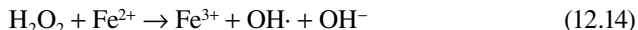
This is a catalytic process that can be propagated via the regeneration of ferrous ions with electrogenerated H_2O_2. This reaction yields hydroperoxyl radical ($HO_2\cdot$), a species that has a much weaker oxidizing power than OH:

$$H_2O_2 + Fe^{3+} \rightarrow Fe^{2+} + HO_2\cdot + H^+ \tag{12.15}$$
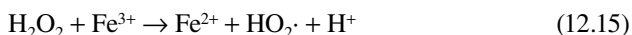
Additionally, reaction of Fe^{3+} with $HO_2\cdot$ and organic radical intermediates is also possible.

Advanced methods, however, can electrochemically generate hydroxyl and hydroperoxyl radicals (Pirvu et al., 2004):

$$H_2O \rightarrow OH\cdot \text{ (ads)} + H^+ + e^- \tag{12.16}$$

$$H_2O_2 \rightarrow HO_2\cdot + H^+ + e^- \tag{12.17}$$
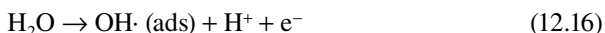
Direct electroreduction methods are typically used for dechlorination of chlorinated pollutants in waters. The easy removal of Cl from chlorinated organics allows conversion of chlorofluorocarbons (CFCs) into hydrochlorofluorocarbons (HCFCs), hydrofluorocarbons (HFCs), and even fluorocarbons (FCs). ECFCs are much less destructive to the atmospheric ozone than CFCs, but HFCs and FCs are harmless to atmospheric ozone, although they may contribute to the greenhouse effect.

The proposed reactions for the reduction of $CFCl_3$ at Hg or Pb cathodes can be represented as

$$CFCl_3 \xrightarrow{+2e^-,-Cl^-} CHFCl_2 \xrightarrow{+2e^-,-Cl^-} CH_2FCl \xrightarrow{+2e^-,-Cl^-} CH_3F \tag{12.18}$$
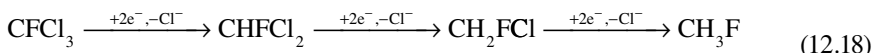
The electrochemical reactions proceed in ethanol-water or methanol-water mixtures. Alternatively, gas diffusion electrodes can be used.

A variety of methods exploit porous materials for environmental treatments. For instance, Hayes et al. (1994) developed several methods for decomposing environmental toxins by application of voltages up to 10 V to zeolite suspensions in waters, whereas lead and tin oxide thin films can be used for the electrochemical degradation of a variety of organic pollutants (Grimm et al., 1998; Borrás et al., 2003; Monteiro et al., 2006).

Electrodes based on doped SnO_2 have received attention in the last years. In its pure form, SnO_2 is an n-type semiconductor with relatively high electrical conductivity due to a level of nonstoichiometric impurities. This electrical conductivity can be enhanced upon addition of small amounts of dopants such as Sb, F, Cl, and Br. Good performances have been reported by codoped materials; for instance, Gd-Sb–doped SnO_2 deposited over Ti plates (Feng et al., 2008) exhibits a significant performance for the electrocatalytic decomposition of phenol.

12.8   DEGRADATION/GENERATION

Cogeneration strategies were described in Chapter 10 with regard to the simultaneous production of energy and chemicals in fuel cells. A similar concept can be applied in environmental chemistry because electrochemical degradation of most contaminants can yield useful products and eventually produce energy.

One of the most significant cases is that of CO_2, which can be used as a starting product to generate useful chemicals. The electrochemical reduction of CO_2 to CO ($E^{\circ} = -0.41$ V versus SHE at pH = 5) can be homogeneously catalyzed by several species, in particular, by Ni(II)-cyclam complexes (Beley et al., 1984). Alternatively, different electrodes can use heterogeneous catalysis. As a result, CO_2 can be used for electrocarboxylations to give a variety of carboxylic acids. Two possible pathways can be considered, having in common the generation of a radical anion of the organic compound (Sánchez-Sánchez et al., 2004):

$$R \rightarrow R^{\cdot -} - e^{-} \tag{12.19}$$

The generated radical anion can react as a nucleophile attacking the CO_2, and yielding a carboxylated radical anion further electrochemically reduced

$$R^{\cdot -} + CO_2 \rightarrow R\text{-}COO^{\cdot -} \tag{12.20}$$

$$R\text{-}COO^{\cdot -} + H^{+} + e^{-} \rightarrow RH\text{-}COO^{-} \tag{12.21}$$

or, alternatively, can reduce CO_2, giving a $CO_2^{\cdot -}$ radical anion, which is subsequently coupled with the parent radical:

$$R^{\cdot -} + CO_2 \rightarrow R + CO_2^{\cdot -} \tag{12.22}$$

$$R^{\cdot -} + CO_2^{\cdot -} + H^{+} \rightarrow RH\text{-}COO^{-} \tag{12.23}$$

Similarly, nitrogen oxides in emissions from automobiles and power plants can be processed in fuel cells using $HClO_4$ as electrolyte, the anodic reaction being hydrogen oxidation to protons (Langer and Pate, 1980). Possible electrochemical reactions are

$$2NO\,(g) + 2H^{+}\,(aq) + 2e^{-} \rightarrow N_2O\,(g) + H_2O\,(l) \tag{12.24}$$

$$2NO\,(g) + 4H^{+}\,(aq) + 4e^{-} \rightarrow N_2(g) + 2H_2O\,(l) \tag{12.25}$$

$$NO\,(g) + 3H^{+}\,(aq) + 3e^{-} \rightarrow NH_2OH\,(aq) \tag{12.26}$$

$$NO\,(g) + 5H^{+}\,(aq) + 5e^{-} \rightarrow NH_3\,(aq) + H_2O\,(l) \tag{12.27}$$
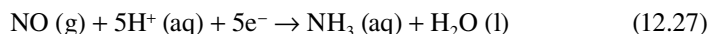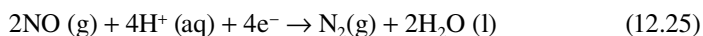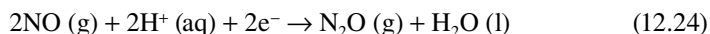
Similarly, sulfur dioxide can also be treated. Here, the cathodic reaction is the oxidation of O_2 to water, while the anodic reaction is

$$SO_2\,(g) + 2H_2O\,(l) \rightarrow H_2SO_4\,(aq) + 2H^{+}\,(aq) + 2e^{-} \tag{12.28}$$
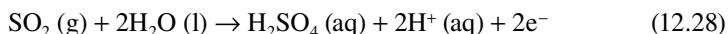
12.9   PHOTOELECTROCHEMICAL DEGRADATION

In most cases, photo assisted electrochemical degradation processes are used. For instance, in the aforementioned Fenton method, formation of complexes of iron ions with some intermediates such as oxalate ions can reduce the effectiveness of the process. Then, photoelectro-Fenton methods involve the use of UV irradiation to produce photolysis of such Fe^{3+} complexes and increase the rate of Fe^{2+} regeneration by means of the photo-Fenton reaction:

$$Fe^{3+} + H_2O + h\nu \rightarrow Fe^{2+} + H^+ + OH\cdot \qquad (12.29)$$
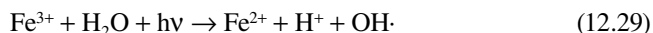
An alternative is the use of a sacrificial Fe anode that continuously supplies Fe^{2+} ions to the solution by means of the electrochemical process:

$$Fe \rightarrow Fe^{2+} + 2e^- \qquad (12.30)$$

Here, ferrous ions are oxidized by electrogenerated hydrogen peroxide so that an Fe^{3+}-saturated solution is obtained, with the excess of this ion precipitating as $Fe(OH)_3$. Then, the pollutants can be removed from the contaminated solution by their degradation with OH· and coagulation with the $Fe(OH)_3$ precipitate (Arias et al., 2004).

Photocatalytic oxidation of organic pollutants on TiO_2-based materials has been extensively investigated. The catalyst is used in the form of a suspension of fine particles or thin film on robust substrates. Figure 12.2 shows the variation of open-circuit potential with time for TiO_2 film electrodes, prepared by anodization of Ti
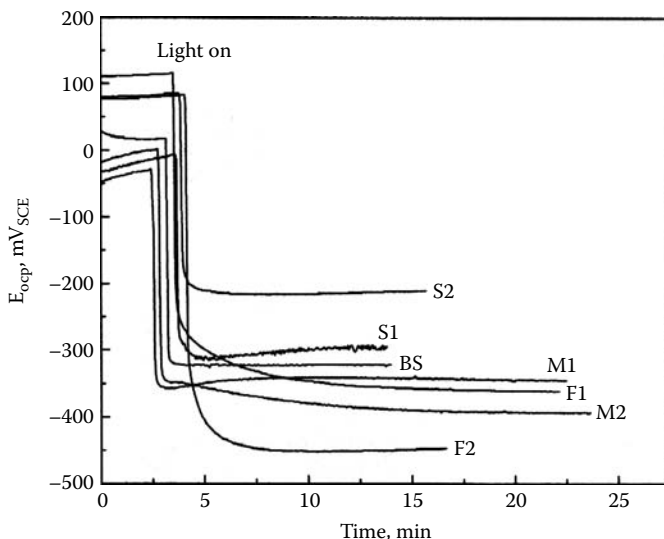
FIGURE 12.2   Variation of open-circuit potential with time for TiO_2 film electrodes, prepared by anodization of Ti, in contact with BS. Base solution; S1 and S2: 0.1 and 0.5 mM salicylic acid; M1 and M2: 1 and 10 mM methanol; F1 and F2: 1 and 10 mM formic acid solutions. (From Li and Shen, 2006. *J. Solid State Electrochem.* 10, 980–986, with permission from Springer.)
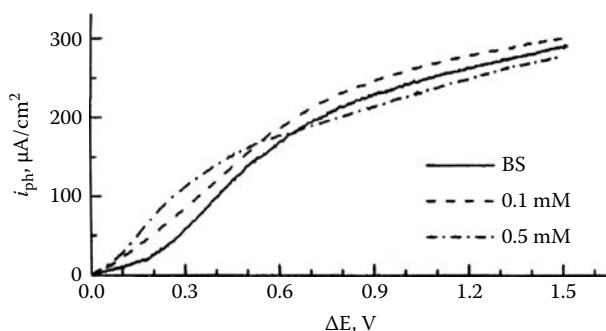
FIGURE 12.3 Variation of the photocurrent density with the bias potential for TiO$_2$ film electrodes in contact with base solution, 0.1 and 0.5 mM salicylic acid. (Adapted from Li and Shen, 2006. *J. Solid State Electrochem.* 10, 980–986, with permission from Springer.)

(see Chapter 6), in contact with solutions of different organic compounds under UV illumination (Li and Shen, 2006). In the base solution, water is oxidized at TiO$_2$ electrode surface by the photogenerated holes, while both water and organics are oxidized. The variation of the photocurrent density, i_{ph}, the tested and base solutions, with the applied potential bias, ΔE, taken as the difference between the applied potential and the open-circuit potential, display s-shaped curves as shown in Figure 12.3 for salicylic acid. At low potential bias, i_{ph} increases slowly on ΔE as a result of the low separation rates of photogenerated e-h pairs under low electric field conditions. At higher bias potentials, there is an almost linear variation of i_{ph} on ΔE. This can be rationalized by assuming that the electron transport in the film becomes rate determining so that the TiO$_2$ photoelectrode behaves as a constant resistance (Jiang et al., 2003). With further increase in ΔE, the photocurrent levels off and tends to stabilize, thus defining a saturation behavior that is attributable to scanty holes that facilitate interface reaction. The variation of the difference photocurrent density, Δi_{ph}, calculated as the
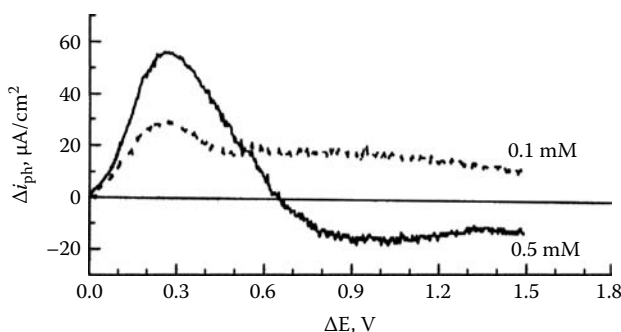
FIGURE 12.4 Variation of the difference photocurrent density with the bias potential for TiO$_2$ film electrodes in contact with base solution, 0.1 and 0.5 mM salicylic acid. (Adapted from Li and Shen, 2006. *J. Solid State Electrochem.* 10, 980–986, with permission from Springer.)

difference between the photocurrents measured for the tested and base solutions, with the applied potential bias, ΔE, is depicted in Figure 12.4 for salicylic acid. Here, a peak in the photooxidation rate appears at a potential bias of 0.26 V. This peak can be attributed to the combination of the current associated to the oxidation of organic molecules and the additional reduction in the e-h recombination rate.

Improving the photocatalytic efficiency of such systems can be fulfilled by using porous TiO_2 films to increase the active area for photoreactions and applying a positive potential bias on the catalyst to suppress markedly the reaction of recombination of photogenerated electrons and holes (Li and Shen, 2006). Hierarchical TiO_2 porous film produces efficient mineralizing gaseous acetaldehyde and liquid-phase phenol, providing the fast transport pathway for reactants, products, and O_2 moving into and out of the catalytic framework (Zhao et al., 2008). These systems illustrate the capabilities of photoelectrochemical methodologies for the degradation of environmental pollutants.

References

Abbà, F., De Santis, G., Fabbrizzi, L., Licchelli, M., Manotti-Lanfredi, A.M., Pallavicini, P., Poggi, A., and Ugozzoli, F. 1994. Níckel(II) complexes of azacyclams: Oxidation and reduction behavior and catalytic effects in the electroreduction of carbon dioxide. *Inorganic Chemistry* 33, 1366–1375.

Abdel Rahim, M.A., Hassan, H.B., and Andel Hamid, R.M. 2006. A systematic study of the effect of OH⁻ and Ni²⁺ ions on the electro-catalytic oxidation of methanol at Ni-S-1 electrode. *Journal of Power Sources* 154, 59–65.

Abraham, K.M., Goldman, J.L., and Holleck, G.L. 1981. Vanadium oxides as cathodes for secondary lithium cells. *Journal of the Electrochemical Society* 128, 271–281.

Adams, R.N. 1958. Carbon paste electrodes. *Analytical Chemistry* 30, 1576.

Alcaide, F., Cabot, P.-L., and Brillas, E. 2004. Cogeneration of useful chemicals and electricity from fuel cells. In *Trends in Electrochemistry and Corrosion at the Beginning of the 21st Century*. Brillas, E., and Cabot, P.-L. Eds. Universitat de Barcelona, Barcelona, pp. 141–165.

Alhalasah, W., and Rolze, H. 2007. Electrochemical bandgaps of a series of poly-3-*p*-phenylthiophenes. *Journal of Solid State Electrochemistry* 11, 1605–1612.

Alkire, R. et al. 2006. *Nanostructured Materials in Electrochemistry*. Wiley-VCH, New York.

Almond, D.P., and West, A.R. 1983. Mobile ion concentration in solid electrolytes from an analysis of a.c. conductimetry. *Solid State Ionics* 9–10, 277–282.

Álvaro, M., Aprile, C., Ferrer, B., and García, H. 2007. Functional molecules from single wall carbon nanotubes. Photoinduced solubility of short single wall carbon nanotube residues by covalent anchoring of 2,4,6-triarylpyrylium units. *Journal of the American Chemical Society* 129, 5647–5655.

Álvaro, M., Carbonell, E., Doménech, A., Fornés, V., García, H., and Narayana, M. 2003. Ship-in-a-bottle synthesis of a large guest occupying two zeolite Y neighbour super-cages. Characterization and photocatalytic activity of encapsulated bipyrylium ion. *Chemical Physics-Physical Chemistry* 4, 483–487.

Álvaro, M., Cabeza, F.J., Corma, A., García, H., and Peris, E. 2007. Electrochemiluminiscence of zeolite-encapsulated poly(p-phenylenevinylene). *Journal of the American Chemical Society* 129, 8074–8075.

Álvaro, M., Cardin, D.F., Colqhoun, H.M., García, H., Gilbert, A., Lay, A.K., and Thorpe, J.H. 2005. Complete filling of zeolite frameworks with polyalkynes formed in situ by transition-metal ion catalysts. *Chemistry of Materials* 17, 2546–2551.

Amarilla, J.M., Tedjar, F., and Poinsignon, C. 1994. Influence of KOH concentration on the γ-MnO_2 redox mechanism. *Electrochimica Acta* 39, 2321–2331.

Amatore, C., and Savéant, J.-M. 1978. Do ECE mechanisms occur in conditions where they could be characterized by electrochemical kinetic techniques? *Journal of Electroanalytical Chemistry* 86, 227–232.

Amatucci, G.G, Badway, F., Dupasquier, A., and Zheng, T. 2001. An asymmetric hybrid non-aqueous energy storage cell. *Journal of the Electrochemical Society* 148, A930–A939.

Ammunsdsen, B., and Paulsen, J. 2001. Novel lithium-ion cathode materials based on layered manganese oxides. *Advanced Materials* 13, 943–956.

Anderson, M.R., Dorn, H.C., and Stevenson, S.A. 2000. Making connections between meta-lofullerenes and fullerenes: Electrochemical investigations. *Carbon* 38, 1663–1670.

Andrieux, C.P., and Savéant, J.-M. 1980. Electron transfer through redox polymer films. *Journal of Electroanalytical Chemistry* 11, 377–381.

مرجع دانشجویان و مهندسین مواد

Andrieux, C.P., and Savéant, J.-M. 1982. Kinetics of electrochemical reactions mediated by redox polymer films: Reversible ion-exchange reactions. *Journal of Electroanalytical Chemistry* 142, 1–30.

Andrieux, C.P., and Savéant, J.-M. 1984. Kinetics of electrochemical reactions mediated by redox polymer films: Pre-activation (CE) mechanisms. *Journal of Electroanaytical Chemistry* 11, 65–93.

Andrieux, C.P., and Savéant, J.-M. 1988. Electroneutrality coupling of electron hopping between localized sites with electroinactive counterion displacement: 1. Potential-step plateau currents. *Journal of Physical Chemistry* 92, 6761–6767.

Andrieux, C.P., Dumas-Bouchiat, J.M., and Savéant, J.-M. 1982. Catalysis of electrochemical reactions at redox polymer electrodes: Kinetic model for stationary voltammetric techniques. *Journal of Electroanaytical Chemistry* 131, 1–35.

Andrieux, C.P., Hapiot, P., and Savéant, J.-M. 1984. Electron-transfer coupling of diffusional pathways: Theory for potential step chronoamperometry and chronocoulometry. *Journal of Electroanaytical Chemistry* 1172, 49–65.

Andrieux, C.P., and Audebert, P. 2001. Electron transfer through a modified electrode with a fractal structure: Cyclic voltammetry and chronoamperometry responses. *Journal of Physical Chemistry B* 105, 444–448.

Andrieux, C.P., Haas, O., and Savéant, J.-M. 1986. Catalysis of electrochemical reactions at redox polymer coated electrodes. Mediation of the Fe(III)/Fe(II) oxido-reduction by a polyvinylpyridine polymer containing coordinatively attached bisbipyridine chlorotuthenium redox centers. *Journal of the American Chemical Society* 108, 8175–8182.

Aprile, C., Abad, A., García, H., and Corma, A. 2005. Synthesis and catalytic activity of periodic mesoporous materials incorporating gold nanoparticles. *Journal of Materials Chemistry* 15, 4408–4413.

Ardizzone, S., Fregonara, G., and Trassati, S. 1990. "Inner" and "outer" active surface of RuO_2 electrodes. *Electrochimica Acta* 35, 263–267.

Arias, C., Brillas, E., Cabot, P.-L., Carrasco, J., Centellas, F., Garrido, J.A., and Rodríguez, R.M. 2004. Advanced electrochemical methods for the degradation of halogenated compounds in waters. In *Trends in Electrochemistry and Corrosion at the Beginning of the 21st Century*. Brillas, E., and Cabot, P.-L., Eds. Universitat de Barcelona, Barcelona, pp. 359–382.

Armstrong, F.A., and Wilson, G.S. 2000. Recent developments in faradaic bioelectrochemistry. *Electrochimica Acta* 45, 2623–2645.

Arnold, D.E. 1967. Maya blue: A new perspective. Master's thesis, University of Illinois, Urbana.

Arnold, D.E. 1971. Ethnomineralogy of Ticul, Yucatan potters: Etics and emics. *American Antiquity* 36, 20–40.

Arnold, D.E., and Bohor, B.F. 1975. Attapulgite and Maya blue. An ancient mine comes to light. *Archaeology* 28, 22–29.

Arnold, D.E., Branden, J.R., Williams, P.R., Feinman, G.M., and Brown, J.P. 2008. The first direct evidence for the production of Maya blue: Rediscovery of a technology. *Antiquity* 82, 152–164.

Asefa, T., and Lennox, R.B. 2005. Synthesis of gold nanoparticles via electroless deposition in SBA-15. *Chemistry of Materials* 17, 2481–2483.

Asoh, H., Nishio, K., Nakao, M., Tamamura, T., and Masuda, H. 2001. Conditions for fabrication of ideally ordered anodic porous alumina using pretextured Al. *Journal of the Electrochemical Society* 148, B152–B156.

Attard, G.A. 2001. Electrochemical studies of enantioselectivity at chiral metal surfaces. *Journal of Physical Chemistry B* 105, 3158–3167.

Auborn, J.J., and Barberio, Y.L. 1987. Lithium intercalation cells without metallic lithium. Molybdenum dioxide/lithium cobalt dioxide and tungsten dioxide/lithium cobalt dioxide. *Journal of the Electrochemical Society* 134, 638–647.

Awad, M.I., Saleh, M.M., and Ohsaka, T. 2008. Oxygen reduction on rotating porous cylinder of modified reticulated vitreous carbon. *Journal of Solid State Electrochemistry* 12, 251–258.

Bach, S., Henry, M., and Livage, M. 1990. Sol-gel synthesis of manganese oxides. *Journal of Solid State Chemistry* 88, 325–333.

Back, R.P. 1987. Diffusion-migration impedances for finite, one-dimensional transport in thin-layer and membrane cells: Part II. Mixed conduction cases: $Os(III)/Os(II)ClO_4$ polymer membranes including steady-state *I–V* responses. *Journal of Electroanalytical Chemistry* 219, 23–48.

Baker, M.D., Senaratne, C., and McBrien, M. 1995. Comment on intrazeolite electron transport mechanism. *Journal of Physical Chemistry* 99, 12367.

Balamurugan, A., and Chen, S.-M. 2007. Silicomolybdate doped polypyrrole film modified glassy carbon electrode for electrocatalytic reduction of Cr(VI). *Journal of Solid State Electrochemistry* 11, 1679–1687.

Balch, A.L., Costa, D.A., and Winkler, K. 1998. Formation of redox-active, two-component films by electrochemical reduction of C_{60} and transition metal complexes. *Journal of the American Chemical Society* 120, 9614–9620.

Bard, A.J., and Faulkner, L.R. 2001. *Electrochemical Methods*, 2nd ed. John Wiley & Sons, New York.

Bard, A.J., Inzelt, G., and Scholz, F., Eds. 2008. *Electrochemical Dictionary*. Springer, Berlin.

Bard, A.J., and Mirkin, M.V., Eds. 2001. *Scanning Electrochemical Microscopy*. Marcel Dekker, New York.

Barisci, J.N., Wallace, G.G., and Baughman, R.H. 2000a. Electrochemical studies of single-wall carbon nanotubes in aqueous solutions. *Journal of Electroanalytical Chemistry* 488, 92–98.

Barisci, J.N., Wallace, G.G., and Baughman, R.H. 2000b. Electrochemical quartz crystal microbalance studies of single-wall carbon nanotubes in aqueous and non-aqueous solutions. *Electrochimica Acta* 46, 509–517.

Barone, V., Hod, O., and Scuseria, G.E. 2006. Electronic structure and stability of semiconducting graphene nanoribbons. *Nano Letters* 6, 2748–2754.

Barrado, E., Pardo, R., Castrillejo, Y., and Vega, M. 1997. Electrochemical behaviour of vanadium compounds at a carbon paste electrode. *Journal of Electroanalytical Chemistry* 427, 35–42.

Barrer, R.M. 1978. *Zeolites and Clay Minerals as Sorbents and Molecular Sieves*. Academic Press, London.

Barrette, W.C., Johnoson, H.W., and Sawyer, D.T. 1984. Voltammetric evaluation of the effective acidities (pK_a') for Bronsted acids in aprotic solvents. *Analytical Chemistry* 56, 1890–1898.

Barrière, F., and Downard, A.J. 2008. Covalent modification of graphitic carbon substrates by non-electrochemical methods. *Journal of Solid State Electrochemistry* 12, 1231–1244.

Basame, S.B., and White, H.S. 1998. Scanning electrochemical microscopy: Measurement of the current density at microscopic redox-active sites on titanium. *Journal of Physical Chemistry B* 102, 9812–9819.

Beck, J.S., Vartuli, J.C., Roth, W.J., Leonowicz, M.E., Kresge, C.T., Smith, K.D., Chu, C.T.-W., Olson, D.H., Sheppard, E.W., McCullen, S.B., Higgins, J.B., and Schlenker, J.L. 1992. A new family of mesoporous molecular sieves prepared with liquid crystal templates. *Journal of the American Chemical Society* 114, 10834–10843.

Bedioui, F., and Devynck, J. 1996. Comment on "Zeolite-modified electrodes, intra- versus extrazeolite electron transfer." *Journal of Physical Chemistry* 100, 8607–8609.

Beley, M., Collin, J.-P., Ruppert, R., and Sauvage, J.-P. 1984. Nickel(II)-cyclam: An extremely selective electrocatalyst for reduction of CO_2 in water. *Journal of the Chemical Society Chemical Communications* 19, 1315–1316.

Berenov, A., Wei, J., Wood, H., Rudkin, R., and Atkinson, A. 2007. Effect of aliovalent doping on the transport properties of lanthanum cuprates. *Journal of Solid State Electrochemistry* 11, 482–489.

Bernard, M.C., Cortes, R., Keddam, M., Takenouti, H., Bernard, P., and Senyarich, S. 1996. Structural defects and electrochemical reactivity of β-Ni(OH)$_2$. *Journal of Power Sources* 63, 247–254.

Bessel, C.A., and Rolison, D.R. 1997a. Topological redox isomers: Surface chemistry of zeolite-encapsulated Co(salen) and [Fe(bpy)$_3$]$^{2+}$ complexes. *Journal of Physical Chemistry B* 101, 1148–1157.

Bessel, C.A., and Rolison, D.R. 1997b. Microheterogeneous dispersion electrolysis with nanoscale electrode-modified zeolites. *Journal of Electroanalytical Chemistry* 439, 97–105.

Bessel, C.A., and Rolison, D.R. 1997c. Electrocatalytic reactivity of zeolite-encapsulated Co(salen) with benzyl chloride. *Journal of the American Chemical Society* 119, 12673–12674.

Blaedel, W.J., and Jenkins, R.A. 1975. Electrochemical oxidation of reduced nicotinamide adenine dinucleotide. *Analytical Chemistry* 47, 1337–1343.

Blandeau, L., Ouvrard, G., Calage, Y., Brec, R., and Rouxel, J. 1987. Transition-metal dichalcogenides from disintercalation processes. Crystal structure determination and Mossbauer study of Li$_2$FeS$_2$ and its disintercalates Li$_x$FeS$_2$ (0.2 ≤ x ≤2). *Journal of Physics C* 20, 4271–4282.

Blauch, D.N., and Anson, F.C. 1991. Effects of interconversion and electron transfer in voltammetric responses for two-component systems with differing diffusion coefficients. *Journal of Electroanaytical Chemistry* 309, 313–318.

Bocchetta, P., Conciauro, F., and Di Quarto, F. 2007. Nanoscale membrane electrode assemblies based on porous anodic alumina for hydrogen-oxygen fuel cell. *Journal of Solid State Electrochemistry* 11, 1253–1261.

Bockris, J.O'M., and Otagawa, T.J. 1984. The electrocatalysis of oxygen evolution on perovskites. *Journal of the Electrochemical Society* 131, 290–302.

Bockris, J.O'M., and Reddy, A.K.N. 1977. *Modern Electrochemistry*. Plenum Press, New York.

Bodoardo, S., Brenet, J., Maja, M., and Spinelli, P. 1994. Electrochemical behaviour of MnO$_2$ electrodes in sulphuric acid solutions. *Electrochimica Acta* 39, 1999–2004.

Bond, A.M., Feldberg, S.W., Miao, W., Oldham, K.B., and Raston, C.L. 2001. Modelling of solid-state, dissolution and solution-phase reactions at adhered solid–electrode–solvent (electrolyte) interfaces, electrochemistry of microcrystals of C$_{60}$ adhered to an electrode in contact with dichloromethane (Bu$_4$NClO$_4$). *Journal of Electroanalytical Chemistry* 501, 22–32.

Bond, A.M., Marken, F., Hill, E., Compton, R.G., and Hügel, H. 1997. The electrochemical reduction of indigo dissolved in organic solvents and as a solid mechanically attached to a basal plane pyrolytic graphite electrode immersed in aqueous electrolyte solution. *Journal of the Chemical Society Perkin Transactions 2*, 1735–1742.

Bond, A.M., Miao, W., and Raston, C.L. 2000. Identification of processes that occur after reduction and dissolution of C$_{60}$ adhered to gold, glassy carbon, and platinum electrodes placed in acetonitrile (electrolyte) solution. *Journal of Physical Chemistry B* 104, 2320–2329.

Booth, C., Nicholas, C.V., and Wilson, D.J. 1989. In *Polymer Electrolyte Reviews—2*. MacCallum, J.R., and Vincent, C.A., Eds. Elsevier, London, p. 229.

Bore, M.T., Pham, H.N., Switzer, E.E., Ward, T.L., Fukuoka, A., and Datye, A.K. 2005. The role of pore size and structure on the thermal stability of gold nanoparticles within mesoporous silica. *Journal of Physical Chemistry B* 109, 2873–2880.

Borosy, A.P., Nyikos, L., and Pajkossy, T. 1991. Diffusion to fractal surfaces—V. Quasi-random interfaces. *Electrochimica Acta* 36, 163–165.

Borrás, C., Laredo, T., and Scharifker, B.R. 2003. Competitive electrochemical oxidation of *p*-chlorophenol and *p*-nitrophenol on Bi-doped PbO$_2$. *Electrochimica Acta* 48, 2775–2780.

Botár, L., and Ruff, I. 1986. Effect of exchange reaction on transport processes, Fick's second law for diffusion on lattice points. *Chemical Physics Letters* 126, 348–351.

Boukamp, B.A., and Wiegers, G.A. 1983. Ionic and electronic processes in AgCrSe$_2$. *Solid State Ionics* 9–10, 1193–1196.

Bowers, R.C., and Murray, R.W. 1966. Voltammetric membrane electrode study of the ion-exchange properties of cellophane membranes. *Analytical Chemistry* 38, 461–465.

Breck, D.W. 1974. *Zeolite Molecular Sieves: Structure, Chemistry, and Use*. Wiley-Interscience, New York.

Bresinska, I., and Drago, R.S. 1990. Gas phase reaction of formaldehyde and hydrogen chloride in the presence of zeolite Y. *Catalysis Letters* 7, 403–408.

Brown, A.P., and Anson, F.C. 1977. Cyclic and differential pulse voltammetric behavior of reactants confined to the electrode surface. *Analytical Chemistry* 49, 1589–1595.

Bruce, P.G., West, A.R., and Almond, D.P. 1983. A new analysis of ac conductivity data in single crystal β-alumina. *Solid State Ionics* 7, 57–60.

Bruhwiler, D., and Calzaferri, G. 2004. Molecular sieves as host materials for supramolecular organization. *Microporous and Mesoporous Materials* 72, 1–23.

Burke, L.D., and Ryan, T.G. 1992. The role of incipient hydrous oxides in the oxidation of glucose and some of its derivatives in aqueous media. *Electrochimica Acta* 37, 1363–1370.

Burke, L.D., and Naser, N.S. 2005. Metastability and electrocatalytic activity of ruthenium dioxide cathodes used in water electrolysis cells. *Journal of Applied Electrochemistry* 35, 931–938.

Burke, L.D., Naser, N.S., and Ahern, B.M. 2007. Use of iridium oxide films as hydrogen gase evolution cathodes in aqueous media. *Journal of Solid State Electrochemistry* 11, 655–666.

Cai, J., Liu, J., Willis, W.S., and Suib, S.L. 2001. Framework doping of iron in tunnel structure cryptomelane. *Chemistry of Materials* 13, 2413–2422.

Calzaferri, G., Lanz, M., and Li, J.-W. 1995. Methyl viologen-zeolite electrodes: Intrazeolite charge transfer. *Chemical Communications* 13, 1313–1314.

Carapuça, H.M., Balula, M.S., Fonseca, and A.P., Cavaleiro, A.M.V. 2006. Electrochemical characterization of glassy carbon electrodes modified with hybrid inorganic-organic single layer of α-kegging type polyoxotung states. *Journal of Solid State Electrochemistry* 10, 10–17.

Casades, I., Constantine, M.S., Cardin, D., García, H., Gilbert, A., and Márquez, F. 2000. "Ship-in-a-Bottle" synthesis and photochromism of spiropyrans encapsulated within zeolite Y supercages. *Tetrahedron* 56, 6951–6956.

Casella, I.G., Cataldi, T.R.I., Salvi, A.M., and Desimoni, E. 1993. Electrocatalytic oxidation and liquid chromatographic detection of aliphatic alcohols at a nickel-based glassy carbon modified electrode. *Analytical Chemistry* 65, 3143–3150.

Cataldi, T.R.I., Guerrieri, A., Casella, I.G., and Desimoni, E. 1995. Study of a cobalt-based surface modified glassy carbon electrode: Electrocatalytic oxidation of sugars and alditols. *Electroanalysis* 7, 305–311.

Cervilla, A., Corma, A., Fornés, V., Llopis, E., Palanca, P., Rey, F., and Ribera, A. 1994a. Intercalation of [MoVIO₂(O₂CC(S)Ph₂)₂]₂⁻ in a Zn(II)-Al(III) layered double hydroxide host: A strategy for the heterogeneous catalysis of the air oxidation of tilos. *Journal of the American Chemical Society* 116, 1595–1596.

Cervilla, A., Doménech, A., Llopis, E., Vicente, F., and Tamarit, R. 1994b. Molybdenum complexes with sterically-hindered thio-carboxylate ligands. Electrochemical properties of the anionic complex bis(2,2-diphenyl-2-mercaptoethanoate) dioxomolybdate(VI) in protic solvents. *Inorganica Chimica Acta* 221, 117–124.

Chen, H.-Y., and Sachtler, W.M.H. 1998. Activity and durability of Fe/ZSM-5 catalysts for lean burn NO_x reduction in the presence of water vapor. *Catalysis Today* 42, 73–83.

Chen, L., and Lasia, A. 1991. Study of the kinetics of hydrogen evolution reaction on nickel-zinc alloy electrodes. *Journal of the Electrochemical Society* 138, 3321–3328.

Chen, L.C. 2008. *Electrochemistry for Biomedical Researchers*. National Taiwan University Press, Taipei.

Chen, N.Y., Degnan, T.F., Jr., and Smith, C.M. 1994. *Molecular Transport and Reactions in zeolites*. VCH, New York.

Chen, Z.-K., Huang, W., Wang, L.-H. Kang, E.-T., Chen, B.J., Lee, C.S., and Lee, S.T. 2000. A family of electroluminescent silyl-substituted poly(*p*-phenylenevinylene)s: Synthesis, characterization and structure—properties and relationships. *Macromolecules* 33, 9015–9025.

Cheng, L., Li, H.-q., and Xia, Y.-y. 2006. A hybrid nonaqueous electrochemical supercapacitor using nano-sized iron oxyhydroxide and activated carbon. *Journal of Solid State Electrochemistry* 10, 405–410.

Choe, S., Cha, Y., Lee, H., Yonn, Y., and Choi, H. 1995. Miscibility of poly(3-hydroxybutyrate-*co*-3-hydroxyvalerate) and poly(vinyl chloride) blends. *Polymer* 36, 4977–4982.

Chretien, M.N., Cosa, G., García, H., and Scaiano, J.C. 2002. Increasing the life expectancy of carbanions by zeolite inclusion. *Chemical Communications* 18, 2154–2155.

Chun, H., Dybstev, D.N., Kim, H., and Kim, K. 2005. Synthesis, x-ray crystal structures, and gas sorption properties of pillared square grid nets based on paddle-wheel motifs: Implications for hydrogen storage in porous materials. *Chemistry—A European Journal* 11, 3521–3529.

Ciolkowski, E.L., Maness, K.M., Cahill, P.S., Wightman, R.M., Evans, D.H., Fosset, B., and Amatore, C. 1994. Disproportionation during electrooxidation of catecholamines at carbon-fiber microelectrodes. *Analytical Chemistry* 66, 3611–3617.

Claye, A.S., Nemes, N.M., Janossy, A., and Fischer, J.E. 2000. Structure and electronic properties of potassium-doped single-wall carbon nanotubes. *Physical Review B: Condensed Matter and Materials Physics* 62, R4845–R4848.

Cofré, P., and Sawyer, D.T. 1986. Electrochemical reduction of dioxygen to perhydroxyl ($HO_2 \cdot$) in aprotic solvents that contain Bronsted acids. *Analytical Chemistry* 58, 1057–1062.

Colomer, M.T. 2006. Proton conductivity of nanoporous anatase xerogels prepared by a particulate sol–gel method. *Journal of Solid State Electrochemistry* 10, 54–59.

Colomer, M.T., and Anderson, M.A. 2001. High porosity silica xerogels prepared by a particulate sol–gel route: Pore structure and proton conductivity. *Journal of Non-Crystalline Solids* 290, 93–104.

Conway, B.E. 1991. Transition from "supercapacitor" to "battery" behavior in electrochemical energy storage. *Journal of the Electrochemical Society* 138, 1539–1548.

Corbin, D.R., Seidel, W.C., Abrams, L., Herron, N., Stucky, G.D., and Tolman, C.A. 1985. Shape selectivity in olefin hydrogenation using rhodium-containing zeolites. *Inorganic Chemistry* 24, 1800–1803.

Corma, A., Fornes, V., Martín-Aranda, R.M., García, H., and Primo, J. 1990. Zeolites as base catalysts: Condensation of aldehydes with derivatives of malonic esters. *Applied Catalysis*. 59, 237–248.

Corma, A., García, H., Primo, A., and Doménech, A. 2004. A test reaction to assess the presence of Brönsted acids and the softness-hardness of Lewis acid sites in palladium supported catalysts. *New Journal of Chemistry* 28, 361–365.

Cox, J.A., Jaworski, R.K., and Kulesza, P.J. 1991. Electroanalysis with electrodes modified by inorganic films. *Electroanalysis* 3, 869–877.

Cuentas-Gallegos, K., Lira-Cantú, M., Casañ-Pastor, N., and Gómez-Romero, P. 2004. Electroactive organic-inorganic hybrid materials. From electrochemistry to multifaceted applications. In *Trends in Electrochemistry and Corrosion at the Beginning of the 21st Century*. Brillas, E., Cabot, P.-L., Eds. Universitat de Barcelona, Barcelona, pp. 243–258.

Cummings, C.Y., Sott, S.J., Bonné, M.J., Edler, K.J., King, P.M., Mortimer, R.J., and Marken, F. 2008. Underpotential surface reduction of mesoporous CeO_2 nanoparticle films. *Journal of Solid State Electrochemistry* 12, 1541–1548.

Dahms, H. 1968. Electronic conduction in aqueous solution. *Journal of Physical Chemistry* 72, 362–364.

Dai, Z.H., Liu, S.Q., and Ju, H.X. 2004. Direct electron transfer of cytochrome *c* immobilized on a NaY zeolite matrix and its application in biosensing. *Electrochimica Acta* 49, 2139–2144.

Damertzis, M., and Evmiridis, N.P. 1986. Potentials of ion-exchanged synthetic zeolite–polymer membranes. *Journal of the Chemical Society Faraday Transactions I* 82, 3647–3655.

Dassas, Y., and Duby, P. 1995. Diffusion toward fractal interfaces. Potentiostatic, galvanostatic, and linear sweep voltammetric techniques. *Journal of the Electrochemical Society* 142, 4175–4180.

Daum, P., Lenhard, J.R., Rolison, D., and Murray, R.W. 1980. Diffusional charge transport through ultrathin films of radiofrequency plasma polymerized vinylferrocene at low temperature. *Journal of the American Chemical Society* 102, 4649–4653.

De Castro-Martins, S., Tuel, A., and Ben Taârit, Y. 1994. Characterization of titanium silicalites using cyclic voltammetry. In *Zeolites and Related Microporous Materials: State of the Art 1994*. Weitkamp, J., Karge, H.G., Pfeifer, H., and Holderich, W., Eds. *Studies in Surface Science and Catalysis*. 84, 501–508.

De Guzman, R.N., Shen, Y.-F., Neth, E.J., Suib, S.L., O'Young, C.-L., Levine, S., and Newsam, J.M. 1994. Synthesis and characterization of octahedral molecular sieves (OMS-2) having the hollandite structure. *Chemistry of Materials* 6, 815–821.

de Levie, R., and Vogt, A. 1990. On the electrochemical response of rough electrodes: Part II. The transient response in the presence of slow faradaic processes. *Journal of Electroanalytical Chemistry* 281, 23–28.

de Silva, A.P., Gunaratne, H.Q.N., and McCoy, C.P. 1997. Molecular photoionic and logic gates with bright fluorescence and "off–on" digital action. *Journal of the American Chemical Society* 119, 7891–7892.

Dell'Era, A., and Pasquali, M. 2009. Comparison between different ways to determine diffusion coefficient by solving Fick's equation for spherical coordinates. *Journal of Solid State Electrochemistry* 13, 849–859.

Delmas, C., Cognac-Auradou, H., Cocciantelli, J.M., Menetrier, M., and Doumerc, J.P. 1994. The $Li_xV_2O_5$ system: An overview of the structure modifications induced by the lithium intercalation. *Solid State Ionics* 69, 257–264.

Denny, R.A., and Sangaranarayan, M.V. 1998. Dynamics of electron hopping in redox polymer electrodes using kinetic Ising model. *Journal of Solid State Electrochemistry* 2, 67–72.

Derouane, E.G., André, J.M., and Lucas, A.A. 1988. Surface curvature effects in physisorption and catalysis by microporous solids and molecular sieves. *Journal of Catalysis* 110, 58–73.

Desilvestro, J., and Haas, O. 1990. Metal oxide cathode materials for electrochemical energy storage: A review. *Journal of the Electrochemical Society* 137, 5C–22C.

Devaraj, G., Guruviah, S., and Seshadri, S.K. 1990. Pulse plating. *Materials Chemistry and Physics* 25, 439–461.

DeWilde, W., Peeters, G., and Lunsford, J.H. 1980. Synthesis and spectroscopic properties of tris (2,2′-bipyridine)ruthenium(II) in zeolite Y. *Journal of Physical Chemistry* 84, 2306–2310.

Dharuman, V., and Chandrasekara Pillai, K. 2006. RuO_2 electrode surface effects in electrocatalytic oxidation of glucose. *Journal of Solid State Electrochemistry* 10, 967–979.

Di Cosmo, R., Burrington, J.D., and Grasselli, R.K. 1986. Oxidative dehydrodimerization of propylene over a Bi_2O_3---La_2O_2 oxide ion-conductive catalyst. *Journal of Catalysis* 102, 234–239.

Diggle, J.W., Downie, T.C., and Goulding, C.W. 1969. Anodic oxide films on aluminium. *Chemical Reviews* 69, 365–405.

Doherty, A.P., and Vos, J.G. 1992. Electrocatalytic reduction of nitrite at an $[Os(bipy)_2(PVC)_{10}Cl]$ Cl-modified electrode. *Journal of the Chemical Society Faraday Transactions* 88, 2903–2907.

Doménech, A. 2004. A model for solid-state voltammetry of zeolite-associated species. *Journal of Physical Chemistry B* 108, 20471–20478.

Doménech, A., and Alarcón, J. 2002a. Determination of hydrogen peroxide using glassy carbon and graphite/polyester composite electrodes modified by vanadium-doped zirconias. *Analytica Chimica Acta* 452, 11–22.

Doménech, A., and Alarcón, J. 2002b. Electrochemistry of vanadium-doped tetragonal and monoclinic ZrO_2 attached to graphite/polyester composite electrodes. *Journal of Solid State Electrochemistry* 6, 443–450.

Doménech, A., and Alarcón, J. 2003. Vanadium-doped zircon and zirconia materials prepared from gel precursors as site-selective electrochemical sensors. *Instrumentation, Science & Technology* 31, 121–139.

Doménech, A., and Alarcón, J. 2007. Microheterogeneous electrocatalytic chiral recognition at monoclinic vanadium-doped zirconias: Enantioselective detection of glucose. *Analytical Chemistry* 79, 6742–6751.

Doménech, A., Ribera, A., Cervilla, A., and Llopis, E. 1998. Electrochemistry of hydrotalcite-suported bis(2-mercapto-2,2-diphenyl-ethanoate)dioxomolybdate complexes. *Journal of Electroanalytical Chemistry* 458, 31–41.

Doménech, A., Doménech, M.T., García, H., and Galletero, M.S. 1999a. Electrocatalysis of neureotransmitter catecholamines by 2,4,6-triphenylpyrylium ion immobilized inside zeolite Y supercages. *Journal of the Chemical Society Chemical Communications* 2173–2174.

Doménech, A., Casades, I., and García, H. 1999b. Electrochemical evidence for an impeded attack of water to anthracene and thianthrene radical ions located on the outermost layers of zeolites. *Journal of Organic Chemistry* 64, 3731–3735.

Doménech, A., Formentín, P., García, H., and Sabater, M.J. 2000a. Combined electrochemical and EPR studies of manganese Schiff base complexes encapsulated within the cavities of zeolite Y. *European Journal of Inorganic Chemistry* 2000(6), 1339–1344.

Doménech, A., Corma, A., García, H., and Valencia, S. 2000b. Electrochemical characterization of two different framework Ti(IV) species in Ti/Beta zeolites in contact with solvents. *Topics in Catalysis* 11–12, 401–407.

Doménech, A., Doménech, M.T., Gimeno, J.V., Bosch, F., Saurí, M.C., and Sánchez, S. 2001. Electrochemistry of iron oxide pigments (earths) from pictorial microsamples attached to graphite/polyester composite electrodes. *Analyst* 126, 1764–1722.

Doménech, A., Formentín, P., García, H., and Sabater, M.J. 2002a. On the existence of different zeolite-associated topological redox isomers. Electrochemistry of Y zeolite-associated Mn(salen)N_3 complex. *Journal of Physical Chemistry B* 106, 574–582.

Doménech, A., García, H., Doménech, M.T., and Galletero, M.S. 2002b. 2,4,6-Triphenylpyrylium ion encapsulated into zeolite Y as a selective electrode for the electrochemical determination of dopamine in the presence of ascorbic acid. *Analytical Chemistry* 74, 562–569.

Doménech, A., Sánchez, S., Doménech, M.T., Gimeno, J.V., Bosch, F., Yusá, M.D., and Saurí, M.C. 2002c. Electrochemical determination of the Fe(III)/Fe(II) ratio in archaeological ceramic materials using carbon paste and composite electrodes. *Electroanalysis* 14, 685–696.

Doménech, A., Pérez, J., Kapteijn, F., Ribera, A., and Moulijn, J.A. 2002d. Characterization of iron centers in ex-framework FeZSM-5 catalyst by electrochemical methods. *Catalysis Letters* 78, 302–312.

Doménech, A., Pérez, J., Ribera, A., Mul, G., Kapteijn, F., and Arends, I.W.C.E. 2002e. Electrochemical characterization of iron sites in ex-framework FeZSM-5. *Journal of Electroanalytical Chemistry* 519, 72–84.

Doménech, A., García, H., Alvaro, M., and Carbonell, E. 2003a. Study of redox processes in zeolite Y-associated 2,4,6-triphenylthiopyrylium ion by square-wave voltammetry. *Journal of Physical Chemistry B* 107, 3040–3050.

Doménech, A., Alvaro, M., Ferrer, B., and García, H. 2003b. Electrochemistry of mesoporous organosilica of MCM-41 type containing 4,4′-bipyridinium units: Voltammetric response and electrocatalytic effect on 1,4-dihydrobenzoquinone oxidation. *Journal of Physical Chemistry B* 107, 12781–12788.

Doménech, A., Moyá, M., and Doménech, M.T. 2004a. Standard addition method applied to solid-state striping voltammetry. Determination of zirconium in minerals and ceramic materials. *Analytical and Bioanalytical Chemistry* 380, 146–156.

Doménech, A., Aucejo, R., Alarcón, J., and Navarro, P. 2004b. Electrocatalysis of the oxidation of methylenedioxyamphetamines at electrodes modified by cerium-doped zirconias. *Electrochemistry Communications* 6, 719–723.

Doménech, A., Torres, F.J., and Alarcón, J. 2004c. Electrochemistry of vanadium-doped ZrSiO$_4$. Site-selective electrocatalytic effect on nitrite oxidation. *Electrochimica Acta* 49, 4623–4632.

Doménech, A., Torres, F.J., and Alarcón, J. 2004d. Electrochemical characterization of cobalt cordierites attached to paraffin-impregnated graphite electrodes. *Journal of Solid State Electrochemistry* 8, 127–137.

Doménech, A., García, H., Casades, I., and Esplá, M. 2004e. Electrochemistry of 6-nitro-1′,3′,3′-trimethylspiro[2*H*-1-benzopyran-2,2′-indoline] associated to zeolite Y and MCM-41 aluminosilicate. Site-selective electrocatalytic effect on *N,N,N′,N′*-tetramethylbenzidine oxidation. *Journal of Physical Chemistry B* 108, 20064–20075.

Doménech, A., Costero, A.M., Bañuls, M.J., and Aurell, M.J. 2004f. Magnetoelectrochemical modulation of preorganization processes in a 4,4′-dinitrobiphenyl azacrown macrocyclic lactam. *Electrochemistry Communications* 6, 908–912.

Doménech, A., García, H., Marquet, J., and Herance, J.R. 2005a. Electrochemical monitoring of compartmentalization effects in the stability of Mesenheimer anions supported in hydrotalcite and X and Y zeolites. *Journal of the Electrochemical Society* 152, J74–J81.

Doménech, A., Ferrer, B., Fornés, V., García, H., and Leyva, A. 2005b. Ship-in-a-bottle synthesis of triphenylamine inside faujasite supercages and generation of the triphenylamminium radical ion. *Tetrahedron* 61, 791–796.

Doménech, A., García, H., and Carbonell, E. 2005c. Electro- and magneto-electrochemistry of zeolite Y- and MCM-41-associated bipyrylium ion. *Journal of Electroanalytical Chemistry* 577, 249–262.

Doménech, A., Doménech, M.T., Gimeno, J.V., and Bosch, F. 2006a. H-point standard addition method applied to solid state stripping voltammetry. Application to the determination of lead and tin in archaeological glazes. *Analytical and Bioanalytical Chemistry* 385, 1552–1561.

Doménech, A., García, H., Marquet, J., Bourdelande, J.L., and Herance, J.R. 2006b. Modelling electrocatalysis of hydroquinone oxidation by nicotinamide dinucleotide coenzyme encapsulated within SBA-15 and MCM-41 mesoporous aluminosilicates. *Electrochimica Acta* 51, 4897–4908.

Doménech, A., Doménech, M.T., and Vázquez, M.L. 2006c. Dehydroindigo: A new piece into the Maya blue puzzle from the voltammetry of microparticles approach. *Journal of Physical Chemistry B* 110, 6027–6039.

Doménech, A., García, H., Doménech, M.T., and Llabbrés-i-Xamena, F. 2006d. Electrochemical nanometric patterning of MOF particles: Anisotropic metal electrodeposition in Cu/MOF. *Electrochemistry Communications* 8, 1830–1834.

Doménech, A., Torres, F.J., Ruiz de Sola, E., and Alarcón, J. 2006e. Electrochemical detection of high oxidation states of chromium (IV and V) in chromium-doped cassiterite and tin-sphene ceramic pigmenting systems. *European Journal of Inorganic Chemistry* 638–648.

Doménech, A., Galletero, M.S., García, H., and Peris, E. 2006f. Electrolyte-driven electrochemical amplification by poly(thienylacetylene) encapsulated within zeolite Y. *Electrochemistry Communications* 8, 1335–1339.

Doménech, A., Doménech, M.T., and Vázquez, M.L. 2007a. Indigo/dehydroindigo/palygorskite complex in Maya blue: An electrochemical approach. *Journal of Physical Chemistry C* 111, 4585–4595.

Doménech, A., Doménech, M.T., and Vázquez, M.L. 2007b. Chemometric study of Maya blue from the voltammetry of microparticles approach. *Analytical Chemistry* 79, 2812–2821.

Doménech, A., Doménech, M.T., and Vázquez, M.L. 2007c. Electrochemical monitoring Maya Blue preparation from Maya's ancient procedures. *Journal of Solid State Electrochemistry* 11, 1335–1346.

Doménech, A., García, H., Doménech, M.T., and Llabrés-i-Xamena, F. 2007d. Electrochemistry of metal-organic frameworks: A description from the voltammetry of microparticles approach. *Journal of Physical Chemistry C* 111, 13701–13711.

Doménech, A., Coronado, E., Lardies, N., Martí, C., Doménech, M.T., and Ribera, A. 2008. Solid-state electrochemistry of LDH-supported polyaniline hybrid inorganic-organic material. *Journal of Electroanalytical Chemistry* 624, 275–286.

Doménech, A., Doménech, M.T., Sánchez del Río, M., and Vázquez, M.L. 2009. Comparative study of different indigo-clay Maya Blue-like systems using the voltammetry of microparticles approach. *Journal of Solid State Electrochemistry*, 13, 869–878.

Duic, L., and Grigic, S. 2001. The effect of polyaniline morphology on hydroquinone/quinone redox reaction. *Electrochimica Acta* 46, 2795–2803.

Dutta, P.K., and Turbeville, W. 1992. Intrazeolitic photoinduced redox reactions between tris(2,2′-bipyridine)ruthenium(2+) and methylviologen. *Journal of Physical Chemistry* 96, 9410–9416.

DuVall, S., and McCreery, R.L. 1999. Control of catechol and hydroquinone electron transfer kinetics on native and modified glassy carbon electrodes. *Analytical Chemistry* 71, 45594–45602.

DuVall, S., and McCreery, R.L. 2000. Self-catalysis by catechols and quinones during heterogeneous electron transfer at carbon electrodes. *Journal of the American Chemical Society* 122, 6759–6764.

Echegoyen, L.E., Herranz, M.A., Echegoyen, L. 2006. Carbon, fullerenes. In *Inorganic Electrochemistry. Encyclopedia of Electrochemistry*, vol. 7. Bard, A.J., Stratmann, M., Schoilz, F., and Pickett, C.J., Eds. Wiley-VCH, Weinheim, pp. 143–201.

Edgell, R.G., Goodenough, J.B., Hammett, A., and Naish, C.J. 1983. Electrochemistry of ruthenates: Part 1. Oxygen reduction on pyrochlore ruthenates. *Journal of the Chemical Society Faraday Transactions I* 79, 893–912.

Eftekhari, A. Ed. 2008. *Nanostructured Materials in Electrochemistry*. Wiley-VCH, Weinheim.

Egbe, D.A.M., Cornelia, B., Nowotny, J., Günther, W., and Klemm, E. 2003. Investigation of the photophysical and electrochemical properties of alkoxy-substituted arylene−ethynylene/arylene−vinylene hybrid polymers. *Macromolecules* 36, 5459–5469.

Evans, D.H. 1990. Solution electron-transfer reactions in organic and organometallic electrochemistry. *Chemical Reviews* 90, 739–751.

Fahidy, T.Z. 1983. Magnetoelectrolysis. *Journal of Applied Electrochemistry* 13, 553–653.

Fahidy, T.Z. 1999. The effect of magnetic fields on electrochemical processes. In *Modern Aspects of Electrochemistry*, no. 32. Conway, B.E., Bockris, O.M., and White, R.E., Eds. Kluwer/Plenum, New York, pp. 333–354.

Farin, D., Volpert, A., and Avnir, D. 1985. Determination of adsorption conformation from surface resolution analysis. *Journal of the American Chemical Society* 107, 3368–3370.

Feng, Y., Cui, Y., Logan, B., and Liu, Z. 2008. Performance of Gd-doped Ti-based Sb-SnO$_2$ anodes for electrochemical destruction of phenol. *Chemosphere* 70, 1629–1636.

Férey, G., Millange, F., Morcrette, M., Serre, C., Doublet, M.-L., Grenèche, J.-M., and Tarascon, J.-M. 2007. Mixed-valence Li/Fe-based metal-organic frameworks with both reversible redox and sorption properties. *Angewandte Chemie International Edition* 46, 3259–3263.

Fois, E., Gamba, A., and Tilocca, A. 2003. On the unusual stability of Maya blue paint: Molecular dynamics simulations. *Microporous and Mesoporous Materials* 57, 263–272.

Forster, R.J. 1994. Microelectrodes: New dimensions in electrochemistry. *Chemical Society Reviews* 23, 289–297.

Frackowiak, E., and Beguin, F. 2002. Electrochemical storage of energy in carbon nanotubes and nanostructured carbons. *Carbon* 40, 1775–1787.

Freund, M.S., and Brajter-Toth, A. 1992. Semi-integral analysis in cyclic voltammetry: Determination of surface excess and concentration in the presence of weak adsorption and thin films. *Analytical Chemistry* 96, 9400–9406.

Friedrich, A., Hefele, H., Mickler, W., Mönner, A., Uhlemann, E., and Scholz, F. 1998. Voltammetric and potentiometric studies on the stability of vanadium(IV) complexes. A comparison of solution phase voltammetry with the voltammetry of microcrystalline solid compounds. *Electroanalysis* 10, 244–248.

Funke, K., Roling, B., and Lange, M. 1998. Dynamics of mobile ions in crystals, glasses and melts. *Solid State Ionics* 105, 195–208.

Fusalba, F., and Bélanger, D. 2000. Electrochemical characterization of polyaniline–molybdenum trisulfide electrode in non-aqueous media. *Electrochimica Acta* 45, 3877–3883.

Gabel, J., Vonau, W., Shuk, P., and Guth, U. 2004. New reference electrodes based on tungsten-substituted molybdenum bronzes. *Solid State Ionics* 169, 75–80.

Galal, A., Darwish, S.A., and Ahmed, R.A. 2007. Hybrid organic/inorganic films of conducting polymers modified with phthalocyanines: II. EIS studies and characterization. *Journal of Solid State Electrochemistry* 11, 531–542.

Gao, M., Dai, L., and Wallace, G.G. 2003. Glucose sensors based on glucose-oxidase-containing polypyrrole/aligned carbon nanotube coaxial nanowire electrodes. *Syntheticmet* 137, 1393–1394.

García, H., and Roth, H.D. 2002. Generation and reactions of organic radical cations in zeolites. *Chemical Reviews* 102, 3947–4007.

Garcia, P., Pernaut, J.M., Witgens, V., Valat, P., Gaunier, F., and Delabouglise, D. 1992. Effect of end substitution on electrochemical and optical properties of oligothiophenes. *Journal of Physical Chemistry* 97, 513–516.

Gasik, M., Ed. 2008. *Materials for Fuel Cells*. CRC-Woodhead, Cambridge.

Gaupp, C.L., Welsh, D.M., Rauh, R.D., and Reynolds, J.R. 2002. Composite coloration efficiency measurements of electrochromic polymers based on 3,4-alkylenedioxythiophenes. *Chemistry of Materials* 14, 3964–3970.

Gefen, Y., Aharony, A., and Alexander, S. 1983. Anomalous diffusion on percolating clusters. *Physical Review Letters* 50, 77–80.

Gemborys, H.A., and Shaw, B.R. 1986. Electrochemical behavior of methyl viologen in zeolite particle films. *Journal of Electroanalytical Chemistry* 208, 95–107.

Ghosh, P.K., Mau, A.W.-H., and Bard, A.J. 1984. Clay-modified electrodes: Part II. Electrocatalysis at bis(2,2′-bipyridyl) (4,4′-dicarboxy-2,2′-bipyridyl)Ru(II)-dispersed ruthenium dioxide—hectorite layers. *Journal of Electroanalytical Chemistry* 169, 315–317.

Giona, M., and Roman, H.E. 1992. Fractional diffusion equation for transport phenomena in random media. *Physica A* 185, 87–97.

Girdauskaite, E., Ullmann, H., Al Daroukh, M., Vashook, V., Bülow, M., and Guth, U. 2006. Oxygen non-stoichiometry and electrical conductivity of $Pr_{2-x}Sr_xNiO_{4\pm\delta}$ with $x = 0$–0.5. *Solid State Ionics* 167, 1163–1171.

Girdauskaite, E., Ullmann, H., Al Daroukh, M., Vashook, V., Bülow, M., and Guth, U. 2007. Oxygen stoichiometry, unit cell volumes, and thermodynamic quantities of perovskite-type oxides. *Journal of Solid State Electrochemistry* 11, 469–477.

Giustetto, R., Llabrés i Xamena, F.X., Ricchiardi, G., Bordiga, S., Damin, A., Gobetto, R., and Chierotti, M.R. 2005. Maya blue: A computational and spectroscopic study. *Journal of Physical Chemistry B* 109, 19360–19368.

Go, J.-Y., and Pyun, S.-I. 2004. A study on lithium transport through fractal $Li_{1-\delta}CoO_2$ film electrode by analysis of current transient based upon fractal theory. *Electrochimica Acta* 49, 2551–2562.

Go, J.-Y., and Pyun, S.-I. 2007. A review of anomalous diffusion phenomena at fractal interface for diffusion-controlled and non-diffusion-controlled transfer processes. *Journal of Solid State Electrochemistry* 11, 323–334.

Gómez-Romero, P., and Sánchez, C., Eds. 2004. *Functional Hybrid Materials*. Wiley, New York.

Grandqvist, C.G. 1999. Progress in electrochromics: Tungsten oxide revisited. *Electrochimica Acta* 44, 3005–3015.

Grimm, J., Bessarabov, D., Maier, W., Storck, S., and Sanderson, R.D. 1998. Sol-gel film-preparation of novel electrodes for the electrocatalytic oxidation of organic pollutants in water. *Desalination* 115, 295–302.

Grodzka, E., Grabowska, J., Wysocka-Zolopa, M., and Winkler, K. 2008. Electrochemical formation and properties of two-component films of transition metal complexes and C_{60} or C_{70}. *Journal of Solid State Electrochemistry* 12, 1267–1278.

Gründler, P. 2007. *Chemical Sensors*. Springer, Berlin.

Grygar, T., Marken, F., Schröder, U., and Scholz, F. 2002. Voltammetry of microparticles: A review. *Collection Czechoslovack Chemical Communications* 67, 163–208.

Guglielmetti, R. 1990. In *Photochromism, Molecules and Systems*. Durr, H. and Bonas-Laurent, H., Eds. Elsevier, Amsterdam, pp. 855–878.

Guha, S., and Nakamoto, K. 2005. Electronic structures and spectral properties of endohedral fullerenes. *Coordination Chemistry Reviews* 249, 1111–1132.

Guidelli, R. 1971. Diffusion toward planar, spherical, and dropping electrodes at constant potential. *Journal of Electroanalytical Chemistry* 33, 303–317.

Guo, G.H., Tao, Y.T., Song, Z.P., and Zhang, K.L. 2007. Zinc tetrathiomolybdate as novel anodes for rechargeable lithium batteries. *Journal of Solid State Electrochemistry* 11, 90–92.

Guth, U., Gerlach, F., Decker, M., Oelssner, W., and Vonau, W. 2009. Solid-state reference electrodes for potentiometric sensors. *Journal of Solid State Electrochemistry* 13, 27–39.

Hah, H.J., Kim, J.S., Jeon, B.J., Koo, S.M., and Lee, Y.E. 2003. Simple preparation of monodisperse hollow silica particles without using templates. *Chemical Communications* 14, 1712–1713.

Hamachi, I., Fujita, A., and Kunitake, T. 1997. Protein engineering using molecular assembly: Functional conversion of cytochrome *c* via noncovalent interactions. *Journal of the American Chemical Society* 119, 9096–9102.

Hanson, R.M. 1991. The synthetic methodology of nonracemic glycidol and related 2,3-epoxy alcohols. *Chemical Reviews* 91, 437–475.

Hasse, U., and Scholz, F. 2001. In situ atomic force microscopy of the reduction of lead oxide nanocrystals immobilised on an electrode surface. *Electrochemistry Communications* 3, 429–434.

Hattori, H. 1995. Heterogeneous basic catalysis. *Chemical Reviews* 95, 537–558.

Hayes, E.A., Stemple, J.Z., and Rolison, D.R. 1994. In *Water Purification by Photoelectrochemical, Photochemical, and Electrochemical Methods*, vol. 94–19. Rose, T.L., Conway, B.E., and Murphy, O.J. Eds., The Electrochemical Society, Pennington, NJ, p. 121.

Hazzazi, O.A., Attard, G.A., and Wells, P.B. 2004. Molecular recognition in adsorption and electro-oxidation at chiral platinum surfaces. *Journal of Molecular Catalysis A: Chemical* 216, 247–255.

Heering, H.A., Wiertz, F.G.M., Dekker, C., and de Vries, S. 2004. Direct immobilization of native yeast iso-1 cytochrome *c* on bare gold: Fast electron relay to redox enzymes and zeptomole protein-film voltammetry. *Journal of the American Chemical Society* 126, 11103–11112.

Herance, J.R., Concepción, P., Doménech, A., Bourdelande, J.L., Marquet, J., and García, H. 2005. Anionic organic guests incorporated within zeolites. Adsorption and reactivity of the Meisenheimer complex in faujasites. *Chemistry A European Journal* 11, 6491–6502.

Hirsch, A. 1993. The chemistry of the fullerenes: An overview. *Angewandte Chemie International Edition* 32, 1138–1141.

Hirsch, A., Li, Q., and Wudl, F. 1991. Globe-trotting hydrogens on the surface of the fullerene compound $C_{60}H_6(N(CH_2CH_2)_2O)_6$. *Angewandte Chemie International Edition* 30, 1309–1310.

Honda, K., and Fujishima, A. 1972. Electrochemical photolysis of water at a semiconductor electrode. *Nature* 238, 37.

Honders, A., and Broers, G.H.J. 1985. Bounded diffusion in solid solution electrode powder compacts: Part I. The interfacial impedance of a solid solution electrode (M_xSSE) in contact with a m^+-ion conducting electrolyte. *Solid State Ionics* 15, 173–183.

Howell, J.O., and Wightman, R.M. 1984. Ultrafast voltammetry and voltammetry in highly resistive solutions with microvoltammetric electrodes. *Analytical Chemistry* 56, 524–529.

Howie, J.K., Houts, J.J., and Sawyer, D.T. 1977. Oxidation-reduction chemistry of DL-α-lipoic acid, propanedithiol, and trimethyllene disulfide in aprotic and in aqueous media. *Journal of the American Chemical Society* 99, 6323–6326.

Hozumi, A., Yokogawa, Y., Kameyama, T., Hiraku, K., Sugimura, H., Takai, M., and Okido, M. 2000. Photocalcination of mesoporous silica films using vacuum ultraviolet light. *Advanced Materials* 12, 985–987.

Hu, C.C., and Tsou, T.W. 2002. Ideal capacitive behavior of hydrous manganese oxide prepared by anodic deposition. *Electrochemistry Communications* 4, 105–109.

Hubbard, B., Kuang, W., Moser, A., Facey, G.A., and Detellier, C. 2003. Structural study of Maya blue: Textural, thermal and solid-state multinuclear magnetic resonance characterization of the palygroskite-indigo and sepiolite-indigo adducts. *Clays and Minerals* 51, 318–326.

Iijima, S., 1991. Helical microtubules of graphitic carbon. *Nature* 354, 56–57.

Ilangovan, G., and Chandarasekara Pillai, K. 1997. Unusual activation of glassy carbon electrodes for enhanced adsorption of monomeric molybdate(VI). *Journal of Electroanalytical Chemistry* 431, 11–14.

Inagaki, S., Guan, S., Fukushima, Y., Oshuna, T., Terasaki, O. 1999. Layer-by-layer assembly of zeolite crystals on glass with polyelectrolytes as ionic linkers. *Journal of the American Chemical Society* 121, 9611–9614.

Ingersoll, D., Kulesza, P.J., and Faulkner, L.R. 1994. Polyoxometallate-based layered composite films on electrodes. Preparation through alternate immersions in modification solutions. *Journal of the Electrochemical Society* 141, 140–147.

Jamnik, J., Kalnin, J.R., Kotomin, E.A., and Maier, J. 2006. Generalised Maxwell-Garnett equation: Application to electrical and chemical transport. *Physical Chemistry Chemical Physics* 8, 1310–1314.

Janiak, C. 2003. Engineering coordination polymers towards applications. *Journal of the Chemical Society Dalton Transactions* 14, 2781–2804.

Janska, J., and Dousek, F.P. 1973. Electrochemical corrosion of polytetrafluorethylene contacting lithium amalgam. *Electrochimica Acta* 18, 673–674.

Jiang, D., Zhao, H., Zhang, S., and John, R. 2003. Characterization of photoelectrocatalytic processes at nanoporous TiO_2 film electrodes: Photocatalytic oxidation of glucose. *Journal of Physical Chemistry B* 107, 12774–12780.

Jiang, Y., Mallat, T., Krumeich, F., and Baiker, A. 2008. Copper-based metal-organic framework for the facile ring-opening of epoxides. *Journal of Catalysis* 257, 390–395.

Jiang, Y., Yentekakis, I.V., and Vayenas, C.G. 1994. Methane to ethylene with 85 percent yield in a gas recycle electrocatalytic reactor-separator. *Science* 264, 1563–1566.

Jiang, Y.-X., Si, D., Chen, S.-P., and Sun, S.-G. 2006. Self-assembly film of zeolite y nano-crystals loading palladium on an au electrode for electrochemical applications. *Electroanalysis* 18, 1173–1178.

Johansson, G., Risinger, L., and Faelth, L. 1977. A cesium-selective electrode prepared from a crystalline synthetic zeolite of the mordenite type. *Analytica Chimica Acta* 119, 25–32.

Jonscher, A.K. 1983. The measurement and interpretation of dielectric properties. *Thin Solid Films* 100, 329–334.

Joo, S.H., Lee, H.I., You, D.J., Kwon, K., Kim, J.H., Choi, Y.S., Kang, M., Kim, J.M., Pak, C., Chang, H., and Seung, D. 2008. Ordered mesoporous carbons with controlled particle sizes as catalyst supports for direct methanol fuel cell cathodes. *Carbon* 46, 2034–2045.

José-Yacamán, M., Rendón, L., Arenas, J., and Serra Puche, M.C. 1996. Maya blue paint: An ancient nanostructured material. *Science* 273, 223–224.

Joyner, R., and Stockenhuber, M. 1999. Preparation, characterization, and performance of Fe–ZSM-5 catalysts. *Journal of Physical Chemistry B* 103, 5963–5976.

Jung, K.-N., and Pyun, S.-I. 2006a. Effect of pore structure on anomalous behaviour of the lithium intercalation into porous V_2O_5 film electrode using fractal geometry concept. *Electrochimica Acta* 51, 2646–2655.

Jung, K.-N., and Pyun, S.-I. 2006b. The cell-impedance-controlled lithium transport through $LiMn_2O_4$ film electrode with fractal surface by analyses of ac-impedance spectra, potentiostatic current transient and linear sweep voltammograms. *Electrochimica Acta* 51, 4649–4658.

Juzeliunas, E. 2007. Advances in detection of magnetic fields induced by electrochemical reactions—A review. *Journal of Solid State Electrochemistry* 11, 791–798.

Kallenberg, A., Vaszilcsin, N., and Brandl, W. 2007. Roughness factor evaluation of thermal arc sprayed skeleton nickel electrodes. *Journal of Solid State Electrochemistry* 11, 84–89.

Kant, R., and Rangarajan, S.K. 1995. Diffusion to rough interfaces: Finite charge transfer rates. *Journal of Electroanalytical Chemistry* 396, 285–301.

Katz, E., Lioubashevsky, O., and Willner, I. 2004. Electromechanics of a redox-active rotaxane in a monolayer assembly on an electrode. *Journal of the American Chemical Society* 126, 15520–15532.

Kavan, L. 1997. Electrochemical carbon. *Chemical Reviews* 97, 3061–3082.

Kavan, L., and Hlavaty, J. 1999. Carbon nanostructures from perfluorinated hydrocarbons. *Carbon* 37, 1863–1865.

Kavan, L., Rapta, P., and Dunsch, L. 2000. In situ Raman and VIS NIR spectroelectrochemistry of single wall carbon nanotubes. *Chemical Physics Letters* 328, 361–366.

Kavan, L., Rapta, P., Dunsch, L., Bronikowski, M.J., Willis, P., and Smalley, R.E. 2001. Electrochemical tuning of electronic structure of single-walled carbon nanotubes: In situ Raman and Vis-NIR study. *Journal of Physical Chemistry B* 105, 10764–10771.

Kavan, L., Hlavaty, J., and Janda, P. 2004. Electrochemical approach to carbon nanostructures. In *Trends in Electrochemistry and Corrosion at the Beginning of the 21st Century*. Brillas, E., and Cabot, P.-L., Eds. Universitat de Barcelona, Barcelona, pp. 77–101.

Kaye, S.S., and Long, J.R. 2005. Hydrogen storage in the dehydrated Prussian blue analogues $M_3[Co(CN)_6]_2$ (M = Mn, Fe, Co, Ni, Cu, Zn). *Journal of the American Chemical Society* 127, 6506–6507.

Keita, B., and Nadjo, L. 1987. New aspects of the electrochemistry of heteropolyacids: Part II. Coupled electron and proton transfers in the reduction of silicotungstic species. *Journal of Electroanalytical Chemistry* 217, 287–304.

Keita, B., and Nadjo, L. 1988. Surface modifications with heteropoly and isopoly oxometalates: Part I. Qualitative aspects of the activation of electrode surfaces towards the hydrogen evolution reaction. *Journal of Electroanalytical Chemistry* 243, 87–103.

Keita, B., and Nadjo, L. 2006. Electrochemistry of isopoly and heteropoly oxometalates. In *Inorganic Chemistry. Encyclopedia of Electrochemistry*, vol. 7b. Bard, A.J., Stratmann, M., Scholz, F., and Pickett, C.J., Eds. Wiley-VCH, Weinheim.

Kessler, T., Visintin, A., Bolzan, A.E., Andreasen, G., Salvarezza, R.C., Triaca, W.E., and Arvia, A.J. 1996. Electrochemical and scanning force microscopy characterization of fractal palladium surfaces resulting from the electroreduction of palladium oxide layers. *Langmuir* 12, 6587–6596.

Khan, A.I., and O'Hare, D. 2002. Intercalation chemistry of layered double hydroxides: Recent developments and applications. *Journal of Materials Chemistry* 12, 3191–3198.

Kharton, V.V., Marques, F.M.B., and Atkinson, A. 2004. Transport properties of solid oxide electrolyte ceramics: A brief review. *Solid State Ionics* 174, 135–149.

Kharton, V.V., Naumovich, E.N., Yaremchenko, A.A., and Marques, F.M.B. 2001. Research on the electrochemistry of oxygen ion conductors in the former Soviet Union. *Journal of Solid State Electrochemistry* 5, 160–187.

Khorkunov, B.A., Näfe, H., and Aldinger, F. 2006. Relationship between the ionic and electronic partial conductivities of co-doped LSGM ceramics from oxygen partial pressure dependence of the total conductivity. *Journal of Solid State Electrochemistry* 10, 479–487.

Khotari, H.M., Kulp, E.A., Boonsalee, S., Nikiforov, M.P., Bohannan, E.W., Poizot, P., Nakanishi, S., and Switzer, J.A. 2004. Enantiospecific electrodeposition of chiral CuO films from copper(II) complexes of tartaric and amino acids on single-crystal Au(001). *Chemistry of Materials* 16, 4232–4244.

Kickelbick, G., Ed. 2007. *Hybrid Materials. Synthesis, Characterization, and Applications.* Wiley-VCH, Weinheim.

Kida, T., Guan, G., Minami, Y., Ma, T., and Yoshida, A. 2003. Photocatalytic hydrogen production from water over a $LaMnO_3$/CdS composite prepared by the reverse micelle method. *Journal of Materials Chemistry* 13, 1186–1191.

Kim, Y.J., Horie, Y., Ozaki, S., Matsuzawa, Y., Suezaki, H., Kim, C., Miyashita, N., and Endo, M. 2004. Correlation between the pore and solvated ion size on capacitance uptake of PVDC-based carbons. *Carbon* 42, 1491–1500.

Kim, D.W., Park, J.K., and Rhee, H.W. 1996. Conductivity and thermal studies of solid polymer electrolytes prepared by blending poly(ethylene oxide), poly(oligo[oxyethylene] oxysebacoyl) and lithium perchlorate. *Solid State Ionics* 83, 49–56.

Kim, T.-W., Park, I.-S., and Ryoo, R. 2003. A synthetic route to ordered mesoporous carbon materials with graphitic walls. *Angewandte Chemie International Edition* 42, 4275.

Kitagawa, S., Kitaura, R., and Noro, S. 2004. Functional porous coordination polymers. *Angewandte Chemie International Edition* 43, 2334–2375.

Kleber, R, Masschelein-Kleiner, L., and Thissen, J. 1967. Study and identification of Maya blue. *Studies in Conservation* 12, 41–56.

Klessinger, M., and Lüttke, W. 1963. Theoretical and spectroscopic investigation of indigo dyes II. The chromophore system of the indigo dyes. *Tetrahedron Letters* 19 (suppl. 2), 315–335.

Koffyberg, F.P., and Benko, F.A. 1982. A photoelectrochemical determination of the position of the conduction band and the valence band edges of *p*-type CuO. *Journal of Applied Physics* 53, 1173–1177.

Kokoh, K.B., Leger, J.-M., Beden, B., and Lamy, C. 1992. "On line" chromatographic analysis of the products resulting from the electrocatalytic oxidation of D-glucose on Pt, Au and adatoms modified Pt electrodes—Part I. Acid and neutral media. *Electrochimica Acta* 37, 1333–1342.

Konaka, R., Terabe, S., and Kuruma, K. 1969. Mechanism of the oxidation reaction with nickel peroxide. *Journal of Organic Chemistry* 34, 1334–1337.

Kondintsev, I.M., and Trasatti, S. 1994. Electrocatalysis of H_2 evolution on RuO_2 + IrO_2 mixed oxide electrodes. *Electrochimica Acta* 39, 1803–1808.

Kornic, S., and Baker, M.D. 2002. Nanoporous zeolite film electrodes. *Chemical Communications* 16, 1700–1701.

Koutecky, J., and Brdicka, R. 1947. Fundamental equation for the electrolytic current when depending on the formation rate of the depolarizer and the rate of diffusion, polarographic verification. *Collection of Czechoslovack Chemical Communications* 12, 337–355.

Koza, Z. 2000. Diffusion coefficient and drift velocity in periodic media. *Physica A* 285, 176–186.

Kröger, F.A., and Vink, H.J. 1956. Relations between the concentrations of imperfections in crystalline solids. *Solid State Physics* 3, 307–435.

Kroto, H.W., Heath, J.R., O'Brien, S.C., Curl, R.F., and Smalley, R.E. 1985. C_{60}: Buckminsterfullerene. *Nature* 318, 162.

Kruk, M., Javoniec, M., Ko, C.H., and Ryoo, R. 2000. Characterization of the porous structure of SBA-15. *Chemistry of Materials* 12, 1961–1968.

Kuang, F., Zhang, D., Li, Y., Wan, Y., and Hou, B. 2009. Electrochemical impedance spectroscopy analysis for oxygen reduction reaction in 3.5% NaCl solution. *Journal of Solid State Electrochemistry* 13, 385–390.

Kuchi, V., Oliver, A.M., Paddon-Row, M.N., and Howe, R.F. 1999. Long-lived charge separation in a donor-acceptor dyad adsorbed in mesoporous MCM-41. *Chemical Communications*, 1149–1150.

Kuwana, T., and French, W.G. 1964. Electrooxidation or reduction of organic compounds into aqueous solutions using carbon paste electrode. *Analytical Chemistry* 36, 241–242.

Lai, C.-Z., Fierke, M.A., Stein, A., and Bühlmann, P. 2007. Ion-selective electrodes with three-dimensionally ordered macroporous carbon as the solid contact. *Analytical Chemistry* 79, 4621–4626.

Lai, C.-Z., Joyer, M.M., Fierke, M.A., Petkovich, N.D., Stein, A., and Bühlmann, P. 2009. Subnanomolar detection limit application of ion-selective electrodes with three-dimensionally ordered macroporous (3DOM) carbon solid contacts. *Journal of Solid State Electrochemistry* 13, 123–128.

Lainé, P., Lanz, M., and Calzaferri, G. 1996. Limits of the in situ synthesis of tris(2,2′-bipyridine) ruthenium(II) in the supercages of zeolite Y. *Inorganic Chemistry* 35, 3514–3518.

Langer, S.H., and Yurchak, S.J. 1969. Electrochemical reduction of the Benzene Ring by electrogenerative hydrogenation. *Journal of the Electrochemical Society* 116, 1228.

Langer, S.H., and Pate, K.T. 1980. Electrogenerative reduction of nitric oxide. *Nature* 284, 434–435.

Langer, S.H., and Colucci-Rios, J.A. 1985. Chemicals with power. *Chemtech* 15, 226–233.

Larose, S., and Akbar, S.A. 2006. Synthesis and electrical properties of dense $Bi_2Al_4O_9$. *Journal of Solid State Electrochemistry* 10, 488–498.

Laviron, E. 1979. General expression of the linear potential sweep voltammogram in the case of diffusionless electrochemical systems. *Journal of Electroanalytical Chemistry* 101, 19–28.

Laviron, E. 1980. A multilayer model for the study of space-distributed redox modified electrodes: Part I. Description and discussion of the model. *Journal of Electroanaytical Chemistry* 112, 1–9.

Laviron, E. 1984. Electrochemical reactions with protonations at equilibrium: Part X. The kinetics of the *p*-benzoquinone/hydroquinone couple on a platinum electrode. *Journal of Electroanalytical Chemistry* 164, 213–227.

Ledney, M., and Dutta, P.K. 1995. Oxidation of water to dioxygen by intrazeolitic $Ru(bpy)_3^{3+}$. *Journal of the American Chemical Society* 117, 7687–7695.

Lee, G.S., Lee, Y.-J., and Yoon, K.B. 2001. Layer-by-layer assembly of zeolite crystals on glass with polyelectrolytes as ionic linkers. *Journal of the American Chemical Society* 123, 9769–9779.

Leger, C., Bach, S., and Pereira-Ramos, J.P. 2001. The sol–gel chromium-modified V_6O_{13} as a cathodic material for lithium batteries. *Journal of Solid State Electrochemistry* 11, 71–76.

مرجع دانشجویان و مهندسین مواد

Lei, L., Hu, M., Gao, X., and Sun, Y. 2008. The effect of the interlayer anions on the electrochemical performance of layered double hydroxide electrode materials. *Electrochimica Acta* 54, 671–676.

Le Mehaute, A., and Crepy, G. 1983. Introduction to transfer and motion in fractal media: The geometry of kinetics. *Solid State Ionics* 9–10, 17–30.

Leroux, F., Raymundo-Piñero, E., Fedelec, J.-M., and Béguin, F. 2006. Textural and electrochemical properties of carbon replica obtained from styryl organo-modified layered double hydroxide. *Journal of Materials Chemistry* 16, 2074–2081.

Leventis, H.C., Streeter, I., Wildgoose, G.G., Lawrence, N.S., Jiang, L., Jones, T.G.J., and Compton, R.G. 2004. Derivatised carbon powder electrodes: Reagentless pH sensors. *Talanta* 63, 1039–10551.

Leventis, N., Dass, A., and Chandrasekaran, N. 2007. Mass transfer effects on the electropolymerization current efficiency of 3-methylthiophene in the magnetic field. *Journal of Solid State Electrochemistry* 11, 727–735.

Levi, M.D., and Aurbach, D. 2007. The application of electroanalytical methods to the analysis of phase transitions during intercalation of ions into electrodes. *Journal of Solid State Electrochemistry* 11, 1031–1042.

Li, H.-Y., and Anson, F.C. 1985. Electrochemical behavior of cationic complexes incorporated in clay coatings on graphite electrodes. *Journal of Electroanalytical Chemistry* 184, 411–417.

Li, J., Papadopoulos, C., Xu, J.M., and Moskovits, M. 1999. Highly-ordered carbon nanotube arrays for electronics applications. *Applied Physics Letters* 75, 367–369.

Li, J., and Zeng, H.C. 2006. Preparation of monodisperse Au/TiO_2 nanocatalysts via selfassembly. *Chemistry of Materials* 18, 2770–2777.

Li, J.-W., Pfanner, K., and Calzaferri, G. 1995. Silver-modified electrodes: An intrazeolite electron transport mechanism. *Journal of Physical Chemistry* 99, 2119–2126.

Li, J.-W., Pfanner, K., and Calzaferri, G. 1995. Reply to "Comment on intrazeolite electron transport mechanism." The importance of the manner to prepare zeolite-modified electrodes. *Journal of Physical Chemistry* 99, 12368–12369.

Li, M.C., and Shen, J.N. 2006. Photoelectrochemical oxidation behaviour of organic substances on TiO_2 thin-film electrodes. *Journal of Solid State Electrochemistry* 10, 980–986.

Li, X., Cheng, F., Zhang, S., and Chen, J. 2006. Shape-controlled synthesis and lithium-storage study of metal-organic frameworks $Zn_4O(1,3,5$-benzenetribenzoate$)_2$. *Journal of Power Sources* 160, 542–547.

Li, Z., Lai, C., and Mallouk, T.E. 1989. Self assembling trimolecular redox chains at zeolite Y modified electrodes. *Inorganic Chemistry* 28, 178–182.

Liang, Y.-Y., Bao, S.-J., and Li, H.-L. 2007. Nanocrystalline nickel cobalt hydroxides/ ultrastable Y zeolite composite for electrochemical capacitors. *Journal of Solid State Electrochemistry* 11, 571–576.

Licht, S., Wang, B., Xu, G., Li, J., and Naschitz, V. 1999. Insoluble Fe(VI) compounds: Effects on the super-iron battery. *Electrochemistry Communications* 1, 522–526.

Licht, S., Naschitz, V., Lin, L., Chen, J. Ghosh, S., and Liu, B. 2001. Analysis of ferrate(VI) compounds and super-iron Fe(VI) battery cathodes: FTIR, ICP, titrimetric, XRD, UV/ VIS, and electrochemical characterization. *Journal of Power Sources* 101, 167–176.

Limmer, S.J., Kulp, E.A., and Switzer, J.A. 2006. Epitaxial electrodeposition of ZnO on Au(111) from alkaline solution: Exploiting amphoterism in Zn(II). *Langmuir* 22, 10535–10539.

Lin, S.-Y., Chen, Y.-C., Wang, C.-M., and Liu, C-C. 2008. Effect of heat treatment on electrochromic properties of TiO_2 thin films. *Journal of Solid State Electrochemistry* 12, 1481–1486.

Liu, B., Shioyama, H., Akita, T., and Xu, Q. 2008. Metal-organic frameworks as a template for porous carbon synthesis. *Journal of the American Chemical Society* 130, 5390–5391.

Liu, X.-X., Bian, L.-J., Zhang, L., and Zhang, L.-J. 2007. Composite films of polyaniline and molybdenum oxide formed by electrocodeposition in aqueous media. *Journal of Solid State Electrochemistry* 11, 1279–1286.

Liu, Z.P., Ma, R.Z., Osada, M., Iyi, N., Ebina, Y., Takada, K., and Sasaki, T. 2006. Synthesis, anion exchange, and delamination of Co–Al layered double hydroxide: Assembly of the exfoliated nanosheet/polyanion composite films and magneto-optical studies. *Journal of the American Chemical Society* 128, 4872–4880.

Lodi, G., Zucchini, G.L., De Battisti, A., Giatti, A., Battaglin, G., and Della Mea, G. 1991. Proton exchange in group VIII metal-oxide films. *Surface Science*, 251–252, 836–840.

Logothetis, E.M. 1980. Resistive-type exhaust gas sensors. *Ceramic Engineering Science Proceedings* 1, 281–301.

Lovric, M. 2002. Square-wave voltammetry. In *Electroanalytical Methods*. Scholz, F., Ed. Springer, Berlin.

Lovric, M., Hermes, M., and Scholz, F. 1998. The effect of the electrolyte concentration in the solution on the voltammetric response of insertion electrodes. *Journal of Solid State Electrochemistry* 2, 401–404.

Lovric, M., Hermes, M., and Scholz, F. 2000. Solid state electrochemical reactions in systems with miscibility gaps, *Journal of Solid State Electrochemistry*, 4, 394–401.

Lovric, M., and Scholz, F. 1997. A model for the propagation of a redox reaction through microcrystals. *Journal of Solid State Electrochemistry* 1, 108–113.

Lovric, M., and Scholz, F. 1999. A model for the coupled transport of ions and electrons in redox conductive microcrystals, *Journal of Solid State Electrochemistry* 3, 172–175.

Loy, D.A., and Assink, R.A. 1992. Synthesis of a fullerene C_{60}-*p*-xylylene copolymer. *Journal of the American Chemical Society* 114, 3977–3978.

Ly, Y.P., and Cheng, Y.-L. 1997. Diffusion in heterogeneous media containing impermeable domains arranged in parallel arrays of variable orientation. *Journal of Membrane Science* 133, 207–215.

Lyons, M.E.G. 1994. Electrocatalysis using electroactive polymers, electroactive composites and microheterogeneous systems. *Analyst* 119, 805–826.

Lyons, M.E.G., and Burke, L.D. 1987. Mechanism of oxygen reactions at porous oxide electrodes: Part 1. Oxygen evolution at RuO_2 and $Ru_xSn_{1-x}O_2$ electrodes in alkaline solution under vigorous electrolysis conditions. *Journal of the Chemical Society Faraday Transactions I* 83, 299–321.

Lyons, M.E.G., Lyons, C.H., Michas, A., and Bartlett, P.N. 1992. Amperometric chemical sensors using microheterogeneous systems. *Analyst* 117, 1271–1280.

Lyons, M.E.G., Fitzgerald, C.A., and Smyth, M.R. 1994. Glucose oxidation at ruthenium dioxide based electrodes. *Analyst* 119, 855–861.

Ma, L., Li, Y., Yu, X., Zhu, N., Yang, Q., and Noh, C.-H. 2008. Electrochemical preparation of $PMeT/TiO_2$ nanocomposite electrochromic electrodes with enhanced long-term stability. *Journal of Solid State Electrochemistry* 12, 1503–1509.

MacCallum, J.R., Smith, M.J., and Vincent, C.A. 1981. The effect of radiation-induced cross-linking on the conductance of $LiClO_4$·PEO electrolytes. *Solid State Ionics* 11, 307–312.

Mahmoud, A., Keita, B., Nadjo, L., Oung, O., Contant, R., Brown, S., and Kochkovski, Y. 1999. Coupled electron and proton transfers: Compared behaviour of oxometalates in aqueous solution or after entrapment in polymer matrices. *Journal of Electroanalytical Chemistry* 463, 129–145.

Malinger, K.A., Ding, Y.-S., Sithambaram, S., Espinal, L., Gomez, S., and Suib, S.L. 2006. Microwave frequency effects on synthesis of cryptomelane-type manganese oxide and catalytic activity of cryptomelane precursor. *Journal of Catalysis* 239, 290–298.

Mandelbrot, B. 1982. *The Fractal Geometry of Nature*. Freeman, San Francisco.

Marnellos, G., Zisekas, S., and Stoukide, M. 2001. Synthesis of ammonia at atmospheric pressure with the use of solid state proton conductors. *Journal of Catalysis* 193, 80–87.

Martel, D., and Kuhn, A. 2000. Electrocatalytic reduction of H_2O_2 at $P_2Mo_{18}O_{62}^{6-}$ modified glassy carbon. *Electrochimica Acta* 45, 1829–1836.

Martín, E., Torres-Costa, V., Martín-Palmar, J., Bousoño, C., Tutor-Sánchez, J., and Martínez-Duart, J.M. 2006. Photoluminescence of naphthalimide derivatives deposited onto nano-structured porous silicon. *Journal of the Electrochemical Society* 153, D134–D137.

Martos, M., Morales, J., and Sánchez, L. 2000. Cation-deficient $Mo_ySn_xO_2$ oxides as anodes for lithium ion batteries. *Electrochimica Acta* 46, 83–89.

Masliy, A.I., Poddubny, N.P., Medvedev, A.Zh., Zherebilov, A.F., and Sukhorukov, D.V. 2008. Electrodeposition on a porous electrode with low initial conductivity: Effect of the oxidant on the dynamics of the cathode deposit mass. *Journal of Electroanalytical Chemistry* 623, 155–164.

Meulenkamo, E.A., Nelly, J.J., and Blasse, G. 1993. Electrochemically induced characteristic luminescence of metal ions at anodic valve metal oxides. *Journal of the Electrochemical Society* 140, 84–91.

Michaels, J.N., and Vayenas, C.G. 1984. Styrene production from ethylbenzene on platinum in a zirconia electrochemical reactor. *Journal of the Electrochemical Society* 131, 2544–2550.

Milchev, A., and Heerman, L. 2003. Electrochemical nucleation and growth of nano- and microparticles: Some theoretical and experimental aspects. *Electrochimica Acta* 48, 2903–2913.

Miller, C.J., and Majda, M. 1986. Microporous aluminum oxide films at electrodes: Part II. Studies of electron transport in the Al_2O_3 matrix derivatized by adsorption of poly(4-vinylpyridine). *Journal of Electroanalytical Chemistry* 207, 49–72.

Miller, C.J., and Majda, M. 1988. Microporous aluminum oxide films at electrodes. Dynamics of ascorbic acid oxidation mediated by ferricyanide ions bound electrostatically in bilayer assemblies of octadecyltrichlorosilane and an octadecylviologen amphiphile. *Analytical Chemistry* 60, 1168–1176.

Miller, J.S. 1993a. Conducting polymers—Materials of commerce. *Advanced Materials* 5, 587–589.

Miller, J.S. 1993b. Conducting polymers—Materials of commerce. *Advanced Materials* 5, 671–676.

Mintova, S, Olson, N.H., Valtchev, V., Bein, T. 1999. Mechanism of zeolite A nanocrystal growth from colloids at room temperature. *Science* 283, 958–960

Mioc, U.B., Milonjic, S.K., Malovic, D., Stamenkovic, V., Colomban, Ph., Mitrovic, M.M., and Dimitrijevic, R. 1997. Structure and proton conductivity of 12-tungstophosphoric acid doped silica. *Solid State Ionics* 97, 239–246.

Moiroux, J., and Elving, P.J. 1978. Effects of adsorption, electrode material, and operational variables on the oxidation of dihydronicotinamide adenine dinucleotide at carbon electrodes. *Analytical Chemistry* 50, 1056–1062.

Moiroux, J., and Elving, P.J. 1979. Optimization of the analytical oxidation of dihydronicotinamide adenine dinucleotide at carbon and platinum electrodes. *Analytical Chemistry* 51, 346–350.

Molina, V.M., Frías, A., González, J., Montiel, V., González, D., Domínguez, M., and Aldaz, A. 2004. Design and development of filter-press type electrochemical reactors for their application in the resolution of environmental problems. In *Trends in Electrochemistry and Corrosion at the Beginning of the 21st Century*. Brillas, E., and Cabot, P.-L., Eds. Universitat de Barcelona, Barcelona, pp. 383–399.

Monteiro, O.C., Mendonça, M.H.M., Pereira, M.I.S., and Nogueira, J.M.F. 2006. Electrodegradation of organic pollutants at lead and tin oxide thin films. *Journal of Solid State Electrochemistry* 10, 41–47.

Moon, S.-M., and Pyun, S.-I. 1998. Growth mechanism of anodic oxide films on pure aluminium in aqueous acidic and alkaline solutions. *Journal of Solid State Electrochemistry* 2, 156–161.

Morales-Saavedra, O.G., Sánchez-Vergara, M.E., Ortiz-Rebollo, A., and Ortega- Martínez, R. 2007. Electrical and optical properties of Jäger-nickel (II)-based molecular-material thin films prepared by the vacuum thermal evaporation technique. *Journal of Physics and Chemistry of Solids* 68, 1571–1582.

مرجع دانشجویان و مهندسین مواد

Mozalev, A., Magaino, S., and Imai, H. 2001. The formation of nanoporous membranes from anodically oxidized aluminium and their application to Li rechargeable batteries. *Electrochimica Acta* 46, 2825–2834.

Mueller, U., Schubert, M., Teich, F., Puetter, H., Schierle-Arndt, K., and Pastré, J. 2006. Metal-organic frameworks-prospective industrial applications. *Journal of Materials Chemistry* 16, 626–636.

Murray, R.W., Ewing, A.G., and Durst, R.A. 1987. Chemically modified electrodes molecular design for electroanalysis. *Analytical Chemistry* 59, 379A–390A.

Nakanishi, S., Sakai, S.-I., Nagai, T., and Nakato, Y. 2005. Macroscopically uniform nanoperiod alloy multilayers formed by coupling of electrodeposition with current oscillations. *Journal of Physical Chemistry B* 109, 1750–1755.

Naono, H., Hakuman, M., Tanaka, T., Tamura, N., and Nakai, K. 2000. Porous texture and surface character of dehydroxylated and rehydroxylated MCM-41 mesoporous silicas—Analysis of adsorption isotherms of nitrogen gas and water vapor. *Journal of Colloid and Interface Science* 225, 411–425.

Nazri, G.A., and Pistoia, G. 2004. *Lithium Batteries: Science and Technology*. Kluwer, Boston.

Nguyen, T., Martini, I.B., Liu, J., and Schwartz, B. 2000. Controlling interchain interactions in conjugated polymers: The effects of chain morphology on exciton–exciton annihilation and aggregation in MEH–PPV films. *Journal of Physical Chemistry B* 104, 237–255.

Nicholson, R.S. 1965a. Some examples of the numerical solution of nonlinear integral equations. *Analytical Chemistry* 37, 667–671.

Nicholson, R.S. 1965b. Theory and application of cyclic voltammetry for measurement of electrode reaction kinetics. *Analytical Chemistry* 37, 1351–1355.

Nicholson, R.S., and Shain, I. 1964. Theory of stationary electrode polarography. *Analytical Chemistry* 36, 706–723.

Nieto, F., Jr., and Tucceri, R.I. 1996. The effect of pH on the charge transport at redox polymer-modified electrodes: An a.c. impedance study applied to poly(*o*-aminophenol) film electrodes. *Journal of Electroanalytical Chemistry* 416, 1–24.

Novoselov, K.S., Geim, A.K., Morozov, S.V., Jiang, D., Zhang, Y., Dubonos, S.V., Grigorieva, I.V., and Firsov, A.A. 2004. Electric field effect in atomically thin carbon films. *Science* 306, 666–669.

Nyikos, L., and Pajkossy, T. 1986. Diffusion to fractal surfaces. *Electrochimica Acta* 31, 1347–1350.

Nyikos, L., and Pajkossy, T. 1990. Electrochemistry at fractal interfaces: The coupling of ac and dc behaviour at irregular electrodes. *Electrochimica Acta* 35, 1567–1572.

Nyikos, L., Pajkossy, T., Borosy, A.P., and Martenyanov, S.A. 1990. Diffusion to fractal surfaces: IV. The case of the rotating disc electrode of fractal surface. *Electrochimica Acta* 35, 1423–1424.

Oberlin, A., and Endo, M. 1976. Filamentous growth of carbon through benzene decomposition. *Journal of Crystals Growth* 32, 335–349.

Obretenov, W., Petrov, I., Nachev, I., and Staikov, G. 1994. The kinetics of structural changes in Cu adlayers on Au(111). *Journal of Electroanalytical Chemistry* 371, 101–109.

O'Brien, R.N., and Santhanam, K.S.V. 1997. Magnetic field assisted convection in an electrolyte of nonuniform magnetic susceptibility. *Journal of Applied Electrochemistry* 27, 573–578.

O'Dea, J.J., Osteryoung, J., and Osteryoung, R.A. 1981. Theory of square-wave voltammetry for kinetic systems. *Analytical Chemistry* 53, 695–701.

O'Dea, J.J., and Osteryoung, J.G. 1993. Characterization of quasi-reversible surface processes by square-wave voltammetry. *Analytical Chemistry* 65, 3090–3097.

Ohtsuka, T., Iida, M., and Ueda, M. 2006. Polypyrrole coating doped by molybdo-phosphate anions for corrosion prevention of carbon steels. *Journal of Solid State Electrochemistry* 10, 714–720.

Oldham, K.B. 1991. Steady-state microelectrode voltammetry as a route to homogeneous kinetics. *Journal of Electroanaytical Chemistry* 313, 3–16.

Oldham, K.B. 1998. Voltammetry at a three-phase junction. *Journal of Solid State Electrochemistry* 2, 367–377.

Oldham, K.B., and Myland, J.C. 1994. *Fundamentals of Electrochemical Science*. Academic Press, San Diego.

Oliveira, P.P., Patrito, E.M., and Sellers, H. 1994. Hydrogen peroxide synthesis over metallic catalysts. *Surface Science* 313, 25–40.

O'Neill, R.D. 1994. Microvoltammetric techniques and sensors for monitoring neurochemical dynamics *in vivo*. A review. *Analyst* 119, 767–779.

Ono, T., Hasei, M., Kunimoto, A., and Miura, N. 2004. Improvement of sensing performances of zirconia-based total NO$_x$ sensor by attachment of oxidation-catalyst electrode. *Solid State Ionics* 175, 503–506.

Ouf, A.M.A., Abd Elhafeez, A.M., and El-Shafei, A.A. 2008. Ethanol oxidation at metal-zeolite-modified electrodes in alkaline medium: Part 1. Gold-zeolite-modified graphite electrode. *Journal of Solid State Electrochemistry* 12, 601–608.

Ozeki, S. 1985. Estimation of pore and surface structures of solids by dye adsorption: The preadsorption method and fractal analysis. *Langmuir* 5, 186–191.

Packheiser, R., Jakob, A., Ecorchard, P., Walfort, B., and Lang, H. 2008. Diphenylphosphinoferrocene gold(I) acetylides: Synthesis of heterotri- and heterotetrametallic transition metal complexes. *Organometallics* 27, 1214–1226.

Pahdi, A.K., Nanjundaswamy, K.S., and Goodenough, J.B. 1997. Mapping of transition metal redox energies in phosphates with NASICON structure by lithium intercalation. *Journal of the Electrochemical Society* 144, 2581–2586.

Pajkossy, T. 1991. Electrochemistry at fractal surfaces. *Journal of Electroanalytical Chemistry* 300, 1–11.

Pandurangappa, M., and Ramakrishnappa, T. 2008. Derivatization and characterization of functionalized carbon powder via diazonium salt reduction. *Journal of Solid State Electrochemistry* 12, 1411–1419.

Panov, G.I., Uriarte, A.K., Rodkin, M.A., and Sobolev, V.I. 1998. Generation of active oxygen species on solid surfaces. Opportunity for novel oxidation technologies over zeolites. *Catalysis Today* 41, 365–385.

Pasierb, P., and Rekas, M. 2009. Solid-state potentiometric gas sensors-current status and future trends. *Journal of Solid State Electrochemistry* 13, 3–25.

Pastore, H.O., Ozin, G.A., Poe, and A.J. 1993. Intrazeolite metal carbonyl kinetics: Substitution reactions of molybdenum carbonyl (Mo$_{12}$(CO)$_6$) in sodium zeolite Y. *Journal of the American Chemical Society* 115, 1215–1230.

Patermarakis, G. 2006. Aluminium anodizing in low acidity sulphate baths: Growth mechanism and nanostructure of porous anodic films. *Journal of Solid State Electrochemistry* 10, 211–222.

Patermarakis, G., Chandrinos, J., and Masavetas, K. 2007. Formulation of a holistic model for the kinetics of steady state growth of porous anodic alumina films. *Journal of Solid State Electrochemistry* 11, 1191–1204.

Patermarakis, G., and Moussoutzanis, K. 2001. Formulation of a criterion predicting the development of uniform regular and non-uniform abnormal porous anodic alumina coatings and revealing the mechanisms of their appearance and progress. *Corrosion Science* 43, 1433–1464.

Patermarakis, G., and Moussoutzanis, K. 2002. Solid surface and field catalysed interface formation of colloidal Al$_2$(SO$_4$)$_3$ during Al anodizing affecting the kinetics and mechanism of development of structure of porous oxides. *Journal of Solid State Electrochemistry* 6, 475–484.

Patermarakis, G., and Nikolopoulos, N. 1999. Catalysis over porous anodic alumina film catalysts with different pore surface concentrations. *Journal of Catalysis* 187, 311–320.

Patermarakis, G., and Pavlidou, C. 1994. Catalysis over porous anodic alumina catalysts. *Journal of Catalysis* 147, 140–155.

Pérez-Inestrosa, E., Montenegro, J.-M., Collado, D., Suau, R., and Casado, J. 2007. Molecules with multiple light-emissive electronic excited states as a strategy toward molecular reversible logic gates. *Journal of Physical Chemistry C* 111, 6904–6909.

Pérez-Ramírez, J., Kapteijn, F., Groen, J.C., Doménech, A., Mul, G., and Moulijn, J.A. 2003. Steam-activated FeMFI zeolites. Evolution of iron species and activity in direct N_2O decomposition. *Journal of Catalysis* 214, 33–45.

Pérez-Ramírez, J., Mul, G., Kapteijn, F., Moulijn, J.A., Overweg, A.R., Doménech, A., Ribera, A., and Arends, I.W.C.E. 2002. Preparation and characterization of isomorphously substituted FeZSM-5 during activation. *Journal of Catalysis* 207, 113–126.

Pichon, C., Dolbecq, A., Mialane, P., Marrot, J., Rivière, E., Goral, M., Zynek, M., McCormac, T., Borshch, S.A., Zueva, E., and Sécheresse, F. 2008. Fe_2 and Fe_4 clusters encapsulated in vacant polyoxotungstates: Hydrothermal synthesis, magnetic, electrochemical properties, and DFT calculations. *Chemistry - A European Journal* 14, 3189–3199.

Pirvu, C., Brillas, E., Radovici, O., Banu, A., and Marcu, M. 2004. Electrochemical study of 2-chlorophenol oxidation. In *Trends in Electrochemistry and Corrosion at the Beginning of the 21st Century*. Brillas, E., and Cabot, P.-L., Eds. Universitat de Barcelona, Barcelona, pp. 443–452.

Pletcher, D., and Walsh, F.C. 1990. *Industrial Electrochemistry*. Chapman and Hall, New York.

Pleus, S., and Schulte, B. 2001. Poly(pyrroles) containing chiral side chains: Effect of substituents on the chiral recognition in the doped as well as in the undoped state of the polymer film. *Journal of Solid State Electrochemistry* 5, 522–530.

Pournaghi-Azar, M.H., and Habibi, B. 2007. Electropolymerization of aniline in acid media on the bare and chemically pre-treated aluminum electrodes: A comparative characterization of the polyaniline deposited electrodes. *Electrochimica Acta* 52, 4222–4230.

Prakash, R. 2002. Electrochemistry of polyaniline: Study of the pH effect and electrochromism. *Journal of Applied Polymer Science* 83, 378–385.

Quayle, W.H., and Lunsford, J.H. 1982. Tris(2,2′-bipyridine)ruthenium(III) in zeolite Y: Characterization and reduction on exposure to water. *Inorganic Chemistry* 21, 97–103.

Ragsdale, S.R., Grant, K.M., and White, H.S. 1998. Electrochemically generated magnetic forces. Enhanced transport of a paramagnetic redox species in large, nonuniform magnetic fields. *Journal of the American Chemical Society* 120, 13461–13468.

Ragsdale, S.R., Lee, J., Gao, X., and White, H.S. 1996. Magnetic field effects in electrochemistry. Voltammetric reduction of acetophenone at microdisk electrodes. *Journal of Physical Chemistry* 100, 5913–5922.

Raistrick, I.D., and Huggins, R.A. 1982. The transient electrical response of electrochemical systems containing insertion reaction electrodes. *Solid State Ionics* 7, 213–218.

Ramaley, L., and Krause, M.S. 1969. Theory of square-wave voltammetry. *Analytical Chemistry* 41, 1362–1365.

Rassaei, L., Sillanpää, M., Milson, E.V., Zhang, X., and Marken, F. 2008. Layer-by-layer assembly of Ru^{3+} and $Si_8O_{20}^{8-}$ into electrochemically active silicate films. *Journal of Solid State Electrochemistry* 12, 747–755.

Reddy, Ch.V.S., Zhu, Q.-Y., and Mai, L.-Q. 2007. Electrochemical studies on PVC/PVdF blend-based polymer electrolytes. *Journal of Solid State Electrochemistry* 11, 543–548.

Reinen, D., Köhl, P., and Müller, C. 2004. The nature of the colour centres in 'Maya blue'—The incorporation of organic pigment molecules into the palygorskite lattice. *Zeitschrift Anorganische Allgemeine Chemie* 630, 97–103.

Ren, J.X., Zhou, Z., Gao, X.P., and Yan, J. 2006. Preparation of porous spherical α-$Ni(OH)_2$ and enhancement of high-temperature electrochemical performances through yttrium addition. *Electrochimica Acta* 52, 1120–1126.

Retter, H., and Lohse, H. 2005. Electrochemical impedance spectroscopy. In *Electroanalytical Methods*. Scholz, F., Ed. Springer, Berlin.

Reviriego, F., Navarro, P., Doménech, A., and García-España, E. 2002. A new macrocyclic dipyrazolate salt of diazatetraester structure able to efficiently and selectively interact with psychotropic phenethylammonium salts. Influence of the amine substituents on the stability of the ammonium dipyrazolate complexes. *Journal of Supramolecular Chemistry* 2, 115–122.

Reyes-Valerio, C. 1993. De bonampak al templo mayor. In *La Histroria del azul Maya en Mesoamérica*. Siglo XXI, México.

Rice, C., Ha, S., Masel, R.I., and Wieckowski, A. 2003. Catalysts for direct formic acid fuel cells. *Journal of Power Sources* 115, 229–235.

Rincón, M.E., Trujillo, M.E., Ávalos, J., and Casillas, N. 2007. Photoelectrochemical processes at interfaces of nanostructured TiO_2/carbon black composites studied by scanning photoelectrochemical microscopy. *Journal of Solid State Electrochemistry* 11, 1287–1294.

Rolison, D.R. 1990. Zeolite-modified electrodes and electrode-modified zeolites. *Chemical Reviews* 90, 867–878.

Rolison, D.R. 1994. The intersection of electrochemistry with zeolite science. In *Advanced Zeolite Science and Applications*. Jansen. J.C., Stöcker, M., Karge, H.G., and Weitkamp, J., Eds. *Studies in Surface Science and Catalysis* 85, 543–587.

Rolison, D.R., and Bessel, C.A. 2000. Electrocatalysis and charge-transfer reactions at redox-modified zeolites. *Accounts of Chemical Research* 33, 737–744.

Rolison, D.R., and Stemple, J.Z. 1993. Electrified microheterogeneous catalysis in low ionic strength media. *Chemical Communications* 1, 25–27.

Rolison, D.R., Bessel, C.A., Baker, M.D., Senaratne, C., and Zhang, J. 1996. Reply to the comment on "Zeolite-modified electrodes: Intra- versus extrazeolite electron transfer." *Journal of Physical Chemistry* 100, 8610–8611.

Rolison, D.R., Nowak, R.J., Welsh, T.A., and Murray, C.G. 1991. Analytical implications of zeolite overlayers at electrodes. *Talanta* 38, 27–35.

Roncali, J. 1992. Conjugated poly(thiophenes): Synthesis, functionalization, and applications. *Chemical Reviews* 92, 711–738.

Rowsell, L.C., and Yaghi, O.M. 2005. Strategies for hydrogen storage in metal-organic frameworks. *Angewandte Cheie International Edition* 117, 4748.

Rowsell, J.L.C., and Yaghi, O.M. 2006. Effects of functionalization, catenation, and variation of the metal oxide and organic linking units on the low-pressure hydrogen adsorption properties of metal-organic frameworks. *Journal of the American Chemical Society* 128, 1304–1315.

Ruiz, V., Blanco, C., Granda, M., Menéndez, R., and Santamaría, R. 2008. Effect of the thermal treatment of carbon-based electrodes on the electrochemical performance of supercapacitors. *Journal of Electroanalytical Chemistry* 618, 17–23.

Ruthstein, S., Frydman, V., Kabbaya, S., Landau, M., and Goldfarb, D. 2003. Study of the formation of the mesoporous material SBA-15 by EPR spectroscopy. *Journal of Physical Chemistry B* 107, 1739–1748.

Ryoo, R., Joo, S.H., and Jun, S. 1999. Synthesis of highly ordered carbon molecular sieves vie template-mediated structural transformation. *Journal of Physical Chemistry B* 103, 7743–7746.

Ryoo, R., Joo, S.H., Kruk, M., and Jaroniec, M. 2001. Ordered mesoporous carbons. *Advanced Materials* 13, 677–680.

Sabater, M.J., Corma, A., Doménech, A., Fornés, V., and García, H. 1997. Chiral salen manganese complex encapsulated with zeolite Y: A heterogeneous enantioselective catalyst for the epoxidation of alkenes. *Journal of the Chemical Society Chemical Communications* 14, 1285–1286.

Sadakane, M., and Steckhan, E. 1998. Electrochemical properties of polyoxometalates as electrocatalysts. *Chemical Reviews* 98, 219–237.

Saito, S. 1997. Carbon nanotubes for next-generation electronics devices. *Science* 278, 77–78.

Saleh, M.M. 2007. Simulation of oxygen evolution reaction at porous anode from flowing electrolytes. *Journal of Solid State Electrochemistry* 11, 811–820.

Salgado,L., Tejo, G., Meas, Y., and Zayas, T. 2006. Cyclic voltammetry and electrochemical quartz crystal microbalance studies of a rhodized platinum electrode in sulfuric acid solution. *Journal of Solid State Electrochemistry* 10, 230–235.

Saliba, R., Mingotaud, C., Argoul, R., and Ravaine, S. 2002. Spontaneous oscillations in gold electrodeposition. *Electrochemistry Communications* 4, 629–632.

Sánchez del Río, M., Martinetto, P., Somogyi, A., Reyes-Valerio, C., Dooryhée, E., Peltier, N., Alianelli, L., Moignard, B., Pichon, L., Calligaro, T., and Dran, J.-C. 2004. Microanalysis study of archaeological mural samples containing Maya blue pigment. *Spectrochimica Acta Part B* 1619–1625.

Sánchez del Río, M., Sodo, A., Eeckhout, S.G., Neisius, T., Martinetto, P., Dooryhée, E., and Reyes-Valerio, C. 2005. Fe *K*-edge XANES of Maya blue pigment. *Nuclear Instruments and Methods in Physics Research B* 238, 50–54.

Sánchez-Sánchez, C.M., Expósito, E., Batanero, B., Montiel, V., Barba, F., and Aldaz, A. 2004. Electrochemical carboxylation. Carbon dioxide could be useful compound for synthesis. In *Trends in Electrochemistry and Corrosion at the Beginning of the 21st Century*. Brillas, E., and Cabot, P.-L., Eds. Universitat de Barcelona, Barcelona, pp. 431–442.

Santos-Peña, J., Soudan, P., Otero-Areán, C., Turnes-Palomino, G., and Franger, S. 2006. Electrochemical properties of mesoporous iron phosphate in lithium batteries. *Journal of Solid State Electrochemistry* 10, 1–9.

Sarangapani, S., Lessner, P., Forchione, J., Griffith A., and Laconti, A.B. 1990. Advanced double layer capacitors. *Journal of Power Sources* 29, 355–364.

Scaiano, J.C., and García, H. 1999. Intrazeolite photochemistry: Toward supramolecular control of molecular photochemistry. *Accounts of Chemical Research* 21, 783–793.

Scavetta, E., Berrettoni, M., Nobili, F., and Tonelli, D. 2005. Electrochemical characterisation of electrodes modified with a Co/Al hydrotalcite-like compound. *Electrochimica Acta* 50, 3305–3311.

Schindler, P.W., and Stumm, W. 1987. In *Aquatic Surface Chemistry*. Stumm, W., Ed. Wiley, New York, pp. 83–110.

Scholz, F., and Hermes, M. 1999. The determination of the redox state of a dissolved depolariser by cyclic voltammetry in the case of electrochemically reversible systems. *Electrochemistry Communications* 1, 345–348. See corrigendum (2000) in *Electrochemistry Communications* 2, 814.

Scholz, F., and Lange, B. 1992. Abrasive stripping voltammetry—An electrochemical solid state spectroscopy of wide applicability. *Trends in Analytical Chemistry* 11, 359–367.

Scholz, F., and Meyer, B. 1994. Electrochemical solid state analysis—State of the art. *Chemical Society Reviews* 23, 341–347.

Scholz, F., and Meyer, B. 1998. Voltammetry of solid microparticles immobilized on electrode surfaces. *Electroanalytical Chemistry, A Series of Advances* 20, 1–86.

Scholz, F., Gulaboski, R., Mirceski, V., and Langer, P. 2002. Quantification of the chiral recognition in electrochemically driven ion transfer across the interface water/chiral liquid. *Electrochemistry Communications* 4, 659–662.

Scholz, F., Nitschke, L., and Henrion, G. 1989. A new procedure for fast electrochemical analysis of solid materials. *Naturwissenschaften* 76, 71–72.

Scholz, F., Nitschke, L., Henrion G., and Damaschun, F. 1989. A new technique to study the electrochemistry of minerals. *Naturwissenschaften* 76, 167–168.

Scholz, F., Schröder, U., and Gulabowski, R. 2005. *Electrochemistry of Immobilized Particles and Droplets*. Springer, Berlin.

Schröder, U., Oldham, K.B., Myland, J.C., Mahon, P.J., and Scholz, F. 2000. Modelling of solid state voltammetry of immobilized microcrystals assuming an initiation of the electrochemical reaction at a three-phase junction. *Journal of Solid State Electrochemistry* 4, 314–324.

Schultz, F.A., and Kuwana, T. 1965. Electrochemical studies of organic compounds dissolved in carbon-paste electrodes. *Journal of Electroanalytical Chemistry* 10, 95–103.

Schultze, J.W., and Lohrengel, M.M. 1983. Nucleation and growth of anodic oxide films. *Electrochimica Acta* 28, 973–984.

Senaratne, C, Zhang, J., Baker, M.D., Bessel, C.A., and Rolison, D.R. 1996. Zeolite-modified electrodes: Intra- versus extrazeolite electron transfer. *Journal of Physical Chemistry* 100, 5849–5862.

Sharifker, B., and Hills, G. 1983. Theoretical and experimental studies of multiple nucleation. *Electrochimica Acta* 28, 879–889.

Shaw, B.R., and Creasy, K.E. 1988. Carbon composite electrodes containing alumina, layered double hydroxides, and zeolites. *Journal of Electroanalytical Chemistry* 243, 209–217.

Shaw, B.R., Creasy, K.E., Lancycjki, C.J., Sargeant, J.A., and Tirhado, M. 1989. Voltammetric response of zeolite-modified electrodes. *Journal of the Electrochemical Society* 135, 869–876.

Shepard, A.O. 1962. Maya blue: Alternative hypothesis. *American Antiquity* 27, 565–566.

Shi, G., Qu, Y., Zhai, Y., Liu, Y., Sun, Z., Yang, J., and Jin, L. 2007. $\{MSU/PDDA\}_n$ LBL assembled modified sensor for electrochemical detection of ultratrace explosive nitroaromatic compounds. *Electrochemistry Communications* 9, 1719–1724.

Shi, W., Zeng, H., Sahoo, Y., Ohulchansky, T.Y., Ding, Y., Wang, Z.L., Swihart, M., and Prasad, P.N. 2006. A general approach to binary ternary hybrid nanocrystals. *Nano Letters* 6, 875–881.

Shirakawa, H., Louis, E.J., MacDiarmid, A.G., Chiang, C.K., and Heeger, A.J. 1977. Synthesis of electrically conducting organic polymers: Halogen derivatives of polyacetylene, $(CH)_x$. *Journal of the Chemical Society Chemical Communications* 474, 578–580.

Silva, L.M.D., De Faria, L.A., and Boodts, J.F.C. 2003. Electrochemical ozone production: Influence of the supporting electrolyte on kinetics and current efficiency. *Electrochimica Acta* 48, 699–709.

Simmons, W., Gonnissen, D., and Hubin, A. 1997. Study of the initial stages of silver electrocrystallisation from silver thiosulphate complexes: Part I. Modelling of the silver nuclei formation during the induction period. *Journal of Electroanalytical Chemistry* 433, 141–151.

Sinha, N.N., and Munichandraiah, N. 2008. Synthesis and characterization of submicron size particles of $LiMn_2O_4$ by microemulsion route. *Journal of Solid State Electrochemistry* 12, 1619–1627.

Skinner, S.J., and Munnings, C. 2002. Electrical properties of iron-substituted $La_{6.4}Sr_{1.6}Cu_8O_{20\pm\delta}$. *Materials Letters* 57, 594–597.

Smith, B.W., Monthioux, M., and Luzzi, D.E. 1998. Encapsulated C_{60} in carbon nanotubes. *Nature* 396, 323.

Smith, D.F., Willman, K., Kuo, K., and Murray R.W. 1979. Chemically modified electrodes: XV. Electrochemistry and waveshape analysis of aminophenylferrocene bonded to acid chloride functionalized ruthenium, platinum, and tin oxide electrodes. *Journal of Electroanalytical Chemistry* 95, 217–227.

Soudan, P., Pereira-Ramos, J.P., Farcy, J., Gregoire, G., and Baffier, N. 2000. Sol-gel chromium–vanadium mixed oxides as lithium insertion compounds. *Solid State Ionics* 135, 291–295.

Squella, J.A., Cassels, B.K., Arata, M., Bavestrello, M.P., and Núñez-Vergara, L.J. 1993. Electrochemical oxidation of methylenedioxyamphetamines. *Talanta* 40, 1379–1384.

Srinivasan, V., and Weinder, J.W. 2000. Studies on the capacitance of nickel oxide films: Effect of heating temperature and electrolyte concentration. *Journal of the Electrochemical Society* 147, 800–885.

Strasser, P., Eiswirth, M., and Koper, M.T.M. 1999. Mechanistic classification of electrochemical oscillators—An operational experimental strategy. *Journal of Electroanalytical Chemistry* 478, 50–66.

Strauss, E., Golodnitsky, D., and Peled, E. 2002. Elucidation of the charge-discharge mechanism of lithium/polymer electrolyte/pyrite batteries. *Journal of Solid State Electrochemistry* 6, 468–474.

Stromme, M., Niklasson, G.A., and Granqvist, C.Q. 1995. Voltammetry on fractals. *Solid State Communications* 3, 151–154.

Stromme, M., Niklasson, G.A., and Granqvist, C.Q. 1996a. Fractal dimension of Li insertion electrodes studied by diffusion-controlled voltammetry and impedance spectroscopy. *Physical Review B* 54, 2968–2971.

Stromme, M., Niklasson, G.A., and Granqvist, C.Q. 1996b. Fractal surface dimension from cyclic *I-V* studies and atomic-force microscopy: Role of noncontiguous reaction sites. *Physical Review B* 54, 17884–17887.

Su, L.-H., Zhang, X.-G., and Liu, Y. 2008. Electrochemical performance of Co-Al layered double hydroxide nanosheets mixed with multiwall carbon nanotubes. *Journal of Solid State Electrochemistry* 12, 1129–1134.

Sun, Z., Li, Y., Zhou, T., Liu, Y., Shi, G., and Jin, L. 2008. Direct electron transfer and electrocatalysis of haemoglobin in layer-by-layer films assembled with Al-MSU-S particles. *Talanta* 74, 1692–1698.

Sunde, S. 1996. Monte Carlo simulations of conductivity of composite electrodes for solid oxide fuel cells. *Journal of the Electrochemical Society* 143, 1123–1133.

Sunde, S. 1997. Calculations of impedance of composite anodes for solid oxide fuel cells. *Electrochimica Acta* 42, 2637–2648.

Sunseri, C., Spadaro, C., Piazza, S., and Volpe, M. 2006. Porosity of anodic alumina membranes from electrochemical measurements. *Journal of Solid State Electrochemistry* 10, 416–421.

Suresh, P., Shukla, A.K., and Munichandraiah, N. 2002. Temperature dependence studies of a.c. impedance of lithium-ion cells. *Journal of Applied Electrochemistry* 32, 267–273.

Surridge, N.A., Sosnoff, C.S., Schmehl, R., Facci, J.S., and Murria, R.W. 1994. Electron and counterion diffusion constants in mixed-valent polymeric osmium bipyridine films. *Journal of Physical Chemistry* 98, 917–923.

Switzer, J.A., Hung, C.J., Huang, L. Y., Switzer, E.R., Kammler, D.R., Golden, T.D., and Bohannan, E.W. 1998. Electrochemical self-assembly of copper/cuprous oxide layered nanostructures. *Journal of the American Chemical Society* 120, 3530–3531.

Szucs, A., Tolgyesi, M., Nagy, J.B., Novak, M., and Lamberts, L. 1996. Photoelectrochemical behaviour of C_{60} films in various oxidation states. *Journal of Electroanalytical Chemistry* 419, 39–46.

Taniguchi, I., and Bakenov, Z. 2005. Spray pyrolysis synthesis of nanostructured $LiFe_xMn_{2-x}O_4$ cathode materials for lithium-ion batteries. *Powder Technology* 159, 55–62.

Teraoka, Y., Zhang, H.M., Furukawa, S., and Yamazoe, N. 1985. Oxygen permeation through perovskite-type oxides. *Chemical Letters* 1743–1746.

Teunisson, E.H., van Santen, R.A., Jansen, A.P.J., and Van Duijneveldt, F.B. 1993. NH_4^+ in zeolites—Coordination and solvation effects. *Journal of Physical Chemistry* 97, 203–210.

Tolman, C.A., and Herron, N. 1988. The selective catalytic oxidation of hydrocarbons in zeolites under mild conditions. *Catálisis Today* 3, 235–243.

Tomic, E.A.J. 1965. Glass transition temperatures of poly(methyl methacrylate) plasticized with low concentrations of monomer and diethyl phthalate. *Applied Polymer Science* 9, 3745–3818.

Tominaga, M., Shimazoe, T., Nagaashima, M., Kusuda, H., Kubo, A., Kuwahara, Y., and Taniguchi, I. 2006. Electrocatalytic oxidation of glucose at gold–silver alloy, silver and gold nanoparticles in an alkaline solution. *Journal of Electroanalytical Chemistry* 590, 37–46.

Trasatti, S. 1994. Transition metal oxides: Versatile materials for electrocatalysis. In *The Electrochemistry of Novel Materials*. Lipkowski, J., and Ross, P.N., Eds. VCH, New York, pp. 207–295.

Trasatti, S., and Logi, G. 1981. In *Electrodes of Conductive Metal Oxides*, Trasatti, S, Ed. Elsevier, Amsterdam, Part B, pp. 521–626.

Trejo, G., Ruiz, H., Borges, R.O., and Meas, Y. 2001. Influence of polyethoxylated additives on zinc electrodeposition from acidic solutions. *Journal of Applied Electrochemistry* 31, 685–692.

Tsipis, E.V., and Kharton, V.V. 2008. Electrode materials and reaction mechanisms in solid oxide fuel cells: A brief review. *Journal of Solid State Electrochemistry* 12, 1367–1391.

Tsuji, T., Tatsuyama, Y., Tsuji, M., Ishida, K., Okada, S., and Yamaki, J. 2007. Preparation of $LiMn_2O_4$ nanoparticles for Li ion secondary batteries by laser ablation in water. *Materials Letters* 61, 2062–2065.

Turro, N.J., and García-Garibay, M. 1991. In *Photochemistry in Organized Media*, Ramamurthy, V., Ed., VCH, New York, pp. 1–38.

Uchida, H., Ikeda, N., and Watanabe, M. 1997. Electrochemical quartz crystal microbalance study of copper adatoms on gold electrodes: Part II. Further discussion on the specific adsorption of anions from solutions of perchloric and sulfuric acid. *Journal of Electroanalytical Chemistry* 424, 5–12.

Uchida, H., Ikeda, N., and Watanabe, M. 1998. Electrochemical quartz crystal microbalance study of copper adatoms on Au(111) electrodes in solutions of perchloric and sulfuric acid. *Journal of Electroanalytical Chemistry* 452, 97–106.

Ullmann, H., and Trofimenko, N.J. 2001. Estimation of effective ionic radii in highly defective perovskite-type oxides from experimental data. *Journal of Alloys and Compounds* 316, 153–158.

Van Olphen, H. 1967. Maya blue: A clay mineral-organic pigment? *Science* 154, 465–467.

Velaski, R., Muchenski, F., Mello, R.M.Q., Micaroni, L., Roman, L.S., and Hümmelgen, I.A. 2006. Sulfonated polyaniline/poly(3-methylthiophene)-based photovoltaic devices. *Journal of Solid State Electrochemistry* 10, 24–27.

Villegas, M.A., and Alarcón, J. 2002. Mechanism of crystallization of Co-cordierites from stoichiometric powdered glasses. *Journal of the European Ceramic Society* 22, 487–494.

Vitale, M., Castagnola, N.B., Ortins, N.J., Brooke, A., Vaidyalingam, A., and Dutta, P.K. 1999. Intrazeolitic photochemical charge separation for $Ru(bpy)_3^{2+}$–Bipyridinium system: Role of the zeolite structure. *Journal of Physical Chemistry B* 103, 2408–2416.

Vonau, W., and Guth, U. 2006. pH Monitoring: A review. *Journal of Solid State Electrochemistry* 10, 746–752.

Walcarius, A., and Bessière, J. 1999. Electrochemistry with mesoporous silica: Selective mercury(II) binding. *Chemistry of Materials* 11, 3010–3011.

Walcarius, A., Ganesan, V., Larlus, O., and Valtchev, V. 2004. Low temperature synthesis of zeolite films on glassy carbon: Towards designing molecularly selective electrochemical devices. *Electroanalysis* 16, 1550–1554.

Wang, B.H., Wang, J.D., Liu, R., Yie, Y.H., and Li, Z.J. 2007. Synthesis of ammonia from natural gas at atmospheric pressure with doped ceria –$Ca_3(PO_4)_2$-K_3PO_4 composite electrolyte and its proton conductivity at intermediate temperature. *Journal of Solid State Electrochemistry* 11, 27–31.

Wang, J. 1985. *Stripping Analysis. Principles, Instrumentation and Applications*. VCH, Weinheim.

Wang, J., and Musameh, M. 2003. Carbon nanotube/Teflon composite electrochemical sensors and biosensors. *Analytical Chemistry* 75, 2075–2079.

Wang, J., and Walcarius, A. 1996. Zeolite-modified carbon paste electrode for selective monitoring of dopamine. *Journal of Electroanalytical Chemistry* 407, 183–187.

Wang, M.Y., Chen, J.H., Fan, Z., Tang, H., Deng, G.H., He, D.L., and Kuang, Y.F. 2004. Ethanol electro-oxidation with Pt and Pt-Ru catalysts supported on carbon nanotubes. *Carbon* 42, 3257–3260.

Wang, X., Lin, H., Bi, Y., Chen, B., and Liu, G. 2008. An unprecedented extended architecture constructed from a 2-D interpenetrating cationic coordination framework templated by $SiW_{12}O_{40}^{4-}$ anion. *Journal of Solid State Chemistry* 181, 556–561.

Waskaas, M. 1993. Short-term effects of magnetic fields on diffusion in stirred and unstirred paramagnetic solutions. *Journal of Physical Chemistry* 97, 6470–6476.

Waskaas, M. 1996. Magnetic field effect on electrode reactions: III. Effects on the anodic polarization of an iron electrode in an iron(III) chloride solution under potentiostatic conditions. *Acta Chemica Scandinavica* 50, 526–530.

Waskaas, M. 1997. Comment on "Short-term effects of magnetic fields on diffusion in stirred and unstirred paramagnetic solutions." *Journal of Physical Chemistry* 100, 8612.

Waskaas, M., and Kharkats, Y.I. 1999. Magnetoconvection phenomena: A mechanism for influence of magnetic fields on electrochemical processes. *Journal of Physical Chemistry B* 103, 4876–4833.

Watanabe, M., Nagano, S., Sanvi, K., and Ogata, N. 1987. Structure-conductivity relationship in polymer electrolytes formed by network polymers from poly[dimethylsiloxane-*g*-poly(ethylene oxide)] and litegum perchlorate. *Journal of Power Sources* 20, 327–332.

Wieckzorek, W., and Stevens, J.R. 1997. impedance spectroscopy and phase structure of polyether-poly(methyl methacrylaye)-LiCF$_3$SO$_3$ blend-based electrolytes. *Journal of Physical Chemistry B* 101, 1529–1534.

Wildgoose, G.G., Leventis, H.C., Davies, I.J., Crossley, A., Lawrence, N.S., Jiang, L., Jones, T.G.J., and Compton, R.G. 2005. Graphite powder derivatised with poly-L-cysteine using "building-block" chemistry—A novel material for the extraction of heavy metal ions. *Journal of Materials Chemistry* 15, 2375–2382.

Wiles, P.G., and Abrahamson, J. 1978. Carbon fibre layers on arc electrodes—I: Their properties and cool-down behaviour. *Carbon* 16, 341–349.

Willner, I., Pardo-Yissar, V., Katz, E., and Ranjit, K.T. 2001. A photoactivated 'molecular train' for optoelectronic applications: Light-stimulated translocation of a β-cyclodextrin receptor within a stoppered azobenzene-alkyl chain supramolecular monolayer assembly on a Au-electrode. *Journal of Electroanalytical Chemistry* 497, 172–177.

Winkler, K., Balch, A.L., and Kutner, W. 2006. Electrochemically formed fullerene-based polymeric films. *Journal of Solid State Electrochemistry* 10, 761–784.

Wright, J.D., and Sommerdijk, N. 2000. *Sol-Gel Materials: Their Chemistry and Biological Properties*. Taylor & Francis, London.

Wu, B.L., Lincot, D., Vedel, J., and Yu, L.T. 1997. Voltammetric and electrogravimetric study of manganese dioxide thin film electrodes: Part 1. Electrodeposited films. *Journal of Electroanalytical Chemistry* 420, 159–165.

Wu, X.Z., Kitamori, T., and Sawada, T. 1992. Monitoring of ion diffusion in Langmuir-Blodgett multilayers by a variable observation angle fluorescence method. *Journal of Physical Chemistry* 96, 9406–9410.

Xia, Y., and Yoshio, M. 1996. An investigation of lithium ion insertion into spinel structure Li-Mn-O compounds. *Journal of the Electrochemical Society* 143, 825–833.

Xie, Q., Pérez-Cordero, E., and Echogoyen, L. 1992. Electrochemical detection of C_{60}^{6-} and C_{70}^{6-}: Enhanced stability of fullerides in solution. *Journal of the American Chemical Society* 114, 3978–3980.

Xie, X., Zhao, X.B., Cao, G.S., Zhong, Y.D., and Zhao, M.J. 2003. Ex-situ XRD studies of CoSb$_3$ compound as the anode material for lithium ion batteries. *Journal of Electroanalytical Chemistry* 542, 1–6.

Xie, Y., and Huber, C.O. 1991. Electrocatalysis and amperometric detection using an electrode made of copper oxide and carbon paste. *Analytical Chemistry* 63, 1714–1719.

Xing, W., Li, F., Yan, Z.F., and Lu, G.Q. 2004. Synthesis and electrochemical properties of mesoporous nickel oxide. *Journal of Power Sources* 134, 324–330.

Xiong Zhang, X., and Yang, W. 2007. Electrophoretic deposition of a thick film of layered manganese oxide. *Chemistry Letters* 36, 1228.

Xu, B., Wu, F., Su, Y., Xao, G., Chen, S., Zhou, Z., and Yang, Y. 2008. Competitive effect of KOH activation on the electrochemical performances of carbon nanotubes fro EDLC: Balance between porosity and conductivity. *Electrochimica Acta* 53, 7730–7735.

Xu, M.-W., Bao, S.-J., and Li, H.-L. 2007. Synthesis and characterization of mesoporous nickel oxide for electrochemical capacitor. *Journal of Solid State Electrochemistry* 11, 372–377.

Yaghi, O.M., Li, H., and Groy, T.L. 1996. Construction of porous solids from hydrogen-bonded metal complexes of 1,3,5-benzenetricarboxylic acid. *Journal of the American Chemical Society* 118, 9096–9101.

Yamagishi, A., and Aramata, A. 1984. A clay-modified electrode with stereoselectivity. *Journal of the Chemical Society Chemical Communications* 7, 452–453.

Yamamoto, O. 2000. Solid oxide fuel cells: Fundamental aspects and prospects. *Electrochimica Acta* 45, 2423–2435.

Yamamoto, T., Fang, Q., and Morikita, T. 2003. New soluble poly(aryleneethynylene)s consisting of electron-accepting benzothiadiazole units and electron-donating dialkoxybenzene units. Synthesis, molecular assembly, orientation on substrates, and electrochemical and optical properties. *Macromolecules* 36, 4262–4267.

Yamanaka, I., Hasegawa, S., and Otsuka, K. 2002. Partial oxidation of light alkanes by reductive activated oxygen over the (Pd-black + VO (acac) (2) / VGCF) cathode of H-2-O-2 cell system at 298 K. *Applied Catalysis A: General*. 226, 305–315.

Yamawaki, H., Yoshida, M., Kakadate, Y., Usuba, S., Yokoi, H., Fujiwara, S., Aoki, K., Ruoff, R., Malhorta, R., and Lorents, D.C. 1993. Infrared study of vibrational property and polymerization of fullerene C_{60} and C_{70} under pressure. *Journal of Physical Chemistry* 97, 11161–11163.

Yamazoe, N., and Miura, N. 1996. Dynamically compacted rechargeable ceramic lithium batteries. *Solid State Ionics* 86–88, 897–902.

Yan, H., and Bein, T. 1992. Molecular recognition on acoustic wave devices: Sorption in chemically anchored zeolite monolayers. *Journal of Physical Chemistry* 96, 9387–9393.

Yan, H., Downes, J., Boden, P.J., and Harris, S.J. 1996. A model for nanolaminated growth patterns in Zn and Zn-Co electrodeposits. *Journal of the Electrochemical Society* 143, 1577–1583.

Yang, Q., Xu, W., Tomita, A., and Kyotani, T. 2005. The template synthesis of double coaxial carbon nanotubes with nitrogen-doped and boron-doped multiwalls. *Journal of the American Chemical Society* 127, 8956–8957.

Yang, S., Song, Y., Zavalij, P.Y., and Whittingham, M.S. 2002. Reactivity, stability and electrochemical behavior of lithium iron phosphates. *Electrochemistry Communications* 4, 239–244.

Yarger, M.S., Steinmiller, E.M.P., and Choi, K.-S. 2008. Electrochemical synthesis of Zn-Al layered double hydroxide (LDH) films. *Inorganic Chemistry* 47, 5859–5865.

Ye, S.H., Lv, J.Y., Gao, X.P., Wu, F., and Song, D.Y. 2004. Synthesis and electrochemical properties of $LiMn_2O_4$ spinel phase with nanostructure. *Electrochimica Acta* 49, 1623–1628.

Ye, S.H., Wang, X.-S., Zhao, H., and Xiong, R.-G. 2005. High stable olefin-Cu(I) coordination oligomers and polymers. *Chemical Society Reviews* 34, 208–225.

Yoshimura, M., and Gallage, R. 2008. Direct patterning of nanostructured ceramics from solution-differences from conventional printing and lithographic methods. *Journal of Solid State Electrochemistry*. 12, 775–782.

Yoshimura, S., and Chang, R.P.H., Eds. 1998. *Supercarbon. Synthesis, Properties and Applications*. Springer, Berlin.

Yu, H.C., and Fung, K.Z. 2003. $La_{1−x}Sr_xCuO_{2.5−δ}$ as new cathode materials for intermediate temperature solid oxide fuel cells. *Materials Research Bulletin* 38, 231–239.

Yu, J., Chen, Y., Yang, H., and Huang, Q. 1999. The influences of organic additives on zinc electrocrystallization from KCl solutions. *Journal of the Electrochemical Society* 146, 1789.

Yu, J.-J., Lu, S., Li, J.-W., Zhao, F.-Q., and Zeng, B.-Z. 2007. Characterization of gold nano-particles electrochemically deposited on amine-functionalized mesoporous silica films and electrocatalytic oxidation of glucose. *Journal of Solid State Electrochemistry* 11, 1211–1219.

Yu, X., and Licht, S. 2008. Recent advances in synthesis and analysis of Fe(VI) cathodes: Solution phase and solid-state Fe(VI) syntheses, reversible thin-film Fe(VI) synthesis, coating-stabilized Fe(VI) synthesis, and Fe(VI) analytical methodologies. *Journal of Solid State Electrochemistry* 12, 1523–1540.

Yuan, C.-Z., Dou, H., Gao, B., Su, L.-H., and Zhang, Z.-G. 2008. High-voltage aqueous symmetric electrochemical capacitor based on $Ru_{0.7}Sn_{0.3}O_2·nH_2O$ electrodes in 1 M KOH. *Journal of Solid State Electrochemistry* 12, 1645–1652.

Yuan, Z.-Y., and Su, B.-L. 2004. An inherent macroperiodic assembly or an artificial beauty? *Studies in Surface Science and Catalysis* 154B, 1525–1531.

Zen, J.-M., and Chen, P.-J. 1997. A selective voltammetric method for uric acid and dopamine detection using clay-modified electrodes. *Analytical Chemistry* 69, 5087–5093.

Zhang, K., Gekhtmann, D., Dresselhaus, M., and Ying, J. 1999. Processing and characterization of single-crystalline ultrafine bismuth nanowires. *Chemistry of Materials* 11, 1659–1665.

Zhang, L., and Lian, J. 2008. The electrochemical polymerization of *o*-phenylenediamine on l-tyrosine functionalized glassy carbon electrode and its application. *Journal of Solid State Electrochemistry* 12, 757–763.

Zhang, M.Z., Wang, M., Zhang, Z., Zhu, J.M., Peng, R.W., and Wang, N.M. 2004. Periodic structures of randomly distributed Cu/Cu_2O nanograins and periodic variations of cell voltage in copper electrodeposition. *Electrochimica Acta* 49, 2379–2383.

Zhang, Y., Chen, F., Shan, W., Zhuang, J., Dong, A., Cai, W., and Tang, Y. 2003. Fabrication of ultrathin nanozeolite film modified electrodes and their electrochemical behavior. *Microporous and Mesoporous Materials* 65, 277–285.

Zhao, K., Song, H., Zhuang, S., Dai, L., He, P., and Fang, Y. 2007. Determination of nitrite with the electrocatalytic property to the oxidation of nitrite on thionine modified aligned carbon nanotubes. *Electrochemistry Communications* 9, 65–70.

Zhao, X.S. 2006. Novel porous materials for emerging applications. *Journal of Materials Chemistry* 16, 623–625.

Zhao, Y., Zhang, X., Zhai, J., He, J., Jiang, L., Liu, Z., Nishimoto, S., Murakami, T., Fujishima, A., and Zhu, D. 2008. Enhanced photocatalytic activity of hierarchically micro-/nano-porous TiO_2 films. *Applied Catalysis B: Environmental* 1–2, 24–29.

Zhao, Y.-D., Zhang, W.-D., Luo, Q.-M., and Li, S.F.Y. 2003. The oxidation and reduction of nitrite at carbon nanotube powder microelectrodes. *Microchemical Journal* 75, 189–198.

Zheng, J.P., Jow, T.R. 1995. A new charge storage mechanism for electrochemical capacitors. *Journal of the Electrochemical Society* 142, L6–L8.

Zhong, X., Chen, J., Liu, B., Xu, Y., and Kuang, Y. 2007. Neutral red as electron transfer mediator: Enhance electrocatalytic activity of platinum catalyst for methanol electro-oxidation. *Journal of Solid State Electrochemistry* 11, 463–468.

Zhuiykov, S., Ed. 2007. *Electrochemistry of Zirconia Gas Sensors*. CRC Press, Boca Raton, FL.

Zicovich-Wilson, D.M., Corma, A., and Viruela, P. 1997. Electronic confinement of molecules in microscopic pores. A new concept which contributes to the explanation of the catalytic activity of zeolites. *Journal of Physical Chemistry* 98, 10863–10870.

Zuo, X., Xu, C., and Xin, H. 1997. Simulation of voltammogram on rough electrode. *Electrochimica Acta* 42, 2555–2558.

Index

COLOR FIGURE 4.11 Image of Maya wall paintings in the Substructure I of Calakmul (Campeche, México), Early Classical Maya period. Photograph courtesy of María Luisa Vázquez de Agredos Pascual. (From Doménech et al., 2007b. *Anal. Chem.* 79, 2812–2821, with permission.)

$$\{Cat^{red}\} + S^{ox} \longrightarrow \{Cat^{ox}\} + S^{red} + nM^+$$

$$\{Cat^{ox}\} + e^- \longrightarrow \{Cat^{red} \cdots nM^+\}$$
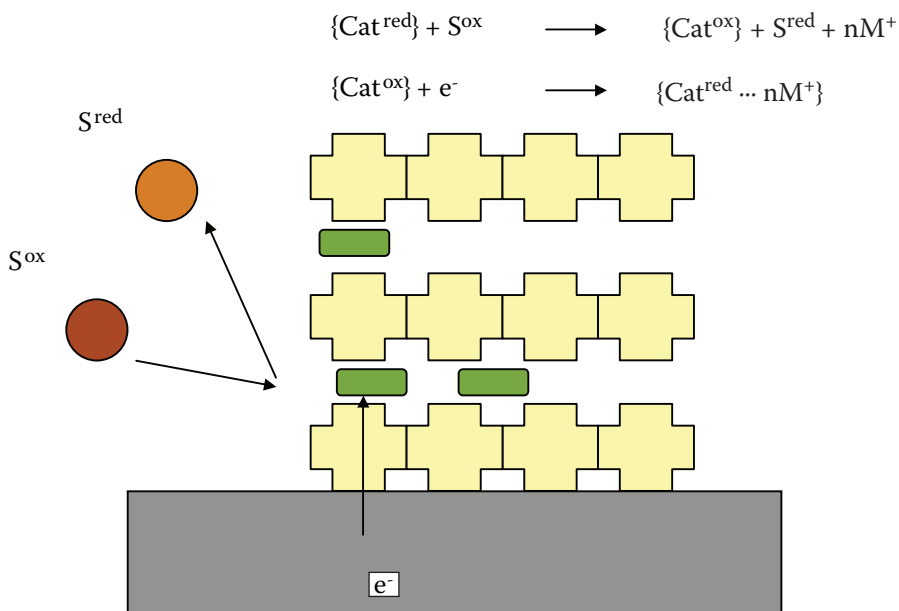
COLOR FIGURE 3.4 Diagram for possible electrocatalytic processes involving immobilized catalyst species ($E_S^{o\prime} > E_{cat}^{o\prime}$).
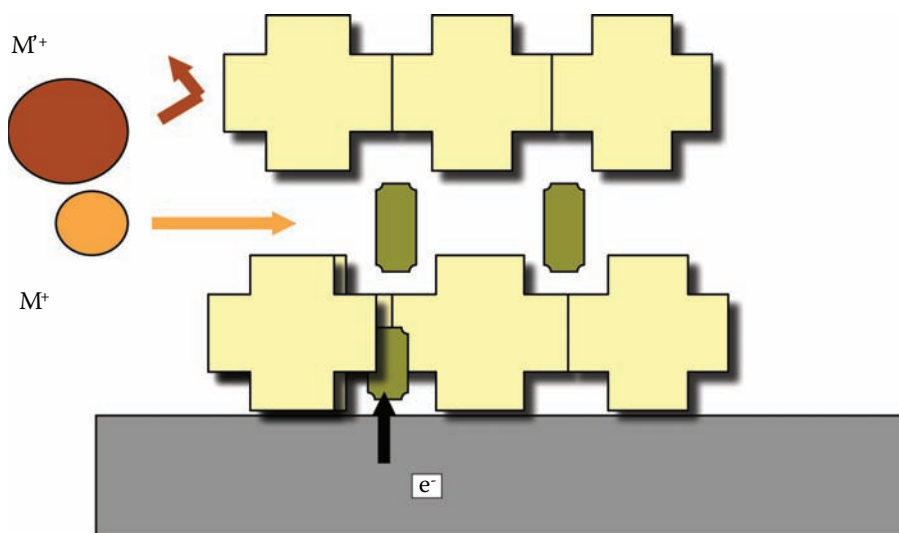
COLOR FIGURE 4.8 Schematics for the electrochemical reduction of a species immobilized into the voids of a porous aluminosilicate involving the ingress of size-allowed electrolyte cations (M^+). Size excluded electrolyte cations cannot contribute to intrazeolite redox conductivity.
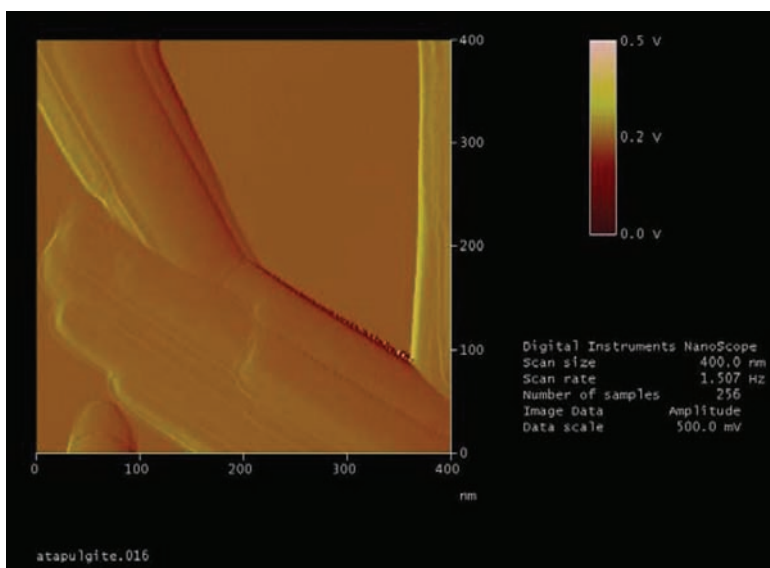
(a)
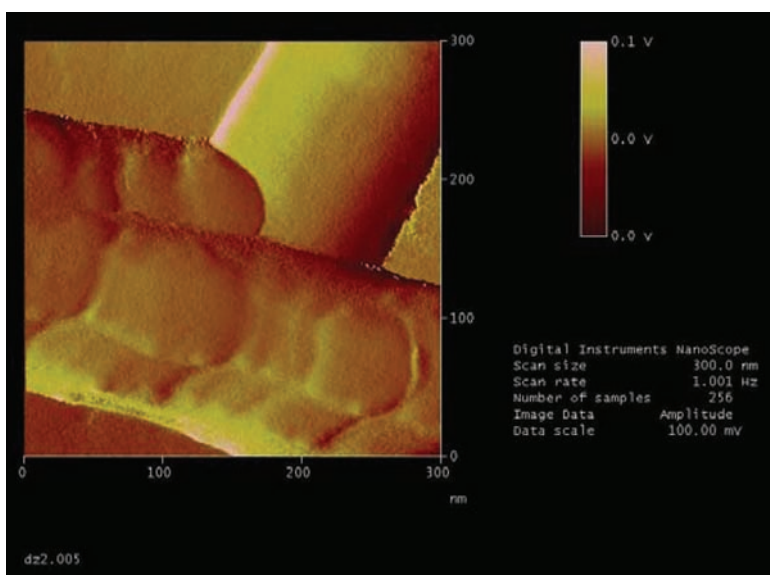
(b)

COLOR FIGURE 4.15 AFM images for (a) pristine palygorskite crystals from Sacalum and (b) MB sample from Dzibilnocac (Yucatán, Maya Late Classical period). (From Doménech et al., 2006c. *J Phys. Chem. B* 110, 6027–6039, with permission.)
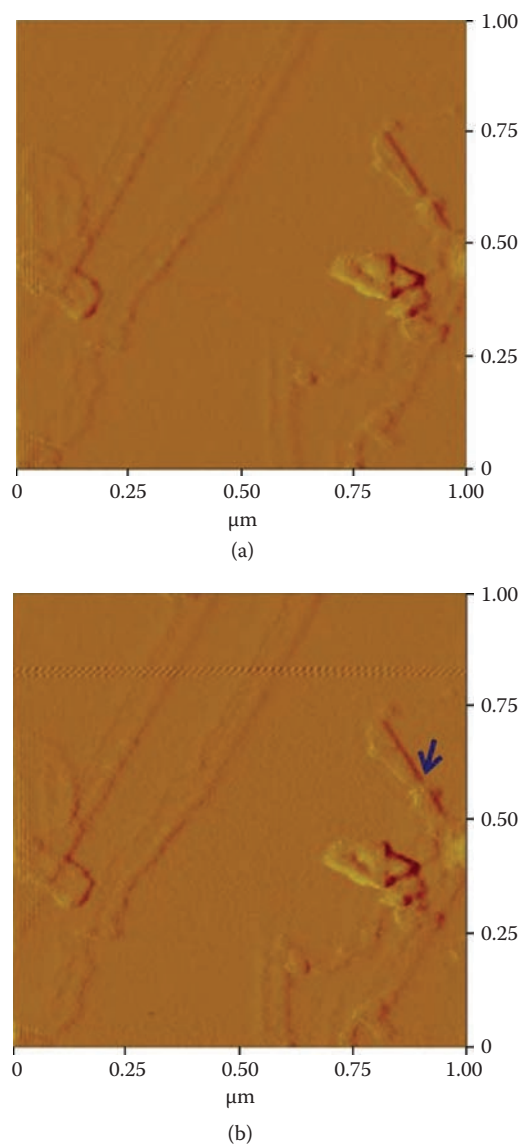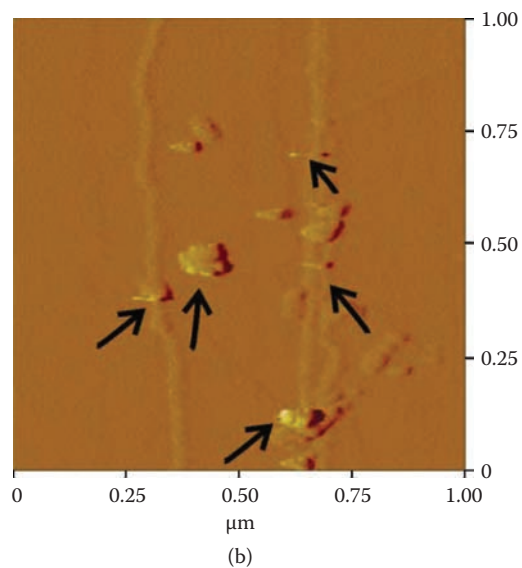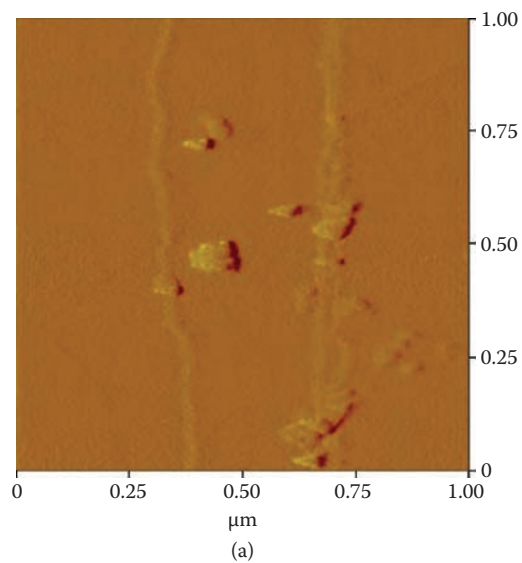
COLOR FIGURE 5.8 AFM images recorded on a Cu-MOF modified electrode in contact with 0.50 M acetate buffer (pH 4.85): (a) pristine sample; (b) after application of a potential step at −250 mV for 5 min. (Adapted from Doménech et al. 2007d. *J. Phys. Chem. C* 111, 13701–13711, with permission.)
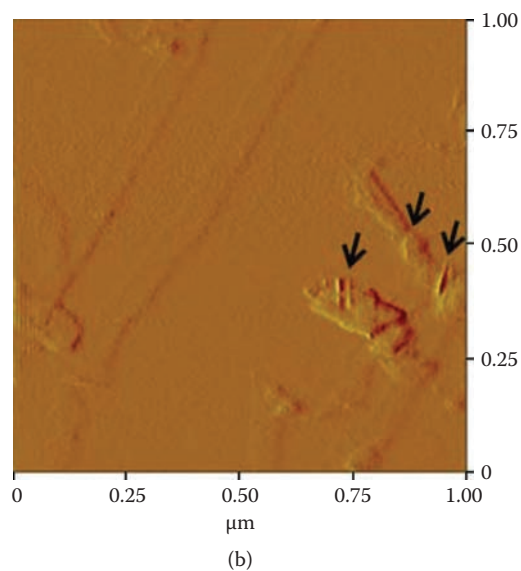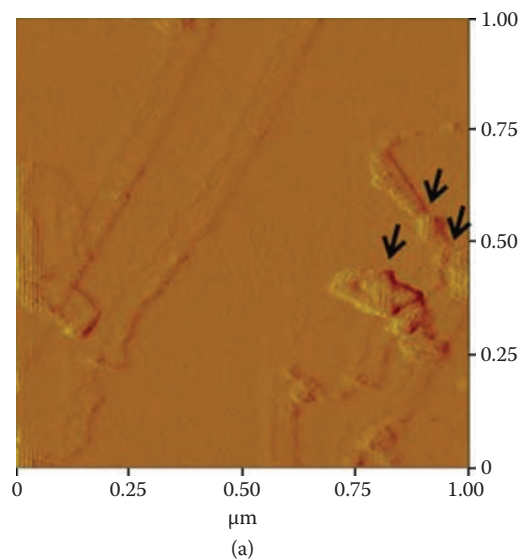
COLOR FIGURE 5.10 AFM images recorded on a Cu-MOF modified electrode in contact with 0.50 M acetate buffer (pH 4.85): (a) after application of a potential step at −0.50 V for 5 min; (b) id. at −0.85 V. (Adapted from Doménech et al. 2007d. *J. Phys. Chem. C* 111, 13701–13711, with permission.)

COLOR FIGURE 5.11 AFM images of Zn-MOF-modified electrode immersed into acetate buffer: (a) pristine sample; (b) after application of a potential step at −935 mV for 5 min.
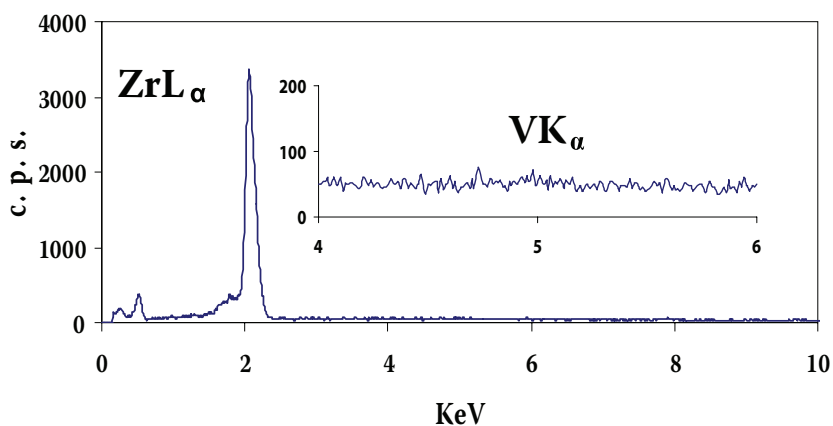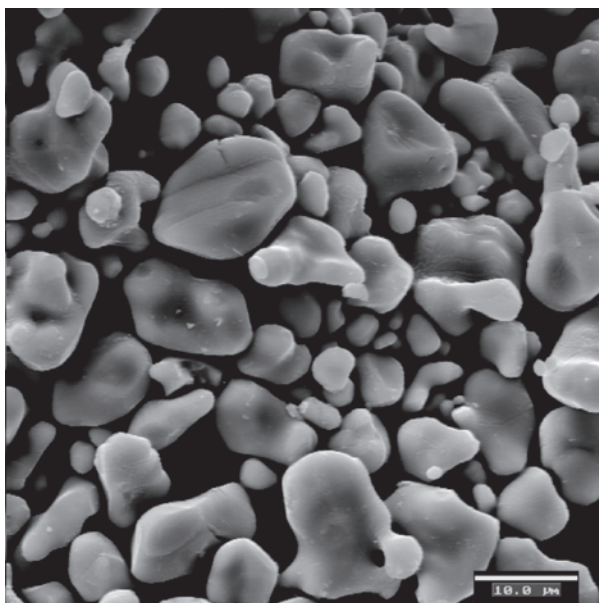
COLOR FIGURE 6.10 Field emission scanning electron micrograph and energy-dispersive x-ray spectroscopy of monoclinic $V_{0.075}Zr_{0.925}O_2$ solid solution prepared after heating gels at 1300°C for 3 h. (From Doménech and Alarcón, 2007, *Anal. Chem.* 79, 6742–6751, with permission.)
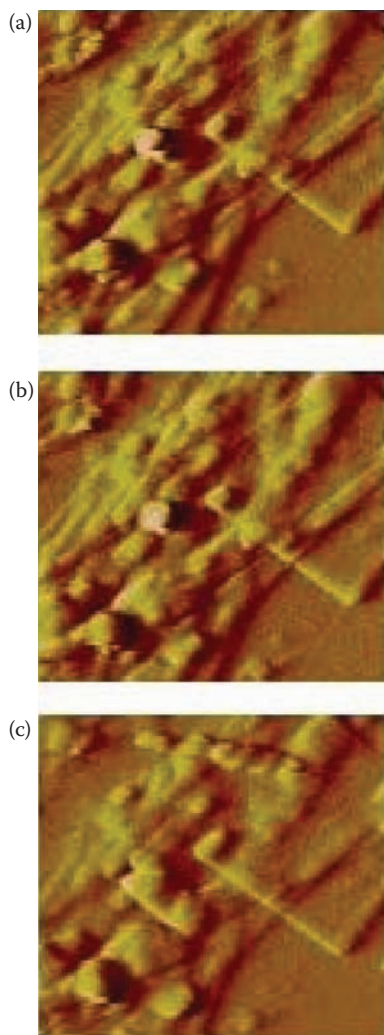
COLOR FIGURE 8.11 AFM images (750–750 nm in size) recorded for a ZnAlNO$_3^-$-LDH-PANI deposit on graphite plate immersed into 0.50 M phosphate buffer at: (a) open-circuit conditions, (b) upon scanning the potential to +1.20 V at 10 mV/sec, and (c) upon scanning again the potential from +1.20 to −1.00 V at 10 mV/sec. (From Doménech et al. 2008. *J. Electroanal. Chem.* 624, 275–286, with permission.)

Electrochemistry of Porous Materials

Porous materials continue to attract considerable attention because of their wide variety of scientific and technological applications, such as catalysis, shape- and size-selective absorption and adsorption, gas storage, and electrode materials. Both research and applications of porous materials—via electroanalysis, electrosynthesis, sensing, fuel cells, capacitors, electro-optical devices, and other means—heavily rely on electrochemistry.

Electrochemistry of Porous Materials focuses on generalized theoretical modeling and describes redox processes for different porous materials, assessing their electrochemical applications. Considering the large variety of materials that can be classified as porous, the text focuses on nanostructured micro- and mesoporous materials. Using this approach, the book offers a more focused and practical analysis of key porous materials that are considered relatively homogeneous from an electrochemical point of view. These include:

- Porous silicates and aluminosilicates
- Porous metal oxides and related compounds
- Porous polyoxometalates
- Metal-organic frameworks
- Porous carbons, nanotubes, and fullerenes
- Porous polymers and certain hybrid materials

With its detailed presentation of advances in electrochemistry of nanostructured materials, this text specifically addresses the foundation and applications of the electrochemistry of microporous materials. It incorporates the latest breakthroughs in applied fields (development of fuel cells, supercapacitors, etc.) and fundamental research (in areas including fractal scaling, photoelectrocatalysis, magnetoelectrochemistry, etc.). Designed to make the topic accessible and understandable for researchers and graduate students working in the field of material chemistry, this volume approximates porous materials chemistry to electrochemists. Selective and streamlined, it culls a wide range of relevant and practically useful material from the extensive literature on the subject, making it an invaluable reference for readers of all levels of understanding.